

MASTER

ANL - 7010

REACTOR PHYSICS DIVISION
ANNUAL REPORT

July 1, 1963 to June 30, 1964

January 1965

Argonne National Laboratory
Argonne, Illinois

DISCLAIMER

This report was prepared as an account of work sponsored by an agency of the United States Government. Neither the United States Government nor any agency Thereof, nor any of their employees, makes any warranty, express or implied, or assumes any legal liability or responsibility for the accuracy, completeness, or usefulness of any information, apparatus, product, or process disclosed, or represents that its use would not infringe privately owned rights. Reference herein to any specific commercial product, process, or service by trade name, trademark, manufacturer, or otherwise does not necessarily constitute or imply its endorsement, recommendation, or favoring by the United States Government or any agency thereof. The views and opinions of authors expressed herein do not necessarily state or reflect those of the United States Government or any agency thereof.

DISCLAIMER

Portions of this document may be illegible in electronic image products. Images are produced from the best available original document.

LEGAL NOTICE

This report was prepared as an account of Government sponsored work. Neither the United States, nor the Commission, nor any person acting on behalf of the Commission:

A. Makes any warranty or representation, expressed or implied, with respect to the accuracy, completeness, or usefulness of the information contained in this report, or that the use of any information, apparatus, method, or process disclosed in this report may not infringe privately owned rights; or

B. Assumes any liabilities with respect to the use of, or for damages resulting from the use of any information, apparatus, method, or process disclosed in this report.

As used in the above, "person acting on behalf of the Commission" includes any employee or contractor of the Commission, or employee of such contractor, to the extent that such employee or contractor of the Commission, or employee of such contractor prepares, disseminates, or provides access to, any information pursuant to his employment or contract with the Commission, or his employment with such contractor.

This report has been reproduced directly from the best available copy.

Printed in USA. Price \$7.00. Available from the Clearinghouse for Federal Scientific and Technical Information, National Bureau of Standards, U. S. Department of Commerce, Springfield, Virginia 22151.

ANL-7010
Reactor Technology
(TID-4500, 38th Ed.)
AEC Research and
Development Report.

Argonne National Laboratory
9700 South Cass Avenue
Argonne, Illinois 60440

REACTOR PHYSICS DIVISION
ANNUAL REPORT

July 1, 1963 to June 30, 1964

Robert Avery, Division Director

January, 1965

Operated by The University of Chicago
under
Contract W-31-109-eng-38
with the
U. S. Atomic Energy Commission

THIS PAGE
WAS INTENTIONALLY
LEFT BLANK

Foreword

This is the first annual report published by the Reactor Physics Division. It is a summary of work accomplished during the year since the inception in July, 1963 of the Division in the split of the Reactor Engineering Division. Since this is the first publication, in some instances it was necessary, for the sake of clarity, to describe work done at an earlier date than the reporting period, although in all cases the work continued to be in progress during the reporting period.

It has been decided to orient this report in the direction of describing the separate technical accomplishments achieved by the members of the Division, as opposed to stressing the programmatic aspects of the work. A large portion of the work included in this publication has been reported more exhaustively in journal articles or in other reports. In order to aid those who might wish to pursue any article to greater depth, a list of pertinent references is included with each article. In addition, a complete list of publications by Reactor Physics staff from April 1963 through March 1964 is published at the end of this report.

THIS PAGE
WAS INTENTIONALLY
LEFT BLANK

Table of Contents

SECTION I

FISSION PROPERTIES AND CROSS SECTION DATA

I-1.	Fast Neutron Scattering.....	3
	A. B. SMITH, W. G. VONACH, S. G. BUCCINO, J. A. M. DEVILLIERS, ¹ D. REITMANN ¹ and C. ENGELBRECHT ¹	
I-2.	Fast Neutron Total Cross Sections.....	8
	W. G. VONACH, J. F. WHALEN and A. B. SMITH	
I-3.	Fast Neutron Capture.....	9
	S. A. COX, J. W. MEADOWS and J. F. WHALEN	
I-4.	Gamma Rays From Inelastic Neutron Scattering.....	10
	J. F. BARRY ² and D. STUPEGIA ³	
I-5.	Energy Dependence of Prompt $\bar{\nu}$ for Neutron-Induced Fission of U-235.....	11
	J. W. MEADOWS and J. F. WHALEN	
I-6.	Fission Neutron Yield Experiment.....	13
	A. DEVOLPI and K. G. PORGES	
I-7.	Mass and Kinetic Energy Distributions in MeV Neutron Induced Fission.....	14
	J. W. MEADOWS and J. F. WHALEN	
I-8.	Nuclear Reaction Theory and Optical Model Studies.....	16
	P. A. MOLDAUER	
I-9.	Neutron Yields From High Energy Proton Bombardment.....	18
	J. W. MEADOWS, J. F. WHALEN, A. B. SMITH and G. R. RINGO ⁴	
I-10.	Stripping Reactions.....	19
	S. G. BUCCINO, A. B. SMITH, D. S. GEMMELL, ⁴ L. L. LEE, JR. ⁴ and J. P. SCHIFFER ⁴	

SECTION II

THERMAL REACTORS

II-1.	Remarks on the Definition of k_{eff} for Off-Critical Reactors—I.....	23
	D. H. SHAFTMAN	
II-2.	Remarks on the Definition of k_{eff} for Off-Critical Reactors—II.....	25
	D. H. SHAFTMAN	
II-3.	Use of Depleted Uranium in Thermal Reactors with Slightly Enriched Fuel to Achieve High Neutron Economy and High Burnup.....	27
	H. P. ISKENDERIAN	
II-4.	Dynamic Analysis of Coolant Circulation in Boiling Nuclear Reactors.....	28
	C. K. SANATHANAN, J. C. CARTER and F. MIRALDI ⁵	
II-5.	Further Developments in Dynamic Analysis of Coolant Circulation in Boiling Water Nuclear Reactors.....	29
	C. K. SANATHANAN	

¹ South African Atomic Energy Board, Republic of South Africa

² On leave from Atomic Weapons Research Establishment, Aldermaston, England

³ Chemical Engineering Division, Argonne National Laboratory

⁴ Physics Division, Argonne National Laboratory

⁵ Case Institute of Technology, Cleveland, Ohio

II-6.	Space Dependent Kinetics of Boiling Reactors.....	31
	C. K. SANATHANAN	
II-7.	High Conversion Critical Experiment.....	33
	A. R. BOYNTON, Q. L. BAIRD, J. M. CHRISTENSON, K. E. PLUMLEE, W. C. REDMAN, W. R. ROBINSON and G. S. STANFORD	
II-8.	Hi-C Uniform Lattice Calculations.....	44
	E. M. PENNINGTON	
II-9.	Evaluation of Flux Trap Experiments in D ₂ O-Moderated Thorium-Uranium Cores..	46
	K. E. PLUMLEE	
II-10.	PuO ₂ -UO ₂ Fueled Thermal Critical Experiments.....	52
	C. E. TILL	
II-11.	Argonne Advanced Research Reactor—Physics Advantages of Intermediate Cores for Research Reactors.....	54
	C. N. KELBER	
II-12.	Argonne Advanced Research Reactor—Optimization of the AARR Core and Reflector Design for Flux Enhancement.....	56
	C. N. KELBER	
II-13.	Argonne Advanced Research Reactor—Physics Calculations.....	57
	B. N. KRISTIANSON and C. N. KELBER	
II-14.	Argonne Advanced Research Reactor—Shielding Analysis of Plant Design.....	63
	H. F. REED	
II-15.	Argonne Advanced Research Reactor—Critical Experiment Planning and Hazards Analysis.....	63
	C. N. KELBER	
II-16.	Preparation of Critical Experiment for Argonne Advanced Research Reactor (AARR) Design.....	66
	K. E. PLUMLEE, E. GROH and G. S. STANFORD	
II-17.	Argonne Advanced Research Reactor—Sample Optimization.....	68
	C. N. KELBER and H. F. REED	
II-18.	Argonne Advanced Research Reactor—Preliminary Safety Analysis.....	69
	C. N. KELBER	
II-19.	EBWR Plutonium Recycle Experiment.....	69
	B. J. TOPPEL	
II-20.	EBWR Plutonium Recycle Safety Analysis.....	73
	P. H. KIER	
II-21.	Experimental Boiling Water Reactor (EBWR) Physics Review.....	74
	H. P. ISKENDERIAN	

SECTION III

FAST REACTORS

III-1.	Predicted Doppler Effects for Some Typical Large Ceramic Fueled Fast Reactors..	79
	H. H. HUMMEL and A. L. RAGO ⁶	
III-2.	Interference Interaction in Doppler Theory for Fast Reactors.....	81
	R. N. HWANG	
III-3.	Doppler Effect Experiments.....	82
	G. FISCHER, J. FOLKROD, ⁷ E. GROH and D. MENELEY	
III-4.	Sodium Void Effect.....	86
	H. H. HUMMEL, L. KVITEK, K. E. PHILLIPS and A. L. RAGO ⁶	

⁶ Applied Mathematics Division, Argonne National Laboratory

⁷ Reactor Engineering Division, Argonne National Laboratory

III-5.	Comparison of SNG, DSN, DTK, and REX Calculations.....	86
	J. WHITE	
III-6.	Studies with the ELMOE Program for Fast Critical Analyses.....	88
	D. MENEGHETTI	
III-7.	Publication of Lecture Notes on Fast Reactor Physics Analysis.....	90
	D. MENEGHETTI	
III-8.	Investigations of a 600-Liter Uranium Carbide Core (ZPR-VI Assembly No. 2)....	91
	G. K. RUSCH, E. R. BÖHME, ⁸ L. R. DATES, S. GRIFONI, ⁹ W. Y. KATO, G. W. MAIN, H. H. MEISTER, ⁸ M. NOZAWA, ¹⁰ and R. L. STOVER	
III-9.	Recent Calculations for Representative ZPR-III Fast Assemblies.....	110
	D. MENEGHETTI and J. R. WHITE	
III-10.	Comparison of ZPR-III Shape Factor Calculations By Transport and Diffusion Methods.....	113
	D. MENEGHETTI	
III-11.	Feasibility Study of Zone Loading for Fast Critical Facilities.....	114
	F. H. HELM	
III-12.	Physics Measurements in Tungsten-Based Aluminum Reflected Fast Reactors....	116
	R. C. DOERNER, K. K. ALMENAS, R. A. KARAM, W. Y. KATO, W. G. KNAPP and W. B. LOEWENSTEIN	
III-13.	Parametric Survey of Homogeneous Unmoderated Rocket Reactors.....	123
	W. B. LOEWENSTEIN and J. WHITE	
III-14.	Super-Prompt Critical Excursions in Unmoderated Cores with Moderating Reflectors.....	127
	W. B. LOEWENSTEIN and J. WHITE	
III-15.	Natural Tungsten Cross-Sections for Fast and Intermediate Neutron Spectra.....	129
	R. KAISER and W. B. LOEWENSTEIN	
III-16.	Verification of Tungsten Cross Sections.....	131
	K. ALMENAS	
III-17.	The Neutronics of Reactor Control with Reflector Materials.....	134
	K. ALMENAS	
III-18.	Investigation of a Rocket Fuel Test Reactor.....	138
	J. T. MADELL and D. R. MACFARLANE	
III-19.	EBR-II Physics.....	141
	W. B. LOEWENSTEIN	
III-20.	Proposed Physics Measurements in FARET.....	147
	P. J. PERSIANI	
III-21.	FARET Fuel Performance Program.....	149
	T. R. BUMP, ¹² J. HANDWERK, ¹¹ W. J. KANN, ¹² E. L. MARTINEC, ¹² P. J. PERSIANI, G. F. POPPER, ¹² S. B. SKLADZIEN ¹² and A. B. SMAARDYK ¹²	
III-22.	Preliminary Considerations on the Safety Analysis of FARET.....	152
	P. J. PERSIANI, A. WATANABE, U. WOLFF, ¹³ S. GRIFONI, ⁹ and B. WARMAN	
III-23.	Nuclear Performance of Large Fast Power Reactors.....	155
	W. B. LOEWENSTEIN and D. OKRENT ¹⁴	
III-24.	Physics Studies of Some Molten-Salt-Fueled Fast Reactor Systems.....	156
	D. BUTLER and D. MENEGHETTI	
III-25.	Fast Reactor Reactivity Coefficients; The Effect of Excess Reactivity.....	159
	W. B. LOEWENSTEIN	

⁸ Kernreaktor, Karlsruhe, Germany

⁹ Comitato Nazionale Per L'Energia Nucleare, Italy

¹⁰ Japan Atomic Energy Research Institute, Japan

¹¹ Metallurgy Division, Argonne National Laboratory

¹² Reactor Engineering Division, Argonne National Laboratory

¹³ Allgemeine Electricitats-Gesellschaft, Germany

¹⁴ Laboratory Director's Office, Argonne National Laboratory

III-26.	Paper withdrawn prior to publication.....	160
III-27.	The Control of Fast Reactors; Current Methods and Future Prospects..... W. B. LOEWENSTEIN	161
III-28.	Sodium Void Coefficient for "Heterogeneous" Fast Reactors..... W. B. LOEWENSTEIN	161
III-29.	Fuel Cycle Studies..... G. J. FISCHER and L. E. LINK ¹⁵	162
III-30.	Theoretical Investigation of a Major Excursion Caused by Fuel Element Failure... V. Z. JANKUS	164
III-31.	Coolant Pressures During Transients..... R. O. BRITAN	165
III-32.	Equation of State for Mixture of Materials in Reactor Excursion..... V. Z. JANKUS	169
III-33.	Behavior of Irradiated Metallic Fuel Elements Exposed to Nuclear Excursions in TREAT..... J. H. MONAWECK, ¹⁶ C. E. DICKERMAN and E. S. SOWA ¹⁶	171
III-34.	TREAT Study of the Penetration of Molten Uranium and Uranium-5 w/o Fission Alloy Through Type 304 Stainless Steel..... C. M. WALTER ¹⁷ and C. E. DICKERMAN	173
III-35.	Photographic Experiments on Meltdown of Irradiated Metallic Fuel Pins..... C. E. DICKERMAN and L. E. ROBINSON	173
III-36.	Calculations on Coherence of Failure in Hypothetical Meltdown Accidents in an EBR-II-Like Reactor..... D. V. GOPINATH, ¹⁸ C. E. DICKERMAN and L. BRYANT ¹⁹	174
III-37.	Behavior of Uranium Sulfide Fast Reactor Type Fuel Specimens Under Transient Heating in TREAT..... L. E. ROBINSON, C. E. DICKERMAN and C. AUGUST	175
III-38.	In-Pile Experiments on Meltdown of EBR-II Mark I Fuel Elements in Stagnant Sodium..... C. E. DICKERMAN, E. S. SOWA, ¹⁶ J. H. MONAWECK ¹⁶ and A. BARSELL ¹⁶	176

SECTION IV

EXPERIMENTAL TECHNIQUES AND FACILITIES

IV-1.	Orthonormal Expansion of Neutron Spectra with Activation Measurements..... R. GOLD	181
IV-2.	An Iterative Solution of the Matrix Representation of Detection Systems..... R. GOLD	185
IV-3.	A Statistical Method for the Measurement of β_{eff} R. A. KARAM	188
IV-4.	Analysis of Fast Neutron-Spectrum Measurements by Magnetic Analysis of Charged Particles Produced by Neutron Interactions..... R. A. KARAM	190
IV-5.	Comparison of Linear and Square-Law Detectors for Noise Measurements..... C. E. COHN	192
IV-6.	Note on the Simulation of Higher-Order Linear Systems with Single Operational Amplifiers..... C. E. COHN	194

¹⁵ Laboratory Director's Office, Argonne National Laboratory¹⁶ Reactor Engineering Division, Argonne National Laboratory¹⁷ Metallurgy Division, Argonne National Laboratory¹⁸ Atomic Energy Establishment, Trombay, India¹⁹ Applied Mathematics Division, Argonne National Laboratory

IV-7.	Expediting Danger-Coefficient Measurements by Measuring Two Samples At Once . . .	195
	C. E. COHN	
IV-8.	Argonne Fast Critical Facilities	196
	W. Y. KATO, L. R. DATES, R. L. STOVER, W. G. KNAPP and G. K. RUSCH	
IV-9.	Automatic Foil Activity Counting Facility and Data-Reduction Program	199
	J. M. CHRISTENSON, K. E. PLUMLEE, W. R. ROBINSON and G. S. STANFORD	
IV-10.	A Calibrated Gamma Counting Facility	202
	R. J. ARMANI	
IV-11.	Attenuation of Epicadmium Neutrons by Cadmium Foil Covers	203
	G. S. STANFORD	
IV-12.	The Activation of Gold Foils and Spheres for Non-Isotropic Neutron Incidence . . .	206
	F. H. HELM	
IV-13.	A Study of the Applicability of Simple Reactor Kinetics to the Interpretation of Reactor Noise Experiments	209
	C. E. COHN	
IV-14.	Errors in Noise Measurements Due to the Finite Amplitude Range of the Measuring Instrument	211
	C. E. COHN	
IV-15.	Improvements in Particle and Radiation Detection	213
	A. DEVOLPI and K. PORGES	
IV-16.	Automated Data Acquisition and Processing with an On-Line Computer	216
	J. F. WHALEN, J. W. MEADOWS, A. B. SMITH and W. F. MILLER ²⁰	
IV-17.	Development of Solid State Fission Counters	217
	G. W. MAIN	
IV-18.	Preparation of Source and Source Mount for Beta Counting on a 4π Proportional Counter	219
	D. M. SMITH	
IV-19.	4π Recoil Counter Neutron Spectrometers	221
	E. F. BENNETT	
IV-20.	In-Core Fast Neutron Spectroscopy	225
	E. F. BENNETT and J. HAUGSNES	
IV-21.	A Study of Rossi-Alpha Measurements in Critical Facilities	227
	F. H. HELM	
IV-22.	Radiochemical Measurement Techniques in ZPR-VI and-IX	228
	R. J. ARMANI	
IV-23.	Rejection of Gamma Background in Hornyak Fast Neutron Detectors	229
	K. PORGES, A. DEVOLPI and P. POLINSKI ²¹	
IV-24.	EBR-II Fuel Element Failure Detector	231
	K. G. PORGES	
IV-25.	Fuel Meltdown Monitoring in TREAT by Fast Neutron Detection	232
	A. DEVOLPI	

SECTION V

MISCELLANEOUS

V-1.	Some Problems in Reactor Theory	237
	B. I. SPINRAD	
V-2.	Effects of Resonance Interference	243
	C. N. KELBER	
V-3.	Resonance Parameter Analysis	246
	E. M. PENNINGTON	

²⁰ Applied Mathematics Division, Argonne National Laboratory²¹ Electronics Division, Argonne National Laboratory

V-4.	An Importance-Weighting Procedure for Averaging Group Parameters in Multi-group Diffusion Theory	246
	D. H. SHAFTMAN and H. GREENSPAN ²²	
V-5.	Neutron Attenuation Calculations and Intercomparison	251
	M. GROTENHUIS, ²³ C. N. KELBER, A. E. MCARTHY and A. D. ROSSIN ²⁴	
V-6.	Thermionic Energy Conversion with a Plasma Thermocouple	251
	H. K. RICHARDS	
V-7.	Flux Monitoring of Radiation Damage Experiments	254
	R. J. ARMANI and A. D. ROSSIN ²⁴	
V-8.	Comparison of Accelerators and Reactors for Steady Neutron Flux Production	255
	C. N. KELBER	
V-9.	Evaluation of a Rotating Power Generating System	256
	A. J. ULRICH, J. C. CARTER, R. O. BRITTAN and R. G. POST ²⁵	
V-10.	Investigation of a Direct Nucleonic Process in the Production of High Temperature Effluent	259
	M. B. RODIN and J. C. CARTER	
V-11.	Zero Gradient Synchrotron Vertical Beam Study	260
	H. MOSES, ²⁶ R. L. MARTIN, ²⁷ J. KASTNER ²⁶ and A. J. ULRICH	
V-12.	Evaluation of a Thermionic Diode for Space Power Using a Liquid Metal Electron Collector	261
	A. J. ULRICH	
V-13.	Numerical Integration by Iterative Procedures and by Rational Osculatory Interpolation	262
	H. C. THACHER, JR.	
V-14.	Evaluation of Functions by Shifted Chebyshev Polynomials	263
	H. C. THACHER, JR.	
V-15.	Generalized Recursive Interpolation	264
	P. M. LUKEHART	
V-16.	Kutta-Merson Solutions of Differential Equations	265
	P. M. LUKEHART	
V-17.	Nuclear Data Compilation Activities	266
	A. B. SMITH and W. G. VONACH	
V-18.	Reactor Physics Constants Center	266
	L. J. TEMPLIN	
V-19.	Resonance Integrals for Dilute Solution	266
	P. J. PERSIANI, A. E. MCARTHY and J. J. KAGANOVE ²²	
V-20.	A FORTRAN Code for Cylindrical Lattice Collision Probabilities (B692/RP)	268
	E. M. PENNINGTON	
V-21.	Foil Activation Programs, B512/RP	269
	E. M. PENNINGTON	
V-22.	Multigroup Constants Code MC ²	270
	D. M. O'SHEA	
V-23.	Ancillary Computing Programs	271
	L. C. KVITEK	
V-24.	Solution Techniques for Elasticity Problems in Cylindrical Coordinates	271
	C. K. YOUNGDAHL	
V-24a.	The Exact Elastic Stress Distribution in the Vicinity of a Hole in a Thick Plate Loaded in Uniaxial Tension	273

²² Applied Mathematics Division, Argonne National Laboratory

²³ Personnel Division, Argonne National Laboratory

²⁴ Metallurgy Division, Argonne National Laboratory

²⁵ University of Arizona, Tucson, Arizona

²⁶ Radiological Physics Division, Argonne National Laboratory

²⁷ Particle Accelerator Division, Argonne National Laboratory

V-24b. Thermoelastic Problem for Fuel Rod with Cladding	283
V-24c. Thermal Stresses in Reactor Fuel Plates	284
V-25. Gain Stabilization of Analog Amplifiers in the Nanosecond Regime.....	285
K. G. PORGES and J. B. BJORKLAND ²⁸	
V-26. A Simple, Compact Control Rod Drive Using a Stepping Motor.....	286
E. F. GROH and C. E. COHN	

SECTION VI

**PUBLICATIONS AND REPORTS
REACTOR PHYSICS DIVISION
(April 1, 1963—March 31, 1964)**

Open Literature.....	289
Reports	290

²⁸ Electronics Division, Argonne National Laboratory

Section I

Fission Properties and Cross Section Data

In close support of the reactor program, experimental and theoretical studies of neutron interactions with those nuclei found in the structural and fuel components of reactor systems are being carried out. A major portion of the effort is devoted to those processes which involve fast neutrons. Particular attention is given to the experimental studies of neutron scattering, neutron capture, and to the properties of the neutron-induced fission process. Of necessity, considerable effort is also devoted to the design, optimization, and increased efficiency of the requisite experimental systems. The theoretical interpretations deal principally with average neutron resonance properties and reaction mechanisms in medium and heavy nuclei.

I-1. Fast Neutron Scattering

A. B. SMITH, W. G. VONACH, S. G. BUCCINO, J. A. M. DEVILLIERS,* D. REITMANN* AND C. ENGELBRECHT*

OBJECTIVE AND METHOD

A systematic study of fast neutron elastic and inelastic scattering has been in progress. The measurements have extended over an appreciable portion of the periodic table with emphasis upon the structural, fertile, and fissile materials employed in fast reactors. Results obtained as of now have given a good picture of the scattering process in many regions of the periodic table and permit the rational consideration of the theoretical concepts underlying the scattering process.

Fast neutron scattering studies usually demand a neutron spectrometer with high resolution. One such device is the powerful time-of-flight system employed in this work. It consists of a pulsed Van de Graaff machine supplying an intense pulsed beam of charged particles, a magnetic bunching system, and timing and storage equipment including an on-line digital computer. Major aspects of the apparatus are shown in Fig. I-1-1. The system is kept at peak performance by constant modification and development. With this equipment, it is possible to achieve excellent scattered neutron resolution. As an example, Fig. I-1-2 shows a time spectrum resulting from the scattering from 1.0 MeV neutrons from W-184. Elastically and inelastically scattered components are clearly resolved. Similar measurements throughout the incident energy interval 0.3–1.5 MeV and at a number of scattering angles have yielded detailed microscopic cross sectional values for a wide range of nuclei. These results are fully corrected for experimental perturbations, such as multiple scattering, and are stored upon punched cards for direct use in reactor and in nuclear theory calculations.

RESULTS

Resumes of the experimental results have been presented in several review papers.^{1,2,3}

In addition to these reviews, detailed results are given in a number of published papers as follows.

Elastic and Inelastic Scattering of Fast Neutrons from Co, Cu, and Zn⁴

Cross sections and angular distributions were measured for the elastic and the inelastic scattering of

* South African Atomic Energy Board, Republic of South Africa.

neutrons from natural Co, Cu, and Zn in the energy range 300 keV to 1.5 MeV. The measured values are compared with the results of optical model calculations using spin assignments which are either known or consistent with shell model predictions. The effect of resonance width fluctuations is investigated.

Scattering of Fast Neutrons from Natural Zr and Nb⁵

Fast time-of-flight techniques were used to measure the differential cross sections for the elastic scattering of neutrons from natural Zr and Nb (see Fig. I-1-3). The measurements were made at ≈ 50 keV intervals throughout the incident neutron energy range 0.3 to 1.5 MeV. In addition, the cross sections for the excitation by inelastic neutron scattering of a 0.92 MeV level in Zr and 0.74, 0.81, 0.96, and 1.08 MeV levels in Nb were measured. The results of these measurements are compared with those obtained in other experiments and with optical model calculations. Tentative spin assignments for the low lying levels in Nb-93 are made on the basis of Hauser-Feshback calculations and shell model predictions.

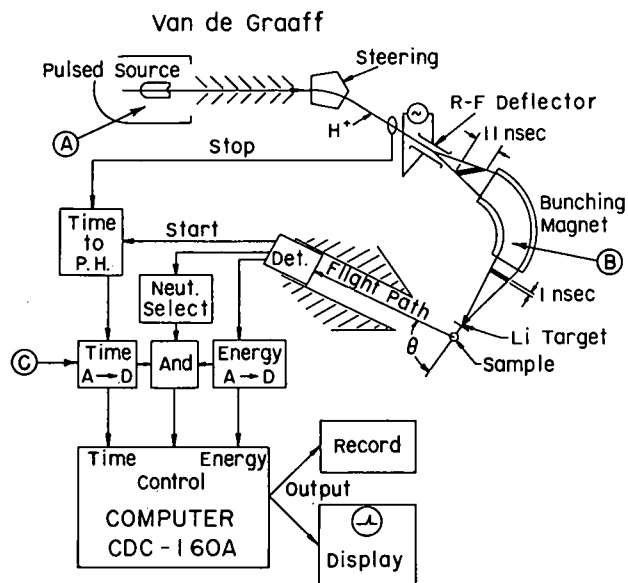


FIG. I-1-1. Schematic Diagram of the Fast Time-of-Flight Apparatus. (A. The Pulsed Van de Graaff Accelerator; B. The Magnetic Bunching System; C. The Timing Circuitry and Digital Computer.)

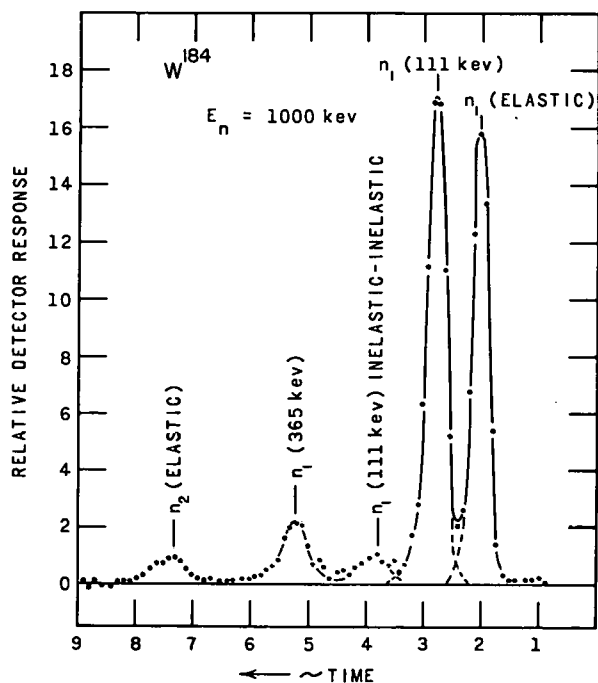


FIG. I-1-2. Time Spectrum Obtained by Scattering 1.0 MeV Neutrons from W-184. The Elastic Group and the Inelastic Components Leading to the First Excited State (110 keV, 2+) and the Second Excited State (365 keV, 4+) are Evident.

Fast Neutron Scattering from Ta-181⁽⁶⁾

The spectrum of neutrons scattered from Ta-181 was measured at incident neutron energies ranging from 0.3 to 1.5 MeV. Time-of-flight techniques were employed to resolve the elastically and the inelastically scattered components. The angular distribution of the elastically scattered neutrons was measured at $\lesssim 50$ -keV intervals with an incident spread of neutron energy of ~ 20 keV. Inelastically scattered neutron groups resulting in the excitation of residual nuclear levels at 140 ± 10 , 300 ± 10 , 620 ± 20 , 725 ± 25 , 900 ± 30 keV were observed. The measurements indicated that the levels at 725 and 980 keV were composed of two or more components. In addition, inelastic scattering to a 480 ± 20 -keV level was tentatively observed. The magnitudes of the differential elastic cross sections and of the inelastic excitation functions were determined relative to the known elastic scattering cross section of carbon. The experimental results were compared with those obtained in previous measurements and a qualitative comparison was made with theoretical calculations.

The Scattering of Fast Neutrons from W-184⁽⁷⁾

Neutrons with energies of 0.3 to 1.5 MeV are scattered from W-184. Pulsed-beam, fast time-of-flight techniques including a magnetic bunching system are

utilized to resolve the elastically scattered neutrons from those inelastically scattered. The differential elastic cross section is measured at 50 keV intervals with an ~ 20 keV incident neutron energy spread. The differential cross sections for inelastic scattering resulting in the excitation of residual nuclear levels at 111 ± 5 , 365 ± 10 , 690 ± 40 , 900 ± 25 , 1000 ± 30 , and 1120 ± 30 keV are determined, (see Fig. I-1-4). In all instances the inelastically scattered neutrons are emitted, within experimental error, isotropically. The experimental results are compared with those obtained in previous work and with the predictions of theory.

Elastic and Inelastic Scattering of Fast Neutrons from Au, Hg, and Tl⁸

The elastic and the inelastic scattering of 300–1500 keV neutrons from Tl, Hg, and Au was studied using time-of-flight techniques. The respective differential cross sections were measured at incident neutron intervals of $\lesssim 50$ keV. The inelastic excitation of a number of states was observed including, a) 205, 280, 620, 680, 920, and 1080 keV levels in Tl; b) 160, 210, 350, 440, 650, and 980 keV levels in Hg; and c) 77, 270, 540, 830, 940, and 1220 keV levels in Au. A number of the observed states have not been previously reported. The measured elastic scattering was compared with optical model calculations using the spherical potential of Moldauer. The Hauser-Feshbach method is used to obtain inelastic excitation functions for comparison with experiment.

A final report of the above work is now in preparation. These three elements are essentially symmetric and lie near the doubly closed shell at $A = 208$. The elastic scattering results, extended with those of Bi and Pb, should show any effect on the scattering potential due to the approach to the doubly closed nuclear shell at $A = 208$. Such was found as illustrated in Fig. I-1-5. Here the measured differential elastic cross sections for Au, Hg, Tl, Pb, and Bi are compared with the cross section calculated from the optical model. A steady decrease in the imaginary (nuclear absorption) potential is noted as the doubly closed shell is approached (solid curves). A note describing this effect has been submitted to "Physics Letters".

Elastic Scattering of Fast Neutrons from U235⁽⁹⁾

The differential cross section for the elastic scattering of neutrons from U-235 was measured at ~ 50 -keV intervals throughout the incident neutron energy range 0.3 to 1.5 MeV. Pulsed-beam time-of-flight techniques were employed to resolve the elastically scattered neutrons from those inelastically scattered and from the spectrum of fission neutrons. The experi-

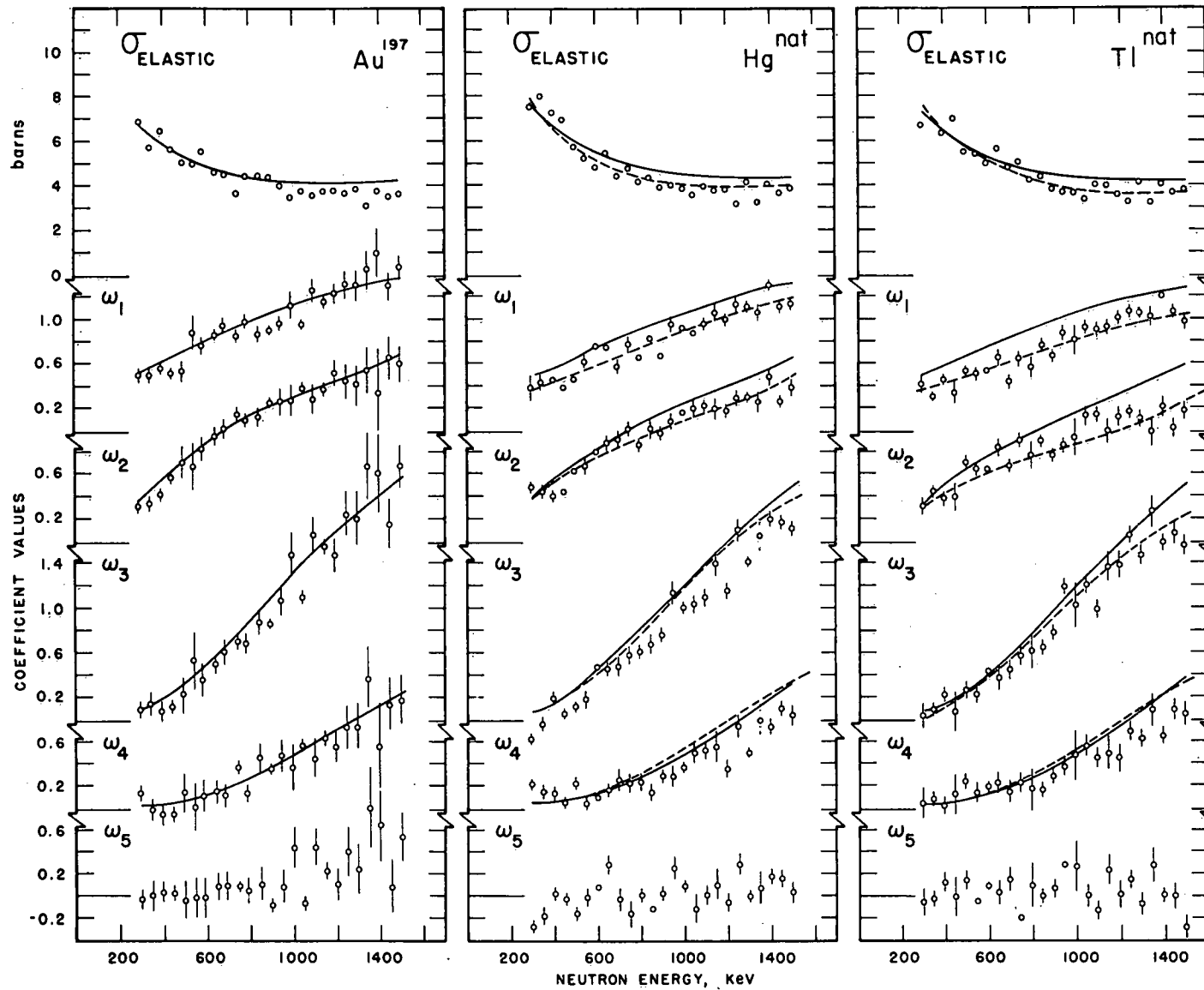


FIG I-1-3. The Differential Elastic Scattering Cross Sections of Au, Hg, and Tl Expressed as a Five Term Legendre Series. The ω_i Values are the Coefficients of the Respective Polynomial Terms.

mental resolution extended from ~25 to ~65 keV at respective neutron energies of 0.3 and 1.5 MeV. All neutrons incurring an energy loss at the time of scattering, equal to or less than the respective resolution function, were considered "elastically" scattered. The experimental results were expressed in the form

$$\frac{d\sigma(el)}{d\Omega} = \frac{\sigma(el)}{4\pi} \left[1 + \sum_{i=1}^5 W_i P_i \right]$$

where $\sigma(el)$ is the total elastic cross section, P_i are Legendre polynomials, and W_i are experimentally determined coefficients. The elastic transport cross section was derived from the measurements.

Scattering from the fissile nuclei such as U-235 is complicated by the profusion of low lying excited nuclear states. Despite this difficulty, the available experimental apparatus made it possible to obtain the above results with precision.

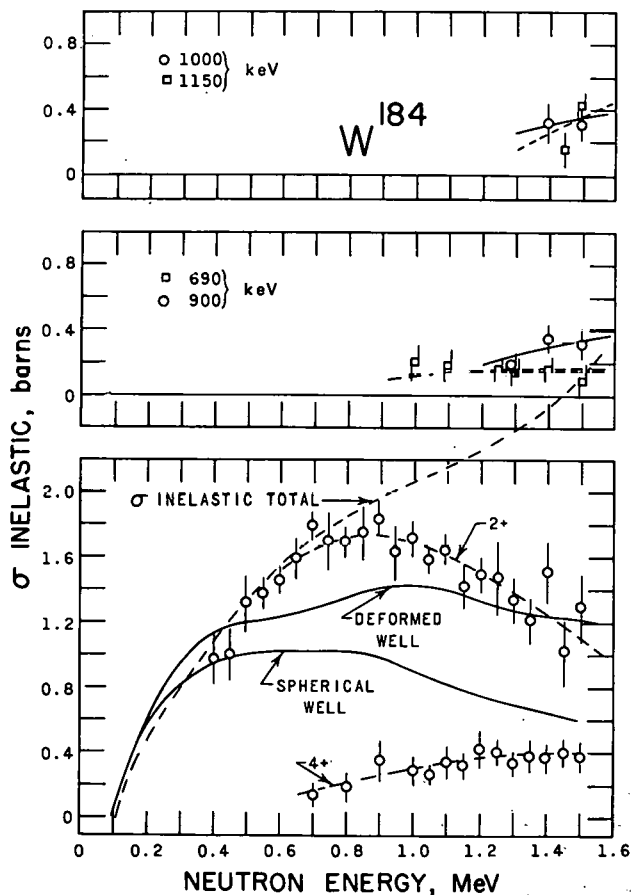


FIG. I-1-4. The Inelastic Scattering Cross Sections of W-184. The Illustrated Values are Typical of Those of High Temperature Structural Materials. (Unless noted the solid curves denote the results of theoretical calculations employing both spherical and deformed nuclear wells.)

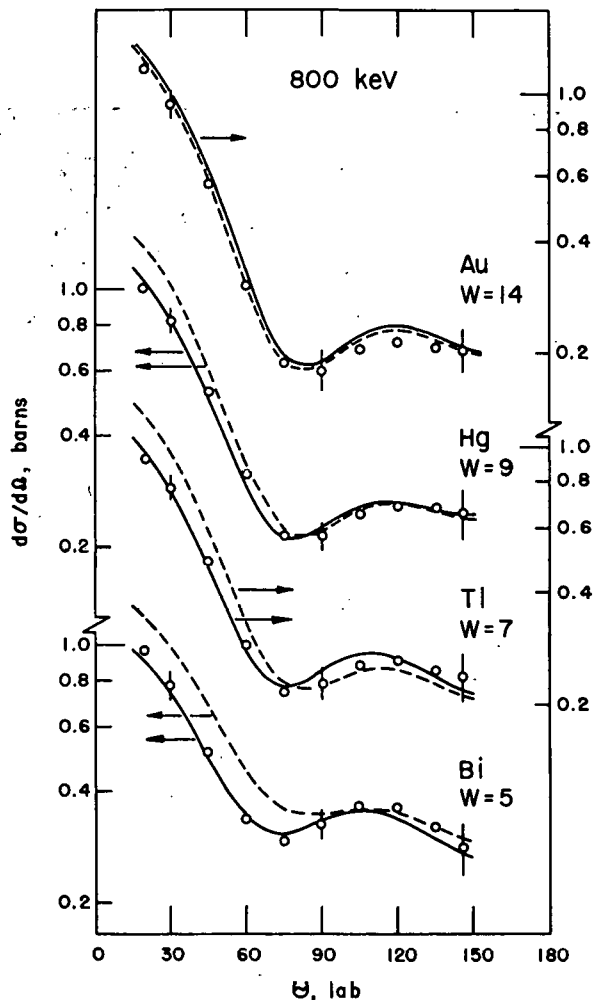


FIG. I-1-5. The Differential Elastic Scattering Cross Sections of Au, Hg, Tl, Pb, and Bi. The Circles Represent the Data Points; the Dotted Curves, Optical Calculations Using a 14 MeV Imaginary Potential; and the Solid Curves Represent the Calculations Using a Potential that is Reduced (14 → 7 MeV) as the Doubly Closed Shell is Approached as Indicated.

Scattering of Fast Neutrons from Natural Uranium¹⁰

The elastic and inelastic scattering of fast neutrons from natural uranium was studied. The incident neutron energy was varied from 0.3 to 1.5 MeV. Time-of-flight techniques were utilized to determine the energy spectrum of scattered neutrons. The differential elastic scattering cross section was determined at incident neutron energy intervals of ~50 keV. The cross sections for the inelastic excitations of residual nuclear levels at 45 ± 3 , 150 ± 5 , 630 ± 20 , 720 ± 20 , 930 ± 30 , 1000 ± 30 , and 1050 ± 30 keV were measured, (Fig. I-1-6). The differential cross section for inelastic scattering to the 45 keV level was essentially symmetric about 90 degrees. The remaining inelastic

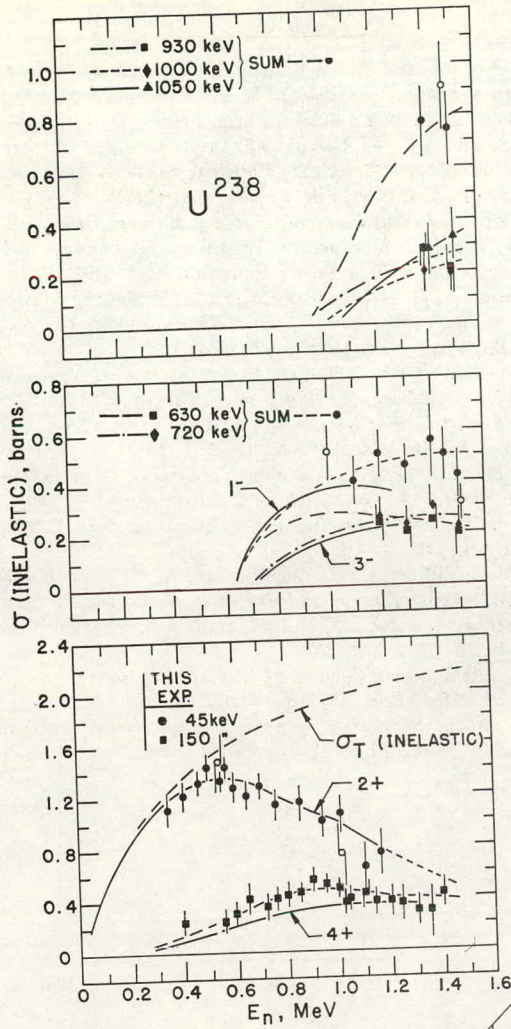


FIG. I-1-6. The Measured Inelastic Excitation Functions of Natural Uranium.

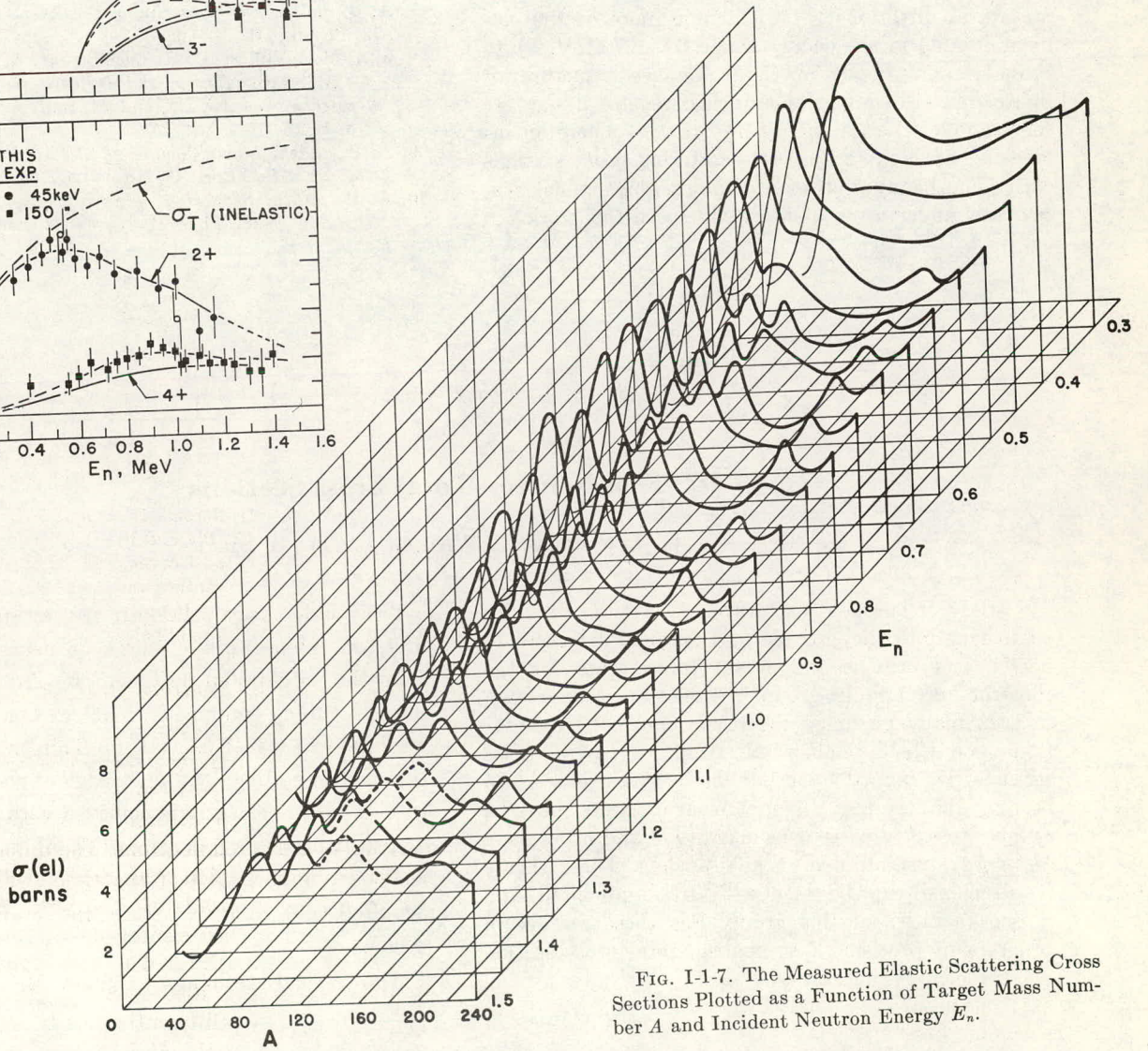


FIG. I-1-7. The Measured Elastic Scattering Cross Sections Plotted as a Function of Target Mass Number A and Incident Neutron Energy E_n .

groups were emitted isotropically. All cross sections were determined relative to the known elastic scattering cross section of carbon. The experimental results were compared with Hauser-Feshbach theory and possible evidence for direct interaction processes is discussed.

SUMMARY

This systematic study has already resulted in a much improved understanding of fast neutron scattering. This is indicated in Fig. I-1-7 where these measured elastic scattering cross sections are shown three dimensionally as a function of incident neutron energy and target mass number. The work is being extended in several directions; a) to include more of the elemental table in the energy range 0.3–1.5 MeV, b) to provide more detail in the resonance structure of lighter nuclei of importance in fast reactor design, Fe for example, c) to higher energy regions where an increasing demand for precise scattering cross sections exist. The installation of a complex ten channel system now underway should greatly speed this work.

REFERENCES

1. W. G. Vonach and A. B. Smith, *A Compendium of Fast Neutron Scattering Studies*, Proc., International Conference on Nuclear Physics, Paris, France, 2 July, 1964.
2. A. B. Smith, *Neutron Microscopy*, Invited Paper, Chicago Meeting of the American Physical Society, October, 1963, Bull. Am. Phys. Soc. **8**, No. 7, 531 (1963).
3. A. B. Smith, *Recent Changes in Heavy Element Cross Sections*, Proc., Conference on Breeding, Economics, and Safety in Large Fast Power Reactors, ANL-6792 (1963).
4. D. Reitmann, C. H. Engelbrecht and A. B. Smith, *Elastic and Inelastic Scattering of Fast Neutrons from Co, Cu, and Zn*, Phys. Rev. **135**, 76–82 (1964).
5. D. Reitmann and A. B. Smith, *Scattering of Fast Neutrons from Natural Zr and Nb*, Nucl. Phys. **48**, No. 4, 593 (1963). See, also, *Inelastic Scattering of Fast Neutrons from Cu, Zr, and Nb*, Bull. Am. Phys. Soc. **8**, 1 (1963).
6. A. B. Smith, *Fast Neutron Scattering from Ta-181*, ANL-6727 (1963).
7. A. B. Smith, *The Scattering of Fast Neutrons from W-184*, Z. Physik, **175**, 242 (1963).
8. J. A. M. deVilliers, C. H. Engelbrecht, W. G. Vonach and A. B. Smith, *Elastic and Inelastic Scattering of Fast Neutrons from Au, Hg, and Tl*, Bull. Am. Phys. Soc. **9**, No. 4, 461 (1964).
9. A. B. Smith, *Elastic Scattering of Fast Neutrons from U-235*, Nucl. Sci. Eng., **18**, No. 1, 126 (1964).
10. A. B. Smith, *Scattering of Fast Neutrons from Natural Uranium*, Nucl. Phys. **47**, No. 4, 633 (1963).

I-2. Fast Neutron Total Cross Sections

W. G. VONACH, J. F. WHALEN AND A. B. SMITH

A study of fast neutron total cross sections provides an insight into the average and detailed structure of nuclei, and provides important information for the construction of multi-group fast reactor cross section sets. In many instances the results form the foundation upon which the normalizations of partial cross sections determined by other methods are based. To be of value, the experimental measurements must be reliable to a few percent in magnitude and often have an energy resolution of 1 keV or less. These severe requirements can be met with the automated and pulsed facilities of this group. For these reasons, a program of precision fast neutron total cross section measurements is underway.

The studies have employed two techniques. In the first, an intense white source of neutrons available from the pulsed Van de Graaff is used together with the fast timing equipment to achieve an experimental resolution of 0.15–0.05 nsec/m. This excellent resolution provides a detailed knowledge of resonance structure in light nuclei and is achieved with a high degree of productivity as the method is inherently a multi-channel approach. All of the time-of-flight data are acquired and processed with the on-line computer system.

The second technique utilizes the conventional

monoenergetic source method to obtain high precision cross sections with a resolution of a few keV. In this method the entire experiment, including the accelerator and the detection equipment, is fully automated and under the programmed control of the digital computer. All data processing and logical decisions are made by the computer system. The result is a rapid acquisition of total cross sections of high quality with essentially no manual supervision. As in all proper applications of "process control", the saving in time leads to a very real economy and increased productivity.

Experimental results have been obtained for the light nuclei Al, S, Mg, and F, the medium weight nuclei Co and Fe, and the heavy nuclei U-Nat, U-235, W and Re. Examples are shown in Fig. I-2-1. The Fe curve at the top of the figure was obtained using the timing techniques while the two lower cross sections pertaining to Al and to U were determined with a monoenergetic source and the automated system. All of the experimental results are stored on punched cards. These can be used directly to derive multi-group reactor cross section sets and to carry out resonance or optical model calculations. A program for resonance fitting the data has been developed by members of the Theoretical Reactor Physics Section.

The future work will emphasize the light nuclei employed as reactor coolants and the heavy fertile and fissile materials (Na and U-235 for example).

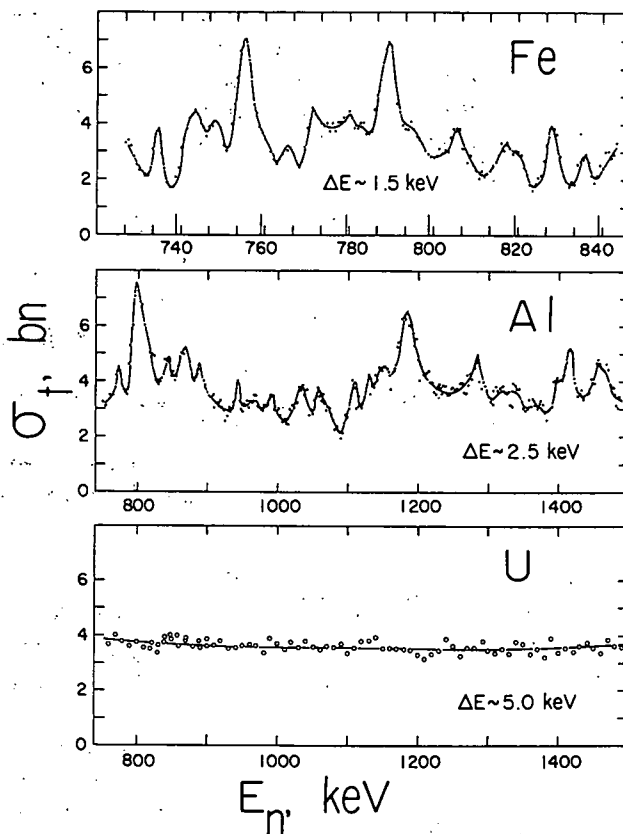


FIG. I-2-1. The Measured Fast Neutron Total Cross Sections of Fe, Al, and U.

I-3. Fast Neutron Capture

S. A. COX, J. W. MEADOWS AND J. F. WHALEN

Studies of fast neutron capture are not a primary concern of this group since other laboratories devote considerable attention to such processes. However, specific measurements (activation cross sections) are carried out to provide requested information and to resolve discrepancies in important quantities. Two sets of experiments have been completed during the past year.

Neutron Activation Cross Sections of Br-79, Br-81, Rh-103, In-115, I-127, and Ta-181⁽¹⁾

Neutron activation cross sections of Br-81, Br-79, Rh-103, In-115, I-127, and Ta-181 have been measured in the incident neutron energy range 130 to 1800 keV. The results agree rather well with other activation measurements. The activation measurements are combined to form the total neutron capture cross sec-

tions of the natural elements and compared with the capture gamma-ray data of B. Diven, et al.² and S. Gibbons, et al.³ The elemental cross sections agree rather well with the results cited in Ref. 2 but do not agree with the lower results cited in Ref. 3.

Ni-58(n,p)Co-58m,g Cross Section and Isomer Ratio from 1.04 to 2.67 MeV⁴

The cross sections and isomer ratios for the Ni-58(n,p)Co-58m,g reaction have been measured relative to the U-235(n,f) reaction for neutron energies of 1.04 to 2.67 MeV. The absolute yield of Co-58 was determined by counting coincidences between the 0.800 MeV gamma-ray and annihilation radiation of the positrons from the decay of the Co-58 ground

state. The observed cross sections and isomer ratios are compared with calculated values obtained by assuming compound nucleus formation and proton emission only to the 5⁺ and 2⁺ states in Co-58.

REFERENCES

1. S. A. Cox, *Neutron Activation Cross Sections of Br-79, Br-81, Rh-103, In-115, I-127, and Ta-181*, Phys. Rev. **133**, 378 (1964). See also Bull. Am. Phys. Soc. **8**, 375 (1963).
2. B. C. Diven, et al., *Radiative Capture Cross Sections for Fast Neutrons*, Phys. Rev. **120**, 556 (1960).
3. S. H. Gibbons, et al., *Average Radiative Capture Cross Sections for 7- to 170-keV Neutrons*, Phys. Rev. **122**, 182 (1961).
4. J. W. Meadows and J. F. Whalen, *Ni-58(n,p)Co-58m,g Cross Section and Isomer Ratio from 1.04 to 2.67 MeV*, Phys. Rev. **130**, 2022 (1963).

I-4. Gamma Rays from Inelastic Neutron Scattering

J. F. BARRY* AND D. STUPEGIA†

A study of the γ -rays following inelastic neutron scattering can yield valuable information about the level schemes of nuclei. In certain cases, it can also yield neutron inelastic scattering cross sections, of particular value at energies close to each inelastic threshold where cross sections cannot easily be obtained by neutron detection methods. In this threshold region, experimental data provides an especially sensitive test of reaction model predictions of cross sections.

Experiments are in progress to measure cross sections and angular distributions of γ -rays following inelastic neutron scattering in the elements Fe, Au, Zr, Nb, Ag, Ho, and Re for neutron energies up to 1.5 MeV. The method employs a 5 cm x 5 cm sodium iodide scintillation counter for γ -ray detection and a time-of-flight system to provide a high degree of discrimination against background. Neutrons from a pulsed source bombard a hollow cylindrical sample and the resultant γ -rays are detected in the heavily shielded scintillator which can be rotated about the sample position. Pulses from the detector are recorded only if they bear the correct time relationship to the pulse from the neutron source. This eliminates approximately 90% of the time-uncorrelated background as well as pulses from scattered neutrons and from γ -rays originating at the neutron source which

scatter into the detector. The remainder of the background is measured in a run with the sample removed. Neutron flux is monitored with a long counter.

Figure I-4-1 is an example of the γ -ray spectra obtained and shows spectra from neutrons of various energies incident on niobium. The γ -rays observed correspond to excitation of known levels. The 335 keV γ -ray appearing at the highest neutron energy results from decay of the 1076 keV level which goes through the level at 741 keV. This contribution to the γ -rays of 741 keV energy must be taken into account when determining the cross section for inelastic scattering to the level at that energy.

Analysis of the γ -ray spectra to obtain the counts in each of the total absorption peaks requires a knowledge of the line shapes due to monoenergetic γ -ray. This is obtained for the geometry used from measurements with sources prepared from suitable γ -ray emitters distributed throughout a laminated sample. The counting efficiency of the system is also obtained from this measurement since the sources used are of known strength.

It is planned to improve the gamma spectra measurements before making an analysis to obtain cross sections. A larger and more efficient shielding tank is being constructed to minimize neutron and γ -ray backgrounds. Inside this tank the detector will be surrounded with an 11 in. diameter plastic scintillator operating in anti-coincidence with the detector. This reduces considerably the Compton contribution

* On leave from Atomic Weapons Research Establishment, Aldermaston, England.

† Chemical Engineering Division.

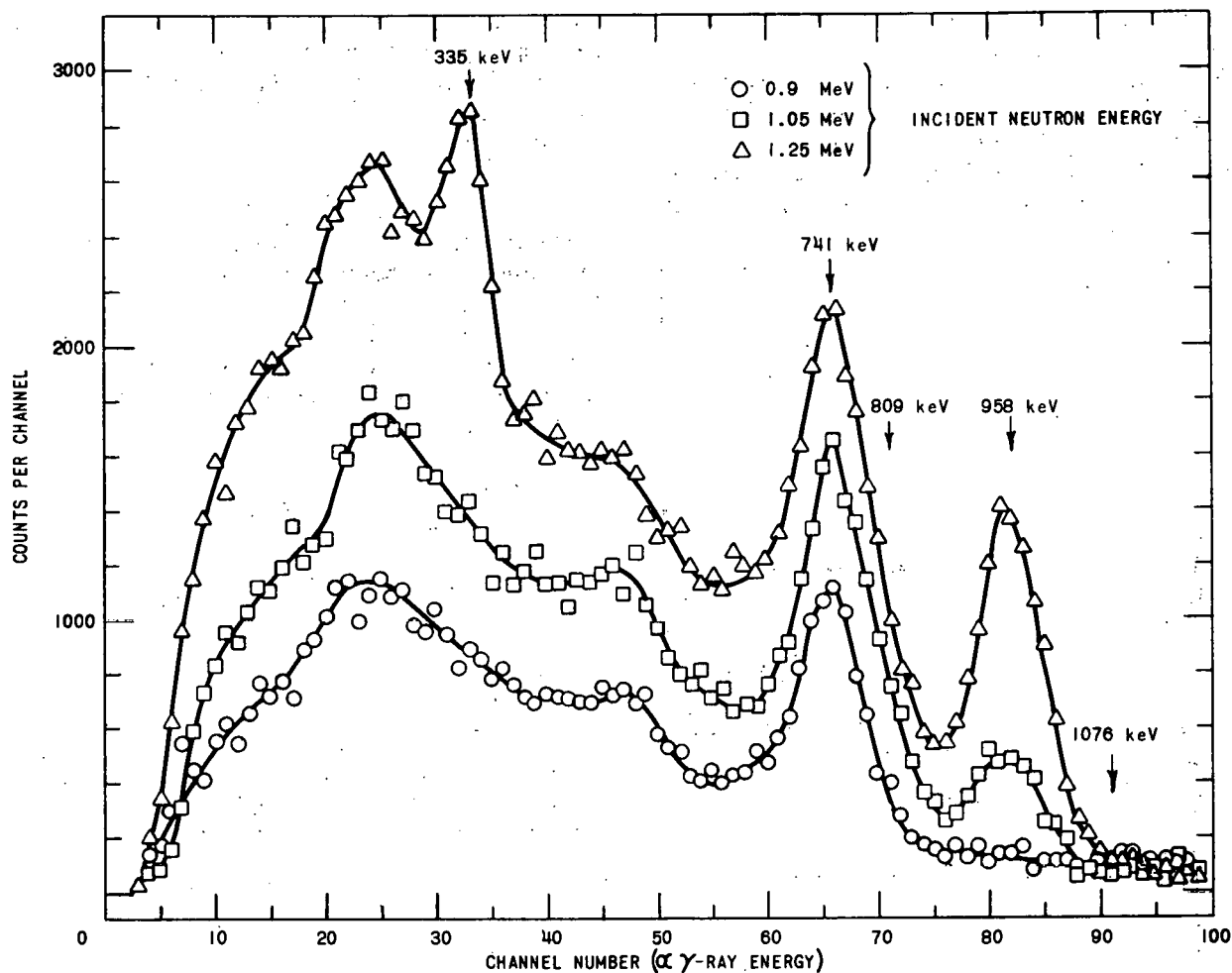


FIG. I-4-1. Spectra of γ Rays from Neutron Inelastic Scattering in Nb-93 at Different Incident Neutron Energies.

to the γ -ray line shapes and also reduces the detector background. A further improvement to the line shapes will result from replacing the relatively thick-

walled cylindrical samples with thin plates which have an absorption of 10% or less for the γ -rays of interest.

I-5. Energy Dependence of Prompt ν for Neutron-Induced Fission of U-235

J. W. MEADOWS AND J. F. WHALEN

INTRODUCTION

The measurement of the energy dependence of the number of prompt neutrons, $\bar{\nu}_p$, emitted for neutron induced fission of U-235 reported in a previous paper¹ is being extended to higher neutron energies. Results in the energy range 3.9 to 6.4 MeV are reported below.

EXPERIMENTAL METHOD

In this work all measurements of $\bar{\nu}_p$ for U-235 are made relative to $\bar{\nu}_p$ for spontaneous fission of Cf-252. The experimental method involves the counting of coincidences between a fission detector and a neutron detector. In order to avoid errors due to a change in the accidental coincidence rate or in the overall neutron

detection efficiency, measurements on U-235, Cf-252, and the accidental rate are made simultaneously. The two fission detectors are placed in a common container in a tube through the center of the neutron detector. Neutrons from the $D(d,n)T$ reaction enter through a collimator. Fission pulses from either fission detector start a time analyzer which records the neutron count

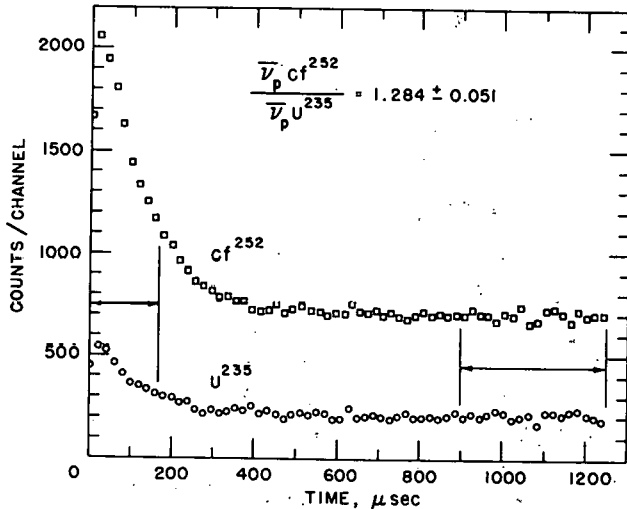


FIG. I-5-1. Time Dependence of Neutron Count Rate after a Fission.

rate for the following 1200 μsec . Figure I-5-1 shows the time spectra from a typical run. Fission neutrons plus accidentals are counted in the first 170 μsec of the time sweep while the accidentals are counted in the last 340 μsec .

RESULTS

The results are listed in Table I-5-I. Column 3 of this table lists the measured values of the ratio, $\bar{\nu}_p(\text{Cf-252})/\bar{\nu}_p(\text{U-235})$. A number of corrections totaling $\sim 4.7\%$ must be applied to these data. These are:

1. Analyzer Dead Time. This correction can be accurately determined from the time spectra. A typical value is $+0.6\%$.

TABLE I-5-I. EXPERIMENTAL RESULTS FOR $\bar{\nu}_p(\text{U-235})$ RELATIVE TO $\bar{\nu}_p(\text{Cf-252}) = 3.782$

E_n , MeV	ΔE_n , MeV	$\bar{\nu}_p(\text{Cf-252})/\bar{\nu}_p(\text{U-235})$		$\bar{\nu}_p(\text{U-235})$	Statistical Error, %
		Measured	Corrected		
3.910	0.260	1.324	1.296	2.918	0.63
4.520	0.152	1.301	1.261	3.000	0.54
5.540	0.086	1.271	1.232	3.069	0.67
5.760	0.080	1.245	1.208	3.132	0.88
6.360	0.074	1.183	1.148	3.293	0.52

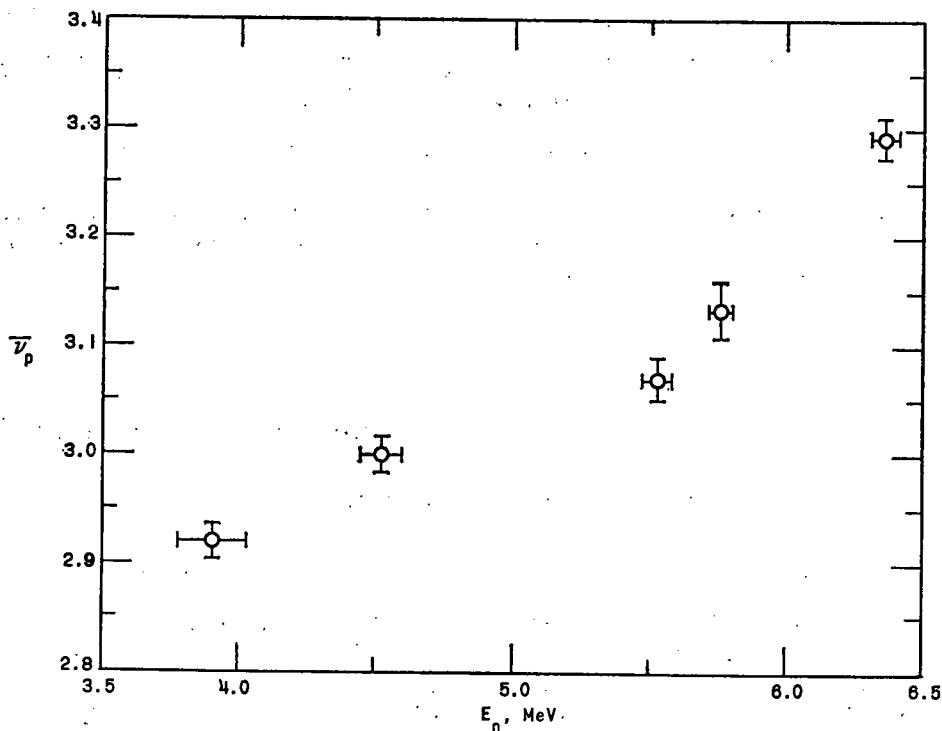


FIG. I-5-2. Energy Dependence of $\bar{\nu}_p$ for U-235. (The vertical bars give the established error only. The horizontal bars give the energy spread due to target thickness.)

2. Geometric Asymmetry of the Neutron Detector. The efficiency of the neutron detector may be different for the two fission neutron sources due to their difference in location. This is measured by making traverses through the volumes occupied by the fissionable material with a small Ra- γ -Be neutron source. For the data presented here the correction is -0.2% .

3. Thermal Neutron Fission. This can be measured accurately using a pulsed source method. No measurements have as yet been made at these energies but measurements at lower energies indicate a correction $\sim +2.4\%$.

4. Energy Dependence of the Neutron Detector Efficiency. The difference in the energy spectra of the neutrons from U-235 and Cf-252 results in a small correction which varies slowly with the excitation energy of the fission fragments. A typical value of this correction is $+0.5\%$.

5. Angular Dependence of the Neutron Detector Efficiency. This is due to the angular anisotropy of the U-235 fission fragments. Although accurate determination of this correction awaits the results of a Monte-Carlo calculation, preliminary estimates indicate a value of -1.0% .

Preliminary values of $\bar{\nu}_p(\text{Cf-252})/\bar{\nu}_p(\text{U-235})$ based on the approximate correction factors are listed in column 4 of Table I-5-I. Column 5 and Fig. I-5-2 give the corresponding values for $\bar{\nu}_p$ of U-235 based on 3.782 for $\bar{\nu}_p$ of Cf-252. Due to the present uncertainty in corrections (3) and (5), only the errors from counting statistics are listed in column 6.

REFERENCES

1. J. W. Meadows and J. F. Whalen, *Energy Dependence of Prompt $\bar{\nu}$ for Neutron Induced Fission of U-235*, Phys. Rev. **126**, 197 (1962).

I-6. Fission Neutron Yield Experiment

A. DE VOLPI AND K. G. PORGES

The fundamental parameter ν_{th} , the average number of neutrons emitted in thermal fission, has not been directly measured with a precision better than 2%; the best values are derived indirectly from cross sections and neutrons-per-absorption experiments. There is a growing body of agreement in absolute measurements of Cf-252 spontaneous fission neutron yields, which then provides a reference for calibration of U-235 determinations. It is noteworthy that all of these Cf-252 results are obtained from the use of large liquid scintillators, which require efficiency calibrations based on the number of detected events per incident neutron and on simulation of the fission neutron energy spectrum. To avoid these particular restrictions, a measurement by a completely different technique has been in preparation for some time.

The approach underway has been to determine the number of fissions by absolute counting in a fission counter and to evaluate the number of neutrons emitted by use of the manganese bath technique. For both U-235 and Cf-252, precision counting of fragments is improved by fission-neutron coincidences. With the aid of a large hydrogenous integrating neutron detector, nearly all neutrons supplied by the fission chamber (located at the sphere center) are intercepted. This can be done for both the spontaneous

fission source and for a thermal beam impinging on U-235.¹ A separate experiment in which the concentration is varied is required to find the ratio of H/Mn absorption. The activated manganese is assayed in a liquid counter designed for high efficiency and long-term stability.

All this equipment has been constructed and tested. It is necessary to intercalibrate the liquid monitor, which is a large volume gamma-gamma coincidence unit, with an absolute 4π beta-gamma coincidence system. Thus ultimate reliance has been placed on well-tested precision techniques of coincidence counting and on one relative measurement of absorption ratio which avoids the need for significant cross section corrections.

Absolute techniques require careful attention to a multiplicity of details normally ignored in less precise work. Thus, in order to aim at an over-all measurement of 1% accuracy or better, each component must be tested for proper and reliable behavior. For example, beta-gamma results are being compared to 4π beta proportional counting data and other standardizations. The liquid counter is intercalibrated daily with the reference system, and activations of the 42-in. diameter manganese bath are currently being conducted with a radium-beryllium source to check long-term reproducibility. In addition, a con-

centration run to obtain the manganese to hydrogen capture ratio with a hard spectrum neutron source (radium-beryllium) is being carried out; this should be of use to groups involved in absolute neutron standardization of such sources.

REFERENCE

1. A. De Volpi and K. Porges, *Direct and Absolute Measurement of Average Yield of Neutrons from Thermal Fission of U-235*, International Conference on Nuclear Physics with Reactor Neutrons, October 15-17, 1963, ANL-6797, (1963), pp. 450-454.

I-7. Mass and Kinetic Energy Distributions in MeV Neutron Induced Fission

J. W. MEADOWS AND J. F. WHALEN

INTRODUCTION

One of the more interesting problems in the study of the fission process has been the dependence of the mass and kinetic energy distributions of the fragments on the excitation energy. Measurement by many experimenters have been made over a large range of excitation energies for many different nuclei.¹ However, in much of this work, the identity of the fissioning nucleus and its excitation energy is uncertain due to the possibility of neutron emission before fission. Consequently we have undertaken a study of the mass and total kinetic energy distribution in neutron induced fission below the threshold for (n, n') reactions (~ 6 MeV). Results for thermal neutron fission of U-235 and Pu-239, 1.0 MeV neutron fission of U-235, and 1.5 MeV neutron fission of U-238 are reported below.

EXPERIMENTAL METHOD

The experimental method involves the simultaneous detection of a pair of fission fragments in two solid state detectors and storing the pulse heights in a 64 x 64 array with the rows representing the pulse height of one fragment and the columns the pulse height of the other. Bias levels and amplifier gains are set so that only the energy range between ~ 40 to ~ 120 MeV is covered. The pulse heights are converted to energies and corrected for energy loss in the source and detector windows, for the pulse height defect, and for center of mass motion. The first two corrections are based on work by J. Alexander and M. Gazdik,² and H. Britt and H. Wegner.³ These energies are related to the total kinetic energy, E_k , and the mass ratio by

$$E_k = E_1 + E_2$$

$$\frac{M_1}{M_1 + M_2} = \frac{E_2}{E_1 + E_2}$$

where E_1 and E_2 are the energies of the fission fragments.

RESULTS

The results are illustrated in Figs. I-7-1 and I-7-2 and some average quantities are listed in Table I-7-I. Fission fragment masses determined by the method used in this experiment are subject to a dispersion due to the decrease in fragment energy caused by neutron emission.⁴ The mass yields in Fig. I-7-1 have not been corrected for this effect; consequently the mass peaks are broader and the valleys somewhat shallower than is actually the case. However, the distributions of \bar{E}_k in Fig. I-7-2 have been corrected. If it is assumed that on the average each fragment emits an equal number of neutrons, then for a given mass split

$$\Delta E_k = \frac{E_k}{2(M_1 + M_2)} \left(\frac{M_1}{M_2} + \frac{M_2}{M_1} \right)$$

The average neutron number per pair of fragments, $\bar{\nu}$, is estimated from

$$\bar{\nu} = \frac{E_f + \epsilon_n - E_\gamma - E_k}{B_{n,p} + 1.21}$$

where E_f is the energy obtained by splitting the fissioning nucleus into two fragments with masses M_1 and M_2 , ϵ_n is the kinetic energy of the incident neutron, E_γ is the energy emitted from the fragments in the form of gamma rays, $B_{n,p}$ is the average neutron separation energy of the fragments and 1.21 is the average kinetic energy of the emitted neutron.

As yet there is not enough data to warrant any conclusions. However, the values of $\sigma^2(M)$ listed in Table I-7-I show that the mass distribution for 1.0 MeV neutron fission of U-235 is appreciably broader than in thermal neutron fission. This increase is more than can be accounted for by the increased number of prompt neutrons. Also, most of the additional width appears on the asymmetric side.

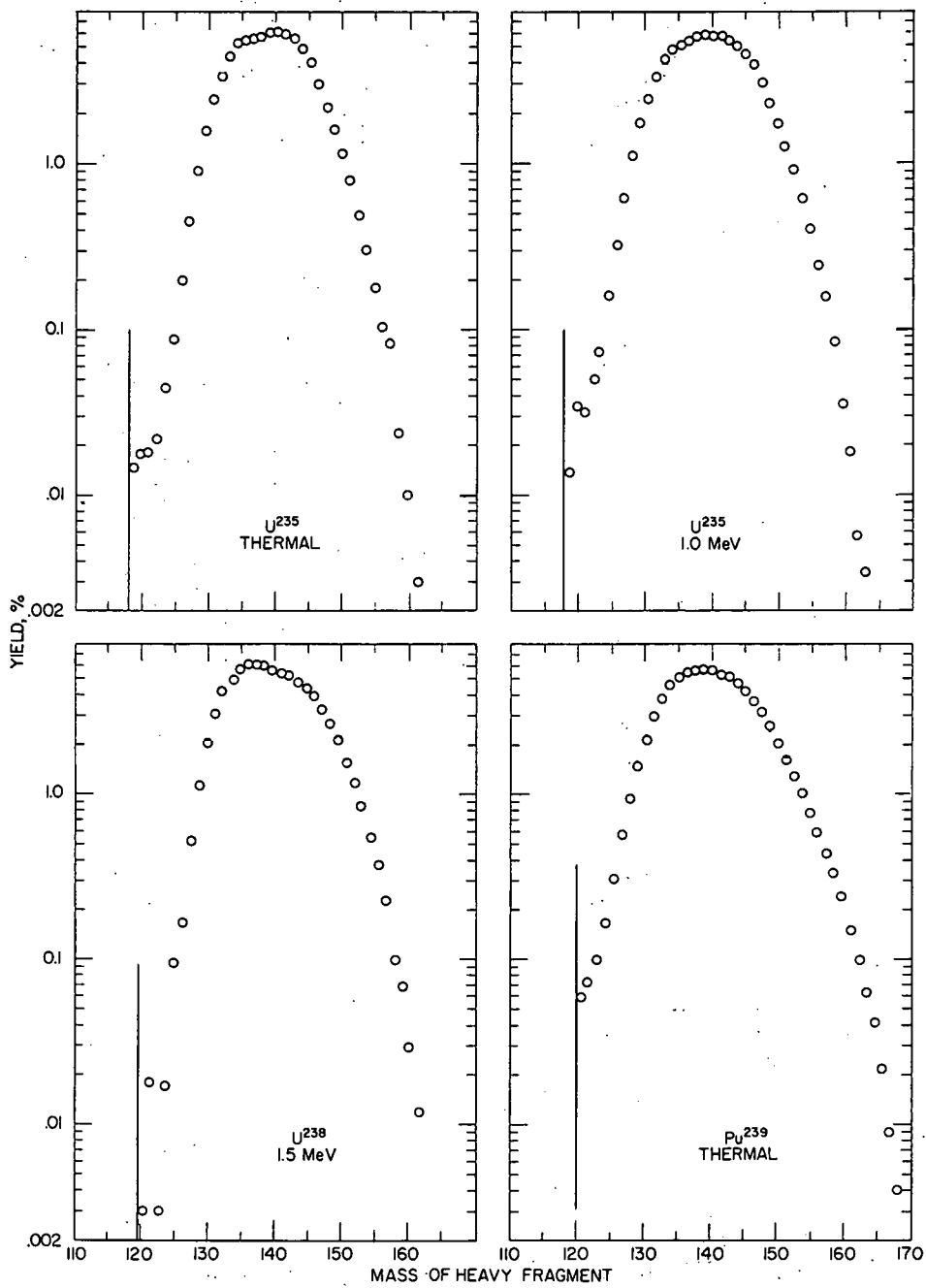


FIG. I-7-1. Mass Distribution.

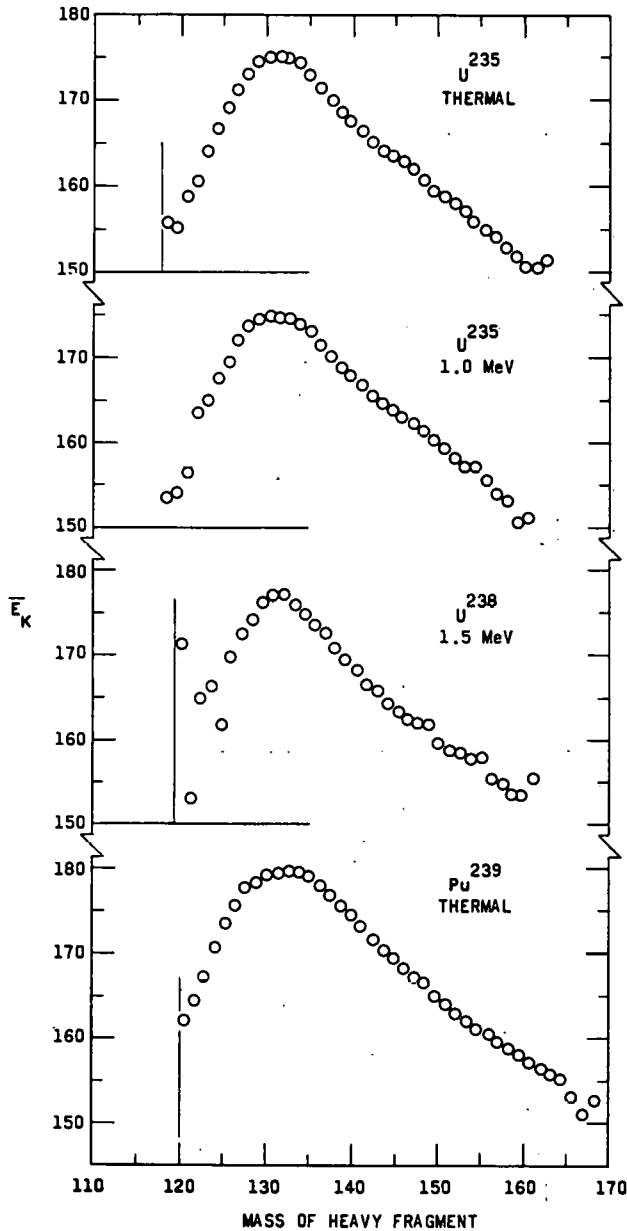


FIG. I-7-2. Total Kinetic Energy Versus Mass of the Heavy Fragment.

TABLE I-7-I. AVERAGE TOTAL KINETIC ENERGIES ($\overline{E_{KT}}$), MASSES (\overline{M}_L , \overline{M}_H), AND THE VARIANCE OF THE MASS DISTRIBUTION [$\sigma^2(M)$].

Target N Nucleus	Neutron Energy	$\overline{E_{KT}}$, MeV	\overline{M}_L	\overline{M}_H	$\sigma^2(M)$
U-235	Thermal	168.1	96.2	139.6	34.9
U-235	1 MeV	168.0	96.2	139.6	38.5
Pu-239	Thermal	172.9	99.4	140.3	48.0
U-238	1.5 MeV	169.4	98.8	139.2	37.8

REFERENCES

1. I. Halpern, *Nuclear Fission*, Ann. Rev. Nucl. Sci. **9**, 1959, p. 245 (Stanford California, Annual Reviews).
E. K. Hyde, *A Review of Nuclear Fission*. Part 1—*Fission Phenomena at Low Energy*, UCRL-9036 (January, 1960). Part 2—*Fission Phenomena at Moderate and High Energy*, UCRL-9065 (February, 1960).
2. J. R. Huizenga and R. Vandenbosch, *Nuclear Fission in Nuclear Reactions*, Vol. II, edited by P. M. Endt and P. B. Smith (North Holland Publishing Company, Amsterdam, 1962) p. 42-112.
3. H. C. Britt and H. E. Wegner, *Response of Semi-Conductor Detector to Fission Fragments*, Rev. Sci. Instr. **34**, No. 3, 274 (1963).
4. J. Terrell, *Neutron Yields from Individual Fission Fragments*, Phys. Rev. **127**, 880 (1962).

I-8. Nuclear Reaction Theory and Optical Model Studies

P. A. MOLDAUER

This theoretical program has been pursued with the objective of improving the fundamental understanding of neutron induced nuclear processes. In addition, these theoretical studies have proved an in-

valuable aid in guiding and interpreting experimental efforts and extrapolating measured results to provide data of importance to the nuclear energy program. The results have been submitted or reported in

journals or at conferences under the following titles and abstracts or summaries.

*Widths of Single Particle Bound States*¹

The radial shape of the nuclear optical model absorptive potential, $W(r)$, is shown to affect the distribution of single particle wave function components among highly excited nuclear bound states. Deuteron stripping and gamma-ray scattering experiments are suggested by means of which it may be possible to determine the shape of $W(r)$.

*Resonance Statistics and Average Cross Sections*²

The effects upon average cross sections of the statistical distributions and correlations of nuclear resonance parameters are discussed.

*Nuclear Cross Section Fluctuations*³

The dependence of the amplitudes of the energy fluctuations of nuclear cross sections upon resonance parameter statistics and resonance width to spacing ratios are discussed.

*Average Compound Nucleus Cross Sections*⁴

A brief historical review of average cross section theories is followed by a new classification of average cross sections and a summary of the latest theoretical results, together with comparisons of their predictions with the measured neutron inelastic scattering data.

*Optical Model of Low Energy Neutron Interactions with Spherical Nuclei*⁵

The optical model is used to study available data on absorption, scattering and polarization by spherical nuclei of neutrons with energies below 1 MeV. A good fit is obtained with a diffuse surface model having a sharply peaked absorptive shell at the surface. The sensitivity of various cross sections to changes in optical model parameters is discussed, both qualitatively and quantitatively.

*Average Resonance Parameters and the Optical Model*⁶

Averages over resonances of the elements of the collision matrix are derived from R -matrix theory for the general many-channel use. Of special interest are the average diagonal elements because of their relation to the complex phase shifts of optical models for the channels. In the absence of correlations among channel width amplitudes, the formula relating an average diagonal element to the average resonance parameters is found to be the same as that obtained by R. Thomas⁷ for the single channel case, or when

competing channels have small transmission factors. The evaluation of this formula with the aid of the single particle level picture of A. Lane, R. Thomas, and E. Wigner⁸ is discussed, as well as the effect of correlations among channels which are indicative of direct reaction effects.

*Statistical Theory of Nuclear Collision Cross Sections*⁹

A formalism is developed for a statistical treatment of the energy variations of nuclear scattering and reaction cross sections. A statistical collision matrix U^s is defined which has the form of an energy-independent direct-transition matrix plus a fixed simple resonance-pole expansion, the matrix residues of which are products of complex channel-width amplitudes. By direct comparison with the Wigner-Eisenbud¹⁰ and Kapur-Peierls¹¹ collision matrices it is found that under widely applicable conditions the statistical collision matrix may be used to calculate averages of observables over energy intervals containing many resonances and many total widths. The problem of determining the statistical properties of the parameters of U^s is defined and is solved for several special cases by relating it to the statistics of R -matrix parameters. Using these methods, averages and mean-square fluctuations of total and reaction cross sections are calculated under general conditions admitting direct and compound processes and arbitrary average values of the total widths Γ and the resonance spacings D . The results are expressed in terms of the direct-reaction matrix elements and the statistical properties of resonance parameters appropriate to the energy region under consideration, and are related to the locally applicable optical-model phase shifts and transmission coefficients. Simplifications are obtained under special assumptions such as uncorrelated width amplitudes, small and large Γ/D , pure compound-nucleus reactions, many competing open channels, and many competing direct processes. In the limit of small Γ/D one obtains the leading terms of an expansion of the average cross section which had previously been derived from R -matrix theory directly. In the limit of large Γ/D , many competing channels, and no direct reactions, the nonelastic fluctuation (or average compound nucleus) cross sections approach the Hauser-Feshbach formula. Except in this limit, corrections due to partial-width fluctuations and resonance-resonance interference are applicable. The former are sensitive to the magnitudes of direct reaction matrix elements, the latter to the correlations of resonance energies. Competing direct reactions are shown to require reductions of the transmission co-

efficients. The mean-square fluctuations of cross sections are found to approach T. Ericson's results¹² in the limit of large Γ/D and many competing channels, but are in general much larger for moderate Γ/D and few channels. They are also sensitive to the details of resonance parameter statistics.

*Distributions of the Poles and Residues of the Collision Matrix*¹³

The relationship between the statistical properties of the parameters defining the R -matrix and the distributions and correlations of the poles and residues of the statistical collision matrix are explored by means of some limited numerical computations involving models for reactions in the presence of large numbers of competing strongly absorbed channels. The results shed light on the distributions of resonance energies and widths and on the relationship between the partial widths to spacing ratios and the channel transmission coefficients. The calculations also yield substantial channel-channel and resonance-resonance correlations in the complex amplitudes which define the collision matrix pole residues. These are important for their effects on average cross section and fluctuation calculations. It is found that the investigated statistical relationships depend on the choice of R -matrix boundary conditions and the implications of this for the choice of boundary conditions are discussed.

*Problem of Measurement*¹⁴

A discussion of questions dealing with the interpretation of the measuring process in quantum me-

chanics is given. It is argued that the conventional interpretation does not give rise to real conceptual difficulties.

REFERENCES

1. P. A. Moldauer, *Widths of Single Particle Bound States*, Phys. Rev. Letters **10**, 525 (1963).
2. P. A. Moldauer, *Resonance Statistics and Average Cross Sections*, Proc., Symposium on Statistical Properties of Atomic and Nuclear Spectra, State University of New York, 1963.
3. P. A. Moldauer, *Nuclear Cross Section Fluctuations*, Phys. Letters **8**, No. 1, 70 (1964).
4. P. A. Moldauer, *Average Compound Nucleus Cross Sections*, Rev. Mod. Phys. (to be published).
5. P. A. Moldauer, *Optical Model of Low Energy Neutron Interactions with Spherical Nuclei*, Nucl. Phys. **47**, No. 1, 65 (1963).
6. P. A. Moldauer, *Average Resonance Parameters and the Optical Model*, Phys. Rev. **129**, 754 (1963).
7. A. Lane and R. Thomas, *R-Matrix Theory of Nuclear Reactions*, Rev. Mod. Phys. **30**, 257 (1958).
8. A. Lane, R. Thomas, and E. Wigner, *Giant Resonance Interpretation of the Nucleon-Nucleus Interaction*, Phys. Rev. **98**, 693 (1955).
9. P. A. Moldauer, *Statistical Theory of Nuclear Collision Cross Sections*, Phys. Rev. (to be published).
10. E. Wigner and L. Eisenbud, *Higher Angular Momenta and Long Range Interaction in Resonance Reactions*, Phys. Rev. **72**, 29 (1947).
11. P. Kapur and R. Peierls, *The Dispersion Formula for Nuclear Reactors*, Proc., Royal Soc. (London) **A166**, 277 (1938).
12. T. Ericson, *A Theory of Fluctuations in Nuclear Cross Sections*, Ann. Phys. (New York) **23**, 390 (1963).
13. P. A. Moldauer, *Distributions of the Poles and Residues of the Collision Matrix*, Phys. Rev. (to be published).
14. P. A. Moldauer, *Problem of Measurement*, Am. J. Phys. **32**, No. 2, 172 (1964).

I-9. Neutron Yields from High Energy Proton Bombardment

J. W. MEADOWS, J. F. WHALEN, A. B. SMITH AND G. R. RINGO*

The yield of neutrons resulting from the bombardment of various target material with high energy protons is of interest for space shielding and for the assaying of the suitability of high energy accelerators for the production of intense neutron sources. For these reasons the following two investigations were carried out.

*Neutron Production by 450-MeV Protons*¹

Measurements on neutron production in U, Pb, Al, and D₂O targets inside an hydrogenous moderator

* Physics Division

have been made with a beam extracted from the University of Chicago cyclotron. With targets 10 cm in diameter and 15 cm thick, U gave 5.7 ± 1.4 neutrons per proton and a maximum flux in the moderator of about 0.012 ± 0.002 neutrons cm⁻² proton⁻¹, Pb gave about one-half as much, and Al and D₂O much less.

*Thick Target Neutron Yields for 6 BeV Protons*²

Evaluation of the possible use of very high energy accelerators as neutron sources for time-of-flight spectroscopy requires a knowledge of neutron pro-

TABLE I-9-I. NEUTRON YIELD PER INCIDENT PROTON FROM HIGH ENERGY PROTON BOMBARDMENT

Target Length, cm	Target			
	U	Pb	Al	D ₂ O
5	34	8	—	—
10	74	18	—	—
15	113	27	1.7	1.7

duction in thick targets. Accordingly, we have made several measurements of thick target neutron yields for 6 BeV protons. The experimental procedure consisted of allowing the protons to strike a thick target

in the center of a large water tank then measuring the neutron flux distribution in the water by gold foil activation. The proton beam intensity was measured by the Al-27(*p,3pn*) Na-24 reaction. The results in neutrons per incident proton for various targets 10 cm in diameter are given in Table I-9-I.

REFERENCES

1. J. W. Meadows, G. R. Ringo and A. B. Smith, *Neutron Production by 450-MeV Protons*, Nucl. Instr. Methods **25**, No. 2, 349 (1964).
2. J. W. Meadows, J. F. Whalen and A. B. Smith, *Thick Target Neutron Yields for 6 BeV Protons*, Bull. Am. Phys. Soc. **9**, No. 4, 461, (1963).

I-10. Stripping Reactions

THE Be⁹(*d,n*)B¹⁰ REACTION (S. G. Buccino and A. B. Smith)

Measurements of the angular distribution of neutrons from the Be⁹(*d,n*)B¹⁰ reaction have been made using the pulsed-beam time-of-flight facility on the Reactor Physics Division's 3 MV Van de Graaff. The measurements were carried out at incident neutron energies of 2.6, 3.0, 3.1, and 3.2 MeV, and in 10 deg intervals from 0 deg to 70 deg. The target consisted of metallic Be (20 keV thick to 3 MeV deuterons) evaporated on a 10 mil tantalum backing.

At bombarding energies of ~3 MeV, 8 distinct neutron groups were seen in the data corresponding to the ground state and the first seven excited states of B¹⁰. The energy resolution at an 18 m flight path was sufficient to clearly resolve the doublet at 5.11 and 5.16 MeV excitation. There is no indication of unreported levels below 5.16 MeV nor any evidence for a level at 5.18 MeV which had been previously reported. Figure I-10-1 shows a typical time spectrum at a bombarding energy of 3.0 MeV and an angle of 20 deg. The data are being reduced to relative differential cross sections and the Butler theory of stripping reactions is being used to extract *l*-values.

THE Fe-54(*d,n*)Co-55 REACTION (D. S. Gemmell,* L. L. Lee, Jr.,* J. P. Schiffer,* and A. B. Smith)

A time-of-flight system incorporating the pulsed deuteron beam of the Physics Division's tandem Van de Graaff accelerator, a 9.5 m flight path and a 4 in. diameter liquid scintillator was used to study angular distributions from the Fe-54(*d,n*)Co-55 reaction with

7-MeV deuterons. Preliminary results indicate six prominent groups at the following excitation energies with *l*-values in parentheses: 0.0 MeV (3), 2.12 (1), 2.54 (1), 2.92 (1), 3.60 (3,4), 4.10 (1). The errors in the energies are less than 50 keV.

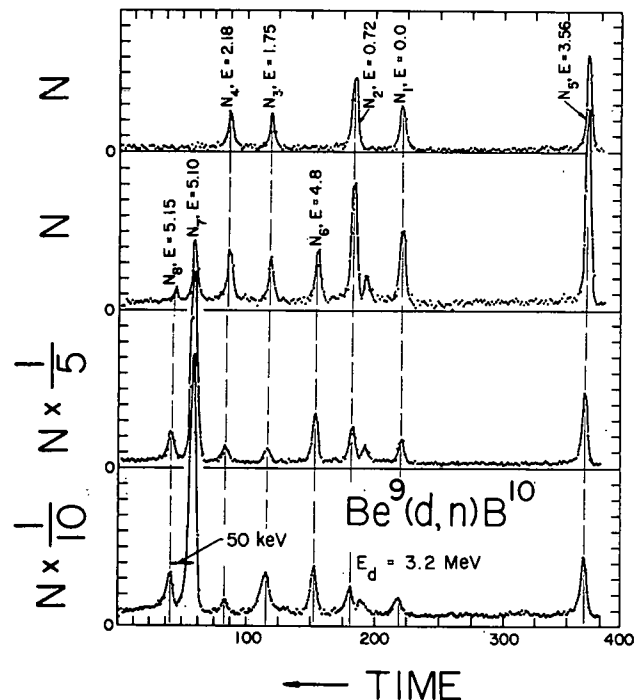


FIG. I-10-1. The Time Distribution of Neutrons Resulting from the Be-9(*d,n*)B-10 Reaction. The First Seven Excited States in B-10 are Evident. The Curves are Taken with Respectively Lower Energy Neutron Sensitivity Top to Bottom, thus the Inset of the Lower Energy Neutron Groups can be Clearly Observed.

* Physics Division

Section II

Thermal Reactors

Work in this section ranges from general reactor theory motivated by analysis of thermal reactors to detailed design problems associated with specific programs: Plutonium Recycle in EBWR and the Argonne Advanced Research Reactor.

Studies applicable to a wide range of existing designs of thermal reactors, such as boiling water reactor kinetics, are included in this section.

In the area of fuel conservation in burner reactors, studies were conducted on the use of depleted uranium as a fertile control material and on the analysis of water lattices with high conversion ratios (the Hi-C lattices).

Some interesting experiments on the U-D₂O systems with "flux traps" are reported here; these include the lattices with predicted $k_{\infty} < 1$. These lattices were made critical by moderation of neutrons to energies below the resonance capture range while in the reflector regions.

II-1. Remarks on the Definition of k_{eff} for Off-Critical Reactors—I

D. H. SHAFTMAN

MODIFICATION OF THE FOUR-FACTOR FORMULA AND k_{eff} FOR OFF-CRITICAL REACTORS

In its usual form, the "four-factor formula" relates the infinite multiplication factor, k_{∞} , to neutron-loss and neutron-gain processes in a 3-group partitioning of the neutron energy range. In the formula $k_{\infty} = (\eta f)\epsilon p$, the factor ϵ takes account of the fast fissions in fertile material. The factor p accounts for resonance neutron absorption in fertile material. The factor (ηf) therefore must account for all other neutron source and sink terms in the infinite medium. In the original application of the four-factor formula, which was to well-thermalized media, (ηf) was calculated as the number of fission spectrum neutrons produced per *thermal*-neutron absorption.

In this approach, for a finite reactor, the effective multiplication factor, k_{eff} , typically is evaluated as a product of k_{∞} and an appropriate combination of non-leakage probabilities for the neutrons in the various energy groups. The accuracy of this implicit assumption of the separability of absorption processes and leakage processes depends upon the detailed properties of the reactor medium being studied. There is, however, a more basic difficulty, in the manner in which k_{∞} frequently is determined, namely, by simulating the cascading of neutrons as they slow down from fission-spectrum energies.

The problem is stated in the context of a 3-group diffusion-theory model which is analogous to the physical model of the four-factor formula. Assume that the reactor is a source-free, uniform sphere of radius r_0 , and that the group fluxes all vanish at the surface of this sphere of geometric buckling B^2 . Assume that neutrons are not scattered up from lower energies to higher energies. For much more general conditions, G. Habetler and M. Martino¹ have proved the existence of a positive dominant eigenvalue, λ_0 , for the multigroup system:

$$0 = \nabla \cdot D_j \nabla \phi_j - \Sigma_{rem,j} \phi_j + \sum_{k < j} \Sigma_s^{k \rightarrow j} \phi_k + \lambda \chi_j \sum_k (\nu \Sigma_f)_k \phi_k; \quad (1)$$

$$1 \leq j \leq n,$$

and therefore, in particular, for this 3-group problem. The group fluxes, ϕ_j , are positive inside the sphere and vanish at its surface.

If $\lambda_0 = 1$, the system will be said to be "critical." More generally, whether the system is critical or not, k_{eff} will be defined to be $1/\lambda_0$.

For the case of the bare sphere, the group fluxes are well known. They are of the form

$$\phi_j = A_j \frac{\sin \frac{\pi}{r_0} r}{r},$$

where the functions A_j are constants which depend upon the diffusion theory parameters and upon the flux normalization. The problem of solving for the eigenvalue, λ_0 , therefore may be simplified to the problem of solving for the dominant positive eigenvalue of the system:

$$0 = -[D_j B^2 + \Sigma_{rem,j}] \phi_j(0) + \sum_{k < j} \Sigma_s^{k \rightarrow j} \phi_k(0) + \lambda \chi_j \sum_k (\nu \Sigma_f)_k \phi_k(0); \quad (2)$$

$$1 \leq j \leq 3.$$

In Eq. (2),

$$\Sigma_{rem,j} \equiv \Sigma_{c,j} + \Sigma_{f,j} + \Sigma_{s,l,j}$$

and

$\Sigma_{s,l,j} \equiv$ macroscopic cross section for slowing down into groups ($k > j$) of lower energies.

Equation (2) is the familiar "fundamental-mode" system, and $k_{eff} \equiv 1/\lambda_0$ corresponds to the usual definition of k_{eff} . Clearly, if, in Eq. (2), the $(\nu \Sigma_f)_k$ were replaced uniformly by $(\nu \Sigma_f)'_k \equiv \lambda_0 (\nu \Sigma_f)_k$, the resulting fictional medium would be "critical". In particular, if, in Eq. (2), $\sum_k (\nu \Sigma_f)'_k \phi_k(0)$ were set equal to unity, then the calculated group fluxes, $\phi_k(0)$, would satisfy $1 = \sum_k (\nu \Sigma_f)'_k \phi_k(0)$, and $\phi_k(0) \equiv \phi_k(0)$. Therefore, $k_{eff} = \sum_k (\nu \Sigma_f)'_k \phi_k(0)$. Equivalently, k_{eff} may be determined by formally introducing this unit source density in the actual system, solving for the group fluxes, $\{\phi_k(0)\}_k$, and setting $k_{eff} = \sum_k (\nu \Sigma_f)_k \phi_k(0)$. Indeed, this usually is the method for determining k_{eff} for the fundamental-mode model.

In Eq. (2), the non-fission neutron source events may be grouped either with $\chi_j (\nu \Sigma_f)_k$ or with $\Sigma_s^{k \rightarrow j}$. With the former choice, such processes as $(n, 2n)$ reactions are treated in a manner similar to the treatment of the fission process—and this seems to be a natural thing to do. With the latter choice, $\sum_{k > j} \Sigma_s^{j \rightarrow k}$ is larger than the cross section, $\Sigma_{s,l,j}$, for slowing down out of group j .

The extra "slowing-down" terms are the source contributions, to groups of lower energy, from $(n,2n)$ reactions in group j . In $\Sigma_{remj} \equiv \Sigma_{cj} + \Sigma_{fj} + \Sigma_{slj}$, the term Σ_{cj} includes the $(n,2n)$ capture cross section, $\Sigma_{(n,2n)j}^{(0)}$, minus the $(n,2n)$ source contribution for group j .

Let us solve the 3-group system in detail, to obtain formulas for k_∞ and for k_{eff} . Assume that age-diffusion applies, in the sense that neutron slowing down is entirely from the one group to the next group down, i.e., $\Sigma_s^{j \rightarrow k} = 0$ if $k \neq (j+1)$. Then, with the additional simplifying assumption that $\chi_3 = 0$, Eq. (2) may be solved readily for λ_0 , and, after some algebra, we obtain:

$$k_{eff} = \left\{ \epsilon_{eff} p(\eta f) \left[1 + \frac{(\nu \Sigma_f)_2 / \Sigma_s^{2 \rightarrow 3}}{(\nu \Sigma_f)_3 / \Sigma_{rem3}^*} \right] \right\} L_1^* L_2 L_3. \quad (3)$$

In Eq. (3),

$$\epsilon_{eff} = \left[1 + \frac{\lambda_0 \chi_1 (\nu \Sigma_f)_1 - (1 + \alpha_1) \Sigma_{f1}}{\Sigma_{rem1} - \lambda_0 \chi_1 (\nu \Sigma_f)_1} \right] \cdot \left[\chi_1 + \frac{\chi_2}{p_1 L_1} \right], \quad (4)$$

$$p_j \equiv \frac{\Sigma_s^{j \rightarrow (j+1)}}{\Sigma_{remj}}; \quad p \equiv p_2,$$

$$L_j \equiv \frac{1}{1 + \tau_j B^2}; \quad \tau_j \equiv \frac{D_j}{\Sigma_{remj}},$$

$$L_1^* \equiv \frac{1}{1 + \tau_1^* B^2}; \quad \tau_1^* \equiv \frac{D_1}{\Sigma_{rem1} - \lambda_0 \chi_1 (\nu \Sigma_f)_1}$$

$$\eta f \equiv \frac{(\nu \Sigma_f)_3}{\Sigma_{rem3}},$$

$$\Sigma_{rem3}^* \equiv D_3 B^2 + \Sigma_{rem3}.$$

If the Group-2 fissions are included in the definition of an "effective (ηf) "; a formula of the more familiar type is obtained:

$$k_{eff} = \epsilon_{eff} p(\eta f) L_1^* L_2 L_3, \quad (5)$$

where

$$(\eta f)_{eff} \equiv \frac{(\nu \Sigma_f)_3}{\Sigma_{rem3}} \left[1 + \frac{(\nu \Sigma_f)_2 / \Sigma_s^{2 \rightarrow 3}}{(\nu \Sigma_f)_3 / \Sigma_{rem3}^*} \right], \quad (6)$$

and the other notation is defined above.

As defined, $\epsilon_{eff} L_1^*$ is the total source rate into group 2 if the total rate of production of fission spectrum neutrons from groups 2 and 3 is unity. The product $p L_2$ is the probability that a neutron introduced into group 2 does not capture or leak out while in group 2. The factor $(\eta f)_{eff} L_3$ is the total rate of production of fission spectrum neutrons from groups 2 and 3 if the source rate into group 3 is unity.

Thus, $\epsilon_{eff} L_1^*$ is the generalization of ϵ to the finite, off-critical system. For an infinite, off-critical system, the formula for ϵ becomes [see Eq. (4)]:

$$\epsilon_{eff} = \left[1 + \frac{\lambda_0 \chi_1 (\nu \Sigma_f)_1 - (1 + \alpha_1) \Sigma_{f1}}{\Sigma_{rem1} - \lambda_0 \chi_1 (\nu \Sigma_f)_1} \right] \left[\chi_1 + \frac{\chi_2}{p_1} \right].$$

If $\chi_2 = 0$, this reduces to

$$\epsilon_{eff} = 1 + \frac{\lambda_0 (\nu \Sigma_f)_1 - (1 + \alpha_1) \Sigma_{f1}}{\Sigma_{rem1} - \lambda_0 (\nu \Sigma_f)_1},$$

instead of²

$$\epsilon = 1 + \frac{(\nu \Sigma_f)_1 - (1 + \alpha_1) \Sigma_{f1}}{\Sigma_{rem1} - (\nu \Sigma_f)_1}.$$

The usual derivation of the fast-fission factor, ϵ , from consideration of the cascade processes of fissions and of diffusion in group 1, does not correspond to Eq. (2). Rather, for the case $\chi_2 = 0 = \chi_3$, it corresponds to Eq. (2') with $B^2 = 0$:

$$\left. \begin{aligned} 0 &= -[\Sigma_{rem1} + (\nu \Sigma_f)_1] \phi_1(0) \\ &\quad + \lambda^* \sum_{k=2}^3 (\nu \Sigma_f)_k \phi_k(0), \\ 0 &= -\Sigma_{remj} \phi_j(0) + \Sigma_s^{(j-1) \rightarrow j} \phi_{j-1}(0); \\ &\quad j = 2, 3. \end{aligned} \right\} \quad (2')$$

The resulting definition of k_{eff}^* , as the reciprocal of the dominant positive eigenvalue, λ_0^* , of Eq. (2'), yields $k_{eff}^* \neq k_{eff}$ unless $k_{eff} = 1$. By comparison of Eqs. (2) and (2'), it is clear that: (a) if $\lambda_0 < 1$, then $\lambda_0^* < \lambda_0$; and (b) if $\lambda_0 > 1$, then $\lambda_0^* > \lambda_0$. Equivalently, if the reactor is "subcritical" (i.e., $\lambda_0 > 1$), then $k_{eff}^* < k_{eff}$. If the reactor is "supercritical" (i.e., $\lambda_0 < 1$), then $k_{eff}^* > k_{eff}$. Note that it is k_{eff} which is obtained from the standard multigroup programs (e.g., Argonne's REX program), not k_{eff}^* .

Equation (5) looks like a modified version of the formulation of k_{eff} as a product of k_∞ and group non-leakage probabilities. However, $\lambda_0 = 1/k_{eff}$ appears non-linearly in the formula for ϵ_{eff} , and Eq. (5) defines k_{eff} implicitly, not explicitly. The explicit solution for k_{eff} is obtained readily, but it is not of the form of a single product of terms.

It is significant that the critical system is unambiguously defined as the case where $k_{eff} = 1$. In this case, the modified formula for k_{eff} , Eq. (5), reduces to a standard formula when the approximations otherwise match, e.g., $\chi_1 = 0$, or $(\nu \Sigma_f)_2 = 0$, etcetera. For the case where $k_{eff} \neq 1$, the numerical difference between k_{eff} [as defined by Eq. (5)] and k_{eff} as defined by one of the more familiar formulas may be quite important with respect to the kinetics problem. For $k_{eff} \neq 1$, it is not necessary to adhere to the definition of k_{eff} as the reciprocal of the dominant positive eigenvalue, λ_0 , of Eq. (1). It is important to define the kinetics problem correctly, but this may be done without introducing the concepts of k_{eff} and of the mean prompt neutron lifetime, ℓ . (see Paper No. II-2).

REFERENCES

1. G. J. Habetler and M. A. Martino, *Existence Theorems and Spectral Theory for the Multigroup Diffusion Model*, Proceedings of the Eleventh Symposium in Applied Mathematics of the American Mathematical Society, *Nuclear Reactor Theory*, 1961, pp. 127-139.
2. *Reactor Physics Constants*, ANL-5800 Second Edition (1963), pp. 150-155.

II-2. Remarks on the Definition of k_{eff} for Off-Critical Reactors—II

D. H. SHAFTMAN

RELATIONSHIP BETWEEN DEFINITIONS OF k_{eff} AND THE MEAN PROMPT NEUTRON LIFETIME, ℓ IN MULTIGROUP DIFFUSION THEORY

Modified pseudo-statics formulas for k_{∞} and k_{eff} are developed in Paper No. II-1. With these modifications, the definitions of these terms correspond to the definitions used in the standard programs of multigroup diffusion theory.

Actually, it is a substantive question as to what is meant by a single, time-independent $k_{eff} \neq 1$ unless the time-dependent multigroup equations have dominating solutions which are separable, asymptotically in time, into simple products of functions of space position and energy, and a single function of time. For quite general conditions on the multigroup parameters of one-dimensional systems, G. Habetler and M. Martino¹ have proved asymptotic separability of the solutions of a simplified form of the time-dependent multigroup diffusion equations. The following discussion will be within the context of multigroup diffusion theory for source-free media. It will be assumed that non-trivial solutions exist and that these group fluxes are separable, asymptotically in time. The multigroup parameters are assumed to be constant in time. To simplify the geometric setting of the remarks, it is assumed that the reactor is a bare homogeneous sphere, and that the fluxes all vanish at the outer surface of this sphere. Finally, attention is restricted to a model where all neutrons are emitted promptly.

A. Weinberg and E. Wigner² have derived a time-dependent diffusion equation for one-group theory, a form of the Telegrapher's Equation, which involves a second partial derivative with respect to time. A modification of this equation will be considered wherein only the first partial derivatives appear, in a multigroup version:

$$(1/\bar{v}_j)[\partial\phi_j(\mathbf{r},t)/\partial t] = (\nabla \cdot D_j \nabla - \Sigma_{remj})\phi_j(\mathbf{r},t) + \sum_{k=1}^m \Sigma_{source}^{k \rightarrow j} \phi_k(\mathbf{r},t), \quad (1)$$

$$1 \leq j \leq m.$$

In Eq. (1), \bar{v}_j is an effective velocity of the neutrons

in energy group j (see Ref. 2). The term $\Sigma_{source}^{k \rightarrow j}$ includes all processes which introduce neutrons into group j from group k , other than scatterings within the group.

Let the normalized solutions, $\{\phi_j\}_j$, of Eq. (1) have the asymptotic form $\phi_j(\mathbf{r},t) \approx \psi_j(\mathbf{r})T(t)$. For m -group theory, there are m sets of solutions, $\psi_{jp}(\mathbf{r})T_p(t)$, where $T_p(t) \equiv \exp(-\alpha_p t)$. It is assumed that there exists a real eigenvalue, α_0 , which is algebraically larger than the real part of all other eigenvalues, α_p . (Habetler and Martino have proved that such an α_0 exists, for a wide variety of one-dimensional systems.¹) If this α_0 exists, then an effective multiplication factor, k_{eff} , and a mean prompt neutron lifetime, ℓ , may be defined.

If, with respect to the particular theoretical model or to its particular application, there is no flux component which is asymptotically separable and dominant, it is difficult to see what advantage would be served by introducing a time-dependent k_{eff} and some sort of an average mean lifetime, $\ell(t)$. The space-time problem is described already by Eq. (1), together with pertinent auxiliary conditions. Equation (1) may be solved for the group fluxes, $\phi_j(\mathbf{r},t)$, without interjecting concepts of $k_{eff}(t)$ and $\ell(t)$ —even if a dominant α_0 does exist. However, often it may be psychologically useful to employ the concepts of an importance-weighted rate of production of excess neutrons, $k_{eff} - 1$, and a mean prompt neutron lifetime, ℓ , as assists to physical insight.

For the sphere, of buckling B^2 , substitution of $\psi_j(\mathbf{r})T(t)$ for $\phi_j(\mathbf{r},t)$ in Eq. (1) yields:

$$0 = -[D_j B^2 + \Sigma_{remj} + (\alpha/\bar{v}_j)]\psi_j(0) + \sum_{k=1}^m \Sigma_{source}^{k \rightarrow j} \psi_k(0), \quad 1 \leq j \leq m \quad (2)$$

We may rewrite Eq. (2) in matrix form:

$$(A - \alpha I)\psi = \phi, \quad (3)$$

where I is the $m \times m$ identity matrix and ψ is the flux vector. The matrix A has m characteristic roots: $\alpha_0, \alpha_1, \dots, \alpha_{m-1}$. Note that the value of the real, dominant, simple eigenvalue, α_0 , is not affected by the particular choice of definition of k_{eff} (see Paper No. II-1). The

TABLE II-2-I. TWO-GROUP PARAMETERS FOR THE CORE*
 (Data from Ref. 3)

Parameter	Group 1	Group 2
D , cm	3.2325	2.2140
$\Sigma_c + \Sigma_f$, cm ⁻¹	0.00646	0.00568
$\nu\Sigma_f$, cm ⁻¹	0.01612	0.00976
Σ_s^{1-2} , cm ⁻¹	0.03397	—
χ	0.574	0.426
\bar{v} , cm/sec	2.13×10^9	6.67×10^8

* This core was studied experimentally in the ZPR-III facility of Argonne National Laboratory.

familiar first-order formula relating “ k_{eff} ” and “ ℓ ” and α_0 is $\alpha_0 \approx (k_{eff} - 1)/\ell$. More generally, α_0 is a function of k_{eff} and ℓ , and k_{eff} and ℓ must be defined so as to provide the correct value of α_0 . Also, all “coefficients of reactivity” must be defined so as to be consistent with the definition of k_{eff} . This is not a trivial point, since we are accustomed to working with coefficients of reactivity rather than with “coefficients of asymptotic reactor period”. In the simplified model adopted in the present discussion, the existence of an asymptotic reactor period is assumed. For many reactor operations, the concept of “coefficient of asymptotic reactor period” should be at least as useful as the concept of coefficient of reactivity.

In Paper No. II-1, on modification of the four-factor formula, it was noted that the k_{eff} of multigroup diffusion theory could be defined in more than one way. Let us examine the implications of this ambiguity in the context of two-group theory. It will be assumed that: (1) all fission neutrons are emitted promptly; (2) the fission spectrum distribution is independent of the energy of the neutron causing the fission; (3) there are no processes of neutron multiplication other than fission; and (4) neutrons do not upscatter to groups of higher energy upon a scattering collision.

With these simplifying assumptions, Eq. (2) may be rewritten as:

$$\left. \begin{aligned} 0 &= -[D_1 B^2 + \Sigma_{rem1} - \chi_1(\nu\Sigma_f)_1 + (\alpha/\bar{v}_1)]\psi_1(0) \\ &\quad + \chi_1(\nu\Sigma_f)_2\psi_2(0), \\ 0 &= -[D_2 B^2 + \Sigma_{rem2} - \chi^2(\nu\Sigma_f)_2 + (\alpha/\bar{v}_2)]\psi_2(0) \\ &\quad + [\Sigma_s^{1-2} + \chi_2(\nu\Sigma_f)_1]\psi_1(0). \end{aligned} \right\} (5)$$

In Eq. (5), the terms $[\alpha/\bar{v}_j]\psi_j(0)$ and $[-\chi_j(\nu\Sigma_f)_j]\psi_j(0)$ are treated as effective loss terms, grouping them with the actual loss terms $D_j B^2 \psi_j(0)$ and $\Sigma_{remj} \psi_j(0)$. This treatment corresponds to the grouping of terms in Eq. (2') of Paper No. II-1. From Eq. (5) a first-order solution for α_0 is obtained:

$$\alpha_0 \approx (k_{eff}^* - 1)/\ell^*, \quad (6)$$

where the effective multiplication factor is defined to be:

$$k_{eff}^* \equiv \frac{\chi_1(\nu\Sigma_f)_2}{\Sigma_{R2}} \left[\frac{\Sigma_s^{1-2} + \chi_2(\nu\Sigma_f)_1}{\Sigma_{R1}} \right], \quad (7)$$

and the mean prompt neutron lifetime is defined by:

$$\ell^* \equiv (1/\bar{v}_1 \Sigma_{R1}) + (1/\bar{v}_2 \Sigma_{R2}), \quad (8)$$

with $\Sigma_{Rj} \equiv D_j B^2 + \Sigma_{remj} + \chi_j(\nu\Sigma_f)_j$.

Alternatively, the grouping corresponding to Eq. (2) of Paper No. II-1 may be chosen:

$$\left. \begin{aligned} 0 &= -[D_1 B^2 + \Sigma_{rem1} + (\alpha/\bar{v}_1)]\psi_1(0) \\ &\quad + \chi_1 \sum_{k=1}^2 (\nu\Sigma_f)_k \psi_k(0), \\ 0 &= -[D_2 B^2 + \Sigma_{rem2} + (\alpha/\bar{v}_2)]\psi_2(0) \\ &\quad + \chi_2 \sum_{k=1}^2 (\nu\Sigma_f)_k \psi_k(0) + \Sigma_s^{1-2} \psi_1(0). \end{aligned} \right\} (9)$$

To first order, from Eq. (9) we obtain:

$$\alpha_0 \approx (k_{eff} - 1)/\ell, \quad (10)$$

where

$$k_{eff} \equiv \frac{\chi_1(\nu\Sigma_f)_1}{D_1 B^2 + \Sigma_{rem1}} + \frac{(\nu\Sigma_f)_2}{D_2 B^2 + \Sigma_{rem2}} \left[\chi_2 + \frac{\chi_1 \Sigma_s^{1-2}}{D_1 B^2 + \Sigma_{rem1}} \right], \quad (11)$$

and

$$\ell \equiv \left[1 - \frac{\chi_1(\nu\Sigma_f)_1}{D_1 B^2 + \Sigma_{rem1}} \right] \cdot \left[1 - \frac{\chi_2(\nu\Sigma_f)_2}{D_2 B^2 + \Sigma_{rem2}} \right] \left[\frac{1}{\bar{v}_1 \Sigma_{R1}} + \frac{1}{\bar{v}_2 \Sigma_{R2}} \right], \quad (12)$$

or

$$\ell = \frac{\Sigma_{R1} \Sigma_{R2}}{[\Sigma_{R1} + \chi_1(\nu\Sigma_f)_1][\Sigma_{R2} + \chi_2(\nu\Sigma_f)_2]} \ell^*. \quad (13)$$

If non-fission source reactions occur, e.g., ($n,2n$) events, then an additional ambiguity exists in the definition of k_{eff} . Should these source events be treated in a manner similar to fission source events, or should they be included as additional net slowing down? Of course, the numerical magnitude of k_{eff} is affected. The usual procedure is to treat ($n,2n$) reactions strictly in terms of removal plus additional slowing-down, and this decision is reflected in the definition of ℓ . (see Paper No. II-1.)

In Equations (7) and (8), it has been assumed implicitly that neither Σ_{R1} nor Σ_{R2} vanishes. If one of the Σ_{Rj} vanishes, but not the other, then the right hand side of Eq. (6) exists although the approximation to α_0 might be very poor. In this case, of course, neither Eq. (7) nor Eq. (8) is meaningful, independently. Equation (13) is exact, and it is valid if at least one of the Σ_{Rj} 's differs from zero.

TABLE II-2-II. APPROACH TO CRITICALITY BY VARYING THE BUCKLING

Buckling (B^2), cm^{-2}	k_{eff} [Eq. (11)]	k_{eff} [Eq. (7)]	$\frac{k_{eff}^* - 1}{k_{eff} - 1}$
0.002045	1.0000	1.0000	2.100
0.002036	1.0020	1.0042	2.103
0.001999	1.0100	1.0212	2.116
0.001954	1.0200	1.0427	2.133

If both Σ_{R_i} 's vanish, then Eq. (5) may be solved directly for α_0 , getting:

$$\alpha_0 = \sqrt{[\Sigma_s^{1-2} + \chi_2(\nu\Sigma_f)_1]v_1[\chi_1(\nu\Sigma_f)_2]v_2}. \quad (14)$$

It is assumed that neither Σ_{R_i} vanishes. It is easily shown that the following exact relationship holds:

$$\frac{k_{eff}^* - 1}{k_{eff} - 1} = \frac{\ell^*}{\ell} = \left[\frac{D_1 B^2 + \Sigma_{rem1}}{\Sigma_{R_1}} \right] \left[\frac{D_2 B^2 + \Sigma_{rem2}}{\Sigma_{R_2}} \right] > 1. \quad (15)$$

Thus, if the reactor is not critical and it is made to approach criticality by varying some parameter, e.g., B^2 , then separately $k_{eff} \rightarrow 1$ and $k_{eff}^* \rightarrow 1$, but $(k_{eff}^* - 1)/(k_{eff} - 1)$ may approach a value quite different from unity. It is therefore essential that the definition of

mean prompt neutron lifetime be consistent with the definition of k_{eff} , and this consistency is equivalent to the condition implied by Eq. (10), namely, that

$$\frac{(k_{eff}^* - 1)/\ell}{\alpha_0} \rightarrow 1 \text{ as } k_{eff} \rightarrow 1.$$

Consider the following example of a two-group model for a fast reactor,³ chosen to illustrate the numerical differences in the values of the effective multiplication factor. The two-group parameters for the bare core are listed in Table II-2-I.

The results of an approach to criticality by varying the buckling, B^2 , are shown in Table II-2-II. Note that

$$[(k_{eff}^* - 1)/(k_{eff} - 1)] \approx 2.1,$$

and that this ratio is insensitive to the value of B^2 over the range in question.

REFERENCES

1. G. J. Habetler and M. A. Martino, *Existence Theorems and Spectral Theory for the Multigroup Diffusion Model*, Proceedings of the Eleventh Symposium in Applied Mathematics of the American Mathematical Society: *Nuclear Reactor Theory*, 1961, pp. 127-139.
2. A. M. Weinberg and E. P. Wigner, *The Physical Theory of Neutron Chain Reactors*, (The University of Chicago Press, Chicago, 1958) p. 235.
3. D. Meneghetti, Argonne National Laboratory (Private Communication).

II-3. Use of Depleted Uranium in Thermal Reactors with Slightly Enriched Fuel to Achieve High Neutron Economy and High Burnup¹

H. P. ISKENDERIAN

The use of depleted uranium has been proposed for long-term shim control in EBWR. In the proposed scheme, "D" fuel elements of depleted uranium (0.2% enriched) are distributed in such a manner as to break up local critical zones that could result from the use of 2.7% enriched "E" elements only. This scheme can be compared with a core uniformly enriched to 2.07%. The thermal flux in the "D" elements is relatively high. These elements, by virtue of their geometric positions and high thermal fluxes, have high importance functions. Endowed with this property, the "D" elements make it feasible:

1. Initially, to obtain control of reactivity for a cold shutdown with a minimum of control rods; i.e., minimize use of poison for shim control.

2. To obtain a buildup of reactivity for an appreciable length of reactor operating time, followed by a slow

loss of reactivity due to the buildup of fission products. The buildup of reactivity is possible because of the greater reactivity worth of a Pu-239 or Pu-241 atom in a "D" element with a high importance function than the reactivity worth due to a loss of U-235 or Pu-239 atom in an "E" element. This advantage is largest when the power in the "D" elements is lowest; thus, even though the initial conversion ratio is less than one, an appreciable reactivity gain may be realized. Eventually as power becomes more uniformly distributed the advantage tends to be lost.

Three group reactivity and burnup calculations made on a pressurized core of EBWR size but tighter lattice with H₂O/UO₂ volume ratio of 1.29, and an average initial enrichment of 2.07% have shown that there would be burnup of 14,500 MWd/tonne and 8,500 MWd/tonne in the "E" and "D" elements, re-

spectively, before k_{eff} of the core returned to its initial value.

The maximum to average radial power ratio in the proposed core is at least as good as that in a core having uniform enrichment. This is achieved by careful placement of "D" elements, in which the thermal flux peaks, thus raising the power in neighboring "E" elements located far from the core center.

II-4. Dynamic Analysis of Coolant Circulation in Boiling Nuclear Reactors

C. K. SANATHANAN, J. C. CARTER AND F. MIRALDI*

This paper constitutes an abridged account of a basic study of the dynamics of coolants in boiling reactors.¹ Initially the work applied to water although it may be extended to other coolants. Further developments are described in Paper No. II-5.

The dynamics of two-phase flow through the coolant channels of a natural circulation boiling water nuclear reactor were studied analytically. One-dimensional conservation equations describing the flow through each channel were written in the linearized, perturbed form. A systematic procedure has been developed to approximate the solution of these space-time dependent equations which yield: (1) the transient void distribution along a coolant channel and (2) an understanding of the hydrodynamic stability. Having (1), it is then possible to estimate the void contribution to the feedback reactivity for a given reactivity worth distribution. This is not attempted in this paper, however.

One of the dependent variables $\Delta\alpha(z,t)$, the perturbed portion of the void fraction, was expressed as:

$$\Delta\alpha(z,t) = b_0(t)P_0(z) + b_1(t)P_1(z) + b_2(t)P_2(z) + \dots,$$

where the coefficients b_0, b_1, \dots , are unknown functions of time only and P_0, P_1, \dots , are orthogonal functions of the space variable z . Similar expressions were used for the other dependent variables. The nature of the problem and the boundary conditions suggested the use of Legendre polynomials for the above series expansion. The coefficients b_0, b_1, \dots , were obtained by substituting the series expansions of the unknown variables into the conservation equations and applying orthogonality conditions. This method of series approximation of the solution is useful only if the series converges fast enough for practical application. Further, one may note that it is necessary that the so-

The conclusion thus reached is that the suggested use of intermixed depleted and enriched fuel elements is of potential value for advanced converter water reactors.

REFERENCE

1. H. P. Iskenderian, *Use of Depleted Uranium in Thermal Reactors With Slightly Enriched Fuel to Achieve High Neutron Economy and High Burnup*, ANL-6843 (1964).

lution converge in both space and time. An absolute proof of convergence is not available at the present time. However, a detailed demonstration of convergence in both space and time has been made for a typical problem.¹

Laplace transformation of the equations in time en-

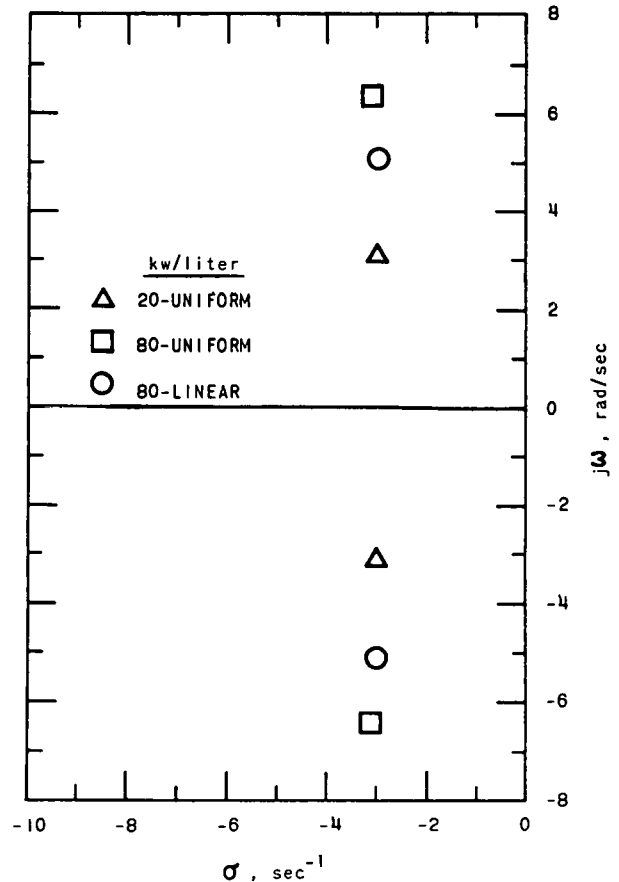


FIG. II-4-1. Variation of Major Pole Locations With Channel Heat Flux.

* Case Institute of Technology, Cleveland, Ohio.

ables one to write transfer functions such as that between $\Delta V_f(z,t)$ and $\Delta \phi(z,t)$, the perturbed portions of the liquid velocity and the channel heat flux respectively, and thus to investigate the hydrodynamic stability.

It was found that the solution may be oscillatory both in time and space, and that the stability depends largely upon the nature of the steady state profile of the heat flux along the channel. The locations of the major pole positions which dictate the flow dynamics of a channel (length 4 ft and diameter 1 in.) corresponding to three different heat flux profiles are illustrated in Fig. II-4-1. Since the real parts of the poles are negative, all three cases are stable in the absolute sense. However, the angular position with respect to the origin indicates that the 20 kW/liter channel with uniform heat distribution is relatively more stable than the other two. Similarly, the linear heat distribution case is relatively more stable than the uniform case for equal power density.

Many complementary problems were also investigated. For the same steady state distribution of void fraction and velocity, it was demonstrated that the longer the channel, the more oscillatory the transient flow in it would be.

It has been observed in the past that the introduc-

tion of a constriction at the inlet to a channel, in order to increase the inlet pressure drop, tends to stabilize the flow. A theoretical verification of this was made. Further, it was shown that the acceleration pressure drop in the downcomer also stabilizes the flow. Increased acceleration pressure drop in the downcomer may be achieved by increasing its length or by reducing its cross sectional area, or both. An experimental confirmation of this predicted effect is not yet reported in the literature.

The study of the parallel channel system led to the conclusion that in the case of a natural circulation boiling water power reactor one may neglect the coupling between the channels and treat the stability of each channel individually. This is possible because in a reactor of usual design, the cross sectional area of the downcomer is large and its length is nearly equal to that of the channels; consequently, the acceleration and friction pressure drops in the downcomer are negligible.

It may be noted that the analytical techniques developed during this study are applicable to both natural and forced circulation systems.

REFERENCE

1. C. K. Sanathanan, *Dynamic Analysis of Coolant Circulation in Boiling Water Nuclear Reactors*, ANL-6847, (1964).

II-5. Further Developments in Dynamic Analysis of Coolant Circulation in Boiling Water Nuclear Reactors

C. K. SANATHANAN

This paper recounts results of further developments on the theme of Paper No. II-4. This work may also be extended to other coolants.

In a boiler or a boiling water reactor, the makeup water introduced is usually below saturation temperature. Consequently, boiling does not occur immediately at the inlet to the heated channels. It has been found possible to dispense with the simplifying assumption made in work reported in Paper No. II-4; namely, that the inlet water is at saturation temperature.

A more realistic system is considered in which the inlet subcooling is constant. The earlier analytical method¹ cannot be applied directly to a system in which subcooling is not negligible. This is so because the boundary condition that the void fraction is zero just at the inlet at all times is insufficient. It is, in fact, zero in the entire nonboiling portion of the channel. Further, in the latter case, the boiling length becomes a function

of time during transients and hence introduces another unknown quantity into the conservation equations.

The following is a brief illustration of the method used to consider the more general case of coolant circulation in boiling reactors, including subcooling.

The equations describing the space-time dependent flow through a channel written in accordance with the principles of conservation of mass and energy are:†

$$(\partial \bar{\rho}^* / \partial t) + (\partial G^* / \partial z) = 0, \quad (1)$$

$$\frac{\partial}{\partial t} (\bar{\rho}^* \bar{H}^*) + \frac{\partial}{\partial z} (G^* H^*) = \Phi^*, \quad (2)$$

where the dependent variable $\rho^*(z,t)$ is the volume weighted mean density, $\bar{H}^*(z,t)$ is the volume weighted mean enthalpy, $H^*(z,t)$ is the flow weighted or mixing

† See Ref. 2 for a detailed derivation of these equations and the quantitative definitions of the dependent variables.

cup enthalpy, G^* is the mass flow rate in the positive z direction (upwards), and $\Phi^*(z,t)$ is the heat flux per unit length of the channel.

There are two boundary conditions:

1. In the case of a natural circulation reactor, the sum of the pressure drops around a closed hydraulic loop consisting of the channel, its inlet, its outlet and the downcomer is zero.

In the case of a forced circulation system, it is reasonable to consider that the sum of the pressure drops along the channel, at the inlet and at the exit is a constant (i.e., there is no downcomer).

2. $H^*(0,t)$ is a constant, since it is assumed that the inlet subcooling is constant.

In Eqs. (1) and (2) it is noted that there are two different enthalpy terms; namely, \bar{H}^* and H^* . They are different because of the presence of slip flow.

The obvious difficulty in solving Eqs. (1) and (2) is that there are too many dependent variables.

A reasonable way to reduce the number of dependent variables is suggested by J. E. Meyer.² It is assumed that \bar{p}^* and \bar{H}^* are functions of H^* only, and that these functional relations are known through suitable experiments. In other words, one may evaluate \bar{p}^* and \bar{H}^* solely from the knowledge of H^* . The implication of this assumption is that during transients, the slip ratio is not a function of time. This was explicitly assumed in the previous formulation, outlined in Paper II-4 (see also Ref. 1).

It is further assumed that all fluid properties correspond to a certain reference pressure. Consequently, given $\Phi^*(z,t)$, there remains only $G^*(z,t)$ and $H^*(z,t)$ to be determined in Eqs. (1) and (2). An analytic solution to these nonlinear equations is found to be impossible. However, it is felt that the solution to their linearized perturbed form would be adequate to understand the transient behavior of the flow for small changes in the heat flux, and the stability in the neighborhood of a known steady operating condition.

Each of the dependent variables is expressed as a sum of its steady state part and its perturbation. For example,

$$G^*(z,t) = G(z) + \Delta G(z,t). \quad (3)$$

Substituting the form given in Eq. (3) for the dependent variables in Eqs. (1) and (2), and eliminating the steady state part and terms with the second or higher degree for the perturbations one may write:

$$\left(\frac{\partial \bar{p}}{\partial \bar{H}}\right) \frac{\partial \Delta H}{\partial t} + \frac{\partial \Delta G}{\partial z} = 0, \quad (4)$$

$$\left[\bar{p} \frac{d\bar{H}}{dH} + (\bar{H} - H) \frac{d\bar{p}}{dH}\right] \frac{\partial \Delta H}{\partial t} + G \frac{\partial \Delta H}{\partial z} + \frac{dH}{dz} \Delta G = \Delta \Phi. \quad (5)$$

Note that the quantities in parenthesis in the left hand side of Eqs. (4) and (5) are known functions of H , and hence known functions of z . It is assumed that $\Delta \Phi(z,t)$ is a product of a known function of time and a known function of space.

It is the object of this paper to solve for ΔH and ΔG in Eqs. (4) and (5) analytically.

The two boundary conditions now are:

1. In the case of a natural circulation reactor, the sum of the perturbed pressure drops around a closed hydraulic loop consisting of the channel, its inlet, its outlet and the downcomer, is zero.

In the case of forced circulation systems, one equates the sum of the perturbed pressure drops in the channel, at the inlet, and at the exit, to zero (i.e., there is no downcomer).

2. Since it is assumed that subcooling is constant the perturbation in the mixing cup enthalpy at the inlet is equal to zero for all t :

$$\Delta H(0,t) = 0.$$

A series approximation of the quantities ΔH and ΔG is utilized. For example, ΔH is expressed as follows:

$$\Delta H(z,t) = h_0(t)P_0(z) + h_1(t)P_1(z) + h_2(t)P_2(z) + \dots, \quad (6)$$

where the coefficients h_0, h_1, h_2, \dots , are unknown functions of time only, and P_0, P_1, P_2, \dots , are orthogonal functions of the variable z . An analogous expression is also written for ΔG . The unknown coefficients in the expressions for ΔH and ΔG may be evaluated using earlier techniques,¹ namely, by applying the boundary and the orthogonality conditions. It is found that the series expansion given by Eq. (3) converges rapidly.

If the time dependence of $\Delta \Phi$ is kept arbitrary, say $c(t)$, one may evaluate the transfer functions, such as $[h_0(s)/c(s)]$, $[h_1(s)/c(s)]$, where s is the Laplace transform variable. The transfer functions are used to investigate stability.

Subcooled boiling is also considered in this study. It is assumed that subcooled boiling results in a certain change in the coolant density, enthalpy, etc., and the appropriate steady state z -variations of these quantities are used in the conservation equations.

It is found in general that subcooling does improve the system stability. This is in agreement with previous experimental observations, such as those for EBWR.³

REFERENCES

1. C. K. Sanathanan, *Dynamic Analysis of Coolant Circulation in Boiling Water Nuclear Reactors*, ANL-6847 (1964).
2. J. E. Meyer, *Conservation Laws in One-Dimensional Hydrodynamics*, Bettis Technical Review (September, 1960).
3. EBWR Test Reports, compiled by V. M. Kolba, ANL-6229 (1960).

II-6. Space Dependent Kinetics of Boiling Reactors

C. K. SANATHANAN

A need has arisen to develop methods of arriving at a good understanding of the transient behavior of boiling reactors. It has been recognized in the past that the classical method of obtaining a solution to the kinetic equations of a reactor by separating the time and space variables and assuming the nuclear parameters to be space independent is erroneous, particularly in the case of the boiling reactor. The nuclear parameters are strongly space dependent due to considerable variations in the coolant density throughout the core.

A rigorous dynamic analysis of such systems must include the simultaneous solution of the space dependent neutron kinetic equations along with the space-time dependent conservation equations of mass, energy and momentum of the coolant flow through the heated channels in the core. Since the equations are highly nonlinear, their analytical solution necessarily becomes cumbersome. Consequently, it is necessary to resort to use of digital computers,¹ rather than to seek closed analytical solutions which invariably demand oversimplification of the problem.

However, for the purposes of understanding the stability and the transient behavior of the system in the neighborhood of a known steady operating condition, one may resort to the analytic solution of the linearized perturbed form of the kinetic equations. In attempting to do this here, the usual simplifying assumption of the knowledge of the reactor thermal power distribution during transients is not made, in view of the strong coupling between the neutron flux and the coolant thermal energy.

In many boiling reactors, the only significant spatial dynamic effects are those associated with the coolant along the axial dimension of the reactor, the other two dimensions being assigned point model properties. Hence, the kinetic equations are solved as a set of two-dimensional partial differential equations in the distance along the core axis and in time. Only the one group diffusion model for the neutrons is considered in the analysis presented here. This is done merely to simplify the algebra so that the new mathematical techniques can be clearly illustrated.

GENERAL APPROACH TO THE PROBLEM

The neutron kinetics equations in two-dimensional form (length z along the core axis and time) are written as follows:

$$D \frac{\partial^2 \Psi}{\partial z^2} - \Sigma_a \Psi + S_1 + \lambda C = \frac{1}{v} \frac{\partial \Psi}{\partial t}, \quad (1)$$

$$-\lambda C + S_2 = \frac{\partial C}{\partial t},$$

where Ψ is the neutron flux, C is the precursor concentration, and S_1 and S_2 are suitable source terms for neutron flux and the precursor. S_1 and S_2 depend upon the void fraction in the core and are expressed approximately as follows:

$$S_1 = (1 - \beta)F_1(\alpha)\Psi, \quad (2)$$

$$S_2 = \beta F_1(\alpha)\Psi,$$

where α is the steam void fraction, β the fraction of the fission neutrons that are delayed, and $F_1(\alpha)$ is a known function of α .

In Eq. (1), D and Σ_a are assumed to be known functions of α and $(\partial D/\partial z)$ to be negligible. Perturbing Eq. (1), removing the steady state portion and retaining only the linear part of the perturbed quantities, one obtains:

$$D(\alpha_0) \frac{\partial^2 \Delta \Psi}{\partial z^2} - \Sigma_a(\alpha_0) - (1 - \beta)F_1(\alpha_0)\Delta \Psi$$

$$+ (1 - \beta)\delta_1 \Delta \alpha \Psi_0 + \lambda \Delta C - \Delta \Sigma_a \Psi_0 = \frac{1}{v} \frac{\partial \Delta \Psi}{\partial t}, \quad (3)$$

$$-\lambda \Delta C + \beta F_1(\alpha_0)\Delta \Psi - \delta_1 \beta \Psi_0 \Delta \alpha = \frac{\partial \Delta C}{\partial t},$$

where the subscript $_0$ indicates steady state quantities and $\Delta \Psi$, ΔC , and $\Delta \alpha$ are perturbations in Ψ , C , and α respectively. $\delta_1 \Delta \alpha$ is the linear term in the expansion of $F_1(\alpha_0 + \Delta \alpha)$ around α_0 .

Following are the boundary conditions:

$$\Delta \Psi(0,t) = \Delta \Psi(L,t) = 0 \quad \text{for all } t,$$

$$\Delta C(0,t) = \Delta C(L,t) = 0 \quad \text{for all } t,$$

$$\Delta \Psi(z,0) = \Delta C(z,0) = 0 \quad \text{for all } z.$$

$L \equiv$ Length of the channel.

In Eq. (3), $\Delta \Sigma_a$ is expressed as

$$\Delta \Sigma_a = \Delta \Sigma_{a_1} + \Delta \Sigma_{a_2}, \quad (4)$$

where $\Delta \Sigma_{a_1}$ is due to fluctuations in the void fraction, and $\Delta \Sigma_{a_2}$ is due to external (arbitrary) addition or withdrawal of poison. $\Delta \Sigma_{a_1}$ is considered as a linear function of $\Delta \alpha$. $\Delta \Sigma_{a_2}$ is assumed to be of the form $f_1(z)f_2(t)$ where f_1 and f_2 are known functions.

The problem is to solve for $\Delta \Psi(z,t)$ and $\Delta C(z,t)$ in

Eq. (3), given $\Delta\Sigma_{a_2}(z,t)$. To accomplish this, it is necessary that $\Delta\alpha(z,t)$ be known.

For any perturbation $\Delta\Psi$ in neutron flux, there is a corresponding perturbation in the heat flux in the reactor. With a time lag characteristic of the fuel element, cladding and coolant thermophysical properties, this heat enters the coolant channels, and a corresponding perturbation in the void fraction, $\Delta\alpha$, along each channel is produced. $\Delta\alpha(z,t)$ is determined by the conservation equations that dictate the two phase flow through the coolant channels.

Many attempts^{2,3,4,5} have been made in the past to obtain a suitable relationship between $\Delta\alpha(z,t)$ and $\Delta\Psi(z,t)$. All except the numerical approaches have some oversimplifying assumptions with regard to the space-time dependence of $\Delta\alpha$, and therefore the results from these are not reliable. In the present study the oversimplifications with respect to the space or time dependence of $\Delta\alpha$ during small transients have been successfully dispensed with.

INTRODUCTION TO THE PRESENT METHOD

The dependent variables $\Delta\Psi$ and ΔC of Eq. (3) are expressed as a series of orthogonal functions. For example,

$$\Delta\Psi(z,t) = \theta_0(t)P_0(z) + \theta_1(t)P_1(z) + \theta_2(t)P_2(z) + \dots, \quad (5)$$

where the coefficients $\theta_0, \theta_1, \theta_2, \dots$, are unknown functions of time only, and P_0, P_1, P_2, \dots , are orthogonal functions of variable z . A similar expression for ΔC may also be written. The problem is solved if the coefficients of the series expansion are determined.

The coefficients $\theta_0, \theta_1, \theta_2, \dots$, are determined by substituting the series expansions for $\Delta\Psi$ and ΔC in Eq. (3) and applying the suitable boundary and orthogonality conditions. But, before proceeding to do this the effect on the nuclear parameters due to the neutron flux perturbation must be known. It is assumed that the nuclear parameters are primarily affected by the local transient void formation. This implies that a suitable relation between $\Delta\Psi$ and $\Delta\alpha$ must be established. Note that the temperature changes are considered small enough that they do not affect these parameters.

The heat flux $\Delta\phi(z,t)$ corresponding to $\Delta\Psi$ may be expressed as follows:

$$\Delta\phi(z,s) = \frac{F_2(z)}{1 + sT} [\theta_0(s) + \theta_1(s)P_1(z) + \theta_2(s)P_2(z) + \dots], \quad (6)$$

where s is the Laplace transform variable in the place of t , $F_2(z)$ is a space dependent function to convert the neutron flux to the equivalent heat flux, and T is the time delay before this heat enters the coolant channels. More complicated forms for the time delay may be necessary in some cases.

Each term on the right hand side of Eq. (6) is of the form $C_k(s)P_k(z)$. The author has developed a method⁶ of obtaining $\Delta\alpha(z,s)$ corresponding to a heat flux perturbation along a channel in the above form. In doing so, no simplifying assumption is made with respect to the space or time dependence of $\Delta\alpha$ as was done in earlier works. The perturbations in the void fraction due to each of the terms $C_k(s)P_k(z)$ of the perturbation in the heat flux in Eq. (6) may be added together to obtain the total perturbation $\Delta\alpha(z,s)$ due to $\Delta\Psi$.

Since it is assumed that the nuclear parameters are linear functions of $\Delta\alpha$, they may now be expressed as linear functions of $\Delta\Psi$ by the above procedure. It is thus that the feedback in the boiling reactors is taken into consideration in the present approach.

Equation (3) now contains only the unknown coefficients of expansion of $\Delta\Psi$ and ΔC . These coefficients may be evaluated by the orthogonality conditions and the existing boundary conditions.

Attempt is being made to apply the above techniques to specific problems, and thereby obtain a better understanding of the space-time behavior of the neutron flux in a boiling reactor.

REFERENCES

1. A. N. Nahavandi and R. F. von Hollen, *A Digital Computer Solution for Space Dependent Neutron Kinetics Equations*, Nucl. Sci. Eng. **18**, No. 3, 335-350, (1964).
2. J. E. Meyer and R. P. Rose, *Application of Momentum Integral Model to the Study of Parallel Channel Boiling Flow Oscillations*, Trans. ASME, Ser C: J. Heat Transfer **85**, (February 1963).
3. E. R. Quandt, *Analysis and Measurement of Flow Oscillations*, Chem. Eng. Progr. Symp. Ser. Heat Transfer, Buffalo **57**, No. 32, (1961).
4. J. A. Fleck, Jr., *The Dynamic Behavior of Boiling Water Reactors*, J. Nucl. Energy: Pt. A **11**, (1960).
5. G. B. Wallis and J. H. Heasley, *Oscillations in Two Phase Flow Systems*, Trans. ASME, Ser C: J. Heat Transfer **83**, (1961).
6. C. K. Sanathanan, *Dynamic Analysis of Coolant Circulation in Boiling Water Nuclear Reactors*, ANL-6847 (1964).

II-7. High Conversion Critical Experiment

A. R. BOYNTON, Q. L. BAIRD, J. M. CHRISTENSON, K. E. PLUMLEE, W. C. REDMAN, W. R. ROBINSON
and G. S. STANFORD

INTRODUCTION

Reactors with high conversion coefficients to allow high burnup are expected to become increasingly important in the utilization of nuclear energy. The current High Conversion Critical Experiment Program (Hi-C) was undertaken to extend the range of investigations with light water-moderated, slightly enriched, uranium oxide cores. The program takes its name from the fact that as the moderator fraction is decreased, the conversion ratio goes through a maximum for any given size or enrichment. Although no specific reactor design is planned from these investigations, they are of interest for several reasons. For example, the undermoderated condition is not unlike the situation existing in a boiling water reactor, and so this information should be of use in understanding the reactor physics of boiling systems.

Previously, few studies of uranium-water systems have extended into the range of H to U-238 atom ratios covered in the Hi-C investigations. Systems having H:28 atom ratios from 5 to as low as 1 have been assembled. These H:28 ratios correspond to water-to-UO₂ volume ratios ranging from 1.7 to 0.3.

The fuel used in the Hi-C cores was 3.04 w/o enriched uranium in the form of UO₂ pellets loaded in either stainless steel or aluminum cladding tubes. In addition, the boiling zone fuel for BORAX-V was available for a short time and studies with H:28 atom ratios from 5 to 3 were done with it. This fuel was 4.95 w/o enriched UO₂ pellets in stainless steel cladding tubes. The details of the fuels and claddings are given in Table II-7-I.

The several H to U-238 atom ratios were obtained by using square and triangular grids of various pitches. In addition, some loadings were done with fuel pins removed in a uniform pattern. The loading in which every ninth fuel pin is removed is referred to as the 8/9 loading, the loading in which every sixth fuel pin is removed is referred to as the 5/6 loading, etc. A description of the different cores is given in Table II-7-II. Because of a finite fuel supply several of the cores were not critical with a uniform loading and required a feeder zone of a higher H:28 ratio for criticality. Some stainless steel cores were composed of a central zone of stainless steel clad fuel pins located inside an annulus of aluminum clad pins with a uniform lattice throughout. About 400 stainless steel clad pins were normally used, resulting in a central zone about 12-14 cm in

radius. All cores were cylindrical unless noted otherwise.

The Hi-C program is being conducted in the ZPR-VII Critical Facility^{1,2} at Argonne. Figure II-7-1 shows core No. 11 loaded in the ZPR-VII tank.

TABLE II-7-I. HI-C AND BORAX-V FUEL AND CLADDING DESCRIPTION

	BORAX-V	Hi-C	
<i>Fuel:</i>			
Enrichment, w/o	4.95	3.04	
Diameter, cm	0.871	0.935	
Length, cm	61	122	
Oxide density, g/cc	10.2	10.17	
<i>Cladding:</i>			
Type	304 SS	6061-T6 Al	304 SS
Inner diameter, cm	0.879	0.962	0.958
Outer diameter, cm	0.955	1.058	1.057
Wall thickness, cm	0.0381	0.048	0.0496

TABLE II-7-II. HI-C AND BORAX-V CORE DESCRIPTIONS

Core No.	Lattice Pitch, cm	Type	H:28
<i>BORAX V Fuel</i>			
1	1.27 square	Uniform SS clad	4.65
2	1.27 triangular	Uniform SS clad	3.53
<i>Hi-C Fuel</i>			
3	1.27 square ^a	—	3.24
4	1.24 square	3/4 loading SS clad	5.16
5	1.24 square	7/8 loading SS clad	3.90
6	1.24 square	Uniform SS clad	2.93
7	1.24 square	Uniform SS zone	2.93
8	1.24 square	Uniform Al clad	2.93
9	1.27 triangular	Uniform Al clad	2.30
10	1.27 triangular	Uniform SS zone	2.30
11	1.166 triangular	Uniform Al clad	1.33
12	1.166 triangular	Uniform SS zone ^b	1.33
13	1.127 triangular	5/6 loading Al clad	1.96
14	1.127 triangular	8/9 loading Al clad	1.60
15	1.127 triangular	11/12 loading Al clad	1.43
16	1.127 triangular	15/16 loading Al clad ^c	1.31
17	1.127 triangular	Uniform SS zone ^b	0.99
18	1.127 triangular	Uniform Al zone ^b	0.99

^a This core refers to measurements in the peripheral zone of the superheater critical experiment.

^b These cores required an outer feeder zone of higher H:28 ratio for criticality.

^c This core was rectangular.

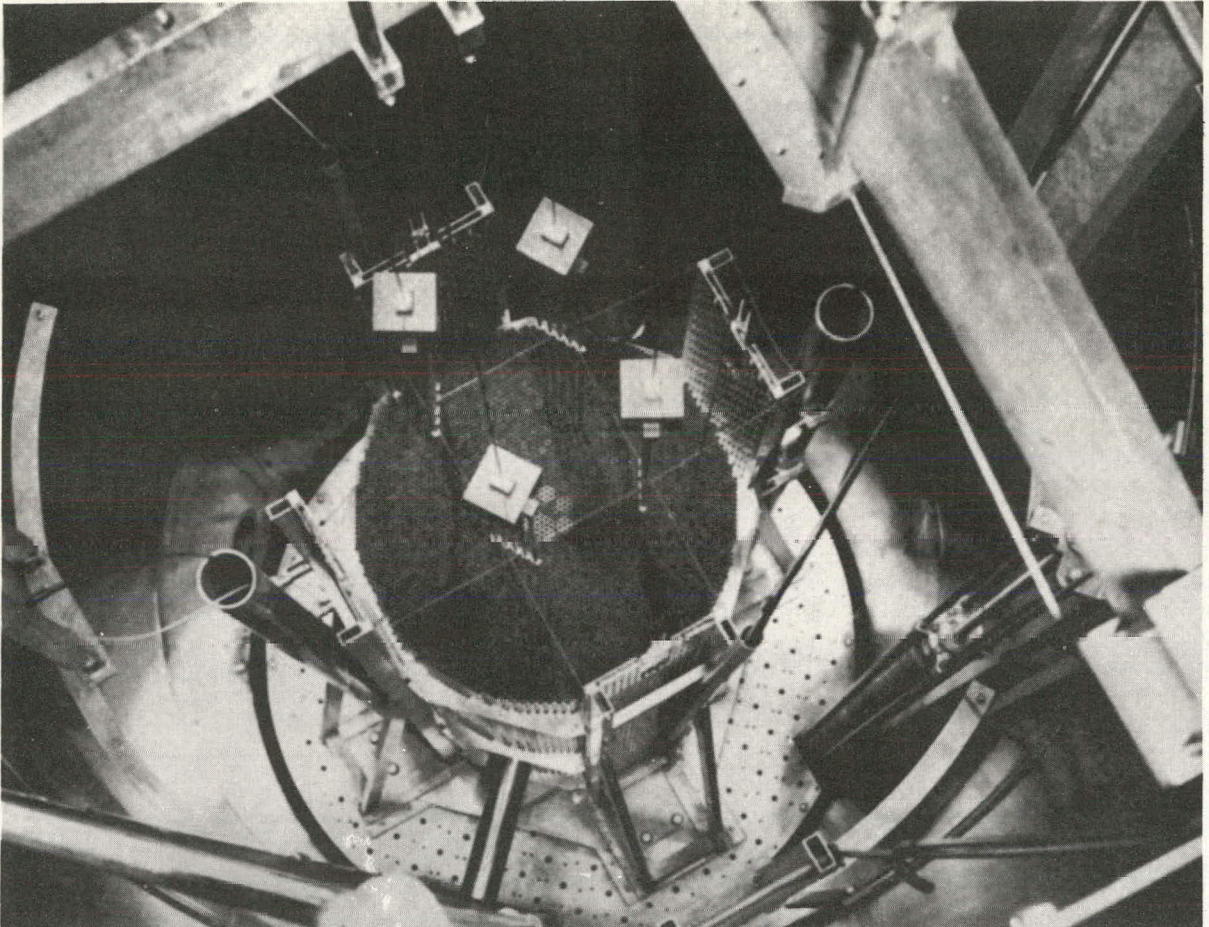


FIG. 11-7-1. Hi-C Core in ZPR-VII Critical Facility.

For each of the cores, measurements related to control and safety must of necessity be done. These include: control rod worth, reactivity worth of the top reflector, reactivity worth of various poisons added during measurements, such as cadmium foil covers, and the reactivity worth of in-core and peripheral fuel pins. In each of the non-zoned cores measurements of critical masses, bucklings, and cadmium ratios were made. In some cores the temperature coefficient of reactivity was determined. In each of the uniform and zoned stainless steel clad cores the initial conversion ratio was measured as well as the following other microparameters: thermal disadvantage factors, U-238 to U-235 fission ratios, and cadmium ratios for U-235 fission and U-238 capture. The results of many of these measurements have been reported.^{3,4} In these reports preliminary comparisons of the experimental results with theory have been made. The study by J. Bengston and R. Hellens⁵ has been used for theoretical compari-

son. Their computations (for unclad oxide rods) were made utilizing MUFT-IV and SOFOCATE to generate constants for three fast groups and one thermal group. While considerable disagreement was found between experimental and calculated bucklings, the calculated microparameters, such as the initial conversion ratio, appear to be in reasonable agreement with the experimental values within the range of H:28 ratios reported. Whether this agreement will exist at still lower H:28 ratios will be determined in future experiments.

A description of the parameter measurements made to date follows.

BUCKLINGS AND CRITICAL MASSES

Axial and radial relative activation distributions were measured in the various cores with two or more of the following foil materials: 0.21 w/o uranium, highly enriched uranium-aluminum alloy, dysprosium-aluminum alloy, gold, lutetium-aluminum alloy, and

manganese. Both bare (aluminum-covered) and cadmium-covered irradiations were made with the various materials.

The traverses were made by sandwiching the foils between fuel pellets in specially slotted fuel pins.

The value of the critical buckling was obtained from the clean critical core size and cosine and Bessel function fits of the axial and radial activation traverses. It was found in fitting the radial distributions that the flux was not influenced by the reflector to about 55-60% of the extrapolated dimension. In the axial direction it extended to 70%. The criterion used for this determination was constancy of the extrapolated dimension with reduction of the radius or length for which data were used in the fitting. This test was done in all of the uniform cores (Nos. 1, 2, 6, 8, 9, and 11). Critical masses and critical core sizes were determined for control-rod free, fully reflected, cylindrical cores. These values were obtained by evaluating the reactivity worth of peripheral and in-core fuel pins in a core of known loading and known excess reactivity. The results of these bucklings and critical parameters are seen in Table II-7-III. In addition, plots of critical mass and critical buckling versus H to U-238 atom ratio are seen in Figs. II-7-2 and II-7-3.

INITIAL CONVERSION RATIO (ICR)

The ICR is the ratio of the Pu-239 production rate to the U-235 destruction rate in a fresh core. It was measured by comparing the relative activity of foils irradiated in the Hi-C fuel to the activity of foils irradiated simultaneously in a reference thermal spectrum.^{6,7} For this spectrum the relative activity can be calculated using the Westcott formulation.⁸ The ICR was computed from

$$ICR = \frac{N^{28}}{N^{25}} \left(\frac{P}{R} \right) \left(\frac{\sigma_{c,thermal}^{238}}{\sigma_{f,thermal}^{235}} \right) \left(\frac{1}{1 + \alpha^{25}} \right). \quad (1)$$

Here, N^{28} and N^{25} are the atom densities for the fuel, the cross sections are the effective values for the thermal column spectrum and α^{25} is the average capture-to-fission ratio in the Hi-C spectrum. P is the ratio of the relative plutonium production in a foil irradiated in the Hi-C fuel to the relative plutonium production in a foil irradiated in the thermal column. R is the ratio of the U-235 fission of a foil irradiated in the Hi-C fuel to the U-235 fission of a foil irradiated in the thermal column.

Uranium metal foils, of various enrichments (usually 0.21 and 3.23 w/o) and the same diameter as the fuel pellets, were irradiated in the fuel pins in flux-symmetric positions. Similar foils were placed in the thermal column of the Argonne Thermal Source Reactor (ATSR) and both sets of foils irradiated simultaneously.

The relative amount of Pu-239 produced in the foils

TABLE II-7-III. CRITICAL PARAMETERS FOR CYLINDRICAL LOADINGS OF HI-C AND BORAX-V CORES

Core No.	1	2	4	5	6	8	9	11	13	14	15	16
H to U-238 atom ratio	4.65	3.53	5.16	3.90	2.93	2.93	2.93	1.330	1.96	1.60	1.43	1.31
Peripheral fuel pin worth, % (Δk/k)/pin	0.028	—	—	—	0.0070	0.0168	0.0112	0.00161	0.00858	—	0.00275	0.0011
In-core pin worth, % (Δk/k)/pin	—	—	—	—	-0.020	-0.0480	-0.0108	-0.0292	-0.0406	—	-0.017	-0.0137
Clean critical number of fuel pins	647 ± 2	967 ± 3	769 ± 1	1093 ± 1	1766 ± 6	950 ± 1	1417 ± 3	5091 ± 13	1862 ± 3	2788 ± 15	3680 ± 18	4618 ± 118 ^a
Clean critical loading, kg of U-235	10.45 ± 0.03	15.63 ± 0.05	17.60 ± 0.02	25.02 ± 0.02	40.42 ± 0.14	21.75 ± 0.02	32.44 ± 0.07	115.69 ± 0.29	42.82 ± 0.07	63.82 ± 0.34	85.92 ± 0.40	105.04 ± 2.68 ^a
Critical radius, cm	18.18 ± 0.05	20.74 ± 0.06	22.40 ± 0.02	24.73 ± 0.02	29.40 ± 0.09	21.56 ± 0.02	25.10 ± 0.03	43.68 ± 0.01	27.96 ± 0.02	33.15 ± 0.09	37.49 ± 0.09	41.53 ± 0.53 ^a
Effective unit cell radius, cm	0.7149	0.6653	0.8078	0.7479	0.6996	0.6996	0.6668	0.6122	0.6479	0.6278	0.6181	0.6113
Radial reflector savings, cm	7.35 ± 0.27	7.55 ± 0.10	6.58 ± 0.06	7.26 ± 0.11	7.69 ± 0.08	8.13 ± 0.16	8.77 ± 0.17	10.73 ± 0.14	8.86 ± 0.40	—	10.67 ± 0.40	10.78 ± 0.50 ^a
Extrapolated radius, cm	25.53 ± 0.27	28.29 ± 0.12	28.98 ± 0.06	31.99 ± 0.11	37.09 ± 0.12	29.69 ± 0.16	33.87 ± 0.08	54.41 ± 0.14	36.82 ± 0.40	—	48.16 ± 0.41	52.31 ± 0.79
Radial buckling, cm ⁻¹ × 10 ⁴	88.74 ± 1.80	72.27 ± 0.62	68.87 ± 0.29	56.52 ± 0.30	42.04 ± 0.27	65.61 ± 0.71	50.42 ± 0.24	19.54 ± 0.10	42.66 ± 0.93	31.20 ± 0.74	24.94 ± 0.42	21.13 ± 0.13 ^a
Axial reflector savings, cm	11.32 ± 0.50	10.74 ± 0.50	13.28 ± 0.49	12. ± 0.45	12.89 ± 0.27	16.52 ± 0.31	19.11 ± 0.18	21.17 ± 0.19	18.03 ± 0.50	—	22.70 ± 0.50	21.78 ± 0.50
Extrapolated height, cm	72.28 ± 0.50	71.70 ± 0.50	135.20 ± 0.49	134.30 ± 0.45	134.81 ± 0.27	138.44 ± 0.31	141.03 ± 0.18	143.09 ± 0.19	139.95 ± 0.50	—	144.62 ± 0.50	143.70 ± 0.50
Axial buckling, cm ⁻¹ × 10 ⁴	18.89 ± 0.26	19.20 ± 0.27	5.40 ± 0.04	5.47 ± 0.04	5.43 ± 0.02	5.15 ± 0.02	4.96 ± 0.01	4.82 ± 0.01	5.04 ± 0.04	4.80 ± 0.07	4.72 ± 0.03	4.78 ± 0.03
Buckling, cm ⁻¹ × 10 ⁴	107.63 ± 1.90	91.47 ± 0.68	74.27 ± 0.29	61.99 ± 0.39	47.47 ± 0.27	70.76 ± 0.71	55.38 ± 0.24	24.36 ± 0.10	47.70 ± 0.93	36.00 ± 0.74	29.66 ± 0.42	25.91 ± 0.14

^a These values were computed from the data obtained in a rectangular core.

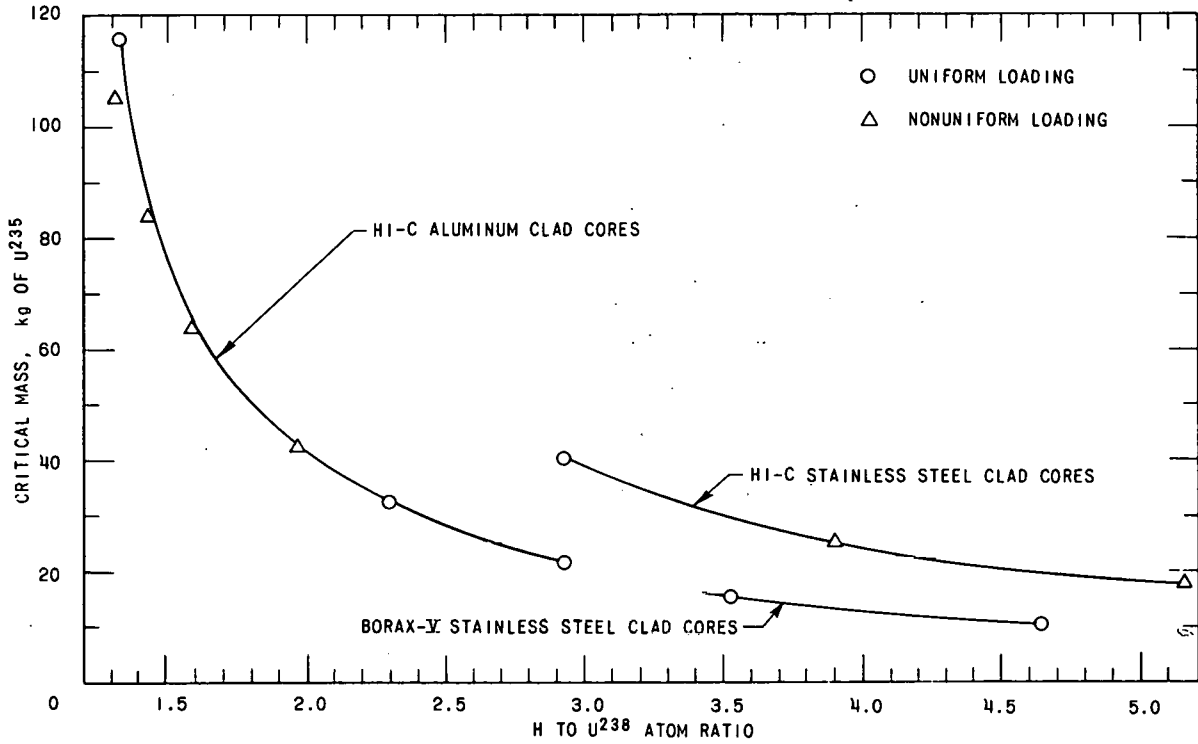


FIG. II-7-2. Critical Masses for Cylindrical Hi-C and BORAX-V Cores.

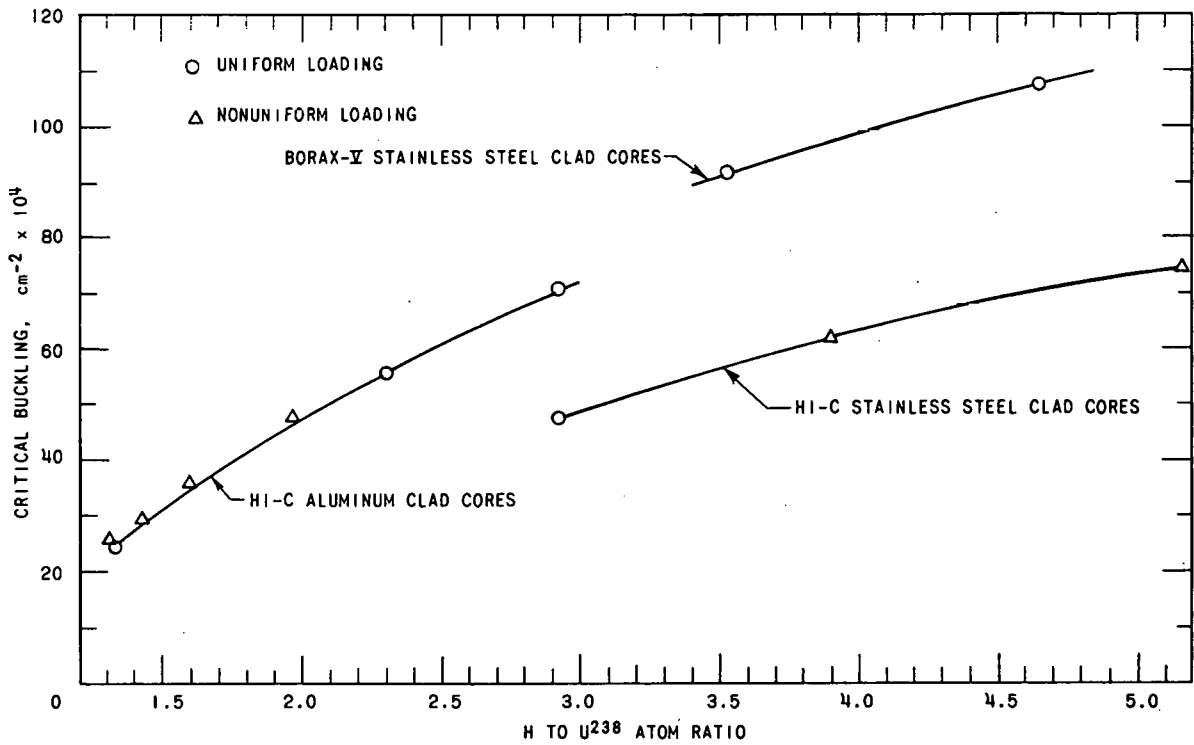


FIG. II-7-3. Critical Bucklings for Hi-C and BORAX-V Cores.

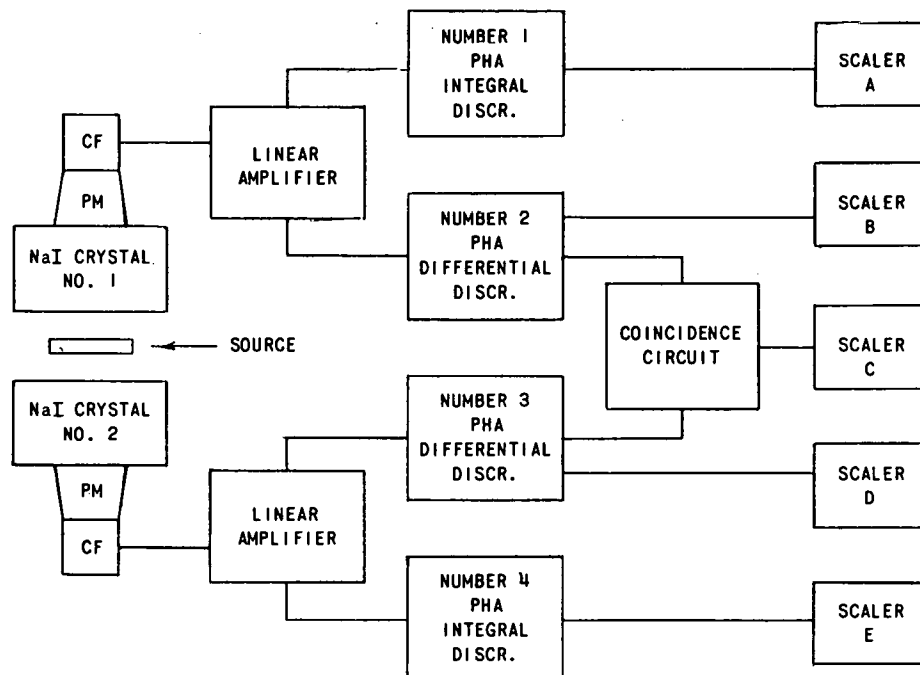


FIG. II-7-4. Block Diagram of Coincidence Counting Circuit.

was determined by the gamma-gamma coincidence technique.⁹ About half of the beta decays of the Np-239 result in an excited state of Pu-239 which emits a 106-keV gamma ray followed mainly by either a 228- or a 278-keV gamma ray. The 228- and 278-keV gamma rays have large internal *K*-conversion coefficients giving rise to X-rays of comparable intensity to the 106-keV gamma ray. A nominal 100-keV peak is then formed by the roughly equal mixture of unresolved 106-keV gamma rays and the Pu-239 X-rays. Thus, a most satisfactory measurement of Pu-239 production is based on observing coincidences between the 106-keV gamma ray and the Pu-239 X-ray.

For foils in the thermal column, all of the fission product activity is considered to be the result of U-235 fission; however, for foils in Hi-C an appreciable part of this activity is the result of fast fission in U-238 and it is necessary to irradiate foils of two isotopic concentrations to identify the component of the activity that is due to U-235 fission.

The foils were gamma-counted in a double detection setup as shown in Fig. II-7-4. Two well-shielded NaI crystals were used as the detectors. Two analyzers were centered on the nominal 100-keV compound peak from the Pu-239 cascade. The channel width used was a compromise between rejection of fission product gamma rays and increased coincidence count rate and was usually 36 keV wide. The outputs from these differential selectors were fed into a slow coincidence circuit with a resolving time of 0.5 μ sec, as well as being

recorded individually. In addition, two other analyzers were used in the integral mode as discriminators to select gamma pulses above 411 keV to be used as a measure of fission rate.

Repeated checks of the relative Pu-239 production as determined by the coincidence counting of uranium metal foils has agreed, within experimental errors, with radio-chemical separation methods on irradiated oxide pellets.

The average U-235 capture-to-fission ratio in the lattice spectrum, α^{25} , was determined by a semi-empirical method in which the subcadmium and epicadmium α 's are weighted by the fission cadmium ratio as follows:

$$\alpha^{25} = \alpha_s \frac{(CR)_f - 1}{(CR)_f} + \frac{\alpha_e}{(CR)_f}. \quad (2)$$

Here, the α_s and α_e values used were results of GAM-1 and THERMOS calculations for the Hi-C cores and MUFT and SOFOCATE calculations for the BORAX-V cores. The U-235 fission cadmium ratios used were the experimental values.

Table II-7-IV presents the results of the *ICR* measurements as well as the values used in Eq. (1) to compute the *ICR*. In Fig. II-7-5 the values of the *ICR* obtained are plotted versus H:28 ratio.

U-238 CAPTURE CADMIUM RATIO (C_{28})

The U-238 capture cadmium ratio, C_{28} , was determined by two methods. The first was the straightfor-

TABLE II-7-IV. INITIAL CONVERSION RATIOS IN HI-C AND BORAX-V CORES

Core No.	H:28	(CdR) _f	α_s	α_c	α^{28}	ICR	$\bar{\sigma}_c^{28}$, b	$\bar{\sigma}_f^{28}$, b	(CdR) _{Au} Thermal Column ATSR
1	4.65	4.94	0.182	0.470	0.241	0.271 ± 0.027	2.92	567.90	90
2	3.53	3.90	0.184	0.469	0.255	0.349 ± 0.035	3.075	567.89	50
7	2.93	4.49	0.179	0.509	0.252	0.495 ± 0.004	2.89	567.98	115
10	2.30	3.75	0.180	0.509	0.268	0.561 ± 0.030	2.89	567.98	115
12	1.33	2.55	0.185	0.507	0.312	0.798 ± 0.007	2.90	567.91	105
17	0.99	2.15	0.185	0.525	0.3419	0.921 ± 0.016	2.89	567.98	115

Note:

$$\bar{\sigma}_c^{28}(\text{th}) = 2.72 \text{ b.}$$

$$\bar{\sigma}_f^{28}(\text{th}) = 581.95 \text{ b.}$$

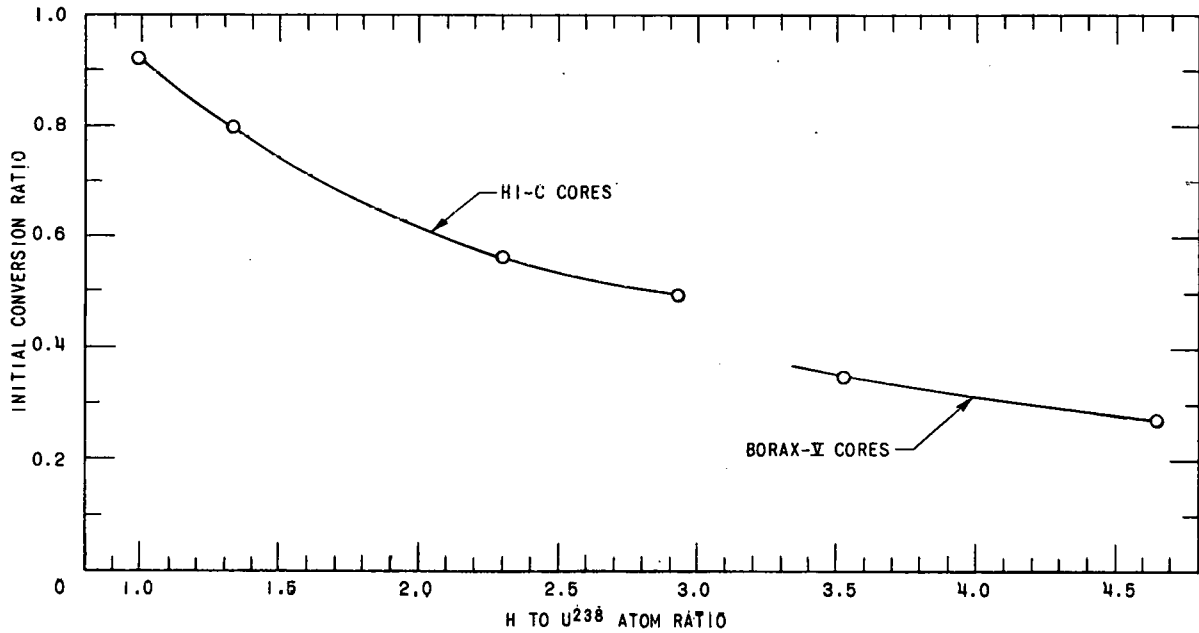


FIG. II-7-5. Initial Conversion Ratios in HI-C and BORAX-V Cores.

ward method of irradiating both bare and cadmium-covered depleted uranium metal foils and computing the cadmium ratio from the measured Np-239 activity as determined by the coincidence counting method previously described. This was the only method used to obtain C_{28} in the BORAX-V cores. This direct method, however, becomes unsatisfactory and gives large error limits when C_{28} approaches unity.

Of interest is the ratio of epicadmium-to-subcadmium captures in U-238, ρ_c^{28} , which is given by

$$\rho_c^{28} = [1/(C_{28} - 1)]. \quad (3)$$

A 1% error in C_{28} , when its value is 1.06, results in a 16% error in ρ_c^{28} . A second method for the determination of C_{28} , designed to give increased accuracy as C_{28} approaches unity, is the thermal activation method of R. Lewis, et al.¹⁰ The method is designed to allow the

determination of $C_{28} - 1$ directly and was used in all of the HI-C lattices.

Briefly stated, the technique compares total absorptions in U-238 to thermal absorptions in an intermediate material, usually dysprosium, having a much higher probability of thermal absorptions. Then, the thermal absorptions in the intermediate material and uranium are normalized in a thermal irradiation. The technique allows the cadmium-covered uranium measurement to be eliminated, and thus avoids cadmium perturbations. The capture cadmium ratio was evaluated from

$$\frac{C_{28} - 1}{C_{28}} = \left(\frac{A_x^b}{A_{28}^b} \right)_t \left(\frac{C_x - 1}{C_x} \right)_t \cdot \left(\frac{A_{28}^b}{A_x^b} \right)_n \left(\frac{C_{28} - 1}{C_{28}} \right)_n \left(\frac{C_x}{C_x - 1} \right)_n K, \quad (4)$$

where the A's signify weight-normalized activities

(Np-239 in the depleted uranium foils), the subscript 28 refers to U-238 and x to the intermediate material, the superscript b refers to a bare irradiation, ℓ denotes an irradiation in the critical experiment lattice, n denotes an irradiation in a normalizing thermal flux, and C is the cadmium ratio. All the factors in Eq. (4) are measurable except K . It is noted that K will depart from unity when the intermediate material departs from a $1/v$ behavior in the ℓ - and n -irradiations. When copper is used, $K = 1.000$; however, when dysprosium is used, K must account for its slight non- $1/v$ behavior.

The results of both the direct and thermal activation measurements of C_{28} are given in Table II-7-V. The K factor given for each core is for dysprosium as the intermediate material. In core No. 17 both copper and dysprosium were used. The value for C_{28} for this core was found to be independent of the intermediate material, indicating that the non- $1/v$ correction for dysprosium was satisfactory. The error limits shown on C_{28} are computed from the data scatter as the standard deviations from the mean. It is readily apparent that the thermal activation method gives the smaller error limits. A plot of the C_{28} values is given in Fig. II-7-6. The epicadmium-to-subcadmium U-238 capture ratio, ρ_c^{28} , was computed from the C_{28} obtained by the thermal activation method in the Hi-C cores and from the C_{28} obtained by the direct method in the BORAX-V cores.

U-238 TO U-235 FISSION RATIO (δ^{28})

The U-238 to U-235 fission ratio, δ^{28} , was measured in cores Nos. 1, 2, 6, 10, 12, and 17. The method as developed by V. Grob, et al.,¹¹ and D. Klein, et al.,¹² was used. In this method, the time-dependent ratio of the measured fission product activity per uranium atom of a partially depleted foil to the measured fission product activity per uranium atom of an enriched foil, $\gamma(t)$, is related to δ^{28} by a factor $P(t)$. This factor is the time dependent ratio of the gamma activity per fission from the fission products of U-238 to the gamma activity

TABLE II-7-V. CAPTURE CADMIUM RATIO IN HI-C AND BORAX-V

Core No.	H:28	C_{28} (Direct)	C_{28} Thermal Activation	ρ_c^{28}	K for Dysprosium
1	4.65	1.182 ± 0.041	—	5.49 ± 1.24	—
2	3.53	1.188 ± 0.083	—	5.32 ± 2.35	—
7	2.93	1.236 ± 0.011	1.243 ± 0.002	4.12 ± 0.03	1.022
10	2.30	1.176 ± 0.011	1.185 ± 0.003	5.41 ± 0.09	1.026
12	1.33	1.105 ± 0.007	1.100 ± 0.001	10.0 ± 0.1	1.039
17	0.99	1.107 ± 0.022	1.069 ± 0.002	14.5 ± 0.4	1.049

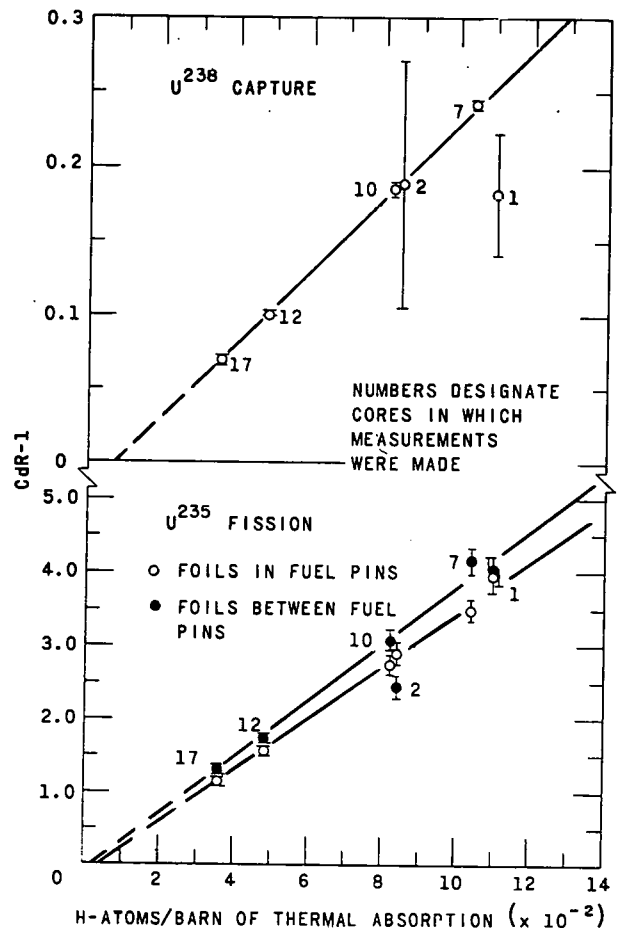


FIG. II-7-6. U-238 Capture and U-235 Fission Cadmium Ratios in Hi-C and BORAX-V Cores.

per fission from the fission products of U-235. The correction factor $P(t)$ as determined by A. Futch¹³ was used in arriving at the values for δ^{28} .

The quantity $\gamma(t)$ was measured by irradiating enriched uranium metal foils and depleted foils in flux symmetric positions in fuel pins. After irradiation the foils were removed and the fission product activity counted with a NaI scintillation counter. The counter was biased to reject pulses due to gammas below 1.2 MeV, eliminating pulses due to Bremsstrahlung from U-239 beta rays. Radiochemical fission analysis was performed for some foils, as a check on counting methods.

The results of these measurements are presented in Table II-7-VI. All $\gamma(t)$ measurements were taken in stainless steel clad cores.

THERMAL DISADVANTAGE FACTOR (ζ)

The thermal disadvantage factor, ζ , was determined in cores Nos. 1, 2, 7, 10, 12, and 17 by obtaining the

TABLE II-7-VI. U-238 TO U-235 FISSION RATIOS IN HI-C AND BORAX-V CORES

Core No.	H:28	δ^{28}
1	4.65	0.0650 \pm 0.006
2	3.53	0.1190 \pm 0.010
7	2.93	0.1014 \pm 0.0007
10	2.30	0.1160 \pm 0.0016
12	1.33	0.1539 \pm 0.0037
17	0.99	0.1877 \pm 0.0020

U-235 fission cadmium ratio in both the fuel and moderator and the bare moderator-to-bare fuel fission ratio.

The foil material used was uranium-aluminum alloy of 17.5 w/o uranium enriched to 92.75 w/o U-235. After irradiation the foils were assayed for fission product activity by gamma counting in a scintillation counter biased to reject pulses from gammas whose energies were below 411 keV. Before irradiation the foils were intercalibrated by counting the natural gamma activity.

tor volume of the unit fuel-moderator cell. Small strips of foil material, placed in cadmium tubing which was flattened to fit into the moderator volume, were used for the cadmium-covered moderator volume foils in the three tightest lattices. In the Hi-C lattices, the cadmium ratios were corrected for thermal self-shielding and extrapolated to zero mass of cadmium. The results of these measurements are assembled in Table II-7-VII. Plots of the fission cadmium ratio are shown in Fig. II-7-6.

It is of interest to compare the Hi-C disadvantage factors with the recent calculations and experimental values reported by H. Honeck¹⁴ and the calculations of E. Pennington.¹⁵ Both calculations were THERMOS multigroup problems using the Nelkin scattering kernel. Figure II-7-7 presents this information as a plot of thermal disadvantage factor versus water-to-oxide volume ratio. It should be noted that Honeck's data and calculations are for 3.00 w/o enriched, 1.128-cm diameter, 0.071-cm thick stainless steel-clad oxide rods, while the Hi-C fuel is in the form of 3.04 w/o enriched, 0.935-cm diameter, 0.0496-cm thick stainless

TABLE II-7-VII. U-235 FISSION CADMIUM RATIOS AND THERMAL DISADVANTAGE FACTORS IN HI-C AND BORAX-V CORES

Core No.	1	2	7	10	12	17
H:28	4.65	3.53	2.93	2.30	1.33	0.99
Fission cadmium ratio in fuel	4.94 \pm 0.20	3.90 \pm 0.16	4.49 \pm 0.11	3.75 \pm 0.08	2.55 \pm 0.06	2.15 \pm 0.05
Fission cadmium ratio in moderator	5.04 \pm 0.20	3.44 \pm 0.15	5.19 \pm 0.15	4.14 \pm 0.10	2.72 \pm 0.08	2.33 \pm 0.08
Bare moderator-to-bare fission ratio	1.159 \pm 0.049	1.197 \pm 0.051	1.118 \pm 0.007	1.075 \pm 0.009	1.054 \pm 0.004	1.051 \pm 0.008
Thermal disadvantage factor f_{25}	1.165 \pm 0.052	1.142 \pm 0.051	1.162 \pm 0.016	1.110 \pm 0.015	1.097 \pm 0.025	1.110 \pm 0.038
Epicadmium-to-subcadmium U-235 fission ratio, ρ_f^{25}	0.274 \pm 0.007	0.345 \pm 0.011	0.286 \pm 0.009	0.364 \pm 0.011	0.645 \pm 0.025	0.870 \pm 0.038

The fuel foils were the same diameter as the fuel and irradiated between fuel pellets in the slotted fuel pins. The cadmium-covered irradiation was obtained by placing cadmium discs between the foil and the fuel pellets, as well as placing a cadmium sleeve over the fuel pin. Several lengths of cadmium sleeve were used.

The moderator foils for the bare irradiations were shaped to fit the roughly triangular moderator area enclosed by three fuel pins in the triangular lattices, and either the whole or one quarter of the cross-like moderator area enclosed by four fuel pins in the square pitch lattices. The foils were held in position between lucite pieces which were shaped to match the foils.

The small triangular pitch in cores Nos. 10, 12, and 17 made it impossible to irradiate a foil covered with a cadmium cover that was shaped to the moderator area. It had been found, however, that in tight, water-uranium oxide lattices the epicadmium flux is flat enough so that the cadmium-covered moderator foils need not be matched to the cross section of the modera-

TABLE II-7-VIII. FOIL MATERIALS USED FOR CADMIUM RATIO MEASUREMENTS IN HI-C AND BORAX-V CORES

Target Nuclide	$T_{1/2}$	Energy of Principal Resonance, eV	Foil Material	Nominal Thickness of Foil, mil
Dy-164	2.3 h	—	Alloy: 3.7% Dy, 96.3 Al	9
Lu-176	6.8 day	0.142	Alloy: 2.5% Lu, 97.5% Al	10
Lu-175	3.7 h	—	Alloy: 2.5% Lu, 97.5% Al	10
In-115	54.0 min	1.457	Metallic indium	1.2
Au-197	2.7 day	4.91	Metallic gold	1.1
Mn-55	2.58 h	337	Alloy: 90% Mn, 10% Cu	2.5
Cu-63	12.8 h	580	Metallic copper	2
U-235	—	—	U-Al alloy: 17.5 w/o U, 92.75 w/o enriched	2, 5, 10, 15 and 25
U-238	56.3 h	—	Metallic uranium, 0.21% depleted	5

steel-clad oxide rods. The disadvantage factors measured in the Hi-C lattices are U-235 fission disadvantage factors while the data Honeck presents are dysprosium-activation disadvantage factors. Honeck reports that ζ_{Dv} and ζ_{25} have been found to agree to within less than 3%. Both the calculations of Pennington and Honeck give number density disadvantage factors rather than neutron flux disadvantage factors.

Honeck¹⁴ noted a systematic discrepancy between the experimental and calculated values of the disadvantage factor. He states that theory predicts disadvantage factors that are 3-5% higher than measured, the 3% corresponding to the largest lattices (water to uranium ratio about 4) and the 5% to the smallest lattices (ratio about 1.2) for which he had experimental data. It would appear from the Hi-C data that this trend continues in the very tight Hi-C lattices. For the tighter Hi-C lattices, the theory predicts disadvantage factors from 6 to 10% larger than measured.

CADMIUM RATIOS IN HI-C CORES

Cadmium ratio measurements have been made in all of the uniform Hi-C lattices—specifically in cores Nos. 1, 2, 3, 6, 8, 9, 10, 11, 12, 17, and 18. Tables II-7-I and II-7-VIII give descriptions of the cores and foil materials, respectively, and the results of the

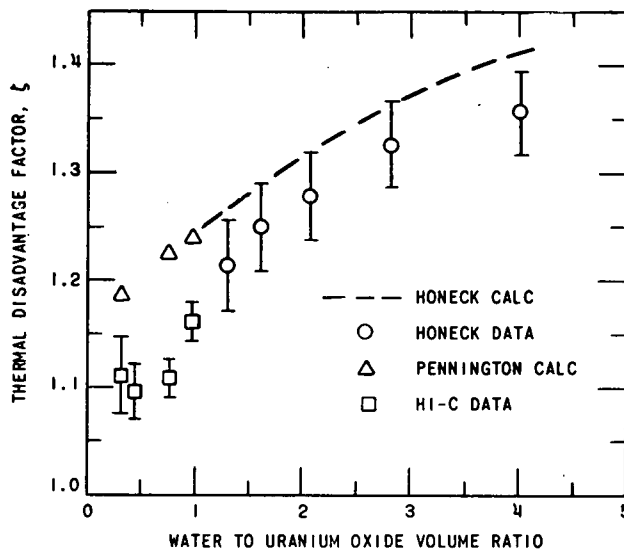


FIG. II-7-7. Thermal Disadvantage Factor in Hi-C and Similar Lattices.

cadmium ratio measurements are contained in Table II-7-IX.

The methods used in making these measurements varied somewhat from core to core, and will not be discussed in detail. For the most part, however, the

TABLE II-7-IX. CADMIUM RATIOS IN HI-C AND BORAX-V CORES

Core No.	H:28	H: σ_T ^a $\times 10^{-2}$	Dy	Lu-176	Lu-175	In 21.9 mg/cm ²	Au 53.9 mg/cm ²	Mn	Cu	U ²³⁵	U ²³⁸
17 (SS)	0.99	3.58	7.6 ± 3	—	—	—	1.152 ± 15	1.587 ± 20	1.500 ± 30	2.15 ± 5	1.069 ± 2
Between pins	—	—	—	—	—	—	—	—	—	2.33 ± 8	—
18 (Al)	0.99	3.96	7.1 ± 3	4.6 ± 7	1.027 ± 15	1.204 ± 20	1.177 ± 10	1.574 ± 30	1.526 ± 30	—	—
12 (SS)	1.33	4.80	8.73 ± 12	—	—	1.234 ± 5	1.201 ± 5	1.80 ± 2	1.67 ± 4	2.55 ± 6	1.100 ± 1
Between pins	—	—	—	—	—	—	—	—	—	2.72 ± 8	—
11 (Al)	1.33	5.31	9.18 ± 30	—	—	1.260 ± 8	1.221 ± 8	1.863 ± 15	1.801 ± 30	—	—
10 (SS)	2.30	8.25	13.8 ± 15	—	—	1.373 ± 7	1.346 ± 15	2.63 ± 10	2.40 ± 4	3.75 ± 8	1.185 ± 3
Between pins	—	—	—	—	—	—	—	—	—	4.14 ± 10	—
9 (Al)	2.30	9.11	14.1 ± 8	—	—	1.398 ± 15	1.361 ± 15	2.58 ± 6	2.49 ± 5	—	—
6 (SS)	2.93	10.41	17.4 ± 7	11.1 ± 16	1.065 ± 15	1.469 ± 8	1.435 ± 8	3.00 ± 3	2.750 ± 20	—	—
Between pins	—	—	—	—	—	1.483 ± 20	1.442 ± 8	3.19 ± 5	3.02 ± 3	—	—
7 (SS)	2.93	10.41	—	—	—	—	—	—	—	4.49 ± 11	1.243 ± 2
Between pins	—	—	—	—	—	—	—	—	—	5.19 ± 15	—
8 (Al)	2.93	11.50	16.4 ± 5 ^c	—	—	1.68 ± 5 ^b	1.455 ± 10	3.118 ± 30	2.950 ± 30	—	—
Between pins	—	—	18.0 ± 5 ^c	—	—	1.482 ± 15	1.85 ± 5 ^c	3.367 ± 20	3.160 ± 20	—	—
						1.518 ± 20	1.503 ± 15	3.367 ± 20	3.160 ± 20	—	—
3 (Al)	3.24	12.74	20.9 ± 6	9.5 ± 8	1.083 ± 20	1.551 ± 30	1.522 ± 30	3.515 ± 30	3.352 ± 50	—	—
2 (SS)	3.53	8.42	13.4 ± 10	7.4 ± 10	1.056 ± 30	1.383 ± 30	1.288 ± 30	2.61 ± 8	2.43 ± 10	3.90 ± 16	1.188 ± 83
Between pins	—	—	14.2 ± 11	9.0 ± 4	1.075 ± 25	1.392 ± 40	1.337 ± 40	2.70 ± 8	2.57 ± 15	3.44 ± 15	—
1 (SS)	4.65	10.98	17.7 ± 7	—	—	1.472 ± 20	1.414 ± 25	3.20 ± 6	3.10 ± 7	4.94 ± 20	1.182 ± 41
Between pins	—	—	17.7 ± 14	—	—	1.531 ± 40	1.495 ± 45	3.46 ± 6	3.39 ± 7	5.04 ± 20	—

^a H: σ_T is the number of hydrogen atoms per thermal barn of absorption in the core.

^b Errors quoted are in the last digits given; e.g., 1.566 ± 15 means 1.566 ± 0.015, 13.8 ± 15 means 13.8 ± 1.5, and 1.19 ± 2 means 1.19 ± 0.02.

^c Measurement made in early loading (July 1961).

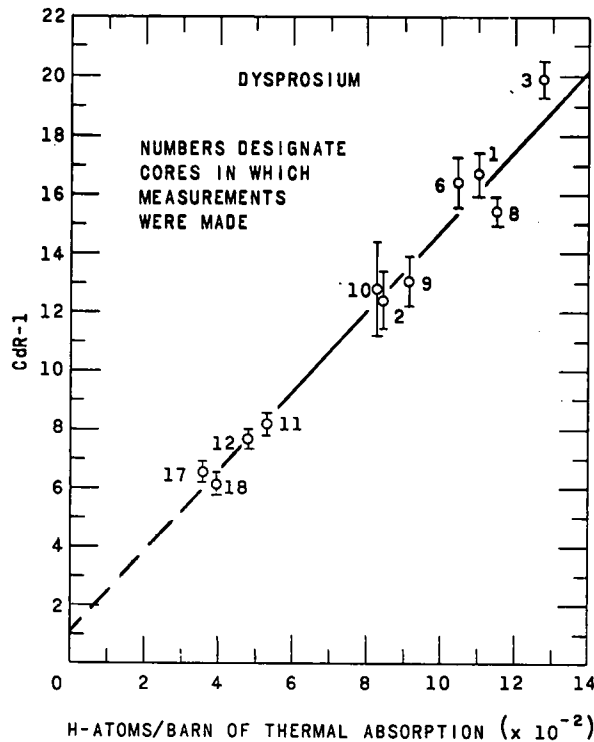


FIG. II-7-8. Dysprosium Cadmium Ratio in Hi-C and BORAX-V Cores.

foils had a diameter of 0.82 cm, and were enclosed in 20-mil thick capsules made of cadmium or aluminum. For the measurements in the fuel pins, the capsules were sandwiched between fuel pellets, while for the measurements in the moderator between the pins, the capsules were in a vertical position, taped to plastic or stainless steel strips slipped horizontally through the core.

In Figs. II-7-6, II-7-8, II-7-9, and II-7-10 are plotted the measured cadmium ratios as a function of the ratio H/σ_T , the number of hydrogen atoms per barn of thermal absorption. Consistent with experimental precision, the resulting curves are linear, although they do not in general extrapolate to the origin. Results from two cores using the more highly enriched BORAX-V fuel (cores Nos. 1 and 2) are consistent with the Hi-C curves. Application to fuel elements of different sizes or shapes is less certain, although at least rough agreement is to be expected.

The linearity of the results plotted in Figs. II-7-6, II-7-8, II-7-9, and II-7-10 is probably due, at least in part, to a fortuitous cancellation of errors since the data are uncorrected for several effects which should in principle be allowed for:

(a) The quantity σ_T (barns per unit volume in the core) was calculated as though the core were homo-

geneous, i.e., with no allowance for self-shielding or local flux depression.

(b) Since the foils were sandwiched between fuel pellets, their activation would be nonuniform, particularly the thermal activation. While this factor should be roughly the same for all the Hi-C cores, it should be different for the BORAX-V fuel, where the enrichment was higher. The directions of effects (a) and (b) are such that they would tend to cancel.

(c) The magnitude of (b) is mitigated by the use of 20-mil aluminum capsules, permitting some streaming of thermal neutrons.

The utility of these plots is enhanced by their simplicity—the fact that the data, uncorrected for effects that are tedious to calculate, are empirically linear.

As an explanation of the observed linearity, it may be noted that the ratio $H:\sigma_T$ should be at least approximately proportional to the ratio of the thermal (moderated) neutron density to the epithermal density

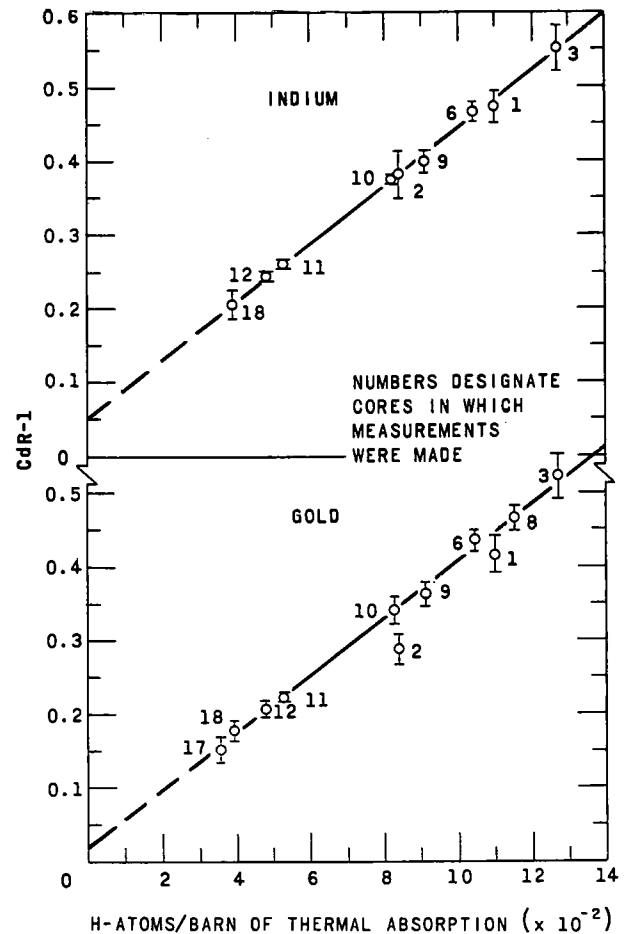


FIG. II-7-9. Indium and Gold Cadmium Ratios in Hi-C and BORAX-V Cores.

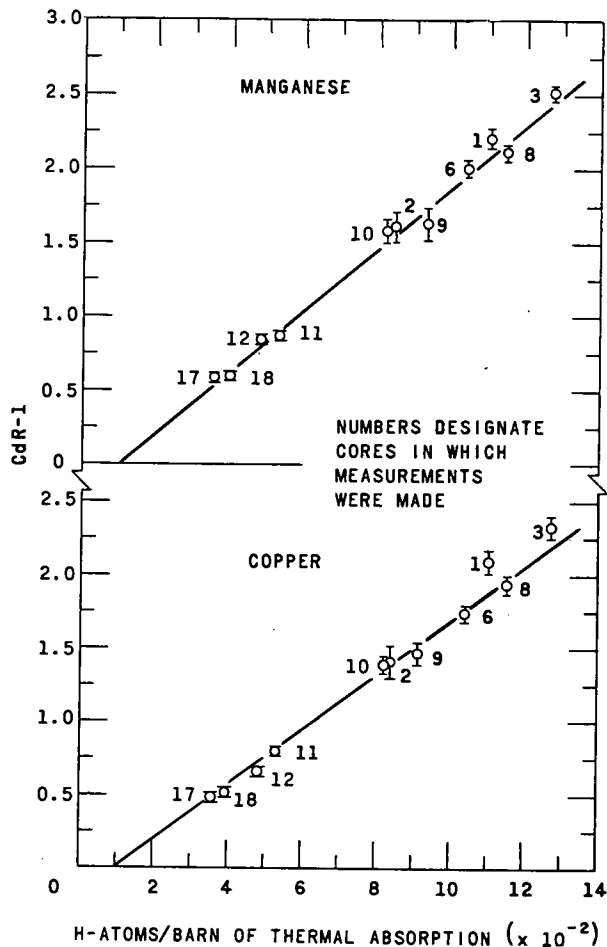


FIG. II-7-10. Manganese and Copper Cadmium Ratios in Hi-C and BORAX-V Cores.

TABLE II-7-X. TEMPERATURE COEFFICIENT OF REACTIVITY IN HI-C AND BORAX-V CORES

Core No.	H:28	Temperature Coefficient, % $(\Delta k/k)/^{\circ}\text{C}$
1	4.65	-0.0131 ± 0.0005
2	3.53	-0.0098 ± 0.0005
6	2.93	-0.0104 ± 0.0004
9	2.30	-0.0101 ± 0.0007
11	1.33	-0.0095 ± 0.0005

—i.e., to the ratio of subcadmium-to-epicadmium activation, which is the cadmium ratio minus one. To explain the failure of the curves to extrapolate to the origin would require further elaboration.

TEMPERATURE COEFFICIENT OF REACTIVITY

The temperature coefficient of reactivity has been

determined for core Nos. 1, 2, 6, 9, and 11. Two methods were utilized: the change in the critical control rod setting of a previously calibrated control rod versus change in moderator temperature; and positive period measurements to a fixed point versus change in moderator temperature. The temperature of the moderator spanned approximately 20°C . Results of these measurements are shown in Table II-7-X.

REFERENCES

1. W. C. Redman, J. A. Thie and L. R. Dates, *Hazards Summary Report on the Oxide Critical Experiments*, ANL-5715 (1957).
2. D. S. Craig, L. R. Dates and K. E. Plumlee, *Hazards Summary Report—High Conversion Critical Experiments*, ANL-5715-Addendum II (1960).
3. Q. L. Baird and A. R. Boynton, *Bucklings, Disadvantage Factors, and δ^{28} Measurements in Some Undermoderated Slightly Enriched Cores*, Trans. Am. Nucl. Soc. 6, No. 2, 248 (1963).
4. Q. L. Baird, A. R. Boynton, W. R. Robinson and J. M. Christenson, *Initial Conversion Ratio and Epicadmium to Subcadmium Uranium-238 Capture Rate Measurements in Very Undermoderated Slightly Enriched Oxide Cores*, Trans. Am. Nucl. Soc. 7, No. 1, 80 (1964).
5. J. Bengston and R. L. Hellens, *A Survey of the Beginning of Life Characteristics of Uranium-Fueled, Water-Moderated Lattices*, CEND-137 (1961).
6. P. R. Tunnicliffe, D. J. Skillings and B. G. Chidley, *A Method for the Accurate Determination of Relative Initial Conversion Ratios*, Nucl. Sci. Eng. 15, No. 3, 268-283 (1963).
7. A. Weitzberg, I. Kaplan and T. J. Thompson, *Measurements of Neutron Capture in U-238 in Lattices of Uranium Rods in Heavy Water*, NYO-9659 (1962).
8. C. H. Westcott, *Effective Cross Section Values for Well-Moderated Thermal Reactor Spectra*, CRP-960, 3rd Ed. Corrected (1960).
9. R. Sher, *Gamma-Gamma Coincidence Method for Measuring Resonance Escape Probability in U-238 Lattice*, Nucl. Sci. Eng. 7, No. 5, 479-480 (1960).
10. R. H. Lewis, et al., *Thermal Activation Method for ρ_{28} Measurements in Slightly Enriched Uranium Oxide Lattices*, BAW-1268 (1963).
11. V. Grob, et al., *Measurement of Parameters Leading to ρ^{28} , f , and ϵ in Light Water Moderated 4.48% and 2.73% Enriched Lattices*, Nucl. Sci. Eng. 7, No. 6, 514-524 (1960).
12. D. Klein, et al., *Measurement of Thermal Utilization, Resonance Escape Probability, and Fast Effect in Water Moderated, Slightly Enriched Uranium and Uranium Oxide Lattices*, Nucl. Sci. Eng. 3, No. 4, 403-427 (1958).
13. A. H. Futch, Jr., *Fast Fission Effect in Lattices of Natural Uranium and Heavy Water*, Nucl. Sci. Eng. 5, No. 1, 61-67 (1959).
14. H. C. Honeck, *The Calculation of the Thermal Utilization and Disadvantage Factor in Uranium/Water Lattices*, Nucl. Sci. Eng. 18, No. 1, 49-68 (1964).
15. E. M. Pennington, Argonne National Laboratory (Private Communication).

II-8. Hi-C Uniform Lattice Calculations

E. M. PENNINGTON

INTRODUCTION

Preliminary calculations of four-group constants and material bucklings have been carried out for the light water moderated, high conversion (Hi-C) lattices in the ZPR-VII critical assembly. Calculations were also done for lattices using BORAX-V fuel. These were studied experimentally at the beginning of the Hi-C program. The Hi-C fuel consists of pellets of UO_2 approximately 3% enriched and clad in either Al or SS; while the BORAX-V fuel is UO_2 of approximately 5% enrichment and clad in SS.

The constants for the three fast groups were determined from the GAM-I code,¹ while those for the thermal group were found using the THERMOS code.² The lower energy limits for the fast groups were 1.35 MeV, 1.23 keV, and 0.414 eV. Cross sections in the GAM-I code are obtained using a 68 group library and either the P-1 or B-1 approximation. Resonance absorption in U-238 is treated according to the methods of F. Adler, G. Hinman and L. Nordheim.³ Except for the calculation of resonance absorption in U-238, the constituents of the lattice cell are treated as a homogeneous mixture.

THERMAL PARAMETERS

The THERMOS code computes the scalar thermal neutron spectrum as a function of position in a lattice by solving numerically the integral transport equation with isotropic scattering. Thirty thermal groups and 20 space points are allowed in the code. Free gas scattering kernels are used except for hydrogen for which the Nelkin, Brown-St. John, and free gas models are all available. The slowing down source for the problems reported here was taken as being due to hydrogen only and was spatially flat in the H_2O region. Since the transport kernels in THERMOS are derived on the basis of mirror image reflection at the cell boundary, the method of H. Honeck⁴ was used in which an extra region consisting of a heavy scatterer was placed outside the actual unit cell boundary. This method produces an essentially isotropic distribution of the neutrons returning to the actual unit cell.

THERMOS one-group calculations were also done using cross sections averaged over the first 27 groups (0-0.415 eV) of the Nelkin kernel multigroup problems. These one-group cross sections were also used in the three-region collision probability code B692/RP to yield average thermal fluxes in the framework of the flat flux approximation.

Use of the three scattering kernels for hydrogen yields cell parameters which do not differ greatly from each other except in the case of the average scattering cross section. Some of the parameters are compared in Table II-8-I for the case of the Hi-C square lattice with 1.24 cm pitch and Al clad fuel.

Table II-8-II compares fluxes for the Hi-C and BORAX-V lattices obtained from multigroup THERMOS, one-group THERMOS, and B692/RP problems. Subscripts 1, 2, and 3 on $\bar{\phi}$ refer to fuel, clad, and H_2O regions respectively.

FAST FISSION CALCULATIONS

Fast fission calculations have been done for some of the lattices using constants obtained by averaging either GAM-I or MUFT-4 cross sections over the fission spectrum above 1.35 MeV. Both the homogeneous method and a transport approximation⁶ involving collision probabilities were used. The transport approximation was, roughly speaking, an approximation to the B692/RP code which had not been written when the calculations were made. For some homogeneous cases the cross sections from the output of GAM-I problems above 1.35 MeV were also used. MUFT-4 cross sections resulted in higher values of δ^{28} and lower values of ϵ than GAM-I cross sections, where δ^{28} is the ratio of the number of fissions in U-238 to fissions in U-235 and ϵ is the fast fission factor. The heterogeneous values of δ^{28} and ϵ were not much larger than the corresponding homogeneous ones since the long mean free paths for fast neutrons and the close spacing of the fuel rods result in little peaking of the fast flux in the rods. GAM-I output cross sections led to values of δ^{28}

TABLE II-8-I. THERMAL PARAMETERS FOR HI-C 1.24 CM SQUARE LATTICE, AL CLAD FUEL

Parameter	Hydrogen Scattering Kernels		
	H Gas	Brown-St. John	Nelkin
f^{28}	0.83642	0.83624	0.83605
f^{fuel}	0.94599	0.94570	0.94602
η^{28}	2.0625	2.0633	2.0619
η^{fuel}	1.8236	1.8246	1.8223
η^f	1.7251	1.7254	1.7239
$\bar{\Sigma}_a, \text{cm}^{-1}$	0.14594	0.14847	0.14251
$\nu\bar{\Sigma}_f, \text{cm}^{-1}$	0.25176	0.25618	0.24572
$\bar{\Sigma}_s, \text{cm}^{-1}$	1.0177	1.4348	1.3753
$\bar{\phi}^{\text{fuel}}$	1.0000	1.0000	1.0000
$\bar{\phi}^{\text{clad}}$	1.0966	1.0934	1.0894
$\bar{\phi}^{\text{H}_2\text{O}}$	1.1584	1.1656	1.1572

TABLE II-8-II. THERMAL FLUX RATIOS FOR HI-C AND BORAX-V LATTICES
 (Data in part from Ref. 5)

Core and Lattice	Flux Ratio	27 Group THERMOS	One Group THERMOS	B692/RP	Core and Lattice	Flux Ratio	27 Group THERMOS	One Group THERMOS	B692/RP
BORAX-V	$\bar{\phi}_2/\bar{\phi}_1$	1.1150	1.1125	1.1173	Hi-C Al	$\bar{\phi}_2/\bar{\phi}_1$	1.0853	1.0865	1.0870
1.27 cm \square	$\bar{\phi}_3/\bar{\phi}_1$	1.2535	1.2462	1.2394	1.166 cm Δ	$\bar{\phi}_3/\bar{\phi}_1$	1.1286	1.1299	1.1299
BORAX-V	$\bar{\phi}_2/\bar{\phi}_1$	1.1124	1.1105	1.1142	Hi-C SS	$\bar{\phi}_2/\bar{\phi}_1$	1.0781	1.0789	1.0801
1.27 cm Δ	$\bar{\phi}_3/\bar{\phi}_1$	1.2299	1.2249	1.2203	1.166 cm Δ	$\bar{\phi}_3/\bar{\phi}_1$	1.1375	1.1391	1.1397
Hi-C Al	$\bar{\phi}_2/\bar{\phi}_1$	1.0894	1.0890	1.0902	Hi-C Al	$\bar{\phi}_2/\bar{\phi}_1$	1.0831	1.0848	1.0858
1.24 cm \square	$\bar{\phi}_3/\bar{\phi}_1$	1.1572	1.1551	1.1497	1.127 cm Δ	$\bar{\phi}_3/\bar{\phi}_1$	1.1271	1.1299	1.1260
Hi-C SS	$\bar{\phi}_2/\bar{\phi}_1$	1.0819	1.0815	1.0836	Hi-C SS	$\bar{\phi}_2/\bar{\phi}_1$	1.0772	1.0785	1.0798
1.25 cm \square	$\bar{\phi}_3/\bar{\phi}_1$	1.1709	1.1687	1.1634	1.127 cm Δ	$\bar{\phi}_3/\bar{\phi}_1$	1.1367	1.1395	1.1363
Hi-C Al	$\bar{\phi}_2/\bar{\phi}_1$	1.0880	1.0879	1.0887					
1.27 cm Δ	$\bar{\phi}_3/\bar{\phi}_1$	1.1486	1.1477	1.1413					
Hi-C SS	$\bar{\phi}_2/\bar{\phi}_1$	1.0807	1.0807	1.0824					
1.27 cm Δ	$\bar{\phi}_3/\bar{\phi}_1$	1.1615	1.1607	1.1544					

and ϵ slightly lower than those from calculations using cross sections averaged over a fission spectrum. In terms of reactivity, heterogeneous calculations increased reactivity only by the order of 0.1% from that for homogeneous calculations. However, use of MUFT-4 constants in place of GAM-I constants decreases reactivity by 1 to 2%. Thus use of accurate cross sections is much more important than heterogeneous effects in the fast fission energy range.

CRITICALITY CALCULATIONS

Material bucklings calculated using GAM-I parameters for nonthermal neutrons and THERMOS parameters for thermal neutrons are much higher than experimental bucklings. The differences become greater as the moderator-to-fuel volume ratio is decreased. Calculations using the B-1 option in GAM-I yield somewhat higher values of B^2 than those using the P-1 option mainly because of the differences in diffusion constants. For the Hi-C 1.24 cm square lattice with Al clad and the Hi-C 1.166 cm triangular lattice with Al clad, the calculated reactivities using B-1 constants are 4.0% and 7.6% higher than experimental reactivities, respectively. Corresponding values for P-1 calculations are 3.4% and 7.5%.

The following considerations of possible sources of inaccuracy show that much of the large reactivity discrepancy must be attributed (by the process of elimination) to the GAM-I cross sections. As mentioned above, transport effects are of little importance in the fast fission region. The use of the THERMOS code with an extra scattering region should yield good thermal parameters. In the resonance region, the Adler-Hinman-Nordheim treatment should give an adequate value for the U-238 resolved resonance integral provided a reasonably accurate value for the Dancoff factor is used. In the unresolved region, calculations

 TABLE II-8-III. RADIAL REFLECTOR SAVINGS
 FOR HI-C LATTICES

Lattice	λ_R (B-1), cm	λ_R (P-1), cm	λ_R (Experimental), cm
1.24 cm \square Al clad	8.07	8.27	8.13 \pm 0.16
1.24 cm \square SS clad	7.46	7.58	7.69 \pm 0.08
1.27 cm Δ Al clad	8.63	8.79	8.77 \pm 0.07

are made for $\ell = 0$ neutrons only (ℓ is the orbital angular momentum). An increase in the unresolved resonance integral is necessary to allow for absorption with higher ℓ values, but this increase would decrease calculated reactivities by only about 1%. The U-235 resonance absorption in GAM-I is treated in the infinite dilution approximation. Considerations of shielding of U-235 resonances would decrease reactivity somewhat, although capture and fission effects would tend to cancel. Shielding of U-235 would be important for computation of the initial conversion ratio.

Recently new versions of U-235 and U-238 for the GAM-I library have been obtained from Hanford. They differ from the original versions in the values of σ_c , σ_f , $\nu\sigma_f$ and in the U-238 resonance parameters. Use of these modified values in a GAM-I problem for the Hi-C 1.24 cm square lattice with Al clad led to a calculated reactivity 1.0% higher than the experimental value rather than 4.0% higher as obtained using the original library. More work will be done in connection with the use of different cross sections in the GAM library.

REFLECTOR SAVINGS

Radial reflector savings calculations were made for the Hi-C 1.24 cm square lattice with both types of clad and for the 1.27 cm triangular lattice with Al clad using the RE-122 (REX) multigroup diffusion code. Both four-group and two-group problems were done

using THERMOS constants and GAM-I constants for the core in both B-1 and P-1 approximations. GAM-I and THERMOS constants were also used for the radial H₂O reflector. Corresponding four-group and two-group values of reflector savings, λ_R , differed by less than 1 mm, while P-1 calculations produced values of λ_R one or two mm larger than those from B-1 calculations. Although the core constants used predicted reactivity very poorly, they led to values of λ_R in rather good agreement with experiment. Four-group values of λ_R are presented along with experimental values in Table II-8-III.

REFERENCES

1. G. D. Joanou and J. S. Dudek, *GAM-I: A Consistent P-1 Multigroup Code for the Calculation of Fast Neutron Spectra and Multigroup Constants*, GA-1850 (June, 1961).
2. H. C. Honeck, *THERMOS, A Thermalization Transport Code for Reactor Lattice Calculations*, BNL-5826 (September, 1961).
3. F. T. Adler, G. W. Hinman and L. W. Nordheim, *The Quantitative Evaluation of Resonance Integrals*, Proc., 1958 Geneva Conference, 16, Paper No. 1988, pp. 155-171.
4. H. C. Honeck, *Some Methods for Improving the Cylindrical Reflecting Boundary Condition in Cell Calculations of the Thermal Neutron Flux*, Trans. Am. Nucl. Soc. 5, No. 2 350 (1962).
5. E. M. Pennington, *Collision Probabilities in Cylindrical Lattices*, Nucl. Sci. Eng. 19, 215 (1964).
6. H. Soodak and R. Sullivan, *A Method for Calculating the Reactivity of D₂O-Moderated Natural Uranium Lattices with Clustered Rod Fuel Elements*, NDA-2131-38 (June, 1961).

II-9. Evaluation of Flux Trap Experiments in D₂O-Moderated Thorium-Uranium Cores

K. E. PLUMLEE

INTRODUCTION

As research continues, there are an increasing number of experiments which are limited by the neutron flux intensities available from current irradiation facilities. The need for higher neutron flux and beam intensities for research purposes has resulted in increasing interest in the design of reactors which produce large flux peaks in internal thermal columns (ITC) or flux traps. Such facilities are of interest since they have the ability to produce very high flux at modest reactor power levels, and to produce a very high thermal neutron source with a relatively small fast neutron component.

An ITC may be visualized as an internal reflector region surrounded by a fuel region. The resulting flux peak may be several times larger than would be obtained in an external reflector because an internal reflector has a more favorable geometry.

The experimental physics work carried out at Argonne with heavy water flux traps was limited to the use of existing fuel and facilities. While the resulting data are very encouraging, it is likely that improvements could be obtained by further work with an experimental system specifically designed for experimentation with heavy water-moderated cores and incorporated flux traps.

DESCRIPTION OF CORES AND FLUX TRAPS

Three types of fuel elements¹ were utilized for flux trap cores. These were designated by their atom ratios

(Th/U-235) which were 15/1, 25/1, and 50/1. Average weights of oxide per fuel element were estimated to be 434.6, 357.2, and 349.8 g, respectively. Nominal length of the stacked pellet columns was 152.5 cm. The 15/1 fuel was contained in nominal 0.793-cm o.d., Type 110 aluminum tubing weighing 34.5 g in 155-cm length. The 25/1 and 50/1 fuel were contained in nominal 0.793-cm o.d., Type 1100 aluminum tubing weighing 81.5 g in 155-cm length.

Lattice spacings were A_0 (0.953-cm or $\frac{3}{8}$ -in.), $2 A_0$, $3 A_0$, and $6 A_0$, all being based on an equilateral triangle lattice in the same grid.

DISCUSSION

Experiments have been performed with 25 D₂O and 3 small H₂O-filled internal thermal columns inside annular thorium-uranium-fueled cores. Moderator and reflector were D₂O. A wide range of dimensions and several fuel loading densities were used. These data are given in Tables II-9-I and II-9-II. The largest ITC was 104 x 104 cm. A fairly densely loaded fuel zone 10 cm thick (forming the boundary) was sufficient for criticality. Very densely loaded annular fuel zones as thin as 3 cm were found to be sufficient for criticality with ITC radii in the range 16 to 28 cm. One such core is shown in Fig. II-9-1.

ITC activation peaks in radial traverses at the midplane of the reactor were as great as ten times the two-dimensional (midplane) average in the fuel zone. The ITC peak was roughly three times that obtained

TABLE II-9-I. ACTIVATION RATIOS AND ASSEMBLY DESCRIPTION

Loading and Run Nos.	Approx. ϕ_{peak} /Specific Power, Fuel Zone		Ratio of Central Peak to Midplane Fuel Zone Activity		Flux Trap		Approx. Fuel Zone Dimensions, cm		Critical H ₂ O Height in Fuel and Trap, cm	No. of Fuel Pins	Lattice Spacing, cm	Fuel Type
	Average	Maximum	Average	Maximum	Material	Dimensions, cm	Inner	Outer				
449-1, -4	Not measured		Not measured		D ₂ O	67.9 × 67.9	67.9 × 67.9	83.8 × 83.8	148.8 ⁺	488	1.905	15/1
448-1	Not measured		Not measured			64.6 × 64.6	64.6 × 64.6	83.8 × 83.8	116.1			
447-1, -2	Not measured		Not measured			63.5 × 63.5	63.5 × 63.5	83.8 × 83.8	107.7 ⁻			
446-1, -2	Not measured		Not measured			104.0 × 104.0	104.0 × 104.0	124.5 × 124.5	142.3			
399-1	0.033	0.023	6.9	4.9		27.7 ⁻ radius	27.7 ⁻ radius	30.5 radius	115.9 ⁻			
398-1, -3	0.035	0.025	7.4	5.3 ⁺		26.9	26.9	30.5	108.6 ⁻			
397-1, -4	0.032	0.026	6.7 ⁻	5.4		25.4	25.4	28.1	118.5 ⁻			
396-1	—	—	—	—		16.4	16.4	19.3 ⁻	142.2			
395-1, -2	0.025	0.015	5.2	3.2		15.3	15.3	—	135.9			
394-1, -4	0.048	0.019	10.0	4.0		13.8	13.8	—	145.2			
393-1	—	—	—	—	10.6	10.6	—	Not critical				
391-1	—	—	—	—	None	None	0	Not critical				
374-1, -2	—	—	—	—	D ₂ O	~28.0 radius	~28.0 radius	~41.0 radius	147.8 ⁻	1.905	25/1	
367-1, -2	0.154	0.052	4.4	1.5	H ₂ O	5.1	Hex. 5.6 ⁻	29.0 ⁺	161.9			
365-1	0.164	0.070	4.7	2.0	—	—	equiv. radius	—	812			
364-1, -6	—	—	—	—	—	—	Hex. 5.2	30.5	139.1			
363-1	—	—	—	—	—	—	equiv. radius	—	893			
361-1, -4	0.182	0.091	5.2	2.6	—	—	5.6 ⁻ radius	30.5	138.2			
359-1, -2	0.136	0.084	3.9 ⁻	2.4 ⁺	—	—	~7.9	30.8	Not critical			
358-1, -3	0.112	0.066	3.2 ⁻	1.9 ⁻	—	—	5.6 ⁻	30.5	137.0			
357-2	—	—	—	—	Void	2.5 ⁺	4.4	27.6	140.9			
357-1	—	—	—	—	D ₂ O	2.6 ⁺	2.6 ⁺	—	132.6			
356-1, -2	0.031	0.021	0.88	0.61	None	None	0	—	137.4			
(central ϕ)	0.070	0.049	(central) 2.0	1.4	None	None	0	—	131.7			
(reflector ϕ)	0.115	0.080	(radial reflector) 3.3 ⁺	2.3 ⁻	None	None	0	—	133.2 ⁺			
271-2	0.136	0.080	3.9 ⁻	2.3 ⁻	D ₂ O	30.5 radius	30.5	44.5	123.2	970	—	
270-2	0.150	0.098	4.3 ⁺	2.8	—	—	—	—	91.0 ⁻			
269-1	0.112	0.084	3.2 ⁻	2.4	—	—	—	—	76.8 ⁻			
268-3	0.129	0.076	3.7	2.2 ⁺	—	—	—	—	152.6			
266-2	0.115	0.070	3.3	2.0	—	—	—	—	137.2 ⁻			
265-1	0.091	0.066	2.6 ⁺	1.9	—	—	—	—	651			
264-2	0.070	0.049	2.0	1.4	—	—	—	—	118.6			
263-2	—	0.059	—	1.7	—	—	—	—	743			
262-2	0.78 ^b	0.42	2.4	1.3 ⁻	None	None	0	—	108.0 ⁻			
261-1	0.78 ^b	0.36	2.4	1.1 ⁺	D ₂ O	11.1 radius	11.1	99.0	103.3 ⁻			
253-3	0.78	0.36	2.4 ⁻	1.1 ⁻	—	—	—	—	104.5			
252-1	0.32	0.32	1.0	1.0 ⁺	None	None	0	—	122.7			
251-3	(central ϕ) 0.72	0.32	(reflector ϕ) 2.2	1.0 ⁺	None	None	0	—	113.5			
									108.2	5.715	—	
									107.6			
									105.3			
									1082			
									1082			
									1082			
									1082			
									1082			
									1082			
									1082			

^a Ratio of estimated thermal flux in flux trap peak to fissions per liter-sec in the fuel region, at the midplane.

^b Calibrated measurements of thermal flux intensity and fission rate.

TABLE II-9-II. DESCRIPTION OF FUEL ZONES

Fuel Ratio, U-235/Th-232	Lattice ^a Pitch	Fuel Pellet Radius, cm	Cell Size, cm ²	U-235 Density, g/liter	Σ_a ^c (Approx. Values)	Σ_f ^c (Approx. Values)
25/1	5.715	0.2972	28.28	2.86	0.0051	0.0031
	2.858	0.2972	7.06	11.46	0.0191	0.0120
	1.905	0.2972	3.14	25.74	0.0406	0.0259
15/1	1.905	0.3302	3.14	49.79	0.0628	0.0445
	0.953	0.3302	0.786	199.0	^b	^b

^a Triangular lattice spacing in cm.

^b Because of the variation in neutron energy spectrum in the thin fuel zones having 1 A₀ lattice spacing, no estimate of Σ_a or Σ_f was made, since these are spectrum dependent and vary with radius.

^c All averaged macroscopic cross sections.

in the radial reflector, and five times the highest level in the fuel zone. Figures II-9-2a, II-9-2b, and II-9-2c show representative traverses taken with very densely loaded fuel zones.

Although only three small H₂O-filled aluminum thimbles were flux mapped, the most effective (and largest) one produced a greater activation peak than was obtained with similar fuel zones and D₂O-filled ITCs. The H₂O-filled ITCs produced greater flux peaks in much smaller dimensions than were obtained with D₂O-filled ITCs. However, greater reactivity losses were involved with H₂O, and increased dependence on fuel zone thickness was indicated. Figures

II-9-3 and II-9-4 show traverses taken with D₂O and H₂O-filled ITCs, respectively.

Although the relation of ITC radius to the magnitude of the accompanying flux peak is also a function of the thickness of the surrounding fuel zone, the effect is shown for a simple case in Fig. II-9-5. Commencing with a core of moderate fuel density, the axial flux trap was produced and enlarged by removal of fuel

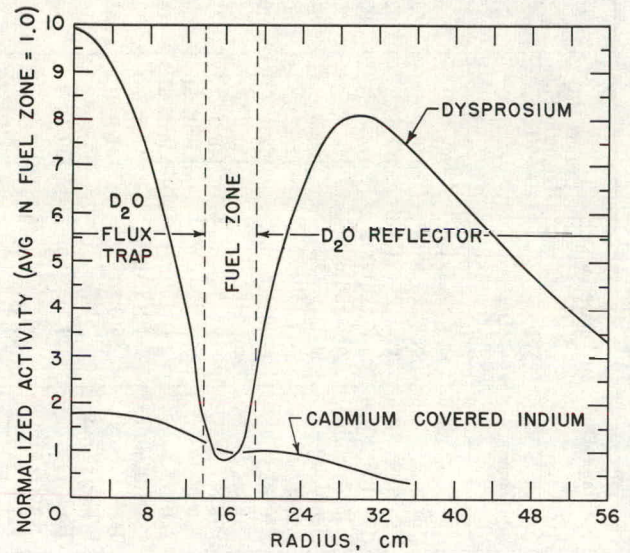


FIG. II-9-2a. Radial Activation Traverse in Core with High Fuel Density—Loading 394.

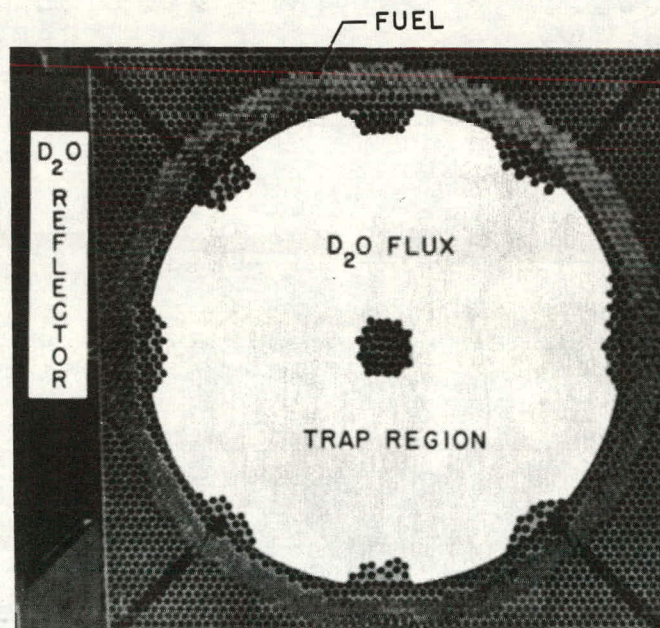


FIG. II-9-1. ~3-cm Thick Annular Fuel Zone Enclosing a Flux Trap.

from the axis or inner edge of the fuel zone. The ITC flux peak increased with ITC radius relative to flux in the fuel region up to a maximum near 16 cm radius. Loading additional fuel on the outer edge of the fuel zone without changing the radius of the ITC resulted in an increased peak.

Reactivity generally increased in these cores as a flux trap radius was increased up to 10 cm. This effect was attributed to the reduction in resonance capture in the fuel region as a larger fraction of neutrons was thermalized in the ITC and was "reflected" back into the fuel zone with energy levels below the Th_{232} resonance. This effect is shown in Fig. II-9-6, for the moderate fuel density loadings.

One of the more interesting categories of flux trap

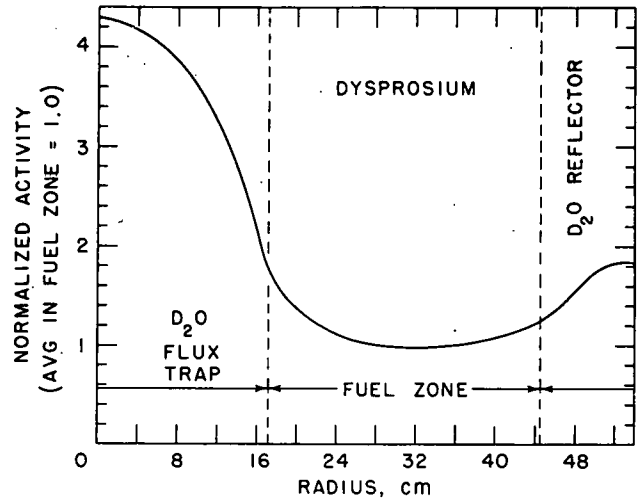


FIG. II-9-3. Radial Activation Traverse in Core with Moderate Fuel Density—Loading 269.

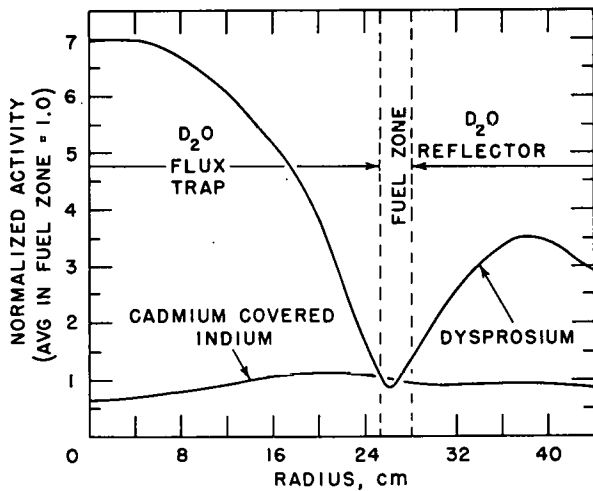


FIG. II-9-2b. Radial Activation Traverse in Core with High Fuel Density—Loading 397.

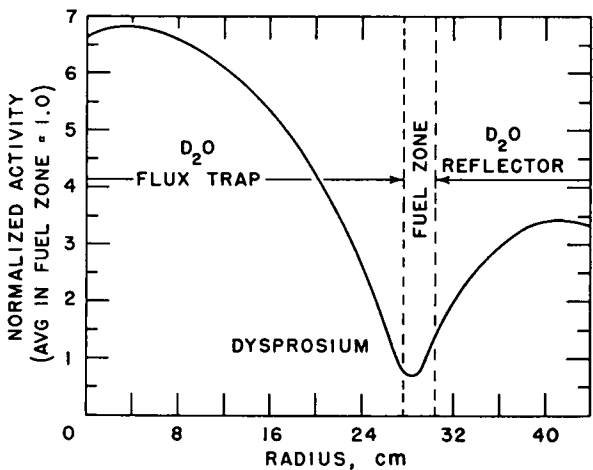


FIG. II-9-2c. Radial Activation Traverse in Core with High Fuel Density—Loading 399.

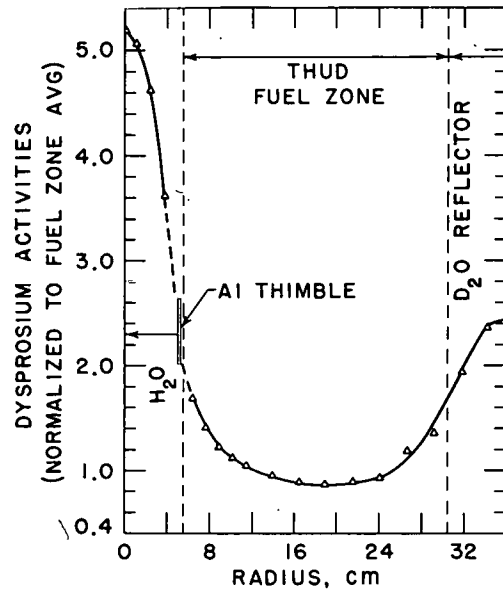


FIG. II-9-4. Radial Activation Traverse in Core with Moderate Fuel Density and H_2O -Filled Flux Trap—Loading 361.

configurations involved very densely loaded fuel zones for which $k_\infty < 1$, as usually defined in the four-factor formula. Such cores are shown in Fig. II-9-1 and Table II-9-I, Loadings 391-399. The small value of resonance escape probability resulting from the very close packing of $\text{ThO}_2\text{-UO}_2$ fuel in such a fuel zone precluded criticality in a fully reflected cylindrical core containing 1,482 fuel elements (see Table II-9-I Loading No. 391). Installation of an internal reflector resulted in a larger fraction of neutrons reaching thermal energy,

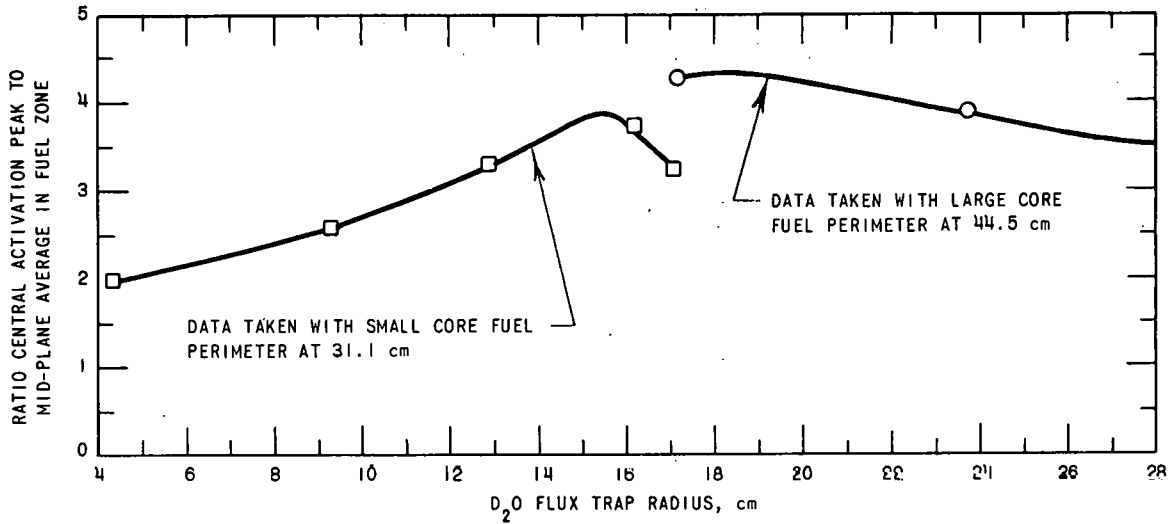


FIG. II-9-5. Effect of Flux Trap Radius on Activation Distribution of Cores with Moderate Fuel Density.

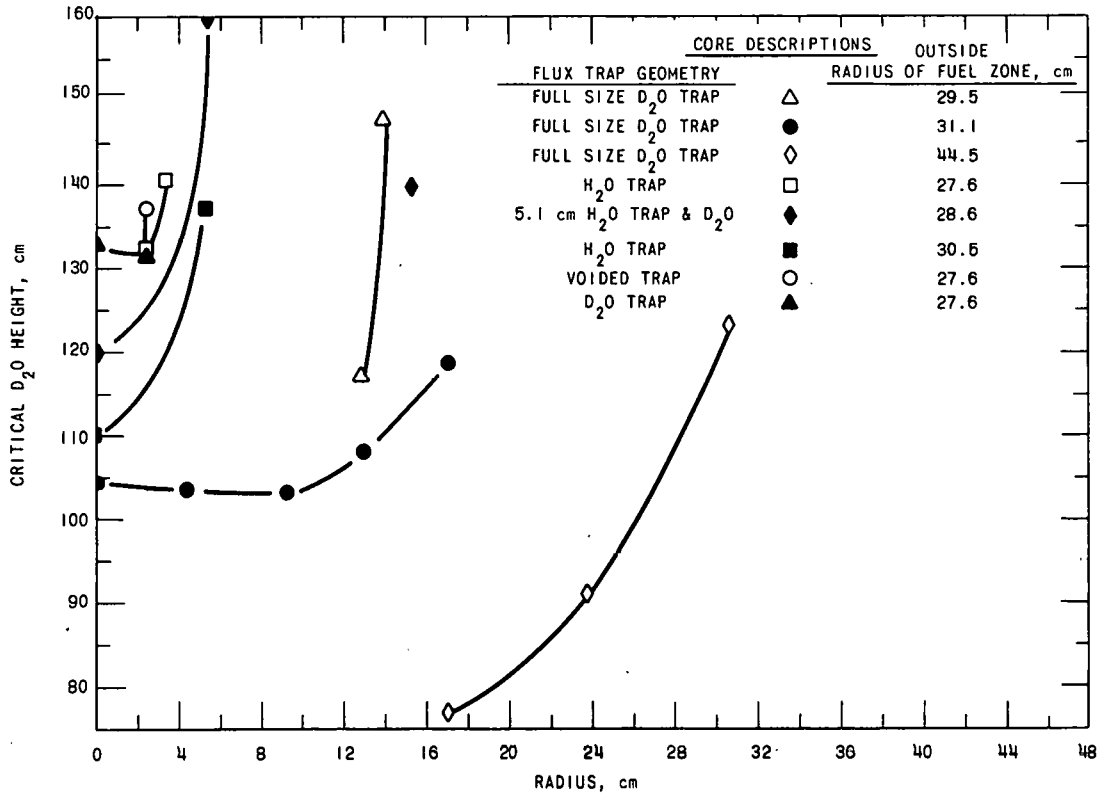


FIG. II-9-6. Critical D₂O Height Versus Flux Trap Radius for Cores with Moderate Fuel Density.

and consequently, in increased reactivity. This is shown in Loadings Nos. 393 to 396. Loading No. 396 consists of the 403 fuel elements at or nearest the periphery of Loading No. 391, and was obtained by stepwise removal of a total of 1,079 fuel elements from

Loading No. 391. Loading No. 396 was critical, yet Loading No. 391 containing nearly four times as much fuel was well subcritical. The gain in reactivity was indicated to be a function of thickness of the annular fuel region with an optimum thickness of 3.5-4.0 cm

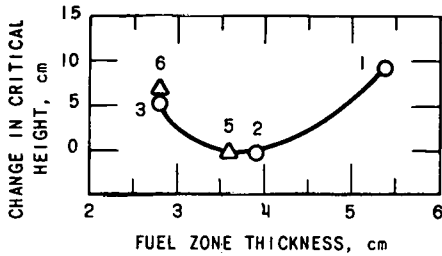


FIG. II-9-7. Variation in Critical D₂O Height for Cores with High Fuel Density.

optimum was not found during experiments with this fuel loading density. Apparently increasing the ITC radius beyond 13.8 cm, the smallest size with which criticality was obtained, resulted in a gain in reactivity although there were superimposed variations accompanying reductions in fuel zone thickness, in the sequence of experiments performed as shown in Fig. II-9-8.

EXTRAPOLATED POWER REQUIRED TO PRODUCE 10¹⁶ PEAK THERMAL FLUX

Rough estimates of the power levels required to produce 10¹⁶ peak thermal flux are given in Table

TABLE II-9-III. EXTRAPOLATED POWER TO PRODUCE 10¹⁶ PEAK THERMAL FLUX

Loading No.	Cell Dis-advantage Factor	U-235 Density, g/liter	Volume of Fuel Zone, liter	Estimated Power Level for 10 ¹⁶ Flux, MW
399	1.28	199.0	59	418
398			70	468
397			54	357
395			59	549
394			87	420
367	1.20	25.74	412	621
365			395	559
361			387	494
359			329	561
358			315	652
271			406 ⁺	821
270			400	693
269			407	631
268			291	603
266			263	473
265			272	549
264			285	728
263			308	1022
261	1.24	2.86	3731	1110
253			3471	1033
252			3322	989

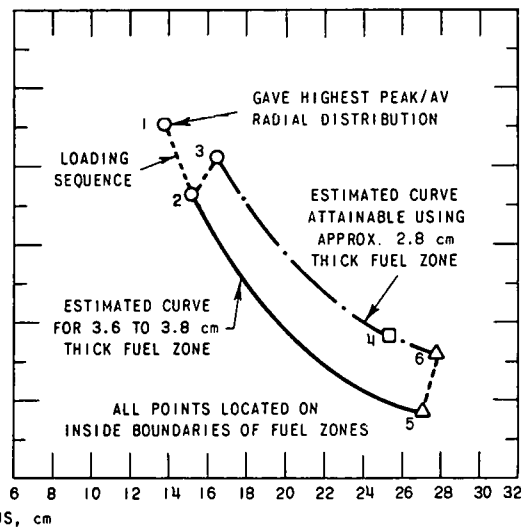
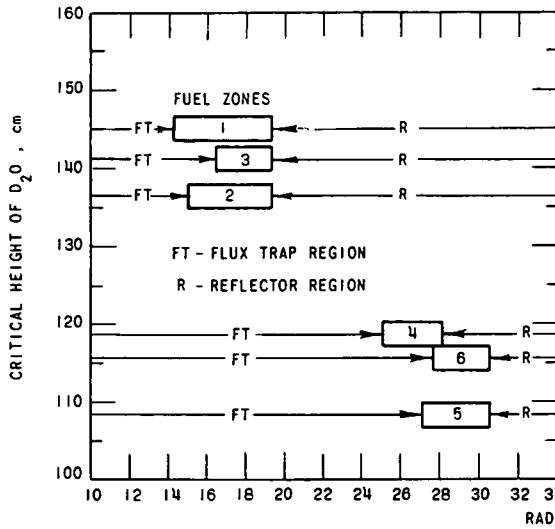


FIG. II-9-8. Critical D₂O Height Versus Flux Trap Radius for Cores with High Fuel Density.

as shown in Fig. II-9-7. Reactivity was also found to be a function of the radius of the ITC although an II-9-III. The lowest power, approximately 357 MW, was indicated for Loading No. 397. This extrapolation does not account for the effects of power coefficients of xenon poisoning.

Absolute flux and fission rate measurements were made during two runs. These measurements agreed

well with the values obtained by applying standard corrections in calculating the ratio of peak flux to reactor power from the radial and axial activation traverses. It was necessary to use flux-averaged cross sections,³ fuel disadvantage factors,^{1,3} and foil flux perturbation⁴ corrections in this comparison. The radial activation traverses were with 0.584-cm diameter, 0.0086-cm thick 90% manganese-10% copper alloy foils

for loadings numbered lower than 357; and were 0.584-cm diameter, 0.0023-cm thick 3.7% dysprosium-86% aluminum alloy for the remaining loadings.

REFERENCES

1. W. C. Redman, S. G. Kaufmann, K. E. Plumlee and Q. L. Baird, *Critical Experiments with Thoria-Urania Fuel in Heavy Water*, ANL-6378 (1961).
2. K. E. Plumlee, *Flux Trap Experiments in D₂O-Moderated Thorium-Uranium Cores*, ANL-6915 (to be published).
3. E. M. Pennington, *Calculations for ZPR-VII Flux Trap Reactors with Heavy Water-Moderated Cores*, ANL-6406 (1961).
4. F. H. Helm, *Numerical Determination of Flux Perturbation by Foils*, Nucl. Sci. Eng. **16**, No. 2, 235-238 (1963).

II-10. PuO₂-UO₂ Fueled Thermal Critical Experiments

C. E. TILL

A study was carried out to outline the important problem areas and requirements for a proposed program of critical assembly work with plutonium fuel moderated by light water. Calculations have indicated that Pu has considerable potential as a thermal reactor fuel, but very little integral information as yet exists on the physics behavior of this material in thermal systems.

FUEL MATERIAL

The fuel material selected was natural UO₂ containing a small percentage of PuO₂. The high cross section and prominent low-lying resonances of all the Pu isotopes mean that self shielding of the Pu will strongly affect the physics of this type of fuel. The fuel fabrication should be such that the fuel material is sufficiently homogenized that any self shielding effects due to local concentrations of Pu, over and above the self shielding present in a homogeneous element, are not significant. This also means that the PuO₂ particle size should be kept small. For example, calculation indicates that for a typical case, self shielding in the thermal region would be about 7% greater than that of a homogeneous blend in which the PuO₂ is distributed in the form of 100- μ diameter spheres. This extra self shielding would be correspondingly greater in the resonances and the reactivity effects caused by the discrete particle size could be very difficult to take into account properly.

The possibility of using fused microspheres of PuO₂ as the Pu portion of the mixed oxide was considered. The contamination-free properties of these spheres are very attractive. However, if their size is decreased to the point where particle self shielding is not significant, they would, if released to the air, remain airborne for a considerable time and thereby present a clear ingestion hazard. Calculation indicates

the compromise between self shielding and ready dispersion in the air cannot be a good one.

FUEL CLADDING MATERIAL

The high toxicity of Pu demands that the fuel cladding be inviolate at all times. Aluminum is a suitable cladding from the material viewpoint of ease of interpretation of results. Calculations based on the SPERT series of oxide fuel transient tests¹ indicate that for the severest credible excursion, the clad temperature will remain close to the boiling point of water. Thus the fuel element should retain its integrity in spite of the low melting point of the cladding material.

The requirement that the fuel be clad at all times presents serious problems for reaction rate measurements in the fuel. The streaming path introduced on either side of any measuring foil in the fuel by the presence of a cladding over the adjacent ends of the fuel can introduce a significant error, particularly where resonance effects are important.

PLUTONIUM ISOTOPIC COMPOSITION

The physics behavior of plutonium in a thermal reactor is very sensitive to its isotopic composition. Isotopic composition was a variable of major interest in this proposed program. Isotopic contents of interest range from pure Pu-239 to material that contains up to 70% of the higher Pu isotopes. The behavior of Pu with low concentrations of the higher isotopes is of interest in connection with long-burnup, uranium-fueled, once-through reactors which build in significant quantities of Pu, but which do not burn the Pu to the point that large fractions of the higher isotopes are produced. The compositions of interest to reactors on a Pu-recycle scheme have contents of higher isotopes ranging from 30% to 70%. At this time, availability may dictate a first-loading composition under 20% in the content of higher isotopes.

REACTIVITY CALCULATIONS

Survey calculations were done for $\text{PuO}_2\text{-UO}_2$ mixed oxide fueled, water moderated lattices for the 27 combinations possible using three values each of the three principal variables: PuO_2 content, Pu isotopic composition and water to oxide volume ratio. The PuO_2 contents were 2, 4 and 6 w/o; the isotopic compositions were 100% Pu-239, and ratios of 90:10 and 80:20 Pu-239 to Pu-240; the water to oxide volume ratios were 1, 3 and 5. The uranium was natural UO_2 . The lattice was assumed to be made up of $\frac{1}{2}$ -in. diameter rods clad in 40 mils of Al. The calculational method used was four-group treatment that gave satisfactory agreement with the measured buckling values of the Hanford Pu-Al alloy subcritical experiments and a homogeneous aqueous critical experiment.^{2,3,4}

RESULTS

Results of the calculations of bucklings are shown in Table II-10-I, which illustrates the rather complex interplay of the three variables (PuO_2 content, isotopic composition and water to oxide ratio) on the lattice reactivity.

The column $V_{\text{H}_2\text{O}}/V_{\text{oxide}} = 1$ (Table II-10-I) illustrates the effect of increasing the Pu-240 content in a tight lattice. The reactivity of the lattices in which the Pu was pure Pu-239 steadily increases with increasing enrichment over the range covered here. This is similar to the behavior expected for U-235 enrichment. With Pu containing 10% or 20% Pu-240, however, the buckling versus Pu content relationship is almost flat; in the 10% case the buckling appears to peak at an enrichment of about 4%, while for the 20% case the buckling actually decreases with increasing enrichment over the entire range covered. This latter effect has previously been noted by K. Puechl,⁵ whose calculations, however, indicated that the effect is much greater than do the calculations presented here. The effect is due to spectral hardening with increasing enrichment which results in a progressively larger fraction of neutrons being captured in the low-lying Pu-240 resonance. As the lattice pitch is increased and the spectrum thus softened, the effect tends to disappear, as illustrated by the columns in Table II-10-I corresponding to volume ratios of 3 and 5.

Based on the bucklings listed in Table II-10-I calculations of the number of fuel rods needed to maintain criticality as the lattice is tightened to a volume ratio of unity show that this number is fairly insensitive to enrichment. It depends mainly on the isotopic composition, approximately doubling for each 10% increase in Pu-240 content. The amount of Pu required, however, increases approximately linearly

TABLE II-10-I. CALCULATED BUCKLING VERSUS PLUTONIUM CONTENT, ISOTOPIC COMPOSITION AND WATER-TO-OXIDE VOLUME RATIO

$\text{Pu}^{239}\text{O}_2$, %	$\text{Pu}^{240}\text{O}_2$, %	Buckling B^2 ($\times 10^4$) cm^{-2}		
		$\frac{V_{\text{H}_2\text{O}}}{V_{\text{oxide}}} = 1$	$\frac{V_{\text{H}_2\text{O}}}{V_{\text{oxide}}} = 3$	$\frac{V_{\text{H}_2\text{O}}}{V_{\text{oxide}}} = 5$
2	0	79	123	115
4	0	93	149	152
6	0	101	160	166
1.8	0.2	47	101	94
3.6	0.4	51	122	129
5.4	0.6	50	130	142
1.6	0.4	30	86	80
3.2	0.8	29	103	111
4.8	1.2	28	111	124

with enrichment. Thus the effect of boosting the PuO_2 content above 2% is only to increase the Pu inventory; the core sizes and number of rods required remain almost the same. The lower the PuO_2 content, the less the external hazard in handling the fuel, and at 2% PuO_2 the characteristics of the fuel are dominated by the Pu anyway. Hence there seems to be little incentive to go above 2% PuO_2 content. Also, a compromise between once-through and recycle usages is offered by 2% PuO_2 , so all-in-all this is probably a good choice for these experiments.

BIOLOGICAL HAZARDS

In addition to Pu being highly toxic in a chemical sense, the radiological hazard set by the combination of high alpha particle energy, long biological lifetime and bone-seeking character of plutonium result in a very low maximum-allowable body burden. Handling and monitoring procedures were worked out to ensure essentially that an intact barrier between the fuel and its environment exists at all times that personnel might be exposed to the environment. The fuel also presents an external hazard and exposure times during loading changes must be suitably limited.

NEUTRONIC HAZARD CONSIDERATIONS

The delayed neutron fraction of Pu-239 and its effective neutron lifetime both tend to be shorter than those in comparable U-235 fueled assemblies and hence the excess must be more carefully controlled.

The Doppler effect of the fuel containing a few per cent PuO_2 should be about as strongly negative as it is for comparable U-235 enrichment. Similar amounts of U-238 are present and its resonance capture will be practically unaffected by the small amount of Pu-239 present. The calculations of Section D indicate that the Pu-239 resonances are not very strongly self shielded at these concentrations, so this potentially

positive contribution to the Doppler effect is expected to be small. Further balancing any positive effect is the presence of the 240 isotope which these calculations indicate is strongly self shielded in its 1 eV capture resonance.

The effect of increased neutron temperature is expected to be negative at these Pu concentrations. Thus a prompt negative temperature coefficient of the same magnitude as that for a comparable U-238:U-235 system is to be expected. Calculations indicate that any credible excursion would be safely terminated without core damage by a prompt negative temperature coefficient of this magnitude.

REFERENCES

1. A. H. Spano, et al., *Self-Limiting Power Excursion Tests of a Water-Moderated Low-Enrichment UO₂ Core in SPERT-1*. IDO-16751 (February, 1962).
2. V. I. Neeley, et al., *Neutron Multiplication Measurements with Plutonium-Aluminum Alloy Rods in Light Water*, Trans. Am. Nucl. Soc. **3**, No. 1, 292 (1960).
3. W. P. Stinson and L. C. Schmid, *Subcritical Measurements with 1.8 w/o Pu-Al Rods in Light Water*, HW-74190 (July, 1962).
4. E. F. Kraesi, et al., *Critical Mass Studies of Pu Solutions*, HW-24514 (1952).
5. K. H. Puechl, *The Potential of Pu as a Fuel in Near-Thermal Converter Reactors*, Nucl. Sci. Eng. **12**, No. 2, 135-150 (1962).

II-11. Argonne Advanced Research Reactor—Physics Advantages of Intermediate Cores for Research Reactors¹

C. N. KELBER

The outstanding reason for the use of low cross section materials in research reactor fuels is the fact that in a homogeneous medium the thermal neutron flux is inversely proportional to the absorption cross section. The demand for higher fluxes (hence power densities) coupled with increasingly complex experimental arrays has led to the design of research reactors in which neutrons are thermalized in specific locations well removed from the core. Under these conditions the penalty in flux level and reactivity from the use of moderately high cross section materials may be small.

As the fuel investment increases, however, it is expected that the incremental reactivity of fuel added for burnup will decrease, so that the reactivity swing over a cycle of given length is decreased; alternatively longer cycle times are available without the use of unusual control methods. Of at least as great importance is the possibility of retaining complete xenon override even at power densities of the order of a few megawatts per kilogram of fuel, or more. This implies a core of intermediate neutron energy, and this is the case. The disadvantages of such cores are well known and, hence, will not be discussed.

In a typical AARR core design the median energy of fission varies from 15eV at the core center to 1eV at the edge. The effective value of η , the neutrons released from fission (of U-235) per absorption in U-235, also varies. A typical value of η is 1.81 in the center of a fresh core. Eta increases with burnup to 2.05 at the edge of a heavily burnt core. In this way,

the incremental reactivity worth of fuel increases with burnup.

The hardness of the spectrum also implies a reduction in the worth of typical control rod materials. Thus, hafnium or europium in the core are expected to be three to four times as effective as cadmium. In a typical thermal reactor core massive hafnium rods are commonly 15 to 20% more effective than cadmium rods; but in cores such as those being discussed the flux in the range 1 to 10eV (the region of hafnium resonances) is 5 to 10 times that in the range 0 to 0.4eV. At the core edge this is not the case; the discrepancy between cadmium and hafnium is much less there.

Concomitant with the reduction of effective cross section of thermal resonance absorbers such as cadmium is a reduction in Xe-135 and Sm-149 worth. Except for small regions near the core edges the effective xenon cross section is much less than that encountered in typical thermal reactor cores.

In a high flux thermal core the xenon residence time is governed almost completely by the lifetime to absorption; in these cores the lifetime to absorption is about the same as the decay time and the mean residence time is thus very long. In terms of recovery from partial or complete scrams this means the kinetic behavior of the system at 100 MW resembles that of a thermal reactor in the $1-5 \times 10^{13}$ flux range. The necessary response time is long; typically an hour or more is allowed for recovery if only 1% δk is available.

TABLE II-11-I. A TYPICAL NEUTRON INVENTORY BASED ON ONE VIRGIN NEUTRON PER REACTOR

Note: Leakage—0.18.

	Captures	Fission
Fuel		
U-235 plus equilibrium Xe and Sm-149.....	0.17	0.43
Fission products.....	0.01	—
Burnable poison (Sm).....	0.005	—
	0.185	0.43
Hydrogen		
In core.....	0.003	—
In I.T.C. ^a	0.02	—
In Be.....	0.03	—
	0.053	
Light elements		
O.....	0.001	—
Be.....	0.02	—
Al or Zr.....	0.01	—
	0.031	
Heavy metals		
Fe.....	0.02	—
Ni.....	0.007	—
Cr.....	0.004	—
	0.031	
Power Flatteners	0.09	
Total	0.390	0.43

^a Internal Thermal Column.

Even more important, the total δk needed for over-ride at any time is small, $\sim 2.3\%$ at 100 MW, so that recovery from scrams need be considered a problem only near the end of a fuel cycle. For the same reason Sm-149 is not a problem even in irradiated cores stored for a long time; the reactivity gain from decay of xenon more than compensates for the buildup of samarium.

By way of summary a typical neutron inventory is given in Table II-11-I. The U-235 captures include the captures in equilibrium xenon and samarium. These two hold down about 3% in k . The term "fission products" refers to non-saturating fission products. The core studied here included some burnable poison, samarium, and a small amount of poison is still present at this stage, which is about halfway through a core cycle. Captures directly associated with the fuel are thus 0.185 (per virgin neutron).

Captures in hydrogen (in water) account for 0.053 while the remaining moderator or light elements capture only 0.031 neutrons. The stainless steel captures are (coincidentally) also 0.031, so that the parasitic capture in hydrogen is actually larger than that of stainless steel. In this core design, power flattening shims were employed and they captured excessively: 0.09 neutrons per virgin neutron. Spatial fuel variation accomplishes the same end; excessive parasitic losses are at the same time decreased. It is concluded that the stainless steel does not add an objectionable amount of parasitic capture.

The full utilization of such heavily loaded cores requires as large a fuel inventory as can be achieved and controlled in the design. With 37 w/o UO₂ dispersed in stainless steel plates, cores have been designed with cycle lengths of 35 to 90 days at 100 MW. Later results show that much longer cycle times (~ 150 days at 100 MW) may be achieved if loading densities of 1 kg U-235 per liter of core can be realized. The plates themselves, however, can probably take irradiations of 120–150 days. It is desirable that the reactivity life be comparable to the irradiation life in costly cores. Desirable improvements in these fuels center on increasing the fuel content. Alternative fuels include dispersions in zircalloy or zirconium-clad, metal fuels.

The use of heavily loaded cores implies some disadvantages. At the interfaces of the core and reflector or flux trap, incoming thermal neutrons are readily absorbed by the fuel and a power peak is created. This may be avoided by the use of shims which absorb mainly thermal neutrons or by special variation of the fuel loading. The latter has been found to be the more satisfactory method. Since the diffusion area for thermal neutrons in such cores is typically of the order of 0.1 cm², fuel variations must be sizeable over distances of 0.3 cm (0.1 in.) or less.

Another problem is that a heavily absorbing core in a diffusive medium creates a thermal neutron sink and hence a neutron concentration gradient in the reflector; this depletes the neutron flux in the reflector. A crude estimate of this depletion is $2\exp(-2\sqrt{\tau/L^2})$. In H₂O this is small, but in pure beryllium the relative variation can be extremely large, approximately a factor of 2.5.

REFERENCE

1. C. N. Kelber, *Physics Advantages of Stainless Steel Cores*, Research Reactor Fuel Element Conference, September 17–19, 1962, Gatlinburg, Tennessee, TID-7642 (Vol. I).

II-12. Argonne Advanced Research Reactor—Optimization of the AARR Core and Reflector Design for Flux Enhancement¹

C. N. KELBER

The design of the Argonne Advanced Research Reactor has reached the stage where the effects of small design changes on the flux can be profitably studied. In particular, a strong effort was made to find those design changes which yielded at the experimental facilities the maximum thermal neutron flux per unit power.

The first problem investigated was that of correlating the results of calculations in idealized geometry with the actual design. An approximation which has been used for many years is to preserve the relative volumes of various regions. This approximation usually gives good prediction of reactivity but it is not obvious that the flux will be so well predicted; indeed, comparison of calculations in square and circular geometries showed this was not the case.

If one is concerned with predicting the maximum thermal flux in an internal thermal column (ITC), then the following argument can be used.

Suppose the flux of fast neutrons on the column periphery is uniform and isotropic. Assume two group theory applies in the ITC. Then the source of slow neutrons arising from fast neutrons emitted at a point on the periphery is proportional to the mean chord length from that point, and the average source density of slow neutrons in the ITC is proportional to the mean chord length. (It is assumed that if the ITC is not convex, the surrounding region is non-moderating.) Calculations of fluxes in square or circular geometries confirm that ITC's of the same mean chord length have very nearly the same maximum flux.

On the basis of preserving the mean chord length the basic hexagonal pattern of the ITC core was chosen to yield an optimum mean chord length (distance between flats) of 14 cm. The basic hexagonal side is then 8.083 cm.

The problem of power distribution was the next to be considered. Since the power must be flattened it was necessary to find the effect of such flattening on

the peak fluxes. The inner 10% of the core volume gives rise to almost one-half the central flux and 80% the central flux comes from the inner 35% of the core. Hence, the power should be at a maximum over the inner 10% of the core and decrease slowly over the next 25% of core volume. The situation with respect to external reflector fluxes is similar at the outer core edge, but not so severe.

There is little effect of core blackness on thermal neutron fluxes once the fuel concentration is high. Substitution of aluminum for stainless steel at AARR fuel loadings makes a difference in experimenters' fluxes of less than 2%, for a given power distribution.

To enhance the flux in experimental beam facilities the power density is increased at the outer edge (a small marginal gain) and a composite reflector is introduced.

A thin layer (~2.5 cm) of beryllium suffices to moderate most of the neutrons leaving the core to the point that they are rapidly thermalized in water. The effective slowing down length in water is so small for these neutrons that a layer of water 4 cm thick enhances the available thermal flux by 25%. The water layer is followed by a beryllium reflector. This array is superior to other constructions of water and beryllium.

Increasing the leakage from the core by decreasing the moderator density obviously increases the available flux. Changing from metal to water volume ratios of 1:1 to 5:3 yields a 25% increment in flux at the expense of reactivity loss and increased heat removal difficulties.

Finally, the use of fuels such as U-233 or Pu-239 will increase the available flux because of the increase in the number of excess neutrons available per fission.

REFERENCE

1. C. N. Kelber, *Enhancement of Experimenters' Fluxes in the Argonne Advanced Research Reactor (AARR)*, Trans. Am. Nucl. Soc. 5, 1 (1963).

II-13. Argonne Advanced Research Reactor—Physics Calculations

B. N. KRISTIANSON and C. N. KELBER

Calculations performed in support of the Argonne Research Reactor include flux and power distributions; spatial distributions of equilibrium Xe-135 and Sm-149; prompt neutron lifetime and effective delayed neutron fractions; and distributed void worths and other distributed perturbation effects. The power coefficient was also determined, using temperature-dependent cross section sets. All calculations assume the reactor to be near the start of its lifetime.

The core composition used for the calculations is based on a physically realizable configuration. The use of variable loading to flatten power is represented by the designation of two compositions, fuel and diluent. The fuel composition represents the core composition when loaded with 37 w/o UO₂ fuel plates. The diluent composition represents the core composition when stainless steel is substituted for UO₂. The core volume fractions and elemental densities at STP are given in Table II-13-I.

A circular cylindrical configuration with an active core height of 45 cm was assumed. In addition, a vertical reflector saving of 15 cm was assumed. Regional radii and compositions are given in Table II-13-II.

The fine core dimensions are used so that a varying UO₂ loading from one plate to the next may be used. The water gap in the reflector regions overestimates the reactivity loss there since it will not extend over the entire height of the reflector. Also, this gap may be eliminated in those regions where a higher, smoother fast flux is desired.

The basic cross section set used was that of Hansen and Roach.¹ The U-235 self shielding at 300 b/atom scattering was taken into account, and the treatment below 1 eV was altered. Two types of sets were used—three sets (at 21, 85, and 100°C) with 18 energy groups each with downscattering into 5 groups and upscattering into 3 groups, and the second type, a set with 16 energy groups with downscattering into 5 groups and no upscattering. All the sets were identical in the energy range above 1 eV. In the 18-group sets, the energy range below 1 eV was divided into 5 groups: 0.64–1.0 eV, 0.4–0.64 eV, 0.1–0.4 eV, 0.02–0.10 eV, and 0–0.02 eV. A 1/E spectrum was assumed for the range 0.64–1.0 eV. The spectrum in the lower energy groups was generated by a 19-group Radkowski kernel using the SLOP-1 code.² In the consistent P-1 approximation, this code computes the spatial thermal flux distribution in the reactor model and yields the few

TABLE II-13-I. AARR CORE VOLUME FRACTIONS AND ELEMENTAL NUMBER DENSITIES (STP) USED IN PHYSICS CALCULATIONS

Material	Volume Fractions	
	Fuel	Diluent
H ₂ O	0.502577	0.502577
SS	0.371301	0.495721
UO ₂	0.124420	0
Zr	0.0017	0.0017
	Element	Elemental Densities, atoms/b-cm
H ₂ O	H	0.064472
	O	0.032236
SS	Fe	0.063310
	Ni	0.006582
	Cr	0.016433
<i>UO₂ (10 g/cc, 93.7% U-235 in U)</i>		
	U-235	0.021110
	U-238	0.001419
	O	0.04506
Zr	Zr	0.0423.

TABLE II-13-II. IDEALIZED REGIONAL RADII AND COMPOSITION

Region No.	Outer Radius, cm	Composition
1	2.65962	Sample
2	6.85	Water
3	6.95	Stainless steel
4	7.00	Water
5	7.1883	Core
6	7.3718	Core
7	7.5508	Core
8	7.7257	Core
9	7.8967	Core
10	8.0641	Core
11	8.2281	Core
12	8.3887	Core
13	8.5467	Core
14	23.2172	Core
15	23.613	Core
16	23.8084	Core
17	24.0022	Core
18	24.2	Core
19	24.7	Zr (followers)
20	27.2	Inner Be reflector
21	31.5	Water
22	55.5	Outer Be reflector

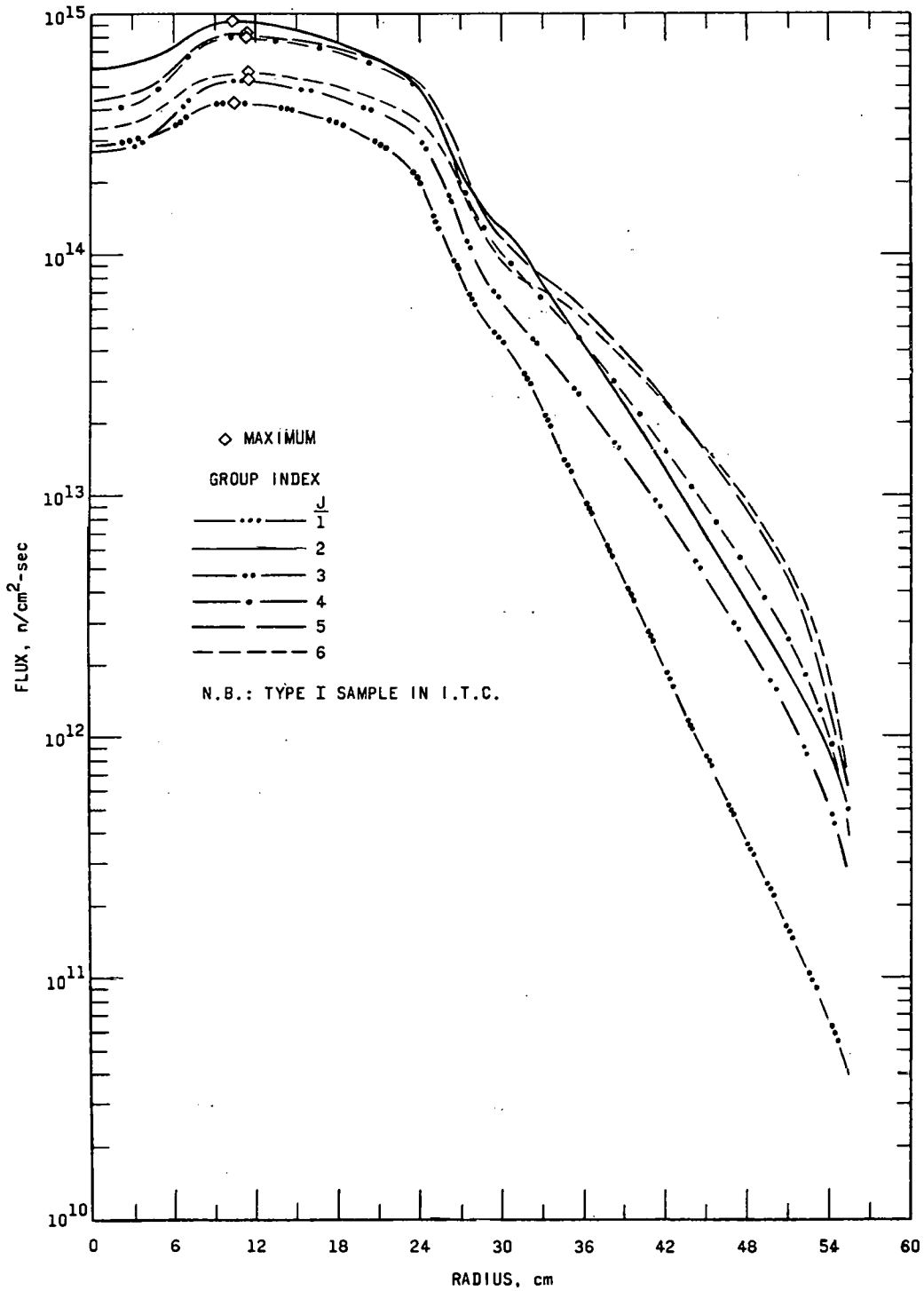


FIG. II-13-1. Axially Averaged Fluxes in AARR at 240 MW (Groups 1-6).

thermal group cross section averages. Moderation is by hydrogen alone. The energy dependence of the cross sections is that given in Ref. 3. Beryllium cross sections were generated separately and were based on a mass 9

free gas model. The 16-group set (at room temperature) was based largely on the Hansen and Roach set¹ except that the thermal groups were generated by the SOFO-CATE code.⁴ Each type of set contained some cross

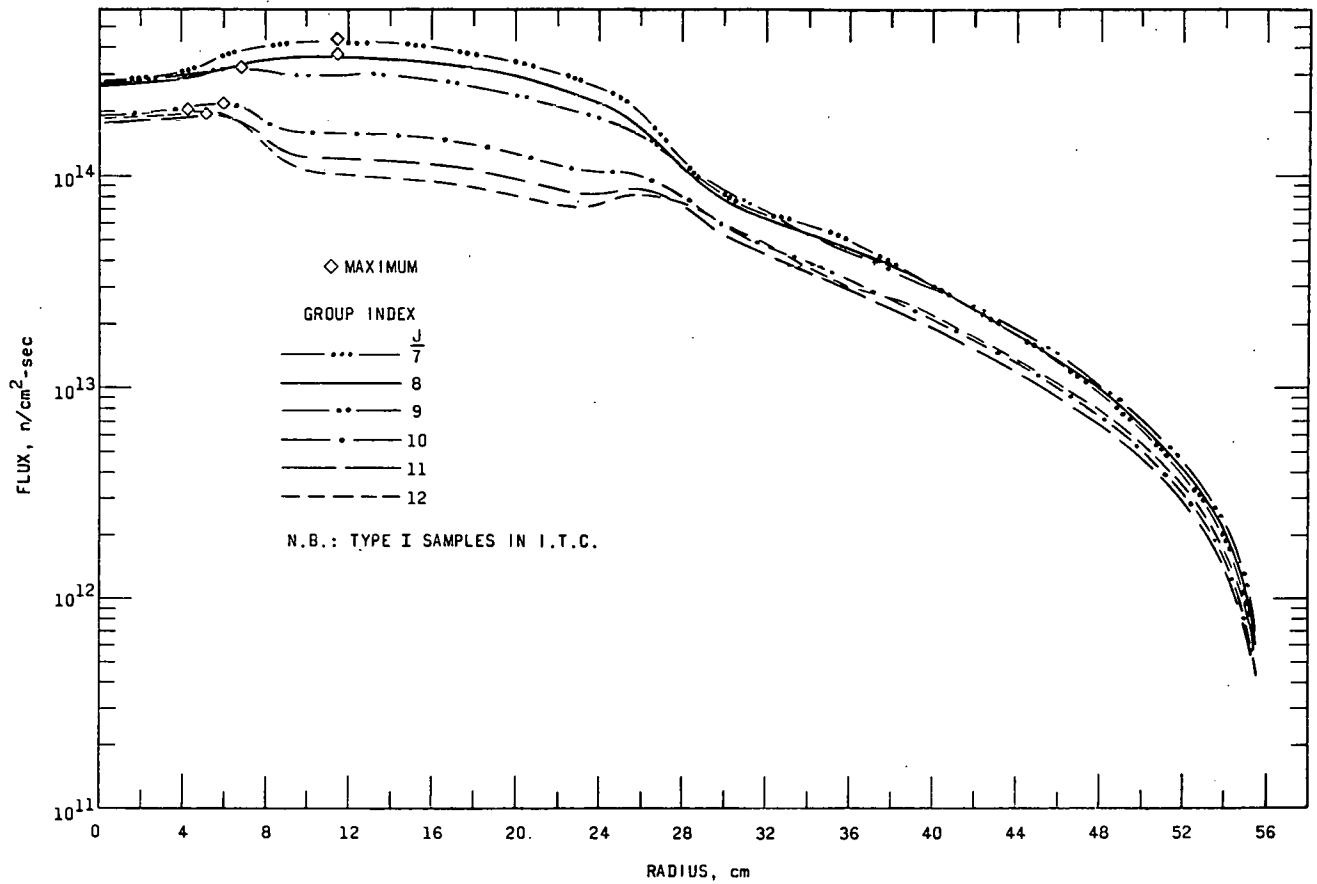


FIG. II-13-2. Axially Averaged Fluxes in AARR at 240 MW (Groups 7-12).

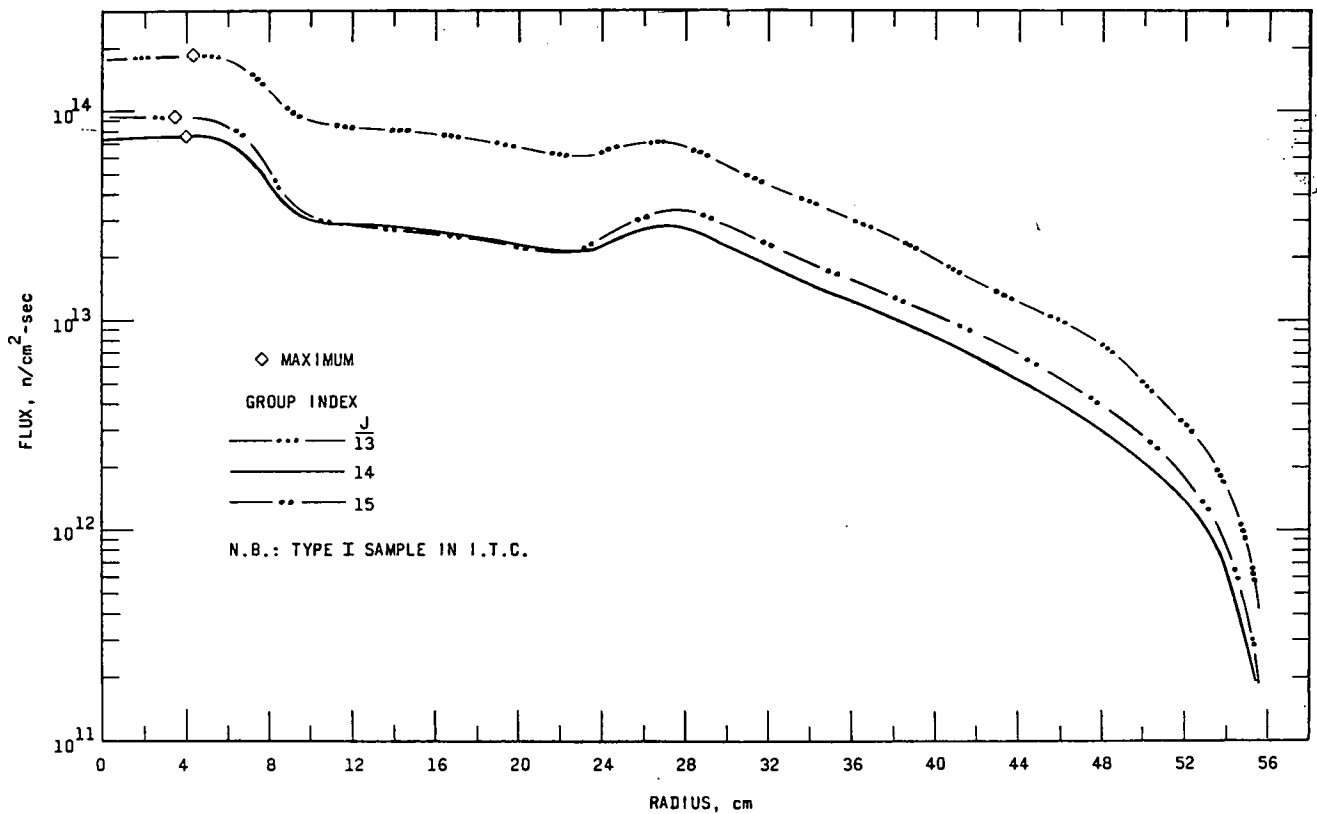


FIG. II-13-3. Axially Averaged Fluxes in AARR at 240 MW (Groups 13-15).

sections of materials not in Ref. 1. These were generated by GAM-1⁽⁶⁾ except for fission products which were taken from Nephew's compilation.⁶

Fluxes, reactivities, power distributions, and overall reactivity coefficients were calculated using REX, the multigroup diffusion theory code.⁷ The effective

delayed neutron fractions and prompt neutron lifetime were calculated using ANL code 1188/RP.⁸ (The prompt neutron lifetime calculations were deficient because the spatial variation in the average reciprocal velocity in the thermal groups could not be taken into account. For this reason the resulting numbers are

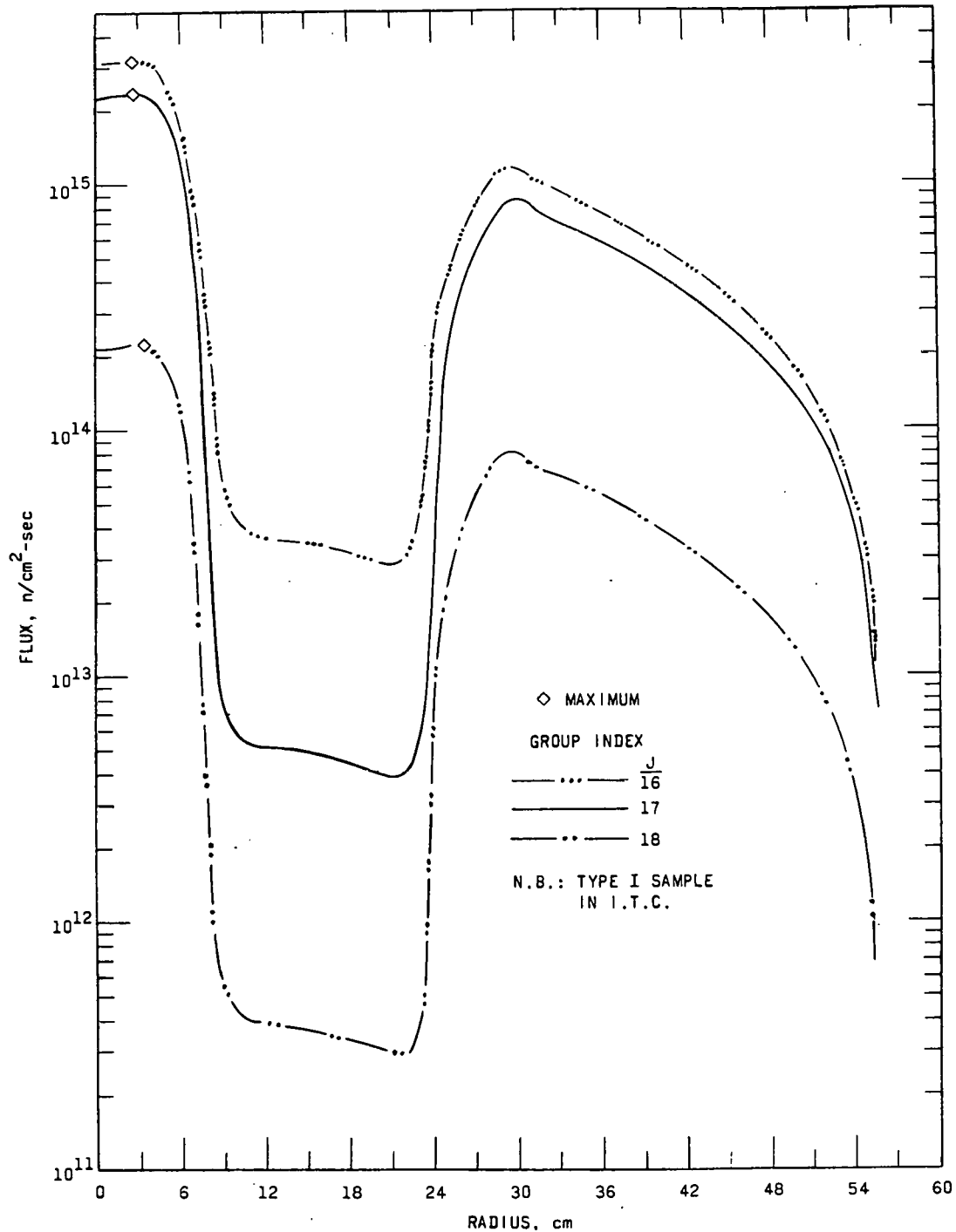


FIG. II-13-4. Axially Averaged Fluxes in AARR at 240 MW (Groups 16-18).

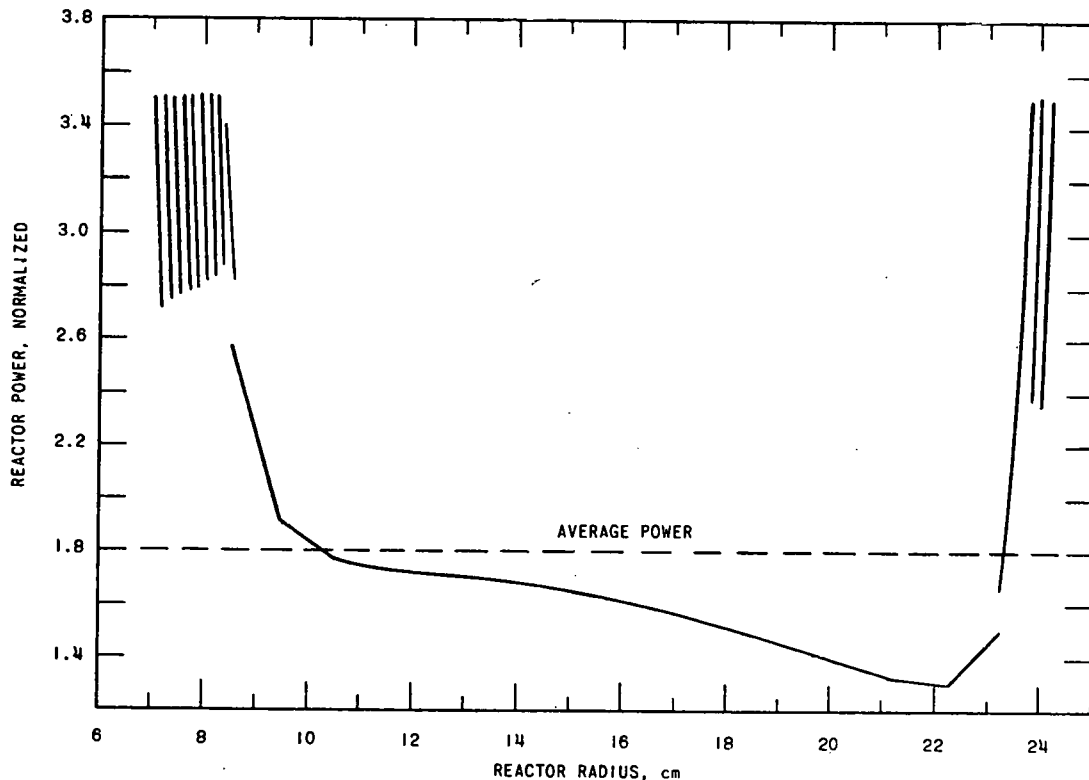


FIG. II-13-5. AARR Core Power Distribution at Operating Temperature (240 MW Power).

lower limits.) The PERT code (RP-254) calculated changes in reactivity due to various perturbations inserted in the reactor. A new code (2166/RP) was written to calculate the concentrations of Xe-135 and Sm-149 in the reactor. A least squares code (RP-167) was used in some instances for curve fitting purposes.

The fluxes and power distribution plots at the start of life with all rods out and with equilibrium Xe-135 and Sm-149 concentrations are given in Figs. II-13-1 through II-13-5. The values are normalized to a power of 240 MW. The first six energy groups represent fast neutrons above 17 keV. The entire fission spectrum is contained in these groups. The intermediate energy spectrum, from 17 keV to 3 eV, is represented by the next six groups. Except for a small amount below 3 eV, all self shielding of U-235 occurs in the intermediate range.

The power distribution is normalized to one virgin neutron per reactor. Discontinuities in the plot correspond to changes in enrichment from one region to another. The enhancement distribution, S_i , that yields the power plot is given in Table II-13-III. A value of S_i equal to unity corresponds to a region in which there is 37 w/o UO₂ in stainless steel cermet.

The prompt neutron lifetime and the effective delayed neutron fractions at the start of life as determined by the perturbation theory code (1188/RP) us-

TABLE II-13-III. REGIONAL FUEL LOADINGS

Core Region	S_i^a
5	0.17590
6	0.22828
7	0.29319
8	0.37420
9	0.47550
10	0.60148
11	0.75588
12	0.93988
13	1.10000
14	1.00000
15	1.10000
16	1.09982
17	0.75047
18	0.50244

^a $S_i = \text{fuel}/(\text{diluent} + \text{fuel})$.

ing an 18-group cross section set are displayed in Table II-13-IV. The prompt neutron lifetime was not corrected for the spatial variation of neutron velocity in each group or for the fact that the flux distributions used correspond to a supercritical system. The latter correction should yield a 10–20% increase in the prompt neutron lifetime. For each delayed neutron, 0.967 was assumed born in the energy range 0.4–0.9 MeV, and 0.033 was assumed born in the energy range 0.1–0.4 MeV.

TABLE II-13-IV. EFFECTIVE DELAYED NEUTRON FRACTIONS, β_{eff} , AND PROMPT NEUTRON LIFETIME, ℓ_p

Group	$\lambda_i, \text{sec}^{-1}$	$\beta_{eff,i}$
1	0.01244	0.000255
2	0.03051	0.00170
3	0.11140	0.00152
4	0.3014	0.00308
5	1.136	0.000896
6	3.014	0.000325

$\beta_{eff} = 0.00778$
 $\ell_p = 9.98 \mu\text{sec}$

TABLE II-13-V. DISTRIBUTED PERTURBATIONS ($\Delta k/k \times 10^3$)

Region	Perturbation				
	1 cm ³ Void	1 g U-235	1 g SS	1 g Be	1 g Zr
1	+1.047				
2	+0.978				
3	No water		-0.301135		
4	+1.013				
5	+0.678	6.09116	-0.258799		
6	+0.380	4.32945	-0.208335		
7	+0.216	3.087	-0.163690		
8	-0.055	2.20226	-0.125351		
9	-0.299	1.52458	-0.093414		
10	-0.440	1.09826	-0.067694		
11	-0.541	0.812852	-0.047703		
12	-0.607	0.624150	-0.032713		
13	-0.643	0.499600	-0.021862		
14	-0.622	0.216542	+0.005582		
15	-0.400	0.200045	+0.010734		
16	-0.353	0.305786	+0.008354		
17	-0.267	0.472125	-0.004334		
18	-0.139	0.763912	-0.02192		
19	No water				
20	+0.001			+0.110713	+0.0025
21	+0.0682				
22	+0.00819			+0.001719	-0.000082

The 16-group cross section set was used in the perturbation theory code to determine the changes in reactivity due to the removal of various volumes of materials from the reactor. The resulting reactivity changes due to these perturbations are given in Table II-13-V.

The reactivity change induced by a coolant temperature change has been determined and related to the temperature increase in various portions of the reactor. The reactivity change is related to the temperature and density changes by the equation:

$$\begin{aligned} d \ln k = & (2.6 + 0.019 T_R) 10^{-5} dT_R - 0.019 d \ln \rho_r \\ & - 1.9 \times 10^{-5} dT_c + 0.19 d \ln \rho_c \\ & - 0.37 \times 10^{-5} dT_m, \end{aligned}$$

where

T_R = reflector coolant temperature, °F

T_c = core coolant temperature, °F

T_m = fuel temperature, °F

ρ_r = reflector coolant density

ρ_c = core coolant density.

The Doppler effect has been omitted from the above equation. Of the terms in the equation, the least certain are the terms proportional to dT_R and dT_c . These are most sensitive to the thermalization model and to small changes in cross section. The equation is based on 18-group calculations. By using the 16-group cross section set in the calculations, the term in dT_R was about half the size given here.

REFERENCES

1. G. E. Hansen and W. H. Roach, *Six and Sixteen Group Cross Sections for Fast and Intermediate Critical Assemblies*, LAMS-2543 (December, 1961).
2. H. Bohl, et al., *SLOP-1—A Thermal Multigroup Program for the IBM-704*, WAPD-TM-188 (October, 1960).
3. H. J. Amster, *A Compendium of Thermal Neutron Cross Sections Averaged Over the Spectra of Wigner and Wilkins*, WAPD-TM-185 (January, 1958).
4. H. J. Amster and R. Suarez, *The Calculation of Thermal Constants Averaged Over a Wigner-Wilkins Flux Spectrum: Description of the SOFOCATE Code*, WAPD-TM-39 (January, 1957).
5. G. D. Joanou and J. S. Dudek, *GAM-1: A Consistent P₁ Multigroup Code for the Calculation of Fast Neutron Spectra and Multigroup Constants*, GA-1850 (June, 1961).
6. E. A. Nephew, *Thermal and Resonance Absorption Cross Sections of the U-233, U-235, and Pu-239 Fission Products*, ORNL-2869 (March, 1960).
7. *Reactor Physics Constants*, ANL-5800, 2nd Edition, (1963), pp. 761-762 (N. B.—RP-122 is also referred to as REX).
8. L. C. Kvitek, *Multigroup Calculations of Effective Delayed Neutron Fractions, Prompt-Neutron Lifetime, and Related Kinetics Parameters*, ANL-6511 (1962).

II-14. Argonne Advanced Research Reactor—Shielding Analysis of Plant Design

H. F. REED

Shielding analyses and further study of the AARR design suggest certain modifications to the tentative 240 MW design.^{1,2,3}

The use of a special holdup tank to protect quality resins in the primary coolant deionizer system against N^{16} radiation is unnecessary. Experiments indicate some resins lose only 1% of their exchange capacity at exposures of 4×10^8 r.⁴ Without holdup, the N^{16} dose rate to the deionizer resin is about the same as the design value for the resin activity during normal operation; i.e., 10^3 r/hr. For low quality resins and/or to minimize the deionizer cubicle shielding requirements for N^{16} radiation, the degassifier output can be used for the deionizer input. This has the attendant advantage of low pressure design for the deionizer system.⁵

From the standpoint of shielding and heat transfer, the operating experience with the Canadian National Research Universal Reactor (NRU) indicates the possibility of operating AARR with a heavily contaminated coolant.⁶ Should such operation prove feasible with respect to other factors such as corrosion and gas concentrations in the coolant, it would eliminate the need for extensive decontamination of the primary coolant system except when access to the system is required. In this connection, system decontaminating facilities might be simplified or incorporated with the primary coolant deionization system.

The use of a 6-in. steel shadow shield within and circumscribing the top closure of the reactor vessel allows a three foot reduction in the depth of the reactor pool. It also reduces the thermal stresses in the top closure, thereby permitting a smaller thickness. A tertiary feature is one of safety should the reactor pool water drain to the level of the fuel transfer chute. In this case the shielding, axially above the shutdown core, is increased from 8 to 11 ft of water equivalence thereby limiting the dose rate to 1 r/hr at shutdown. Another possibility is the reduction in the reactor building height.

REFERENCES

1. D. H. Lennox, et al., *Status Report on the Argonne Advanced Research Reactor*, ANL-6451 (1961).
 2. M. S. Silberstein, Editor, *Preliminary Feasibility and Cost Study for AARR*, UNC-5024, (July, 1962).
 3. S. A. Davis, Editor, *Revised Preliminary Cost Study for AARR*, UNC-5066, (September, 1963).
 4. F. C. Nachod and J. Schubert, Eds., *Ion Exchange Technology*, (Academic Press, Inc., New York, 1956).
 5. J. F. Mech, Argonne National Laboratory (Private Communication).
 6. H. K. Rae, *The Behavior of Uranium and Aluminum in the NRU Heavy-Water System*, Trans. Am. Nucl. Soc. **16** (Supp.), 39 (October, 1963).
- See also: J. B. Violette, et al., *Operating Experience with Ruptured Fuel in the Vallecitos Boiling Water Reactor*, Trans. Am. Nucl. Soc. **16** (Supp.), 39 (October, 1963).

II-15. Argonne Advanced Research Reactor—Critical Experiment Planning and Hazards Analysis

C. N. KELBER

The course of ramp-input accidents in the AARR critical experiment has been calculated in an approximate manner through use of the assumptions and approximations which are set out in connection with each example. Rapid transients have been described semiquantitatively through reference to SPERT data¹ from cores of similar properties.

The basic methods used have been multigroup diffusion theory and, where applicable, transport theory. The one-dimensional code RE-122⁽²⁾ was used for most calculations; rod worths and water height effects were determined from two-dimensional PDQ³ calculations.

The cross sections were taken from G. Hansen and W. Roach.⁴ SOFOCATE⁵ was used to compute constants of the thermal groups. Some cross sections, when not found in Ref. 4 were derived from GAM-1⁽⁶⁾ or MUFT⁷ libraries. Kinetics calculations were performed using the RE-129⁽⁸⁾ code. RE-254⁽⁹⁾ has been used for one-dimensional perturbation calculations.

Cores composed of fuel plates containing 0.0127 cm of highly enriched uranium foil, and clad or backed by seven times this thickness of stainless steel moderated by water channels of 1 mm have been calculated. Three core sizes are forecast:

1. A clean core with outer beryllium reflector containing 10% water by volume; the total loading is 13.45 kg of U-235 with 1 kg of excess loading corresponding to about 2% excess k .
2. The same core and reflector as in item 1 but poisoned uniformly with B-10 to a concentration of 1 atom of B-10 for each 26.7 atoms of U-235; the total loading is 26.9 kg of U-235 with 1 atom of B-10 per 31 atoms of U-235 corresponding to reactivity gain of 2%.
3. Maximum non-uniform loading for power flattening, with distributed poison concentration of 1 atom of B-10 per 13.9 atoms of U-235; the total loading of uranium is 70.3 kg.

Control rod worths vary during the course of experimental work, but typical values range from 1 to 2 dollars per rod. Successful execution of the experiments requires that in general the rods be withdrawn from the core to a position of low worth (the so-called clean core position). In this case, most of the excess reactivity will be held down by fixed poison in the form of B-SS plates clamped to the fuel. A small amount of reactivity, typically less than 0.5%, is required for operational control. There are exceptional experiments, e.g., to find the power distribution near a partly inserted rod. When the reactor is critical, under these conditions, as much as one dollar of reactivity might be added by removing the rod; but the rate at which this may be done is mechanically and electrically restrained, so that reactivity may not be added at rates greater than 0.05%/sec. Under these conditions the transient induced by this reactivity addition would cause a scram through action of the period and the high level flux trips.

The various reactivity effects listed in Table II-15-I

TABLE II-15-I. REACTIVITY EFFECTS

Void effects		
Void in fuel zone.....	-0.22%	$\Delta k/\%$ void
10% void over all internal thermal column.....	0.040%	$\Delta k/k$ per % void
60% void over all internal thermal column.....	0.018%	$\Delta k/k$ per % void
Temperature change in fuel zone only, (no density change, no Doppler effect).....	+0.00086	$\Delta k/^\circ\text{C}$
Temperature change in fuel zone (fuel plate expansion with radially restrained fuel-zone boundaries, no water density change, no Doppler effect).....	≈ 0	
Doppler effect.....	-10^{-5}	$[(\Delta k/k)/^\circ\text{K}]$ at $T_f = 300^\circ\text{K}$; coefficient proportional to $1/T_f$. (T_f = fuel temp.)

TABLE II-15-II. PARAMETERS USED IN TRANSIENT EFFECT STUDIES

Delayed Neutrons		
Lifetime, λ , sec	Abundance, β	β_{eff}
1.244×10^{-2}	2.28×10^{-4}	2.549×10^{-5}
3.051×10^{-2}	1.52×10^{-3}	1.7×10^{-3}
1.114×10^{-1}	1.36×10^{-3}	1.52×10^{-3}
3.014×10^{-1}	2.75×10^{-3}	3.0745×10^{-3}
1.136	8.0×10^{-4}	8.944×10^{-4}
3.014	2.9×10^{-4}	3.252×10^{-4}
Prompt neutron lifetime.....	16 μsec	
Heat capacity of U.....	7.6×10^3 W/sec/ $^\circ\text{C}$ (based on 60 kg U)	
Heat capacity of SS.....	120.2×10^3 W/sec/ $^\circ\text{C}$	
Heat capacity of water.....	150.5×10^3 W/sec/ $^\circ\text{C}$ (in core only)	
Change of water density (ρ_{H_2O}) with temperature.....	$d \ln (\rho_{H_2O}/\rho_0)/dt = 0.207 \times 10^{-3}/^\circ\text{C}$	
H ₂ O density at 20 $^\circ\text{C}$	ρ_0	
Diffusivity of air.....	0.179 cm ² /sec	
Diffusivity of SS.....	0.173 cm ² /sec	
Long-term shutdown coefficient..	-1.6×10^{-4} $\delta k/\text{MW-sec}$ (water expulsion)	
Doppler coefficient (short term only).....	-0.244×10^{-6} $\delta k/\text{W-sec}$ (average over range 300 to 800 $^\circ\text{K}$)	
Heat to raise hottest fuel plates to melting (5% of the fuel)		
Insulated fuel.....	3.8 MW-sec	
All steel and U in thermal equilibrium.....	63.9 MW-sec	
Entire core in thermal equilibrium.....	139.0 MW-sec	
Heat to melt all fuel, insulated plates.....	14.0 MW-sec	
Heat to cause bulk boiling.....	27.8 MW-sec	

have been calculated for the heavily loaded core 3 with power flattening since most of the experimental program will be devoted to this core. The Doppler coefficient listed last in Table II-15-I was taken from the results given in Ref. 10 for systems whose median energy of fission and fission distribution are similar to those of AARR. Similar results have been obtained by A. McWhirter and A. Goodjohn.¹¹

The parameters used in transient effect calculations are listed in Table II-15-II. The gap between the foil and the steel clad is assumed to be of the order of 2.5×10^{-4} cm (0.0001 in.) and possibly as large as 2.5×10^{-3} cm. A thermal relaxation time, $\tau = (\Delta x)^2/a^2$ where Δx = gap width and a^2 = diffusivity can then be estimated. The diffusivity of air is 0.179 cm²/sec and of stainless steel 0.173 cm²/sec. Even for very large gaps (2.5×10^{-3} cm) the relaxation time across the gap

is but 36 μ sec, so that the gap does not insulate the plate unless the period of a transient is extremely small ($\delta k \sim \$65$).

The relaxation time across a fuel plate, shim stock, and backing plate bundle, is about 0.06 sec so that for periods longer than 60 msec those approximations are good.

The analysis of the effects of fast transients follows the suggestions of S. Forbes, et al.¹ The suggestion is made there that, following a large step insertion, the maximum reactor power and the energy produced to the time of peak power correlate with the reciprocal period and scale approximately as $\sqrt{C_v/\ell}$, where C_v is the void coefficient (% $\Delta k/\text{cm}^2$) and ℓ is the lifetime. Ramp insertions with a given maximum reciprocal period produce about the same effect as step insertions characterized by the same reciprocal period.

For the AARR critical $C_v/\ell \approx 30$; C_v and ℓ and their ratio are similar to the parameters of two plate-type cores discussed in Ref. 1. One, designated B-24/32, is an aluminum core while the other, P-18/19, is a stainless steel core. Since the AARR critical is a stainless steel core the scale factor $\sqrt{C_v/\ell}$ was taken with respect to the data for core P-18/19. The scale factor in this core is 1.3. Using this factor the data presented in Ref. 1 may be scaled to estimate the results of step or ramp insertions in AARR.

From Table II-15-II it is found that the smallest amount of heat needed to cause fuel melting is 3.8 MW-sec. To find the excursion corresponding to this energy release and to determine that the time constant is short enough that the fuel may be considered thermally insulated, reference is made to Fig. II-15-1 (Fig. 13 of Ref. 1) and the scale factor of 1.3 is applied to the ordinate. From the P-18/19 curve, a stored energy of 3.8 MW-sec at a reciprocal period of 50 sec^{-1} is expected. This corresponds to a step insertion of \$1.11 or a ramp insertion of 30¢/sec. Under these conditions the time constant is too long for the fuel to be considered thermally insulated.

Continuing this process it is noted from Table II-15-II that 63.9 MW-sec stored energy is needed to melt the hottest fuel if all the steel is heated. Such an energy release corresponds to very large reciprocal periods for which sufficient data do not exist. More conservatively, however, if only the uranium and the steel clad are heated, 12.4 MW-sec are needed to heat the hottest fuel to melting; referring again to Fig. II-15-1 (Fig. 13 of Ref. 1) it is found that such an energy release corresponds to a reciprocal period of 250 per sec, which, in turn, represents a step insertion of \$1.50 or a ramp rate greater than 50¢/sec. Since the time constant is small enough under these conditions to consider the fuel and clad to be thermally insulated, this is regarded as

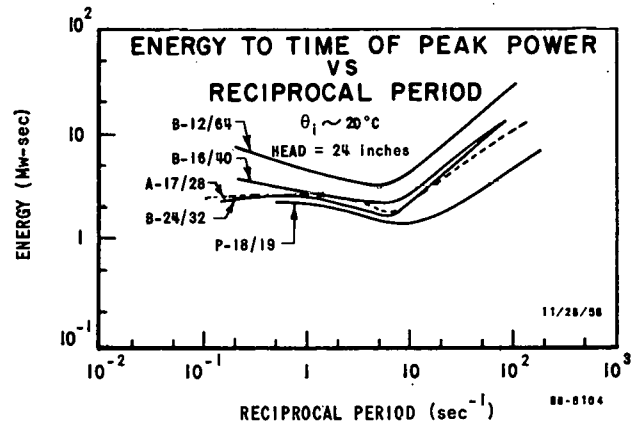


FIG. II-15-1. Energy to Time of Peak Power Versus Reciprocal Period (Fig. 13 in Ref. 1).

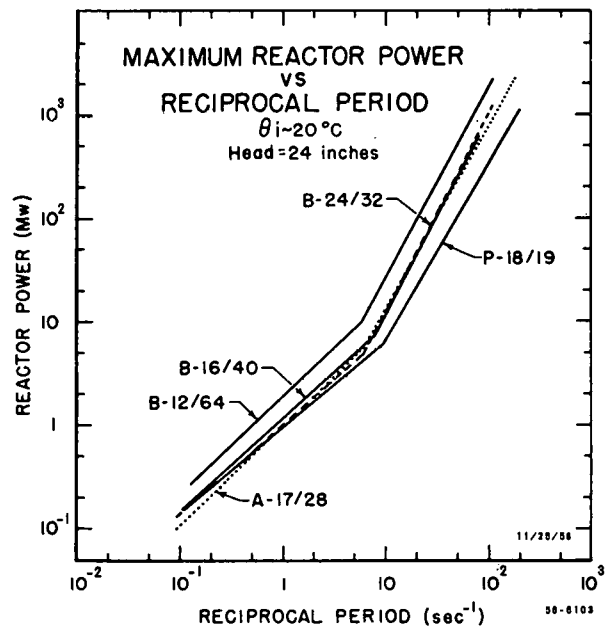


FIG. II-15-2. Maximum Reactor Power Versus Reciprocal Period (Fig. 12 in Ref. 1).

the most reasonable estimate of the excursion required to melt the fuel.

The total energy dissipated in the excursion is estimated at 1.5 times the energy-to-peak-power (nuclear) or 18.6 MW-sec, plus the heat of combination of 12 kg U with water—about 25 MW-sec. The steel does not react with the water.

The total number of fissions is 5.8×10^{17} ; melting the hottest 5% of the fuel lowers the reactivity by about 5% so that the nuclear reaction is shut down.

Credence is lent to the SPERT data by the suggestion that ramp rate studies be correlated on the basis of the minimum period. Comparison of the data given in

Fig. II-15-2 (Fig. 12 of Ref. 1), using a 1.3 scale factor with the slow excursions tabulated previously, indicates good agreement.

REFERENCES

1. S. G. Forbes et al., *Analysis of Self-Shutdown Behavior in the SPERT-I Reactor*, IDO-16528, (July 1959).
2. M. K. Butler and J. M. Cook, *Univac Programs for the Solution of One-Dimensional Multigroup Reactor Equations*, ANL-5437, (1956).
3. W. Cadwell, *PDQ-3, A Program for the Solution of the Neutron Diffusion Equations in Two Dimensions on the IBM-704*, WAPD-TM-179, (March, 1960).
4. G. E. Hansen and W. H. Roach, *Six and Sixteen Group Cross Sections for Fast and Intermediate Critical Assemblies*, LAMS-2543 (November 1961).
5. H. Amster and R. Suarez, *The Calculation of Thermal Constants Averaged Over a Wigner-Wilkins Flux Spectrum: Description of the SOFOCATE Code*, WAPD-TM-39, (January, 1957).
6. G. D. Joanou and J. S. Dudek, *GAM-I: A Consistent P-1 Multigroup Code for the Calculation of Fast Neutron Spectra and Multigroup Constants*, GA-1850, (June 28, 1961).
7. H. Bohl, Jr., E. N. Gelbard and G. H. Ryan, *MUFT-4 Fast Neutron Spectrum Code for IBM-704*, WAPD-TM-72, (July, 1957).
8. R. O. Brittan, *Some Problems in the Safety of Fast Reactors*, ANL-5577, (1956).
9. G. Jensen, Argonne National Laboratory, (Private Communication).
10. *Physics of Intermediate Spectrum Reactors*, Naval Reactor Handbook (J. R. Stehn, Ed., UC-81), Vol. II (September 1958).
11. A. D. McWhirter and A. J. Goodjohn, *The Temperature Coefficient Due to Doppler Broadening of U-235 Resonances*, Trans. Am. Nucl. Soc. 5, No. 2, 364-365 (1962).

II-16. Preparation of Critical Experiment for Argonne Advanced Research Reactor (AARR) Design

K. E. PLUMLEE, E. GROH and G. S. STANFORD

A critical experiment is being assembled to provide a facility for zero-power measurements of characteristics of the AARR core design. The facility includes an axial H₂O internal reflector or flux trap (volume—4.8 liters) in a hexagonal fuel zone (volume—78 liters) which is enclosed by a beryllium radial reflector (see Fig. II-16-1). Fuel density is 0.9 kg/liter and metal-to-water volume ratio is unity in the fuel region. The fuel is 93% enriched uranium metal foil in pieces 0.011 x 5.7 x 45.7 cm in size and the cladding is a 0.007 cm thick stainless steel envelope with welded closure. Burnable poison is simulated by 1% boron stainless steel foil. A fuel plate consists of a fuel foil, a boron or a plain stainless steel foil, and clips which secure these pieces. Each rhombic fuel assembly contains 27 fuel plates 0.10 cm thick with 0.20 cm center-to-center spacing. Forty-five assemblies comprise the fuel region. The internal and external hexagonal boundaries have sides 6.4 and 25 cm wide, respectively. Six hafnium control blades are located in the fuel region and six hafnium safety (or cutoff) blades separate the fuel region from the beryllium reflector.

A major purpose of the experiment is to measure and to optimize the power distribution in the reactor. Design studies have indicated that a peak central thermal neutron flux of 10^{16} nV may be obtained at a power level of approximately 240 MW. This requires an average power density of about 3 MW/liter.

Consequently it is necessary to flatten the power distribution so that the greatest local power density remains reasonably near the average (i.e. within a factor of ~ 2).

Spatial variations in power density and in neutron density will be measured by foil activation techniques. The ratio of central thermal flux to reactor power as well as the peak-to-average power density will be determined.

Reactivity worth and reaction rates of various core component materials must be measured to provide information on the amount of fuel and poison required for criticality, and to forecast burnout rates in various parts of the core during its lifetime. Since fuel and poison will be consumed rapidly in the high flux reactor, both the reaction rates and the reactivity effects accompanying the burnup must be known. These measurements are particularly important because of the dependence of reaction cross sections on neutron energy. The subcadmium flux will be strongly depressed in the densely loaded fuel region and as a result a large fraction of the fissions will result from epithermal neutron reactions. Although most of the cross sections are known for this range of energy, little prior information is available from nuclear reactor measurements involving a similar neutron energy spectrum. Moreover at the core boundaries there will be rather abrupt spatial variations both in

I DRY THIMBLES FOR FLUX DETECTORS
(ROMAN NUMERAL INDICATES
CHANNEL NUMBER)

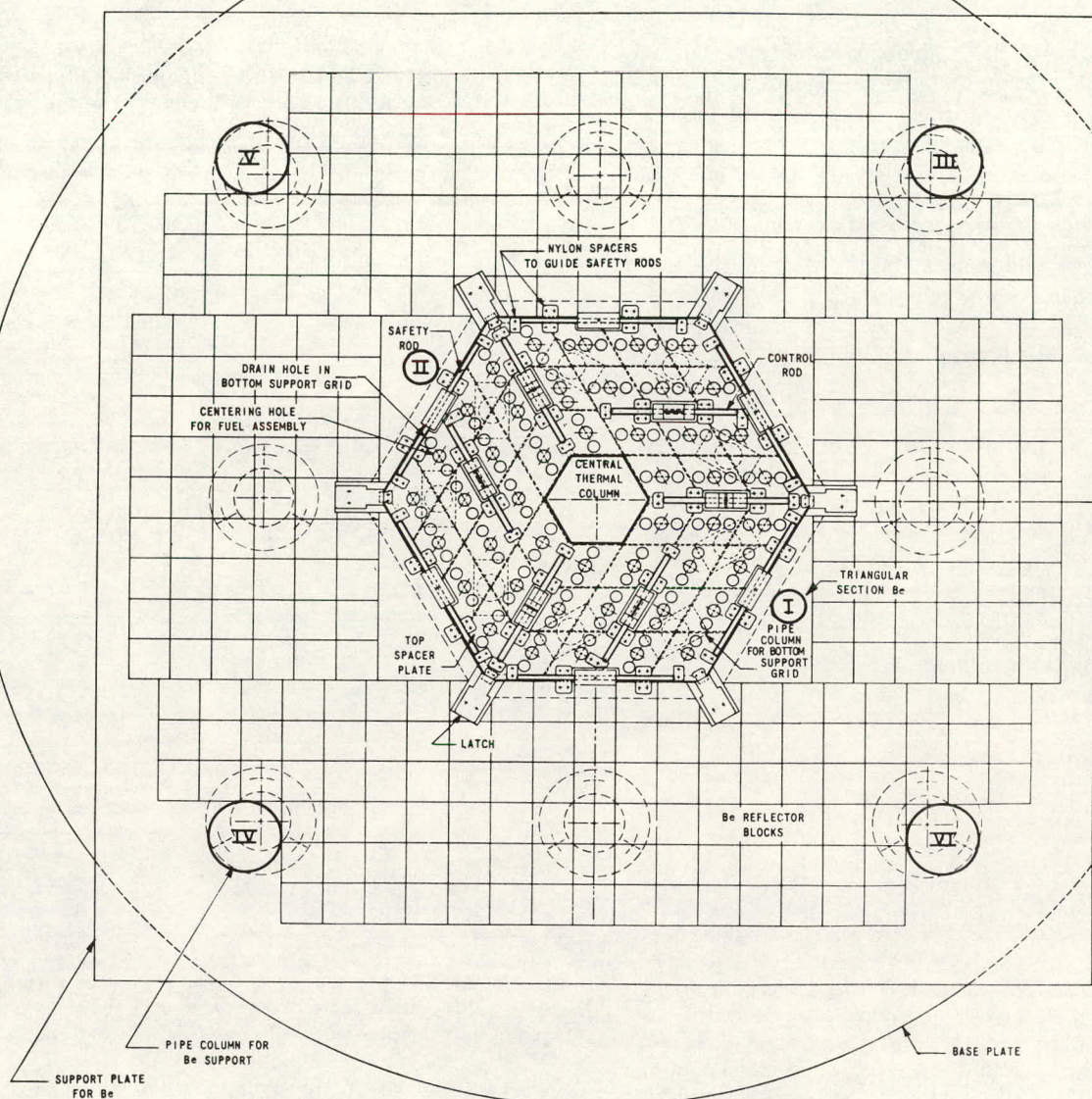


FIG. II-16-1. Top View of AARR Critical Core.

the neutron flux intensity and in the neutron energy distribution, both of which affect the reaction rates.

Experiments will be performed to determine the effect of various methods of flux suppression for control of power peaking near the fuel-reflector interfaces. These may include volume displacement of reflector to reduce the thermal neutron density locally, insertion of poison for flux suppression, or reduction of fuel density to reduce the fission rate in regions where the power density is high.

Measurement of critical masses, reactivity coefficients, and control blade worth will be made to verify

calculated results. Because of the hardened neutron energy spectrum, resonance effects and epithermal reactions will be much more significant than in more thermal reactor systems. Various materials will be compared for effectiveness as control rod constituents, burnable poisons, and flux suppressors.

The experimental program may continue into the period of operation of the AARR since it is likely that further development may be done for the second and subsequent cores. The immediate purpose is to measure characteristics of the design core and any subsequent modifications which may be made.

II-17. Argonne Advanced Research Reactor—Sample Optimization

C. N. KELBER and H. F. REED

Physics work has been done to ascertain the Internal Thermal Column (ITC) diameter plus the sample radius and absorption area which will provide the greatest reaction rate in the target material. Calculations were made for a 70 liter or larger fuel zone uniformly loaded with about 50 kg of U-235 as UO_2 and containing 46 v/o H_2O plus 40 v/o stainless steel. Although large differences between the spectral-temperature reactivity coefficients for this core and the core variably loaded with fuel (which more closely resembles the design core) are apparent, such core differences are less important for reaction rates in the sample.*

The results of the study are presented in Table II-17-I. In variation 2 the metal cross sections for neutron energies up to 0.4 eV were averaged over a water spectrum which is harder than the spectrum calculated in the ITC. For the other two variations a fuel zone spectrum, which is harder still, was used for the averaging.

It is observed that a maximum reaction rate can be expected in the sample target material for target absorption areas in excess of 100 cm^2 , for sample radii larger than 3.5 cm, and an ITC diameter of about 14 cm.

The larger the sample radius the greater the re-

* The optimization calculations are to a large extent independent of core details; thus an early core design was used in these calculations; later designs call for a larger UO_2 inventory.

TABLE II-17-I. SAMPLE OPTIMIZATION AND CORE REACTIVITY

Variation 1: Flux versus absorption area (ITC diameter—11.4 cm; sample radius—3.15 cm; sample volume—1.38 liters including 0.69 liter of H_2O ; fuel zone volume—70.6 liters).

Sample Absorption Area, cm^2			Perturbed Neutron Fluxes for 100 MW ($\times 10^{15}$)
Metal	H_2O	Total	
6.75	13.9	20.7	3.01
13.5	13.9	27.4	2.79
119.0	13.9	133.0	1.18

Variation 2: Flux versus ITC diameter (sample radius—3.15 cm; sample volume—1.38 liters including 0.69 liter of H_2O ; absorption area constant at 27.4 cm^2 ; fuel zone thickness constant at 17.4 cm).

ITC Diameter, cm	Fuel Zone Volume, liter	Perturbed Neutron Flux	
		at 100 MW ($\times 10^{15}$)	at 1.42 MW/liter ($\times 10^{15}$)
11.4	70.6	2.79	2.79
14.0	76.8	3.01	3.28
16.0	81.7	2.88	3.33

Variation 3: Flux versus radius (metal absorption area constant at 17.5 cm^2 ; ITC diameter—14 cm; fuel zone volume—76.8 liters).

Sample Radius, cm	Total Sample Absorption Area, cm^2	Perturbed Neutron Flux at 100 MW ($\times 10^{15}$)
3.15	31.4	2.87
3.45	37.5	2.93
3.72	44.8	2.97

ITC Diameter, cm	Relative Core Reactivity (Sample as in variation 2)	
	Constant fuel zone volume of 70.6 liters	Constant fuel zone thickness of 17.4 cm
11.4	1.0	1.0
14.0	0.91	0.99
16.0	0.85	0.982

Notes: 1. The non-design neutron fluxes in units of n/cm^2 sec lie within the 0–0.1 eV energy range (as do the absorption areas) and represent the radial average over the sample mid-plane. 2. The sample and core have a height of 44.5 cm.

activity increase of the system when the sample is voided of its water. For the largest sample studied about \$1 of excess reactivity would result if the sample were completely voided. It is possible to reduce this source of reactivity to \$1 or less by the use of low absorption structure-cladding plus filler materials such as zirconium and beryllium in sufficient amounts to keep the water volume in the sample below 10–12% of the ITC volume.

II-18. Argonne Advanced Research Reactor—Preliminary Safety Analysis

C. N. KELBER

The preliminary safety analysis of the Argonne Advanced Research Reactor (AARR) reveals that a heavy burden is placed on control by rods and burnable poison. Design criteria are:

1. Eleven out of twelve rods sufficient for shutdown.
2. Prompt shutdown margin at least ten dollars to insure prompt decrease to emergency power level on scram.
3. Approximately four per cent δk available initially to compensate for reactivity to be held up in Xe and Sm at equilibrium.
4. Movable rod insertion at power limited to prevent severe power distortions.
5. It is desirable to have as much override of Xe available as possible.

Rod worths were determined by a series of calculations using four group, flux weighted cross sections in $x-y$ geometry. Later calculations using multigroup cross sections in $r-\theta$ geometry failed to converge; one dimensional calculations in cylindrical geometry also were used successfully. In the course of these calculations a negligible difference was found between the use of black boundary conditions and diffusion theory in the thermal group. This is a reflection of the small number of thermal neutrons in the core.

The safety rods (at the core-outer-reflector interface) are found to be worth eight to nine per cent in reactivity, the six control rods to be worth eleven to twelve per cent. Since the clean cold reactivity is 22%,

it is found that there must be at least five per cent reactivity held up in burnable poison initially just to satisfy criterion 1. Actually we expect to have much more.

Criteria 2 and 3 imply that initially no more than 7.5% δk be held up in movable control in addition to the 4% δk used to compensate for Xe and Sm. After equilibrium Xe and Sm is reached the total held up in movable control can be as high as 11.5%; but this violates criterion 4.

Xenon recovery calculations show that about 6% Δk is needed for complete xenon override at 240 MW while 3% Δk should give several hours recovery time. Earlier AARR core designs had too little fuel content and samarium was useful as a poison. Even though it burned out rapidly, it was sufficient to compensate for excess reactivity until enough fuel was lost to keep the maximum δk in rods to about 6%. With the newer core loadings, samarium burns out much too fast and rod insertion a little beyond 11.5% is required.

Alternative burnable poison choices include B-10 (which burns out a little too slowly), europium, non-uniform B-10 loading, or Sm and B-10 combinations.

Criterion 5 can be met by using grey rods to give a better power distribution or, possibly, half rods may be used. The latter must be carefully examined to see that on scram they do not add reactivity as half rod sections leave the core and full rod sections enter.

II-19. EBWR Plutonium Recycle Experiment

B. J. TOPPEL

The potential advantages of plutonium recycle have been long recognized. In the fast reactor area these advantages are primarily, if not exclusively, related to the possibility of achieving a fuel cycle with a substantial breeding gain. At Argonne a vigorous program is being pursued in connection with the fast system. In the thermal area, the potential advantages are perhaps less clear cut, though not necessarily less real. It is probably true that plutonium recycle in thermal reactors is primarily motivated by the desire to achieve irradiations not otherwise possible, either longer irradiations, or the use of a lower

enrichment feed. In either the fast or thermal area the ultimate justification must, of course, come from consideration of the economics of the system.

A joint Argonne-Hanford program, which will make use of the EBWR facility is now underway for the purpose of obtaining information useful for the utilization of plutonium as a fuel in light water thermal systems. Such utilization could be made in either an all thermal plutonium recycle system, or as the thermal part of a mixed fast-thermal reactor complex.

An example of the latter system is the following. A normal fast power reactor is used. The blanket

fuel elements are irradiated until the desired plutonium concentration is achieved. The blanket elements are then transferred without reprocessing to the thermal reactor where they are used as fuel. The fuel elements are irradiated in the thermal reactor to as high a burnup as is achievable. The fuel, which contains a considerable amount of the higher plutonium isotopes is reprocessed, and the plutonium is used as make-up material for the fast reactor core.

An encouraging facet to this cycle is that studies carried out on fast systems have indicated that the blanket may not be able to pay for itself in such systems. The above system would alleviate the charges against the blanket since these costs would be the same as those required for fueling the thermal core. Calculations indicate that plutonium containing much of the higher isotopes is advantageous, in terms of neutron economy, as fast reactor feed material.

The physics information required for the development of either the all-thermal or mixed fast-thermal concept is essentially the same. Since the attainment of certain rather basic numbers, in particular obtaining data on the isotopic behavior of plutonium as it is irradiated in a thermal reactor, is the main objective, it appears desirable that the experiment be made as simple as possible while still yielding this information so that it would be most amenable to analysis.

In specifying an EBWR experiment which would be useful in the plutonium recycle program the following considerations were kept in mind. It is advisable that modifications to EBWR should be kept to a minimum. It should remain a boiling H_2O system. EBWR should be used primarily as an irradiation facility rather than in support of an active reactor experimental program. In the planned experiment on EBWR, the 148 element core is divided into four zones; the central 6 x 6 square, the immediately adjacent 28 element ring, the next 32 element ring (excluding the fuel elements on the 45 degree symmetry lines), and the remaining 52 outside elements. One of the outside elements will be replaced with an Sb-Be neutron source.

Each fuel element contains a square 6 x 6 array (10.569 in. pitch) of zircaloy tubes about 0.372 in. i.d. with 0.025 in. walls. These elements are similar to those of the EBWR Core 2 reference design.¹

The central zone represents the plutonium test region. It contains mixed plutonium-uranium oxides with 1.5 w/o PuO_2 in UO_2 . The Pu will initially contain about 8% Pu-240.

The two rows surrounding the Pu region may be referred to as the enriched uranium oxide shim zones,

and it is these rows which may have their composition periodically altered in order to vary the reactivity of the over-all system. They will be enriched to 6% in U-235 and will initially be identical and contain europium oxide and samarium oxide burnable poisons to minimize the reactivity variation with burnup. Initially the shim fuel will contain 0.158 w/o Eu_2O_3 and 0.0288 w/o Sm_2O_3 .

The outer 52 elements contain natural uranium oxide and will not be replaced during the experiment.

The core loading described above is the result of physics studies which proceeded in the following manner. Various loadings were considered and the properties of each system were determined. The loadings were of three different types—one, two, or three zone. This classification refers only to the core. One zone refers to an initially uniform core; two zone refers to a central 36 element Pu region surrounded by a driver uranium region of a single enrichment; three zone refers to a central 36 element Pu region surrounded by a one row region (28 element) with uranium of one enrichment which in turn is surrounded by a uranium region of a second (lower) enrichment.

Two fuel element designs were considered. One was the EBWR Core 2 reference element design¹ consisting of a 6 x 6 pin array of fuel tubes with outer diameter of 1.07 cm. The other design consisted of the same element and tube size except in a 5 x 5 pin array. Various initial Pu-239 enrichments in the range of 0.005 to 0.05 were considered for the central region. Fuel for the uranium region had the 6 x 6 pin array in all cases. The Pu enrichment range of most interest to current technology is from 0.015 to 0.035.

The central plutonium zone system was favored over the uniform system for several reasons. It reduces the necessary plutonium inventory without materially reducing the information obtained from the experiment. Furthermore, reactivity may have to be periodically restored to the system and in terms of the analysis of the experiment it would be best if this were done in a region outside of that where one is studying the long term behavior. Higher plutonium enrichments in the central region are ruled against largely by control requirements. They would have too large a cold to hot void reactivity variation. Lower plutonium enrichments are ruled against since too small a fraction of the total reactor power would be generated in this region. The plutonium would, of course, reach its asymptotic isotopic composition at an earlier date if a lower enrichment were used, which in itself would be highly desirable. The system,

however, would again be one which is not of greatest interest.

Enrichment of 1.5% in the Pu zone and the shim zone containing 60 elements, as indicated above, resulted from the desire to achieve a nine control rod shutdown without boric acid requirement, at the same time attaining a reasonable power level. The interdependence of the enrichment and the shutdown criterion comes about in the following manner. Although the control rod worth does not change significantly, the void reactivity coefficient increases significantly with plutonium enrichment. This occurs because the core is effectively smaller as the enrichment increases since more of the reactivity of the system is concentrated in the center. If one were to retain the 9 rod shutdown without boric acid requirement in a 2.5% Pu region, the power which could be reached would be unreasonably low. A reasonable power can be achieved if the void coefficient is decreased by using a 1.5% enriched Pu zone.

Generally, one anticipates that the enrichment of most interest in plutonium recycle will be initially of the order of 1.5% and will gradually increase as higher burnup systems are contemplated.

The plutonium fuel elements are designed for a burnup of 0.025 (~25,000 MWd/tonne), although no definite duration has been set for the experiment. It should be continued as long as feasible and as long as useful information on isotopic change behavior can be obtained. It is anticipated that the interesting range may only be up to about 9,000 MWd/tonne. The higher design burnup allows for continuation if deemed worthwhile.

The fuel element boxes in the central region are somewhat different from those in the remainder of the core. They are of a "take apart" design and allow the withdrawal and replacement of individual rods within the element. This feature is necessary to permit isotopic analysis studies of the central region as the burnup proceeds. These studies are the main objective of the experiment.

To provide a greater degree of control to accommodate the planned experiment changes have been made in the control rods as compared to previous EBWR operation. One of the control rods will be similar to that used previously, being fabricated from hafnium and it will again be used for oscillator measurements. The remaining eight control rods will be boron-stainless steel rods as before but the boron will be enriched to approximately 90% in B¹⁰ rather than containing natural boron. The greater worth compared with natural rods is due to the increased epithermal absorption afforded by the higher boron enrichment.

Prior to the start of irradiation, critical experiments will be performed. These experiments will be

performed partly at Hanford, where experiments will be performed on rods similar to those to be shipped to Argonne for assembly into the fuel elements. At Argonne, critical experiments will be performed within the EBWR vessel. In particular, it will be highly desirable to obtain a clean, i.e., no control rods inserted, critical configuration of only the plutonium fuel elements where the system is controlled with boric acid. The usual reactivity coefficient and other standard measurements will also be made. In particular transfer function measurements to test the system stability will be made after loading of the driver zones and during the approach to power. The system will then be irradiated a predetermined amount, of the order of 2,000 MWd/tonne. This will require an elapsed time of about 4 months, assuming sustained operation at an initial power of about 40 MW. At this point a major investigation of the irradiated system will be undertaken. This will consist of removal of some plutonium rods from the system. A selection of the order of 10 rods should be sufficient to give a thorough mapping of the plutonium region. Among these will be a selection of special rods supplied by Hanford designed to yield information on the irradiation of fuel of varying initial compositions. The rods will then be examined for isotopic analysis. Further measurements will at this time be made on the reactivity of the system. It would again be highly desirable to come to a clean condition, that is, where the assembly contains only the plutonium elements and the system is made critical by the addition of the proper amount of boric acid. Further measurements of items related to various reactivity coefficients will also be made at this time. After these measurements are made the irradiation will proceed for the next major time step, perhaps again of the order of 2,000 MWd/tonne. Owing to burnup of the plutonium zone and redistribution of the power, this second step will require an elapsed time of about 5 months, again assuming sustained operation of a power of about 40 MW.

The observed reactivity and control rod worth variations during the course of the irradiation will determine the desirability of alteration of the enrichment or poison content of the shim zone. It is expected that if such variation is desirable, it would be accomplished by altering the composition of the shim zones.

Related theoretical calculations will be made during execution of the experiment to aid in interpretation of data and to serve as a guide to subsequent experimental effort.

The program of irradiation and periodic sampling and analysis of the plutonium fuel outlined above

will be continued as long as the useful information derived thereby is consistent with the interest in the experiment and the effort required to achieve the required irradiation. Measurements of the U and Pu isotopic composition of the fuel as the irradiation proceeds are by far the most important aspect of the EBWR plutonium experiment.

Comparison of the isotopic analyses obtained for the plutonium fuel with calculational predictions during the course of the irradiation will facilitate the setting up of a mathematical model which should serve as the basis for future calculations for prototype systems of either the all-thermal recycle type or of the fast-thermal complex.

During the routine portion of the irradiations, studies will be made in support of Argonne's interest in the mixed fast-thermal reactor complex. These will include theoretical fast reactor blanket studies to relate plutonium buildup to associated burnups. Experimental experience may be gained by irradiation in EBWR and subsequent analysis of special fuel elements designed to mock up material derived from a fast reactor blanket.

In preparing for the experiment, detailed physics calculations have been performed to determine the initial core characteristics and the core behavior under irradiation. These calculations have been influenced by the experimental information obtained from the EBWR operating experience and by various other available experimental data.

The computational model has involved the use of the GAM-1² and SOFOCATE³ codes to generate multigroup cross sections for use in one and two-dimensional neutron diffusion theory codes.

Many of the results obtained have been useful in preparing the Safety Analysis for the planned experiment. Some of the results of this Safety Analysis are presented here.

In considering the safety of a plutonium loaded reactor, the two distinguishing areas of concern are related to the potential hazard associated with dispersal of the plutonium and effect on the kinetic behavior due to the reduced delayed neutron fraction. It has been shown in the safety analysis that the proposed experiment and the previous EBWR core are closely related in regard to plutonium content and effective delayed neutron fraction, as well as plant configuration.

The initial core contains only about 50% more plutonium than did EBWR at the time of shutdown after the previous 100 MW operation. In addition, since oxide fuel is to be used exclusively, the proposed experiment has a significant safety advantage over the

previous EBWR core with regard to the degree to which plutonium could be dispersed if a fuel rod failed.

The β_{eff} of the full system varies from about 0.005 initially to over 0.006 at a plutonium zone burnup of 0.006. By comparison, the β_{eff} for EBWR was about 0.0054 at the end of the 100 MW operation.⁴ For the plutonium critical configuration, since Pu-239 is the only fissile isotope, β_{eff} is lower and has a value of about 0.003.

Even though the expected operating power is less than that previously attained safely in EBWR, the stability of the proposed system is not being taken for granted. The stability of the system will be investigated during the approach to power using essentially the same techniques and equipment which were successfully used during the previous 100 MW program.

The proposed system exhibits the same inherent safety characteristics as did the previous EBWR cores. In addition, the present oxide fuel loading has significant advantages, from a safety point of view, over the previous metal fuel core loadings. Events which previously did not lead to serious core damage will again not be damaging for the present core. Events which previously would have caused core damage may now not be damaging. For example, whereas the previous core could, by virtue of the Doppler effect combined with metal expansion, sustain a step reactivity insertion of about 0.3% above prompt critical, the corresponding conservative value for the present core based solely on the Doppler effect is about 1%.

The same potential "maximum credible accident" is postulated for the present experiment as was postulated for the previous core. This accident which involves no nuclear violation corresponds to complete loss of water during full power operation and results in melting of the fuel. The consequences of this accident would be less severe for the proposed experiment because the use of oxide fuel implies a lower likelihood and level of chemical reaction with the water and subsequent plutonium dispersal when compared with the previous predominantly metal fueled cores.

It has been concluded that the plutonium recycle experiment is as safe as the system previously used in EBWR; in fact, that it represents a significantly more reliable reactor plant configuration. The chief reasons are: plant improvements, the use of an oxide core, benefit of experience from past operation, and similarity of the plutonium recycle experiment to the previous system.

REFERENCES

1. R. Avery and C. N. Kelber, *Physics Analysis of Proposals for EBWR Core 2*, ANL-6306 (1961).
2. C. D. Joanou and J. S. Dudek, *GAM-1: A Consistent P1 Multigroup Code for the Calculation of Fast Neutron Spectra and Multigroup Constants*, GA-1850 (June 28, 1961).
3. H. Amster and R. Suarez, *The Calculation of Thermal Constants Averaged over a Wigner-Wilkins Flux Spectrum: Description of the SOFOCATE Code*, WAPD-TM-39 (January, 1957).
4. *EBWR Test Reports (100 Mw Operation)*, Test Report No. 100-I, ANL-6703 (1964).

II-20. EBWR Plutonium Recycle Safety Analysis

P. H. KIER

FAST TRANSIENT SHUTDOWN

For a rapid reactivity insertion, the only inherent shutdown mechanism available for preventing melting of the oxide fuel of the Plutonium Recycle Experiment is Doppler broadening of the resonances of U-238, Pu-239, and Pu-240. Calculations were made to determine the largest step insertion of k_{eff} that can be introduced without causing the oxide fuel to melt. A realistic configuration is all control rods inserted except a corner rod, which has the greatest reactivity worth.

The first step in the calculational procedure was to obtain cross section changes due to elevation of the fuel temperature. The next step was to determine the spatial temperature distribution in the case for a variety of conditions and energy inputs to the system. Because it was assumed that heat is not transferred to the moderator, the temperature distribution was easily related to the spatial power distribution by using tabulated values of the specific heat of UO_2 . When a corner rod is removed, the power distribution is dependent on azimuthal angle so the two-dimensional PDQ¹ code was used to obtain the Doppler coefficient of reactivity due to the energy inputs. The reactivity feedback obtained for the Doppler coefficient was then used in the A129 RP code² to compute integrated energy as a function of reactivity insertion. Finally, the assumed power distribution and specific heat of UO_2 were again used to obtain the spatial temperature distributions resulting from various reactivity insertions.

The specific heat of UO_2 is such that the melting point will be reached for an energy density of 8.22 kW-sec/cm³. Table II-20-I gives the reactivity insertion and total energy release for which this energy density will occur at the hottest point in the assembly. Included in the table for reference are calculations for cores without control rods.

For reactivity insertions that carried the center of

TABLE II-20-I. STEP REACTIVITY INSERTIONS LEADING TO FUEL MELTING

System	Step k_{eff} , %	Integrated Energy Release, MW-sec	Reactor Period, msec
Cold, 0 Burnup unrodded	1.6	1000	2.4
Cold, 0.006 Burnup unrodded	1.5	1100	3.0
Cold, 0 Burnup only corner rod not inserted	0.95	190	6.2
Cold, 0.006 Burnup only corner rod not inserted	1.1	170	5.8
Cold, 0 Burnup unrodded, Pu critical configuration	1.5	390	3.3

the oxide fuel to several hundred degrees above the melting point, calculations predicted that the outer surface of the oxide would not melt and that thermal stresses in the cladding would just reach the elastic limit of about 18,000 psi for zircaloy-2. These calculations showed that the present oxide core greatly exceeds the previous EBWR metal fueled system with regard to its ability to sustain, without permanent damage, severe reactivity insertions. This result is expected from SPERT-1 experience.³

FUEL STORAGE

Calculations were made of the reactivity of fuel from the Plutonium Recycle Experiment when placed in the existing EBWR storage racks. The calculations predicted that the south rack, when loaded with fuel from the shim zone with 0.006 burnup would have an infinite multiplication constant within a few percent of unity. To preclude the possibility that the rack can become critical, a new rack, consisting of a rectangular array of 148, 4-in. square boxes formed by interlocking $\frac{1}{4}$ -in. thick sheets of stainless steel containing a nominal 1.2 w/o boron, is being manufactured. The new rack will be subcritical by some 20%.

WATERLOGGING

The mixed oxide fuel is constructed such that if a crack develops in the cladding, water can leak into and remain in the interior of the fuel pin. Calculations were made of the reactivity effect of this "waterlogging" when it is assumed that ten percent of the volume of all the mixed oxide fuel pins is water. The results of these calculations showed that "waterlogging" would not change the reactivity of the

plutonium critical but would cause a decrease of 0.3% in the multiplication constant of the full system.

REFERENCES

1. W. Cadwell, *PDQ-3, A Program for the Solution of the Neutron Diffusion Equations*, WAPD-TM-179 (1960).
2. *Reactor Physics Constants*, ANL-5800 Second Edition, (1963), p. 815.
3. J. E. Houghtaling, et al., *Calculation and Measurement of the Transient Temperature in a Low-Enrichment UO₂ Fuel Rod During Large Power Excursions*, IDO-16773 (1962).

II-21. Experimental Boiling Water Reactor (EBWR) Physics Review

H. P. ISKENDERIAN

100 MW(t) PERFORMANCE, REACTIVITY VERSUS POWER

Core loading 1A, described in Ref. 1, had as its objective an operating level of 100 MW(t). In planning for EBWR operation at 100 MW, the number of boron-stainless steel strips attached to the highly enriched "spike" elements were to be adjusted to provide sufficient reactivity to overcome the effects of steam voids at 100 MW while still satisfying cold shutdown requirements. The predicted increment in the multiplication factor had been estimated to be $\Delta k_{eff} = 0.054$ for 100 MW(t) operation. Following procedures outlined in Ref. 1, it was determined that the average number of boron-stainless steel strips per spike should be 1.57 to compensate for $\Delta k_{eff} = 0.054$.

POWER RUNS ZERO TO 60 MW(t)

This increment in k_{eff} (0.054) was in fact used up when the power level reached 60 MW(t). The source of the discrepancy was investigated and, at the same time, more reactivity was added by reducing the boron-stainless steel strips to an average of one per spike. The performance characteristics of EBWR in the range zero-60 MW(t) are summarized in Ref. 2. A graphical summary of reactivity versus power is shown in Fig. II-21-1.

It was found that the discrepancy in reactivity held up in voids stemmed from two sources:

a. The power-void iterations in Ref. 1 systematically underestimated the mean void content of the core as a function of power. At 100 MW(t) the mean void content was estimated to be 20.8%. The principal reason for the underestimate was a lack of knowledge of steam behavior in the downcomer.²

b. The reactivity coefficient predicted in Ref. 1 was 25% too high. Two changes dependent on void concentration had been omitted: the changes in the Dancoff factor and in the fast fission factor.

With revised steam void calculations yielding a 27% mean void content at 60 MW(t) and a lower void coefficient, the revised computed value of 0.052 for Δk_{eff} is in good agreement with the observed value, 0.054.

POWER RUNS ABOVE 60 MW(t)

For powers of up to 60 MW(t), the reactor power was a function of the core input reactivity and carry-under of steam in the downcomer area.²

When the water level in the pressure vessel was low; i.e., nominally 21 in. above the top of the core, the behavior of the reactor at powers above 60 MW(t) was quite similar to that at lower powers; a maximum of 73 MW(t) was obtained. When the nominal height of the water level in the pressure vessel was raised (Fig. II-21-1, $H > 14$ ft 10 in.) by pumping more water into the core at about 130°F, the reactivity of the core was increased, and the hydrodynamic conditions of flow changed² resulting in greater amounts of steam extraction and of power.

FUEL BURNUP CALCULATIONS

Burnup of U-235 and buildup of plutonium in the fuel elements of EBWR from its initial day of operation (December 1, 1956) to the end of the core life of loading 1A (December 31, 1962) was evaluated. Monthly calculations were made during the operation of the reactor from zero to 100 MW(t) levels. During power runs from June to December 1962 it was noted that:

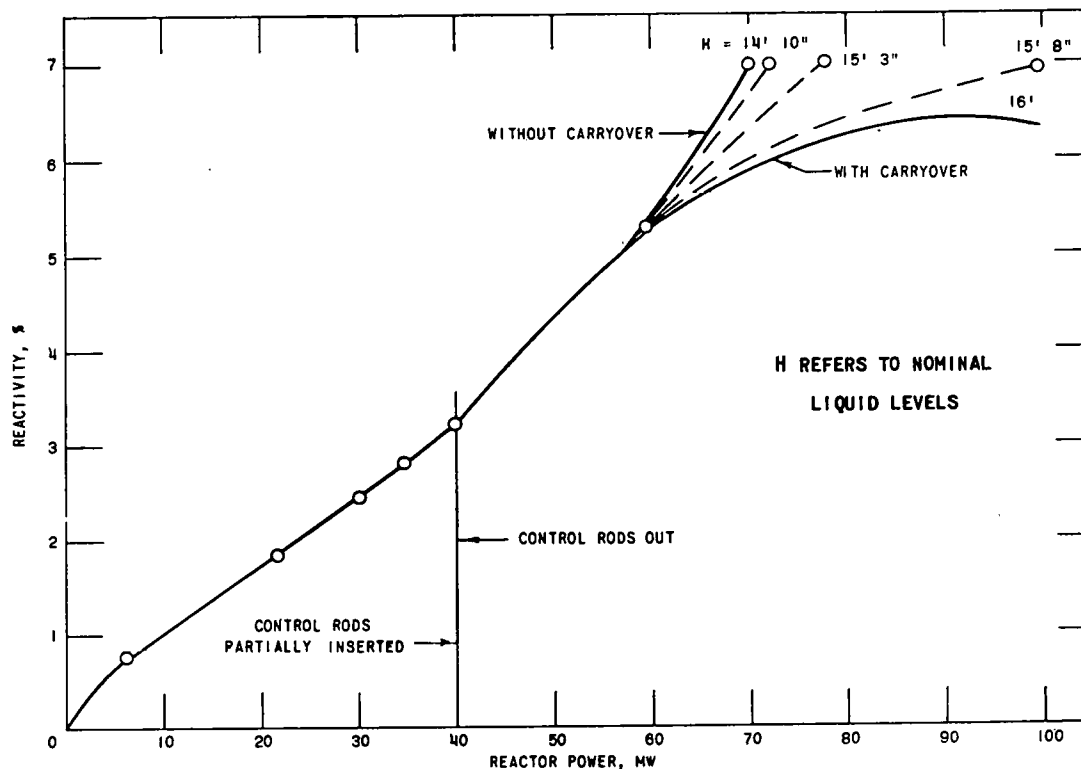


FIG. II-21-1. Reactivity Versus Reactor Power.

Average burnup of U-235/MWd
 = 3015 g/2785 MWd = 1.083 g/MWd;
 Average buildup of Pu/MWd
 = 1153.5 g/2785 MWd = 0.414 g/MWd;
 Average buildup of Pu/Average burnup of U-235
 = 1153.5/3015 = 0.382.

(This work was done in connection with the "Four Reactor Inspection Agreement" between the U.S.A. and the I.A.E.A.)

The method used was based mainly on the approach to core depletion outlined by K. K. Almenas.³ Values of neutron flux in each region of the core (three axial values for each fuel element) were obtained for average burnup conditions of the core (e.g. 5000 MWd is the average exposure for a total exposure of 10,000 MWd). Three group diffusion theory as described in Ref. 1, with allowances for resonance absorption, were used with PDQ code calculations.⁴ Following the history of each fuel element in the core, the exposure time "t" was determined for each element and the time-integrated neutron flux was obtained with the aid of the PDQ calculations. From the plots of the solutions of the appropriate differential equations values of nuclear concentrations were then obtained for each isotope, allowance being made for resonance

absorption. Thermal cross section data were obtained from Ref. 1.

DESIGN CALCULATIONS OF A CASK FOR SHIPMENT OF EBWR FUEL

Design calculations of a cask for the shipment of fuel elements from core 1A, and of Pu fuel elements (Plutonium Recycle project) have been made. These calculations were undertaken to determine the design which would enable the transport of a maximum number of EBWR fuel elements in one shipment. A cylindrical steel cask 106.7 cm (42 in.) in diameter, provided with 7 top holes 13.97 cm (5.5 in.) in diameter (a central hole surrounded by 6 holes separated by 15.24 cm (6 in.) center to center) would result in γ activity of 36 mr/hr at the cask surface, and 5 mr/hr at a point 3 m away from the cask surface, when highly enriched elements fill the cask holes. Thin and heavy slightly enriched elements (TE and HE) should give appreciably lower γ -doses.

The AEC imposed the requirement that the shield be made of steel and that the γ -dosage not exceed 10 mr/hr at a distance 3 m from the cask surface.

The source strength determinations and the overall method of calculations^{5,6} were verified by storage pit measurements at EBWR.

REFERENCES

1. R. Avery, K. K. Almenas, C. Carson, H. P. Iskenderian and C. N. Kelber, *EBWR Core 1A Physics Analysis*, ANL-6305 (1961).
2. E. A. Wimunc, M. Petrick, W. C. Lipinski and H. P. Iskenderian, *Performance Characteristics of EBWR from 0-100 Mwt.*, ANL-6775 (1963).
3. K. K. Almenas, *Burnup Calculations for the Experimental Boiling Water Reactor*, Trans. Am. Nucl. Soc., 2, No. 2, November, 1959.
4. C. C. Bilodeau, et al., *PDQ—An IBM-704 Code to Solve Two-Dimensional Few-Group Neutron-Diffusion Equations*, WAPD-TM-70 (August, 1957).
5. T. Rockwell III, *Reactor Shielding Design Manual*, TID-7004 (March, 1956), Ed. I.
6. M. Grotenhuis, *Lecture Notes on Reactor Shielding*, ANL-6000 (1959).

Section III

Fast Reactors

Activities related to fast reactor development are summarized in this chapter. Most of the studies are oriented toward fast power breeder reactors; some work is directed toward development of a fast spectrum nuclear rocket. Many neutronic problems in the two general areas of application are closely related.

Individual papers fall into a number of related topical categories: General Fast Reactor Research and Development, Support of Project Activities, Fast Reactor Safety, and General Studies of Fast Reactor Concepts with related Evaluations.

III-1. Predicted Doppler Effects for Some Typical Large Ceramic Fueled Fast Reactors

H. H. HUMMEL and A. L. RAGO*

The importance of the Doppler effect to the safety of large fast reactors is now widely recognized. A review of the current computational status of the fast reactor Doppler effect has been given recently.¹

The first calculations made at ANL² used an 18-group set of cross sections, Set 199. This was constructed by taking the first 11 groups of the YOM cross sections,³ extending down to 25 keV, and appending 7 additional groups extending down to 30 eV used by Greebler, *et al.*⁴ Temperature and composition (expressed by σ_p , the equivalent scattering cross section per absorbing atom, in barns) dependent cross sections from Ref. 4 were used in these calculations. Flux calculations were performed using the ELMOE code,⁵ which allows use of hundreds of fine groups in a fundamental mode calculation. Such a calculation requires the use of an effective core temperature and also assumes that the neutron energy spectrum is constant over the core, which is not an unreasonable assumption for a large reactor.

The resonance integral calculations of Greebler, *et al.*⁴ were performed in the narrow resonance approximation, assuming isolated resonances. A similar procedure was subsequently followed at ANL in constructing a 22 group set of cross sections, Set 215. This had the same energy divisions as the 199 set, except that the lower groups were further subdivided, particularly in the vicinity of the 2.85 keV resonance in Na.

A series of calculations for oxide and carbide fueled reactors with 52 v/o Na and stainless steel structural material was performed with the 215 set⁶ with results given in Table III-1-I. Some of these repeated the earlier work with the 199 set,² with results that were not much different. This is not too surprising, as the assumed parameters as well as the method of resonance integral evaluation did not differ greatly from that of Greebler, *et al.*⁴

The sensitivity of the calculated results to the assumed parameters was explored.⁶ It was concluded that for what appeared to be reasonable variations in parameters the Doppler effect was not changed by more than about 20%. However, fissile material properties are quite uncertain and in particular multilevel effects were not examined. On the other hand, the effect of fissile-fertile resonance interaction⁷ makes the calculated fissile material contributions very small. The results in Table III-1-I do not include this interaction effect.

Another source of uncertainty in Doppler effect calculation in addition to the parameters arises from the calculation of the neutron energy spectrum at low energies (<25 keV). There are two aspects to this question. One is the problem of calculating how many neutrons per fission source neutron are slowed down to low energy, and the other is the matter of the spectral distribution of low energy absorptions. There is an uncertainty in inelastic scattering properties which affects the first of these but not the second. The magnitude of this uncertainty is illustrated by the fact that the new Cross Section Set 224⁽⁸⁾ gives 10 to 20% more low energy neutrons than does Set 215. The new set has the same group structure as Set 215, but has updated cross sections. A comparison of results using the various cross section sets is given in Table III-1-II. The Pu-239-U-238 overlap effect is taken into account in Set 224 using calculations of R. Hwang.⁹

The number of neutrons slowing down to low energies is characterized here by q , the fraction of fission neutrons slowing down below 9.1 keV. From 80 to 90% of the Doppler effect in a fast ceramic-fueled reactor occurs below this energy, depending on composition. This quantity is also determined by the values of fission and capture cross sections and by elastic scattering effects. The difference in q between Sets 215 and 224 is really a combined effect of inelastic scattering, fission, and capture; but it is felt that inelastic scattering is the major effect. It is believed that elastic scattering effects are adequately treated by the ELMOE program.

An indication of the sensitivity of the Doppler effect to low energy spectral shape can be obtained from the results in Table III-1-I. It is seen that although both δk and q vary by a factor of two when sodium is removed, for these compositions with 52 v/o Na, $\delta k/q$ is not very sensitive to the presence or absence of sodium. This is true even though the 2.85 keV scattering resonance in Na produces a considerable displacement of the neutron spectrum to lower energies. The $(\delta k)_{\text{Doppler}}$ per neutron absorbed becomes appreciable below about 25 keV and rises rapidly with decreasing energy down to an energy of about 4 keV, below which it does not vary sharply with energy. This behavior makes it plausible that the Doppler effect would be relatively insensitive to the low energy spectral shape. For this reason it seems unlikely that errors in calculating this shape would be important unless they were very gross.

* Applied Mathematics Division.

TABLE III-1-I. DOPPLER EFFECT OF OXIDE- AND CARBIDE-FUELED REACTORS, 750°-1500° K, AS A FUNCTION OF U-238/Pu-239 RATIO
Cross Section Set 215

Fuel	U-238/ Pu-239	52 v/o Na	-% δk	q^a	$-\delta k/q$	Positive Pu-239 Effect as Percentage of Negative U-238 Effect
Oxide (32 v/o fuel @ 10.9 g/cc, 16 v/o steel)	9	Yes	0.87	0.226	0.0384	13
		No	0.38	0.117	0.0324	10
	7	Yes	0.53	0.161	0.0328	17
		No	0.23	0.0775	0.0296	13
		Yes	0.28	0.100	0.0280	23
Carbide (30 v/o fuel @ 13.5 g/cc, 18 v/o steel)	9	Yes	0.068	0.0430	0.0158	38
		No	0.025	0.0208	0.0120	41
	7	Yes	0.59	0.163	0.0362	12
		No	0.25	0.0807	0.0324	9
		Yes	0.36	0.113	0.0318	16
No	0.15	0.0529	0.0284	12		

^a Fraction of fission source neutrons slowing down below 9.1 keV.

TABLE III-1-II. DOPPLER EFFECT, 750°-1500° K,
OF 7 U-238/1 Pu-239 OXIDE-FUELED REACTORS
FOR DIFFERENT CROSS SECTION SETS
(52 v/o Na, 33 v/o Fuel)

Cross Section Set	-% δk	q	$-\delta k/q$	Positive Pu-239 Effect as Percentage of Negative U-238 Effect
199	0.50	0.152	0.0328	21
215	0.53	0.161	0.0304	17
224	0.73	0.188	0.0388	5

A hardening of the spectrum tends to decrease ($\delta k/q$) because a greater fraction of low energy absorptions occur in the upper part of this energy region, in which δk per absorption is less. Any error in the calculated low energy spectral shape would arise from the values assigned to fission and capture cross sections, as elastic moderation effects should be adequately taken into account by ELMOE.

The low energy flux hardens with increasing temperature because of increases in average fission and capture cross sections. It was found that the negative δk for a cross section variation for 750 to 1500°K was about 10% greater if the flux and adjoint for 750°K was used in a perturbation calculation instead of the 1500°K flux. It was likewise found that for a change from 1500 to 2500°K the use of the 1500°K fluxes gave an effect about 10% greater than the use of the 2500°K fluxes. This gives an idea of the probable magnitude of the error occasioned by a mismatch of buffer and test zone temperatures in a zoned loading experiment.

The calculations in Tables III-1-I and III-1-II were based on systems with 52 v/o Na, and with fuel composed only of Pu-239 and U-238. An increase in the Na to fuel ratio to 70 v/o Na with 18 v/o fuel for an oxide system increases the Doppler effect by a factor of two because of the increase in low energy flux.⁶ A substitution of Pu-240 for U-238 to the extent of 0.5 of the Pu-239 decreases the Doppler effect by about 30% for U-238/Pu-239 = 7. Addition of fission products corresponding to 5% burnup decreases the Doppler effect an additional 10%.

It would be expected that the addition of sodium might affect calculated resonance integrals significantly because of the change in σ_p , particularly in the vicinity of the 2.85 keV resonance. This has been found not to be true, however, because of the flux depression in the vicinity of the resonance and because of the slow variation of $\delta\sigma_\gamma$ of U-238 with σ_p in the range of interest. Significant heterogeneity effects might be expected because of the large part of the total scattering cross section associated with pin clad and with sodium. Using the equivalence theory in current use, which involves the flat flux approximation, such effects do not appear to be significant. This is so even for pins as large as 1 in. in diameter, which might be used in reactor or critical experiment measurements of the Doppler effect. More refined calculations are desirable to verify this, however.

REFERENCES

1. R. Avery, et al., *Physics of Fast Reactors*, Proc. 1964 Geneva Conference.
2. M. G. Bhide and H. H. Hummel, *Calculations of the Doppler Coefficient of Large Ceramic-Fueled Fast Reactors*, ANL-6601 (1962).
3. S. Yiftah, D. Okrent and P. A. Moldauer, *Fast Reactor Cross Sections*, (Pergamon Press, New York, 1960).
4. P. Greebler, B. Hutchins and J. Sueoka, *Calculation of Doppler Coefficient and Other Safety Parameters for a Large Fast Oxide Reactor*, GEAP-3646 (1961).
5. H. H. Hummel and A. L. Rago, *An Accurate Treatment of Resonance Scattering in Light Elements in Fast Reactors*, SM-18/45, Proc. of Seminar on Physics of Fast and Intermediate Reactors (1961).
6. H. H. Hummel and A. L. Rago, *Effect of Parameter Variation in Doppler Effect Calculations*, Proc. of the Conf. on Breeding, Economics, and Safety in Large Fast Power Reactors, ANL-6792 (1963), pp. 747-763.
7. J. Codd and P. Collins, *Some Calculations Concerning the Influence of Resonance Overlapping on the Doppler Effect in a Dilute Fast Reactor*, Proc. of the Conf. on Breeding, Economics, and Safety in Large Fast Power Reactors, ANL-6792 (1963), pp. 711-726.
8. D. O'Shea, H. H. Hummel, W. B. Loewenstein and D. Okrent, *26 Group Cross Sections*, ANL-6858 (in publication).
9. R. N. Hwang, *An Improved Method of Doppler Effect Calculation for Fissile Materials in the Intermediate Energy Region*, Proc. of the Conf. on Breeding, Economics, and Safety in Large Fast Power Reactors, ANL-6792 (1963), pp. 727-745.

III-2. Interference Interaction in Doppler Theory for Fast Reactors

R. N. HWANG

Because of great concern about the effect of interference interactions on the Doppler effect calculations, extensive studies have been made in order to include the contribution of these interactions in our current calculations of the Doppler broadened cross sections for fissile isotopes. Two types of interference interactions are of practical significance. The first type, which is referred to as the "self"-overlap effect, is attributed to the interaction of neighboring resonances of a particular fissile isotope. The second type, which is referred to as "accidental"-overlap, is attributed to the interaction between resonances of two or more isotopes in the mixture. The interference interactions give rise to a change in the fine structure of the neutron flux and consequently may bring about a substantial reduction in the Doppler broadening as obtained by the well-known isolated resonance approximation.

The direct evaluation of the temperature dependent effective cross section becomes extremely complicated and time consuming when interference interactions are considered. However, the problem can be simplified greatly by some analytical approximations.

"SELF"-OVERLAP EFFECT

Two methods generally known as "Method A" and "Method B" were used in earlier studies¹ for the Doppler coefficient calculations in the unresolved region. "Method A", in which the Doppler broadened resonances are assumed to overlap strongly, is applicable only in the high energy region, whereas "Method B," in which resonances are treated as isolated, is presumably valid only in the low energy region. However, neither "Method A" nor "Method B" is clearly applicable in the intermediate energy region which is of great concern in the current studies of large fast reactors.

An improved method² based on the narrow resonance approximation and single level formula has been developed to take into account the self-overlap effect in the intermediate energy region. The method can be summarized as follows:

1. In general, the temperature dependent effective cross section can be considered as the superposition of a non-overlapping and an overlapping part; that is,

$$\bar{\sigma}_x = \bar{\sigma}_x^{\text{isolated}} + \sigma_p \sum_{\text{Spin } j} \frac{1}{\langle S \rangle_j} \left[\langle \Gamma_x H \rangle_{\text{over width}} \right]_{\text{over spacing}}$$

where σ_p is the potential scattering cross section per atom of the isotope under consideration; H , the overlap correction term defined in Ref. 2; $\langle S \rangle_j$ average spacing; and Γ_x , the level width of the process x . $\langle \rangle$ and $[]$ repre-

sent the statistical averaging over width and spacing distributions respectively.

For the high energy region, the term $[\langle \Gamma_x H \rangle]$ approaches its asymptotic form² as Eq. 1 becomes identical with "Method A." On the other hand, the overlap term which depends strongly on the ratio of the Doppler width to the average spacing vanishes in the low energy region as Eq. 1 approaches the "Method B" approximation.

2. In order to evaluate the overlap term, it is necessary to determine the function Ω , the probability of finding any level within an interval $d | E_k - E_{k'} |$ at a distance $| E_k - E_{k'} |$ from a given level k . The function Ω is assumed to satisfy a Faltung type integral equation depending on the statistical distribution of the level spacing. In the present work, a χ -square distribution with $\nu = 8$, which gives reasonably good fit to experimental values at low energy, is used for fissile isotopes. For the $\nu = 8$ distribution, the function $\Omega(y)$ becomes

$$\Omega(y) = 1 - e^{-8y} - 2e^{-4y} \sin 4y \quad (2)$$

where

$$y = \frac{|E_k - E_{k'}|}{\langle S \rangle}$$

is the ratio of local to average spacings.

3. Since the typical fast reactor potential scattering cross section Σ_b is generally much larger than the reaction cross section Σ_R of the fissile isotope in the energy region of interest, it is possible to expand the overlap term into a power series. The integration has been carried out for each term in the series. An analytical expression for the overlap term was obtained in terms of Fresnel integrals.² It is therefore possible to evaluate the overlap term more accurately by retaining more terms in the series.

4. Calculations have been made for both U-235 and Pu-239. For U-235, the "self"-overlap causes a reduction in $\delta\bar{\sigma}_f$ and $\delta\bar{\sigma}_\gamma$ varying from about 25% at several hundred eV to 35% at several keV from the corresponding values obtained by the isolated resonance approximation. For Pu-239, the reduction varies from 4% to 25%.

"ACCIDENTAL"-OVERLAP

The effect of the "accidental"-overlap between the fissile and fertile isotopes in a large fast reactor was not fully realized in the earlier work on the Doppler effect. Extensive studies have been made since the discovery by J. Codd and P. Collins.³

A straightforward evaluation of the temperature-

dependent cross section is extremely difficult and time consuming. In order to simplify the problem of numerical integration and utilize the existing code, a method of approximation has been developed as described in Ref. 2. Again, the temperature-dependent effective cross section is expressed as a superposition of a non-overlap and an overlap term. Since there is no correlation between resonances of two different isotopes, the separation of levels in this case is taken as random distribution. It was found that the "accidental," overlap also exhibits asymptotic characteristics. In the very high energy region, the overlap term in $\bar{\sigma}_x$ eventually becomes temperature-independent and hence the effect of the "accidental"-overlap on $\delta\bar{\sigma}_x$ due to temperature vanishes. On the other hand, the effect of the "accidental"-overlap also becomes small in the low energy groups since the number of interfering resonances in the energy interval under consideration decreases with energy. These arguments seem to indicate that the maximum effect occurs somewhere in the intermediate energy region.

Calculations of the Doppler broadenings have been made for both U-235:U-238 and Pu-239:U-238 systems with various enrichment ratios and at various energy groups. It is most convenient to express the interference effect in terms of the percent reduction in δk or δR_x (the change in reaction rate of the process x with temperature) from the corresponding values obtained

by the isolated resonance approximations. The percent reduction in δR_x was found to depend strongly on (1) neutron energy and (2) enrichment ratio at high energy (beyond 2 keV) but less so at low energy. Calculations of δk seem to indicate that the "accidental"-overlap will essentially wipe out or may, in the case of U-235 systems, make negative the positive component of δk due to the fissile isotope.

So far, two types of interference interactions have been considered separately. An attempt is being made to improve the method further in order to include the combined effect of two types of interference interactions. A general expression for an interacting system with more than two resonance absorbers is also under investigation. Since all theoretical studies have been based on the narrow resonance approximation and single level formalism, the validity of these basic assumptions is yet to be investigated.

REFERENCES

1. R. B. Nicholson, *The Doppler Effect in Fast Neutron Reactions*, APDA-139 (1960).
2. R. N. Hwang, *An Improved Method of Doppler Effect Calculation for Fissile Materials in the Intermediate Energy Region*, ANL-6792 (1963).
3. J. Codd and P. J. Collins, *Plutonium 239 and Uranium 238 Resonance Interaction Effect in a Dilute Fast Reactor*, E.A.E.S. Symposium on Advances in Reactor Theory (1963).

III-3. Doppler Effect Experiments

G. FISCHER, J. FOLKROD,* E. GROH and D. MENELEY

GENERAL

These experiments have been or will be done on ZPR-III with zoned loadings. The central zone in which the measurements are made is a mockup of some soft spectrum composition of current interest for large power reactors; this is surrounded by a high reactivity driver. A suitable filter is placed between the zones to provide spectrum matching of the central zone to that of the large reference core. The central zone is designed for relatively flat radial and axial flux distributions in order to minimize expansion reactivity changes upon heating the Doppler elements.

The measurements are made by exchanging hot and cold samples, or samples and dummies in the assembly

* Reactor Engineering Division, Argonne National Laboratory.

while holding the reactor at constant power level. The power level is maintained by moving a fine control rod located in the driver zone. Reactivity changes are determined from the relative positions of this rod. Air cooling is provided for the hot element to prevent the dissipated heat from causing temperature drift of the assembly.

MEASUREMENTS ON ZPR-III ASSEMBLIES 43 AND 43A^{1,2}

Assembly 43 was a zoned mockup of a 5000 liter uranium monocarbide power reactor with sodium volume fraction of 48% and with stainless steel clad and structure. Assembly 43A was constructed by replacing 40% of the sodium in Assembly 43 with graphite in order to increase the low energy fluxes and hence the

Doppler effect. Two matrix tubes, one above and one below the central drawer of the assembly, were voided to allow insertion of two elements. The measurement procedure was to exchange the hot element in one channel with the cold element in the other channel and to observe the reactivity change. The difference in reactivities when both elements were cold was added or subtracted as appropriate to give the reactivity change on heating the element. Results are shown in Table III-3-I. The calculated values shown were derived from cylindrical and spherical 1-D diffusion theory calculations using ANL cross-section set 215.³

These values were obtained from several hot-cold sample exchanges. The overall confidence level is about ± 0.02 Ih. Tests were made to estimate the effects of resonance shielding of the sample by the surrounding U-238, the fraction of the signal due to non-Doppler sources, the error in element position, and possible axial expansion of the sample. These errors were all smaller than 5% of the signal.

The basic sample used in the measurements was 1.4 in. in diameter and 11 in. long, made up of 1-in. pellets. The natural uranium dioxide was ground and pressed to 70% of theoretical density using 1 w/o sodium metasilicate bonding agent. It was found that this type of pellet, when heated, could be restrained from expanding with very little thrust. The sample was contained in a thin-walled Hastelloy tube which served as the electrical heating element. This tube was supported inside a stainless steel outer can with silvered inner surface, by means of a ceramic tube at each end. A bellows at one end of the Hastelloy tube allowed it to expand while the supports maintained the cold length of the sample. The space between the outer and inner cans was evacuated to reduce conductive heat transfer. The vacuum was held to about 1 micron by continuous pumping during the experiment. Power required to heat the element to 800°K was less than 80 W.

Some difficulties were encountered during operation. X-ray examination showed that with continuous cycling the cold length of the sample slowly decreased, indicating that the pellets were deforming when hot. This reduced the effectiveness of the length restraint system. Also the temperature distribution was uneven due to higher resistance and hence greater power input at the bellows end of the Hastelloy inner can. The fuel expansion worths mentioned above showed that the error due to sample expansion was small, and appropriate temperature averaging was done to reduce the non-uniformity error.

These results demonstrated that this type of measurement could be made in a critical assembly with

TABLE III-3-I. REACTIVITY CHANGES ON SAMPLE HEATING, Ih

(In hours per percent reactivity = 444)

Sample Exchanges	Assembly 43	Assembly 43A
2 cold to 1 hot ($\bar{T} = 800^\circ \text{K}$)	-.251	-.593
1 cold to 2 cold ($\bar{T} = 300^\circ \text{K}$)	-.151	-.089
Net	-.402	-.682
1 cold to 2 hot ($\bar{T} = 800^\circ \text{K}$)	-.549	-.765
2 cold to 1 cold ($\bar{T} = 300^\circ \text{K}$)	+.151	+.089
Net	-.398	-.674
Average	-.400	-.678
Calculated	-.444	-.981
Calculated/experimental	1.11	1.447
1 cold to 2 hot ($\bar{T} = 553^\circ \text{K}$)	—	-.437
2 cold to 1 cold ($\bar{T} = 300^\circ \text{K}$)	—	+.089
Net	—	-.348

good accuracy, and they gave some valuable guides to the design of new equipment.

EQUIPMENT FOR FURTHER MEASUREMENTS

Recent work on Doppler effect experiments has been directed along two main lines. The first has been an attempt to measure the effect of sample size on the measured Doppler effect per gram of heated material. It is of interest to estimate errors by comparing these measurements on relatively large diameter samples with smaller prototype power breeder fuel pins. The second has been the preparation of samples containing fissile isotopes and mixtures of fissile and fertile materials.

New equipment has been designed in accordance with the following main principles:

1. The maximum amount of material heated in any one matrix drawer should approximate the amount in a normal drawer of the mockup.
2. Only low capture materials should be used. (This limits the maximum operating temperature to about 1000°C, using Inconel for the sample can.)
3. Flexibility of matrix position and sample composition must be attained.
4. The equipment should be sufficiently rugged to allow measurements of the same samples in several assemblies.
5. Reactivity changes due to sample expansion must be kept to acceptable levels by the proper design of critical assemblies as well as of the fuel elements.
6. Sufficient air cooling must be provided to remove all heat dissipated from the element in order to control reactor drift.
7. Samples must be effectively sealed in two en-

closures while heating—that is, the sample can and the outer vacuum can. (Ion vacuum pumping was made necessary by this requirement).

8. Leakage from the sample can during heating must be detectable. (This led to inclusion of helium inside the can and a helium mass spectrometer in the vacuum system).

9. Temperature differences along the sample length should be held to a minimum.

A cross-section of the element is shown in Fig. III-3-1.

The basic samples are 0.5-in. diameter, 6-in. long

uranium and/or plutonium dioxide, fabricated in 0.5- or 1-in. lengths. The pellets are made in the same fashion as those for the first set of measurements. As before, two of the samples, enclosed in heater cans, are supported at the ends in a silvered stainless steel tube. The heater cans are wound with insulated nichrome heater wire with a closer pitch near the end supports to make the sample temperature more uniform. Quartz spacers inside the cans also serve this purpose. Three thermocouples are placed in a reentrant tube which passes down the axis of each sample.

The sample can is allowed to expand against a spring

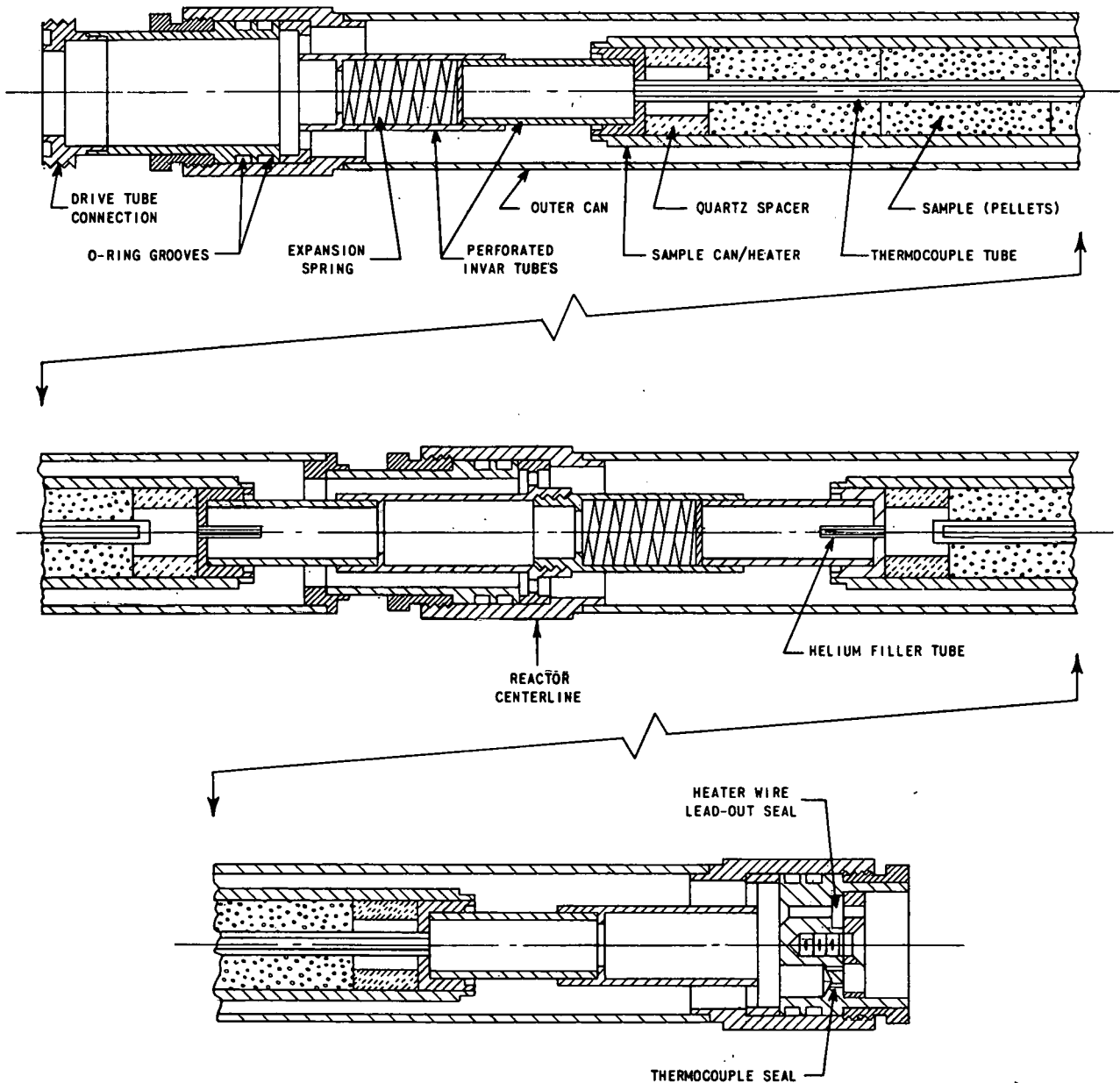


FIG. III-3-1. Doppler Element.

at one end; this spring holds it firmly against the opposite support. One of the fixed supports is located at the end of the sample nearest the reactor centerline while for the other sample it is at the outer end. This layout provides some cancellation of expansion reactivity changes.

The outer can is sealed with O-rings to permit easy changing of samples. The whole assembly, approximately 25 in. long, is placed into a drive tube which in turn moves in fixed guides in the matrix drawer. The outer dimension of these guides is roughly $1\frac{1}{2}$ in. square. The remainder of the drawer is filled with ZPR plates. The drive tube contains space for two $\frac{1}{2}$ in. x 1 ft. ZPR plates in the sections not occupied by the elements. This reduces reactivity changes when moving highly reactive samples. A dummy element drawer is attached to the rear of the drive tube. Up to four complete assemblies as described above may be driven in tandem during a measurement; many combinations of radial position are possible.

A measurement consists of pulling the drive tube out of the assembly to exchange the element and dummy at the reactor center. Hot and cold comparisons are made to complete the measurement.

The movable drive table is positioned at one end of the matrix. This table contains the vacuum manifold, mass spectrometer and ion pump. Maximum stroke of the table is 48 in., with a minimum transit time of 30 sec. This could be reduced by use of a larger drive motor.

Auxiliary equipment includes a roughing pump, heater controls, thermocouple recorders and cooling air refrigeration system. This system will cool 100 scfm of air from 90°F to 50°F for use in element cooling. Condensers, filters, and traps are included as well as a variable heater to adjust the air inlet temperature to balance heat losses. There is also a blower and suction manifold for drawing room air through plutonium bearing assemblies to remove spontaneous fission heat.

Samples being prepared for measurement are natural uranium dioxide, 7:1 U-PuO₂, low Pu-240 content PuO₂, high enrichment UO₂ and 17% enriched UO₂.

A second set of elements has been constructed to accommodate 1 in. and 0.73 in. natural uranium oxide samples in order to investigate rod size effects on this type of Doppler measurement. These elements are similar in detail to the unit described above. The drive table, pumps, etc. may be used for either element.

CONCLUSIONS

While several refinements could be made to improve the design described above, it is felt that not very much more could be gained from building new equipment of this type. The main restrictions of the design are the sample size necessary to give a reasonable signal, the elaborate canning and insulation necessary, and the large amount of cooling required for elements to run at significantly higher temperatures. Also, as F. Storrer⁴ has shown, the "hot sample in cold reactor" error increases markedly for large temperature differences between sample and core material. A method of avoiding this difficulty as suggested by Storrer would be to heat a zone consisting of core materials to some intermediate temperature and then heat a sample inside this zone to a higher temperature. The expansion effect of the buffer zone would not be a spurious factor since it would remain constant throughout the measurement. The difference between the buffer and sample temperatures would be kept to 200-300°C.

A relatively long program of importance concerning the fast reactor Doppler effect measurement is anticipated with the use of the equipment which has just been completed. Plutonium-uranium systems will be studied at ZPR-III, and U-235-U-238 systems will be examined at ZPR-VI. Doppler calculations for FARET and SEFOR will be checked during critical experiments on ZPR-III. The very important recent theoretical prediction that interference absorption by the resonances of U-238 can considerably reduce the positive Doppler coefficient of Pu-239 will be checked.

REFERENCES

1. G. Fischer, H. Hummel, J. Folkrod and D. Meneley, *Experimental Results for U-238 Doppler Measurements in Fast Reactor Spectra*, Proc. Conference on Breeding, Economics and Safety in Large Fast Power Reactors, ANL-6792 (1963), pp. 885-895.
2. G. Fischer, H. Hummel, J. Folkrod and D. Meneley, *Doppler Coefficient Measurements for U-238 in Fast Reactor Spectra*, Nucl. Sci. Eng. **18**, No. 2, 290 (1964).
3. H. H. Hummel and A. L. Rago, *Effect of Parameter Variation in Doppler Effect Calculations*, Proc. Conference on Breeding, Economics and Safety in Large Fast Power Reactors, ANL-6792 (1963), pp. 747-761.
4. F. Storrer, A. Khairallah, and J. Ozeroff, *Measurements of the Doppler Coefficient in Large Fast Power Reactors Using a Fast Critical Assembly and an Experimental Reactor*, Proc. Conference on Breeding, Economics and Safety in Large Fast Power Reactors, ANL-6792 (1963), pp. 823-852.

III-4. Sodium Void Effect

H. H. HUMMEL, L. KVITEK, K. E. PHILLIPS and A. L. RAGO*

A review of the problem of positive sodium void effects in large Pu-fueled fast reactors has been presented recently.¹ Certain aspects have been explored in more detail in another paper.²

The problem arises from the fact that the fission cross section of Pu-239 varies less rapidly with energy than do the capture cross sections of reactor materials. As a result $\eta(E)$, the neutrons produced in the reactor per fission, and the closely related neutron importance function, are monotonically increasing with energy over most of the energy region of interest. The result is that the inelastic and elastic scattering energy transfers provided by sodium reduced reactivity, and conversely a positive effect is produced when sodium is removed. It has been found that this spectral component of the sodium void effect is mainly dependent on core composition and relatively insensitive to core geometry for uniform removal of sodium from a uniformly loaded core. There is another—a smaller positive effect also dependent on the core spectrum—which results from radiative capture in sodium. These components of the sodium void effect are at a maximum at the center of the core and become small at the outer edge. The leakage component of the void effect, which is negative, is zero at the center of the core and its absolute value passes through a maximum in the outer part of the core.

The spectral component becomes more positive as core enrichment decreases because $\eta(E)$ becomes more rapidly varying with energy. Means of dealing with the problem have mainly involved raising core enrichment by increasing core leakage, thereby reducing the positive spectral component. This can be accomplished by reducing one or more core dimensions, or by reducing reflector effectiveness. It has been found³

* Applied Mathematics Division.

that infinite slab cores have a smaller leakage component than spherical cores of the same composition because the increase in reflector effectiveness that accompanies removal of sodium is more important as the minimum dimension of the core decreases.

If reflector effectiveness can be reduced in such a way that neutrons leaving the core have a reduced probability of returning, then less of an increase in effectiveness can occur on sodium voiding. The bare core condition is thus approached, for which the leakage component is a maximum. Reducing reflector effectiveness does, however, introduce problems with the core maximum-to-average power density and also increases the difficulty of capturing all neutrons escaping from the core.

An increase in the leakage component offers the possibility that, if it is permissible to balance a larger negative leakage component against a larger positive spectral component, a lower core enrichment can be permitted. This has the advantage of a larger Doppler effect and a larger core conversion ratio. It is not clear that this balancing is permissible to any extent desired, since a boiling sodium accident may void sodium first from the center part of the core, where the leakage component is not effective. Resolution of this point depends on more information about the possible movement of sodium in such an accident.

REFERENCES

1. R. Avery, H. H. Hummel, R. N. Hwang, D. Meneghetti, P. A. Moldauer, A. B. Smith, P. Greebler, and J. B. Nims, *Physics of Fast Reactors*, Proc. 1964 Geneva Conference.
2. H. H. Hummel, K. E. Phillips and A. L. Rago, Proc. of the Conf. on Breeding, Economics, and Safety in Large Fast Power Reactors, ANL-6792 (1963), pp. 65-74.
3. W. G. Davey and J. M. Chaumont, Argonne National Laboratory (Private Communication).

III-5. Comparison of SNG, DSN, DTK, and REX Calculations

J. WHITE

Comparison calculations have been made for the Godiva¹ and Topsy¹ systems using DSN² and DTK³ with 4, 8, and 16 angular approximations. Convergence criteria were 10^{-5} for Godiva and 10^{-5} or 10^{-6} for Topsy. An SNG⁴ case was also studied. Analyses were

made with 16 energy groups and criticality was obtained by variation of radii for all regions. The differences in critical radii as given by DSN and DTK with $n = 4^*$ were due to the low angular approxima-

* n is the number of angular intervals.

tion and were not caused by the convergence criterion of 10^{-5} . It can be seen in Tables III-5-I and III-5-II that, for the case of the bare system (Godiva), the DTK code gave smaller critical radii than DSN for

TABLE III-5-I. GODIVA

Program	n	Convergence Criterion	Critical Core Radius, cm
DSN	4	10^{-5}	8.7557
DTK	4	10^{-5}	8.7080
DSN	8	10^{-5}	8.8032
DTK	8	10^{-5}	8.78425
DSN	16	10^{-5}	8.8133
DTK	16	10^{-5}	8.8053

TABLE III-5-II. TOPSY

Program	n	Convergence Criterion	Critical Outer ^a Radius, cm
DSN	4	10^{-5}	26.3206
DTK	4	10^{-5}	26.3870
SNG	4	10^{-5}	26.4424
DSN	4	10^{-6}	26.3206
DTK	4	10^{-6}	26.3872
DSN	8	10^{-6}	26.6343
DTK	8	10^{-6}	26.6023
DSN	16	10^{-6}	26.70925
DSN	16	10^{-6}	26.7092
DTK	16	10^{-6}	26.6901

^a Outer radial dimension of the Topsy reflector; ratio of core radius to outer radius is 0.2291.

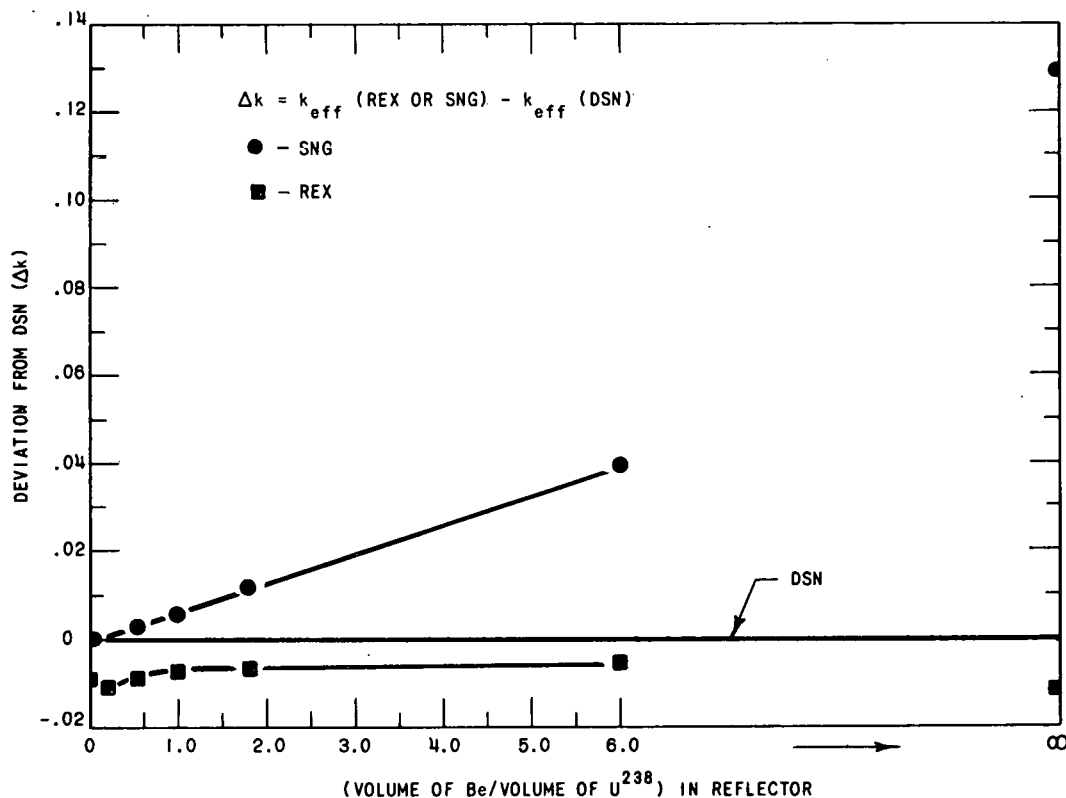


FIG. III-5-1. A Comparison of Diffusion Theory with SNG and DSN.

the low approximation $n = 4$. For the case of the reflected system (Topsy) the DSN code gave smaller critical radii than DTK for $n = 4$.

A comparison has also been made among SNG, DSN, and REX⁵ calculations of a high-void fast core with several reflectors (20 cm thick) consisting of various ratios of Be to U-238. The SNG and DSN calculations utilized $n = 4$ angular intervals. The analyses were with 4 energy groups and in all cases the convergence

criterion was 10^{-6} . Figure III-5-1 summarizes the results of this comparison.

In general, it was found that as the atomic Be density in the reflector increases, the SNG method gives an inadequate description of the system reactivity.

REFERENCES

1. *Critical Mass (U-235, Pu-239, U-233, U-238 and Th Systems)*, ANL-5800, Second Edition (1963), Sec. 7.2.1.

2. B. Carlson, *Numerical Solution of Transient and Steady-State Neutron Transport Problems*, LA-2260 (May, 1959). B. Carlson, C. Lee and J. Worlton, *The DSN and TDC Neutron Transport Codes*, LAMS-2346 (February, 1960). B. Carlson, C. Lee and J. Worlton, *The DSN CODE (Appendix I)*, LAMS-2346 (February, 1960).
3. B. Carlson, *Methods in Computational Physics; The Numerical Theory of Neutron Transport*, (Academic Press, New York), Vol. 1, (1963), pp. 1-42.
4. B. Carlson, *Solution of the Transport Equations by S_n Approximations*, LA-1891, (February, 1955). B. Carlson, *The S_n Method and the SNG and SNK Codes*, AECU-3691 (January, 1958). B. Carlson and G. Bell, *Solution of the Transport Equation by the S_n Method*, Proc., 1958 Geneva Conference, 16, Paper No. 2386, p. 535.
5. M. Butler and J. Cook, *Univac Programs for the Solution of One-Dimensional Multigroup Reactor Equations*, ANL-5437 (1956).

III-6. Studies with the ELMOE Program for Fast Critical Analyses

D. MENEGHETTI

INTRODUCTION

The increasing use of the ELMOE program^{1,2} to determine the group transport and group elastic-transfer cross sections for subsequent use in multigroup multiregion reactor analysis have given rise to numerous questions regarding the suitability and possible errors in its use. For a given composition the ELMOE program solves for the fundamental mode using hundreds of very fine energy groups, and yields coarse-group cross sections for possible use in reactor criticality codes. The details of the elastic scattering resonances present in nonfissile and nonfertile atoms of structural and coolant materials are thus accounted for in the case of a bare core system. Its applicability for determining effective cross sections for multiregion cores differing in regional composition and for determining effective group cross sections in the case of reflectors containing light elements becomes an important consideration. Furthermore as the ELMOE program contains the options: *P-1*, consistent *P-1*, *B-1*, and consistent *B-1*, it is of interest to know the differences in critical masses computed using effective group cross sections based upon the different ELMOE options.

EFFECT OF NEIGHBORING FINE FLUX SPECTRUM UPON EFFECTIVE CROSS SECTIONS

The possible effects of the fine flux spectrum of adjacent regions upon effective cross sections are indicated in the following situation.

Aluminum at lowered density is often used to simulate Na coolant in fast critical experiments. The reactivity effects of Na relative to Al are found by replacement experiments in various regions of the core. Na and Al have different resonance scattering cross section dependence with energy in the neutron range of fast systems. Theoretical analyses of replace-

ment experiments are generally carried out with multigroup cross section parameters having group energy increments which encompass many scattering resonances. Furthermore the multigroup constants may also have been evaluated a-priori, taking into consideration the differing fine group structure of the Na and Al-containing regions. Still unaccounted for is the possible effect of the resonance-produced fine structure flux spectrum of the surrounding Al-containing region upon the effective group cross section of the internal Na-containing region and vice-versa.

Possible effects of the adjacent Al-containing regions in modifying the effective group cross sections for transport and elastic transfer in the Na-containing region are indicated in Table III-6-I. Results are given for an EBR-II assembly and a ZPR-III Assembly 31 core composition. The ratios of effective coarse group cross sections of the Na-containing composition determined by resonance-produced fine group fluxes of the Al-containing composition to those of the Na-containing composition determined by the resonance-produced fine group fluxes of the Na-containing composition are given. The modifying effect is seen to be greater for the elastic removal than for the transport cross sections in these cases. These results were obtained by averaging the fine group cross sections of the ELMOE library for the composition of the Na-containing systems with the fine group fluxes. The latter were determined with the ELMOE code for the Al- and Na-containing cores respectively.

EFFECTIVE CROSS SECTIONS FOR REFLECTORS BY USE OF ELMOE CODE

In the calculation of critical mass of a fast critical assembly the ELMOE code^{1,2} is often employed to obtain the effective group cross sections for transport and elastic-transfer for the core composition. As ELMOE is a fundamental mode analysis code, strictly it

TABLE III-6-I. RATIOS OF TRANSPORT AND OF ELASTIC REMOVAL CROSS SECTIONS

Energy Group ^a	EBR-II		ZPR-III, Assy. No. 31	
	Transport ^b	Elastic removal ^c	Transport ^b	Elastic removal ^c
2	1.00	0.98	1.00	0.97
3	1.00	1.035	1.00	1.06
4	1.00	0.93	1.00	0.94
5	1.01	0.82	1.01	0.81
6	1.00	0.93	1.01	0.91
7	1.00	0.93	1.01	0.90
8	1.00	1.10	0.99	1.175
9	0.99	1.48	0.98	1.61
10	1.02	0.67	1.03	0.59
11	1.00	1.98	0.95	2.02
12	0.975	0.75	0.945	0.525
13	1.00	1.04	1.00	0.99
14	0.99	0.93	0.99	0.97
15	1.07	0.17	1.25	0.19

^a Ref. 5.^b Ratio of total homogenized core cross section for transport.^c Ratio of light element (Na and stainless steel) homogenized core cross sections for elastic transfer.

is neither applicable to the outer regions of a reflected core nor, in particular, to a reflector region containing light scattering materials such as steel, sodium, aluminum, etc. (In the past, critical assemblies such as many of the ZPR-III assemblies,³ had reflectors that contained primarily only U-238. Hence, the question of light element scattering resonances in the reflector did

not enter and fine group averagings for this effect were not necessary.) To obtain an indication of the sensitivity of critical mass to choice of light element group cross sections in a reflector three sets of aluminum cross sections have been considered for the reflector of the aluminum-reflected system, ZPR-IX, Assembly 1.¹⁴ In two cases the ELMOE code was used to generate these cross sections making, however, certain simplifying assumptions on buckling and source spectra.

The three cases are:

- The YOM⁵ aluminum cross sections
- The ELMOE-determined aluminum cross sections in an applied fission spectrum source assuming zero buckling
- The ELMOE-determined aluminum cross sections in an applied source which is constant with respect to energy and assuming zero buckling

The cross section sets are compared in Table III-6-II. The ratio of critical core volumes using Set (b) relative to Set (a) in the reflector was calculated to be 1.17. As the cross sections of Set (c) are closely similar to those of Set (b) no subsequent criticality calculations were made with Set (c).

Current studies of calculated average group cross sections for reflectors containing light materials indicate that the choice of an applied fission source together with the assumption of zero buckling lead to negligible error in reflector group transport cross sections. Such is not the case, however, for the group transfer cross sections. In a reflector region the transport cross sections will generally be more important

TABLE III-6-II. COMPARISONS OF GROUP CROSS SECTIONS FOR ALUMINUM, BARNS

Energy Group	Group Lower Energy MeV	Set a ⁵		Set b		Set c	
		Transport	Elastic transfer	Transport	Elastic transfer	Transport	Elastic transfer
1	3.668	1.37	0.118	(1.37) ^a	(0.118)		
2	2.225	1.60	0.162	1.36	0.238	1.33	0.198
3	1.35	2.00	0.216	1.90	0.321	1.90	0.299
4	0.825	2.48	0.332	2.10	0.378	2.09	0.368
5	0.5	2.97	0.404	2.77	0.481	2.77	0.478
6	0.3	3.17	0.420	2.90	0.466	2.90	0.462
7	0.18	3.82	0.484	2.66	0.468	2.66	0.467
8	0.11	5.02	0.632	2.40	0.547	2.40	0.546
9	0.067	5.98	0.690	2.17	0.497	2.17	0.496
10	0.0407	2.78	0.308	1.97	0.323	1.97	0.323
11	0.025	6.34	0.721	0.639	0.202	0.638	0.202
12	0.015	0.75	0.081	0.711	0.106	0.711	0.106
13	0.0091	1.13	0.121	1.10	0.163	1.10	0.163
14	0.0055	1.51	0.161	1.49	0.184	1.49	0.184
15	0.0021	1.37	0.0507	1.37	0.105	1.37	0.105
16	0.0005	1.37	0	(1.37)	0		

^a Parentheses indicate use of the same value as in Set a for criticality comparison. No ELMOE values were obtained for these groups.

than the transfer cross sections insofar as critical core mass is concerned. Therefore, the factor, 1.17, calculated for the aluminum-reflected assembly should be a reasonable indication of the error which would arise if direct YOM⁵ aluminum cross sections had been used.

EFFECT OF DIFFUSION THEORY AND CONSISTENT
B-1 ELMOE-EFFECTIVE CROSS SECTIONS ON
CRITICAL MASS CALCULATIONS OF ZPR-III
FAST CRITICAL ASSEMBLIES

The ELMOE code^{1,2} was often employed to obtain the effective group cross sections for transport and elastic transfer for several fast critical cores. The critical masses were then usually calculated with the DSN code³ in the S_4 approximation. For these studies the ELMOE averaging has generally been in the $P-1$ approximation. As the ELMOE program also has consistent $P-1$ and consistent $B-1$ options, it was of interest to calculate a few ZPR-III assemblies³ using effective cross sections obtained with the consistent $B-1$ option. Four assemblies (No. 14, with graphite diluent; No. 22, with U-238 diluent; No. 23, with aluminum diluent; and No. 32, with steel diluent) were studied.

The calculated ratios of critical volumes using the consistent $B-1$ averaged cross sections relative to the critical volumes using the simple $P-1$ averaged cross sections are 0.991, 0.993, 0.984, and 0.951, respectively. The ratios correspond to increased calculated reactivities of +0.2%, +0.1%, +0.4%, and +1.2% $\Delta k/k$, respectively. It may be noted that as ZPR-III calculations usually tend to be too reactive, use of consistent $B-1$ averaging (rather than simple $P-1$ averaging) tend to increase the reactivity even further.

REFERENCES

1. H. H. Hummel and A. L. Rago, *An Accurate Treatment of Resonance Scattering in Light Elements in Fast Reactors*, Proc., Seminar on Physics of Fast and Intermediate Reactors, IAEA, Vienna, Vol. I, 231 (1961).
2. A. L. Rago and H. H. Hummel, *ELMOE: An IBM-704 Program Treating Elastic Scattering Resonances in Fast Reactors*, ANL-6805 (1964).
3. *Reactor Physics Constants*, 2nd Edition, ANL-5800, 587 (1963).
4. *Reactor Development Program Progress Report*, ANL-6860 (1964).
5. S. Yiftah, D. Okrent and P. A. Moldauer, *Fast Reactor Cross Sections*, (Pergamon Press, New York, 1960).
6. B. Carlson, C. Lee and J. Worlton, *The DSN and TDC Neutron Transport Codes*, LAMS-2346 (1960).

III-7. Publication of Lecture Notes on Fast Reactor Physics Analysis

D. MENEGHETTI

The lecture series of a seminar course in fast reactor physics analysis presented by the author has been published as a laboratory report.¹ The primary purpose of the lectures was to teach the rudiments of fast reactor physics with emphasis on calculations. The subject matter was chosen as an introduction to fast reactor analysis for persons reasonably familiar with thermal reactor physics. It was the author's intent to present a practical course which would introduce sufficient subject matter to enable the student to sense pitfalls in blindly adhering to recipe calculations. Such calculations are tempting because of the ready availability of multigroup cross section sets and major reactor computing programs.

The subject matter includes discussions of fast reactor characteristics, breeding, multigroup methods, cross section definitions and evaluations, discrete ordinate transport methods, transport approximation, B_N method, asymptotic diffusion theory, equilibrium spectra, resonance effects, perturbation analysis, shape factor, lifetime, delayed-neutron fraction, reactivity-period relations, coupled systems, sodium void effect, and Doppler effect.

REFERENCES

1. D. Meneghetti, *Introductory Fast Reactor Physics Analysis*, ANL-6809 (1963).

III-8. Investigations of a 600-Liter Uranium Carbide Core (ZPR-VI Assembly No. 2)

G. K. RUSCH, E. R. BÖHME,* L. R. DATES, S. GRIFONI,† W. Y. KATO,
G. W. MAIN, H. H. MEISTER,* M. NOZAWA,‡ and R. L. STOVER

INTRODUCTION, COMPOSITION AND CRITICAL MASS

ZPR-VI Assembly No. 2¹ was a nominal 600-liter uranium carbide (UC) core used primarily for sodium versus void reactivity worth studies. The core was reflected both axially and radially with a 30-cm thick blanket of depleted uranium. Table III-8-I details the core and blanket compositions. The height of the bare core, neglecting the 1.6-mm stainless steel gap at the interface of the halves due to the drawer ends, was 91.4 cm. Figure III-8-1 shows an outline of the core and blanket cross section. This configuration contained 550.5 kg of U-235 and had an excess reactivity of 0.205%. Correcting for this excess reactivity by substituting depleted uranium for core materials at the radial boundary of the core resulted in an experimentally determined critical mass of 544.0 kg of U-235. § Using the above numbers for critical mass and core height, the critical diameter of the bare core was calculated to be 92.1 cm, and the critical volume to be 610 liters.

Figure III-8-2 shows a typical drawer loading. Each drawer is 61 cm long, the back 15.2 cm of the drawer being loaded with blanket material. The movable drawer loadings were mirror images of the stationary half drawer loadings.

Besides the sodium-void coefficient studies, central reactivity coefficients of various materials, fission ratios, Rossi- α measurements, and other miscellaneous measurements were of interest. These are discussed below.

CONTROL ROD CALIBRATIONS

The results obtained by using a dynamic-rod calibration technique³ were compared (Table III-8-II and Fig. III-8-3) with results obtained by conventional period and step function (rod drop) reactivity change measurements. In the dynamic-rod calibration technique the rod to be calibrated was continuously withdrawn from the initially critical reactor. The resulting flux decay was analyzed by the usual space-independent kinetic equations using calculated delayed neutron parameters ($\beta = 0.0073$ and $451 \text{ lh} = 1\% \Delta k/k$).

For all rod calibrations the neutron intensity was measured with a U-235 fission chamber operated as a

pulse chamber, a current pulse amplifier,⁴ a prescaler, and a multi-channel analyzer. Control rod position data were obtained from a photocell system wherein a light beam was modulated by a selsyn rod-position indicator.

The calibration curve found by the dynamic-rod technique exhibits oscillatory fluctuations with amplitudes increasing from $\pm 2 \text{ lh}$ at the end of the curve. These non-random variations result from a four-point smoothing procedure used in analyzing the count rate data.

Dynamic rod worth measurements taken at various power levels, rod speeds, and at various positions were consistent.

SPECTRAL INDICES

MEASUREMENT OF FISSION RATIOS

Fission ratios of several isotopes have been determined with a pair of absolute gas-flow fission chambers and also with a set of solid-state detectors. The measurements were made near the center of the core, first in the regular loading pattern with sodium-filled cans throughout the core region, then in a central voided region ($\sim 41 \text{ cm diam} \times 41 \text{ cm long}$) in which the sodium cans were replaced by empty cans.

The gas-flow counters (5 cm diam \times 2.5 cm long) were made of stainless steel, 0.3-mm wall thickness, and were similar to those described by F. Kirn.⁵ Each counter contained a known quantity of fissionable material electroplated with a superficial density of $\sim 100 \mu\text{g}/\text{cm}^2$ on a stainless steel backing plate. Two counters, one of which contained a U-235 coating, were placed in the center of the core so that each of them occupied a void volume, 2.5 cm deep by 5 cm square, in the front part of the central drawers. The pulse cables and gas supply tubes were lead through an axial duct, 2.5 cm \times 1.3 cm wide, located in the middle of the drawers; the loading pattern in the remaining part of these drawers was shifted by 1.6 mm with respect to the normal pattern.

The two solid-state detectors (1.3 cm diam and $\sim 100 \mu\text{g}/\text{cm}^2$ coating thickness) were centered between the two fuel columns of drawers S/M-2321,** about 10

* Kernreaktor, Karlsruhe, Germany.

† Comitato Nazionale Per L'Energia Nucleare, Italy.

‡ Japan Atomic Energy Research Institute.

§ This includes an extra column of enriched fuel—Rod No. 5 (Fig. III-8-1) to increase the worth.

** S/M means stationary and movable drawers; the first two digits of the number indicate the row number in the matrix, and the second two digits indicate the column number. Together they define a particular location in the matrix (see Fig. III-8-1).

TABLE III-8-I. ZPR-VI, ASSEMBLY NO. 2 CORE AND BLANKET COMPOSITIONS

	Core			Blanket ^c		
	Atom density, atom/cm ³ × 10 ²⁴	Average density, ^a g/cm ³	YOM volume ^b fraction	Atom density, atom/cm ³ × 10 ²⁴	Average density, g/cm ³	YOM volume fraction
U-235	0.002285	0.8915	0.04760	8.104 × 10 ⁻⁵	0.03162	0.001688
U-238	0.009853	3.982	0.2052	0.03993	15.777	0.8318
C	0.01290	0.2573	0.1540	—	—	—
Na	0.007910	0.3019	0.3595	—	—	—
Fe	0.01038	0.9621	0.1226	0.004223	0.3916	0.04986
				0.006782	0.6289	0.08008
Cr	0.002983	0.2575	0.03724	0.001214	0.1048	0.01516
				0.001950	0.1683	0.02435
Ni	0.001390	0.1355	0.01522	0.000566	0.0552	0.0062
				0.000909	0.0887	0.0100
SS 304	0.01475	1.355	0.17506	0.006003	0.552	0.07122
				0.00965	0.8865	0.1146

^a Densities were calculated from known weights and volumes.

^b The YOM volume fractions were obtained by dividing the actual (homogenized) atom densities by the corresponding atom densities used by Yiftah, Okrent and Moldauer.²

^c It is noted that two sets of values are given for the stainless steel content of the blanket. This is due to the fact that the inner part of the blanket was contained in stainless steel drawers while the outer portions of the blanket were inserted directly into the matrix tubes. For most calculations, the resulting difference is negligible.

cm radially outward from the center of the core. Ratios of atomic fission cross sections obtained in these experiments are listed in Table III-8-III. The values are corrected for fission contributions of isotopes other than the principal ones. The experimental errors are based on statistical counting accuracies which were better than 0.5%. The uncertainty in the amount of fissionable material deposited was less than 1% in cases where the coatings were prepared from solutions of gravimetrically known concentration. Errors from 1.5% to 4% were assumed where the amount was determined by its alpha activity on the basis of the known isotopic composition.

Except for the Pu-239/U-235 ratio, good agreement between the results of the fission chambers and solid-state detectors is found. This indicates that the spectral perturbations of both detector types are either small or nearly equal.

The comparison between solid-state detector and fission chamber data, however, does not reveal systematic errors in the sample masses since, for most isotopes, the same stock solutions were used to prepare the coatings for both detector types. A comparison of fission chamber data obtained with samples which were prepared from different stock solutions is given in Table III-8-III for the isotopes U-233 and U-238. Agreement within 2% or better indicates that the assumed uncertainties of sample masses are realistic.

FINE STRUCTURE OF U-235 AND U-238 FISSION RATES

The distribution of the U-235 and U-238 fission rates across the heterogeneous structure of a core drawer was

measured by irradiating a set of enriched and depleted uranium foils. Pairs of these foils (9.27 mm diam, 0.13 mm thick) were placed between the mockup plates of drawer S2325 or S2322 at a distance of 10 cm from the interface. Gamma activities above 412 keV were measured relative to enriched and depleted uranium foils which were irradiated during the same run between the sensitive areas of the U-235 and U-238 fission chambers, thus providing a calibration of foil activities in terms of absolute fission rates.

Foil traverses were measured in loading patterns, both with sodium-filled cans and with empty stainless steel cans. Results are shown in Figs. III-8-4 and III-8-5. In either case, there is a very smooth variation of the U-235 fission rate similar to the over-all macroscopic flux distribution, and a pronounced fine structure in the U-238 fission rate with maxima at the fuel columns.

With the sodium-filled cans, the resulting fine structure fission ratio, $\sigma_f^{28}/\sigma_f^{25}$, varies within +10% and -7% about the ratio of the volume-averaged fission rates, $\bar{\sigma}_f^{28}/\bar{\sigma}_f^{25} = 0.0358$.* The U-238/U-235 fission ratios found with the solid-state detectors are 3.9% lower than this value and agree closely with the value $\sigma_f^{28}/\sigma_f^{25} = 0.0344$ taken from the foil traverses at the middle of the drawer ($z = 2.8$ cm) where the solid-state detectors were located. The fission ratio $\sigma_f^{28}/\sigma_f^{25} = 0.0346$ measured with the gas-flow counters is 3.4% below the volume average, showing that the spectrum at the detector position inside the 5-cm cube void volume is slightly different from the volume-averaged spectrum.

* The volume averaged fission rates were determined by averaging the foil fission rate data (Figs. III-8-4 and III-8-5).

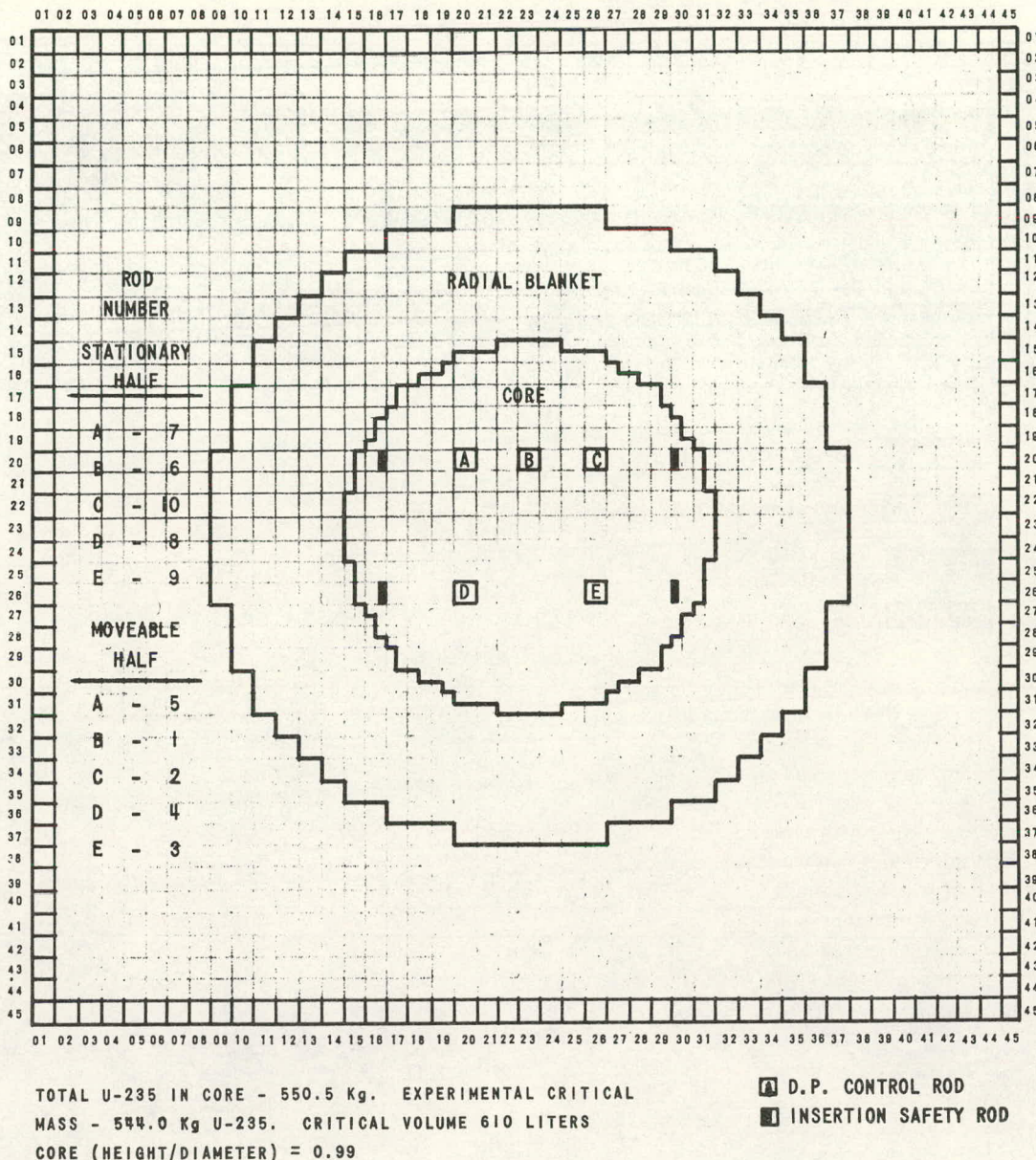


FIG. III-8-1. Outline of Core and Blanket Cross Section.

In the measurement with the empty cans, somewhat smaller fluctuations in the local U-238 fission rate were observed. The U-238/U-235 fission ratio measured with the fission chambers was 2.1% lower than the volume average $\bar{\sigma}_f^{28}/\bar{\sigma}_f^{25}$. Similar measurements were made in an unbunched fuel configuration containing four 0.8 mm fuel columns per drawer. This loading pattern was established in a central region of 3 x 5 drawers in each half. Figure III-8-6 shows a smaller variation ($\pm 5\%$) of the U-238 fission rate, while the fission ratio found with the flow counters was only 2% below the volume

average. Compared to the normal pattern, however, all fission ratios are smaller in this case since each drawer of the test region contained 17% less fuel.

The spectral softening at the fission chamber location inside the central 5-cm cube void volume, which was encountered in all three foil measurements, may be explained in the following way. Among the neutrons entering this voided cube, only those emerging from four sides represent the average neutron spectrum, while those coming from the two surfaces formed by the horizontally adjacent drawers are expected to have a

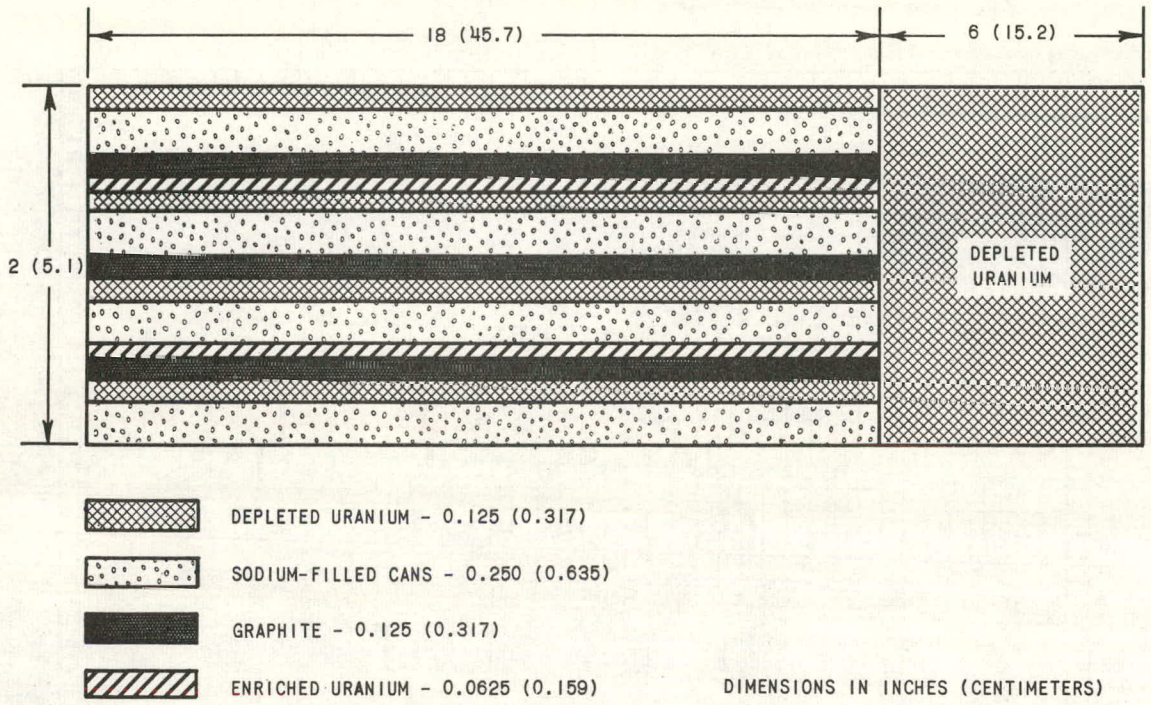


Fig. III-8-2. Stationary Half Core Drawer Loading.

TABLE III-8-II. TOTAL WORTHS OF SOME CONTROL RODS

Control Rod No.	No. of U-235 Columns	Period Measurements, Ih	Digital Method, Ih	Rod Drop, Ih
5	3	100.6 ± 0.8	99.5 ± 1.5	101.5 ± 3
8	2	67.5 ± 0.5	68 ± 1.0	

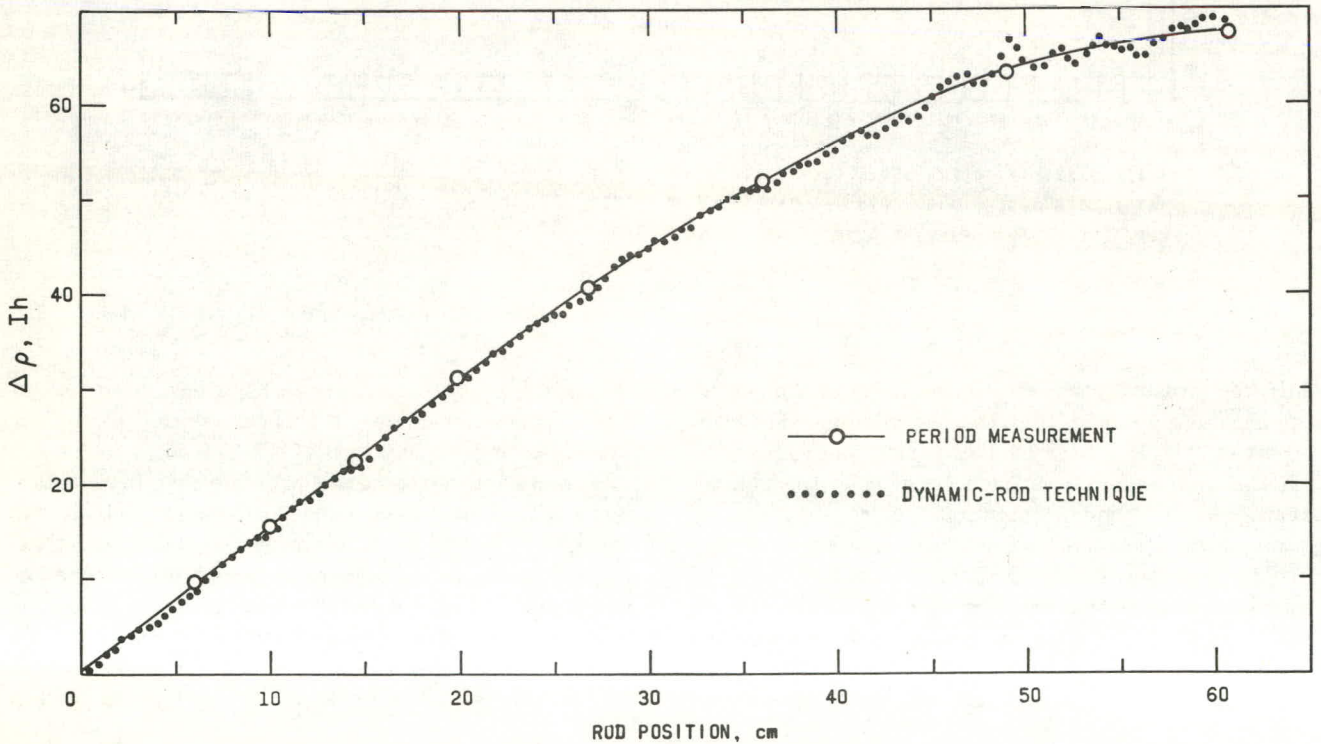


Fig. III-8-3. Calibration of Control Rod No. 8.

TABLE III-8-III. EXPERIMENTAL FISSION RATIOS

Isotope Ratio	Sodium-Filled Region		Void Region	
	Flow counter (σ_f/σ_f^{235})	Solid state counter (σ_f/σ_f^{235})	Flow counter (σ_f/σ_f^{235})	Solid state counter (σ_f/σ_f^{235})
U-233/U-235	1.520 ± 0.020	1.45 ± 0.04	1.526 ± 0.020	1.51 ± 0.04
U-234/U-235	1.522 ± 0.020			
U-236/U-235	0.225 ± 0.004	0.233 ± 0.007	0.250 ± 0.004	0.250 ± 0.007
U-238/U-235	0.074 ± 0.004		0.082 ± 0.004	0.087 ± 0.004
U-238/U-235	0.0346 ± 0.0005	0.0344 ± 0.0010	0.0376 ± 0.0005	0.0375 ± 0.0011
	0.0354 ± 0.0005			
Np-237/U-235	0.174 ^a	0.174 ± 0.006	0.188 ^a	0.187 ± 0.005
Pu-239/U-235	1.045 ± 0.020	1.09 ± 0.006	1.062 ± 0.020	1.12 ± 0.04
Pu-240/U-235	0.249 ± 0.005		0.268 ± 0.005	
Am-241/U-235	0.101 ^a		0.110 ^a	

^a No accurate isotopic analysis is yet available; data are based on an assumed 100% isotopic purity of the Np-237 and Am-241 samples.

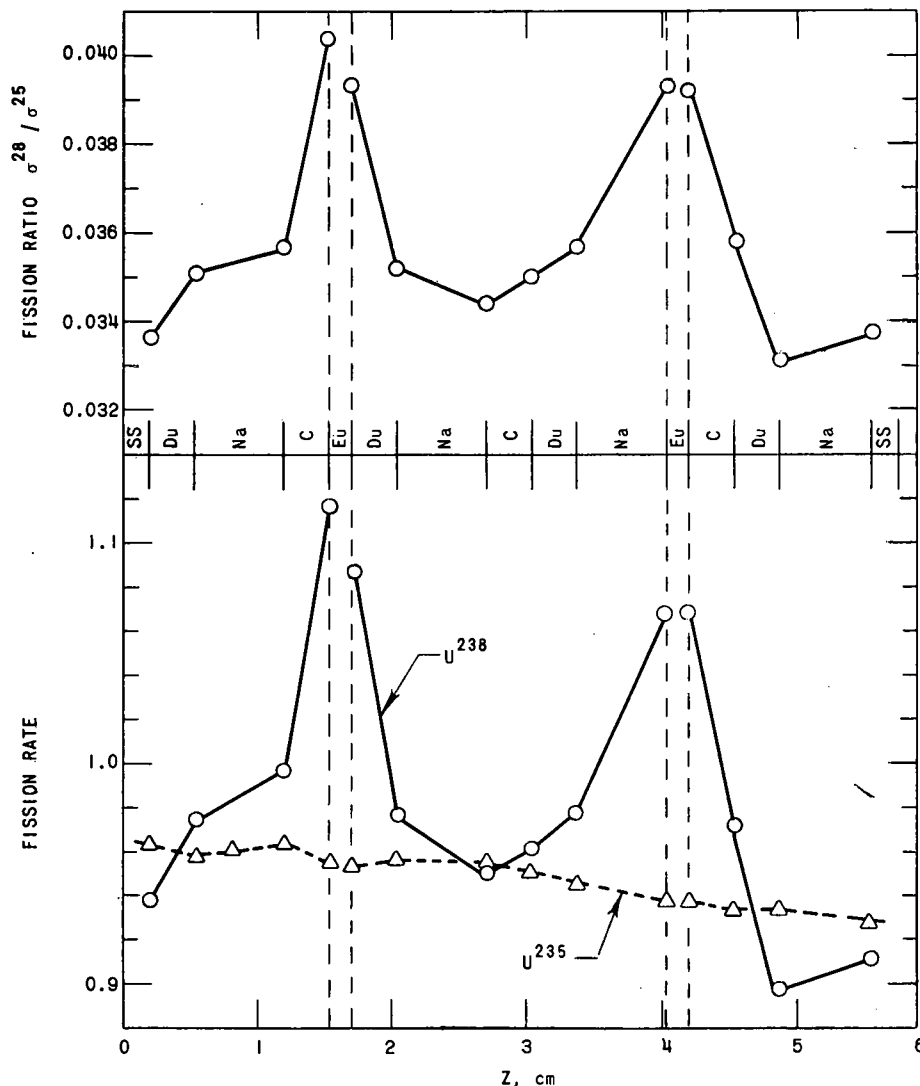


FIG. III-8-4. Relative Distribution of Fissions within Core Drawer with Na Filled SS Cans. (Central Core Region.)

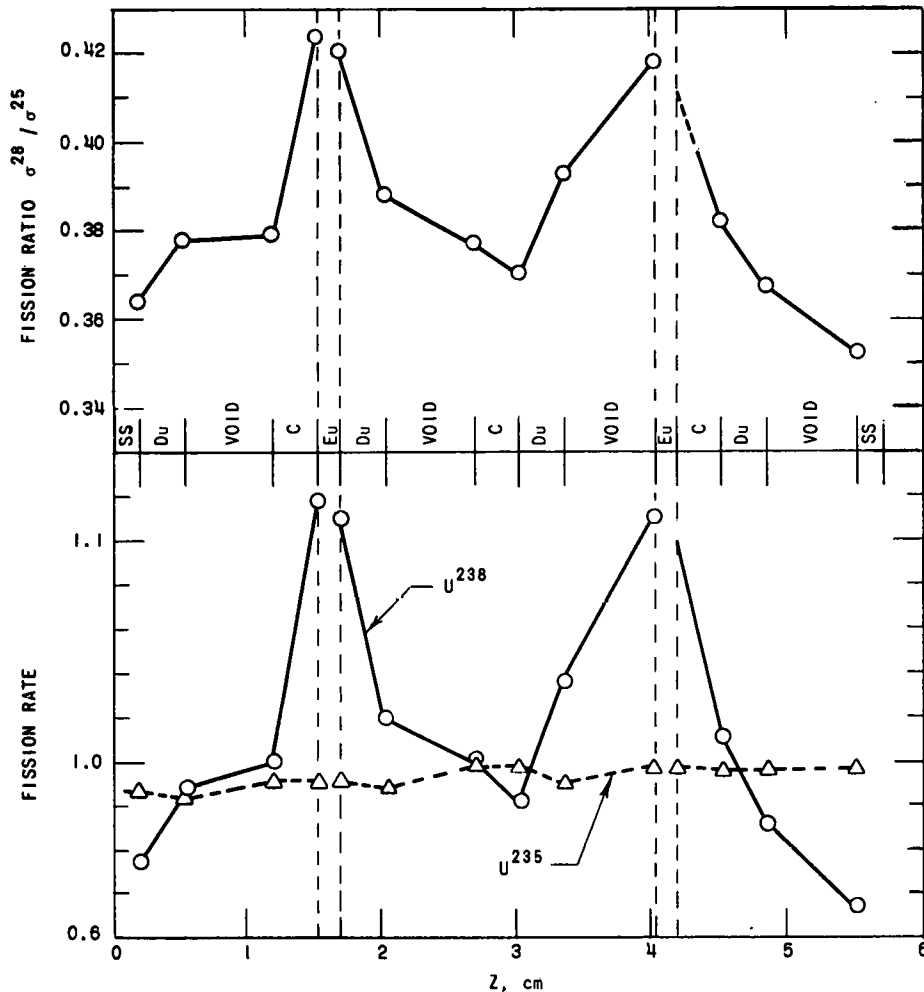


FIG. III-8-5. Relative Distribution of Fissions within Core Drawer with Empty SS (void) Cans. (Central Core Region.)

softer spectrum which is characterized by the lower local fission ratio at the wall of the matrix tube (see Fig. III-8-4 or Fig. III-8-5).

In addition, a spectral softening is expected to occur by inelastic scattering in the surrounding 1.0-mm thick stainless steel walls of the central matrix tube, which represents an excessive amount of stainless steel with respect to the average composition of a drawer. The spectral perturbation by the fission counters themselves adds to this effect, but is probably much smaller.

FOIL IRRADIATION FOR RADIOCHEMICAL ANALYSIS

A pair of enriched and depleted uranium foils was closely attached to the sensitive area of the flow counters and irradiated for a radiochemical analysis of U-235 and U-238 fissions, and U-238 captures (see Table III-8-IV). The radiochemical U-235 fission rates found by the Mo-99 method (see Paper No. IV-23) agree within 3% of those measured directly with the fission chambers during the same run. The radiochemical

fission ratios $\sigma_f^{28}/\sigma_f^{25}$ agree with the fission chamber data within 1%.

COMPARISON OF SPECTRAL INDICES WITH CALCULATED VALUES

For a comparison with calculated values, the experimental data are corrected to represent the fission ratios in the volume-averaged heterogeneous spectrum, which is expected to resemble closely the spectrum in a homogeneous assembly of the same material composition. To this end, the fission ratio of material "x" relative to U-235 is multiplied by the correction factor $f_x = [(\sigma_f^x/\sigma_f^{25})/(\sigma_f^x/\sigma_f^{25})_{\text{Detector}}]$, which is a monotonic function of the threshold energy and is known for the two extreme cases: the U-238/U-235 fission ratio from the foil traverses ($f_{28} = 1.034$ for the reference core, $f_{28} = 1.021$ with the central region voided), and the fission ratio of two non-threshold isotopes where $f_x \approx 1$. Correction factors for the other threshold substances were estimated by interpolation (Table III-8-V).

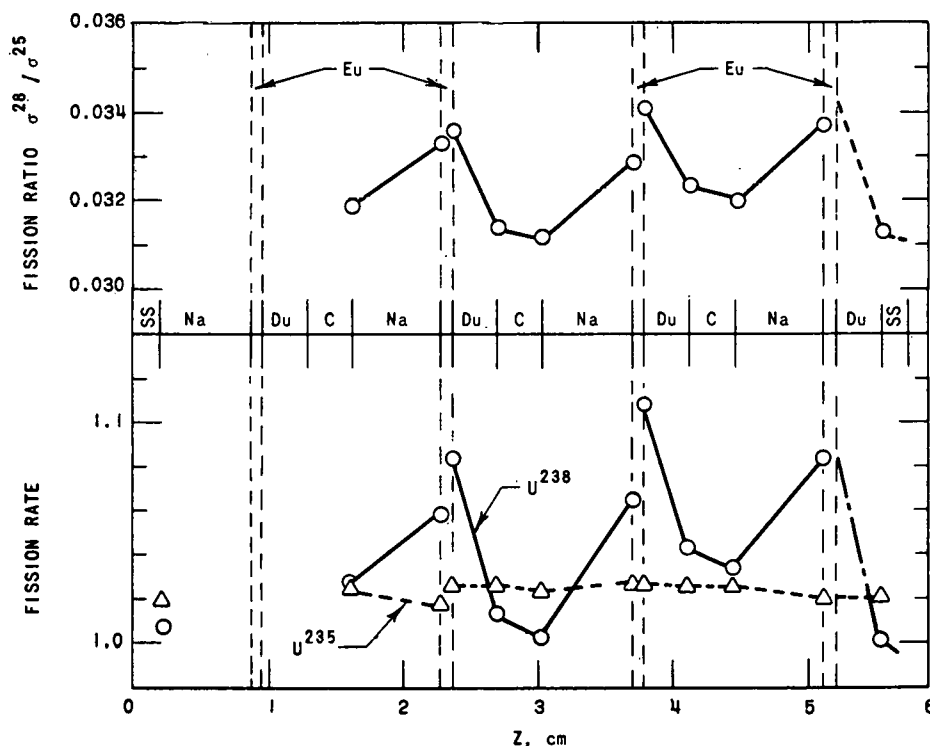


FIG. III-8-6. Relative Distribution of Fissions within Core Drawer with Four Fuel Columns and Na Filled SS Cans. (Central Core Region.)

The corrected experimental fission ratios are compared in Table III-8-V with calculated values. These were derived using 16-group fission cross sections (ANL set 635) and from the neutron spectra in the center of the core which were obtained by 16-group diffusion theory calculations in spherical geometry (Code RE 122). For the isotopes Np-237 and Am-241, 16-group fission cross sections were derived from the cross section curves in BNL-325.

For all threshold detectors, fission ratios relative to U-235 are found to be considerably lower than those derived from the calculated spectra. Deviations range from 6% for U-238 up to about 12% for U-234, U-236 and Pu-240, while deviations as high as 30% are found for Np-237 and Am-241. In the case of Np-237 and Am-241, however, there are considerable uncertainties concerning the attributed sample weights which have been determined by alpha counting on the basis of an uncertain isotopic composition.

The observed non-threshold fission ratios (U-233/U-235 and Pu-239/U-235) are only slightly smaller than the calculated values, with the exception of the Pu-239 fission chamber data which deviate by 5% from those found with the solid state detectors.

In general, the experimental fission ratios indicate that the actual spectrum is considerably softer than the calculated spectrum and that this shift to lower energies

TABLE III-8-IV. RADIOCHEMICAL FISSION AND CAPTURE RATES

	Sodium-Filled Region	Void Region
U-235 fission rate (fissions/min-g U-235)		
Radiochemical	1.279×10^7	1.109×10^7
Fission chamber	1.238×10^7	1.085×10^7
$\sigma_f^{238}/\sigma_f^{235}$		
Radiochemical	0.0345	0.0378
Fission chamber	0.0346	0.0376
$\sigma_c^{238}/\sigma_f^{235}$		
Radiochemical	0.106	0.0991

is more pronounced in the energy region near the U-234 threshold than at higher energies.

The radiochemical capture-to-fission ratios were found to be 20% lower than calculated. If the experimental data are correct, it would imply that either the observed spectrum is considerably harder than the calculated one, in contradiction to all the fission ratio measurements, or that the 16-group capture cross section of U-238 is greatly in error. Both possibilities appear to be very unlikely and it is more conceivable that some calibration error occurred in the radiochemical technique.

A comparison of the spectral indices measured in both

TABLE III-8-V. EXPERIMENTAL FISSION AND FISSION-TO-CAPTURE RATIOS (CORRECTED FOR VOLUME-AVERAGED SPECTRUM) IN COMPARISON WITH CALCULATED VALUES

Isotope Ratio	Method ^a	Sodium-Filled Region			Void Region			Ratio Void/Sodium	
		f_z	Experimental, σ_f/σ_f^{25}	Calc.	f_z	Experimental, σ_f/σ_f^{25}	Calc.	Experimental	Calc.
U ²³³ /U ²³⁵	F	1.00	1.520 ± 0.025	1.5317	1.00	1.526 ± 0.025	1.541	1.004 ± 0.010	1.006
	S	1.00	1.45 ± 0.04		1.00	1.51 ± 0.04		1.041 ± 0.010	
U ²³⁴ /U ²³⁵	F	1.015	0.228 ± 0.005	0.2665	1.01	0.252 ± 0.005	0.2930	1.105 ± 0.010	1.100
	S	1.015	0.236 ± 0.007		1.01	0.252 ± 0.007		1.068 ± 0.11	
U ²³⁶ /U ²³⁵	F	1.025	0.076 ± 0.004	0.0857	1.015	0.083 ± 0.004	0.0934	1.092 ± 0.015	1.090
	S	1.025	—		1.015	0.088 ± 0.004		—	
U ²³⁸ /U ²³⁵	F	1.034	0.0358 ± 0.0005	0.0381	1.021	0.0384 ± 0.0005	0.0409	1.073 ± 0.010	1.079
	S	1.039	0.0358 ± 0.0010		1.024	0.0384 ± 0.0011		1.073 ± 0.015	
Np ²³⁷ /U ²³⁵	F	1.015	0.177	0.2500	1.01	0.190	0.2754	1.073 ± 0.015	1.101
	S	1.015	0.177 ± 0.006		1.01	0.189 ± 0.005		1.068 ± 0.011	
Pu ²³⁹ /U ²³⁵	F	1.00	1.045 ± 0.020	1.1130	1.00	1.062 ± 0.020	1.139	1.016 ± 0.010	1.023
	S	1.00	1.09 ± 0.04		1.00	1.12 ± 0.04		1.027 ± 0.010	
Pu ²⁴⁰ /U ²³⁵	F	1.02	0.254 ± 0.005	0.2730	1.012	0.271 ± 0.005	0.3006	1.067 ± 0.010	1.101
	F	1.025	0.104	0.1505	1.015	0.122	0.1644	1.077 ± 0.015	1.092
			$\sigma_c^{238}/\sigma_f^{25}$			$\sigma_c^{238}/\sigma_f^{25}$			
U ²³⁸ /U ²³⁵	R	1.00	0.106	0.1281	1.00	0.0991	0.1249	0.935	0.9750

^a F = Fission chamber.

S = Solid-state detector.

R = Radiochemical analysis.

core configurations (sodium and void) shows that removing the sodium from the central region of the core causes a hardening of the spectrum as shown by a measurable increase of all fission ratios and a decrease of the U-238 capture to U-235 fission ratio. The observed fractional changes of the fission ratios (which are not affected by uncertainties of sample masses) are in good agreement with the calculated values.

ROSSI-ALPHA MEASUREMENTS

The prompt neutron decay constant α near delayed critical (-7.6 lh) has been determined by the Rossi- α technique. Two fission chambers were used: one of them (located in the central drawer S2323) was used to start the timing cycle, while the pulses of the other chamber (at S2314) were recorded by the time analyzer (channel width 1.5×10^{-6} sec). From the measured distribution of chain-related counts,

$$\alpha = (3.44 \pm 0.12) \times 10^4 \text{ sec}^{-1}$$

was obtained. Measurements with only one fission chamber located at S2323 gave the same result within the experimental error

$$\alpha = (3.52 \pm 0.15) \times 10^4 \text{ sec}^{-1}$$

From the average of both values, the decay constant at delayed critical was found to be

$$\alpha_c = \beta_{eff}/\ell = (3.48 \pm 0.10) \times 10^4 \text{ sec}^{-1}$$

Hence, the prompt-neutron lifetime

$$\ell = (21.4 \pm 0.6) \times 10^{-8} \text{ sec}$$

is obtained on the basis of the calculated delayed-neutron fraction $\beta_{eff} = 0.0073$.

GAP WORTH MEASUREMENTS

Gap worth measurements were performed on Assembly No. 2 so that corrections could be applied to experimental data. Measurements were performed both with air and type 304 stainless steel in the gap, the latter being of interest since the gap is in part attributable to the stainless steel drawer ends.

The air gap measurements were made by bringing the table halves to a preselected separation and establishing criticality. The change in reactivity necessary to achieve criticality with the gap was determined by the positions of calibrated control rods. The table separation is measured with a precision of ± 0.02 mm relative to an arbitrary zero determined by the minimum possible separation of the reactor halves. True zero of the core is different by at least the thickness of the drawer ends, approximately 1.6 mm.

The stainless steel gap worth curve was obtained by placing sheets of stainless steel of known thickness across the entire face of the stationary half of the reactor and driving the movable half firmly against it. Criticality was achieved with calibrated control rods resulting in

data for the gap curve. Figure III-8-7 is a plot of the data thus obtained.

TYPE 304 STAINLESS STEEL—WORTH MEASUREMENTS

The worth of type 304 stainless steel was measured as a function of radial and axial position within the core of Assembly No. 2. The measured values are compared with calculated values.

A set of four radial positions was selected for investigation. At each radial position the steel worth was determined at three axial positions. Figure III-8-8 schematically shows the positions involved. The resulting experimental data are shown on Fig. III-8-9. Figure III-8-10 displays the measured worths, as a function of radial position at the axial center of the core versus calculated worths as a function of radius in a spherical core. The perturbation calculations were made using ANL code 1155/RE 254 and ANL cross section set 199. Spherical shell calculations, in which the density of stainless steel between two spherical radii was varied, were made using ANL diffusion theory code RE 122 and cross section set 635.

SODIUM COEFFICIENT MEASUREMENTS

These experiments are part of a program devoted to an understanding of the sodium versus void coefficient behavior in fast reactors. The experiments consisted of replacing all of the sodium-filled stainless steel cans with empty cans in various regions of the core and observing the change in reactivity. The cans were arranged in the drawers in such a way that modification occurred outside of the region where the sodium void effect was being measured. Empty and full cans of the same size and weight were used in corresponding positions.

Experimental errors as large as ± 0.5 Ih are associated primarily with uncertainties in table and rod positions when relatively small numbers of drawers are handled. When large numbers of drawers (~ 100) are handled, the uncertainties increase to ± 1 Ih.

The experiments are grouped as follows into four sets according to the size and shape of sodium voided regions:

1. three cylindrical central regions ($L \simeq D$)
2. three cylindrical regions ($0.5 \leq L/D \leq 3$)
3. twelve cylindrical rings
4. central regions with different core diluents (Nb,S)

Cylindrical Central Regions

The sodium void effect was measured for the regions and corresponding cross sections shown in Fig. III-8-11 (A),(B),(C). The shapes were as close as possible to cylinders with $L \simeq D$.

Comparisons of the experimental data in cylindrical

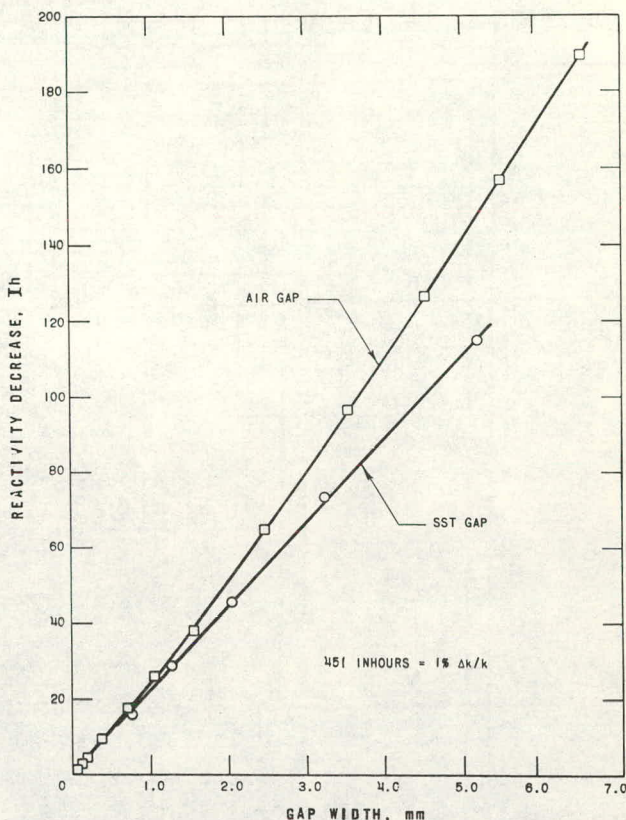


FIG. III-8-7. Variation in Reactivity with Size of Gap.

geometry to the calculated results in spherical geometry require knowledge of a shape factor for the voided region. In this work the same shape factor was used for the voided region as was calculated for the entire core. The cross section sets used in the calculations were the ANL cross section set 635^[6] (which is a modification of the YOM cross section set²) and the ANL cross section set 199. The latter is an 18-group set which was prepared at Argonne.^{7,8}

The results of the experiments, together with the calculated results, are presented in Table III-8-VI. It may be seen that set 199, which includes self shielding, predicts the experimental results much better than set 635 (see for example Ref. 9).

Cylindrical Regions ($0.5 < L/D < 3$)

All of these regions were done in only one half of the reactor and were therefore asymmetrical. A study of a symmetric void region relative to an asymmetric void region showed that the effect of asymmetry was less than the experimental error. Therefore, it was assumed that the measurements in an asymmetric Na region can be used to predict the symmetric Na void coefficient without introducing any significant errors. The cylindrical regions are shown in Fig. III-8-11

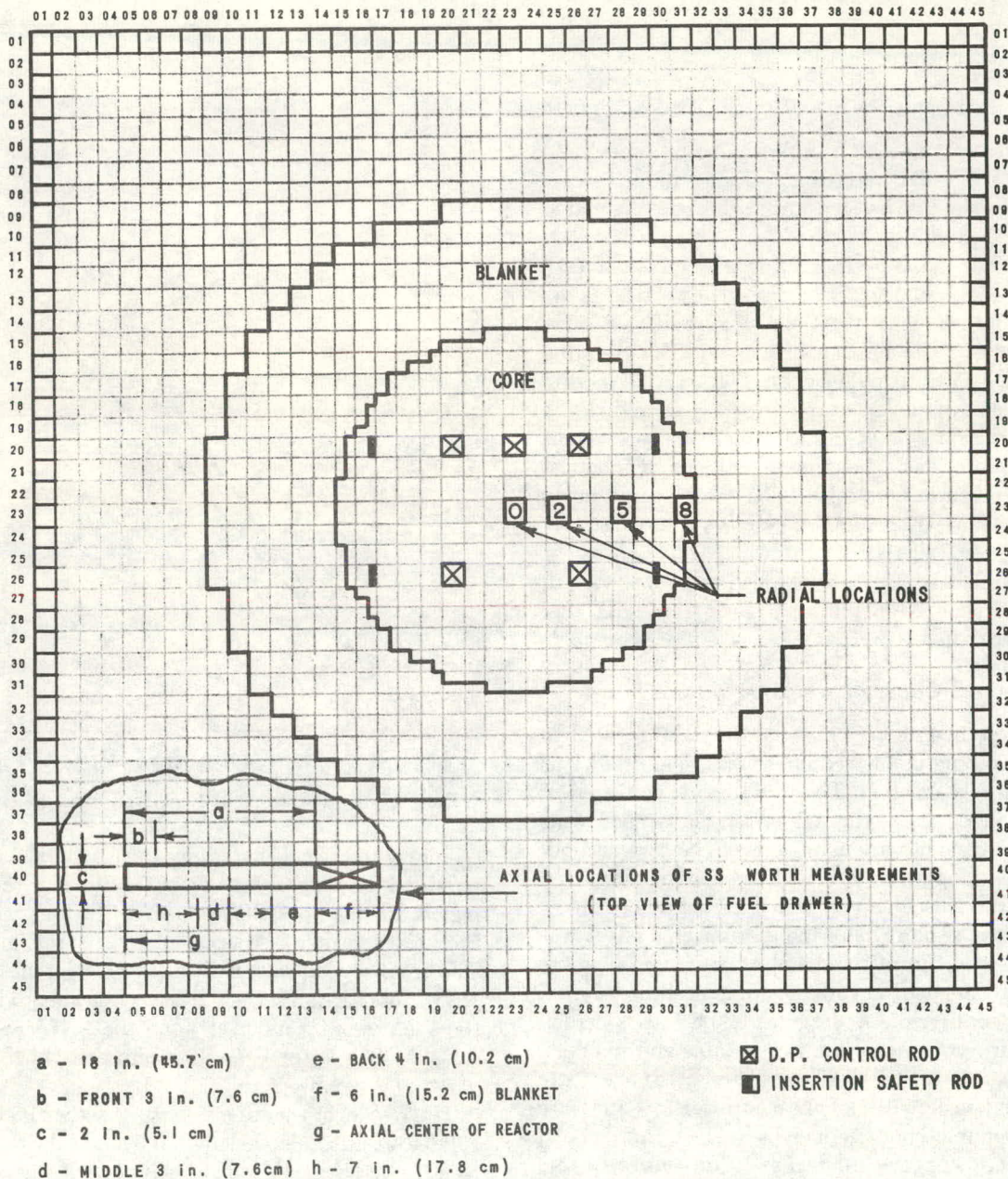


FIG. III-8-8. Location of SS Worth Measurements in Core.

(D),(E),(F). The experimental results for these regions are presented in Table III-8-VII.

Cylindrical Rings

This set of experiments was done to “map” the sodium void coefficient throughout the core. Four ring configurations of various diameters were formed, one at a time, at each of three axial positions. The axial length of each voided region was in every case 10.2 cm; the geometric configurations of the regions are shown in Fig. III-8-11 (G),(H),(I),(J). Experiments involving

the configurations shown in Fig. III-8-11 (H),(J) were performed with half rings after ascertaining that the error involved in extrapolating the results to complete rings was less than the experimental uncertainties associated with a measurement.

The experimental results obtained are compared with calculated values in Table III-8-VIII. Calculations for this set of experiments were performed with a one-dimensional code (RE-122) in slab and cylindrical geometries. Cross section set 199 was used. Only the sum of the values measured for the individual rings at each

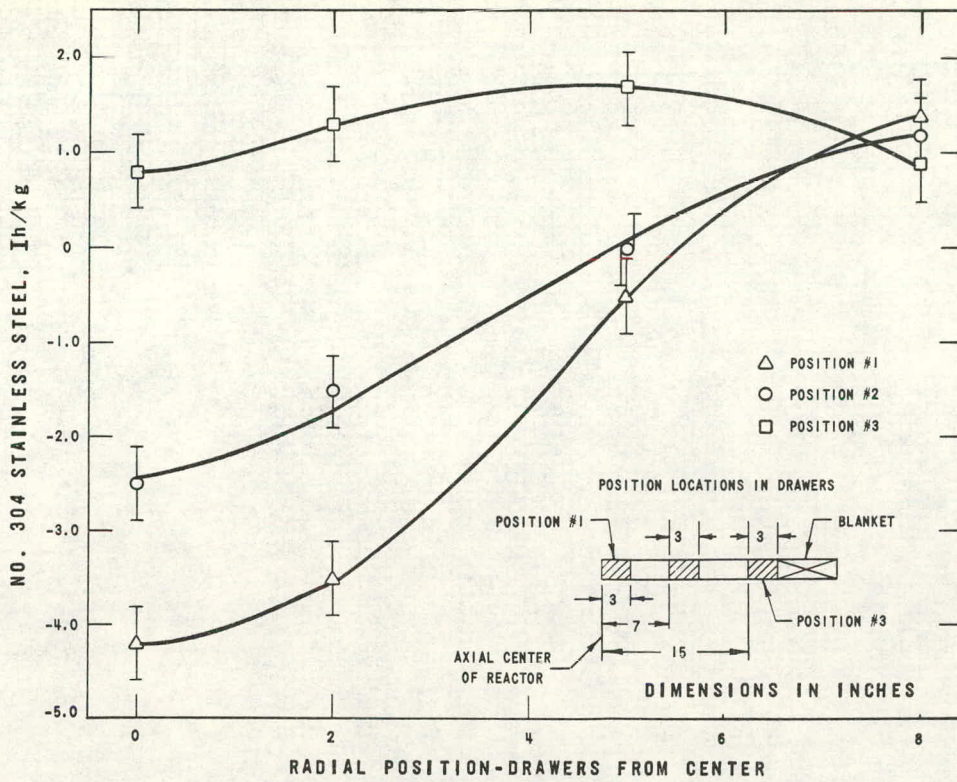


FIG. III-8-9. Radial Worth of Type 304 Stainless Steel.

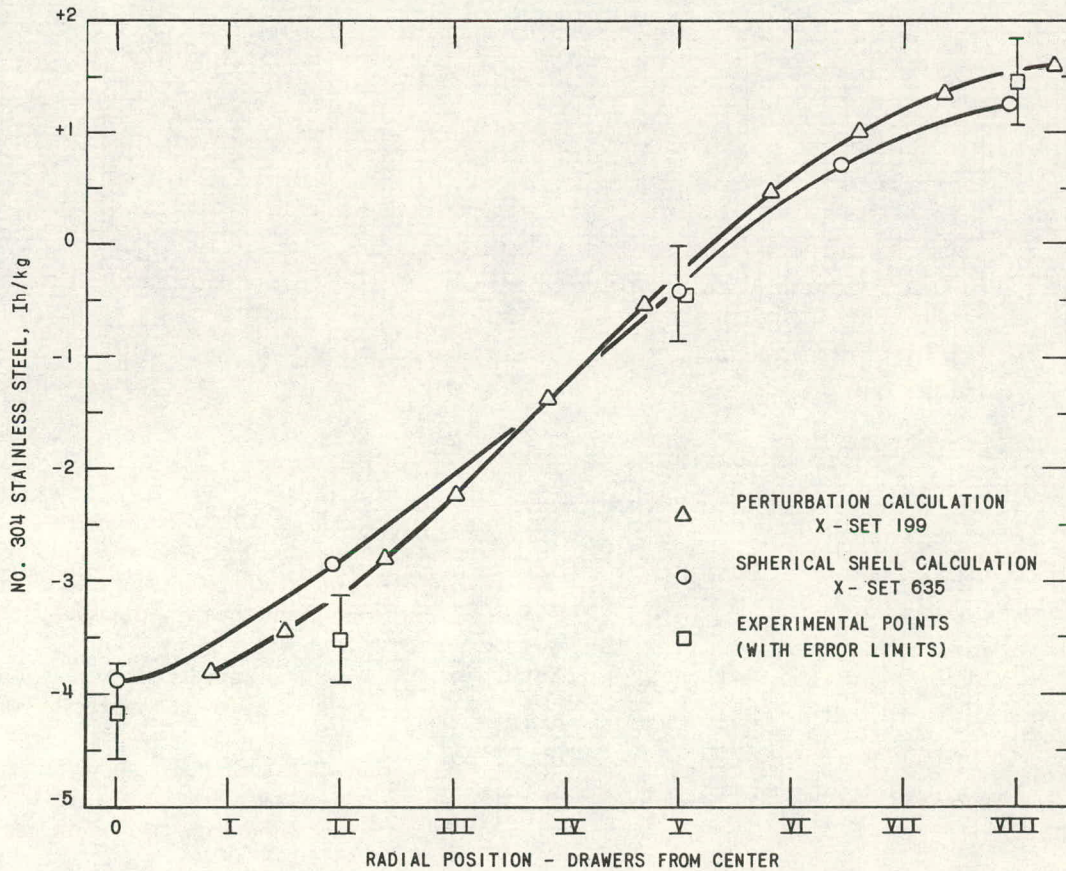


FIG. III-8-10. Comparison of Calculated and Measured SS Worths as Function of Radius. (Axial Center of Core.)

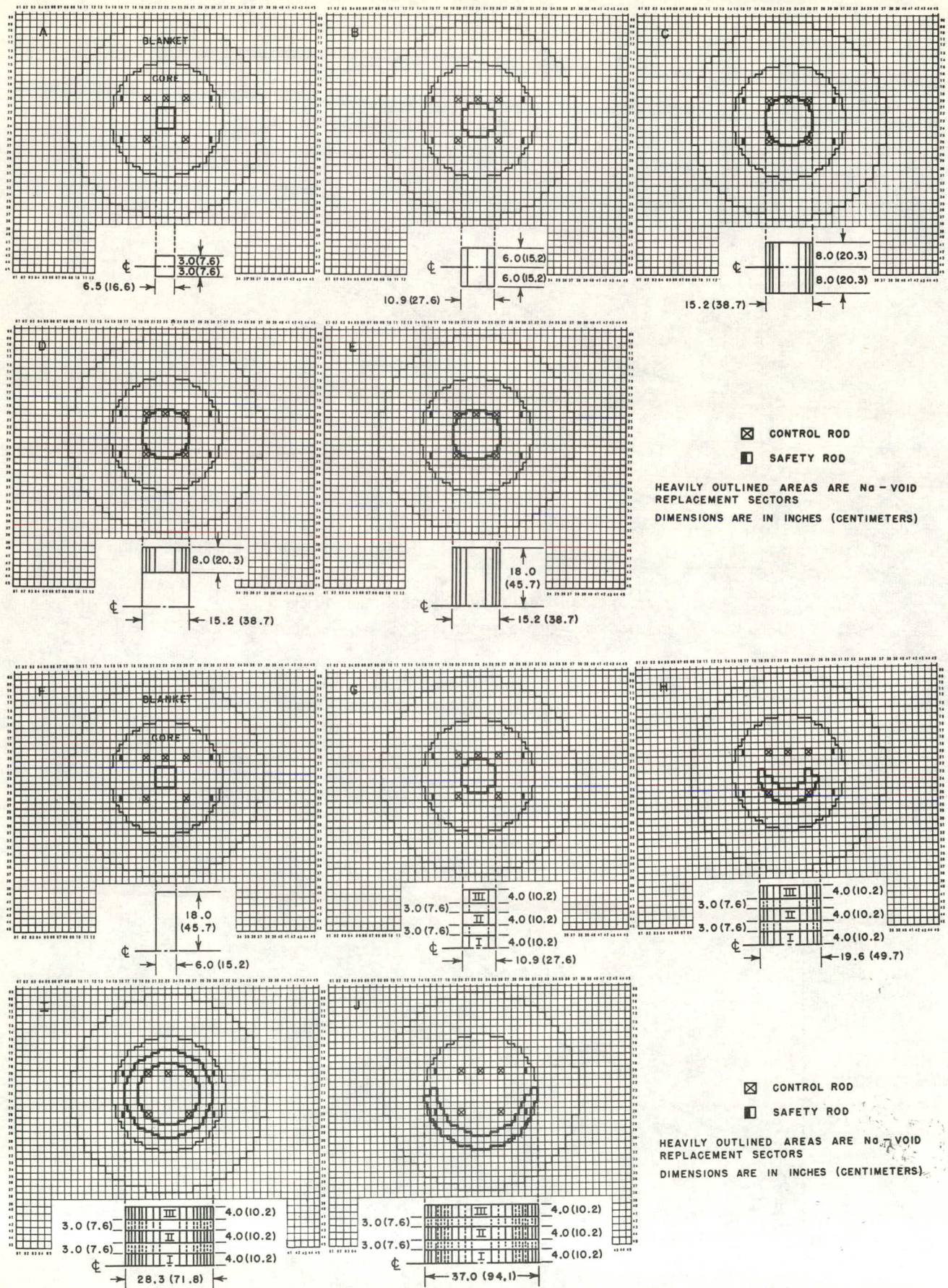


FIG. III-8-11. Sodium Versus Void Experimental Regions.

TABLE III-8-VI. EXPERIMENTAL RESULTS AND ANALYTICAL PREDICTIONS FOR CENTRAL REGIONS

Region ^a	Measured Effect, Ih	Experimental Sodium Coefficient, Ih/kg of Na	Calculated Sodium Coefficient, Set 199, Ih/kg	Calculated Sodium Coefficient, Set 635, Ih/kg
A	-2.0 ± 0.5	-1.6	-1.47	+0.32
B	-11.8 ± 0.5	-2.07	-2.09	-0.44
C	-45.0 ± 1.0	-2.99	-2.80	-1.30

^a Regions refer to core volumes shown in Fig. III-8-II.

TABLE III-8-VII. EXPERIMENTAL RESULTS FOR CYLINDRICAL REGIONS

Region ^a	Measured Effect, Ih	Experimental Sodium Coefficient, Ih/kg
F	17.0 ± 2	-4.5
E	-84.3 ± 1	-4.89
D	-47.7 ± 1	-6.34

^a Regions refer to core volumes shown in Fig. III-8-II.

TABLE III-8-VIII. SUMMARY OF THE CYLINDRICAL RING MEASUREMENTS AND CALCULATIONS

Axial Position (see Fig. III-8-11)	Radial Configuration (see Fig. III-8-11)				Experimental Results for Whole Slab	Calculated Results for Slab	Discrepancy
	G	H	I	J			
	(Negative inhours)						
III	14.75	22.54	30.97	29.25 = 97.5	74.8	+13%	
	8.71 ^a	14.73 ^a	24.00 ^a	27.31 ^a = 74.8 ^a	63.0 ^a	+19%	
II	7.92	17.54	33.13	45.82 = 104.4	86.4	+21%	
	3.78 ^a	13.00 ^a	26.11 ^a	42.71 ^a = 85.6 ^a	64.0 ^a	+34%	
I	3.70	18.29	35.77	62.64 = 120.4	83.4	+44%	
Experimental results for cylindrical shells	38.9	86.1	150.0	207.7	482.7 ^b	371.6 ^c	+30%
Calculated results for cylindrical shells	34.6	82.2	132.8	182.0	431.6 ^d		
Discrepancy	+12%	+5%	+13%	+14%	+12%		

^a Extrapolated values for the zones between the rings.

^b Experimental value for half core.

^c Calculated value for half core in slab geometry.

^d Calculated value for half core in cylindrical geometry.

axial position or the sum of the values measured at the individual axial positions (plus estimated values for the two intermediate axial positions) for each radial configuration can be compared to calculated values because of the limitations imposed by the one-dimensional code.

The agreement between experimental values and calculated values is not as good as was obtained for the first set of experiments when the calculations were performed in spherical geometry. This is probably due to the difficulty in evaluating the correct leakage terms for use in the slab and cylindrical calculations.

The experimental values, plus estimated values for the axial positions where no measurements were taken, are summed over the entire core and compared with calculated (code RE 122) reactivity changes when the entire core is voided of sodium. The results are shown in Table III-8-IX.

In addition, perturbation calculations in spherical geometry, from a 50% voided core (in order to give an average worth of sodium from full to void), were done with cross section set 199. The results of these calculations are presented in Figs. III-8-12 and III-8-13, together with the experimental sodium coefficients from the ring measurements, as functions of height and sodium respectively. The experimental results are shown in these figures by the horizontal lines. The horizontal line in each case represents an average coefficient over the region spanned by the line in the figure. The solid curves were drawn through the experimental points. The detailed shapes of these curves were derived from the results of perturbation calculations. These perturbation calculations, as well as k_{eff} calculations performed

TABLE III-8-IX. EFFECT OF VOIDING THE WHOLE CORE, $\Delta k/k\%$

Experimental	-2.14	sum of all rings
Calculated	sphere	-2.12 all core void
		-2.00 sum of single spherical shell
	slab	-1.76 all core void
		-1.65 sum of single slabs
cylinder	-1.92 sum of single cylindrical shell	

in spherical geometry, which are not reported here, show that cross section set 199 does predict reasonably well the magnitude of the sodium coefficient in the

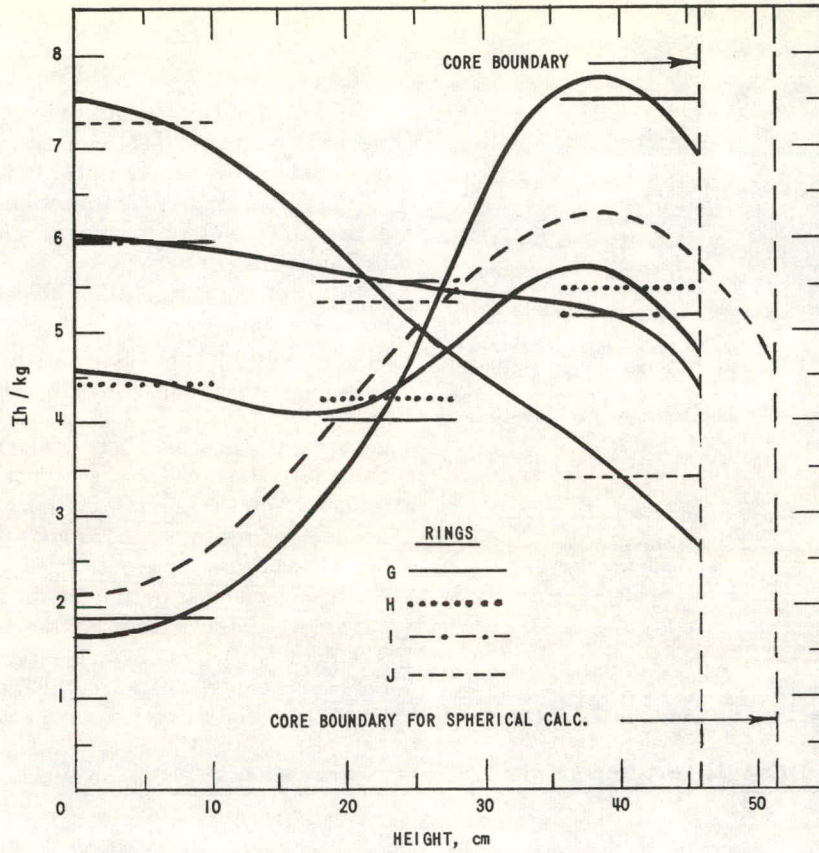


FIG. III-8-12. Na \rightarrow Void Reactivity Coefficients.

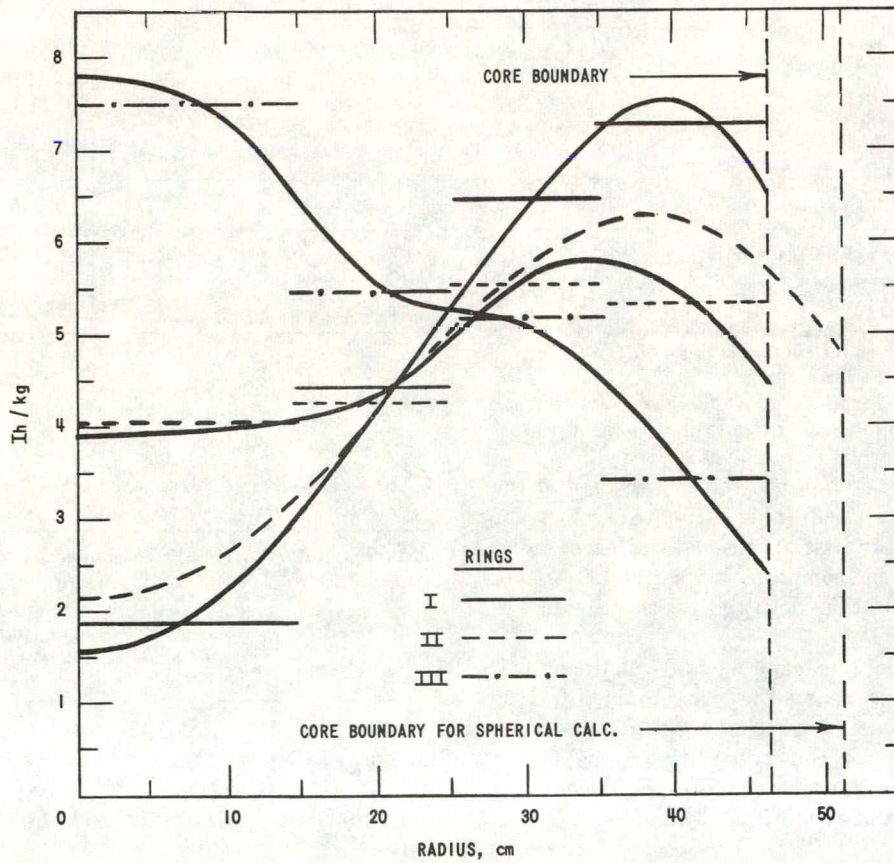


FIG. III-8-13. Na \rightarrow Void Reactivity Coefficients.

center of the reactor and also in the outer regions of the core. However, the increase of the coefficient in going outward from the center of the core is underestimated. It is difficult to rigorously compare the calculated and experimental results because the geometries utilized to obtain them are different. It appears that two dimensional calculations are necessary to obtain higher resolution of the agreement between experimental and calculated results.

Central Regions with Different Diluents

These experiments were performed to determine the effect on the sodium coefficient due to modifying the core composition. Two materials were studied: niobium and sulphur. They would possibly replace the stainless steel for cladding and form US instead of UC for fuel in a fast reactor core. The limited availability of the two materials, however, was such that only a small region could be modified. This region had the same cross section as region (B) in Fig. III-8-11 but was 22.9 cm long in each half. The region in which the void was measured, however, was identical to region (B) in Fig. III-8-11 so that this can be considered as reference.

To compare the niobium with the stainless steel, it was necessary to replace some of the other materials present in the core with these two materials. It was decided to replace the four columns of depleted uranium first with niobium and then with stainless steel, noting the difference in the sodium void effect.

In the case of sulphur, two 6.35 mm thick columns were introduced in place of two 3.18 mm thick columns

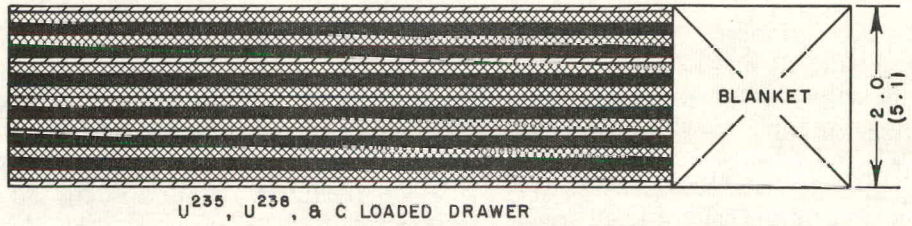
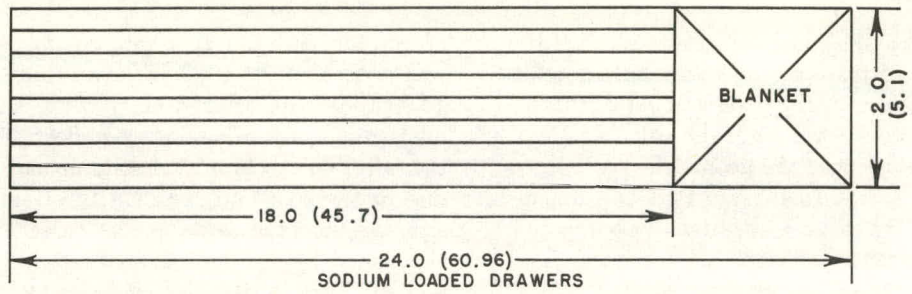
of graphite and one 6.35 mm column of sodium. This was equivalent to replacing two-thirds of the carbon (0.0086×10^{24} nuclei/cm³) with sulphur, (0.0070 nuclei/cm³), resulting in a net decrease of sodium in the core. The columns of sodium had to be removed due to the small atomic density of sulphur. The core size was not the same in the three experiments distinguished by niobium diluent, stainless steel diluent, and sulphur diluent. The core size had to be increased in the case of niobium with respect to the reference core because of the greater negative worth of niobium compared with depleted uranium. The contrary is true for the stainless steel. In the case of sulphur, the core size had to be increased relative to the original core because of the greater absorption of sulphur compared with the replaced materials. The results of these experiments, together with other pertinent data and with the results of calculations, are shown in Table III-8-X. These calculations were done by the same method used for the central regions. It may be seen that the cross-section set 199 predicts the correct change in the sodium coefficient in changing from stainless steel diluent to niobium diluent, while the cross section set 201 (which is basically the Hansen and Roach¹⁰ cross section set) does not give the correct answer for sulphur even if compared with the reference experiment. It may be noted that if the depleted uranium remained in place and if niobium were to be substituted for the stainless steel in the matrix, the drawers and the sodium cans, the sodium coefficient would be about +5.8 Ih/kg pro-

TABLE III-8-X. SODIUM VOID EFFECT WITH DIFFERENT CORE DILUENTS

	Volume Fractions, % and Nuclei/cm ³ × 10 ²⁴							Core ^b Radius and Excess Reactivity with Sodium, Ih/kg	Measured Effect, Ih	Experimental Sodium Coefficient, Ih/kg	Calculated Sodium Coefficient Set 199, Ih/kg	Calculated Sodium Coefficient Set 201, Ih/kg
	U-235	U-238	C	Na	SS	Nb	S					
Reference core	4.8	21	15	36	17	—	—	46.3	—11.8	—2.07	—2.09	0.64
Stainless steel diluent	0.002285	0.009853	0.0129	0.00791	0.01475	—	—	40	—72.3	—12.7	—9.5	—
	4.7	0.3	15	36	38	—	—	44.9				
Niobium diluent	0.002265	0.000166	0.0129	0.00791	0.03221	—	—	51 ^a	—17.0	—2.99	—0.15	—
	4.7	0.3	15	36	17	21	—	47.0				
Sulphur diluent	0.002265	0.000166	0.0129	0.00791	0.01475	0.01123	—	45	—5.3	—1.25	—	—1.09
	4.8	21	5	27	16	—	20	46.7				
	0.002285	0.009853	0.00430	0.00593	0.01348	—	0.00696	43				

^a Four additional drawers had to be added and their worth measured (17.5 Ih/drawer) when the void was made.

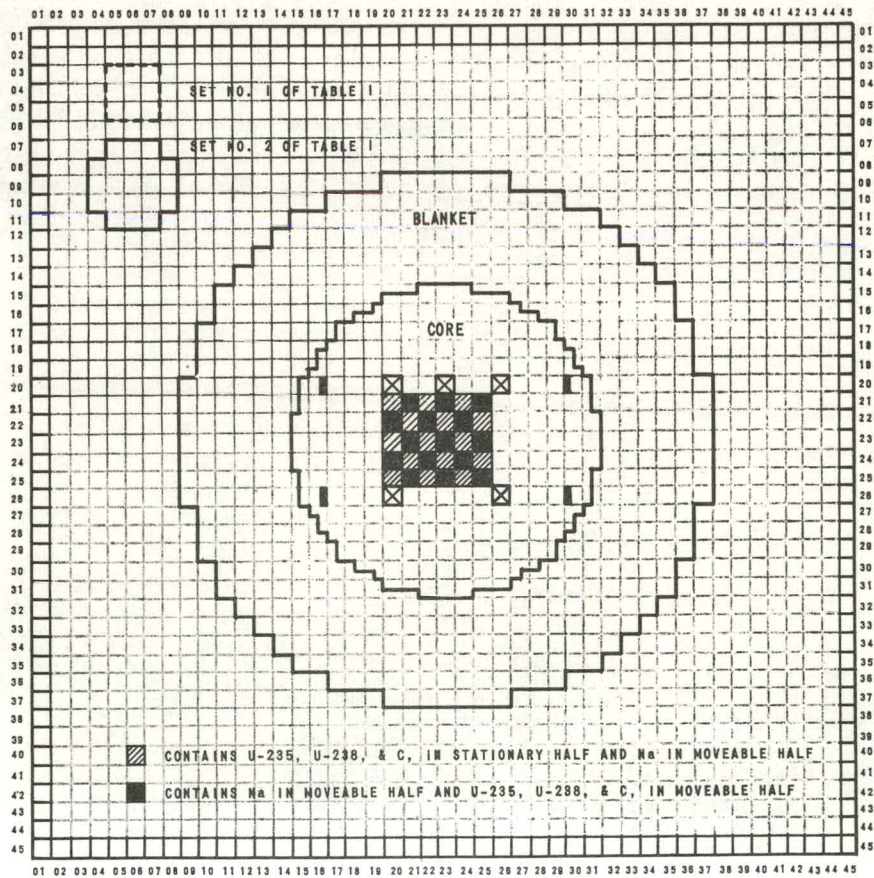
^b The core radius was obtained by equating the actual cross sectional area of the core to an equivalent circular cross section.



- ENRICHED URANIUM
- DEPLETED URANIUM
- CARBON

DIMENSIONS IN INCHES (CENTIMETERS)

Fig. III-8-14. Modified Drawer Loadings for Modified Sodium Versus Void Measurements.



- D.P. CONTROL ROD
- INSERTION SAFETY ROD

Fig. III-8-15. Portion of Core with Modified Drawer Loading.

TABLE III-8-XI. SODIUM LOADED DRAWERS

Set No.	Typical Core Drawers	Equivalent Bunched Pattern
1	S/M-2222, S/M-2223, S/M-2224, S/M-2323, S/M-2323, S/M-2324, S/M-2422, S/M-2423, S/M-2424,	S-2222, S-2224, S-2323, S-2422, S-2424, M-2223, M-2322, M-2324, M-2423,
2	S/M-2122, S/M-2123, S/M-2124, S/M-2221, S/M-2222, S/M-2223, S/M-2224, S/M-2225, S/M-2321, S/M-2322, S/M-2323, S/M-2324, S/M-2325, S/M-2421, S/M-2422, S/M-2423, S/M-2424, S/M-2425, S/M-2522, S/M-2523, S/M-2524,	M-2122, S-2123, M-2124, M-2221, S-2222, M-2223, S-2224, M-2225 S-2321, M-2322, S-2323, M-2324, S-2325, M-2421, S-2422, M-2423, S-2424, M-2425, M-2522 S-2523, M-2524,

TABLE III-8-XII. SODIUM COEFFICIENTS

Drawer Set	Configuration Voided	Typical Loading, Ih/kg	Bunched Sodium, Ih/kg ^a	
			Sodium cans replaced by void ^b	Sodium cans replaced by empty SS cans
1	18 in. of drawer	-4.5	-9.1 ± 0.4	—
1	Front 3 in.	-1.6	—	-3.0 ± 0.4
1	Back 3 in.	—	—	-10.3 ± 0.4
2	Front 7 in.	—	-4.3 ± 0.4	-4.3 ± 0.1
2	Front 4 in.	-1.9	-4.9 ± 0.6	-4.2 ± 0.2
2	Back 4 in.	-7.5	-14.9 ± 0.3	-10.7 ± 0.2
2	18 in.	—	-8.9 ± 0.1	—

^a 451 Ih = 1% ρ.^b Measurements corrected for stainless steel-void worth to correspond with other measurements.

TABLE III-8-XIII. CENTRAL REACTIVITY COEFFICIENTS

Can Wt, g	Material Wt, g	Material	Rod # 5, Δ cm	Rod # 8, Δ cm	Inhours	Can Correction, Ih.	Net Inhours	Ih/kg
—	272.95	U ²³⁵		+18.3	28.5 ± 0.5		+28.5 ± 0.5	+104.4 ± 1.8
20.0 (SS)	123.46	Pu		+12.5	19.5 ± 0.5	-0.069	+19.6 ± 0.5	+158.7 ± 4.1
26.8 (Al)	92.97	Pu		+9.42	14.7 ± 0.5	0.045	+14.7 ± 0.5	+158.1 ± 5.4
19.2 (Al)	177.08	WO ₃ (#0)	-0.206		-0.515 ± 0.05	-0.033 ± 0.006	-0.482 ± 0.056	-2.72 ± 0.32
19.4 (Al)	224.47	W (#5)	-1.038		-2.595 ± 0.05	-0.033 ± 0.006	-2.562 ± 0.056	-11.4 ± 0.25
—	1052	W	-4.605		-11.51 ± 0.05	—	-11.5 ± 0.05	-10.9 ± 0.05
19.5 (Al)	257.85	W (#1)	-1.271		-3.18 ± 0.05	-0.033 ± 0.006	-3.15 ± 0.056	-12.2 ± 0.22
19.2 (Al)	173.74	W (#2)	-0.777		-1.943 ± 0.05	-0.033 ± 0.006	-1.91 ± 0.056	-11.0 ± 0.32
4 (Al)	237.14	W (#3)	-0.972		-2.430 ± 0.05	-0.033 ± 0.006	-2.397 ± 0.056	-10.1 ± 0.24
19.4 (Al)	211.44	W (#4)	-0.711		-1.778 ± 0.05	-0.033 ± 0.006	-1.745 ± 0.056	-8.25 ± 0.27
19.4 (Al)	209.37	W ¹⁸⁶ (#6)	-0.596		-1.490 ± 0.05	-0.033 ± 0.006	-1.457 ± 0.056	-6.96 ± 0.27
19.2 (Al)	163.59	W ¹⁸⁴ O ₃ (#7)	-0.400		-1.000 ± 0.05	-0.033 ± 0.006	-0.967 ± 0.056	-5.91 ± 0.34
—	1154	D.U.	-2.879		-7.198 ± 0.05	—	-7.198 ± 0.05	-6.24 ± 0.04
—	166.9	Al	-0.114		-0.285 ± 0.05	—	-0.285 ± 0.05	-1.71 ± 0.44
4.3 (SS)	155.2	Al ₂ O ₃	+0.149		+0.373 ± 0.05	-0.015 ± 0.001	+0.388 ± 0.051	+2.50 ± 0.32
—	499.6	SS-304	-0.689		-1.723 ± 0.05	—	-1.723 ± 0.05	-3.45 ± 0.1
—	1183.6	Au	-8.719		-21.8 ± 0.05	—	-21.8 ± 0.05	-18.4 ± 0.04
—	103	C	+0.696		+1.74 ± 0.05	—	+1.74 ± 0.05	+16.9 ± 0.5
—	488	Fe	-0.560		-1.400 ± 0.05	—	-1.400 ± 0.05	-2.87 ± 0.10
49.4 (SS)	137.3	Fe ₂ O ₃	-0.075		-0.188 ± 0.05	-0.170 ± 0.005	-0.018 ± 0.055	-0.13 ± 0.40
49.7 (SS)	152.3	UO ₂	-0.328		-0.820 ± 0.05	-0.171 ± 0.005	-0.649 ± 0.055	-4.26 ± 0.36
8 (SS)	220.73	Cr	-0.353		-0.883 ± 0.05	-0.193 ± 0.006	-0.690 ± 0.056	-3.13 ± 0.25
30.3 (SS)	481.20	Nb	-3.294		-8.235 ± 0.05	-0.104 ± 0.003	-8.131 ± 0.053	-16.9 ± 0.11
55.8 (SS)	33.30	B ¹⁰	-15.125	-10.240	-53.8 ± 0.2	-0.193 ± 0.006	-53.6 ± 0.2	-1843.0 ± 7.0
	29.07 (B ¹⁰)							

vided, all effects are additive. If all of the carbon were replaced by sulphur, the sodium coefficient would drop to about -0.5 lh/kg.

SODIUM VERSUS VOID COEFFICIENTS—MODIFIED DRAWER LOADINGS

The drawer loading pattern of Assembly No. 2 was modified to obtain experimental information concerning the dependence of the sodium-void coefficients on the sodium distribution. Alternate drawers were filled with sodium-containing cans and the intermediary drawers were filled with fuel, depleted uranium, and graphite. Mating drawers from opposite halves of the reactor contained different materials; i.e., a sodium-filled drawer in the stationary half of the reactor was opposite a fuel, depleted uranium, and carbon containing drawer in the movable half. Because of the symmetry of the halves, each radial location in this bunched sodium arrangement still contained on the average the same quantity of the same core materials as the typical core drawers. Figure III-8-14 shows the modified drawer loading patterns. Figure III-8-15 shows the drawers contained in two experimental regions for a typical core loading and for the equivalent bunched loading. Table III-8-XI shows the drawers contained in two experimental regions for a typical core loading and for the equivalent bunched loading.

Table III-8-XII contains the results of these measurements compared to the measurements obtained for the

equivalent typical core drawer loadings. It is seen that in general the bunched sodium-void worths are greater than those obtained for typical drawers; the difference approaches a factor of two.

CENTRAL REACTIVITY COEFFICIENTS

Table III-8-XIII contains central reactivity coefficient data. The data with assigned error limits of ± 0.05 lh were obtained using a mechanical sample changer. In these instances the table halves were not separated between reference and sample experiments, and consequently higher precision measurements resulted.

FAT MAN EFFECT

Multiplication measurements were made on Assembly No. 2 to obtain an indication of the possible usefulness of the multiplication technique for predicting the worth of reflecting and moderating material between the separated halves of larger diameter reactor assemblies.

A 20-cm thick moderating material (Fat Man) having an approximate hydrogen density of 5.5×10^{22} atoms/cm³ and large enough to cover the entire face of the core and blanket was used for the moderating reflector. As the initial core loadings were made during the approach to a critical assembly, Fat Man effect measurements were made. The measurements were made with B¹⁰F₃ pulse counters located on top of the reactor assembly as well as with fission pulse counters located in the center of the core.

Normalized inverse counting rates and normalized ratios of the counting rates without the Fat Man to those with the Fat Man are plotted in Fig. III-8-16 versus kg of U-235 loaded into the stationary half of the reactor.* For Assembly No. 2, which had a *L/D* ratio of 0.99 and a critical volume of 610 liters, the Fat Man savings is estimated from the inverse count rate data to be of the order of 60 kg of U-235.

REACTIVITY COEFFICIENTS OF EXPANSION

An expansion experiment was performed with 28 drawers comprising a sector having a volume approximately $\frac{1}{3}$ that of the stationary half of the reactor. The drawers in this region were loaded with 5-cm long plates of enriched uranium, depleted uranium, and graphite, as well as a normal complement of sodium. In addition, the sodium columns were extended through the 15.3 cm of blanket material contained in the back of the drawer. A reference run was then made using the metal spring normally contained in a drawer to hold the drawer constituents firmly against the front of the drawer. The

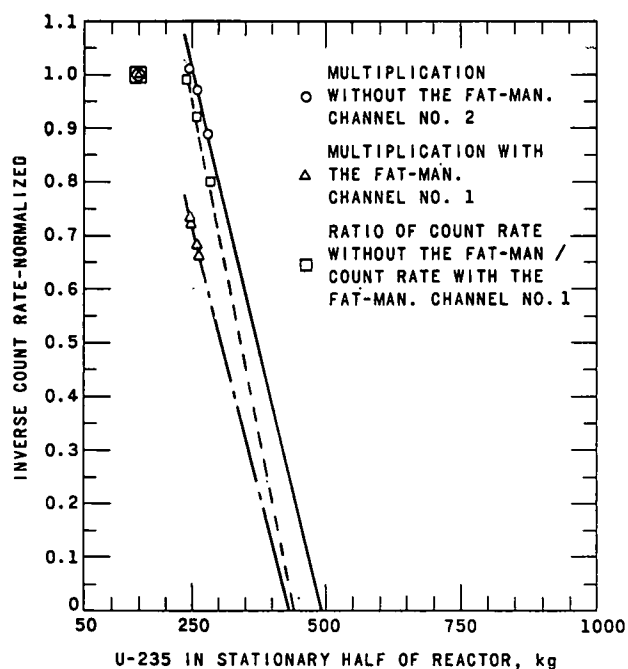


FIG. III-8-16. Multiplication Curves—Fat-Man Experiment.

* Fission chamber data are not shown since the data were not self consistent, apparently due to electronic noise problems.

drawer loading and the sector of the core involved are shown in Fig. III-8-17.

To simulate expansion, the holding spring was removed and the 5 cm plates of uranium and graphite were uniformly spaced (axially) with spacers to obtain an over-all "expansion" of 0.754 cm. The spacers were carefully removed and the drawers were carefully inserted into the reactor to maintain as closely as possible the prescribed spacings. The 15.3 cm of blanket material within the drawer was also moved, as a whole, toward the back of the drawer. The resulting reactivity change measured was -14.3 Ih. This expansion corre-

sponds to a whole core reactivity change of -228 Ih or -0.51% $\Delta k/k$.

Calculations were performed in cylindrical and slab geometry using the ANL one-dimensional diffusion theory code RE-122, and ANL cross section set 199. Using slab geometry with a radial buckling term incorporated, the axial analytical model is as close as possible to the experimental model. The cylindrical calculation assumed an axial buckling term which was modified by increasing the height of the bare core by the amount of the expansion. The two calculations gave respectively 224 and 230 Ih for the entire core.

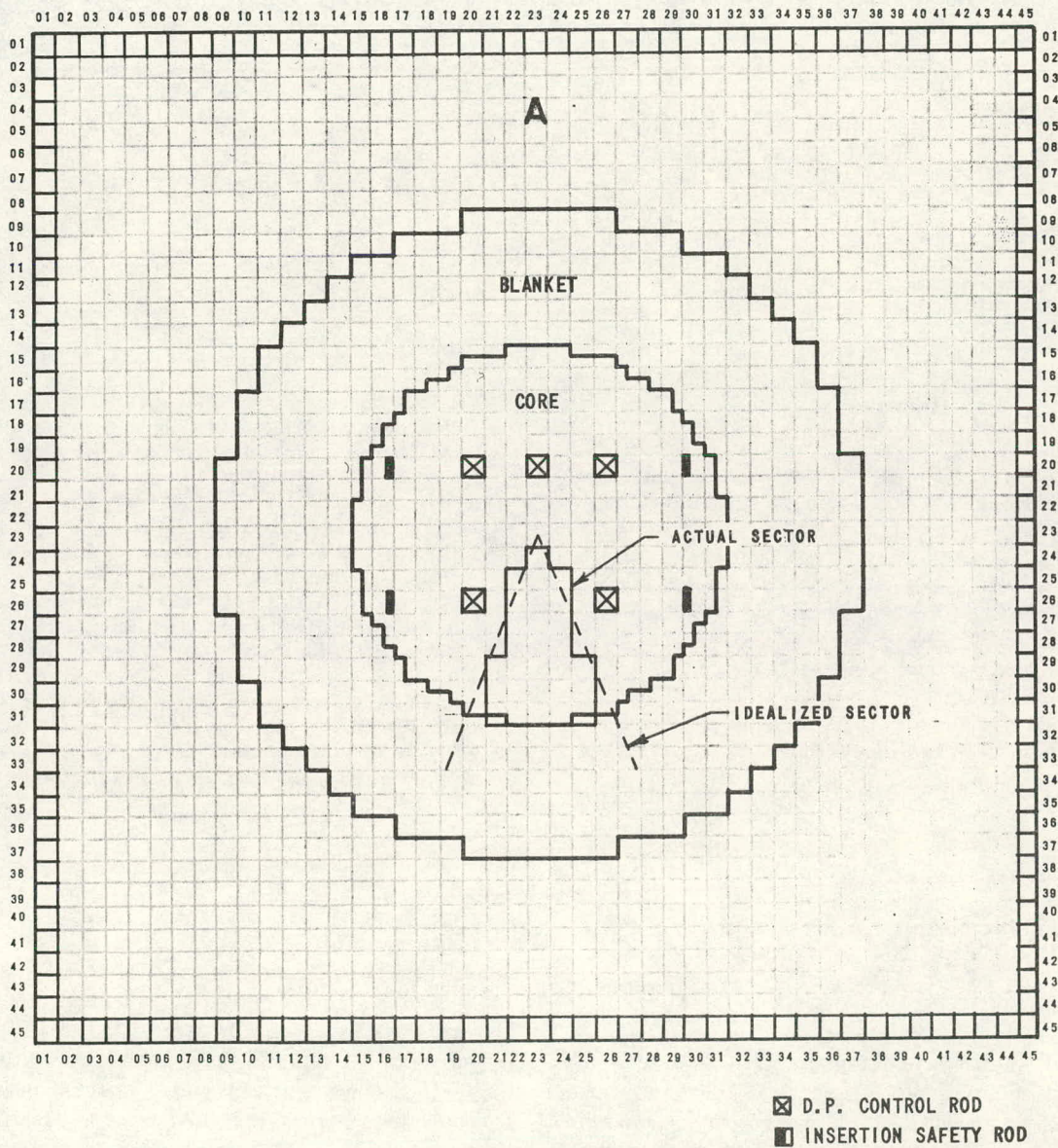


FIG. III-8-17. Simulated Expansion of Drawer Materials (Stationary Half).

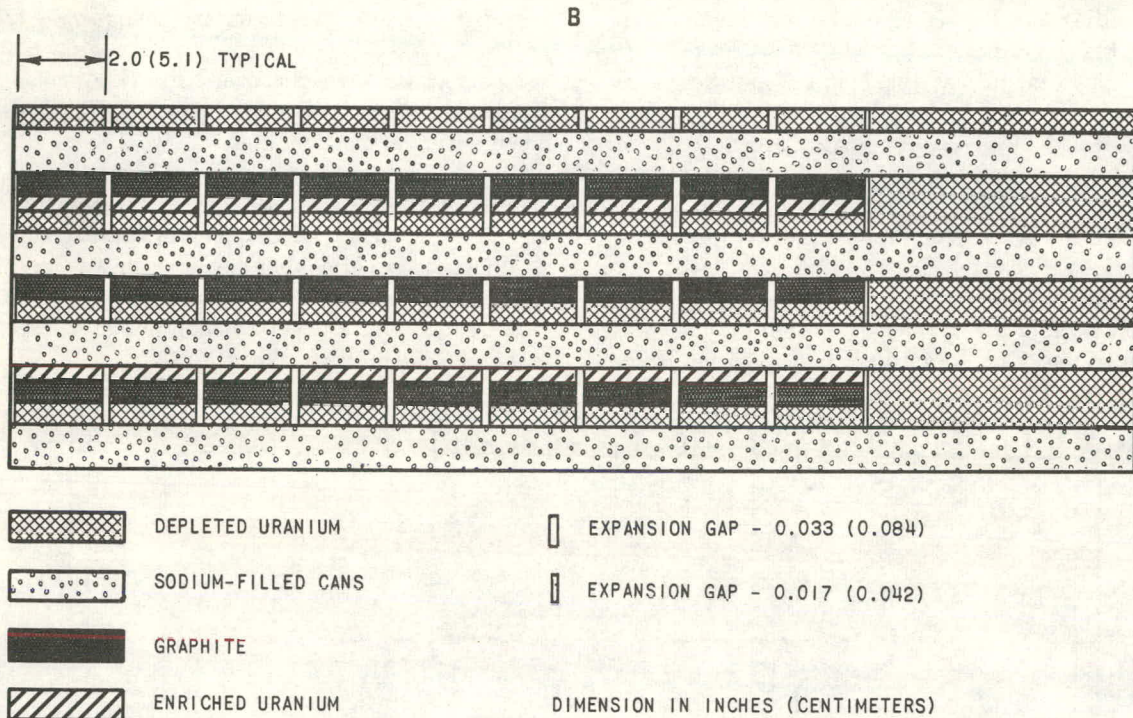


FIG. III-8-17—Continued

REFERENCES

1. G. K. Rusch, E. R. Böhme, L. R. Dates, S. Grifoni, W. Y. Kato, G. W. Main, H. H. Meister, N. Nozawa and R. L. Stover, *ZPR-VI, Assembly No. 2*, ANL Report (to be published).
2. S. Yiftah, D. Okrent and P. A. Moldauer, *Fast Reactor Cross Sections—International Series of Monographs on Nuclear Energy*, (Pergamon Press, New York, 1960).
3. C. E. Cohn and J. J. Kaganove, *Digital Method for Control Rod Calibration*, Trans. Am. Nucl. Soc. **5**, No. 2, 388 (November, 1962).
4. C. J. Rush, *New Technique for Designing Fast Rise Transistor Pulse Amplifiers*, Rev. Sci. Instr. **35**, No. 2, 149-156 (February, 1964).
5. F. S. Kirn, *An Absolute Fission Counter*, Trans. Am. Nucl. Soc. 2nd Winter Meeting, 61 (October, 1957).
6. W. G. Davey, *K Calculations for Assembly No. 22 ZPR-III Fast Reactor Assemblies Using Cross Section Set 635*, ANL-6570 (1962).
7. M. G. Bhide and H. H. Hummel, *Calculations of the Doppler Coefficient of Large Ceramic Fueled Fast Reactors*, ANL-6601 (1962).
8. P. Greebler, B. A. Hutchins and J. R. Sueoka, *Calculations of Doppler Coefficient and Other Safety Parameters for a Large Fast Oxide Reactor*, GEAP-3646 (March, 1961).
9. J. Codd, C. Durston and M. F. Janes, *Some Calculations of Sodium Reactivity Effects in a Dilute Fast Reactor*, AEFW-M225 (April, 1962).
10. W. H. Roach, *Computation Survey of Idealized Fast Breeder Reactors*, Nucl. Sci. Eng. **8**, No. 6 (1960).

III-9. Recent Calculations for Representative ZPR-III Fast Assemblies

D. MENEGHETTI and J. R. WHITE

Improved knowledge of microscopic cross sections together with more involved procedures for determination of multigroup constants have recently led to the development¹ of an up-dated multigroup cross section set. A comparison has therefore been made between experimental results and calculated quantities, using this

recent cross section set, for a representative series of ZPR-III fast critical assemblies. Critical masses, central detector response ratios, and prompt neutron lifetimes have been calculated. Because of the relatively hard neutron flux spectra in these assemblies, the present comparison indicates the characteristics of this

TABLE III-9-I. CALCULATED CRITICAL MASSES AND DETECTOR RESPONSE RATIOS FOR REPRESENTATIVE ZPR III ASSEMBLIES COMPARED WITH EXPERIMENTAL VALUES

Assembly number	Core ^a Volume Fractions							Critical Mass							Detector Response Ratios										Neutron Lifetime (10 ⁻⁸ sec)																	
	U ²³⁵ (N = 0.048)		U ²³⁸ (N = 0.048)		SST ^b (N = 0.0854)		Al (N = 0.0603)		C (N = 0.0717)		O (N = 0.096)		Na (N = 0.0254)		L/D ratio	Estimated shape factor	Estimated reactivity addition due to heterogeneity	Ratio of fractional critical mass increase, $\Delta M/M$, to reactivity, $\Delta k/k$	Spherical homogeneous calculated critical mass, kg U ²³⁵	Critical mass addition due to heterogeneity, kg U ²³⁵	Critical mass addition due to shape factor, kg U ²³⁵	Calculated critical mass corrected for shape and heterogeneity, kg U ²³⁵	Experimental critical mass, kg U ²³⁵	Per cent error critical mass			Per cent error reactivity	Fission counter ^d			Radio-chemical		Calculated		Experimental ^e		Calculated		Experimental ^e		Calculated	
	σ_f (U ²³⁵)	σ_f (U ²³⁸)	σ_f (U ²³⁵)	σ_f (U ²³⁸)	σ_f (U ²³⁵)	σ_f (U ²³⁸)	σ_f (U ²³⁵)	σ_f (U ²³⁸)	σ_f (U ²³⁵)	σ_f (U ²³⁸)	σ_f (U ²³⁵)	σ_f (U ²³⁸)	σ_f (U ²³⁵)	σ_f (U ²³⁸)														Experimental	Calculated	Experimental	Calculated	Experimental	Calculated	Experimental	Calculated	Experimental	Calculated	Experimental	Calculated	Experimental	Calculated	
6F	0.14	0.159	0.123	0.314	—	—	—	—	—	—	—	—	—	SPHERE	—	0.01	4.6	129.3	-5.9	—	123.4	131.1	-5.9	+1.3	—	0.069	0.0729	—	1.564	—	0.459	—	1.263	—	0.485	0.084	0.100	7.7	6.8			
9A	0.117	0.380	0.142	0.215	—	—	—	—	—	—	—	—	—	SPHERE	—	0.01	5.3	149.9	-7.9	—	142.0	146.2	-2.8	+0.5	0.055	—	0.0543	—	1.570	0.447	0.392	1.30	1.233	—	0.409	—	0.106	8.3	6.7			
12	0.095	0.355	0.092	—	0.357	—	—	—	—	—	—	—	—	0.87	0.94	0.01	5.7	165.7	-9.4	+10.0	166.3	176.8	-5.9	+1.0	0.048	0.046	0.0495	1.46	1.544	0.305	0.322	1.10	1.150	—	0.338	0.100	0.116	10.5	8.9			
14	0.094	0.007	0.093	—	—	0.745	—	—	—	—	—	—	—	0.99	0.94	0.012	4.3	125.1	-6.5	+7.6	126.2	136.1	-7.3	+1.7	0.059	0.060	0.0618	1.45	1.503	0.317	0.331	1.05	1.095	—	0.354	0.109	0.116	18.7	15.3			
22	0.094	0.701	0.093	—	—	—	—	—	—	—	—	—	—	0.88	0.93	0.008 ^c	7.2	248.1	-14.3	+17.6	251.4	243.7	+3.2	-0.4	0.039	0.041	0.0398	1.53	1.574	0.305	0.335	1.16	1.209	0.346	0.345	0.091	0.103	7.1	6.3			
23	0.093	0.007	0.092	0.428	—	—	—	—	—	—	—	—	—	0.84	0.944 ^c	0.011 ^c	4.6	237.5	-12.0	+13.4	238.9	258.1	-7.4	+1.6	0.0732	0.079	0.0711	1.48	1.558	0.418	0.438	1.18	1.246	—	0.463	0.089	0.103	12.1	11.0			
25	0.071	0.741	0.093	—	—	—	—	—	—	—	—	—	—	0.90	0.92	0.01	11.6	603.5	-70.0	+46.4	579.9	581.6	-0.3	0.0	0.0315	—	0.0316	—	1.573	0.263	0.292	1.17	1.183	—	0.298	0.092	0.114	8.1	7.5			
20	0.0497	0.0997	0.248	0.244	—	0.145	—	—	—	—	—	—	—	0.79	0.92	0.01	5.3	361.6	-19.2	+29.8	372.2	421.0	-11.6	+2.2	0.0384	—	0.0358	1.47	1.534	0.269	0.253	1.06	1.094	0.301	0.263	0.115	0.124	23.5	21.2			
32	0.093	0.007	0.81	—	—	—	—	—	—	—	—	—	—	1.17	0.932 ^c	0.01	4.3	197.9	-8.5	+13.8	203.2	227.5	-10.7	+2.5	0.0487	—	0.0485	1.51	1.572	0.382	0.387	1.20	1.227	0.397	0.405	—	0.107	12.6	11.3			
33	0.093	0.007	0.636	—	—	—	—	—	—	—	0.158	—	—	1.14	0.93	0.01	4.4	207.0	-9.1	+14.9	212.8	238.0	-10.6	+2.4	0.052	—	0.0542	1.51	1.569	0.385	0.400	1.21	1.232	0.416	0.420	—	0.106	12.5	11.3			
34	0.0467	0.103	0.246	0.255	0.106	—	—	—	—	—	—	—	—	0.94	0.92	0.01	5.4	441.6	-23.8	+36.3	454.1	503.0	-9.7	+1.8	0.0366	0.040	0.0352	1.454	1.537	0.257	0.259	1.067	1.101	0.282	0.270	0.122	0.123	24.7	22.0			
36	0.0937	0.495	0.127	—	—	—	—	—	—	—	0.158	—	—	1.42	0.87	0.01	6.3	219.8	-13.8	+30.8	236.8	242.7	-2.4	+0.4	0.0443	—	0.0460	1.47	1.572	0.324	0.357	1.19	1.217	0.350	0.370	0.097	0.108	7.8	7.2			
41	0.0596	0.291	0.141	0.179	—	—	—	—	—	—	—	—	—	0.98	0.92	0.01	6.6	455.0	-30.0	+37.0	462.0	489.9	-5.7	+0.9	0.0395	—	0.0402	1.430	1.567	0.297	0.322	1.164	1.191	—	0.333	—	0.113	13.1	11.9			

^a Blanket volume fractions: 0.19% U²³⁵, 83.3% U²³⁸, 7.31% stainless steel, except assembly no. 6F which contains in addition 2.27% Al blanket thickness 30 cm.

^b Stainless steel (assuming $N_{SST}^{Fe} = 0.0615$, $N_{SST}^{Cr} = 0.0162$ and $N_{SST}^{Ni} = 0.0077$ in SST).

^c Directly calculated.

^d Includes +8% correction for counter wall thickness [55].

^e Includes +4% correction for counter wall thickness [55].

26 group cross section set only down to about No. 13 having lower energy 9.1 keV.

For any given core composition the effective group cross sections for transport and elastic transfer attributed to structural and simulated coolant materials were obtained by using the ELMOE program.² The latter solves a fundamental mode problem using hundreds of fine groups and yields coarse-group cross sections for use in the subsequent multiregion-multigroup reactor analysis. The details of the elastic scattering resonances present in the light element structural and the coolant atoms were thus taken into account. The data on the light element angular scattering were provided by a library of Legendre polynomial coefficients.

In the present study the effective group cross sections for transport and elastic transfer were determined by ELMOE analysis using the consistent B_1 option.² The subsequent reflected systems criticality analyses were carried out using the DSN neutron transport code³ in the S_4 approximation with spherical geometry. The latter calculations assumed the cores to be homogeneous spheres. The DSN results were then corrected to account for the increased reactivity effect of the thin fuel plate heterogeneities⁴ and, when necessary, for the cylindrical core geometries. The resulting predicted parameters are listed in Table III-9-I. The experimental values^{5,6,7,8} are listed for comparison with the corrected calculated parameter. (The relatively small corrections for experimental irregular boundaries and for assembly center-gap are not included).

The increase in reactivity due to heterogeneity was estimated at 1% $\Delta k/k$ except for a few cases where direct analyses had been made.⁴ The reactivity increment was then related to incremental change in core peripheral fuel mass through calculated $(\Delta M/M)/(\Delta k/k)$ ratios. The latter ratios were calculated using the DSN program in the S_4 approximation. The corrections to convert the calculated spherical heterogeneous systems to cylindrical geometry were based upon estimated shape factors (ratio of spherical critical mass to corresponding cylindrical critical mass) except in the few indicated cases where directly calculated shape factors were available. For the estimated cases the shape factors were taken to be 0.94, 0.93, or 0.92 depending upon whether the core size was considered relatively small, moderate, or large in the limited range of core sizes studied herein. The previous general studies of W. Loewenstein and G. Main^{7,9} and W. Davey¹⁰ together with the few directly calculated values were used as fiducial guides in these choices. As Assembly 36 had quite a large L/D ratio, the shape factor was estimated from available

curves^{7,9,10} of shape factor versus L/D ratio. Because of uncertainties in the shape factor and heterogeneity corrections, it was estimated that the percent error in reactivity of the final adjusted calculated masses relative to the experimental values should be assessed on the estimate that the order of magnitude of error due to these uncertainties may be 0.5 to 1% in k_{eff} . It is noted, furthermore, that the systems containing large amounts of light materials, i.e. Al, Na, steel, C, etc., were calculated to be most overly reactive relative to other selected materials.

Table III-9-I also lists the calculated detector response ratios at the core centers and the calculated prompt neutron lifetimes. For comparison with experimental reported ratios, the experimental values of detector response ratios were corrected for counter wall thickness.¹¹ The lifetimes were calculated by the $1/\nu$ -insertion method. It may be noted that the calculated lifetimes are in better agreement with experiment than previous studies of ZPR-III assemblies using other cross section sets.^{4,5,12}

REFERENCES

1. D. M. O'Shea, H. H. Hummel, W. B. Loewenstein, D. Okrent and B. J. Toppel, *Twenty-Six Group Cross Sections*, ANL-6858 (to be published).
2. A. L. Rago and H. H. Hummel, *ELMOE: An IBM-704 Program Treating Elastic Scattering Resonances in Fast Reactors*, ANL-6805 (1964).
3. B. Carlson, C. Lee and J. Worlton, *The DSN and TDC Neutron Transport Codes*, LAMS-2346 (1960).
4. D. Meneghetti, *Recent Advances and Problems in Theoretical Analyses of ZPR-III Fast Critical Assemblies*, Proc., Seminar on Physics of Fast and Intermediate Reactors, IAEA, Vienna, Vol. I, 457 (1961).
5. G. S. Brunson, R. N. Curran, J. M. Gasidlo and R. J. Huber, *A Survey of Prompt-Neutron Lifetimes in Fast Critical Systems*, ANL-6681 (1963).
6. J. K. Long, A. R. Baker, W. Gemmel, W. P. Keeney, R. L. McVean and F. W. Thalgot, *Experimental Results on Large Dilute Fast Critical Systems with Metallic and Ceramic Fuels*, Proc., Seminar on Physics of Fast and Intermediate Reactors, IAEA, Vienna, Vol. I, 271 (1961).
7. *Reactor Physics Constants*, 2nd Edition, ANL-5800, 594 (1963).
8. R. L. McVean, W. G. Davey and G. J. Fischer, *The Role of the Fast Critical Facility in the Power Reactor Program*, Symposium on Exponential and Critical Experiments, IAEA, Amsterdam, Vol. I, 85 (1963).
9. W. B. Loewenstein and G. W. Main, *Fast Reactor Shape Factors and Shape-Dependent Variables*, ANL-6403 (1961).
10. W. G. Davey, *k Calculations for 22 ZPR-III Fast Reactor Assemblies Using ANL Cross-Section Set 635*, ANL-6570 (1962).
11. W. G. Davey, *A Critical Comparison of Measured and Calculated Fission Ratios for ZPR-III Assemblies*, ANL-6617 (1962).
12. W. G. Davey, *A Comparison of Experimental and Calculated Prompt Neutron Lifetimes and Central Reactivity Coefficients in ZPR-III Assemblies and Their Relationship to Other Reactor Parameters*, ANL-6682 (1963).

III-10. Comparison of ZPR-III Shape Factor Calculations by Transport and Diffusion Methods

D. MENEGHETTI

It has been usual in ZPR-III criticality calculations to apply shape factors to convert calculated spherical critical masses to the analogous cylindrical critical masses. This circumvents the necessity for a multi-group two-dimensional analysis of a reflected fast critical assembly by employing instead a multigroup one-dimensional calculation. Estimates of shape factors are often based upon published^{1,2,3} experimental or calculated curves. These do not necessarily correspond to the particular assembly of interest.

This study calculated explicitly the shape factors for three ZPR-III fast assemblies, using two neutron energy groups, by transport and diffusion theory methods. The lower limits of the energy groups are 1.35 MeV and 9.12 keV. The contributions to reactivity by neutrons below these groups are negligible.

The assemblies calculated are Nos. 23, 32, and 31 which are fueled by U-235 and have as diluents aluminum, steel, and aluminum and steel, respectively.¹ The L/D ratios (height to diameter) of the cores are 0.84, 1.17, and 0.69 respectively.¹

For the cylindrical calculations, TDC, the Los Alamos two-dimensional R-Z transport code⁴ was used. The spherical configurations were calculated using the corresponding one-dimensional DSN transport code.⁴ In all cases the S_4 approximation was used. TDC and DSN calculations give shape factors of 0.944, 0.932, and 0.913 for assemblies Nos. 23, 32, and 31 respectively. It may be noted that the calculated value for assembly No. 31 differs from the experimentally reported value of 0.921 ± 0.002 by about -1%.

The analogous shape factor calculations have also been carried out by diffusion theory, using the two-dimensional PDQ code⁵ and the one-dimensional RE-122 code.⁶ As TDC calculations are comparatively costly, it is of interest to determine what difference in shape factor might be expected by using diffusion theory. In the diffusion theory cylindrical (PDQ) problems, the calculated shape factors derived from transport theory were applied to the diffusion theory critical spherical systems. This determined the cylindrical input volumes for the two-dimensional diffusion analyses. The resulting values of k_{eff} were then 1.0003₁, 0.9991₆, and 1.0007₉. The shape factors by diffusion theory are thereby estimated to differ by +0.1%, -0.4%, and +0.4% from the corresponding S_4 transport values.

Critical core volumes determined by diffusion theory are generally larger than critical core volumes deter-

mined by S_4 calculations. An estimate of this effect upon the shape factor was made by decreasing the diffusion theory critical volume to equal the S_4 critical volume for assembly No. 31. The diffusion theory volume is about 4.9% larger. RE-122 and PDQ calculations for k_{eff} had been carried out assuming the previously calculated critical spherical and cylindrical S_4 volumes. The difference obtained for the resulting non-critical multiplication factors, $k_{eff}(\text{PDQ}) - k_{eff}(\text{RE-122})$, for the reduced volumes was 0.00078. This is essentially equal to the previously obtained difference, $k_{eff}(\text{PDQ}) - 1$, of 0.00079. This suggests that the effect of volume change on shape factor is small, even when compared with the small calculated differences observed between S_4 and diffusion theory. It is, however, interesting to note that the diffusion theory shape factors are not necessarily larger than those derived from S_n calculations. The calculated differences between S_4 and diffusion theory are sufficiently small that diffusion theory shape factor calculations should generally be adequate for analysis.

It may be noted that general shape factor curves^{2,3} should be used with caution for other than the approximate sizes and compositions of cores and reflectors indicated. For example, reactor No. 3 in Refs. 2 and 3 differs from assembly No. 31 only by having 37.6% Na instead of 23.5% Al. It might be expected that reactor No. 3 would be adequate to estimate the shape factor for assembly 31. In fact, from reactor No. 3 of Ref. 2, a diffusion theory shape factor of about 0.91 is estimated. This seems to compare favorably with the directly calculated diffusion theory value of ~ 0.917 reported here. More recent calculations by the same authors,³ have resulted in a lowering of the shape factor for reactor No. 3. The estimated value for assembly No. 31 based on the more recent values³ is about 0.885 which is about 3.5% smaller than the directly calculated 0.917 value reported here.

REFERENCES

1. *Reactor Physics Constants*, 2nd Edition, ANL-5800, 594 (1963).
2. W. B. Loewenstein and G. W. Main, *Fast Reactor Shape Factors and Shape-Dependent Variables*, ANL-6403 (1961).
3. W. B. Loewenstein and G. W. Main, *The Influence of Core Shape on Fast Reactor Criticality*, Trans. Am. Nucl. Soc. 5, No. 1, 61 (1962).
4. B. Carlson, C. Lee and J. Worlton, *The DSN and TDC Neutron Transport Codes*, LAMS-2346 (1960).

5. G. Bilodeau et al., *PDQ, An IBM-704 Code to Solve the Two-Dimensional Few Group Neutron Diffusion Equations*, WAPD-TM-70 (1957).

6. M. K. Butler and J. M. Cook, *Univac Programs for the Solution of One-Dimensional Multigroup Reactor Equations*, ANL-5437 (1956): IBM-704 Code related to REX Code.

III-11. Feasibility Study of Zone Loading for Fast Critical Facilities

F. H. HELM

INTRODUCTION

Measurements of the properties of large dilute reactor cores are often performed in a zoned system.^{1,2} The simplest core consists of two zones, one having the properties of the core to be studied and the second being a driver region containing an economical amount of fuel. When the two are coupled together the system is critical. The driver may be either internal or external to the zone to be studied, depending upon the requirements of the program of measurement. In this report, the results of critical mass calculations are given and the advantages and difficulties in performing reactivity and spectrum measurements are discussed for two right cylindrical zones of equal radii joined axially (see Fig. III-11-1).

For convenience the large dilute zone of interest is referred to as Zone A and the driver zone as Zone B. Either zone made critical by itself is called Core A or Core B and the critical length is called l_A and l_B , respectively.

CRITICAL MASS

In principle, a part of the large dilute Core A is, in the zone system, replaced by the more concentrated driver region, Zone B. In practice, Zone B is assembled first and its critical length, l_B , determined. Half of Core B is then removed and Zone A loaded to determine the total critical length, $l = z_A + (l_B/2)$. The length z_A of Zone A for which the zone system becomes critical is approximately equal to half the critical

length of Core A. This can be shown by the following consideration. If each of the zones were exactly one half of a critical core and if it is assumed that these respective cores have the same spectra and radial flux distributions then, when the two zones are coupled the boundary conditions of continuous flux and current are fulfilled by the same flux distribution which would exist in a system consisting of two identical zones. According to diffusion theory, this implies that the system fulfills boundary conditions and steady-state flux equations in each zone, and is therefore critical.

Actually, however, the neutron spectra in the two zones will be different and there will also be differences in the radial flux distributions. Particularly this is true if there is a radial reflector which yields different reflector savings for the compositions of the two zones.

In order to determine the critical length l_A of Core A, a calculated correction term Δl is applied to the length z_A , such that $l_A = 2(z_A - \Delta l)$. Machine calculations of the correction term Δl were performed for a test case. The compositions and dimensions which were assumed for Cores A and B are listed in Table III-11-I. Δl was calculated using the two-dimensional PDQ code³ with cross section set No. 193 and the one-dimensional DSN-transport code^{4,5} with the cross section set No. 192.

The results of the calculations are shown in Table III-11-II. The values for Δl found with the two codes have different signs but their absolute difference (about 1 cm) corresponds to a difference of only about two per cent in the critical mass.

MEASUREMENTS OF REACTIVITY AND NEUTRON SPECTRA

Central reactivity coefficients cannot be directly measured in the zone system, as the center of Core A corresponds to a point on the interface between Zone A and Zone B. For the same reason the zone system does not allow a direct measurement of a central spectrum. The best approximation to the central spectrum of Core A is the spectrum near the center of Zone A. Results of DSN spectra calculations for Zone A and

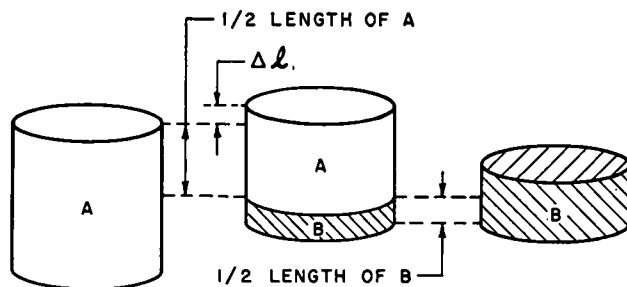


FIG. III-11-1. Two-Zone Loading.

TABLE III-11-I. COMPOSITIONS USED FOR THE ZONE LOADING CALCULATIONS

Core	Core Compositions, v/o				Core Radius, cm	Critical Length, cm	Calculated Critical Mass, kg
	U-235 (93% Enr.)	U-238	Fe	Al (56% density)			
A	4.96 ^a 5.02 ^b	—	12.0	83.04	50	90.0	617
B	10.0 ^a 8.63 ^b	20.0	12.0	58.0	50	27.4	378
Reflector	—	88.0	12.0	—	—	—	—

^a Numbers used in PDQ calculation.

^b Numbers used in DSN calculation.

These numbers were chosen so that the PDQ calculation gave the same results as the DSN calculations for the critical lengths of the Cores A and B.

TABLE III-11-II. RESULTS OF ZONE-LOADING CALCULATIONS

Method	Correction Factor		Fuel Savings, ^b %
	Δl , cm	Per cent of critical mass ^a	
two-group diffusion	0.52	+1.2	19.5
sixteen-group diffusion	-0.47	-1.0	23.6

^a In this column, Δl , was converted into the fraction by which the critical mass measured by the zone technique is greater than the actual critical mass.

^b In this column the percentage of fuel is shown which can be saved when the critical mass is measured by the zone technique instead of by a full size mockup of Core A.

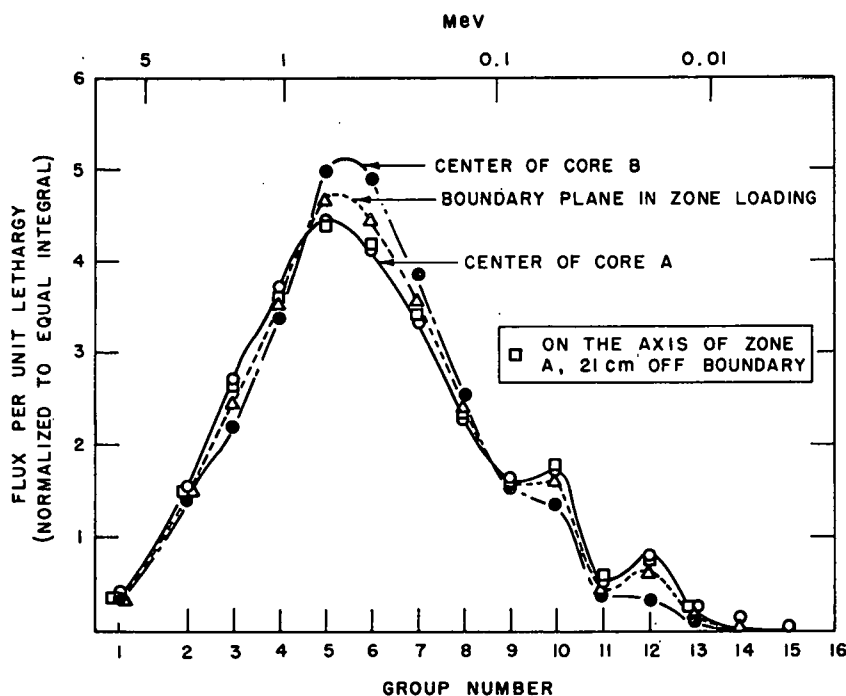


FIG. III-11-2. Neutron Spectra by Sixteen Group DSN Calculation.

Core A are shown in Fig. III-11-2. For the core parameters given in Table III-11-I the DSN calculations showed that in the center of Zone A the spectrum is very similar to the central spectrum of Core A.

While the zone system described here is not very suitable for the measurement of central core parameters it does offer the opportunity of spectra and reactivity measurements at points near the zone boundary for which the conditions in Core A are well simulated.

CONCLUSIONS

The main advantage of the zoned system lies in the fact that the critical mass of a large core can be determined using considerably less fuel than would be necessary for a full-scale mock-up. This difference is shown in the last column of Table III-11-II.

Approximate measurements of the central spectrum are possible, but the measurement of central reactivity coefficients can be done better with the more conventional zone loading in which a central zone with dilute

fuel is surrounded by a driver zone with higher fuel concentration.^{1,2} On the other hand, properties near the core edge can be studied in the zone system described here. This is not possible in a system with a central zone.

REFERENCES

1. P. I. Amundson, R. L. McVean and J. K. Long, *A Two-Zone Fast Critical Experiment (ZPR-III Assembly 42)*, ANL-6733 (1964).
2. L. A. Mountford and V. E. Kistler, *Critical Mass Calculations of a Multispectrum Critical Assembly*, Trans. Am. Nucl. Soc. 5, No. 1, 68 (1962).
3. G. G. Bilodeau, et al., *PDQ—An IBM-704 Code to Solve the Two-Dimensional Few-Group Neutron-Diffusion Equations*, WAPD-TM-70 (August, 1957).
4. B. G. Carlson, C. Lee and J. Worlton, *The DSN and TDC Neutron Transport Codes*, LAMS-2346 (February, 1960).
5. B. G. Carlson, *Numerical Solution of Transient and Steady-State Neutron Transport Problems*, LA-2260 (October, 1959).

III-12. Physics Measurements in Tungsten-Based Aluminum Reflected Fast Reactors

R. C. DOERNER, K. K. ALMENAS, R. A. KARAM, W. Y. KATO, W. G. KNAPP and W. B. LOEWENSTEIN

INTRODUCTION

There have been no studies reported in the literature concerning moderate-volume (100–300 liters) fast reactor cores in which tungsten is a major diluent material. Neither have there been reported studies of aluminum reflectors in cores of this size. The results of a parametric study of the effects of increasing volume fractions of tungsten as a diluent material and of the reactivity effects of an aluminum reflector are reported in this paper. Because of the interest in tungsten-rhenium alloys in high-temperature, high power-density applications, a number of exploratory measurements made with rhenium are also reported. All measurements were made in the Argonne ZPR-IX facility (see Paper No. IV-8) and may be compared to the well known and extensively studied depleted uranium-diluted and reflected assemblies constructed on ZPR-VI (Assembly No. 1) and ZPR-III (Assemblies No. 11 and 22). All of the experimental data obtained from corresponding ZPR-III and VI assemblies were nearly identical and so the results of these measurements are used as reference points for corresponding measurements reported here.

CORE COMPOSITION

The first core studied was the standard 7:1 volume ratio of U-238 to U-235, which differed from the reference assembly only in the use of aluminum rather than depleted uranium as a reflector material. In subsequent assemblies, the U-238 diluent material was replaced in a stepwise manner with tungsten. The physical properties of these assemblies are shown in Table III-12-I.

The calculated critical masses listed in Table III-12-I were determined by a 16-group one-dimensional diffusion theory code² using ANL cross section sets.³ Al-

though this particular U-238 cross section set overestimates the critical mass of U-238 diluted assemblies by 10 to 15% it was used in an identical manner (code, mesh points, convergence criteria, etc.) for all assemblies in order that different cross section sets, particularly for aluminum, could be compared.

One of the major calculational problems in assemblies containing major amounts of full density aluminum is the proper theoretical treatment of the resonance scattering in the 0.1 to 1 MeV region. Another is the difficulty of treating the spatially varying spectrum in the region of the core-reflector interface; these regions have radically different asymptotic spectra. Table III-12-I shows that the error in the experimental critical mass relative to the calculated critical mass decreases as the fraction of tungsten diluent increases or the U-238 content decreases. A study was made on one of the assemblies (No. 1) of the effect of the calculational technique and of the effect of using different aluminum cross section sets, including YOM and an ELMOE⁴ generated sets. The results show that the use of a diffusion theory code compared to the more exact transport theory code (DSN) overestimates the critical mass of similar assemblies by 6 to 10%^{1,5} and that the aluminum contributes an additional 5% because of an overestimate of core leakage. Such an overestimate would result in an increased calculated critical mass and an increase in the reflector fluxes which should lead to higher calculated reaction rates in the reflector. For the limited number of reaction rates measured in the reflector this is indeed the case.

As the core volume increases, errors introduced by the use of diffusion theory and by reflector-induced discrepancies will decrease. Both sources of error are estimated to account for not more than 1% of the experimental-to-calculated critical mass difference. The

TABLE III-12-I. PHYSICAL PROPERTIES OF TUNGSTEN-BASED REACTOR CORES

	Reference Assembly	ZPR-IX Cores			
		Assembly No. 1	Assembly No. 2	Assembly No. 3	Assembly No. 4
Reflector material	U-238	Aluminum	Aluminum	Aluminum	Aluminum
Volume/Density ^a of U-238	87/0.0336	87/0.0338	62/0.0242	44/0.0168	0/0.000486
U-235	9/0.00452	9.5/0.00451	9/0.00451	9/0.00447	14.5/0.00672
W	0/0	0/0	25/0.0123	44/0.0214	81/0.0396
Critical mass, ^b kg U-235	241	278.5	382.6	493.0	285.2
Length/Radius, cm	51.0/29.0	50.8/31.4	60.9/34.1	71.4/35.0	56.2/24.9
Volume, liters	134.7	158	224	283	109.4
Homogeneous critical mass ^c exp/calc	239/278	267/332	366/441	474/562	271/294
(exp-calc)/(calc), % ^d	-14	-19	-17	-16	-7.8

^a The approximate volume percent and the atom density $\times 10^{24}$ for each of the materials.

^b Experimental critical mass corrected only for excess reactivity.

^c Experimental and calculated critical masses corrected for excess reactivity, heterogeneity of the fuel ($+0.6\% \Delta k/k$), central gap ($-0.1\% \Delta k/k$) and converted to equivalent spherical volumes through the shape factor (0.80-0.94, see Ref. 1).

^d Relative percent differences between experimental and calculated critical masses. Predicted parameters are for cores of experimental composition. Core radius was varied to achieve predicted criticality.

important improvement in the agreement is due to the exchange of U-238 for tungsten.

CENTRAL REACTIVITY WORTHS

One of the more sensitive measurements of spectral dependence that can be made is that of a central danger coefficient. In particular, the central reactivity worth of U-238 provides a measure of the flux above the fission threshold energy; that of U-235 reflects the importance weighting for fissions at the core center; and the worth of B-10 tests the softer component of the flux spectrum. A comparison of the tungsten worth relative to that of U-238 for each of the assemblies is a moderately sensitive measure of its inelastic scattering. In some cases, the real and adjoint fluxes were calculated by a 16-group one-dimensional diffusion theory code (RE 269) and used in a perturbation calculation. Results of the measured and calculated worths for these materials are shown in Table III-12-II.

As was the case for the critical mass calculations, predictions of effects associated with tungsten are consistently more accurate than those associated with U-238. Table III-12-II also summarizes the data for Re for which the calculated results are significantly more negative than the experimental values.

A number of separated isotopes of tungsten were made available by Lewis Research, NASA. Central reactivity worths of each of the samples and their isotopic enrichments are given in Table III-12-III.

HYDROGEN-BORON MIXTURE WORTHS

It is of interest from the control point of view to determine the degree to which hydrogen can be used to enhance the central boron worth. Central worths of

various homogeneous mixtures of powdered lucite and amorphous boron were made in Assembly No. 4. Specially fabricated aluminum sample cans were filled with 63 cm³ of mixtures having known weight ratios of lucite to boron. Because of the different densities of the materials, (lucite powder ≈ 0.4 g/cm³, solid lucite ≈ 1.18 g/cm³, powdered boron ≈ 0.6 g/cm³, amorphous boron ≈ 2.34 g/cm³), it was necessary to normalize the measured worths of the samples to unit weights. The measured points are shown in Fig. III-12-1 as circles. From the smoothed curve (A), the worth per gram of boron was determined and is shown as curve B of Fig. III-12-1. It appears that a 65:35 weight percent mixture of lucite to boron has the maximum worth per gram of boron.

A parametric study of the worth per gram for different sample sizes was made in Assembly No. 4 for boron and in assemblies 3 and 4 for lucite and polyethylene. The Assembly No. 3 results are shown in Fig. III-12-2 and those for the all-tungsten diluted core are shown in Fig. III-12-3. Figure III-12-2 clearly illustrates the extreme degree of self shielding that is characteristic of hydrogen samples. In the all-tungsten diluted system, not only is the sign of the hydrogen worth reversed but the self shielding effect is not nearly as prominent. A small correction has been made in Fig. III-12-2 for the carbon in the lucite samples.

SPATIALLY DEPENDENT REACTION RATES

U-235 and U-238 fission rates were determined by foil activation techniques for Assembly Nos. 3 and 4. The Mo-99 was radiochemically separated and counted to determine the fission rate per gram of material. This technique is reported by R. J. Armani (see Paper No.

TABLE III-12-II. CENTRAL REACTIVITY WORTHS, lh/kg

Core Volume	Facility					
	ZPR-III	ZPR-IX				
	Assy. No. 22 (132 liters)	Assy. No. 1 (158 liters)	Assy. No. 2 (224 liters)	Assy. No. 3 (283 liters)	Assy. No. 4 (109 liters)	
U-235	exp.	270	240	189	162	270
	calc.	265	276	248	164	316
	calc.-exp.	+0.02	+0.13	+0.24	~0	+0.14
U-238	exp.	-11.7	-10.9	-9.7	-6.3	-5.5
	calc.	-13.5	-17.9	-12.1	-9.53	-4.7
	calc.-exp.	+0.13	+0.39	+0.20	+0.34	-0.17
B-10	exp.	-2760	-2430	-2395	-2110	-3660
	calc.	-2840	-2645	-2490	-1920	-3740
	calc.-exp.	+0.03	+0.09	+0.04	-0.09	+0.02
W	exp.	-24.6	-23	-17	-14.8	-19.6
	calc.	-27.3	-26	-17	-15.4	-24.1
	calc.-exp.	+0.10	+0.11	~0	+0.11	+0.18
Re	exp.	-64.7	-60	-49.3	-44.3	-71.7
	calc.	-79.5	-84.1	-72.4	-58.5	-121
	calc.-exp.	+0.19	+0.25	+0.32	+0.24	+0.42
Graphite, exp.	-27.3	-37.3	-27.4	-37.9	-22.0	
Gold, exp.		-33.7		-23.4	-39.3	

TABLE III-12-III. CENTRAL WORTHS OF SEPARATED TUNGSTEN ISOTOPE SAMPLES

Sample	% W-182	% W-183	% W-184	% W-186	Weight, g	Worth, lh/kg	
						Assy. No. 1	Assy No. 4
No. 0, normal WO ₃	26.4	14.4	30.6	28.4	117.08	-24.3	-13.7
No. 1, W metal	36.9	17.7	31.5	13.9	257.85	-27.1	-20.2
No. 2, W metal	24.1	14.7	34.2	26.9	173.74	-21.9	-18.7
No. 3, W metal	12.5	9.8	30.8	46.8	237.14	-24.2	-17.0
No. 4, W metal	5.8	5.7	23.3	65.1	211.44	-22.0	-14.7
No. 5, normal metal	26.4	14.4	30.6	28.4	224.47	-24.7	-19.3
No. 6, W-186 metal	1.6	2.1	11.6	84.7	209.37	-21.0	-13.1
No. 7, W-184 O ₃	1.91	1.87	94.3	1.91	163.58	-23.2	-14.6

IV-22). These data, as well as the U-235 to U-238 fission ratios are shown in Fig. III-12-4 for Assembly No. 3 and in Fig. III-12-5 for Assembly No. 4. There is a slight but consistent tendency for the calculated reaction rates to be overestimated in the aluminum reflector. This implies a lower experimental flux in the reflector than calculated and, as noted earlier, indicates that the aluminum cross sections overestimate the core leakage. In all of the assemblies, the calculated U-238 to U-235 fission ratio is about 6% higher than the measured values and is consistent with extensive ZPR-III

experience. W. Davey⁶ ascribes this discrepancy to a low value of the U-235 cross sections, though this is not born by the U-235 central reactivity worth measurements.

KINETIC PARAMETERS

It is standard practice in these assemblies to determine the value of β_{eff} from the measured value of Rossi-alpha ($\equiv \beta_{eff}/\ell$) and the calculated prompt neutron lifetime of the particular assembly. Only recently has it been possible to determine β_{eff} independent of the

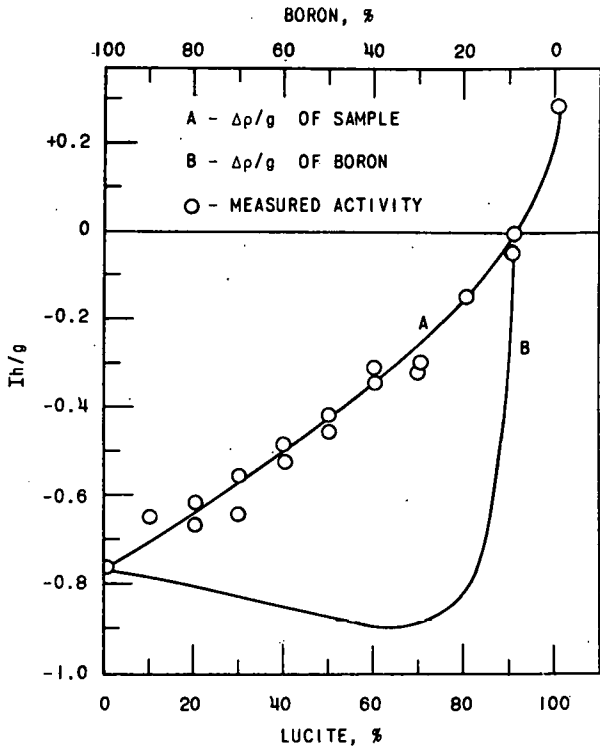


FIG. III-12-1. Central Reactivity Worths of Lucite-Boron Mixtures. (Curve A is the smooth curve through the measured points, and curve B is the worth per gram of Boron as derived from curve A.)

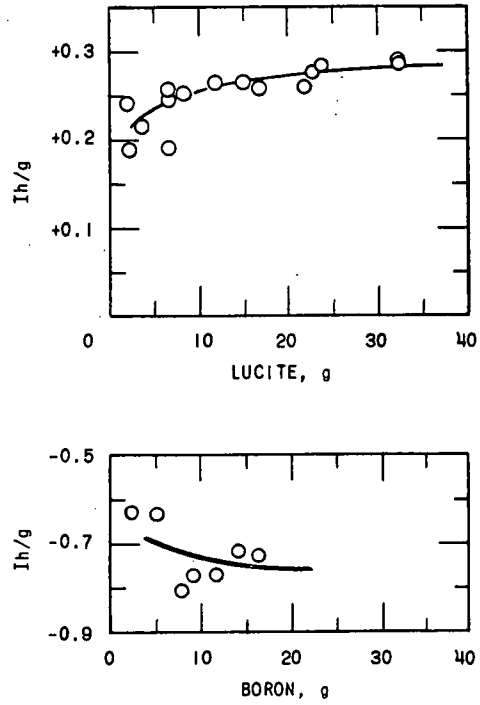


FIG. III-12-3. Central Worth of Lucite and Boron in Assembly No. 4.

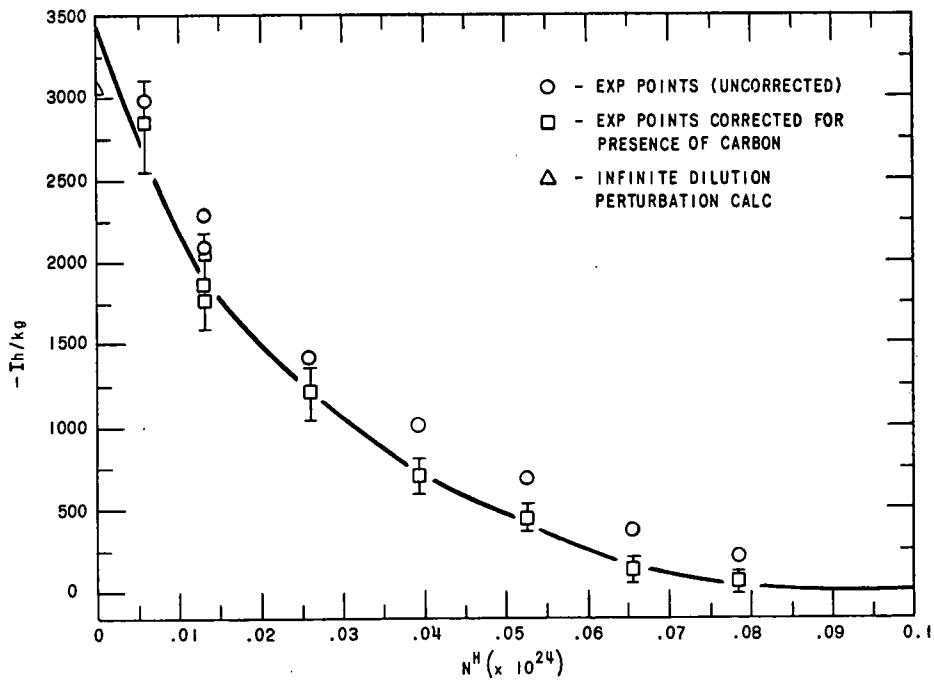


FIG. III-12-2. Central Hydrogen Worth in Assembly No. 3.

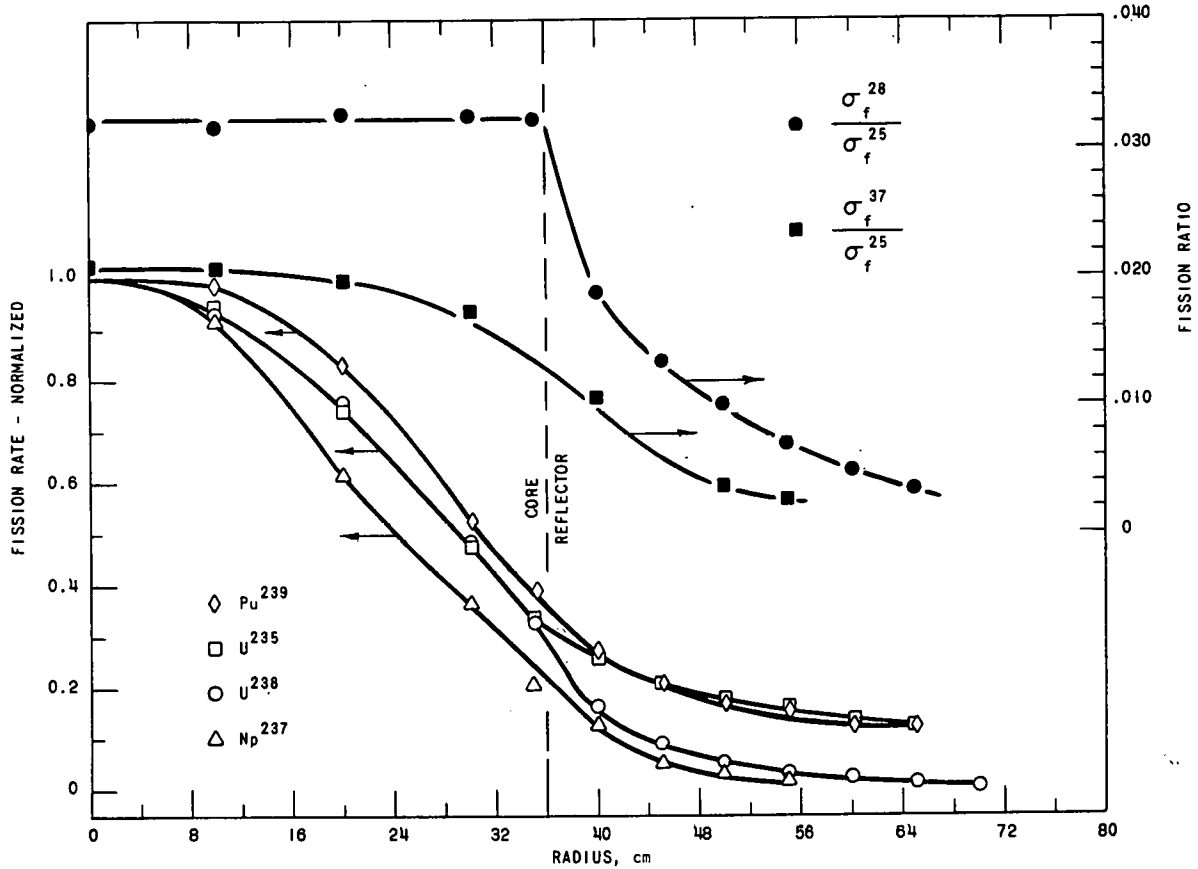


FIG. III-12-4. Relative Fission Rates for Assembly No. 3.

lifetime. This determination is based on the measured variance-to-mean ratio and is reported by R. Karam (see Paper No. IV-3).

Early measurements in aluminum reflected assemblies showed the existence of two components to the Rossi-alpha. The model chosen to evaluate the data was that of a one-group two-region reactor⁷ in which the prompt neutron balance equations for the core and reflector are given as

$$\frac{dN_c}{dt} = \frac{N_c P_c [(1 - \beta) - 1]}{\ell_c} + \frac{N_r L_r}{\ell_c}, \quad (1)$$

and

$$\frac{dN_r}{dt} = -\frac{N_r}{\ell_r} + \frac{N_c L_c}{\ell_c}, \quad (2)$$

where

- P_c \equiv probability of a disappearing core neutron producing a fission neutron in the core,
- L_c and L_r \equiv probabilities of a disappearing core neutron appearing in the reflector and conversely, respectively,

β \equiv effective delayed neutron fraction,
 ℓ_c and ℓ_r \equiv neutron lifetimes in the core and reflector, respectively.

Delayed neutrons and their precursors have been neglected because they do not affect the Rossi-alpha measurement. Solving Eq. (1) for N_r , differentiating with respect to time and equating to Eq. (2) gives a second order differential equation for N_c , having the general solution

$$N_c = A e^{\alpha_1 t} + B e^{\alpha_2 t},$$

where

$$\alpha_1 = -\frac{1}{2} \left\{ \left[\frac{k_{ex} + \beta}{\ell_c} + \frac{1}{\ell_r} \right] - \left[\left(\frac{k_{ex} + \beta}{\ell_c} + \frac{1}{\ell_r} \right)^2 - \frac{4\beta}{\ell_c \ell_r} \right]^{1/2} \right\}$$

$$\alpha_2 = -\frac{1}{2} \left\{ \left[\frac{k_{ex} + \beta}{\ell_c} + \frac{1}{\ell_r} \right] + \left[\left(\frac{k_{ex} + \beta}{\ell_c} + \frac{1}{\ell_r} \right)^2 - \frac{4\beta}{\ell_c \ell_r} \right]^{1/2} \right\}.$$

In these expressions P_c in Eq. (1) has been replaced

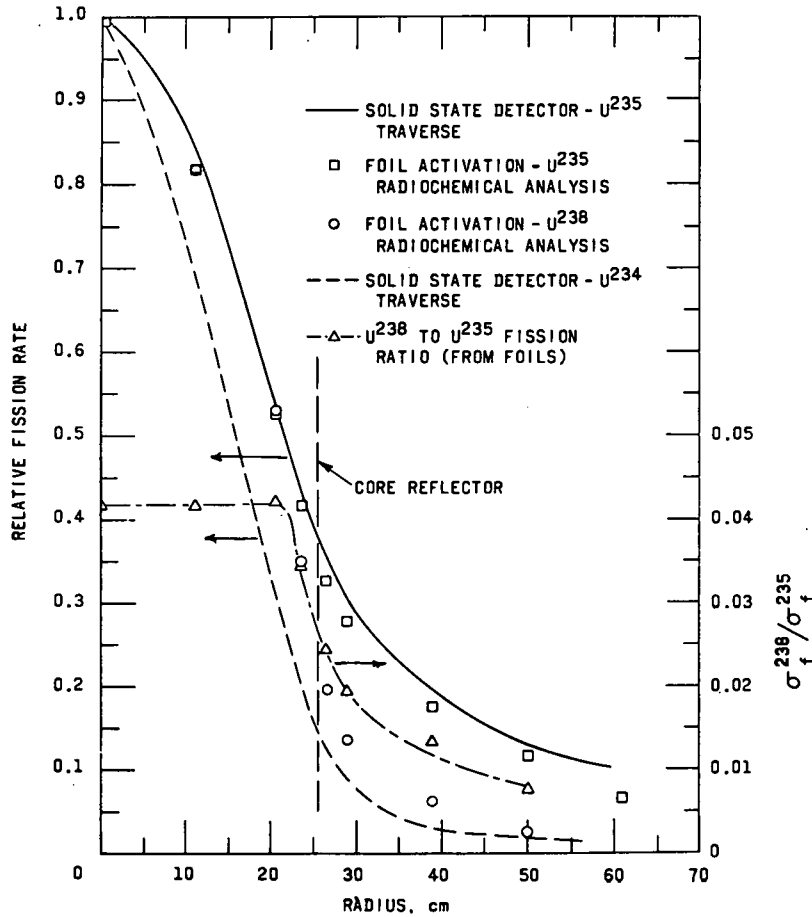


FIG. III-12-5. Assembly No. 4 Reaction Rates and Fission Ratios.

by $(1 - k_{ex})$; at critical the product $L_c L_r = k_{ex}$, (see Paper No. IV-3).

Substituting this solution into Eq. (2) gives a similar expression for the neutron population in the reflector.

The time behavior of prompt neutrons in the whole system is then the sum

$$N_T(t) = N_c(t) + N_r(t) = A'e^{\alpha_1 t} + B'e^{\alpha_2 t},$$

where A' and B' are functions of k_{ex} and β_{eff} .

A parametric study was made of the relationships among different ratios of l_r/l_c , k_{ex} and the products $\alpha_1 l_c$ and $\alpha_2 l_c$. The results are shown in Fig. III-12-6. In all cases, it was assumed $\beta_{eff} = 0.007$. The solid curves go with the $\alpha_2 l_c$ scale to the left of the figure and the $\alpha_1 l_c$ scale to the right is used with the dashed curves.

The spectrum in a depleted uranium reflector of a fast reactor is not expected to differ significantly from the core spectrum and $l_c \approx l_r \equiv l$. To a good approximation

$$\alpha_1 \approx -\frac{1 + k_{ex}}{l} \approx 10^7$$

$$\alpha_2 \approx -\frac{\beta}{l} \approx 10^5.$$

Measurements⁸ on such systems show that if the α_1 component exists, it is at least two orders of magnitude less than α_2 .

A similar argument applied to a thermal reactor in which $l_c \approx l_r \approx 10^{-4}$ sec gives $\alpha_1 \approx 10^4$ and $\alpha_2 \approx 10^2$ and a Rossi-alpha measurement essentially measures the α_1 component.

In the ZPR-IX assemblies, the ratio of l_r to l_c is not known, but the values of α_1 and α_2 can be measured and Fig. III-12-6 can be used to determine both l_c and l_r if k_{ex} is known.

The measured kinetic parameters are compared to the calculated values in Table III-12-IV for the various assemblies. The very large error associated with the calculated lifetimes may be attributed to the calculated spectra being too hard and the average neutron velocity being too high. This conclusion is not entirely supported, however, in the central reactivity worth measurements which use the same real and adjoint fluxes but produce much better agreement.

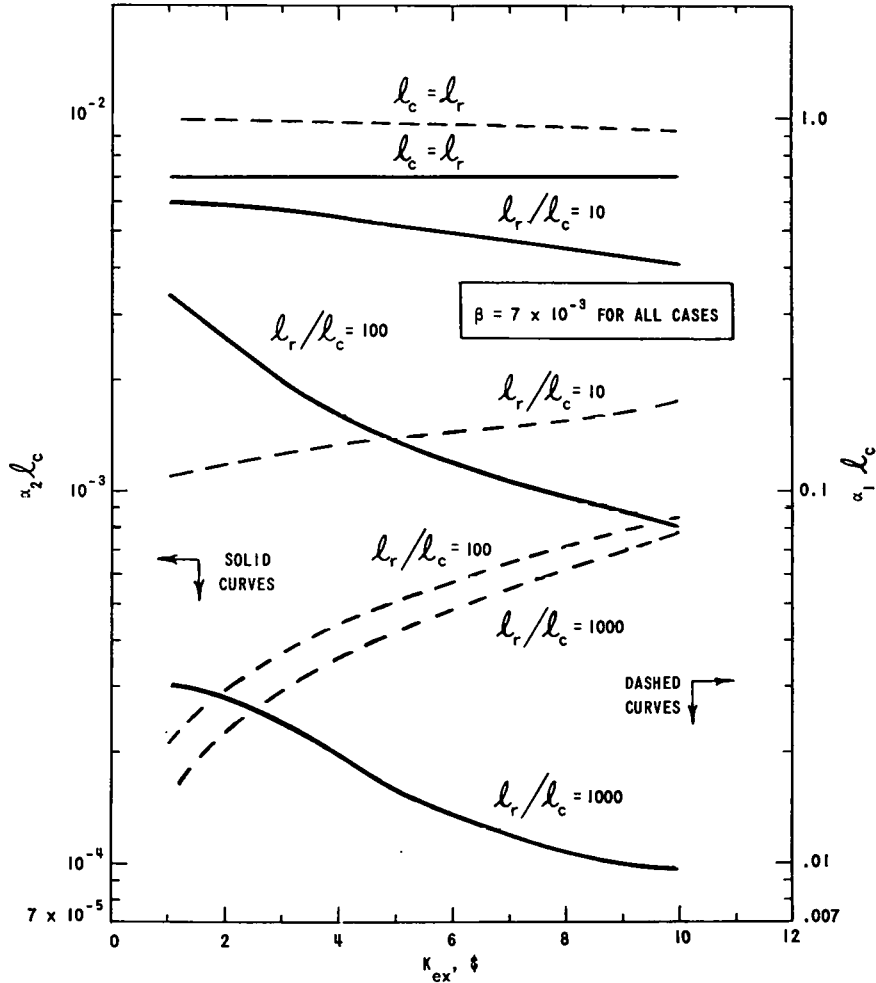


FIG. III-12-6. Parametric Relationship Between α_1 , α_2 , l_c , l_r , and K_{ex} .

TABLE III-12-IV. MEASURED AND CALCULATED KINETIC PARAMETERS

	Reference Core	ZPR-IX			
		Assembly No. 1	Assembly No. 2	Assembly No. 3	Assembly No. 4
β_{eff} (calc.)	0.00738	0.00728	0.00723	0.00708	0.00664
Rossi-alpha $\times 10^{+4} \text{ sec}^{-1}$ (calc.)	11.8	12.0	9.78	8.66	6.99
measured α_1		0.022	0.018	0.025	0.012
measured α_2	10.0 ± 0.5	8.2	6.9	6.57 ± 0.38	5.19 ± 0.28
Prompt lifetime $\times 10^{-9} \text{ sec}$ (calc.)	62.9	60.6	73.9	81.7	95.0
(exp.)	73.8	88.8	105	107	128
(calc.-exp.)/(calc.)	-0.17	-0.47	-0.42	-0.31	-0.35

REFERENCES

- W. G. Davey, *An Analysis of 23 ZPR-III Fast Reactor Critical Experiments*, Nucl. Sci. Eng. **19**, No. 3, 259 (July, 1964).
- Reactor Physics Constants*, ANL-5800, Second Edition, 761 (1963). A slightly modified Hanson and Roach set (material No. 19 of ANL library No. 201). W. H. Roach, *Computation Survey of Idealized Fast Breeder Reactors*, Nucl. Sci. Eng. **8**, No. 6, 621 (December, 1960).
- D. Meneghetti, *Recent Advances in Problems in Theoretical Analysis of ZPR-III Fast Critical Assemblies*, Proc., IAEA Seminar on Physics of Fast and Intermediate Reactors, Vienna, p. 457. See also H. Hummel and A. Rago, *An Accurate Treatment of Resonance Scattering in Light Elements in Fast Reactors*, Proc., IAEA Seminar on

- Physics of Fast and Intermediate Reactors, Vienna, p. 231.
5. W. B. Loewenstein and D. Okrent, *The Physics of Fast Reactors*, Proc., 1958 Geneva Conference 12, Paper No. 637, p. 6.
 6. W. G. Davey, *A Critical Comparison of Measured and Calculated Fission Ratios for ZPR-III Assemblies*, ANL-6617 (1962).
 7. C. E. Cohn, *Reflected-Reactor Kinetics*, Nucl. Sci. Eng. 13, No. 1, 12 (1962).
 8. G. S. Brunson, et al., *Survey of Prompt Neutron Lifetimes in Fast Critical Systems*, ANL-6681 (1963).

III-13. Parametric Survey of Homogeneous Unmoderated Rocket Reactors

W. B. LOEWENSTEIN and J. WHITE

The neutronics of a variety of nuclear rocket concepts were investigated in detail. This study was accompanied by a limited amount of pertinent correlation between theory and experiment. The correlation studies served to emphasize those areas where predicted reactor neutronics for the rocket concepts are uncertain and further neutronic studies are required. These studies include an extension of analytical techniques, accelerator cross-section measurements and pertinent critical experiments.

INTRODUCTION

Conceptual nuclear rocket reactor cores are constituted primarily of those materials that show significant high temperature capability. For neutronic interpretation these may be categorized as follows:

- a. Significant parasitic neutron absorption; e.g. tungsten based cores
- b. Moderate parasitic neutron absorption; e.g. molybdenum based cores
- c. Little parasitic neutron absorption; e.g. mixed carbide cores based on ZrC.

The conceptual reactors may be fueled by a variety of fissile compounds, the use of a specific one being dictated by high temperature capability as well as high temperature compatibility with the base material. Fissile compounds of U-235, U-233 and Pu oxide, carbide and sulfides were parametrically studied. The effect of using low (~2%) and high (~20%) Pu-240 content was also investigated.

The rocket reactor cores were parametrically studied in the 300 to 2500 liter range of core volumes. Each core volume was analyzed with several thicknesses (5-25 cm) of light metal reflector at 70% density. The volumetric provision for propellant in the core parametrically ranged from 20-70 v/o. In principle, the parametric survey covered a wide range of potential power levels and missions; the details of the latter are determined by propellant flow and heat transfer considerations.

The neutronic investigations were designed to give self-consistent quantitative data on:

- a. The critical mass
- b. The critical fuel loading per unit core volume of base material
- c. The power distribution and the critical mass penalty for flattening the power distribution
- d. The prompt neutron lifetime
- e. Reactivity effects including potential control mechanisms, propellant reactivity worth and temperature dependent feedbacks.

Some of the detailed calculations are reported in Refs. 1 and 2. In addition a few metal based reactor cores were analyzed to determine whether non-optimum heterogeneous core dilution with high temperature moderator tends to produce favorable neutronics when compared with the compact homogeneous core. Similarly, the analyses formed a basis for evaluating the fuel penalty for clustering several small nuclear rockets as opposed to a single large nuclear rocket.

The materials of interest in these studies and the anticipated neutron energy distribution for various systems were beyond those common to most fast reactor cross section libraries. The group structure and cross sections from Ref. 3 are appropriate for the purpose of the parametric survey in that the spectral range from 10 MeV to thermal is covered. However, the fast groups are quite broad in lethargy, suggesting that systems with little or insignificant inelastic scattering would be predicted to be too energetic. The systems of most interest feature significant inelastic scattering; hence the constants are quite appropriate except, perhaps, for a precise prediction of interaction between moderating reflector and unmoderated core. With respect to materials the Ref. 3 library was augmented by interim constants for sulfur and tungsten.¹

Most of the calculations utilized multigroup diffusion theory. However, ancillary studies involving gaps and thin regions were verified by multigroup DSN calculations.

FUEL REQUIREMENTS

It was expected that total fuel requirements for the tungsten based cores would exceed those for the molybdenum based cores which in turn would exceed those for the ZrC based cores. However, there had been very little previous work reported on tungsten bearing systems, which were found to be quite parasitic. On a volumetric basis, tungsten is more parasitic than U-238 in fast neutron systems. The measured fast neutron tungsten capture cross section is not more and probably is less than that for U-238; the total tungsten inelastic scattering cross section is probably not more than 10% greater than that for U-238. Thus the more parasitic nature of tungsten is primarily due to the ~30% greater atomic density when compared to U-238 metal. This observation has been experimentally confirmed for some unreflected tungsten "Jemima" assemblies¹ which may be compared to U-238 diluted reference Jemima assemblies.⁴ For example, a critical high density spherical core containing ~38 v/o U-235 requires about 90 to 129 kg of U-235 when diluted with U-238 and tungsten, respectively. Similarly a core containing ~29 v/o U-235 requires about 108 and 174 kg of U-235 when diluted with U-238 and tungsten, respectively. In both of these cores, criticality was achieved in cylindrical geometry by varying core size with fixed core composition.

The molybdenum based system requirements were not surprising. In small core (~300 liters) volumes the Mo enhanced reactivity, while in the larger systems the Mo becomes quite parasitic.

The ZrC based systems were, as expected, found to be very favorable on total fuel requirements, especially in the large (>1000 liters) sizes with low intermediate energy spectra.

Typical calculations for U-235 fueled systems with a 4 in. thick 70% density Be reflector are given in Table III-13-I. Similar calculations with different reflector thickness and systems fueled with both U-233 and Pu are given in Ref. 2. The several hundred liter core volume requirements, especially for high void cores, are quite sensitive to reflector thickness. For example, the reactivity will increase ~10% $\Delta k/k$ by doubling the reflector thickness (4 in. to 8 in.) on a 300 liter, 45% void tungsten based core. On a 70% void core, a similar reflector will change the reactivity by ~20% $\Delta k/k$. Such reflector thickness reactivity effects are roughly halved when analyzing 1500 liter core volume systems.

Equivalent studies with U-233 and Pu fueled systems demonstrated again that fuel requirements for a given system are roughly 40% less than those required for a similar U-235 fueled system.

The results given in Table III-13-I may be used to give semi-quantitative answers on the inventory penalties associated with clustering small systems and core dilution with moderator. For example, a 1500 liter, 45% void, US in W system would require about 2000 kg U-235. Five similar 300 liter systems and two 800 liter systems would require about 2880 and 2410 kg U-235, respectively. The clustering penalty is less than 50% for the smaller systems and on the order of 20% for the two 800 liter systems. The percentage penalty for clustering is more pronounced for the neutronically advantageous ZrC based systems. A 1500 liter, 45% void, carbide based core requires about 490 kg of U-235. Five similar 300 liter and two 800 liter cores require 1515 and 828 kg of U-235, respectively. The percentages are significantly greater than for the similar comparison above on the W based systems.

The inventory advantages of heterogeneous core dilution with moderator may be evaluated only by comparing cores with similar volumes of heat producing material. For example, the homogeneous 1500 liter, 45% void, US in W core requires about 2015 kg of U-235. A 2000 liter core with ~500 liters of heterogeneously distributed Be moderator requires about 1900 kg of U-235. It is not clear that the ~6% saving in fuel offsets the requirement for the increased core size.

The last column in Table III-13-I gives the volume percent of fissionable material in the critical reactor fuel matrix. In general, as this number decreases, the high temperature potential of a given core material tends to increase.

POWER DISTRIBUTION

The relatively high rocket performance requirements place a premium upon knowing and devising means to tailor the power distribution of the system. In general it was found that the moderating reflector produced a near thermal "spike" near the core-reflector boundary. Cores with high void content thus have a "flatter" power distribution than similar cores with heavy metal reflectors. It was found that the total inventory penalty to produce an acceptable radially flat power distribution, by varying fissile loading, is of the order of 10%.

Axial power shaping was also studied by using two slabs of core, having different constituent materials. The inlet reflectors may be Be while the outlet reflector is a heavy metal. The core inlet might be constituted of UC in ZrC while the core outlet is a tungsten based material (UO₂ or US in W). The calculations required essential continuity of power density at the boundary between the core slabs. The shaping parameter is the core height of each slab for a fixed

TABLE III-13-I. A COMPARISON OF REQUIRED FISSIONABLE MATERIAL FOR VARIOUS CORE SYSTEMS^a

Core Volume, liters	Heat Producing Volume, liters	Heat Producing Material	% Void in Heat Producing Material	Core Diluent		Predicted Critical Mass, kg U ²³⁵	Fissionable Material in Fuel Matrix, v/o	
				Material	v/o			
300	300	US in W	20	—	—	647	0.3046	
↓		45	—	—	—	576	0.3946	
↓		70	—	—	—	543	0.6816	
↓		↓	UO ₂ in M ₀	20	—	—	469	0.2404
↓		45	—	—	—	461	0.3436	
↓		70	—	—	—	478	0.6533	
600		20	BeO	50	515	0.265		
↓		45	BeO	50	460	0.342		
↓		70	BeO	50	475	0.662		
300		↓	UC in ZrC	20	—	—	216	0.0746
↓		45	—	—	—	303	0.1525	
↓		70	—	—	—	423	0.3906	
800		800	US in W	20	—	—	1459	0.2577
↓			45	—	—	—	1207	0.3102
↓			70	—	—	—	1025	0.4826
1067	20		Be	~25	~1350	~0.24		
↓	45		Be	~25	~1125	~0.292		
↓	70		Be	~25	~1050	~0.440		
800	↓		UO ₂ in M ₀	20	—	—	969	0.1862
↓	45		—	—	—	883	0.2467	
↓	70		—	—	—	865	0.4435	
1600	20		Be	50	1180	0.227		
↓	45		Be	50	970	0.270		
↓	70		Be	50	870	0.435		
800	↓		UC in ZrC	20	—	—	269	0.0350
↓	45		—	—	—	414	0.0781	
↓	70		—	—	—	655	0.2265	
1500	1500	US in W	20	—	—	2539	0.2392	
↓		45	—	—	—	2015	0.2762	
↓		70	—	—	—	1600	0.4019	
2000		20	Be	25	~2850	~0.23		
↓		45	Be	25	~1900	~0.265		
↓		70	Be	25	~1550	~0.370		
1500		↓	UO ₂ in M ₀	20	—	—	1611	0.1651
↓		45	—	—	—	1392	0.2074	
↓		70	—	—	—	1292	0.3530	
3000		20	BeO	50	~2100	~0.215		
↓		45	BeO	50	~1600	~0.242		
↓		70	BeO	50	~1300	~0.365		
1500		↓	UC in ZrC	20	—	—	305	0.0211
↓		45	—	—	—	488	0.0492	
↓		70	—	—	—	848	0.1565	
2500	2500	US in W	20	—	—	4040	0.2285	
↓		45	—	—	—	3115	0.2563	
↓		70	—	—	—	2343	0.3532	
3300		20	Be	25	~3700	~0.22		
↓		45	Be	25	~2850	~0.25		
↓		70	Be	25	~2100	~0.34		
2500		↓	UO ₂ in M ₀	20	—	—	2489	0.1530
↓		45	—	—	—	2063	0.1844	
↓		70	—	—	—	1813	0.2971	
5000		20	BeO	50	~3300	~0.21		
↓		45	BeO	50	~2400	~0.24		
↓		70	BeO	50	~1800	~0.36		
2500		↓	UC in ZrC	20	—	—	333	0.0138
↓		45	—	—	—	550	0.0332	
↓		70	—	—	—	1029	0.1139	

^a Four-inch thick 70% density Be reflector.

total core volume. Substantial axial power tailoring may be achieved in this manner with some saving of fuel requirements relative to a single tungsten based system. This sort of flux shaping can be achieved in a 300-500 liter core, while axial variation of fuel loading may be more satisfactory for cores larger than 1000 liters. However, the fuel inventory savings for the small cores are less significant than for the larger system.

PROMPT NEUTRON LIFETIME

The average core spectra in these systems are generally quite energetic, especially in the metal based cores. However, the prompt neutron lifetime is not as dependent on core composition as it is upon Be reflector thickness. Some typical calculated prompt neutron lifetimes are given in Table III-13-II.

REACTIVITY EFFECTS

The study focused on only a few, but extremely important, reactivity effects. These included potential control mechanisms, propellant reactivity worth and temperature dependent feedbacks.

The rocket reactor core operates at extremely high temperatures. It is therefore desirable to investigate control mechanisms which do not operate in a high temperature environment. Initial calculations dealt with the movement of reflector material away from the core, the interchange of poison and reflector and finally the interchange of fuel material with poison in a moderating reflector.

Reflector motion does give significant reactivity changes in the smaller (~300 liter) cores. For example, a gross 5 cm radial motion of a 20 cm thick Be reflector can give between 2.5 and 7.0% $\Delta k/k$. However, uncertain propellant distribution in the reflector while

TABLE III-13-II. PROMPT NEUTRON LIFETIMES (45% VOID CORES)

Core Composition	Core Volume, liters	Be Reflector Thickness, in.	Prompt Neutron Lifetime, μsec
UC in ZrC	300	none	0.37
	300	4	1.2
	1500	none	1.5
	1500	4	>2.5
US in W	300	none	<0.11
	300	4	0.49
	300	8	19.0
	1500	none	<0.13
US in W ^a	1500	4	0.28
	1500	8	>4.0
	300	8	>5.0
	1500	8	>2.4

^a 0.5 cm tungsten sheet between core and reflector.

TABLE III-13-III. NATURAL B₄C CONTROL CALCULATIONS

Core Volume, liters	Description	% $\Delta k/k^b$
300	Reference	14.6
1500		5.9
300	0.5 cm W between core and poison	11.3
1500		4.4
300	2.54 cm W between core and poison	11.7
1500		4.8
300	1.28 cm W and 1.28 cm Be between core and poison	5.9
1500		2.2

^a 45% void with 20 cm thick 70% density Be reflector.

^b The B₄C annulus is about 3.8 cm thick at ~70% density.

TABLE III-13-IV. EFFECTIVENESS OF FUEL AND B₄C INTERCHANGE IN REFLECTOR (45% VOID, US IN W SYSTEM)^a

Core Volume, liters	Total kg U-235		Reactivity Change, % $\Delta k/k$
	Core	Reflector	
300	479	0	14.6 ^b
300	433	53	21.5 ^c
1500	1868	0	5.9 ^b
1500	1764	149	10.3 ^c

^a 20 cm thick ~70% density Be reflector.

^b Exchange of B₄C with reflector.

^c Exchange of B₄C with reflector annulus (~3.8 cm) containing fuel.

such motion takes place raises some serious operational questions.

Spherical geometry calculations were used to evaluate the general reactivity behavior of the poison-reflector interchange at the core boundary. Typical results are given in Table III-13-III. Such reactivity changes can probably not be realized in a practical application. They are, however, indicative of potential design difficulties. It is apparent from Table III-13-III that engineering compromises can substantially reduce the available reactivity for such B₄C-Be interchanges. Therefore, the interchange of fuel embedded in a reflector with B₄C was similarly studied. Such results are given in Table III-13-IV.

In general these results in spherical geometry indicate that significant control may be achieved by mechanical material movements in the moderating reflector. Ancillary calculations show that for reasonable ratios of core height to diameter, the values in Tables III-13-III and III-13-IV should be reduced by about 30% to apply in the more realistic cylindrical geometry.

The basic temperature and power coefficients of reactivity for the hard core spectrum propulsion reactors

are similar to those for equivalent fast power reactor systems in the absence of sodium coolant. These effects can be attributed primarily to axial and radial expansion of the core structure. The Doppler coefficient of reactivity may be important in a reactor startup but it is not expected to be significant at high temperature operating conditions. Some typical spherical core expansion calculations are given in Table III-13-V.

Perhaps the most interesting reactivity effects in these systems are due to the gaseous hydrogen propellant in both core and reflector. To a fair degree of approximation, the effect in the core and reflector were found to be essentially additive except for very extreme circumstances; hence each region will be discussed separately. As hydrogen is introduced into the core, the spectrum is softened. At low hydrogen density this can cause either an increase or a decrease in reactivity, depending upon core size and composition (e.g. UO_2 or US). If a reactivity increase is incurred by low density hydrogen introduction, a further densification of the hydrogen does not always cause a further increase in reactivity. In fact, the introduction of extremely dense hydrogen may make the system less reactive than the reference configuration containing no hydrogen. Such effects have been only initially explored, and it is expected that both detailed experiments and analysis will be required for confident understanding.

The reactivity effect of increased hydrogen density in the reflector is frequently positive. It is sensitive to the details of how the reflector is coupled to the core

TABLE III-13-V. ESTIMATED REACTIVITY EFFECTS DUE TO UNIFORM CORE EXPANSION AND ESTIMATED ISOTHERMAL CORE EXPANSION TEMPERATURE COEFFICIENTS (US IN W SYSTEMS)

Core Volume, liters	Void Content, %	Core Expansion by Moving Reflector		Core Expansion into Gap between Core and Reflector	
		$\frac{\Delta k/k^a}{\Delta V/V}$	$\frac{\Delta k/k^b}{\Delta T}$	$\frac{\Delta k/k^a}{\Delta V/V}$	$\frac{\Delta k/k^b}{\Delta T}$
300	45	0.28	4.2×10^{-6}	0.18	2.7×10^{-6}
300	70	0.30	4.5×10^{-6}	0.11	1.7×10^{-6}
1500	45	0.19	2.9×10^{-6}	0.15	2.3×10^{-6}
1500	70	0.27	4.1×10^{-6}	0.16	2.4×10^{-6}

^a Reactivity effect per unit change in core volume (materials conserved).

^b Temperature coefficient of reactivity per °C assuming that $\Delta V/V \approx 15 \times 10^{-6}/^\circ\text{C}$.

and may cause a slight reactivity loss with a lessening of reflector effectiveness.

REFERENCES

1. C. E. Cohn, G. Golden, B. Hoglund, W. Loewenstein, G. Rosenberg, D. Sparks and C. Youngdahl, *Basic Material Resulting from ANL Rocket Study*, ANL-6656 (1963).
2. J. Marchaterre, K. Almenas, G. Golden, B. Hoglund, V. Kolba and W. Loewenstein, *Nuclear Rocket Study Evaluation Report*, ANL-6774 (1963).
3. G. E. Hansen and W. H. Roach, *Six and Sixteen Group Cross Sections for Fast and Intermediate Critical Assemblies*, LAMS-2543 (1961).
4. G. E. Hansen, *Elementary Fast Neutron Critical Assemblies*, Proc., 1958 Geneva Conference, 12, Paper No. 592, p. 84.

III-14. Super-Prompt Critical Excursions in Unmoderated Cores with Moderating Reflectors

W. B. LOEWENSTEIN and J. WHITE

Super-prompt critical excursions for typical fast neutron systems have been extensively studied in the past.^{1,2,3,4} Systems with light element and/or moderating reflectors (e.g. a nuclear rocket or a coupled fast-thermal breeder) have not in the past been subjected to similar detailed analyses. It is therefore of some interest to attempt to compare the super-prompt critical excursions in these systems with those of the extensively studied fast systems. A meaningful comparison of the overall safety of such systems with the extensively studied fast neutron systems is very difficult. It would require detailed comparison of the effect of prompt neutron lifetime and power distribu-

tion, as well as the very important considerations pertaining to the manner in which the prompt period is established (e.g. the manner in which reactivity is inserted at or near prompt critical). No such overall comparison is implied, or attempted, in this study. The detailed analyses were simply addressed to the following question: Assuming certain initial prompt periods, corresponding to some reactivity insertion rates, what is the subsequent behavior of the system? What is the maximum pressure, total liberated energy and liberated kinetic energy from such an excursion?

The analyses were carried out with the AX-I program.⁵ The major absolute uncertainty is related to

TABLE III-14-I. PROMPT CRITICAL EXCURSIONS IN UNMODERATED ROCKET CORES WITH VARIOUS REFLECTORS

Approximate Core Volume, liters	Reflector ^a Material	Core ^b Type	Approximate Prompt Neutron Lifetime, μsec	Initial Prompt Period, μsec	Shortest Prompt Period, μsec	Time Period ^c Becomes Negative, μsec	Energy Liberated, 10^{16} ergs		Peak Pressure, megabars	Time of Peak Pressure, μsec
							Kinetic	Total		
200	Be	H	15-20	1000	715	2600	0.0005	1.9	0.053	2650
		H		250	220	1188	0.04	5.2	0.15	1090
		H		31.7	31.3	327	21.0	98.0	1.23	340
		HL		1000	1000	125	0.004	0.11	—	—
		HL		250	199	453	0.007	0.28	~0.07	~75
250	Be	PF	10-15	1000	950	3020	0.003	3.2	0.10	2900
		PF		345	263	1470	0.10	8.2	0.16	1410
		PF		297	188	1240	0.18	10.8	0.19	1210
		PF		168	129	900	0.54	15.5	0.26	890
		PF		~250	260	2410	0.56	37.0	0.16	2240
900 300 700 700 300 300 800 800	Be-U	H	~0.5	250	228	1060	0.05	2.9	0.15	1140
		H		400	370	1880	0.11	7.3	0.12	2000
		H		250	238	1360	0.33	9.2	0.16	1480
		HL		250	241	400	~0	0.4	0.009	150
		PF		250	227	1080	0.05	2.9	0.25	1160
		PF		400	373	1990	0.10	7.4	0.20	2090
		PF		250	240	1450	0.30	9.7	0.25	1560

^a Be-U = 50 v/o Be and 50 v/o U-238.

^b H = Homogeneous; HL = "Homogeneous" Layered; PF = Power Flattened.

^c After initial prompt period is established.

the propriety of the "usual" equation of state for uranium. To afford a comparison with previous analyses on fast neutron systems, the "Stratton" equation of state¹ was used with appropriate modifications for simulated voids present in the core. The use of this equation of state does imply considerable uncertainty on the absolute values of the calculated parameters of interest; however they may be used for qualitative comparisons under very restricted circumstances. To accommodate the rapid spatial variation of the neutron spectrum near the core boundary, four energy groups (two fast, one intermediate and one thermal) were used for the neutronics calculations. Typical results of the excursion analyses are given in Table III-14-I.

The systems chosen for analysis were U-235 fueled cores with a heavy metal diluent. The cores contained about 45% simulated void. Some systems had a Be reflector, others had a mixture of Be and U-238 in the reflector. The moderating material in the reflector tended to lengthen the prompt neutron lifetime as well as to provide a power density at the core-reflector interface which was higher than that at the core center. During an excursion on such systems, initial material motions may take place near the core boundary. In some cases such motions may tend to shorten the prompt period relative to that used to initiate the excursion (e.g. an autocatalytic effect). This shortening of the period may be due to a change in the prompt neutron lifetime during the excursion. It may also be

due to increased reactivity due to initial material motions. The detailed influence of both these considerations remains to be investigated.

Some additional studies were concerned with the effect of radially "flattening" the power distribution. This was accomplished by discontinuously varying the loading of fuel in the diluent material to provide a "chopped" radial power distribution which is essentially flat. It was found that for given initial prompt periods, the total energy released, liberated kinetic energy, and peak pressures generated tended to be higher in the power-flattened system relative to the system with a homogeneous core composition. The difference was most pronounced for the longer prompt neutron lifetime systems.

Finally, the effect of "layering" the core was found to significantly reduce the severity of these excursions. Layering is accomplished by calculating a system of spherical shells. Some of these contain high density U²³⁵ metal. The others contain diluent materials and simulated void; the overall composition is the same as the single region homogeneous sphere. The effect of layering found here is quite similar to that obtained by Stratton.¹

REFERENCES

1. W. R. Stratton, T. H. Colvin and R. B. Lazarus, *Analysis of Prompt Excursions in Simple Systems and Idealized Fast Reactors*, Proc., 1958 Geneva Conf., 12, Paper No. 431, p. 196.

2. W. J. McCarthy, Jr., R. B. Nicholson, D. Okrent and V. Z. Jankus, *Studies of Nuclear Accidents in Fast Power Reactors*, Proc., 1958 Geneva Conf., **12**, Paper No. 2165, p. 207.
3. V. Z. Jankus, *A Theoretical Study of Destructive Nuclear Bursts in Fast Power Reactors*, Proc., Seminar on Physics of Fast and Intermediate Reactors, IAEA, Vienna **3**, 209 (1962).
4. G. Fischer, E. Barts, S. Kapil and K. Tomabechi, *Major Accident Analyses for Experimental Zero Power Fast Reactor Assemblies*, Proc., Seminar on Physics of Fast and Intermediate Reactors, IAEA, Vienna **3**, 195 (1962).
5. D. Okrent, J. M. Cook, D. Satkus, R. B. Lazarus and M. B. Wells, *AX-I, A Computing Program for Coupled Neutronics-Hydrodynamics Calculations on the IBM-407*, ANL-5977 (1959).

III-15. Natural Tungsten Cross Sections for Fast and Intermediate Neutron Spectra

R. KAISER and W. B. LOEWENSTEIN

Several interim sets of multi-group tungsten cross sections for fast and intermediate spectra have been compiled. The constants are generally based on microscopic cross section data available as of September, 1963. The sixteen group constants were subsequently used to calculate experimental integral parameters (critical size and material replacement effects) where tungsten cross sections are important. The sixteen group structure is the same as adopted by "Hansen-Roach"¹ and all integral analyses utilized their multi-group constants for materials other than tungsten.

The microscopic data were spectrum averaged as follows:

Groups 1, 2 and 3 (900 keV to 10 MeV) used the U²³⁵ fission spectrum.

Groups 4 through 14 (0.4 eV to 900 keV) used a calculated spectrum for a reflector moderated core with tungsten constants from Ref. 2.

Groups 15 and 16 (thermal to 0.4 eV) were averaged over a modified Maxwell-Boltzmann distribution which is flat from 0.2 to 0.4 eV.

Averages were carried out with the following two prescriptions:

$$a) \quad \bar{\sigma}_x = \frac{\int \sigma_x(E) \frac{\varphi(E)}{\sigma_t(E)} dE}{\int \frac{\varphi(E)}{\sigma_t(E)} dE}$$

and

$$b) \quad \bar{\sigma}_x = \frac{\int \sigma_x(E) \varphi(E) dE}{\int \varphi(E) dE},$$

where:

σ_x is the reaction cross section to be averaged

σ_t is the total cross section

φ is the appropriate spectrum.

Elastic removal cross sections were obtained by calculating a "spectrum weighted" logarithmic energy decrement for each group. Table III-15-I summarizes the results.

Inelastic cross sections and transfer matrix are based on available measurements at low energies (<2 MeV). At high energies the statistical model of the nucleus was applied. The resulting matrix was then normalized to be in substantial agreement with the "sphere transmission" measurements³. Table III-15-II gives both the total inelastic and the inelastic transfer cross sections obtained.

Capture (n, γ) cross sections are particularly uncer-

TABLE III-15-I. WEIGHTING SPECTRUM AND SPECTRUM WEIGHTED LOGARITHMIC ENERGY DECREMENTS
(16 Group Format)

Energy Group	Lower Boundary of Energy Group	Weighting Spectrum ^a φ_j	ΔU^b	$\left(\frac{\xi}{\Delta U}\right)^c$
1	3.0 MeV	422.0	1.2	0.041
2	1.4	881.0	0.76	0.020
3	0.9	762.0	0.44	0.026
4	0.4	2593.0	0.81	0.021
5	0.1	3920.0	1.39	0.0093
6	17 keV	1200.0	1.77	0.0049
7	3	165.0	1.74	0.0081
8	0.55	43.6	1.70	0.0077
9	100 eV	9.72	1.71	0.0074
10	30	2.07	1.20	0.0064
11	10	0.34	1.10	0.012
12	3	0.54	1.20	0.029
13	1	1.08	1.10	0.016
14	0.4	0.43	0.92	0.013
15	0.1	0.18	1.39	0.039
16	Thermal	0.12	—	—

^a $\varphi_j \equiv \int_{E_{\text{lower},j}}^{E_{\text{upper},j}} \varphi(E) dE$; used only for groups 4-14.

^b $\ln \frac{E_{\text{upper}}}{E_{\text{lower}}}$.

^c $\xi_{\text{tungsten}} = 0.01084$

TABLE III-15-II. TOTAL INELASTIC AND INELASTIC TRANSFER CROSS SECTIONS FOR TUNGSTEN, barns^a
(16 Group Format)

Energy Group	Lower Group Boundary, MeV	Total σ_{in}	Transfer Cross Section, $\sigma_{in\ j \rightarrow j+k}$					
			K = 0	1	2	3	4	5
1	3.0	3.0	0.60	1.21	0.33	0.54	0.28	0.04
2	1.4	2.85	0.48	0.97	0.99	0.36	0.05	—
3	0.9	2.40	1.08	0.83	0.39	0.08	0.02	—
4	0.4	1.48	1.08	0.38	0.02	—	—	—
5	0.1	0.30	0.18	0.12	—	—	—	—

^a Group structure identical to that of Table III-15-I.

TABLE III-15-III. TOTAL, TOTAL ELASTIC, TRANSPORT AND CAPTURE CROSS SECTIONS FOR TUNGSTEN, barns^a
(16 Group Format)

Energy Group	Lower Boundary of Group	σ_t	σ_s	σ_c	σ_c^b	σ_{tr}^b	σ_{tr}	$1-\bar{\mu}^b$	$1-\bar{\mu}$
1	3.0 MeV	6.14	3.11	0.025	0.026	4.56	3.47	0.41	0.14
2	1.4	6.99	4.07	0.080	0.072	4.63	3.77	0.41	0.20
3	0.9	6.52	4.02	0.10	0.10	4.38	3.81	0.46	0.32
4	0.4	6.60	5.03	0.09	0.09	4.63	4.29	0.60	0.54
5	0.1	7.93	7.50	0.16	0.13	6.64	6.56	0.83	0.82
6	17 keV	10.14	9.87	0.263	—	9.62	—	0.947	—
7	3	12.99	12.34	0.651	—	12.84	—	0.987	—
8	0.55	15.22	13.39	1.824	—	15.17	—	0.996	—
9	100 eV	17.87	14.63	3.238	—	17.81	—	0.996	—
10	30	13.54	12.89	0.645	—	13.49	—	0.996	—
11	10	41.68	33.33	8.359	—	41.56	—	0.996	—
12	3	13.89	6.15	7.745	—	13.87	—	0.996	—
13	1	8.43	5.33	3.101	—	8.41	—	0.996	—
14	0.4	9.26	5.52	3.741	—	9.24	—	0.996	—
15	0.1	12.91	5.58	7.326	—	12.89	—	0.996	—
16	Thermal	20.02	5.61	14.412	—	20.00	—	0.996	—

^a σ_t = total; σ_s = total elastic; σ_c = total capture; σ_{tr} = total transport.

^b Most frequently used for integral analyses; see text.

tain. Some experimental results differ by a factor of two, probably because of normalization difficulties. Table III-15-III summarizes the compiled spectrum averaged cross sections. The most frequently used capture cross sections for analysis are denoted with an asterisk. These represent some judgment as to which of the microscopic data may be normalized consistent with the U²³⁵ fission cross sections.

Table III-15-III also gives appropriate spectrum averaged total (σ_t), total elastic (σ_s) and transport (σ_{tr}) cross sections as well as the constant relating to the average angle of scattering ($\bar{\mu}$) in the laboratory system. With respect to the latter one again finds reported differing data at high energies; hence two sets have been assembled at high energies with the most

frequently used $\bar{\mu}_j$ denoted by an asterisk. These represent some judgement, based on criticality calculations, as to the validity of some reported angular distributions.

A similar set of tungsten multigroup constants was assembled having 24 energy groups to thermal. Here, the high energy inelastic cross sections were not normalized to integral sphere measurements. Subsequent application showed that calculated spectra are probably too energetic although the reactivity of a tungsten "Jemima" assembly² was quite well predicted. Table III-15-IV gives the group structure and all cross-sections except the inelastic transfer cross sections which are given in Table III-15-V. The inelastic transfer cross sections out of groups 1 and 2 on Table III-15-V are particularly uncertain and should be reevaluated before extensive application of these constants.

TABLE III-15-IV. TOTAL, TOTAL ELASTIC, TRANSPORT AND CAPTURE CROSS SECTIONS FOR TUNGSTEN, barns^a
(24 Group Format)

Energy Group	Lower Group Boundary	σ_t	σ_s	σ_c	$1-\bar{\mu}$	σ_{tr}	$\left(\frac{\xi}{\Delta U}\right)$	Weighting Spectrum $\bar{\phi}_j^b$
1	3.67 MeV	5.86	2.61	0.021	0.41	4.35	0.038	0.024
2	2.23	6.83	3.60	0.045	0.41	4.72	0.028	0.164
3	1.35	6.99	3.68	0.086	0.41	4.85	0.025	0.277
4	0.83	6.93	4.19	0.101	0.48	4.75	0.021	0.342
5	0.50	7.04	5.45	0.090	0.62	4.99	0.028	0.472
6	0.30	7.45	6.30	0.181	0.75	5.89	0.025	0.815
7	0.18	8.08	7.31	0.117	0.83	6.86	0.022	1.15
8	0.11	8.66	8.21	0.167	0.88	7.73	0.022	1.21
9	67 keV	9.32	9.11	0.217	0.94	8.81	0.022	1.25
10	41	10.05	9.81	0.238	0.96	9.65	0.022	1.30
11	25	10.88	10.58	0.300	0.97	10.57	0.023	1.34
12	15	11.81	11.42	0.385	0.98	11.57	0.021	1.40
13	9.1	12.66	12.13	0.531	0.98	12.48	0.022	1.44
14	5.5	13.29	12.56	0.729	0.99	13.16	0.022	1.50
15	2.1	14.33	13.26	1.074	0.993	14.24	0.012	1.57
16	0.5	15.39	13.18	2.203	0.996	15.34	0.010	1.91
17	100 eV	20.82	17.24	3.576	0.996	20.75	0.0092	3.51
18	30	15.37	14.58	0.789	0.996	15.32	0.010	5.30
19	10	51.90	41.52	10.378	0.996	51.75	0.012	6.77
20	3	16.15	7.26	8.885	0.996	16.12	0.020	15.6
21	1	8.50	5.38	3.129	0.996	8.49	0.015	63.4
22	0.4	8.67	5.21	3.468	0.996	8.65	0.0081	—
23	0.1	12.98	5.60	7.384	0.996	12.96	0.039	—
24	Thermal	20.12	5.61	14.514	0.996	20.10	—	—

^a σ_{tr} = total transport; σ_t = total; σ_s = total elastic; σ_c = total capture (n, γ).

$\bar{\mu} = \cos i_{lab}$ for elastic scattering.

$\frac{\xi}{\Delta U}$ = spectrum weighted logarithmic decrement.

$${}^b \bar{\phi}_j = \frac{\int_{E_{lower_j}}^{E_{upper_j}} \phi(E) dE}{\Delta E_j}$$

TABLE III-15-V. TOTAL INELASTIC AND INELASTIC TRANSFER CROSS SECTIONS FOR TUNGSTEN, barns^a
(24 Group Format)

Energy Group	Lower Group Boundary, MeV	Total σ_{in}	Transfer Cross Section, ^b $\sigma_{in j \rightarrow j+k}$													
			K = 0	1	2	3	4	5	6	7	8	9	10	11	12	13
1	3.67	3.23	(1.08)	(2.15)												
2	2.23	3.18	(0.706)	(2.326)	(0.148)											
3	1.35	3.22	0.477	2.028	0.466	0.249										
4	0.83	2.64	0.586	1.575	0.096	0.165	0.084	0.052	0.032	0.020	0.012	0.007	0.004	0.004	0.002	0.001
5	0.50	1.50	0.580	0.769	0.063	0.030	0.021	0.014	0.009	0.006	0.003	0.002	0.002	0.001		
6	0.30	0.971	0.370	0.55	0.014	0.015	0.009	0.006	0.004	0.002	0.001					
7	0.18	0.65		0.38	0.23	0.040	—	—	—	—	—					
8	0.11	0.30			0.096	0.081	0.051	0.030	0.018	0.015	0.009					

^a Group structure identical to that of Table III-15-IV.

^b The values indicated in parentheses should be carefully evaluated to be consistent with measured distributions of inelastically scattered neutrons.

REFERENCES

1. G. Hansen and W. H. Roach, *Six and Sixteen Group Constants for Fast and Intermediate Critical Assemblies*, LAMS-2543 (1961).

2. C. Cohn, G. Golden, B. Hoglund, W. Loewenstein, G. Rosenberg, D. Sparks and C. Youngdahl, *Basic Material Resulting From ANL Rocket Study*, ANL-6656 (1963).

3. *Reactor Physics Constants*, ANL-5800, 2nd edition, p. 611.

III-16. Verification of Tungsten Cross Sections

K. ALMENAS

The utility of a series of measurable critical assembly parameters for the verification of tungsten multigroup constants was studied. Measurable parameters as used here refer to experimentally determined quantities such as fission ratios, Rossi- α 's etc. The basic analysis included prediction of the interesting parameters by using five separate sets of tungsten cross sections. These differed from one another primarily in details of averaging the basic microscopic nuclear constants. They also reflected some uncertainties in the knowledge of nuclear data. The calculated differences in the five separate calculations were then analyzed. The objectives of the study were primarily to determine which measurable parameters should be employed in the verification of the tungsten multigroup cross sections.

The measurable parameters included the critical mass, central material replacement data, fission ratios, Rossi- α , and capture cross sections. Most of the measurable parameters were indirectly influenced by the presence of tungsten since the tungsten affects the core spectrum. In the measurements it is necessary that tungsten be a major constituent of the core.

Three critical assemblies have been analyzed:

(1) A core containing U-235, U-238 and tungsten;

this assembly facilitates comparison of the tungsten constants with U-238 constants

(2) A core containing U-235, aluminum and tungsten; the spectrum is determined by and is sensitive to the tungsten inelastic cross sections

(3) A core containing U-235, carbon and tungsten; this assembly has a less energetic spectrum than the above two systems

The influence of several reflectors was also considered. These were fast spectrum assemblies with non-moderating reflectors and were typical of those for the initial ZPR-IX investigations. In such reactors, only the cross sections above 100 eV (groups 1-9) have any significant effect. This is demonstrated in Table III-16-I for the softer spectrum system cited above. All of the calculations utilized the multigroup constants and structure of Ref. 1. The tungsten constants are based on Paper No. III-15.

Some of the results pertinent to the analysis are given below.

CRITICAL MASS

The critical mass is one of the more accurately measured and one of the more important parameters for

TABLE III-16-I. NORMALIZED $\varphi_j\varphi_j^*$ VALUES AT CENTER OF A ZPR-IX ASSEMBLY^a
(~ 35 v/o W, ~ 35 v/o C and ~ 10 v/o U-235)

Energy Group J	Lower Energy Limit	$\varphi_j\varphi_j^*$ at Core Center ^{b, c}				
		W 30	W 35	W 37	W 40	W 43
1	3.0 MeV	0.0398	0.0381	0.0379	0.0380	0.0373
2	1.4 MeV	0.0920	0.0907	0.0903	0.0904	0.0890
3	0.9 MeV	0.0650	0.0810	0.0804	0.0805	0.0798
4	0.4 MeV	0.2008	0.2217	0.2200	0.2203	0.2200
5	0.1 MeV	0.3436	0.3282	0.3337	0.3341	0.3352
6	17 keV	0.1997	0.1913	0.1893	0.1899	0.1901
7	3 keV	0.051	0.0428	0.0426	0.0415	0.0427
8	0.55 keV	0.0076	0.0055	0.0055	0.0050	0.0055
9	100 eV	0.0004	0.00044	0.00044	0.00027	0.00044
10	30 eV	—	0.00003	0.00003	—	0.00003
		1.0	1.0	1.0	1.0	1.0

^a The assembly is reflected by 30 cm of 94% density Al. Calculations are multigroup diffusion theory in spherical geometry.

^b φ_j = neutron flux

φ_j^* = neutron importance.

^c W 37 "Most Frequently Used" from Ref. 2. W 43 "Alternate" from Ref. 2. W 35 and W 40 are similar constants differing primarily in the manner of averaging high energy capture cross sections. The number (W 30, etc) refer to the material designation in ANL Multigroup Set No. 201.

TABLE III-16-II. CALCULATED AND EXPERIMENTAL CRITICAL RADII FOR BARE U-235-U-238-W ASSEMBLIES^a

Core Composition, v/o			Critical Radius, cm				
U-235	U-238	W	Exp. ^b	W 35 ^c	W 37 ^c	W 40 ^c	W 43 ^c
53.5	3.8	42.6	12.67	12.66	12.61	12.61	—
37.5	2.7	59.8	16.00	16.11	—	—	—
28.8	2.1	69.1	19.27	19.43	19.15	19.14	19.67

^a Calculations performed by R. Kaiser and D. Fuller using the DSN code in the S_4 approximation.

^b Unpublished LASL data.

^c See footnote c of Table III-16-I.

TABLE III-16-III. CALCULATED CRITICAL MASSES OF SOME ZPR-IX ASSEMBLIES^a

	Approximate Core Composition (W Cross Section Set ^b)														
	~ 35 v/o W, ~ 35 v/o U-238, ~ 10 v/o U-235					~ 35 v/o W, ~ 16 v/o Al, ~ 10 v/o U-235					~ 35 v/o W, ~ 35 v/o C, ~ 10 v/o U-235				
	W 30	W 35	W 37	W 40	W 43	W 30	W 35	W 37	W 40	W 43	W 30	W 35	W 37	W 40	W 43
Critical radius (cm)	43.1	41.55	40.07	40.0	40.55	39.2	38.0	37.1	37.0	37.6	35.7	35.6	34.9	35.0	35.4
Critical volume (liters)	352	300	269	268	279	253	229	213	212	222	190	188	177	179	185
Critical mass (kg U-235)	651	556	497	495	515	467	423	394	392	410	351	348	328	330	342

^a All calculations are multigroup diffusion theory in spherical geometry. All cores are reflected by a 30 cm thick 94% density Al reflector.

^b See footnote c of Table III-16-I.

cross section studies. Tables III-16-II and III-16-III cite a series of critical mass calculations.

Table III-16-II compares the only available experimental tungsten-diluted critical assembly data (prior to ZPR-IX operation) with calculated values. The critical assemblies were bare, compact and had extremely hard spectra. Only the upper five energy groups (above 0.1 MeV) had any significance in these calculations. Table III-16-II shows that the agreement of the predicted critical radius with the experimental radius is within experimental error. No significant difference exists among the four sets. The BSN analytical program and the U-235 cross sections have been successful in predicting critical radii for this type of system. Therefore, the agreement (Table III-16-II) indicates that reasonable multigroup constants were used for the high energy groups.

Table III-16-III gives critical mass computations for three ZPR-IX assemblies. The spectra of these assemblies were considerably less energetic than those for the assemblies of Table III-16-II. In these cases, the differences in the tungsten cross sections become significant and resulted in differences that may be experimentally detected.

CENTRAL TUNGSTEN WORTH

Central material replacement measurements can give information about the combined effect of capture and inelastic scattering constants. The measurements require only small amounts of tungsten and were performed on a number of ZPR-III systems. A comparison of theory and experiment is given in Table III-16-IV. The perturbation theory calculations have been performed with both unperturbed and perturbed real fluxes. Thus the lower "block" of figures in Table III-16-IV is based on real fluxes (calculated by DSN) which have been perturbed by a 1.2 kg tungsten sample at the center of the core. Two methods of comparing theory and experiments were used. These refer to the manner in which period measurements are re-

TABLE III-16-IV. COMPARISON OF PREDICTED WITH MEASURED TUNGSTEN MATERIAL REPLACEMENT EFFECTS^a

X-section Number ^b	ZPR-III Assembly No. 22						ZPR-III Assembly No. 38						ZPR-III Assembly No. 39					
	Absolute normalization			Relative normalization			Absolute normalization			Relative normalization			Absolute normalization			Relative normalization		
	$(\Delta\rho)^C$ lh/kg	$(\Delta\rho)^E$ lh/kg	$\frac{E-C}{E}$	$\bar{\sigma}_a^C$, mb.	$\bar{\sigma}_a^E$, mb.	$\frac{E-C}{E}$	$(\Delta\rho)^C$, lh/kg	$(\Delta\rho)^E$, lh/kg	$\frac{E-C}{E}$	$\bar{\sigma}_a^C$, mb.	$\bar{\sigma}_a^E$, mb.	$\frac{E-C}{E}$	$(\Delta\rho)^C$ lh/kg	$(\Delta\rho)^E$ lh/kg	$\frac{E-C}{E}$	$\bar{\sigma}_a^C$, mb.	$\bar{\sigma}_a^E$, mb.	$\frac{E-C}{E}$
W 30	-24.43	-24.6	+0.007	-179.4	-170.1	-0.055	-15.03	-14.4	-0.04	-161.2	-159.2	-0.013	-10.46	-7.68	-0.361	-160.6	-128.6	
W 35	-22.60	-24.6	+0.008	-166.1	-170.1	+0.024	-14.33	-14.4	+0.005	-151.1	-159.2	+0.051	-9.21	-7.68	-0.2	-149.4	-128.6	-0.162
W 37	-20.79	-24.6	+0.15	-152.8	-170.1	+0.102	-13.36	-14.4	+0.078	-139.6	-159.2	+0.123	-8.45	-7.68	-0.1	-136.1	-128.6	-0.058
W 40	-20.76	-24.6	+0.16	-152.8	-170.1	+0.102	-13.36	-14.4	+0.072	-139.6	-159.2	+0.123	-8.43	-7.68	-0.09	-136.1	-128.6	-0.058
W 43	-20.76	-24.6	+0.16	-152.8	-170.1	+0.102	-13.47	-14.4	+0.064	-141.8	-159.2	+0.109	-8.44	-7.68	-0.1	-136.1	-128.6	-0.058
W 30	-26.56	-24.6	-0.08	-186.9	-170.1	-0.099	-16.08	-14.4	-0.117	-169.1	-159.2	-0.062	-10.76	-7.68	-0.401	-157.3	-128.6	-0.233
W 35	-24.09	-24.6	+0.02	-175.3	-170.1	-0.031	-15.06	-14.4	-0.046	-158.3	-159.2	+0.006	-10.25	-7.68	-9.335	-150.1	-128.6	-0.167
W 37	-23.11	-24.6	+0.06	-162.8	-170.1	+0.043	-13.97	-14.4	+0.03	-146.8	-159.2	+0.078	-9.4	-7.68	-0.224	-137.9	-128.6	-0.072
W 40	-23.06	-24.6	+0.06	-162.8	-170.1	+0.043	-13.94	-14.4	+0.032	-146.8	-159.2	+0.078	-9.38	-7.68	-0.221	-137.9	-128.6	-0.072
W 43	-23.05	-24.6	+0.06	-162.0	-170.1	+0.048	-13.93	-14.4	+0.033	-146.1	-159.2	+0.082	-9.39	-7.68	-0.223	-137.9	-128.6	-0.072

^a Explanation of table: Superscripts C and E refer to calculated and experimental values, respectively. All calculations based on perturbation theory. Upper "block" utilized perturbed real fluxes (obtained from DSN), lower block utilized unperturbed multigroup diffusion theory. Comparison with experiment was done by two methods: (a) Absolute basis. Calculated β_{eff} and a normalization integral for each assembly. Calculated reactivities were then converted to inhours; (b) Relative basis. An average value of $(\nu - 1 - \alpha)\sigma_f$ Pu-239.

^b See footnote c of Table III-16-I.

TABLE III-16-V. $\sigma_f(\text{Np-237})/\sigma_f(\text{U-235})$ FOR A TYPICAL ASSEMBLY^a

Tungsten Constants ^b	$\sigma_f(\text{Np-237})/\sigma_f(\text{U-235})$				
	W 30	W 35	W 37	W 40	W 43
At core center	0.378	0.406	0.404	0.404	0.402
5 cm from reflector	0.363	0.385	0.382	0.382	0.383
Core average	0.369	0.394	0.391	0.391	0.391
12 cm from core in a W reflector ^c	0.099	0.104	0.099	0.098	0.107

^a Calculated for a core containing ~35 v/o W, ~16 v/o Al and ~10 v/o U-235 reflected by 30 cm of 94% density Al.

^b See footnote c of Table III-16-I.

^c A separate calculation where 30 cm full density W reflector was used.

lated to reactivity. This is done by calculating the relationship between inhours and reactivity or by assuming that one may accurately predict the central worth of PU-239. As shown in Table III-16-IV, the use of perturbed fluxes and the two different methods of correlating calculated and experimental data result

in significant absolute differences. These are sufficiently great that a choice of the "best" set of constants could depend on the method of reactivity correlation.

FISSION RATIOS

The fission ratios of U-238 or Np-237 to U-235 can give an estimate of the neutron flux fraction in the upper three to four energy groups. The ratios are thus a reasonable indication of the accuracy of the slowing down matrix. The high tungsten-content assemblies can provide evidence regarding the inelastic cross sections in groups 1-4. Some typical spatially dependent calculations for $\sigma_f^{\text{Np-237}}/\sigma_f^{\text{U-235}}$ ratios are given in Table III-16-V.

REFERENCES

1. G. E. Hansen and W. H. Roach, *Six and Sixteen Group Cross Sections for Fast and Intermediate Critical Assemblies*, LAMS-2543 (1961).
2. C. Cohn, G. Golden, B. Hoglund, W. Loewenstein, G. Rosenberg, D. Sparks and C. Youngdahl, *Basic Material Resulting from ANL Rocket Study*, ANL-6656 (1963).

III-17. The Neutronics of Reactor Control with Reflector Materials

K. ALMENAS

INTRODUCTION

In some fast reactor applications it is extremely advantageous to control the system without utilizing moving mechanisms in the core. The use of control mechanisms outside of the core is frequently inspired by the high temperature core environment. This causes engineering problems in connection with moving control mechanisms. These problems may be circumvented if it is feasible to relocate such control mechanisms in the reflector adjacent to the core, where the environment is at a lower temperature. This study was initiated to identify the important qualitative and quantitative neutronic parameters related to reflector control mechanisms. The parameters include the nuclear constants of the poison, the reflector and the core as well as the relative importance of their interaction. The analyses distinguished among absorption, energy degradation and leakage phenomena in the reflector. The individual reactions were analyzed as a function of energy and position.

ANALYTICAL METHODS

Eight reflectors were considered. The reference core contained tungsten and highly enriched UO₂ with

about 40% void. The reflectors were assumed to contain a single material for each investigation. They were 25 cm thick and contained about 30% void.

The control poison was simulated in the reflectors with a 2 cm thick concentric region located 4 cm from the core reflector interface. This region was assumed to contain about 50% void. The remainder of the annulus contained 20 v/o control material and 30 v/o reflector material.

DSN calculations in spherical geometry with the 16-group Hansen and Roach cross sections¹ and modifications (see Paper No. III-15) were used in the analysis. The geometric model overestimates the effect of the reflector when compared with realistic finite cylinders with control poison located in the radial reflector only. For this study such an overestimate is advantageous since it tends to emphasize effective neutronic differences of various control and reflector materials.

The following three calculations were carried out for each of the reflectors:

1. A reference problem including a reflector free of poison. The calculated reactivity for this con-

TABLE III-17-I. SUMMARY OF CONTROL PROBLEM RESULTS

Reflector	Poison	Control Span, % ($\Delta k/k$)	Relative Worth of Reflector	Net Outward ^a Leakage Fraction	Total Fraction ^a Absorbed in B	$L_{No B} - L_B^b$	Control Span $\frac{L_{No B} - L_B}{L_B}$
U	No B		0	0.3825			
U	B	1.04		0.3841	0.0462	-0.00165	6.3
U	B + H	1.22		0.3856	0.0359	-0.0031	3.9
Al	No B		-5.0	0.3489			
Al	B	0.52		0.3525	0.0291	-0.00367	1.42
Al	B + H	0.70		0.3525	0.0184	-0.00363	1.94
Al ₂ O ₃	No B		+2.7	0.2763			
Al ₂ O ₃	B	2.66		0.3035	0.0693	-0.0272	0.98
Al ₂ O ₃	B + H	2.40		0.2982	0.0526	-0.0219	1.1
Ni	No B		+1.0	0.3025			
Ni	B	1.51		0.3147	0.0462	-0.0121	1.24
Ni	B + H	1.71		0.3147	0.0392	-0.0122	1.40
Fe	No B		-1.8	0.3239			
Fe	B	1.14		0.3330	0.0389	-0.0091	1.26
Fe	B + H	1.17		0.3311	0.0308	-0.0072	1.6
Mo	No B		+2.1	0.2969			
Mo	B	1.19		0.3058	0.0415	-0.0089	1.33
Mo	B + H	1.36		0.3061	0.0304	-0.0092	1.47
C	No B		+0.67	0.2862			
C	B	3.45		0.3208	0.0893	-0.0346	1.0
C	B + H	3.18		0.3156	0.0725	-0.0293	1.1
Zr	No B		+0.83	0.3033			
Zr	B	1.57		0.3159	0.0422	-0.0126	1.24
Zr	B + H	1.54		0.3130	0.0306	-0.0097	1.54

^a Leakage fractions are normalized to one fission neutron produced in the core.

^b Core leakage of unpoisoned system minus core leakage of poisoned system.

figuration represents the most reactive system configuration.

2. A problem with natural boron in the "poison" region.
3. A problem with one-half of the natural boron volume occupied by water density hydrogen. (Under some circumstances a mixture of poison and moderator was found to be more effective than poison without moderator in the core.²)

RESULTS AND INTERPRETATION

The analytical results are summarized in Table III-17-I. The table presents a comparison of the control-related effectiveness of the various reflectors. The parameter of greatest practical importance is the "control span". This is defined as the reactivity difference existing between the boron-free and boron-containing reactors. This parameter is given in the third column of Table III-17-I. In terms of "control span", aluminum is shown to be the poorest reflector while Al₂O₃ is quite good, second only to carbon.

The fourth column of Table III-17-I illustrates the neutronic differences of the unperturbed reflectors. The predicted reflector worth is given relative to the depleted uranium reflector. The definition of this term is:

[Worth of Reflector A]

$$= \frac{k_{eff}(\text{reflector A}) - k_{eff}(\text{depleted U reflector})}{k_{eff}(\text{depleted U reflector})} \quad (1)$$

The observed difference between aluminum and Al₂O₃ reflectors becomes even more pronounced on this basis than is implied by the "control span".

There is no simple correlation between reflector worth and control span. This may be seen by comparing the values for the carbon and the molybdenum.

The fifth column gives the net leakage from the core. The leakage fractions were evaluated from a detailed energy dependent neutron balance. The energy dependence of the leakage fraction is given in Table III-17-II for the reference reactors. Except for the depleted uranium reflector, the leakages become negative for all cases below 17 keV. This means that for neutron energies below 17 keV, there is a net leakage into the core from the reflector. The absolute value of the back leakage is small. It is, however, very important since the reflector-located poison most directly affects it. Table III-17-II illustrates the disproportionate importance of the lower energy neutrons [17 keV-100 eV] in producing the observed differences in the reflectors. As seen, the total leakage and the group leakages down to 0.1 MeV differ only slightly

TABLE III-17-II. GROUP DEPENDENT CORE LEAKAGE FOR VARIOUS UNPOISONED REFLECTORS

Energy Group	Lower Energy Limit	Depl. Uranium Reflector	Aluminum Reflector	Al ₂ O ₃ Reflector	Nickel Reflector	Iron Reflector	Molybdenum Reflector	Carbon Reflector	Zirconium Reflector
1	3 McV	0.04275	0.02319	0.02773	0.02612	0.02391	0.02582	0.03003	0.02611
2	1.4 MeV	0.08081	0.04043	0.04542	0.04846	0.04730	0.04781	0.05132	0.04729
3	0.9 MeV	0.05713	0.04255	0.04753	0.03489	0.04042	0.03329	0.05112	0.04301
4	0.4 MeV	0.10760	0.10501	0.10896	0.08871	0.09577	0.08261	0.12068	0.08832
5	0.1 MeV	0.06580	0.10670	0.09682	0.09394	0.09787	0.08587	0.10823	0.08936
6	17 keV	0.02768	0.03187	0.000924	0.01708	0.02510	0.02277	0.00690	0.01688
7	3 keV	0.000579	-0.000392	-0.02248	-0.00126	-0.00270	-0.00129	-0.02437	-0.00559
8	0.55 keV	0.000110	-0.000402	-0.01405	-0.00254	-0.00224	-3.32 × 10 ⁻⁸	-0.01962	-0.00175
9	100 eV	6.93 × 10 ⁻⁶	-6.90 × 10 ⁻⁵	-0.00760	-0.00148	-0.000776	+1.75 × 10 ⁻⁶	-0.01357	-0.00317
10	30 eV	1.16 × 10 ⁻⁷	-8.07 × 10 ⁻⁶	-0.00314	-0.00684	-0.000350	+1.75 × 10 ⁻⁷	-0.00699	-4.46 × 10 ⁻⁶
11	10 eV	5.92 × 10 ⁻¹⁰	-1.13 × 10 ⁻⁶	-0.00168	-0.000373	-0.000197	-1.29 × 10 ⁻⁸	-0.00467	-7.81 × 10 ⁻⁶
12	3 eV	1.54 × 10 ⁻¹¹	-1.64 × 10 ⁻⁷	-0.00106	-0.000231	-0.000125	-2.27 × 10 ⁻⁹	-0.00374	-1.53 × 10 ⁻⁶
13	1 eV	4.71 × 10 ⁻¹³	-1.81 × 10 ⁻⁸	-0.000505	-9.02 × 10 ⁻⁸	-5.24 × 10 ⁻⁸	-3.61 × 10 ⁻¹⁰	-0.00232	-2.35 × 10 ⁻⁷
14	0.4 eV	3.66 × 10 ⁻¹⁵	-2.48 × 10 ⁻⁹	-0.000263	-3.01 × 10 ⁻⁸	-1.87 × 10 ⁻⁸	-5.93 × 10 ⁻¹¹	-0.00157	-4.23 × 10 ⁻⁸
15	0.1 eV	-8.14 × 10 ⁻¹⁸	-4.02 × 10 ⁻¹⁰	-0.000194	-9.23 × 10 ⁻⁸	-6.12 × 10 ⁻⁸	-6.49 × 10 ⁻¹²	-0.00164	-8.75 × 10 ⁻⁹
16	Thermal	-5.37 × 10 ⁻¹⁹	-3.80 × 10 ⁻¹¹	-0.000148	-8.14 × 10 ⁻⁷	-6.55 × 10 ⁻⁷	-1.99 × 10 ⁻¹³	-0.00354	-1.17 × 10 ⁻⁹
Total		0.38247	0.34888	0.27626	0.30251	0.32389	0.29688	0.28625	0.30326

for the various reflectors, but the differences below 17 keV in some cases amount to orders of magnitude.

The sixth column of Table III-17-I shows the neutron fraction absorbed in the control poison. The data show that upon introducing hydrogen into the control region the fraction of neutrons absorbed in the boron decreased for all reflectors, even for those for which the hydrogen addition resulted in an increased control

span. This is due to the fact that neutrons can be prevented from re-entering the core by down-scattering as well as by absorption. The energy distribution of the core adjoint function shows a trough in the energy region from 5 keV to 3 eV. This decrease in neutron importance reflects the resonance absorption in tungsten in this energy region. Reactivity can thus be decreased even in the core by down-scattering

TABLE III-17-III. ENERGY DISTRIBUTION OF BORON ABSORPTION IN VARIOUS REFLECTORS
(Source in Boron Free Problems Normalized to 1)

Energy Group	Depl. Uranium	Aluminum	Al ₂ O ₃	Nickel	Iron	Molybdenum	Carbon	Zirconium
1	0.000606	0.000104	0.000148	0.000452	0.0000827	0.0000858	0.0000871	0.0000848
2	0.00140	0.000422	0.000447	0.000767	0.000324	0.000398	0.000428	0.000392
3	0.000607	0.000271	0.000209	0.000398	0.000346	0.000565	0.000223	0.00143
4	0.00366	0.00201	0.00158	0.002802	0.002528	0.00374	0.00144	0.00260
5	0.01972	0.01087	0.01042	0.01280	0.012631	0.01487	0.00861	0.01302
6	0.01512	0.01042	0.01822	0.01431	0.012568	0.01492	0.01486	0.01462
7	0.00449	0.00398	0.01635	0.00664	0.005821	0.00592	0.01765	0.00748
8	0.000555	0.000923	0.01133	0.003851	0.002846	0.000922	0.01687	0.00222
9	0.0000325	0.000143	0.00642	0.002365	0.001094	0.0000683	0.01314	0.000411
10	7.77 × 10 ⁻⁷	0.0000133	0.00237	0.000959	0.000393	2.33 × 10 ⁻⁶	0.00652	4.45 × 10 ⁻⁶
11	8.82 × 10 ⁻⁹	1.21 × 10 ⁻⁶	0.00100	0.000440	0.000178	6.79 × 10 ⁻⁸	0.00366	4.88 × 10 ⁻⁶
12	8.64 × 10 ⁻¹¹	1.09 × 10 ⁻⁷	0.000468	0.000230	0.0000886	3.92 × 10 ⁻⁹	0.00229	5.63 × 10 ⁻⁷
13	8.55 × 10 ⁻¹³	8.66 × 10 ⁻⁹	0.000189	0.000091	0.0000331	3.22 × 10 ⁻¹⁰	0.00128	5.83 × 10 ⁻⁸
14	1.57 × 10 ⁻¹⁴	7.64 × 10 ⁻¹⁰	0.0000755	0.000032	0.0000103	3.51 × 10 ⁻¹¹	0.000706	6.56 × 10 ⁻⁹
15	1.88 × 10 ⁻¹⁶	8.73 × 10 ⁻¹¹	0.0000437	0.000010	3.2 × 10 ⁻⁶	3.32 × 10 ⁻¹²	0.000623	9.34 × 10 ⁻¹⁰
16	8.88 × 10 ⁻¹⁹	6.26 × 10 ⁻¹²	0.0000242	9.3 × 10 ⁻⁷	3.3 × 10 ⁻⁷	9.79 × 10 ⁻¹⁴	0.000882	8.83 × 10 ⁻¹¹
Total	0.04619	0.02914	0.06930	0.04616	0.03894	0.04150	0.08927	0.04220
Control span (% Δk/k)	1.04	0.523	2.66	1.51	1.14	1.19	3.45	1.57

TABLE III-17-IV. ENERGY DISTRIBUTION OF LEAKAGE DIFFERENCE FOR VARIOUS REFLECTORS
(Core Leakage to Unpoisoned Reflector Minus Core Leakage to Poisoned Reflector)

Energy Group	Depl. Uranium	Aluminum	Al ₂ O ₃	Nickel	Iron	Molybdenum	Carbon	Zirconium
1	0.00155	0.00017	0.00190	0.00069	0.00047	0.00036	0.00383	0.00065
2	0.00284	0.00011	0.00239	0.00122	0.00107	0.00072	0.00560	0.00112
3	0.00103	-0.00003	0.00197	-0.00081	-0.00004	-0.00121	0.00385	0.00019
4	-0.00060	-0.00124	0.00124	-0.00335	-0.00227	-0.00289	0.00391	-0.00317
5	-0.00772	-0.00271	-0.00280	-0.00432	-0.00425	-0.00446	-0.00072	-0.00557
6	0.00090	0.00010	-0.00653	-0.00259	-0.00132	-0.00138	-0.00430	-0.00328
7	0.00031	0.00003	-0.00694	-0.00015	-0.00056	-0.00009	-0.00650	-0.00161
8	4.2×10^{-5}	-0.00006	-0.00672	-0.00075	-0.00094	$+4.32 \times 10^{-5}$	-0.00854	-0.00071
9	-1.0×10^{-8}	-3.06×10^{-5}	-0.00532	-0.00088	-0.00053	$+2.18 \times 10^{-6}$	-0.00894	-0.00021
10	-8.0×10^{-9}	-5.9×10^{-6}	-0.00270	-0.00054	-0.00030	$+1.73 \times 10^{-7}$	-0.00577	-3.79×10^{-5}
11	-4.2×10^{-11}	-1.01×10^{-6}	-0.00159	-0.00033	-0.00019	-4.9×10^{-9}	-0.00432	-7.41×10^{-6}
12	-1.4×10^{-12}	-1.6×10^{-7}	-0.00105	-0.00022	-0.00012	-1.96×10^{-9}	-0.00365	-1.52×10^{-6}
13	-3.2×10^{-14}	-1.81×10^{-8}	-0.00050	-8.66×10^{-5}	-5.21×10^{-5}	-3.5×10^{-10}	-0.00230	-2.35×10^{-7}
14	1.49×10^{-15}	-2.48×10^{-9}	-0.00026	-2.76×10^{-5}	-1.87×10^{-5}	-5.89×10^{-11}	-0.00157	-4.23×10^{-8}
15	1.82×10^{-17}	-4.02×10^{-10}	-0.00019	-8.1×10^{-6}	-6.12×10^{-6}	-6.47×10^{-12}	-0.00164	-8.75×10^{-9}
16	-3.29×10^{-19}	-3.8×10^{-11}	-0.00015	-7.02×10^{-7}	-6.55×10^{-7}	-1.99×10^{-13}	-0.00354	-1.17×10^{-9}
Total	-0.00165	-0.00367	-0.02725	-0.01215	-0.00906	-0.00891	-0.03460	-0.01264

neutrons into the resonance region. The effect in the reflector is twofold: first, neutrons are scattered into this lower importance region; second, the lower energy neutrons have a smaller probability of re-entering the core. The absorption fractions thus illustrate that both down-scattering and absorption can be effective methods in decreasing reactivity.

The seventh column of Table III-17-I gives the difference between the net core leakage for the poison free case (corresponding to the most reactive configuration) and the case with the poison section (corresponding to the least reactive configuration). This represents the difference in the neutron fraction reaching the reactor produced by the movement of a control mechanism. This difference would be expected to correlate quite closely with the control span. That this is approximately the case is shown in the last column of Table III-17-I. This gives the ratio of the difference in the leakage to the control span. With the exception of the depleted uranium reflector, the value of the ratio is fairly consistent, varying from 1 to about 2. The systematic increase in this ratio for the boron plus hydrogen control sections again demonstrate the added control that may be produced by the down-scattering of neutrons.

The energy dependence of boron absorption is given in Table III-17-III. The table demonstrates the importance of the absorbed neutron energy. For example, the ratio of the total neutrons absorbed in an Al₂O₃ to an Al reflector is 2.4. However, the resulting control span differs by a factor of 5.

The energy dependence of leakage differences is given in Table III-17-IV. This table shows that the addition of poison to the reflector consistently reduces the leakage from the core for the upper two and in some cases for the upper four energy groups. For some reflectors (e.g. carbon) this reduction in leakage for the high energy neutrons represents a large fraction of the net increase in leakage between the least and most reactive configurations. Such an effect lowers the over-all control span. The introduction of poison decreases the fast neutron source near the core-reflector interface. This decreases leakage for all energy groups, the largest reduction being associated with the high energy neutrons.

SUMMARY

Qualitative conclusions from this study may provide guidelines for subsequent analyses. Zirconium, molybdenum, nickel, and iron were found to have quite similar control characteristics. The study will be extended to cover other materials (e.g. BeO) and other related aspects (e.g. the effect of coolant reactivity and power distribution).

REFERENCES

1. G. E. Hansen and W. H. Roach, *Six and Sixteen Group Cross Sections for Fast and Intermediate Critical Assemblies*, LAMS-2543 (1961).
2. W. Loewenstein, *The Control of Fast Reactors—Current Methods and Future Prospects*, Proc. 1963 IAEA Seminar on the Physics and Material Problems of Reactor Control Rods, Vienna, November 1963, (to be published).

III-18. Investigation of a Rocket Fuel Test Reactor¹

J. T. MADELL and D. R. MACFARLANE

This paper deals with the investigation of a test reactor to evaluate rocket fuel elements. In the initial stages of the investigation it is necessary to decide the major objectives of the test program; that is, which properties of the fuel must be most thoroughly investigated. The test facility may then be designed to carry out these objectives.

Since the nuclear rocket program is in its initial stage and the fuel has not been operated at design conditions, the most critical properties of the fuel have not been determined. It is therefore necessary to envision a general test program, in which the fuel is represented by single elements or clusters in an environment duplicating as closely as possible the environment of the nuclear rocket.

Duplicating the environment of a nuclear rocket presents some severe performance requirements. Both the Kiwi and Argonne types of rocket cores are characterized by a fast neutron spectrum, principally above one keV; a high temperature, greater than 1500°C; and high power densities ranging upward from a few MW/liter. On the other hand, the test facility is assumed to be the product of advanced existing technology: that is, it operates at substantially lower temperatures and power densities than is true

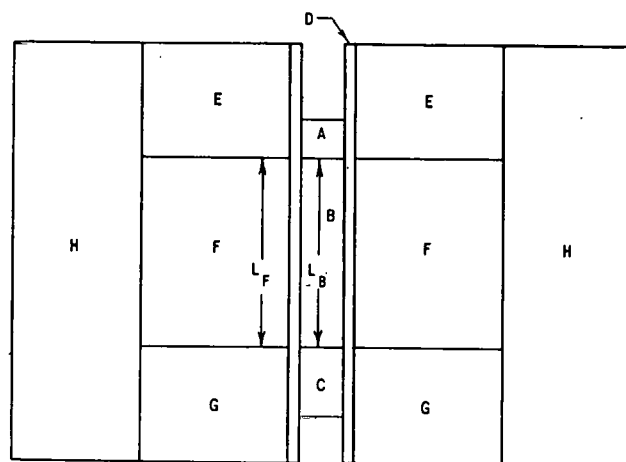
for rocket cores. The major considerations to which this study is addressed are the following:

1. Investigation of a test facility in which the power density in the test section is several times greater than that in the rest of the facility. The ratio of power density in the test section to the power density in the test core (conventional core) is the major criterion in the design.
2. Tailoring the spectrum of the neutrons entering the test section to produce the characteristic power and temperature distribution within the test section.
3. Protection of the test facility from the high temperature hydrogen flowing in the test section.

The general arrangement of the test facility is shown in Fig. III-18-1. This arrangement was used in most of the calculations. The innermost region is the test section. Next to it is a liner which protects the test reactor from the high temperatures in the test section. The next radial region is the test reactor core or a buffer region. The reactor is surrounded by a reflector.

In the study, three approaches were considered to achieve the desired requirements for a test facility. In one approach the test reactor core was of more or less conventional design; that is, a water or sodium cooled system fueled with elements that have been previously fabricated. This approach is discussed using an ANL-type rocket fuel element in the test section. In the ANL design the fuel elements are composed of uranium-oxide and tungsten, and the power densities are assumed to range from a few MW/liter to about 10 MW/liter. Survey calculations were made to investigate the types of reactors which were judged to offer the greatest promise in meeting the design requirements. These types include light- and heavy-water moderated and cooled reactors and sodium cooled reactors fueled with either uranium oxide-beryllium oxide, or uranium-zirconium. The uranium loading in these types of test reactors was selected to be about one-fourth to one-fifth of the loading in the test section in order to achieve the desired power density ratio. The coolant volume was about 50% in all cases. The results of the survey calculations are shown in Fig. III-18-2.

It is seen that light and heavy water systems exhibit lower power density ratios and large power peaks in both the test section and the test reactor, compared to the sodium cooled systems. The results can be



A - TOP TEST REFLECTOR
 B - ACTIVE TEST CORE
 C - BOTTOM TEST REFLECTOR
 D - TEST SECTION LINER
 E - TOP REACTOR REFLECTOR
 F - ACTIVE REACTOR CORE
 G - BOTTOM REACTOR REFLECTOR
 H - RADIAL REFLECTOR
 L_B AND L_F - ACTIVE HEIGHT OF TEST AND REACTOR CORES

FIG. III-18-1. Vertical Section of the Test Section, Test Reactor, and Reflector.

readily explained by looking at the spectrum plots in Fig. III-18-3. The characteristic neutron spectrum of the test section (rocket core) is fast. When a thermal or epithermal system surrounds the test section, power peaks naturally occur at the interface from the thermal or epithermal neutrons entering the test section. The soft spectrum in the test reactor also leads to a greater fissioning rate in the test reactor and this results in a lower power density ratio. That is, the peak power density is limiting in both the test section and the test reactor. A maximum power density is associated with a flat power density distribution in both regions.

The main conclusion of the survey calculations is that a fast test reactor matches more closely the spectrum of the test section and thus a larger power density ratio can be achieved. Therefore, fast systems of uranium oxide-beryllium oxide or uranium-zirconium were studied further. The characteristics investigated were the influence of the uranium and moderator concentrations in the test reactor and the size and uranium loading of the test section on the design goals of power density ratio and spectrum matching. The influence of increasing the moderator concentration is to reduce the critical size and power output at a fixed test reactor power density at the same time producing a poorer match in spectrum and hence a lower power density ratio.

The influence of the parameters—loading of the test reactor, type of test reactor, size, and loading of the test section—are presented in Fig. III-18-4 which indicates the relationship between the test reactor power and the maximum power density ratio. First, increasing the uranium loading in the test reactor reduces both the power density ratio and total power output. The presence of the moderator in this case (uranium oxide-beryllium oxide system) results in a

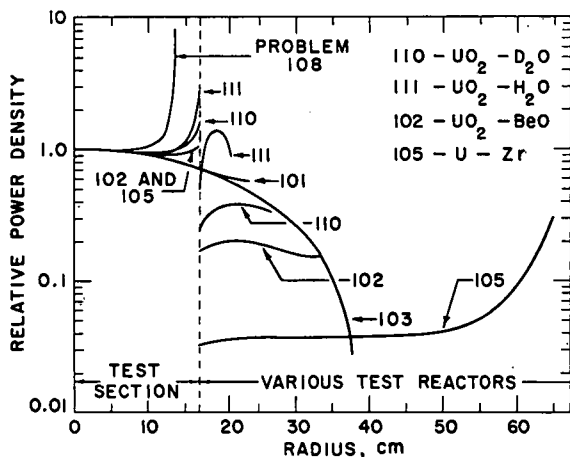


FIG. III-18-2. Relative Power Density Versus Radius for Survey Calculations.

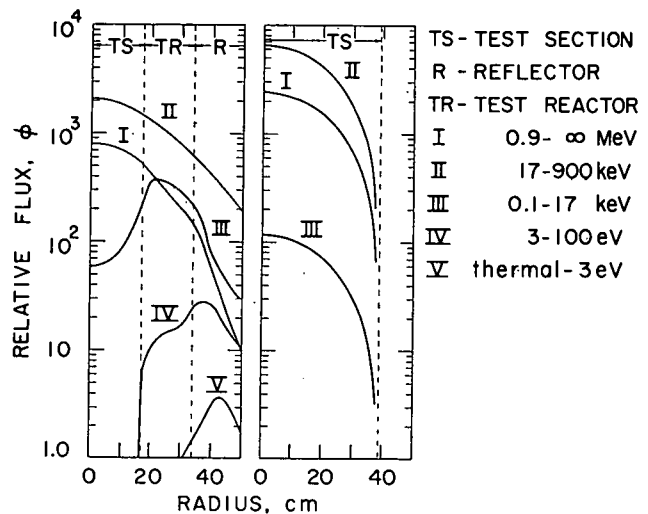


FIG. III-18-3. Relative Flux Versus Radius for Beryllium Moderated Test Reactor with a Nickel Reflector (left panel), and a Bare Test Section (right panel).

lower power production and a poorer spectrum match for a particular power density ratio. The size of the test section does not have a strong influence on the relation between the power and power density ratio, although it is generally true that a larger test section results in a smaller amount of power being produced in the test reactor. The influence of the uranium loading in the test section is quite pronounced in the case of the heaviest uranium loading; the power production is fairly reasonable. For the lightest loaded test section, the total power production is excessive. Some conclusions which are drawn from the study are:

1. A test reactor should have a fast neutron spectrum.
2. Even under most favorable values of uranium loadings in the test section, and moderate values for the maximum power density ratio, the total power production of the test reactor is high so that the facility would be expensive.
3. The systems under study exhibit a desired versatility in the possible dimensions of the test section; that is, the test section may be made larger or smaller without influencing the outer dimension of the test facility.

Other comments are also in order. Improvements are possible in the test reactor design. For example, varying the loading of fuel and moderator to reduce the total power production while keeping the power density ratio constant, and by using a thicker liner or buffer region between the test reactor and the test section. Results of calculations in which the test reactor has a variable loading of fuel and moderator are shown in Table III-18-I. For a maxi-

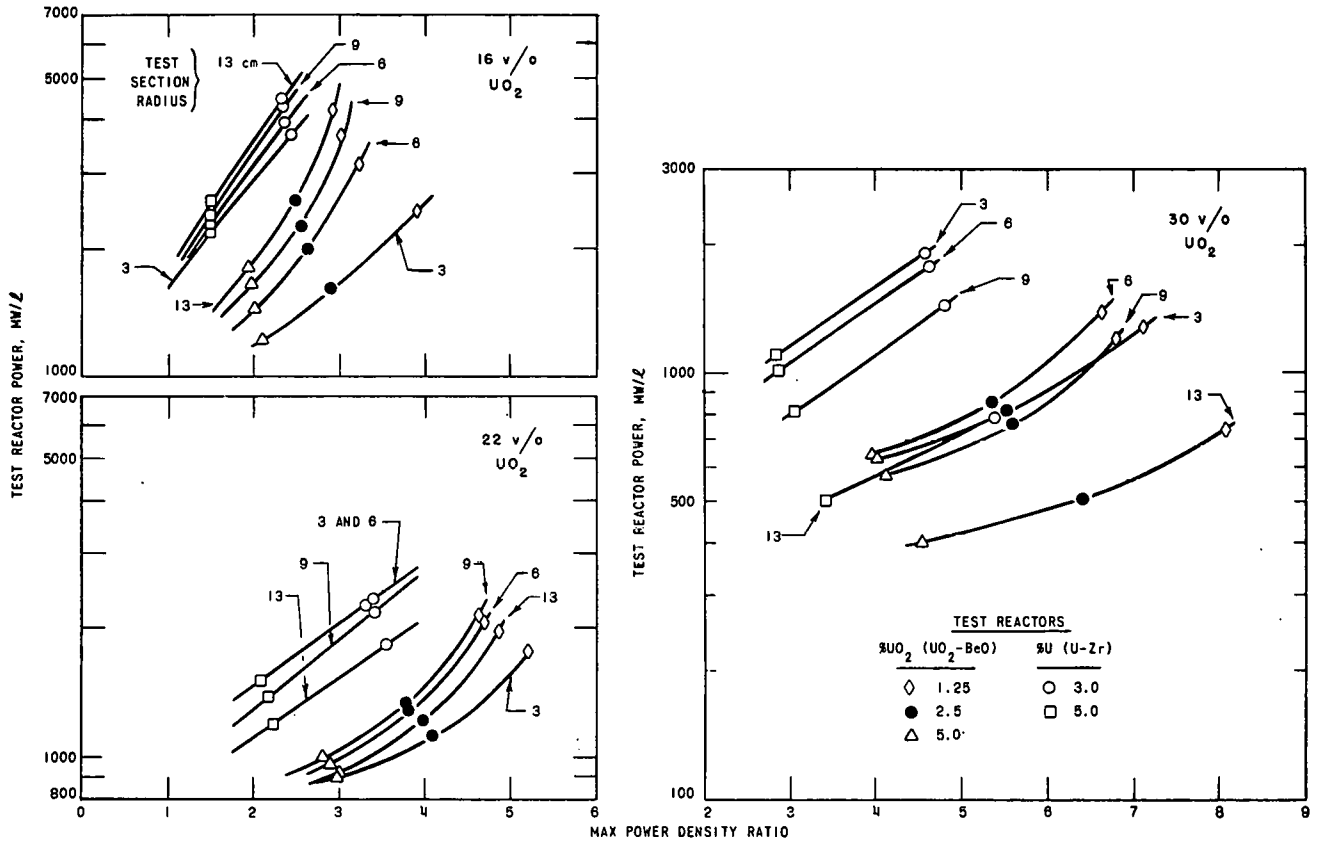


FIG. III-18-4. Test Reactor Power Versus Maximum Power Density Ratio for 16, 22, and 30 v/o UO₂ Test Sections.

TABLE III-18-I. COMPARISON OF UNIFORMLY AND VARIABLY LOADED TEST REACTORS

Type	Max Power Density Ratio	Test Section Max/Av	Volume, liters	Power, MW(l)
Uniform UO ₂ -BeO	4.0	1.17	815	1000
Variable UC ₂ -BeO	4.0	1.11	490	740
Uniform U-ZrH ₂	4.0	1.02	~1370	~2000
Variable U-ZrH ₂	4.0	1.04	920	1380

imum power density ratio of four, a variable loaded system of either uranium oxide-beryllium oxide or uranium-zirconium hydride results in a lower power output and also a better match of the spectrum, as

indicated by the values of maximum-to-average power density in the test section. These values are shown for a moderately loaded test section and are normalized to an arbitrary maximum power density in the test section of 10 MW/liter. Although it is felt that further improvements would be possible, no substantial reduction in the size of the power output is envisioned. Therefore, this approach to the design of a rocket fuel test reactor is severely limited by the size and power output of the system. Other approaches which appear to be more promising have been studied. The results of these studies will be presented at a later date.

REFERENCES

1. D. R. MacFarlane and J. T. Madell, *Investigation of a Rocket Fuel Test Reactor (RFTR)*, Trans. Am. Nucl. Soc. 7, No. 1, 68 (1964).

III-19. EBR-II Physics

W. B. LOEWENSTEIN

INTRODUCTION

The Experimental Breeder Reactor-II (EBR-II)^{1,2,3} is a fast neutron system designed to produce 62.5 MWt with a maximum power density exceeding 1000 kW/liter. The core is fueled with 370 kg of uranium containing 5 w/o fissium² alloy. The uranium is about 48% enriched in the U-235 isotope. The core is surrounded on all sides by a thick depleted uranium blanket. Most of the conversion (~90%) of fertile (U-238) to fissile (Pu-239) atoms takes place in the blanket.

The Dry Critical Experiments (without coolant sodium)⁴ were conducted during the latter half of 1961; the Wet Critical Experiments (with coolant sodium)⁵ were conducted during the latter half of 1963; the Low Power Experiments which were related to and simply extensions of the Wet Critical Experiments were conducted during the spring of 1964. The Approach to Power was initiated during June 1964.

This report is concerned with work performed prior to the initiation of the Approach to Power. Data obtained during this latter period have not yet been analyzed in detail. However, it may be noted that a preliminary measured power coefficient of reactivity of $\sim 4.2 \times 10^{-5}$ ($\Delta k/k$)/MW at full flow compares favorably with predicted values cited in Table III-19-I.

The high intensity unmoderated EBR-II neutron flux also provides a useful tool for irradiating prototype fast reactor fuels. Some considerations and problems pertaining to this application are also described.

POWER COEFFICIENT OF REACTIVITY

The power coefficient of reactivity in the EBR-II depends upon:

1. Thermal expansion of core materials,
2. Fuel subassembly bowing that may be incurred by radial temperature gradients,
3. The position of axially movable control rods relative to the stationary core subassemblies.

The first two major components of the power coefficient have been extensively studied.^{1,2,3} These results are summarized under "Previous Analyses" in Table III-19-I.

There it may be seen that if subassembly bowing is significant there may be power level ranges where a positive power coefficient may prevail. It is expected that bowing will not manifest itself in as pronounced a manner as indicated in Table III-19-I. However, it

is possible that subassembly bowing may cause a significant decrease in the magnitude of the dominant negative power coefficient of reactivity. That the negative sign of the power coefficient is retained even if subassembly bowing were to conform with the most pessimistic predictions² comes from considering the third of the major effects cited above.

In the EBR-II, the core subassemblies are supported near the bottom of the primary tank by the reactor gridplate. The control subassemblies, containing fuel, are supported by the control rod drive mechanisms which are fastened to the smaller of the rotating plugs. As the reactor power increases, the subassemblies supported at the bottom tend to thermally expand upward. The control subassemblies which are supported at their upper extremities tend to thermally expand downward. The overall effect of this relative motion is a reactivity loss. A thermal analysis⁶ shows that ~ 0.46 cm of such relative motion takes place between zero power and 62.5 MW. This relative displacement represents between -0.03 and -0.105% $\Delta k/k$ for twelve control rods. The lower value prevails if the control rods are almost 100% inserted (e.g. essentially no excess reactivity) while the larger value prevails if the control rods are about 50% inserted. Initial reactor operation is intended with most of the control rods about 80% inserted.

These reactivity changes are expressed as contributions to the power coefficient of reactivity under "Present Analysis" in Table III-19-I. Even with control rods 100% inserted, the adverse influence of bowing, if it indeed occurs in a significant manner, is severely reduced by this effect. Furthermore, it may be seen that with lesser effective control rod insertion, all net power coefficients can be made negative or all power levels under all assumed conditions. This is true in a dynamic as well as static sense since the time constant associated with the relative motions is essentially the same as for subassembly bowing and expansion of sodium coolant.

EVALUATION OF DRY CRITICAL EXPERIMENTS

The EBR-II Dry Critical Experiments⁴ were conducted in the reactor prior to filling the primary system with sodium coolant. All mechanical components and reactor fuel used in these experiments were those that are used for normal plant operation. The experimental results have also been compared with similar ones conducted in the sodium filled system.⁷ Reactivity

TABLE III-19-I. POWER COEFFICIENT OF REACTIVITY
 (Full Reactor Flow)

Power Range, MW	System Description	Previous Analyses ^a		Present Analysis ^b			
		Total reactivity change, % $\Delta k/k$	Power coefficient of reactivity, $[(\Delta k/k)/MW] \times 10^5$	Additional contribution to power coefficient of reactivity, $[(\Delta k/k)/MW] \times 10^5$		Revised power coefficient of reactivity, $[(\Delta k/k)/MW] \times 10^5$	
				100% Insertion ^c	50% Insertion ^c	100% Insertion ^c	50% Insertion ^c
0-62.5	No uniform radial expansion	-0.20	-3.2	-0.5	-1.7	-3.7	-4.9
0-62.5	Uniform radial expansion	-0.27	-4.3	-0.5	-1.7	-4.8	-6.0
0-25	The most probable configuration	-0.088	-3.5	-0.5	-1.7	-4.0	-5.2
25-34		+0.086	+1.0	-0.5	-1.7	+0.5	-0.7
34-62.5	Subassembly bowing is significant	-0.11	-4.0	-0.5	-1.7	-4.5	-5.7
0-20		-0.068	-3.4	-0.5	-1.7	-3.9	-5.1
20-56	A possible but improbable subassembly	+0.031	+0.9	-0.5	-1.7	+0.4	-0.8
56-62.5		Bowing configuration	-0.028	-4.3	-0.5	-1.7	-4.8

^a Expansion of core materials and subassembly bowing.

^b Motion of control subassemblies relative to core subassemblies.

^c Control rod insertion.

effects associated with sodium were thus directly obtained. Such comparison may become increasingly important for large core reactor systems where the sign of the sodium void coefficient of reactivity may be in doubt.

In another sense, the Dry Critical Experiments were quite useful in evaluating experimental data pertaining to EBR-II that were obtained during studies of both the basic assembly and reactor mockup on the ZPR-III facility.⁸ As expected, the ZPR-III experiments confirmed the general nature of analytical predictions for the EBR-II. What had not been expected was the fairly good accuracy associated with analytical extrapolations based on the ZPR-III data. These extrapolations were, to a large extent, based upon rather crude material replacement experiments which could not be very accurately predicted at the time.

The Dry Critical Experiments were also instrumental in finalizing a number of design parameters which either were not or could not be precisely measured on ZPR-III. Perhaps the most significant of these is the final control rod design. The mockup experiments on ZPR-III did indicate the general range of control rod worths. However, experiments in the dry reactor with the actual control rods in the actual geometric disposition indicated that the control rod reactivity worths were somewhat greater than anticipated. The greater rod worths obviated the need for providing more effective fuel-poison interchange control rods.

These experiments provided the only data on details of the power distribution within a single reflector subassembly. Such a subassembly adjacent to the core is subject to large gradients in the power density. This is due to the rapid spatial spectral shift between that portion of the subassembly facing the core and that portion of the subassembly facing other reflector subassemblies. All reflector subassemblies contain depleted uranium.

Verification of the low power monitoring capability of the normal reactor instruments was also a result of the Dry Critical Experiments. It was definitely determined from these experiments that in-core instrumentation need not be provided for reactor startup.

The Dry Critical Experiments for EBR-II were part of the pre-operational nuclear investigations which included critical experiments on ZPR-III and analytical studies. The large amount of experimental investigation for the EBR-II was to some extent exploratory to determine how such investigations might be conducted in the future. In retrospect, not all of these experiments need be conducted for a future fast reactor and certainly not for a future EBR-II loading. However, it is envisaged on the basis of EBR-II experience that a careful but not overly lengthy critical assembly program will be useful for future fast reactors. Whether or not this should include a dry critical experiment will depend primarily on the experiments that can be conducted on a zero power critical assembly.

EVALUATION OF WET CRITICAL EXPERIMENTS

The EBR-II Wet Critical Experiments^{5,7} were designed to provide two general, but not mutually exclusive, types of information. First are the data essential for operating the power reactor system. These include control rod worth, neutron source strength, nuclear instrument response, etc.. The second types of data are of more general interest including both the incremental and total worth of the sodium coolant, critical size, and the isothermal temperature coefficient of reactivity.

The most interesting implication of results from the Wet Critical Experiments comes from comparison with predicted parameters and measured results from both the earlier Dry Critical Experiments and the EBR-II Mockup of ZPR-III. In general, it was found that extrapolations of the previous experimental data are in substantial agreement with results from the Wet Critical and Low Power Experiments; they are also in good agreement with theory. The performance of all three types of critical experiments (e.g. Zero Power Mockup, Dry Critical, and Wet Critical Experiments), along with satisfactory extrapolations among the three, does suggest that some of the investigations may, in fact, have been redundant. That this is the case could not have been ascertained with confidence prior to the performance of these experiments. However, the general analytical improvements that have

been developed since this program was initiated, coupled with the EBR-II experience, may serve as a guide toward a judicious choice of experimental neutronics for future fast reactor system investigations. In making such choices one should not overlook the implications of zero power experimental investigations of systems in clean geometry. The latter do not usually feature the exact details of the engineering design.

A summary comparison between measured and predicted values for various reactor parameters is given in Table III-19-II.

The only disturbing comparison between theory and experiment concerns the power calibration. While it is by no means certain, this may easily be attributed to a very small impurity content in the graphite shield where the low power instruments are located.

The Wet Critical Experiments also demonstrate the adequate reactivity behavior of the oscillator mechanism.^{2,4} Finally, no significant reactivity effects related to flowing sodium, at zero power, were measured at 315°F.

EBR-II AS A FUEL IRRADIATION FACILITY

The relatively high core flux in the EBR-II ($\phi_{\text{center}} \approx 3.5 \times 10^{15}$) provides a great incentive to utilize the reactor for prototype fuel sample and fuel element irradiations. Provisions to irradiate prototype fuel elements have been incorporated into the EBR-II pro-

TABLE III-19-II. PREDICTED AND MEASURED EBR-II NUCLEAR PARAMETERS

	Original Prediction (Ref. 1)	ZPR-III Mockup Measurement (Ref. 8)	Dry Critical Measurement (Ref. 5)	Final Prediction (Ref. 2)	Wet Critical Measurement (Ref. 7)
Critical mass, kg U ²³⁵	172	165	228	176-184	181.2
Reactivity worth, % $\Delta k/k$					
Control rod (av)	0.45	0.37	0.35	0.34	0.345
Control rods (12-banked)	—	—	—	—	4.4
Poison (B ¹⁰ C) ^a	—	0.55	0.58	0.55	0.57
Safety rods (2)	1.5	1.36	1.0	1.3	1.2
Sodium					
Total	—	6.9	—	6.0 \pm 0.5	5.8
Core, (% $\Delta k/k$)/kg	0.14	0.116	—	0.116	—
Isothermal temp. coef., [($\Delta k/k$)/°C] $\times 10^{-5}$					
Structure (including fuel)	-1.9	—	-2.6	-2.2 \pm 0.4	—
Coolant	-1.7	—	—	-1.8	—
Total	-3.6	—	—	-4.0 \pm 0.4	-4.3 ^b
Power calibration, counts/W—sec	—	730	—	500	390
Subassembly substitution, % $\Delta k/k$					
Core center	1.43 ^c	1.53 ^c	—	1.26 ^d	1.2 ^d
Row 5 (Radius = 21 cm)	—	0.77 ^c	—	0.64 ^d	0.56 ^d
Row 6 (Radius = 27 cm)	—	—	0.35 ^d	—	0.35 ^d

^a Alternate control rod containing 253 gm of 87% enriched B¹⁰C in upper 7 in. of control rod follower.

^b Measured at 237-315°C.

^c Enriched uranium subassembly versus sodium.

^d Enriched uranium subassembly versus natural uranium subassembly of otherwise identical composition.

gram. However, the relatively small core volume as well as rapid attenuation of neutron flux in the strongly absorbing radial blanket pose some peculiar problems when brought within the framework of realistic heat removal considerations.

CORE IRRADIATIONS

The most important problem associated with the core irradiations is that the prototype fuel element irradiation subassembly holds less reactivity than the standard core subassembly it replaces. This lesser reactivity worth comes from two sources. First, the prototype subassembly contains only 19 fuel elements; the standard core subassembly contains 91 fuel elements. Second, the reactivity per fuel element is limited by decreased fuel enrichment which may be dictated by heat removal considerations.

To provide for the irradiation of a single irradiation subassembly at the center of the core, about 1% $\Delta k/k$ must be provided elsewhere. In principle this may be achieved by increasing the enrichment of the reference fuel alloy. In practice this is a very difficult and expensive approach; it may ultimately be adopted however. With the reference fuel subassembly it will be necessary to add about three fuel subassemblies at the core boundary to provide the same excess reactivity as the unperturbed core. Assuming relatively fixed total heat removal capability (~ 62.5 MW), these provisions tend toward a lower peak fission rate in the irradiation subassembly and a lower power density throughout the core. However, if the irradiation sub-

assembly is placed in a position* of lower reactivity worth, as well as somewhat lower flux only one additional fuel subassembly is required at the core boundary to provide the original excess reactivity. Thus it is evident that about three irradiation subassemblies may be thus located* with about the same reactor system perturbation as one subassembly at the center of the core. The unperturbed peak fission rate at this location* is about 80% of the maximum fission rate at the core center; the average fission rate is in excess of 70% of the maximum.

If, as is anticipated, there is a multiplicity of requests for prototype fuel irradiations, there are advantages to schedule such irradiations in positions that represent a realistic compromise between maximizing flux and minimizing the perturbing reactivity requirements. On the other hand it would not be unreasonable to make up a single subassembly containing prototype fuel elements from all requestors for irradiation in a higher flux position.

BLANKET IRRADIATIONS (W. Loewenstein and D. Fuller)

The EBR-II system is such that for about every two neutrons that are born in the core, roughly one neutron leaks from the core to be absorbed in the fertile blanket. The blanket is very efficient because of the relatively high density fertile material (~ 60 v/o). Because of this efficiency, the leakage flux is rapidly attenuated. If the leakage flux were not rapidly attenuated but merely somewhat degraded in energy, it is possible that fission rates commensurate with those in the core could be obtained. In this connection it may be noted that the EBR-II core spectrum is considerably more energetic than those spectra anticipated in the large power breeder reactors of current interest. In the EBR-II core there are virtually no fissions below 9 keV. In large power breeder reactor systems, core fissions below 9 keV can range from three to thirty percent of the total fissions. Thus there is some practical irradiation interest in spectra that are more degraded than the EBR-II core spectrum, provided the fission rates are commensurate with those in the EBR-II core.

An exploratory study was initiated to produce a fission density in the radial blanket of the EBR-II which is similar to that of the core center. A number of specific calculations were carried out. In each case the U-235 fission density $\left(\sum_{j=1}^N \sigma_{fj}^{25} \phi_j\right)$ was evaluated as a function of radial position. The flux was perturbed by altering the material composition of the radial blanket. Beryllium and carbon were each used in combination

* Approximately midway between the core center and core boundary.

TABLE III-19-III. COMPOSITION AND GEOMETRY OF "ALTERED BLANKET"

Case	Radii of "Altered" Blanket, cm		Moderating Material	Volume Fractions ^a	
	Inner	Outer		Moderator	Steel
1	40	74	Be	0.85	0.07
1a	40	74	Be	0.43	0.49
2	40	65	Be	0.85	0.07
2a	40	65	Be	0.43	0.50
3	40	55	Be	0.85	0.07
3a	40	55	Be	0.43	0.50
4	35	74	Be	0.85	0.07
4a	35	74	Be	0.43	0.50
4b	35	74	Be	0.22	0.71
5	40	74	C	0.85	0.07
5a	40	74	C	0.43	0.50
6	35	74	C	0.85	0.07
6a	35	74	C	0.43	0.50

^a Remaining volume occupied by sodium.

^b Reference blanket contains 60 v/o depleted uranium, 20 v/o steel and 20 v/o sodium. Inner and outer radii are ~ 25 and 79 cm, respectively.

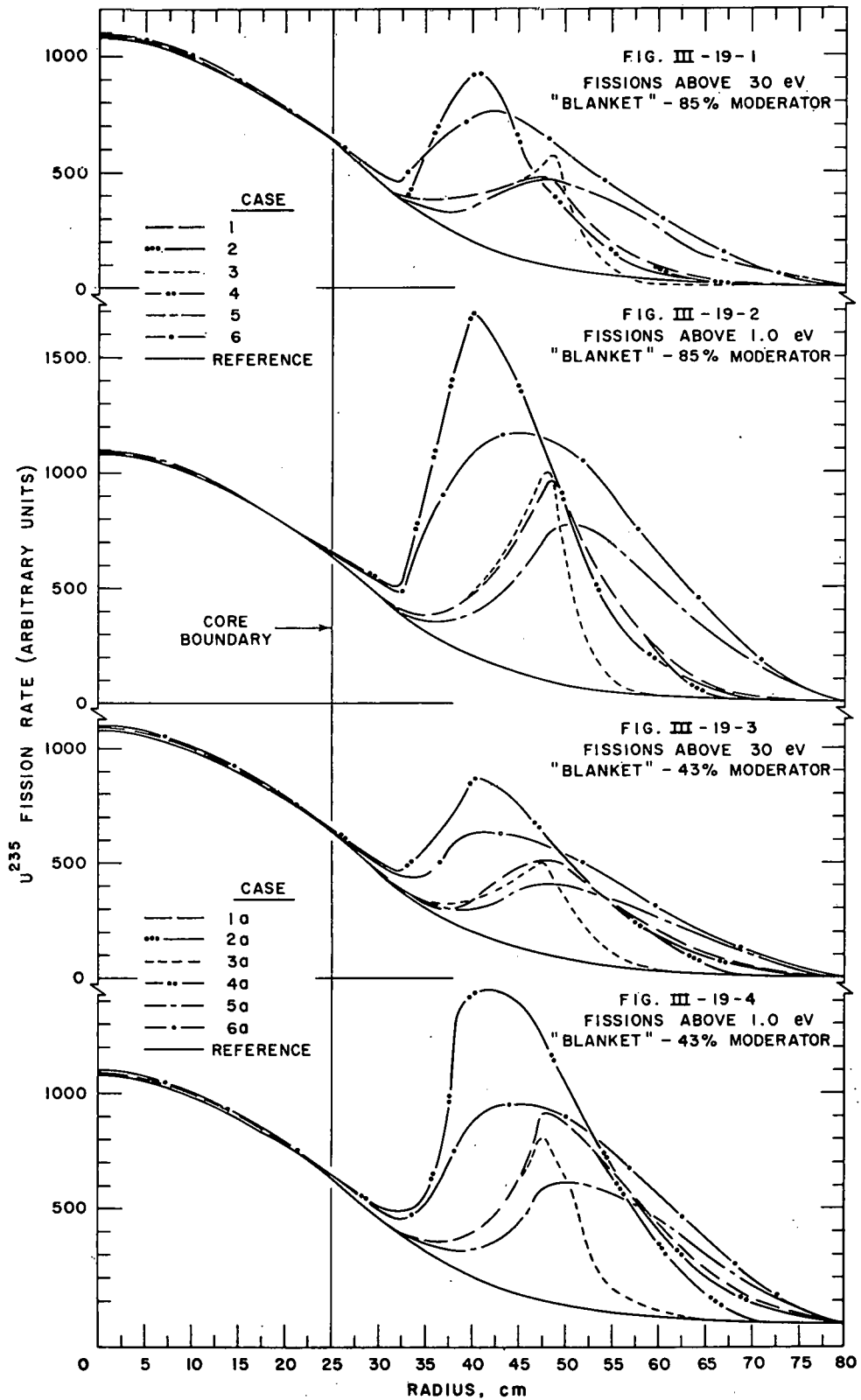


FIG. III-19-1. Fissions Above 30 eV "Blanket"—85% Moderator.
 FIG. III-19-2. Fissions Above 1.0 eV "Blanket"—85% Moderator.
 FIG. III-19-3. Fissions Above 30 eV "Blanket"—43% Moderator.
 FIG. III-19-4. Fissions Above 1.0 eV "Blanket"—43% Moderator.

with sodium for coolant and stainless steel for the structural and diluent material. The volume fractions and the radial thickness of the "altered" radial blanket region were parametrically evaluated. Some calculations simulated gross perturbations of the altered radial blanket due to irradiation "assemblies," assumed to be about 5 cm thick. Other calculations simulated only relatively small sample irradiations.

All of the analyses utilized multigroup diffusion theory in cylindrical geometry with sixteen energy groups⁹ extending to the thermal region. A basic but arbitrary criterion in all the analyses required that there be insignificant neutronic interaction between the core and the "altered" reflector. To achieve this objective, at least a 10 cm (and usually 15 cm) thick region of normal depleted uranium blanket was interspersed between the core and the "altered" reflector.

The data extracted from the analyses were the U-235 fission density as a function of position, "altered" blanket dimension and "altered" blanket composition. Information on the spectrum giving the fission rate may also be extracted. Table III-19-III identifies the basic reactor configurations that were analyzed.

Figures III-19-1 through III-19-5 give the U-235 fission rate as a function of radial position for the various cases described in Table III-19-III. Separate graphs are given for fissions above 1.0 eV and above 30 eV. The influence of fissions below 1.0 eV markedly increases the peak fission rate; however most of these will tend to be or can be significantly eliminated through the use of realistic clad materials and/or thermal neutron absorbing sleeves (e.g. cadmium). The effect of all fissions relative to fissions above 1.0 eV and 30 eV is shown on Fig. III-19-5.

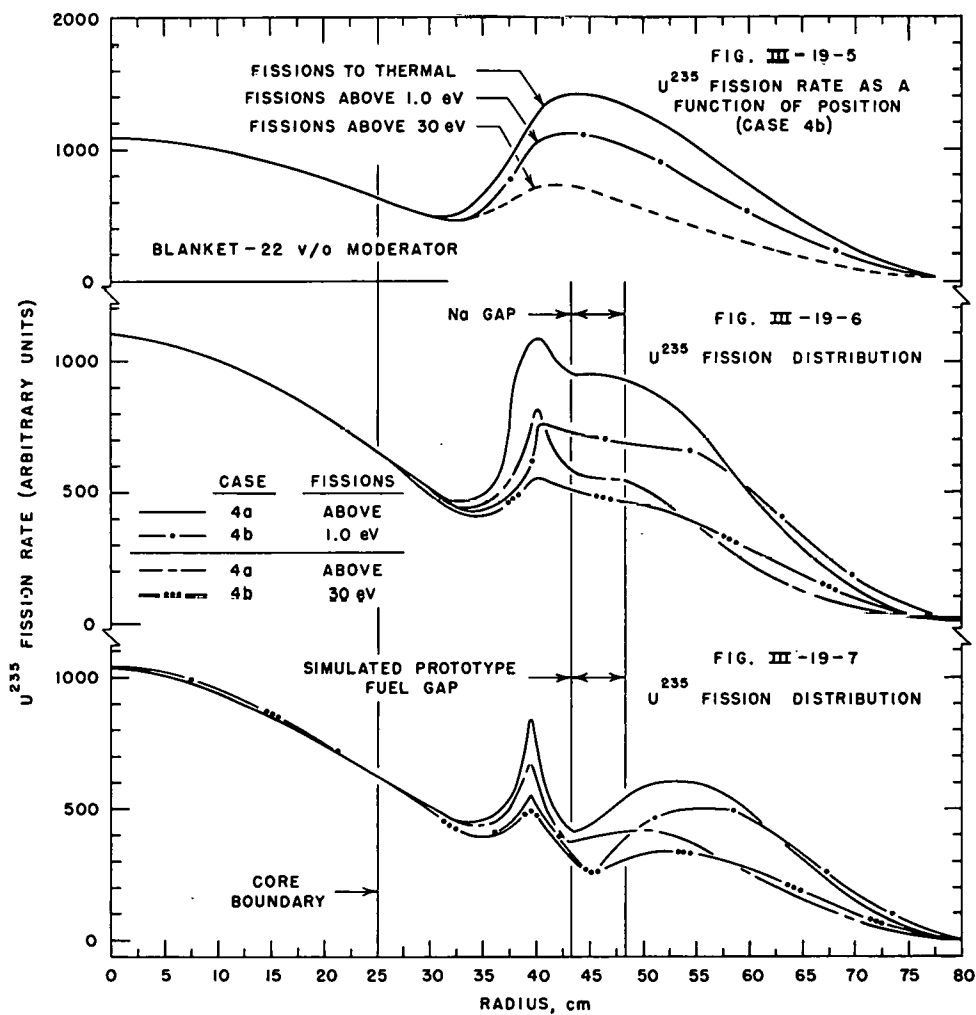


FIG. III-19-5. U²³⁵ Fission Rate as a Function of Position (Case 4b).

FIG. III-19-6. U²³⁵ Fission Distribution.

FIG. III-19-7. U²³⁵ Fission Distribution.

In general it may be seen that fission rates commensurate with those in the core can be obtained for small samples throughout large regions of the "blanket" with a judicious choice of moderator and diluent material. Case 4a, with 43 v/o Be and 50 v/o steel will probably be a "good" blanket for small sample irradiations. Case 6, with 85 v/o carbon, is attractive if the number of small samples exceeds those that can be handled by the rather narrow spatial "peak" of Case 4a.

It may also be noted that the whole radial blanket of the EBR-II need not be substituted to provide the irradiation environment described in Figs. III-19-1 through III-19-5. One or two sectors of the hexagonal radial blanket will be adequate to provide a suitable neutron environment.

The effect of gross perturbations of the "altered" blanket was also studied. The effect was overestimated by assuming an annular perturbation, representing a sodium gap or ring of prototype fuel. Thus the predicted spatial flux and fission rate depressions are overestimates of what will actually be observed if a single prototype fuel subassembly were to be placed in the "altered" blanket environment. (It is to be noted that realistic heat removal considerations and capability have not yet been factored into these analyses.)

Figure III-19-6 shows the effect of a 5 cm thick annular sodium gap upon the U-235 fission rate in Cases 4a and 4b. Figure III-19-7 shows the effect of a 5-cm thick annular simulated prototype fuel gap. The latter region is assumed to consist of 3 v/o U-235, 22 v/o U-238, 25 v/o steel and 50 v/o sodium. These results show that extreme care must be exercised in contemplating the irradiation of large aggregates of strongly absorbing materials under these conditions. Certainly a whole "ring" of prototype fuel, as shown

in Fig. III-19-7 is an inappropriate technique. The problem of irradiating a single subassembly, as opposed to a small sample, in this irradiation environment is the subject of future investigation.

The exploratory calculations cited in Figs. III-19-1 through III-19-7 show that high reaction rate irradiations are feasible in the EBR-II blanket. It appears that an advantageous blanket composition would consist of 40 to 45 v/o Be and 60 to 55 v/o steel and sodium.

REFERENCES

1. W. B. Loewenstein, *The Physics Design of the EBR-II*, ANL-6383 (1961); also Proc. of Seminar on Physics of Fast and Intermediate Reactors, IAEA, Vienna, **3**, 263 (1962).
2. L. J. Koch, W. B. Loewenstein and H. O. Monson, *Addendum to Hazard Summary Report—Experimental Breeder Reactor II*, ANL-5719 Addendum (1962).
3. L. J. Koch, H. O. Monson, D. Okrent, M. Levenson, W. R. Simmons, J. R. Humphreys, J. Haugsnes, V. Z. Jankus and W. B. Loewenstein, *Hazard Summary Report—Experimental Breeder Reactor II*, ANL-5719 (1957).
4. R. L. McVean, G. S. Brunson, B. C. Cerutti, W. B. Loewenstein, F. W. Thalgott, and G. K. Whitham, *EBR-II Dry Critical Experiments—Experimental Results*, ANL-6462 (1962).
5. F. Kirn and W. B. Loewenstein, *EBR-II Wet Critical Experimental Results*, Trans. Am. Nucl. Soc. **7**, No. 1, (1964); also *Results of the Wet Critical Experiments*, ANL-6864 (1964).
6. T. R. Bump, Argonne National Laboratory (private communication).
7. L. J. Koch, F. S. Kirn, G. W. Wensch, C. E. Branyan and E. L. Alexanderson, *Sodium Cooled Fast Breeder Reactors*, Paper submitted to the 1964 Geneva Conference.
8. W. P. Keeney and J. K. Long, *Argonne National Laboratory Idaho Division Summary Report for July, August, September, 1960*, ANL-6301.
9. G. E. Hanson and W. H. Roach, *Six and Sixteen Group Cross-Sections for Fast and Intermediate Critical Assemblies*, LAMS-2543 (1961).

III-20. Proposed Physics Measurements in FARET¹

PAUL J. PERSIANI

The Fast Reactor Test Facility (FARET)² is being designed for the purpose of generating physics and engineering data required in the development of large fast power breeders.

REACTIVITY MEASUREMENTS

This study is concerned with the physics phase of the anticipated experimental program, and in particu-

lar with the measurement of the fuel temperature coefficient of reactivity which is comprised of the fuel expansion and Doppler effects.

The immediate objective of the experimental program being planned for FARET is the measurement of the Doppler coefficient which can be assigned to a reference power reactor. To allow these measurements to be made for several reference reactor systems, zoned

loadings will be utilized. The zoned loading will consist of a relatively small test zone in the center of the reactor, which in turn is surrounded by a buffer region followed by a driver and a reflector section.

The test zone would simulate the composition, structure and neutron spectrum of the reference reactor. The buffer region serves to equilibrate the neutron spectrum in the test zone to that of a corresponding zone in the reference system. The driver section will be fueled with uranium metal and will furnish whatever additional reactivity is required to achieve criticality.

The fuel temperature of the test zone is varied to obtain a static measurement of the corresponding change in reactivity. The measured reactivity coefficient of the test zone can then be extrapolated to the full-size reference reactor by the theoretically determined ratio of the Doppler coefficient of the reference test zone to that of the total core.

The varying power level method is being used to confine a significant temperature change in the fuel elements of the FARET test zone. In this method fuel pellets are slip-fitted inside the clad. The fuel temperature change is dependent on the power density, the conductivity, and the radius of the fuel pin.

The coolant and clad temperature changes in the test zone are minimized by varying the coolant flow rate in direct proportion to the change in the power level. The initial temperatures in the buffer and driver regions are maintained essentially constant by the increased coolant flow.

The initial experiment in the FARET zone system will be the investigation of the Doppler effect for an oxide-fueled, uranium-blanketed reference reactor. The poor conductivity of the uranium oxide allows a significant temperature increase in the fuel pin.

The problem of isolating an interpretable Doppler effect in a reactivity measurement depends on the contributions to the signal by effects due to fuel expansion in the test zone, and the temperature changes of coolant and structure in the whole system. Although the coefficients (other than Doppler) appear to be non-negligible, an error analysis indicates that the Doppler reactivity effect, based on a 500°C fuel temperature rise in the test zone, can be observed with an uncertainty of 20%.

The expected Doppler reactivity change, $\Delta k/k$, for a 500°C fuel temperature increase in the test zone is -410×10^{-6} . The extraneous contribution is predicted to be -232×10^{-6} with a standard deviation of about 12%. Assuming that a series of determinations on the experimental value of -642×10^{-6} yields an error of 10%, the Doppler coefficient can be determined within 20%.

The estimated errors are by no means final. Efforts toward improvements, such as performing critical experiments to determine sodium coefficients, the fuel expansion effects, and associated errors, will be made in order to be able to assign error limits with a good degree of confidence.

To establish more firmly the extraneous contributions to the fuel temperature measurement, the FARET experiment will include the replacing of the test zone fuel elements with non-enriched uranium oxide elements. Criticality will be achieved by adding driver subassemblies in the driver region. This experiment will include errors which may arise from the hydrodynamics of the system.

Sodium void and expansion coefficients will be studied in critical assemblies. However, the multi-region core loading in FARET offers an opportunity to investigate the positive spectral component of a large core by measuring the sodium coefficient of reactivity in the test zone. The coefficient can be determined by varying the coolant flow rate as well as by changing the temperature level of the coolant. With the fuel temperature effect having been determined separately, the sodium effect can be isolated.

CROSS SECTION MEASUREMENTS

Irradiation studies in the center of the zoned system are also planned. The neutron spectrum is similar to that of a large dilute reactor. The integral reaction rate measurements include capture-to-fission cross section ratios of fissile materials and capture cross sections for U-233, U-234, U-235, U-236, U-238, Pu-238, Pu-239, Pu-240, Pu-241, Pu-242, and Np-237. Attempts will be made to measure the capture cross sections of Np-239 and Pa-233 which have relatively short half lives (on the order of days). Measurement of the capture cross sections of various structural materials will also be considered.

The present state of knowledge leads to considerable uncertainty in the reaction rates in a neutron spectrum characteristic of a large dilute fast reactor. More microscopic measurements should be available in the near future. However, confirmation with measurements in a reactor spectrum will be valuable. In some cases, reactor spectrum measurements will be the only source of such data.

At the maximum total power level of 50 MW(t), the power density in the test zone is expected to be approximately 0.061 MW/liter. For a macroscopic fission cross section of 0.0024 cm^{-1} , the average flux in the test zone would be $9 \times 10^{14} \text{ n/cm}^2\text{-sec}$. For a sample reaction cross section of one barn, the reaction rate is about 0.20% per month. Therefore, irradiation of one to two months duration will be sufficient to de-

termine average capture cross sections for isotopes of interest (average cross sections ~ 0.5 – 1.0 b). Isotopic changes of the order of 0.1% can be measured with great accuracy. (Note: The above power densities in the test zone are those calculated for the large core to be used in the physics program: power densities up to 1.5 MW/liter can be obtained with the smaller cores to be used later for the fuel development program).

FIRST CORE SCHEDULE (CALENDAR 1968)

The experiments to be performed on the first core may be summarized as follows:

1. Doppler effect
 - a. Calibration of control rods
 - b. Oscillator tests for measurement of transfer function
 - c. Two power experiment—basic Doppler coefficient measurement
 - d. Small step reactivity changes
 - e. Small ramp reactivity changes
 - f. Reactivity coefficient due to change of flow at zero power
 - g. Na void worth measurements (partly for correction to Doppler measurement)
 - h. Structural and fuel expansion coefficients
 - i. Power coefficient at selected constant flow rates. (Many of the tests (a–i) would be done at various reactor temperatures)
 - j. Dummy test zone (depleted oxide)—repeat tests a–i

2. Reaction rates (effective cross sections) determined from isotopic changes under sustained irradiation. Samples include: Pu-238, Pu-239, Pu-240, Pu-241, Pu-242, U-233, U-234, U-235, U-236, U-238, Np-237, Np-239, Pa-233
3. Repeat the fuel reactivity effect measurements after sustained irradiation in order to study any effects that may have resulted from fuel segregation, movement, or cracking.

ZPR-III critical experiments will be performed on a mockup of the first FARET loading. The initial investigation will be instrumental in establishing fuel specifications. The other main objectives of the FARET critical experiments on ZPR-III are: 1) to investigate spectrum matching characteristics of the buffer zone; 2) to determine reactivity contribution of the test zone; 3) to determine various reactivity effects to facilitate the interpretation of Doppler effect measurements in FARET, and 4) to make Doppler effect measurements in the critical assembly itself.

REFERENCES

1. P. J. Persiani, *Reactivity Coefficient Measurements in FARET*, Proceedings of the Conference on Breeding, Economics, and Safety in Large Fast Power Reactors, (October, 1963), ANL-6792, 873 (1963).
2. T. R. Bump, J. Handwerk, W. J. Kann, E. L. Martinec, P. J. Persiani, G. F. Popper, S. B. Skladzien and A. Smaardyk, *Interim Report: Faret Experimental Program* ANL-6708, (1963).

III-21. FARET Fuel Performance Program¹

T. R. BUMP,* J. HANDWERK,† W. J. KANN,* E. L. MARTINEC,* P. J. PERSIANI, G. F. POPPER,* S. B. SKLADZIEN* and A. B. SMAARDYK*

A primary objective of the FARET experimental program is to investigate fuel or fuel-clad systems under high performance conditions. Areas of investigation related to fuel performance under conditions approaching those expected in a full-scale power reactor include the use of ceramic fuel systems containing plutonium, new fuel cladding concepts and designs, the attainment of high power densities and high temperatures, the achievement of high fissile atom burnup, operating experience with components and systems, fuel stability, and corresponding safe operational reactivity feedback.

* Reactor Engineering Division, Argonne National Laboratory.

† Metallurgy Division, Argonne National Laboratory.

At this stage of development of fast breeder reactors, a number of fuel-clad systems using various fuel element design concepts are under consideration.

Questions or choices related to fuel-clad systems under consideration include:

1. Various fuel types: carbides, oxides, metals, other ceramic or cermets
2. Various claddings: stainless steel, V-Ti alloys
3. Bonding: Na bonding, no bonding
4. Various radial and axial gap sizes: e.g. fuel element vent
5. Stoichiometry effects, including effects of burnup
6. Effects of design, including axial expansion restraint
7. Metal fuel burnup expansion space: enlarged

radial gaps between fuel and clad, axial expansion space

Small, high power density cores, allowing up to 10% burnup in ten months, will be utilized to study fuel performance characteristics in FARET. The design and geometry of a large reactor can be simulated with the small core but the fuel enrichment will be different. The Pu-239 content can be made identical with that of a large reactor by replacing U-238 with U-235 to achieve criticality.

In cases where it is important to mock up the core height, FARET can accept active fuel elements up to three feet in length. Thus, FARET cores having a high L/D ratio will still be able to achieve criticality with total core volumes slightly in excess of 50 liters and, therefore, at full or only slightly reduced power densities.

Fuel systems will be tested to establish their performance at high power density and high temperature. The determination of burnup capability and the effect of power density and temperature on that capability are of particular importance.

The systems may be tested to failure (with extensive instrumentation) in order to establish their specific operational limitations. It is also planned to investigate advanced fuel concepts which present too great a degree of risk to be considered initially in existing reactors. Such concepts will include those which present a high probability of contaminating the primary coolant system as, for example, vented fuel elements. In addition to the capability of reactor operation at temperatures up to 1200°F (650°C), provisions will be made for operation of individual fuel assemblies or small zones of the reactor at higher temperatures.

Provision for considerable core instrumentation with great flexibility of arrangement is one of the salient features of the FARET facility. Special in-core instruments will be required, particularly for the measurement of fuel pin temperatures and neutron and gamma fluxes. The development of thermocouples which will measure fuel pin temperatures greater than 2000°C and perhaps up to the melting point of uranium oxide, is a major phase of the FARET experimental program. Several reference fuel pin thermocouple designs have been selected. A variety of refractory metal sheath materials with thorium insulation in combination with tungsten-rhenium type thermocouples are now being investigated.

Temperature indicators are being explored as a back-up to the thermocouple temperature measuring devices. The indicator technique currently under study uses a variety of perforated refractory metal

foils placed between fuel pellets in two or three axial planes. The metal foils are chosen such that the range of melting points spans the temperature range of interest. This technique has the potential of bracketing the maximum temperature expected in the fuel pin.

To facilitate the discussion of the proposed FARET fuel test program, some of the types of experiments and measurement techniques that will be performed on the facility are described below.

Post Mortem Metallurgical Tests Consisting of the Removal of Representative Fuel Elements at Predetermined Intervals of Exposure for Destructive Testing

The primary function of these tests will be to investigate the dimensional changes, physical properties, and condition of the fuel pellets and cladding materials. Fission gas release measurements and inspection of the temperature indicators will be made at this time. Experimental information on the dimensional behavior of ceramic fuel due to temperature changes, rate of temperature changes, history of the fuel, and degree of irradiation is at present limited. This behavior must be established under conditions which would allow a high degree of understanding and predictability.

Dynamic Reactivity Coefficient Measurements

The small core experiments are primarily intended to develop information relating to fuel performance. However, they will also provide an opportunity to investigate irradiation-induced changes in properties affecting reactivity coefficients. The reactivity of a small, high leakage core is quite sensitive to fuel dimensional changes. Furthermore, the Doppler effect is quite small. Measurement of the temperature and power coefficients of these cores initially and periodically during exposure will provide an indication of reactivity-inducing property changes. The measurement technique will be similar to that used for the zoned core. That is, the fuel temperature will be varied as the clad and coolant temperature changes are minimized (by varying reactor power and flow simultaneously).

Analysis of kinetic behavior, both from transfer function measurement and from response to small ramps and steps of reactivity, will give information about the time constants of the reactivity coefficients.

An important point is that these measurements can be repeated several times on a core which has undergone considerable burnup and thermal cycling.

Measurements in a Closed Loop Facility

It is planned to insert a closed loop into FARET. This will permit a variety of experiments related to fuel failure and fission product release to be performed. The loop could be large enough to displace seven of the FARET subassemblies. In addition, if required, several closed loops can be placed in the reflector region. The power density would only be down approximately a factor of two from that attainable within the core. These loops might be particularly useful for controlled studies of fast neutron irradiation damage to cladding and structural materials.

Tests on Vented Fuels

The degree and type of fission product release as a function of fuel, burnup, operating conditions, and fuel element design will be investigated using closed loops.

Experiments on Proposed Methods of Fuel Element Failure Detection

These experiments will again make use of the closed loop.

Tests of Proposed Special Design Features or Reactor Fuses to Enhance Safety

Examples of a safety design feature are the controlled - expansion fuel element or modifications thereof. The small FARET core is very sensitive to neutron leakage effects on reactivity, making it an excellent diagnostic tool for most such devices. These experiments may or may not require a closed loop depending upon whether any fuel or fission products are likely to be released in the test.

Meltdown Experiments Including Effects of Fuel Transport by Coolant

These experiments, which would be performed in the closed loop, should give information on the mechanism of fuel failure. They are basically similar to meltdown tests in the TREAT sodium loops with two important differences. Reactivity feedback effects due to the meltdown would be significant in FARET and there is a reasonable chance that they may be susceptible to analysis. The second important difference is that the ability of FARET to operate at sustained high power makes possible the study of different mechanisms associated with fuel element failure. One example would be a gradual failure in periods of minutes or longer, due to operation at excessive temperatures. An important feature of any such tests is

the study of the transport of the failed fuel by the coolant. Loss of coolant experiments, e.g., effects due to coolant blockage, could also be studied in the closed loop.

The detailed plans for the FARET program of fuel testing are the following:

CORE II—FUEL PERFORMANCE TEST CORE— JANUARY, 1969 TO JUNE, 1970

1. Fuel types deemed most likely to be relevant to the prototype will be tested. Argonne has a strong interest in high-burnup carbide and metal fuels using vanadium-titanium clad. Oxide fuel is the other major contender. If the number of different kinds of fuels deemed worthy of test is sufficiently large, there may be no single predominant fuel being tested. The mode of operation would then resemble that of a test reactor in which the assemblies under test drive each other.
2. Additional test pins of current interest will be included.
3. Some measurement technique and instrumentation development during this core irradiation is expected.
4. Three to six months of irradiation should be provided before the first prototype core must be specified. At maximum power this would provide a sizeable part of the design burnup.

CORE III—PROTOTYPE I PROOF TEST— JULY, 1970 TO DECEMBER, 1971

1. By this time the first core of the prototype will have been specified. This FARET core will be a proof test on fuel elements mocking up those of the prototype as closely as possible.
2. In all probability these elements will be somewhat different from those tested in Core II. If Core II has been prudently selected, however, at least some of its elements will resemble those of Core III.
3. The loading will be run to and beyond the specifications for the prototype, if possible.

CORE IV—PROTOTYPE I SAFETY AND LIMITS OF PERFORMANCE TEST—JANUARY, 1972 TO JUNE, 1973

1. This core will consist primarily of Prototype I elements. Some of the same elements irradiated in Core III may be used. It may also include special advanced subassemblies.
2. This core will be operated under more extreme conditions to determine the limits of performance.
3. Closed loop tests will be conducted for meltdown experiments.

4. Special fuel elements may be vented to the coolant in a closed loop.

5. Special design features to enhance safety (such as the controlled expansion elements—CEX) may be tested.

CORE V—PROTOTYPE II TEST—JULY, 1973
TO DECEMBER, 1974

1. The second core for the prototype should reflect some of the things learned about high performance elements.

2. Whereas Prototype I will probably be selected as an element which will work satisfactorily but not necessarily with exceptional performance, Prototype II should be a good approximation to a high performance element.

3. Advanced subassemblies will be included in the loading to the extent that they are available.

4. Experiments aimed at determining performance limits will be conducted (in the closed loop if there is significant probability of failure).

CORE VI—NEXT GENERATION FUEL CONCEPTS—
JANUARY, 1975 TO JUNE, 1976

Most of the elements studied in previous cores may not have been of the "far out" category. If elements having greatly increased potential (higher temperatures, higher burnups, vented) will have survived earlier small scale tests, they may be tested at this time. This core might consist of a number of different type elements of this category.

CORE VII—SAFETY STUDIES—JULY, 1976

This could be a series of meltdown experiments in a central test loop or it could be a core specially designed to test our understanding of various accident conditions. These include, flow coastdown on loss of pump power, fuel slumping at meltdown or near-meltdown conditions, etc.

REFERENCE

1. T. R. Bump, J. Handwerk, W. J. Kahn, E. L. Martinec, P. J. Persiani, G. F. Popper, S. B. Skladzien and A. B. Smaardyk, *Interim Report: FARET Experimental Program*, ANL-6708 (1963).

III-22. Preliminary Considerations on the Safety Analysis of FARET¹

P. J. PERSIANI, A. WATANABE, U. WOLFF,* S. GRIFONI,† and B. WARMAN

The Fast Reactor Test Facility (FARET)^{2,3,4} is being designed to accommodate a variety of fast reactor configurations, compositions, sizes, and experiments. The reactor kinetics for a variety of positive reactivity insertion rates and the effects from temperature-dependent negative reactivity feedbacks on a series of incidents which may lead to core melting have been analyzed for the two typical reference core loadings in FARET. The two cores considered were the small core loading which is proposed for the engineering performance experiments and the zoned core loading which is planned for the reactor physics and safety phase of the FARET program. For detailed dimensions and material compositions, see Ref. 1.

The range of external reactivity insertion rates studied for the two systems were those considered to be associated with credible or near-credible conditions for FARET. For example, ramp insertions included dropping a fuel subassembly, unplanned removal of a control rod, and expulsion of the sodium coolant. Small reactivity insertions which resulted in

a slow power rise until the fuel eventually melted and collapsed were also included. These conditions may be associated with possible startup accidents as well as with the slow loss of bulk coolant or coolant flow.

The reactor incidents considered were assumed to terminate only by disassembly of the core. The analysis was separated into two phases; reactivity insertion and core disassembly.

In the disassembly phase, the estimate of energy yield and explosive force of a variety of hypothetical nuclear incidents was made using the AX-1 code.⁵ The input information needed for this computation, in addition to the usual reactor parameters and equations of state, was the inverse power period at the start of disassembly. The energy yield is very sensitive to this parameter, which in turn is dependent upon the reactivity insertion rate during the initial stages of disassembly.

The objective of the reactivity insertion phase was the estimation of the maximum inverse power period for reasonable initial reactivity insertion rates. In this respect, the reactivity insertion eventually resulting from core melting was based on the assumed

* Allgemeine Electricitäts-Gesellschaft, Germany.

† Comitato Nazionale Per L'Energia Nucleare, Italy.

model in which the core collapses under gravity in a time- and space-wise continuous manner. It was further assumed that as the fuel collapses, it is redistributed over the new core configuration by displacing the coolant. The use of this "continuous reactivity" model is a departure from the use of the "reactivity threshold" model in safety analyses. The latter assumes that approximately the upper half of a molten core drops as a single unit into a somewhat more densified lower core region.

The degree and the amount of core which densifies and reassembles is questionable; counter arguments as to the credence of the "threshold reactivity" model have been advanced by H. Bethe.⁸ A situation is advanced by Bethe in which the fuel, as it becomes molten and comes into contact with sodium, vaporizes the sodium which, in turn, expels the molten fuel. This would probably inhibit any extensive, abnormally high concentration of fuel from forming in the lower portion of the core. This is judged to be a reasonable sequence of events for the case of rapid power rises where the fuel becomes molten in tenths of milliseconds before expelling the coolant.

The situation differs in the case of a slow power rise in which the coolant is boiled off before the fuel melting process begins. However, the credibility of the "reactivity threshold" model remains questionable for the following reasons. To rearrange the core and create conditions for the "reactivity threshold" model to be valid would probably require much more than 100 msec. The time required for complete meltdown of the fuel from the start of melt is of the order of tens of msec. During the time between melting in situ and rearrangement of core configuration, it can be argued that some reactivity is inserted by collapse under gravity. This would lead to power periods of several msec. With such periods, the molten fuel could vaporize and create pressures within tens of msec which would tend to inhibit the formation of the pessimistic geometrical configuration suggested by the "reactivity threshold" model.

The assumption made here is that the collapsing of a molten core would result in a positive reactivity insertion during the early stages of collapse. It is during this phase that a "continuous reactivity" model would appear to be more appropriate for the purpose of estimating energy yield.

In the FARET analysis, the collapsing of the core was allowed to proceed until the total energy density input reached a value of about 2×10^4 J/cc of fuel, whereupon the core was assumed to start to disassemble. This was taken as the energy required to vaporize the fuel. The inverse power period corresponding to this energy density was then used as the input pa-

rameter for the computation of the energy yield (AX-1 code). This approach affords a detailed evaluation of core conditions and parameters which may exist during meltdown and reassembly.

The results of the meltdown computations for the small core indicated that the lower external ramp rates could lead to greater reactivity insertions than higher external ramp rates. That is, the extent of collapse of the core was greater for the lower ramp rates since the time interval is longer for a given energy input. This can be seen from the two curves (3 and 4) on Fig. III-22-1.

The reactivity insertion resulting from core collapse was also studied by introducing negative temperature-dependent feedbacks (Doppler effect) of different magnitudes. Two cases shown in Fig. III-22-1 (curves 1 and 2) demonstrate the influence of a Doppler feedback. The effect of Doppler broadening on the inverse power period is illustrated in Fig. III-22-2. It can be seen that a greater reactivity insertion occurred as a result of core collapse for the case with negative feedback. The magnitude of the Doppler coefficient was not large enough to effect a reactor shutdown.

In the case of the zoned system it was generally

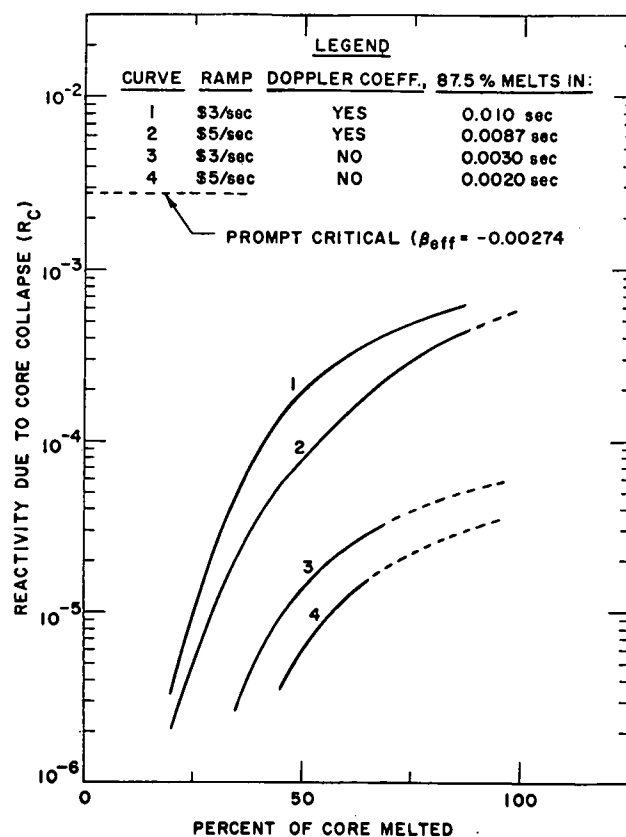


FIG. III-22-1. Reactivity of Collapse Versus Percent of Core Meltdown for Reference Small Core.

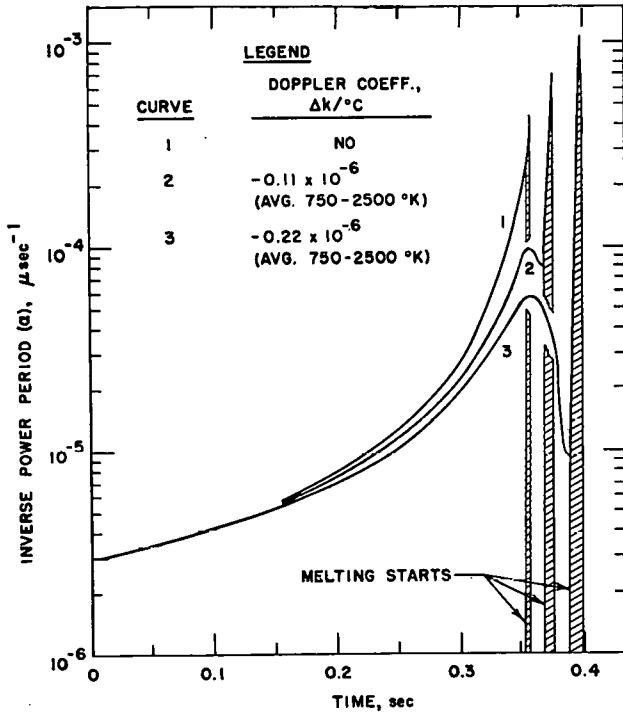


FIG. III-22-2. Inverse Power Period Versus Time for Ramp Reactivity Input of \$3/sec in Reference Small Core. (Curves terminate when 87.5% of core has melted.)

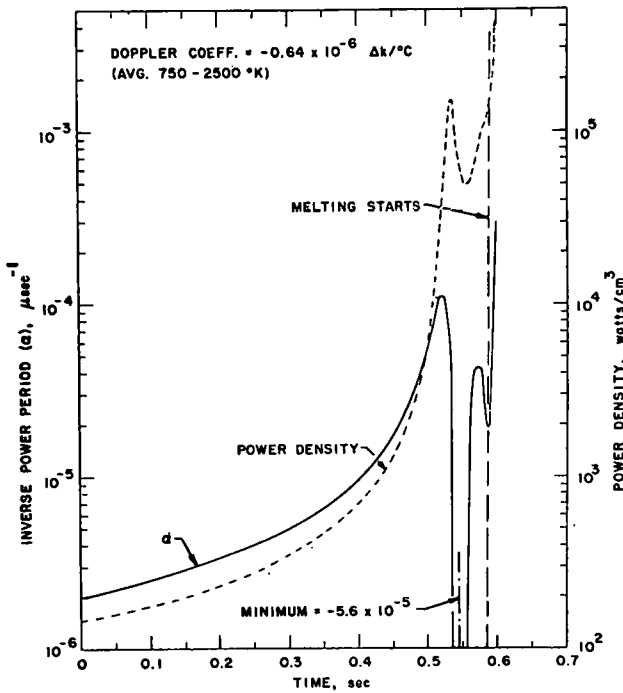


FIG. III-22-3. Inverse Power Period and Power Density Versus Time for Ramp Reactivity Input of \$2/sec in Reference Zoned Core. (Curves terminate when 87.5% of core has melted.)

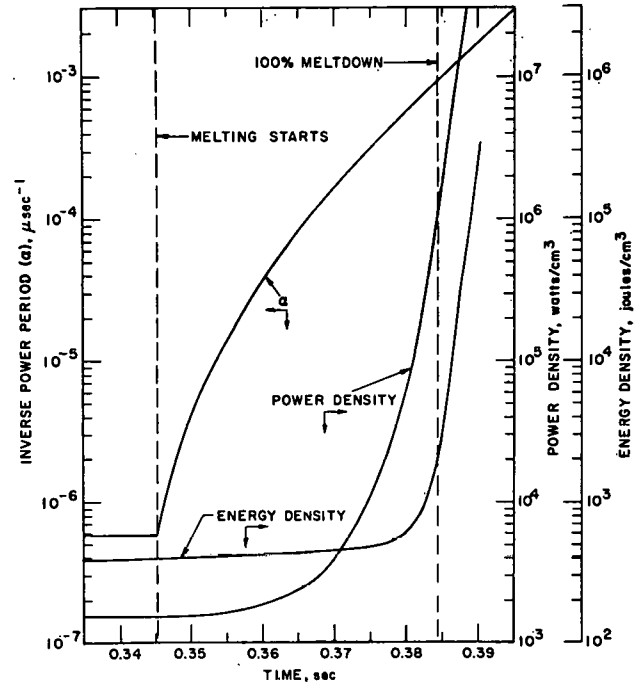


FIG. III-22-4. Net Reactivity Insertion, Inverse Power Period, Power Density, and Energy Density Versus Time for Reference Zoned Core. (Initial power period = 1.7 sec.)

observed that for a range of external ramps studied (\$2/sec to \$10/sec), negligible reactivity was introduced by the collapsing core.

The effect on the inverse power period of introducing a Doppler feedback is shown in Fig. III-22-3. The power was reduced but the Doppler effect was not great enough to completely overcome the externally applied ramp insertion. The core proceeded to melt.

Low initial insertion rates did give shorter power periods resulting from the gravitational collapse of the core. A case studied is presented in Fig. III-22-4. Low initial insertion rates usually resulted in higher energy yields.

REFERENCES

1. T. R. Bump, B. C. Cerutti, I. Charak, S. H. Fistedis, J. D. Geier, A. Hirsch, W. F. Malloy, P. J. Persiani, O. S. Seim, W. R. Simmons, A. Smaardyk and N. J. Swanson, *Preliminary Safety Analysis of the Fast Reactor Test Facility*, ANL-6813 (1964).
2. T. R. Bump, J. Handwerk, W. J. Kann, E. L. Martinec, P. J. Persiani, G. F. Popper, S. B. Skladzien and A. B. Smaardyk, *Interim Report: FARET EXPERIMENTAL PROGRAM*, ANL-6708 (1963).
3. P. J. Persiani, *Reactivity Coefficient Measurements in FARET*, ANL-6792, 873 (1963).
4. P. J. Persiani, A. Watanabe, U. Wolff, S. Grifoni and B. Warman, *Preliminary Consideration on the Safety Analysis of FARET*, ANL-6935 (1964).
5. D. Okrent, J. M. Cook, D. Satkus, R. B. Lazarus and M.

B. Wells, *AX-I: A Computing Program on Coupled Neutronics-Hydrodynamics Calculations on the IBM-704*, ANL-5977 (1959).

6. H. A. Bethe, Testimony of H. A. Bethe, *In the Matter of Power Reactor Development Company*, USAEC, Docket No. 50-16.

III-23. Nuclear Performance of Large Fast Power Reactors

W. B. LOEWENSTEIN and D. OKRENT*

The performance characteristics of a wide range of reactors were calculated in idealized spherical or infinite slab geometry using the first 22 groups (to 30 eV) of a newly developed 26 group (to thermal) cross-section set.¹ The general results are being reported to the 1964 Geneva Conference² while the detailed results are in publication.³

The Pu-U-238 fueled systems analyzed at equilibrium core and blanket compositions show that high-density metallic fueled reactors using steel structure have predicted breeding ratios between 1.6 and 1.9. (Increments of 0.1 to the breeding ratio are possible if blanket leakage can be reduced.) For the lower-density oxide fuel, the predicted breeding ratio ranges from 1.18 to 1.4, the higher breeding accompanying greater fuel concentrations. Carbide breeding ratios fall between those for oxide and metal.

The Doppler effect, $T(dk/dT)$, at operating temperature is estimated to be in the range of -0.001 to -0.0025 for the large metal-fueled reactors considered, and -0.003 to -0.008 for the large oxide- or carbide-fueled reactors treated, when deliberate spectral softening or a strongly absorbing structural material is not used. If all core sodium were lost, spectral hardening would significantly reduce the Doppler effect. This reduction would be most pronounced for initially high sodium-content systems.

Sodium coefficients and the sodium-void reactivity effect are shown to be a strong function of reactor size, composition, and geometry. The effect of core composition at fixed core volume as well as the effect of core size at fixed core composition were separately studied in spherical and infinite slab geometry. Calculated sodium reactivity effects include uniform removal from the whole core as well as the core sodium from only those inner portions which contribute a positive reactivity effect.

For nominal core compositions (30% fuel, 20% steel, and 50% Na) at a given core volume, the sodium-void effect is more positive for the higher-density fuel which has more U-238 present. Thus, at 1000

liters, the metallic fuel gives a positive effect for uniform core removal, the carbide is slightly negative, and the oxide is more negative. If reactors are compared on the basis of equal power output, however, the higher power density capability of the metal and carbide tends to reduce this difference.

A large-volume core having one dimension deliberately foreshortened (e.g., a flat cylinder) will have more neutron leakage, a higher fuel enrichment and critical mass, and a sodium-void effect more characteristic of a small, spherical reactor. However, an infinite slab does have a somewhat more positive sodium-void effect than a sphere of identical composition. The practical reactor of the same composition should have a sodium-void effect between that of sphere and infinite slab. For sphere or slab, in large sizes there may be a large, positive, central sodium-void effect. For small fuel and large coolant concentrations, the sodium-void effect may be strongly negative for uniform core removal, although slightly positive for the central region alone. This "worst case" is not as bad with 15/15/70 as with 30/20/50 composition.

The deliberate introduction of some BeO will degrade the spectrum of either a metal- or ceramic-fueled reactor enough to enhance the Doppler effect markedly. The presence of some fixed moderator appreciably lessens the usual large reduction in Doppler effect due to spectral hardening in the advent of a loss of sodium. The introduction of BeO may result in a tendency for a less positive sodium-void effect. However, the degraded spectrum also results in an appreciable reduction in breeding ratio.

The use of BeO, combined with a strongly capturing structural material like Nb, reduces the breeding ratio drastically and still does not result in a large negative Doppler coefficient. The small Doppler effect is due partly to a lessened low-energy flux and partly to a reduced neutron worth at low neutron energies.

The presence or absence of fission products and Pu-240 in the core, and Pu in the blanket, has significant effects on breeding and reactivity coefficients, large enough to change the sign of the sodium coefficient between a "clean" and an "equilibrium" reactor.

* Laboratory Director's Office, Argonne National Laboratory.

Nuclear performance, with vanadium as the structural material was found to be similar to and perhaps slightly better than that with steel.

Reactor performance calculated with the new ANL 26-group set of nuclear constants is compared with that for the Hansen-Roach⁴ and YOM⁵ sets. The new cross sections lead to a more negative sodium coefficient and more low-energy flux than unmodified 16-group YOM cross sections. Breeding ratios and critical masses are the same, however. With shielded cross sections, the Hansen-Roach set usually gives somewhat higher critical masses and breeding ratios, and somewhat more negative sodium coefficients than the ANL 26-group set. With unshielded Hansen-Roach cross sections, the critical masses rise markedly, and the sodium coefficients become much more positive.

The effect of various potential clad or structural materials on performance was also investigated. Ti, V, Cr, Fe, Ni and Zr are fairly similar in their effect on nuclear performance. The strongly capturing materials Nb, Mo, W, and Ta increase the critical mass, decrease the breeding ratio and lead to less desirable reactivity coefficients.

The performance of "clean" Th-U-233 and U-238-U-233 reactors is also studied. The Th-U-233 combination is now predicted to give somewhat lower breeding ratios than had been previously predicted.

primarily due to a downward revision in $\nu(E)$ for U-233. The sodium-void effects are calculated to be very negative, and the Doppler coefficients appear to be similar to those for corresponding Pu-U-238 fueled reactors.

An approximate multi-multigroup treatment of elastic scattering in lighter elements was used for the survey. "ELMOE"-averaged⁶ elastic transport and moderation cross sections were generated once for each light material in an appropriate calculation, and these were then held fixed throughout the survey. Modest errors were introduced by this procedure.

REFERENCES

1. D. O'Shea, H. H. Hummel, W. B. Loewenstein and D. Okrent, *Twenty-Six Group Cross Sections*, ANL-6858 (To be published).
2. D. Okrent, K. P. Cohen and W. B. Loewenstein, *Some Nuclear and Safety Considerations in the Design of Large Fast Power Reactors*, (Paper presented to the 1964 Geneva Conference).
3. W. B. Loewenstein and D. Okrent, *Nuclear Performance of Large Fast Power Reactors*, ANL-6867 (To be published).
4. G. E. Hansen and W. H. Roach, *Six and Sixteen Group Cross Sections for Fast and Intermediate Critical Assemblies*, LAMS-2543 (1961).
5. S. Yiftah, D. Okrent and P. A. Moldauer, *Fast Reactor Cross Sections*, (Pergamon Press, New York, 1960).
6. A. L. Rago and H. H. Hummel, *ELMOE: An IBM-704 Program Treating Elastic Scattering Resonances in Fast Reactors*, ANL-6805 (1964).

III-24. Physics Studies of Some Molten-Salt-Fueled Fast Reactor Systems

D. BUTLER and D. MENEGHETTI

INTRODUCTION

The neutron statics of several molten-salt-fueled fast reactor systems have been investigated. The systems utilize salt mixtures which contain PuCl₃, UCl₃, MgCl₂, and NaCl.

Three different compositions were studied which correspond to systems suggested for this preliminary physics study by members of the Chemical Engineering Division of Argonne National Laboratory*. The first is an externally cooled homogeneous reactor (labelled Type A in the Tables). The second (labelled Type B) corresponds to a homogeneous salt mixture containing the fuel and fertile materials, but would be internally cooled by sodium metal circulated through channels in the core. The third case (labelled Type C) simulated the core fertile material as metallic elements.

* P. Nelson, N. Chasanov and A. Tevebaugh.

The compositions of the systems studied are given in Table III-24-I. In these calculations no attempt was made to optimize compositions.

METHOD OF ANALYSIS

Critical masses, concentrations, and breeding ratios were determined for each type. The effects of changing from metal to oxide blankets were examined and the sodium void coefficients and thermal expansion coefficients were studied. Finally, some implications of several uncertainties in the cross sections used were determined.

The calculations utilized multi-group diffusion theory with the 16 group cross sections of Hansen and Roach.¹ Spherical geometry was assumed, with no correction made for effects which would probably exist in an actual cylindrical system. Except where

TABLE III-24-I. NUCLEAR CHARACTERISTICS OF MOLTEN SALT SYSTEMS

	Type A, Externally Cooled					Type B, Internally Cooled					Type C, Internally Cooled Metallic Uranium in Core					
	A-1 Refer- ence	A-5 Oxide blanket	A-6 Fluoride	A-7 Self shielded	A-8 Self shielded oxide blanket	B-1 Refer- ence	B-2 No Cl absorp.	B-3 Reduced nickel capture	B-4 Struc- tural material iron	B-5 Self shielded	C-1 Refer- ence	C-2 No Cl absorp.	C-3 Reduced nickel capture	C-4 Struc- tural material iron	C-5 Oxide blanket	C-6 Fluoride
Core volume (liters)	10,000	10,000	10,000	10,000	10,000	20,000	20,000	20,000	20,000	20,000	10,000	10,000	10,000	10,000	10,000	10,000
Critical mass (kg)	2,100	2,093	2,615	2,022	2,002	4,510	4,460	4,264	3,784	4,330	2,817	2,797	2,709	2,482	2,821	3,312
Core volume fractions																
Pu-239 (metal equivalent)	0.011	0.011	0.014	0.011	0.011	0.012	0.012	0.011	0.010	0.011	0.015	0.015	0.014	0.013	0.015	0.018
U-238 (metal equivalent)	0.063	0.063	0.060	0.063	0.063	0.055	0.55	0.055	0.057	0.055	0.083	0.084	0.084	0.086	0.084	0.081
Sodium ^a (metal equivalent)	0.367	0.367	0.367	0.367	0.367	0.397	0.397	0.397	0.397	0.397	0.500	0.500	0.500	0.500	0.500	0.500
Iron						0.007	0.007	0.007	0.127	0.007	0.007	0.007	0.007	0.127	0.007	0.007
Nickel ^b						0.111	0.111	0.111		0.111	0.111	0.111	0.111		0.111	0.111
Molybdenum						0.017	0.017	0.017		0.017	0.017	0.017			0.017	0.017
Core atom densities (in units of 10 ²⁰ per cm ⁻³)																
Pu-239	5.290	5.274	6.591	5.095	5.046	5.676	5.616	5.373	4.768	5.460	7.103	7.053	6.828	6.255	7.110	8.348
U-238	29.410	29.426	28.109	29.605	29.654	25.544	25.600	25.847	26.452	25.759	39.107	39.160	39.382	39.955	39.100	37.862
Blanket volume fractions																
U-238 (metal equivalent)	0.60	0.31	0.60	0.60	0.31	0.600	0.60	0.60	0.60	0.60	0.60	0.60	0.60	0.60	0.31	0.60
Sodium	0.20	0.20	0.20	0.20	0.20	0.200	0.20	0.20	0.20	0.20	0.20	0.20	0.20	0.20	0.20	0.20
Iron	0.20	0.20	0.20	0.20	0.20	0.200	0.20	0.20	0.20	0.20	0.20	0.20	0.20	0.20	0.20	0.20
Leakage from blanket	0.025	0.0035	0.011	0.025	0.025	0.015	0.015	0.014	0.015	0.014	0.017	0.016	0.016	0.018	0.002	0.010
Core breeding ratio	0.73	0.75	0.855	0.69	0.72	0.62	0.69	0.69	0.83	0.57	0.72	0.73	0.78	0.88	0.73	0.74
Total breeding ratio	1.71	1.72	1.39	1.68	1.62	1.17	1.22	1.25	1.49	1.11	1.33	1.34	1.41	1.60	1.34	1.17
$\alpha = \sigma_c/\sigma_f$	0.161	0.168	0.274	0.171	0.182	0.162	0.177	0.176	0.186	0.174	0.153	0.154	0.163	0.169	0.157	0.203

^a Includes sodium metal coolant, sodium chloride in fuel, and magnesium.

^b Includes chromium.

specifically mentioned, 45 cm thick solid metal blankets (60 v/o uranium-238, 20 v/o iron, 20 v/o sodium) were used. It was assumed that the nuclear properties of magnesium and chromium were identical to those of sodium and nickel respectively. Since these were minor constituents, this introduced little error into the calculations.

RESULTS AND DISCUSSION

The characteristics of the reference systems and the results of the calculations are summarized in Table III-24-I.

The highest breeding ratio (neglecting out-of-pile inventory) is found to be that of the externally cooled homogeneous reactor (A-1). The internally cooled homogeneous reactor (B-1) has the smallest breeding gain. The internally cooled reactor with uranium metal in the core has a breeding ratio between the two cited extremes.

The parasitic absorption of neutrons by chlorine (radiative capture and the (n,p) and (n,α) reactions) is of some concern in evaluating fast molten chloride systems. In order to estimate the significance of such absorptions, the second and third types of reactor (B-1 and C-1) were reanalyzed (B-2 and C-2) assuming no chlorine absorptions. It can be seen that the breeding ratio is slightly higher ($\sim 5\%$) without the absorptions. This should not be considered a final test of the deleterious effect of chlorine absorptions. It is possible that the cross section library does not represent the true physics of chlorine. Fast neutron data for this material are very limited.

The calculation shows an even more significant loss

TABLE III-24-II. SODIUM VOID AND EXPANSION EFFECTS

Reactor Type C-1	Reactivity Change
1. Remove 50% of sodium coolant from the core.....	$\Delta k = +0.0124$
2. Remove $\frac{1}{2}\%$ of molten salt fuel from the core ($12\frac{1}{2}^\circ\text{C}$ to 25°C temperature rise).....	$\Delta k = -0.0028$
Reactor Type B-1	
1. Remove 20% of sodium coolant from the core.....	$\Delta k = +0.0072$
2. Remove 50% of sodium coolant from the core.....	$\Delta k = +0.0182$
3. Remove $\frac{1}{2}\%$ of molten salt fuel from the core ($12\frac{1}{2}^\circ\text{C}$ to 25°C temperature rise).....	$\Delta k = -0.0024$
4. Transfer $\frac{1}{2}\%$ of molten salt fuel from the core and add it to the inner 6 cm of blanket.....	$\Delta k = -0.0020$
5. Expand molten salt $\frac{1}{2}\%$ making room for expansion by moving the blanket radially outward.....	$\Delta k = -0.0022$

of neutrons (than that incurred by Cl absorptions) to the structural material required for the internally cooled systems (B-1 and C-1). The high nickel concentration is particularly important. In order to obtain a quantitative estimate of the effect of these absorptions on breeding, the effect of reduced capture in the nickel and iron substituted for nickel, chromium, and molybdenum was studied. The reduced nickel capture cross sections were obtained by reducing the very large number of captures between 3 and 17 keV. The effect of the reduced nickel absorption is shown by cases B-3 and C-3. The breeding ratios are increased in both instances. Substituting iron for the other structural materials (B-4 and C-4) results in an even more favorable breeding ratio than obtained with reduced nickel captures.

Another variation of the systems considered was that of replacing the metal blanket with one made of uranium oxide (60 v/o UO_2 of density 10.16 gm/cm^3 , 20 v/o iron and 20 v/o sodium). A 15 cm thick iron reflector was placed outside the 60 cm oxide blanket to reduce the blanket leakage. The results for the externally cooled homogeneous reactor (A-5) and the internally cooled reactor with metallic uranium in the core (C-5) show that the decrease in breeding ratio is only a few percent when the metal blanket is replaced with oxide. It should be noted that an iron reflector would have improved the breeding in the metal blanketed systems by several percent, so that the net effect of substituting the oxide for the metal blanket is a net reduction in each case.

The use of fluorides rather than chlorides in the fuel was also examined. The cross sections indicate that fluorine has less radiative capture but has greater inelastic plus elastic moderation. The comparison of fluorides with chlorides as fuels is given for cases A-6 and C-6. The fluoride systems show much lower breeding ratios than the corresponding chloride systems. These calculations also indicated that absorptions due to (n,p) reactions in these fluoride systems are about as important as those for the chloride systems.

The calculations indicate that the systems considered here have significant numbers of neutrons in the groups in which resonance effects are important. Because resonance self-shielding can have an appreciable influence on breeding ratio, three analyses utilized self-shielded cross sections. Potential scattering cross sections of 600 barns per atom for Pu-239 and 100 barns per atom for U-238 were used. The results for systems corresponding to the metal blanketed type A-1, the oxide blanketed A-5, and the internally cooled B-1, are labelled types A-7, A-8, and B-5 respectively in Table III-24-I. These results

show somewhat lower breeding ratios than those obtained with the cross sections which assume infinite dilution. For the case of the oxide blanketed system (A-8) the apparent much larger decrease in breeding ratio is due essentially to the omission of the iron reflector in that calculation.

Two properties of the molten salt systems were studied in addition to the neutron inventories. These were the sodium void coefficients for the sodium containing internally cooled reference systems, and reactivity coefficients for thermal expansion of the molten salt. The results are summarized in Table III-24-II and were obtained with infinite dilution cross sections for plutonium and uranium. Since the sodium void effect depends significantly on the effect of resonance self-shielding, the calculations were repeated using the appropriate self-shielded cross sections. The results for both 20% and 50% coolant expulsion showed a decrease of 33% relative to the unshielded cases in

Table III-24-II. It is noted that the Na void effect is positive and the thermal expansion effects of the salt are negative. The last two coefficients listed in the table were obtained to determine what change in the reactivity coefficient of expansion results if the fuel remains in the system. Calculations of the first coefficient assumes that 1/2% of the core salt-mixture is expanded into and mixed with the first 6 cm of blanket. Calculation of the second coefficient assumes the salts in the core to be expanding, and the blanket to be pushed radially outward to accommodate the increased volume of core. In both investigations the difference in the coefficient when compared to that obtained when the fuel is expelled from the reactor system is quite small.

REFERENCE

1. G. E. Hansen and W. H. Roach, *Six and Sixteen Group Cross Sections for Fast and Intermediate Critical Assemblies*, LAMS-2543 (1961).

III-25. Fast Reactor Reactivity Coefficients; the Effect of Excess Reactivity

W. B. LOEWENSTEIN

In order to provide a relatively long uninterrupted fast reactor operating cycle, it is necessary to provide built-in excess reactivity at the start of core life. The amount of such required excess reactivity is a sensitive function of the fuel cycle, reactor schedule and core conversion ratio. Such excess reactivity may be controlled by poisoning the core (e.g. with control rods) at the start of core life. Such poison would then be gradually withdrawn as burnup proceeds. Excess reactivity may also be provided with fuel that initially resides outside of the core and is gradually inserted as burnup proceeds as well as combinations of fuel, moderator and poison. Whatever the control scheme, it is of significant interest to ascertain if important reactor parameters (e.g. Na coefficient, Doppler coefficient and breeding ratio) are significantly affected by the provision of excess reactivity that allows a relatively long uninterrupted reactor operating cycle.

Proposed plans for large fast reactor operation and fuel burnup capability are not too well defined. Therefore the effect of built-in excess reactivity that is controlled with poison was parametrically evaluated on a variety of conceptual fast power breeder reactor systems. These include typical oxide, carbide and metal fueled systems and systems which feature deliberate

spectral softening by introducing BeO in the core. Typical results are given in Table III-25-I.

In evaluating the results it should be noted that core fission product concentration was held fixed throughout the study for each reactor. In actual practice, fission products will "grow in" as reactivity demands will require a less-poisoned core, thus tending to slightly reduce the effects of the cited results.

The systems requiring the most excess reactivity for long core life (e.g. low core conversion ratio) seem to show the most pronounced variation of Na void coefficient with poisoned excess reactivity. Sign changes as well as large changes in the magnitude of the core sodium void coefficient may also be realized.

No specific Doppler effects were calculated here. However, the variation of the number of fissions below 9.1 KeV is indicative of the variation of the Doppler coefficient with core poisoning.

The breeding and core conversion ratios are not significantly affected by poisoning for excess reactivity.

The results in Table III-25-I are only illustrative in that actual details of poisoning the reactor were not specifically considered. If poison rods are used, as opposed to a uniform poison concentration, the effect of local poison concentration can have more marked local

TABLE III-25-I. FAST REACTOR PARAMETERS AS A FUNCTION OF POISONED EXCESS REACTIVITY^a

Spherical ^b Core Volume, liters	Fuel Type	Core Volume Fractions Fuel/Clad/Na/BeO	Poison ^c Material	Poison Atoms per cc × 10 ²⁴	Poisoned Excess Reac- tivity, %Δk/k	$\left(\frac{\text{Pu}^{239} + \text{Pu}^{241}}{\text{Pu}^{240} + \text{U}^{238}} \right)$	Core Na Void Effect, ^d % Δk/k	Fraction of Fissions Below 9.1 keV	Core Con- version Ratio	Breeding Ratio
3000	Oxide	30/20/50/—	—	—	—	0.148	+0.340	0.148	0.79	1.29
3000	Oxide	30/20/50/—	B	0.000134	1.011	0.150	+0.373	0.150	0.775	1.273
3000	Oxide	30/20/50/—	B ¹⁰	0.000029	1.031	0.150	+0.391	0.142	0.775	1.274
3000	Oxide	30/20/50/—	B ¹⁰	0.000067	2.317	0.154	+0.474	0.135	0.753	1.249
5000	Oxide	30/20/50/—	—	—	—	0.134	+0.70	0.157	0.88	1.29
5000	Oxide	30/20/50/—	B	0.000123	1.019	0.136	+0.723	0.153	0.862	1.264
5000	Oxide	30/20/50/—	B ¹⁰	0.000027	1.051	0.136	+0.746	0.151	0.862	1.264
5000	Oxide	30/20/50/—	B ¹⁰	0.000062	2.347	0.139	+0.823	0.144	0.838	1.234
2000	Carbide	30/20/50/—	—	—	—	0.128	+0.31	0.113	0.87	1.46
2000	Carbide	30/20/50/—	B	0.000161	0.858	0.130	+0.335	0.110	0.852	1.438
2000	Carbide	30/20/50/—	B ¹⁰	0.000036	0.884	0.130	+0.350	0.108	0.851	1.439
2000	Carbide	30/20/50/—	B ¹⁰	0.000080	1.920	0.132	+0.408	0.103	0.831	1.417
1000	Metal	30/20/50/—	—	—	—	0.104	+0.43	0.027	0.95	1.75
1000	Metal	30/20/50/—	B	0.000213	1.998	0.106	+0.492	0.0264	0.933	1.726
1000	Metal	30/20/50/—	B ¹⁰	0.000079	2.37	0.107	+0.508	0.0252	0.923	1.717
1000	Metal	30/20/50/—	B ¹⁰	0.000107	2.70	—	+0.525	0.0246	0.915	1.707
3000	Oxide	27.5/17.5/47.5/7.5	—	—	—	0.158	+0.14	0.235	0.77	1.18
3000	Oxide	27.5/17.5/17.5/7.5	B	0.000130	0.984	0.160	+0.159	0.229	0.744	1.202
3000	Oxide	27.5/17.5/47.5/7.5	B ¹⁰	0.000024	0.917	0.160	+0.173	0.228	0.746	1.205
3000	Oxide	27.5/17.5/47.5/7.5	B ¹⁰	0.000065	2.657	0.166	+0.271	0.216	0.719	1.176
2000	Metal	15/15/55/15	—	—	—	0.15	-0.03	0.277	0.76	1.31
2000	Metal	15/15/55/15	B	0.00010	0.836	0.153	+0.006	0.273	0.743	1.30
2000	Metal	15/15/55/15	B ¹⁰	0.000019	0.852	0.153	+0.021	0.272	0.743	1.30
2000	Metal	15/15/55/15	B ¹⁰	0.000050	2.161	0.157	+0.097	0.262	0.724	1.28

^a Reactors similar to those considered in Ref. 1. Multigroup constants used are 22 groups of the ANL-26 group set (Ref. 2).

^b Reactors have 18 in. thick blankets with 6 in. thick reflectors. The blanket composition is 45% fertile material, 20% steel and 35% Na. Except for poison, the core composition is "equilibrium" with fission products equivalent to 5% burnup replacing the core fuel. $\text{Pu}^{240}/\text{Pu}^{239} = 0.15$ for metal, 0.2 for carbide, and 0.25 for oxide. The blanket fertile material type is the same as the core fuel type.

^c Distributed uniformly throughout core.

^d $\Delta k/k$ corresponds to uniform removal of 40% of the Na originally present in the core.

effects than the results in Table III-25-I would indicate. It may also be noted that slight variations may be obtained by poisoning with natural versus enriched boron.

Some preliminary analyses providing excess reactivity with fuel residing outside the core indicate less pronounced variation of reactivity coefficients with the reactor operating cycle.

The implication of these results is simply that it may not be possible to consider a single reactivity coefficient for some reactors. The coefficient must be considered within the framework of the reactor oper-

ating cycle. Finally, the reactor operator and/or an automatic flux level control system must be capable of accommodating to the changes implied by the results of Table III-25-I.

REFERENCES

1. D. Okrent, I. Cohen and W. Loewenstein, *Some Nuclear and Safety Considerations in the Design of Large Fast Power Reactors*, (Presented to the 1964 Geneva Conference).
2. D. O'Shea, H. Hummel, W. Loewenstein and D. Okrent, *Twenty-Six Group Cross Sections*, ANL-6858 (to be published).

III-27. The Control of Fast Reactors; Current Methods and Future Prospects¹

W. B. LOEWENSTEIN

The practical aspects of providing adequate reactivity for the control of fast reactors differ significantly from those used to control thermal neutron systems. The differences are primarily due to the rather small fast neutron cross sections. There are no strong poisons in a fast neutron system. As a result, the strong thermal reactor fission product poisons (e.g. Xe and Sm) require significantly less reactivity override than the reactivity loss due to destruction, by fission and capture, of fissionable material. Because the fast spectrum atomic cross sections are relatively small compared to their thermal counterparts, the atomic density of the material plays an important role in the choice of control materials.

The reactivity for control is dictated by reactor shutdown requirements, the reactor fuel cycle (excess reactivity) and to a lesser extent the dominant feedbacks. The excess reactivity requirements can be quite well specified in terms of a given fuel cycle but

may vary considerably for several similar systems operating on different fuel cycles. The required shutdown reactivity may be almost arbitrarily specified beyond certain limits. Typical power and temperature dependent feedback parameters are used to determine their influence upon the control reactivity requirements.

The methods used to predict the reactivity worth of control mechanisms have evolved from crude estimates to quite reliable calculations which can be confirmed by experimental data from critical assemblies. Exploratory analytical studies demonstrate problems of control for large core volume conceptual systems.

REFERENCES

1. W. Loewenstein, *The Control of Fast Reactors; Current Methods and Future Prospects*, Proc. IAEA Sponsored Symposium of Physics and Material Problems of Reactor Control Rods, Vienna, 1963, (to be published).

III-28. Sodium Void Coefficient for "Heterogeneous" Fast Reactors

W. B. LOEWENSTEIN

Exploratory analyses to determine how a core with an inherently overall positive sodium void coefficient might be assembled to produce a negative sodium void coefficient were considered. In these particular calculations, it was initially assumed that the change in sign of the void coefficient might be produced by providing several loosely coupled cores with a higher fuel enrichment as opposed to the reference single region compact core.

The multigroup diffusion theory calculations utilized one dimensional slab geometry with an appropriate transverse leakage term. The reference reactor was a 1500 liter core. In all subsequent calculations, the transverse radial leakage term was held constant and the sum of the axial core dimensions were held fixed. Thus there was some assurance that systems of equal size and power capability were, in fact, compared. The multigroup constants for these calculations were taken from Ref. 1. The reactor core contains a metallic Pu-U fuel and the reflector contains depleted uranium.

The results of the calculations where the core was separated into several slab regions loosely coupled by interspersed fertile material regions are given in Table III-28-I.

It can be seen that the character of the sodium void coefficient of reactivity may be markedly altered by providing several loosely coupled slabs of smaller thickness rather than a core of one large slab. A most interesting result is the one case where natural uranium was used for the separating slab. This approximates a condition where significant Pu production has taken place in the separating slab. The Na void coefficient is less negative than for the separating slab using depleted uranium.

In all cases, the provision of a negative sodium void coefficient is at the expense of increased fuel requirements. The increased fuel enrichment required to accomplish criticality for the loosely coupled slabs may harden the spectrum sufficiently to improve the overall breeding ratio of the system even though the internal core breeding ratio will suffer. However, the fuel re-

TABLE III-28-I. EXPLORATORY SODIUM VOID CALCULATIONS FOR "HETEROGENEOUS" FAST REACTOR CORES (1500 LITER SYSTEMS: METAL FUEL AND REFLECTOR)

Number of Regions		Axial Thickness of Region, cm		Critical Enrichment, $\frac{N(\text{Pu})}{N(\text{Pu}) + N(\text{U-238})}$		Reactivity Change for 30% Core Na Removal	
Core ^a	Reflector ^b	Core	Reflector ^c	Reference	30% Na removed ^d	Sign	Magnitude ($\% \Delta k/k$)
1	2	142	0	0.08776	0.08763	positive	0.033
2	3	71	10	0.10376	0.10405	negative	0.143
2	3	71	10 ^e	0.10323	0.10350	negative	0.130
2	3	71	5	0.09846	0.09842	positive	0.0188
2	3	71	15	0.10595	0.10645	negative	0.264
2	3	71	20	0.10681	0.10742	negative	—
3	4	48	10	0.10717	0.10708	positive	0.074
3	4	48	15	0.11441	0.11445	negative	0.024
3	4	48	20	0.11972	0.12013	negative	0.187
3	4	48	25	0.12340	0.12408	negative	—
5	6	28	10	0.12422	0.12397	positive	0.16
5	6	28	20	0.15245	0.15289	negative	—

quirements for the 1500 liter "heterogeneous" cores analyzed here seem quite moderate when compared to the reference single slab core.

REFERENCES

1. S. Yiftah, D. Okrent and P. Moldauer, *Fast Reactor Cross Sections*, (Pergamon Press, New York, 1960).

^a Core contains 25 v/o Pu-U metal, 25 v/o steel, 50 v/o Na.

^b Reflector contains 60 v/o depleted U, 20 v/o steel, 20 v/o Na.

^c Only interspersed reflector regions. Outer reflector always ~45 cm thick.

^d From core regions only.

^e Central reflector region contains natural uranium.

III-29. Fuel Cycle Studies

G. J. FISCHER and L. E. LINK*

The economic potential of fast power breeder reactor systems which might be built in the near future, with very little extrapolation of present technology, was recently evaluated. The results of this study are summarized in a paper presented to the 1964 Geneva Conference.¹ This paper contains a partial re-evaluation or normalization of the four 1000 MWe fast reactor studies recently prepared for the USAEC.^{2,3,4,5} The normalization was effected with consistent assumptions on fuel fabrication, processing, and shipping costs.

The 14 fast reactors whose fuel cycle physics and economics were calculated for the Geneva report are briefly described in Tables III-29-I A and B.

The physical dimensions, thermodynamic efficiencies, fuel pin diameters, etc., were chosen to be consistent among the three fuel types, but a careful optimization program was not pursued. The assigned costs and charges shown in Table III-29-II represent those felt to be consistent among the fuel types. Fabricating and processing plant costs are based on a near-future total operating level equivalent to reactors having a power output of 1500 MWe.

* Laboratory Director's Office, Argonne National Laboratory.

TABLE III-29-IA. REACTOR CASE IDENTIFICATION

Case No.	Fuel Type	
1-C	UC-PuC	Reference carbide fuel study, 1250 liters
2-M	U-Pu	Reference metal fuel study, 2 cores, 1000 liters
3-O	UO ₂ -PuO ₂	Reference oxide fuel study, 3000 liters
4-C	UC-PuC	Case 1-C } with average core burnup increased 50%
5-M	U-Pu	
6-O	UO ₂ -PuO ₂	
7-C	UC-PuC	Case 1-C } with } (25% of radial and 50% axial) outer } (25% blankets removed)
8-C	UC-PuC	
9-M	U-Pu	
10-M	U-Pu	
11-O	UO ₂ -PuO ₂	
12-O	UO ₂ -PuO ₂	
13-C	ThC-UC	Thorium-U ²³³ carbide fuel study
14-C	UC	U ²³³ -U ²³⁸ (core) carbide fuel study; ThC blanket

TABLE III-29-IB. REACTOR DIMENSIONS

Case No.	Core (Cylinder Shape)		Blanket Thickness	
	Diam, cm	Ht, cm	Axial, cm	Radial, cm
<i>Reference cases</i>				
1-C	145	75	60	30
2-M ^a	113	100	60	30
3-O	252	60	70	35
<i>Reference cases—core burnup increased 50%</i>				
4-C	145	75	60	30
5-M ^a	113	100	60	30
6-O	252	60	70	35
<i>Blanket thickness variation</i>				
7-C	145	75	45	23
8-C	145	75	30	16
9-M ^a	113	100	45	24
10-M ^a	113	100	30	17
11-O	252	60	53	27
12-O	252	60	35	19
<i>U²³⁵ fuel</i>				
13-C	106	100	60	30
14-C	106	100	60	30

^a Two core system; diameter listed for each core.

TABLE III-29-II. UNIT COSTS AND CHARGES

	Oxide	Carbide
1. Fabrication—ceramic fuels core and axial blanket radial blanket	\$140/kg \$61/kg	\$188/kg \$63/kg
2. Processing—ceramic fuels—\$55 to 90/kg (core and blanket fuel mixed).		
3. Fabrication and pyrometallurgical reprocessing—metal fuel core ≈ \$230/kg ^a radial blanket ≈ \$180/kg.		
4. Shipping charges—total for spent and fabricated fuel—\$24/kg.		
5. Annual charge on value of equilibrium core fissile material—10%.		
6. Annual charge on average fabrication investment in core and blankets—10%.		
7. Losses in fabrication and processing—1.5%.		
8. Fissile material price—\$10/g based on U ²³⁵ , Pu ²³⁹ , Pu ²⁴¹ only.		
9. Cycle thermodynamic efficiency with ceramic fuel—40%. with metallic fuel—35%.		

Note: Costs listed for 1, 2 and 3 are valid for the 1500 MWe scale assumed, 58 MT/yr for metal and 38 MT/yr for carbide and oxide.

^a Valid for core/blanket ratio in reference cases.

TABLE III-29-III. COSTS—mills/kWh

Case No.	Fabrication	Processing	Shipping	Pu Invent. ^a	Fab. Invest. ^b	Pu Credit	Total
<i>Reference cases</i>							
1-C	0.35	0.18	0.06	0.24	0.03	0.46	0.40
2-M	← 1.22 →		0.13	0.34	0.14	0.78	1.05
3-O	0.26	0.17	0.05	0.48	0.04	0.39	0.61
<i>Reference cases—core burnup increased 50%</i>							
4-C	0.24	0.13	0.04	0.21	0.03	0.38	0.27
5-M	← 0.81 →		0.10	0.35	0.14	0.68	0.72
6-O	0.18	0.12	0.04	0.42	0.04	0.32	0.48
<i>Blanket thickness variation</i>							
7-C	0.33	0.16	0.05	0.24	0.03	0.38	0.43
8-C	0.30	0.14	0.04	0.24	0.02	0.25	0.49
9-M	← 1.11 →		0.12	0.35	0.11	0.69	1.00
10-M	← 0.98 →		0.11	0.35	0.09	0.53	1.00
11-O	0.25	0.16	0.05	0.48	0.04	0.30	0.68
12-O	0.23	0.16	0.04	0.49	0.03	0.19	0.76
<i>U²³⁵ fuel</i>							
13-C	0.34	0.19	0.06	0.26	0.02	0.09 ^c	0.78
14-C	0.33	0.16	0.06	0.20	0.02	0.27	0.50

Note: Losses are included in fabrication and processing.

^a Charge for plutonium inventory.

^b Charge for fabrication investment.

^c U²³⁵ credit.

The results of applying these costs and charges to the equilibrium core and blanket cycles of the reactors are shown in Table III-29-III. A partial breakdown of the total costs is given. These results indicate that even for restrictive assumptions of cost estimates based on total fast reactor power limited to 1500 MWe for a given type fuel and about 500 MWe per plant, relatively attractive fuel cycle costs can be hoped for in near-future fast reactor designs.

REFERENCES

1. L. E. Link, G. J. Fischer and E. L. Zebroski, *Fuel Cycle Economics of Fast Reactors*, (Presented to 1964 Geneva Conference).
2. *Liquid Metal Fast Breeder Reactor Design Study*, CEND-200, Vols. I and II, (January, 1964).
3. *Large Fast Reactor Study*, ACNP-64503, (January, 1964).
4. *Liquid Metal Fast Breeder Reactor Design Study*, WCAP-3251-1, (January, 1964).
5. *Liquid Metal Fast Breeder Reactor Design Study*, GEAP-4418, Vols. I and II (January, 1964).

III-30. Theoretical Investigation of a Major Excursion Caused by Fuel Element Failure

V. Z. JANKUS

TREAT experiments have shown¹ that a sodium-bonded stainless-steel-clad metallic fuel pin exposed to transient heating experiences failure when the temperature reaches about 1100° C. At the time of failure an opening develops at about the middle of the pin and the molten uranium is ejected within ~0.15 sec. Similar pin failures in an operating reactor might cause reactivity addition. Increased power, in addition to the possible eutectic action of ejecting molten uranium on stainless steel clad, could cause failure of neighboring pins and thus initiate an autocatalytic excursion. If reactivity insertion would continue unchecked until all the fuel is collected at the reactor midplane, the maximum excess reactivity could reach 0.14 $\Delta k/k$ for EBR-II.² Maximum possible reactivity cannot usually be reached since a reactivity reduction mechanism generally takes over before all available reactivity has been inserted. When the reactivity insertion rate, \dot{k}_0 , is constant, it has been shown³ that the maximum reactivity attained is

$$k_{max} \approx \sqrt{\ell k_0} \sqrt{\ln(Q_1^2 n^{-2}(0) \ell^{-1} \dot{k}_0)}, \quad (1)$$

where ℓ is the prompt lifetime, $n(0)$ is initial power and Q_1 is the heat necessary for effective reactivity reduction. If it is assumed that all pins fail simultaneously at the rate observed in TREAT, one may obtain $\dot{k}_0 \approx 140$ dollars/sec in EBR-II.² However, with increasing pressures the reactivity insertion rate may become even larger. First, the speed of fuel ejection is proportional to the square root of pressure. Secondly, penetrations of the cladding are likely to increase with increasing pressures. Consistent application of this quasistatic model for reactivity insertion may lead to very high insertion rates.

It should be recognized that the quasistatic model is valid only for relatively long periods, so that the generated pressure can traverse the pin several times and become essentially uniform. When inverse periods, α , become larger than c/b (where c is the velocity of sound and b the half-height of the core), reactivity effects of pressure can be adequately represented by neglecting wave propagation⁴:

$$\ddot{k} = \int p \nabla^2 w dV, \quad (2)$$

where the Laplacian of fuel worth, $\nabla^2 w$, is negative and the pressure generated locally results in negative \ddot{k} . Autocatalytic reactivity insertion should be terminated

when

$$\alpha_a \approx k_a/\ell = c/b,$$

where the subscript "a" refers to autocatalytic reactivity. It is assumed that effects initiating the autocatalytic events are not significant. In the initial autocatalytic stage the pressure in the fuel elements can pessimistically be assumed to be spatially uniform.

In the following stage the reactivity is obtained from Eq. (2) and reactivity reduction is initiated. The energy yield can be shown to be a function of k_{max} obtained from Eq. (1). Fortunately, k_{max} is not sensitive to the details of the reactivity insertion mechanism. The autocatalytic reactivity insertion rate is assumed to be caused by generated heat or energy ($\dot{k}_a \approx Q^n$, where n is a constant, Q is the energy density and \dot{k}_a is the "reactivity insertion rate" due to autocatalytic processes). At the end of the autocatalytic insertion it can be shown that:

$$\sqrt{\ell \dot{k}_a} = k_a \sqrt{n/(n+2)}.$$

\dot{k}_a is thus fairly insensitive to the details of the reactivity insertion mechanism. k_{max} depends only logarithmically on the "initial" power, $n(0)$, when k_a has been reached. Thus k_{max} is not very sensitive to the parameters during the autocatalytic insertion stage. Exploratory calculations have shown that $n(0)$ is almost independent of the power when autocatalytic insertion is initiated. The autocatalytic form of reactivity increase causes $n(0)$ to be many times larger than the initial power used earlier,³ in core collapse accident analyses. The autocatalytic excursion is milder than \dot{k}_0 would tend to indicate. The reactivity increase is only about half that of a reactivity insertion caused by mechanical rather than thermal effects.

The energy yield during the last stage of the excursion is known to depend strongly on effective voids in the reactor. These are likely to depend principally upon details of initial reactivity insertion and a few calculations are being performed to obtain some numerical examples. Similarly a more precise definition of k_a would be desirable. However, from present considerations it is already clear that excursions caused by melting pins will not be larger than those calculated for the collapse of reactor core.

REFERENCES

1. C. E. Dickerman, G. H. Golden and L. E. Robinson, *In-Pile Photographic Studies of EBR-II Mark-1 and Fermi*

- Core-A Sample Meltdown, Nucl. Sci. Eng. 14, No. 1, 30 (September 1962).
2. L. J. Koch, W. B. Loewenstein and H. O. Monson, *Addendum to Hazard Summary Report—Experimental Breeder Reactor-II (EBR-II)*, ANL-5719-Addendum (1962).
 3. W. J. McCarthy, R. B. Nicholson, D. Okrent and V. Z. Jankus, *Studies of Nuclear Accidents in Fast Reactors*, Proc. 1958 Geneva Conf. 12, Paper No. 2165, pp. 207.
 4. V. Z. Jankus, *A Theoretical Study of Destructive Nuclear Bursts in Fast Power Reactors*, ANL-6512 (1962).

III-31. Coolant Pressures During Transients

R. O. BRITTAN

INTRODUCTION

The problem of estimating core pressure rises during excursions in water cooled systems has long been studied without success. It was necessary to estimate such pressures in sodium-cooled systems because of the advent of the sodium loop tests in TREAT. This paper constitutes a record of upper limit pressure estimates made for the large sodium loop, during transients in TREAT, and some subsequent investigations. These investigations form the basis for a continuing examination of the problem of predicting such pressures.

It should be noted that in order to assure upper bounds for the pressures estimated, extremely conservative assumptions have been made. It would be the purpose of subsequent investigations to reduce this conservatism, allowing a closer approach to realism.

In this case it was necessary to utilize a physically intuitive approach in making the estimates. Hence, a short description of the system and the phenomenological aspects are needed to gauge the conservatism.

DESCRIPTION OF THE SYSTEM AND PHENOMENON

First, the physical behavior of the coolant in a fuel channel or subassembly during a nuclear transient can be described in terms of the energy release rates, heat transfer rates, the thermal and mechanical inertia of the system, and an equation of state of the coolant.

The system may be simply characterized by a vertical tube containing coolant moving upward through an active (heated) section into an inactive (non-heated) section. Heat is generated in the active section and transferred to the coolant in that section.

The primary nuclear energy release rate for a positive k_{eff} condition is characterized by the nuclear variable $[(1/n)(dn/dt)]^{-1}$ which for constant k_{eff} , and after a short time, becomes the asymptotic period or e-folding time $(1/\alpha)$. This characteristic continues until physical changes bring about a reduction in reac-

tivity, causing $(1/n)(dn/dt)$ to become zero and then negative.

Only the "heat" energy release is of interest. It is manifest from two forms: kinetic energy of the fission fragments and β particles; and energy of the gamma rays. The latter heat the fluid directly by giving up energy on their passage through the fluid. The time from original acquisition of energy to transfer to the fluid is of the order of 10^{-8} sec. Thus, fluid heating rates from this source are characterized by α with no delay. The other transfer path to the fluid is more tortuous: the fission fragments and β 's are slowed down very near to the location of the fission, transforming their kinetic energy to heat in the active tube material.

Fuel elements or subassemblies are small compared to the reactor core; therefore, the fission fragment heat source will be considered uniformly distributed in the active portion and proportional in strength to the average fission rate at the location of the element. This fission fragment heat is stored in and gives rise to a temperature increase in the active material which forces the heat to flow by conduction to the tube-fluid interface (when the fluid is cooler than the tube, of course). The character of the active material with respect to heat storage, temperature rise, and heat conduction is given by dimension, heat capacity, and thermal conductivity as the parameter "thermal diffusivity." This parameter is likened to a thermal "inertia" and introduces a time lag for the heat transferred by conduction between the nuclear energy release and heating of the inactive section.

The backed-up heat in the active section is stored causing a continuing temperature rise in the active material in accordance with the heat capacity. The characteristic time for this temperature rise is governed by α . The heat conducted to the surface of the tube (tube-fluid interface) and transferred to the fluid, has a time lag introduction also characterized by α because the temperature rise increases the "driv-

ing pressure." The combination of the driving pressure acting against the thermal resistance and inertia dictates the time lag for the heating rate of the fluid. This thermal resistance is manifest if the active material is clad. If the cladding is thin and a good heat conductor, or, if the active fuel is directly exposed to the fluid, the heat transfer is characterized by the temperature difference across the interface and by the thermal diffusivity of the coolant.

A third characteristic which is important in some transients is the fluid flow velocity. For very small heat transfer rates and large flow rates, the flow is not significantly altered and no pressure rise occurs, the fluid sweeping away and condensing fluid vapor bubbles. For very small flow velocities and small heating rates (approaching stagnation), the vapor bubble grows slowly and, if there is no mechanical restriction on fluid motion, pressure will not build up.

If α is large, so that the heating rate rapidly becomes large, a rapid expansion of the fluid in the active portion could occur because of the heat dump; however, this expansion may be inhibited by the inertia of the column of fluid in the inactive portion of the tube, resulting in a pressure rise.

It may be possible for heating rates to be small and thermal resistance very large. A specific example would be a case where the cladding is thick and acts as an insulator. Then all the heat would be stored in the fuel material and dumped suddenly on the loss of integrity of the cladding. Sudden expansion of the fuel tube would act like a solid piston on the fluid. This coupled with the sudden heat dump, the inertia of the fluid in the active portions and in the inactive portions, could lead to a pressure rise.

Thus, in the general case, pressure buildup is a function of the rapidity of heat dump to the fluid and the rapidity of expansion of the fuel element into the fluid space. The pressure is linked to the heat dump by the heating and expansion of the fluid and by the increase in vapor pressure.

From this summary of the phenomenology a physically intuitive approach will allow estimates of an upper limit on the pressure buildup in a transient. This can be done by considering two pressure sources separately. That caused by temperature rise of the fluid with inertia restrictions is the first, and that caused by pressure buildup in and sudden expansion of the fuel pin is the second.

PRESSURE RISE IN THE FLUID

The theoretical maximum heating rate is that obtained by assuming instantaneous heat transfer to the fluid so that the temperature of both fuel and coolant

are always equal and the total available heat is divided or apportioned in accordance with the heat capacities. It must also be assumed that the energy release rate corresponds to that in a reactor on an asymptotic period ($1/\alpha$) without reactivity change. Then the total heat available is:

$$H = (1/\alpha)P_0(e^{\alpha t} - 1) = H_f + H_p$$

P_0 = initial heat generation rate in the subassembly at $t = 0$

H_f = total enthalpy of the fluid in the active section

H_p = total enthalpy of the active portion of fuel element.

As the fluid heats up, it expands and drives the fluid in the inactive portion upward. It is assumed that the fluid is incompressible so that any thermal expansion must result in a volumetric displacement of the fluid column in the inactive portion. Using temperature as the index, if a change in specific volume in relation to temperature is known, the variation of vertical displacement of the fluid column can be tabulated. If the relation between enthalpy and temperature is known, the enthalpy versus temperature data can also be tabulated. From the expression relating enthalpy to energy release rate, the corresponding e -folding time may be tabulated. This provides the relation between time and displacement necessary to determine velocities and accelerations. From the accelerations and the inertial mass loadings, the pressures required to accelerate the fluid to allow for expansion are determined.

This relationship continues until the vapor pressure of the fluid becomes greater than the fluid weight and atmospheric head and inertial pressure due to expanding fluid. Continued heating causes increased vapor pressure, and the fluid motion now becomes primarily a function of the pressure, rather than the reverse as originally obtained. Even though the vapor pressure moves the fluid out, leaving an increasing gas space below the whole fluid column, the fluid expansion continues to move the fluid in the inactive portion as before. Surface tension resistance has been neglected, but may be included if important. The relation between temperature, enthalpy, and vapor pressure is maintained at saturation values. Too rapid expansion results in further vaporization using more heat, while too slow an expansion would cause condensation. The amount of heat required to produce the few cubic inches of vapor is small enough to be ignored, but sufficient to guarantee the equilibrium of the saturated condition.

Continuing with temperature as the index, if the variation of vapor pressure in relation to temperature

is known, the vapor pressure may be tabulated and the pressure-time relationship established. By double semi-graphical integration of the pressure-mass-acceleration relation, the vertical motion of the fluid column is obtained. The pressure buildup will continue until the vapor bubble has forced the fluid out of the active region. By this time, heat transfer will have greatly diminished and the corresponding pressure will be an upper limit.

This pressure is of course an over-estimate, since the heat transfer lag, rates, and temperature variations have been ignored.

These "upper limit" calculations were carried out for the EBR-II fuel subassembly, using the information on heat capacities given in Table III-31-I,¹ and the sodium thermodynamic properties given in Ref. 2. The relation between pressure and temperature given in Ref. 2 above 2700°F and up to the suggested critical temperature (3632°F) was altered to:

$$\log p = 1.046202 (\theta/1000) - 0.097203 \text{ (psia)}$$

in order to conform to the suggested critical pressure (343 atm). These calculations were started with the sodium at about 400°F initially to yield maximum heat dump rates at the time the vapor pressure becomes significant.

The variation of limiting pressure and other quantities with α was found to be:

α , 1/sec	1	5	10	20	50
θ , °F/°C	1810/990	1925/1050	2075/1150	2620/1450	3500/1940
v , ft/sec	7.8	14.2	16.6	33	95
p , psia	21	43	84	430	3620
t_{exp} , sec	0.27	0.175	0.126	0.056	0.020
v_{exp} , ft/sec	54	82	116	260	770
E_k , ft-lb	730	1680	3370	16900	148000

where

- α = inverse period
- θ = coolant and fuel temperature at time of peak pressure
- v = velocity of fluid column in riser at time of peak pressure
- p = peak pressure in vapor bubble
- t_{exp} = time after peak pressure to complete expulsion of fluid
- v_{exp} = velocity of coolant at time of expulsion (maximum)
- E_k = kinetic energy of coolant at time of expulsion.

The other mechanism for producing pressure, i.e., pin thermal expansion, was examined briefly. This expansion was treated as augmenting the fluid expansion, in effect only. The largest effect found for the EBR-II-type subassembly was 3% of the fluid expansion.

Subsequently, similar calculations were made substituting water for sodium. With water it was necessary to start the calculations at 32°F, and final tem-

TABLE III-31-I. MATERIAL PROPERTIES¹
(3% U-fissium)

k	ρC_p	Temp. Range, °C	$\rho \Delta H$
0.06617	0.7089	260-630	62.825
0.10780	0.9065	630-1010	0.0
0.1136	4.7873	1010-1100	0.0
0.0852	0.6058	>1100	0.0

k = thermal conductivity [cal/sec-cm²-°C]; ρC_p = density times specific heat [cal/cm³-°C]; $\rho \Delta H$ = density times heat of transformation [cal/cm³].

peratures were of course much lower. The resulting pressure maximums for equal α 's were significantly lower due to larger heat capacities and liquid expansion coefficients, and smaller pressure coefficients.

The effect of degree of subcooling was studied for both sodium and water. For equal α 's, an order of magnitude reduction in pressure was realized by starting the heating at the boiling point instead of the melting point, in both cases.

A single calculational description will suffice to represent all of these. Assumptions made are:

1. The heat of fusion has been added, so that the zero enthalpy reference is just above the melting point of coolant.

2. The specific heat of the uranium pin is assumed constant up to the first phase transformation. It is then increased several fold to a new constant value between the first and second phase transformation. Following this second transformation, it is reduced again to a new constant value up to the mp of uranium. A new constant value is used above this point. Heat added to effect the phase changes is neglected.

3. The specific heat of the coolant is constant; and the heat of vaporization is neglected.

4. The coolant maintains saturated conditions after subcooling becomes zero.

5. Vapor does not appear in the active portion until the vapor pressure balances the inertial resistance to the expanding fluid plus the atmospheric pressure. Hence, this balance point marks the beginning of ejection of the fluid from the active region.

6. The liquid in the active portion expands into the tube (riser) forcing all the non-heated water in the riser ahead of it.

7. The inertial mass loading is that of the column of liquid divided by the cross sectional area of the coolant passages in the active portion.

8. The specific heats, specific volumes, vapor pressures, and enthalpies are known, each as a function of temperature.

9. The power increases exponentially with a constant period.

10. Thermal conductivity is infinite.

On the basis of the foregoing assumptions, calculations are made in the following manner:

(1) Tabulate the ratios of vapor pressure to mass loading for a number of convenient temperatures above atmospheric boiling temperature.

(2) For each temperature increment, calculate and tabulate the total heat which must be added to effect the increment from enthalpies of fuel element and coolant.

(3) Integrate the heat increments and tabulate them.

(4) The velocity of the inertial mass due to fluid expansion alone is equal to the power level multiplied by the derivative of specific heat of coolant w.r.t. total energy release, by the derivative of specific volume, of coolant w.r.t. specific heat of coolant, and the ratio of the weight of fluid to cross sectional area of coolant passage. The power level is equal to the product of the total energy release times the inverse period, plus the initial power. The acceleration or inertial pressure is equal to the velocity times the inverse period. From these relations the inertial pressure can be calculated for each temperature and tabulated.

(5) The net accelerating pressure is obtained next at each temperature by subtracting step (4) from step (1).

(6) The time increment between temperature points is next calculated by dividing the natural logarithm of the sum of one plus the ratio of total heat increment to total heat by the inverse period, and tabulated.

(7) The product of step (6) and the incremental net pressure of step (5) next yield the incremental velocities which are tabulated and integrated to provide velocity at each temperature.

(8) The product of step (6) times the velocity increments of step (7) yields the incremental rise of the column in the inactive portion. These motion increments are integrated and tabulated for each temperature.

(9) The motion of step (8), when multiplied by the ratio of riser cross section to area of coolant passage in the active portion, yields the position of the vapor-liquid interface in the active portion.

(10) When the interface position coincides with the upper end of the active portion, the maximum pressure has been reached and it is equal to the saturated vapor pressure at the corresponding temperature.

This completes the calculational sequence, which may be repeated for any inverse period and degree of subcooling. The pressures attained, for the EBR-II subassembly with sodium, are tabulated for various inverse periods, and for various degrees of subcooling at one inverse period:

Gage Pressures, psi

Inverse Period, α , sec ⁻¹ →	1	5	10	20	50
Degree of subcooling, °F					
↓					
1410 (melting point)	14	41	160	570	7900
1218	6	29	69	415	3600
800				200	
150				44	
0				17	

The calculations also showed that the inertial pressures resisting the expansion of the liquid phase alone can become considerable. Representative values for sodium on reaching atmospheric boiling are:

Inertial Pressures, psi

Inverse Period, α , sec ⁻¹ →	1	10	20	50	100	200	500
Degree of subcooling, °F							
↓							
1410 (melting point)	0.02	2.1	8.5	53	210	850	5300
705	0.01	1.0	4.2	26	105	420	2600
141	0.002	0.21	0.85	5.3	21	85	530
14	0.00003	0.002	0.008	0.053	0.21	0.85	513

All the estimates for water yield pressures far in excess of those actually experienced for these small α 's in SPERT. It has been found experimentally for the water system that significant pressures do not develop until α approaches several hundred/sec. This indicates that the assumptions made to yield upper limits are far too conservative. To continue efforts in predicting pressures, some drastic changes in these assumptions will have to be made. The course of the detailed calculations has pointed up some of the changes which must be made to yield more realistic estimates.

One of the more obvious of these changes is that because of the shape of the power burst curve, and its integral³ the heat release is better characterized by a linear relation after 10% of the total heat has been released than by an indefinitely increasing exponential. In many cases, the heating rates will diminish before coolant ejection is realized.

Another area for change is that the heat transfer characteristics and vapor blanketing effects do not allow realization of the heat dump rates found in the calculations.

In TREAT excursions the shape of the heat release history is prescribed by the nature of the reactor transient, and unaffected by the behavior of the test section. In the SPERT type tests, nuclear shutdown begins before significant pressures can occur and the

heat release rates during development of significant pressures are usually diminishing rapidly. That is, the peak power occurs considerably before the pressure peak, even for very large α . Often the total heat added is insufficient to boil the coolant, and the only motion is due to liquid expansion. The only pressures developed short of fuel melting are those due to inertial resistance to fluid expansion. These can be significant only for very large α . For example, with water at an α of 500, the inertial pressure for 20° subcooling was found to be 250 psi by the time boiling point was reached, but only about 2 psi for an α of 50.

At present it appears that if the history of the heat dump to the coolant is known, the pressure history can be predicted with precision. The principal unknown with respect to heat dump rates to the sodium is the heat transfer rate from the solid fuel element to the coolant. This can be obtained directly by integral experiments in which sodium is heated in a long tube. To couple such basic experiments with reactor excursion

data available for water from the SPERT and KEWB tests, companion experiments with water will be necessary. This conclusion is based on the difference in behavior during calculations made for the two coolants. It is evident from this difference that water cannot be used directly as a substitute to study the behavior of sodium under most dynamic conditions in out-of-pile experiments.

Consideration of these factors is being given in our continuing efforts to predict pressures, and the successes will be determined by comparison with experiments.

REFERENCES

1. A. W. Barsell, Argonne National Laboratory, (Private Communication).
2. E. L. Dunning, *The Thermodynamic and Transport Properties of Sodium and Sodium Vapor*, ANL-6246 (1960).
3. R. Brittan, *Reactor Containment, Including a Technical Progress Review*, ANL-5948 (1959).

III-32. Equation of State for Mixture of Materials in Reactor Excursion

V. Z. JANKUS

In a realistic approach to a major excursion one encounters conditions when not only fuel but also structural material and coolant are present in substantial amounts in the reactor core. The major effect of non-fissioning material is, obviously, reduction of the voids and, because of this, considerable reduction of the severity of the accident. For a detailed calculation of the excursion, other parameters are also of importance (e.g. $(\gamma-1)$ of the Bethe-Tait analysis,¹ velocity of wave propagation, etc.). While these can often be roughly estimated, a more formal approach is appropriate.

A major excursion in a fast reactor takes place in such short time that conduction of heat is negligible. Fuel temperatures reached during this time are too low for appreciable radiative energy loss. Pressures depend only on the local energy input and expansion of the material. For determination of the pressure, an equation of state giving pressure, p , in terms of internal energy, e , and specific volume, v , is required. (If one neglects the Doppler effect, the temperature does not enter explicitly into the computations.) To describe the motion of reactor material attention need be focused only on $e = e(p, v)$ describing the mixture of materials.

This relation can be obtained quite simply by employing two extreme assumptions. The first (isothermal assumption) postulates a case in which all materials are

so finely dispersed that they have the same temperature locally. The second (adiabatic assumption) supposes that only fuel is heated and no heat is transferred to any other material. In the first assumption both internal energy and specific volume for each material are given in terms of pressure and temperature. Eliminating the temperature gives the required relation among pressure, average specific volume (v), where

$$v = \left(\sum_i m_i v_i \right) / \left(\sum_i m_i \right), \quad (1)$$

and average specific internal energy e , where

$$e = \left(\sum_i m_i e_i \right) / \left(\sum_i m_i \right). \quad (2)$$

Here, m_i are the masses of the materials (i).

In the adiabatic assumption the equation of state for the fuel is:

$$e_1 = e_1(p, v_1). \quad (3)$$

Then using the isentropic equations for the second material:

$$v_2 = v_2(p) \quad (4)$$

$$e_2 = e_2(p); \quad (\partial e_2 / \partial p) = -p(\partial v_2 / \partial p), \quad (5)$$

and definitions (1) and (2), the intermediate v_i and e_i

are eliminated to obtain a relation between internal energy, pressure, and specific volume:

$$e = \frac{m_2}{m_1 + m_2} e_2(p) + \frac{m_1}{m_1 + m_2} \cdot e_1 \left[p, \frac{m_1 + m_2}{m_1} v - \frac{m_2}{m_1} v_2(p) \right]. \quad (6)$$

In AX-1 calculations,² the equation of state usually is approximated by that of Stratton.¹ The pressure is assumed to be zero until the threshold temperature, θ^* , is reached. After this the pressure is a linear function of temperature, θ , and density ρ :

$$p = \tau + \alpha\rho + \beta\theta, \quad (7)$$

where τ , α , and β are constants.

The specific heat, c_v , is assumed to be a linear function of the temperature, θ :

$$c_v = (\partial e / \partial \theta)_v = A + B\theta, \quad (8)$$

where A and B are constants.

From these equations a relationship among τ , p , and v can be easily derived:¹

$$e = (A/\beta)(p - \tau - \alpha\rho) + (B/2\beta^2)(p - \tau - \alpha\rho)^2 - \tau v - \alpha \ln v + \text{const.} \quad (9)$$

Thus the energy is expressed as a quadratic function of pressure (when $p > 0$). The specific volume is not expected to change drastically during a contemplated power burst in a fast reactor. One can expand Eq. (9) in a power series in $(v - v^*)$ and keep only first order terms where v^* is the specific volume at the threshold temperature, θ^* .

$$e = a_0 + a_1 p + a_2 p^2 + b_0(v - v^*) + b_1 p(v - v^*) + \dots \quad (10)$$

where numerical values of the coefficients can be obtained from Eq. (9) in a straightforward fashion. Conversely the coefficients in the expansion, Eq. (10), determine the coefficients in Stratton's equations:

$$\alpha = \frac{b_1 v^{*2}}{2a_2}$$

$$\tau = \frac{-2b_0 a_2 + b_1(a_1 - v^*)}{2a_2}, \quad (11)$$

$$\frac{A}{\beta} = -2b_0 a_2 + b_1 a_1 + a_1$$

$$\frac{B}{\beta^2} = 2a_2.$$

Obviously only relations (A/β) and (B/β^2) are obtained since Eq. (10) is not altered by a change in temperature scale.

The coefficient $a_0 = Q^*$ depends upon the initial temperature and the expression for the specific heat used at $p = 0$. The numerical program (AX-I) generally uses Eq. (8) for the specific heat at zero pressure. While Eq. (8) is simple, it is inconsistent with the assumed equation of state for positive pressures. It is known from thermodynamics that

$$(\partial c_v / \partial v)_\theta = \theta (\partial^2 p / \partial \theta^2).$$

Thus, the specific heat given at one density determines the specific heat at other densities when the equation of state, Eq. (7), is known. Where the specific heat for positive pressure is given by Eq. (8) for vanishing pressures, the equation becomes:

$$c_v = A + B\theta + \frac{\alpha\beta^2\theta}{(\tau + \beta\theta)^2}. \quad (12)$$

This expression is used only for $p = 0$ (when saturated vapor pressure is neglected). Its complex appearance may only be condoned as a formal expression used to provide a logical continuation for Stratton's equations (for $p > 0$).

Suppose it is desired to express the equation of state for the mixture in Stratton's form when the equations of state for the components are also given in Stratton's form. When the isothermal assumption is applicable, one can first express the temperature in terms of pressure and volume. Substituting Eq. (7) into Eq. (1),

$$v \sum_i m_i = \sum_i \frac{m_i \alpha_i}{p - \beta_i \theta - \tau_i}. \quad (13)$$

Because Eq. (10) is applicable for positive pressures only, the threshold temperature, θ^* , must first be found. Considerable expansion of materials can be expected until θ^* is attained. Therefore, θ^* is determined numerically from:

$$\sum_i \frac{m_i \alpha_i}{-\tau_i - \beta_i \theta^*} = v_v + \sum_i m_i v_{i0} = v^* \sum_i m_i,$$

where v_{i0} are the initial specific volumes and v_v is the initial volume of voids corresponding to masses m_i . The initial void fraction is $v_v / (v_v + \sum_i m_i v_{i0})$. Coefficients τ_i are determined so that at the initial temperature θ_0

$$v_{i0} = \frac{\alpha_i}{-\tau_i - \beta_i \theta_0}.$$

After θ^* is determined, a power series expansion of Eq. (13) gives

$$\left(\sum_i m_i \right) (v - v^*) = - \sum_i \frac{m_i \alpha_i}{(-\tau_i - \beta_i \theta^*)^2} [p - \beta_i (\theta - \theta^*)] + \sum_i \frac{m_i \alpha_i}{(-\tau_i - \beta_i \theta^*)^3} [p - \beta_i (\theta - \theta^*)]^2 + \dots$$

This equation is solved for $(\theta - \theta^*)$ in terms of the power series in p and $(v - v^*)$. The value obtained is substituted into the equation for the internal energy expressed in a power series of $(\theta - \theta^*)$ and p . When initial terms are collected, the internal energy acquires the form of Eq. (10) and the corresponding Stratton's coefficients are obtained from Eq. (11).

The procedure is simpler when the adiabatic assumption is valid. Then the specific volume of the diluent (which experiences only isentropic compression) can be expressed as a function of pressure:

$$v_2 = v_{20}(1 + c_1 p + c_2 p^2 + \dots); \quad (14)$$

v_{20} is the initial specific volume of the diluent material; c_1 and c_2 are constants. The corresponding change in internal energy is

$$e_2 = -\frac{1}{2}v_{20}c_1 p^2 + \dots \quad (15)$$

If the equation of state for the diluent material is given in Stratton's form, the coefficients c_i are determined from:

$$c_1 = \frac{-v_{20}(A_2\beta_2v_{20} - B_2\tau_2v_{20} - B_2\alpha_2)}{\alpha_2(A_2\beta_2v_{20} - B_2\tau_2v_{20} - B_2\alpha_2) - \beta_2^2v_{20}^2(\tau_2v_{20} + \alpha_2)} \quad (16)$$

$$c_2 = \frac{\alpha_2v_{20}^2(A_2\beta_2v_{20} - B_2\tau_2v_{20} - B_2\alpha_2)^3 - \frac{1}{2}A_2\beta_2^5v_{20}^7(\tau_2v_{20} + \alpha_2)}{[\alpha_2(A_2\beta_2v_{20} - B_2\tau_2v_{20} - B_2\alpha_2) - \beta_2^2v_{20}^2(\tau_2v_{20} + \alpha_2)]^3}$$

Equation (6) may now be rewritten as

$$e = \frac{m_2}{m_1 + m_2} e_2(p) + \frac{m_1}{m_1 + m_2}$$

$$\cdot e_1 \left[p, v_1^* + \frac{m_1 + m_2}{m_1} (v - v^*) - \frac{m_2}{m_1} (v_2 - v_{20}) \right],$$

where $v_1^* = v_{10} + (v_v/m_1)$ is the specific volume of the fuel at the beginning of pressure generation and $v_2^* = v_{20}$ and v and v^* are defined by Eq. (1). If the equation of state for the fuel is taken in the form of Eq. (10), substitution of Eqs. (14) and (15) is straightforward. Collection of initial terms yields the equation of state representing the mixture in the same form.

It may be noted that, for the mixture, the higher powers of pressure in the expression for energy do not vanish, even if the equations for the components are strictly in Stratton's form. In general, neither adiabatic nor isothermal assumptions are strictly satisfied. More thorough treatment of these points does not seem warranted because the thermodynamics of the component materials are not well known under these conditions.

REFERENCES

1. V. Z. Jankus, *A Theoretical Study of Destructive Nuclear Bursts in Fast Power Reactors*, ANL-6512, Appendix A (1962).
2. D. Okrent, J. M. Cook, D. Satkus, R. B. Lazarus and M. B. Wells, *AX-1, A Computing Program for Coupled Neutronics-Hydrodynamics Calculations on the IBM-704*, ANL-5977 (1959).

III-33. Behavior of Irradiated Metallic Fuel Elements Exposed to Nuclear Excursions in TREAT¹

J. H. MONAWECK,* C. E. DICKERMAN and E. S. SOWA*

Previous controlled out-of-pile experiments on the behavior of uranium fuel elements under meltdown or near-meltdown conditions have been performed using direct electrical resistance heating² or furnace heating.^{3,4} These experiments, although not mocking up reactor conditions precisely, indicated that fuel meltdown should be accompanied by significant short-time swelling due to the fission gas inventory in the fuel. However, these data did not appear adequate to permit estimates to be made of failure threshold effects, or rates of fuel movement, under actual meltdown conditions for either Fermi Core A or EBR-II

Mark I fuel. As a step toward obtaining more complete information on reactivity effects accompanying fuel meltdown, the behavior of irradiated EBR-II and Fermi A samples under transient nuclear heating in TREAT has been studied.

The EBR-II elements were irradiated at a calculated maximum center line temperature of 445°C to a maximum burnup of about 1 a/o. The Fermi A elements were irradiated at 460°C maximum center line temperature to a maximum specified burnup of 0.5 a/o.

After irradiation the elements were removed from their containers by remote procedures and examined. The EBR-II samples appeared to be good. These samples were further annealed by furnace heating for

* Reactor Engineering Division, Argonne National Laboratory.

four hours at 550°C. In addition to a check of the external element condition, the fuel-cladding bond was determined to be acceptable by non-destructive tests performed using the cyclograph eddy current technique.⁵ Eddy current scanning of the elements before and after heat treatment showed that the treatment produced a change attributed to changes in the fuel and a tendency toward normalization of the condition of the elements. None of the Fermi A elements tested had visible defects. However, 12 of the total of 20 irradiated displayed detectable swelling and/or clad splitting near the top end fitting. Thermocouples were welded to the cladding of the samples. The elements were then remotely encapsulated in graphite-lined helium-filled stainless steel containers.⁶

Results, and comparison of the effects of TREAT transients on unirradiated fuel elements with those on the pre-irradiated specimens, are as follows:

Uranium—5 w/o Fissium

1. Irradiated and unirradiated pins start swelling at approximately the same excursion conditions.

2. The amount of burnup does not have a great effect on the threshold of failure for the ranges considered.

3. The failure mechanism of very low burnup (~0.09 a/o) samples is essentially the same as that of unirradiated samples.

4. The meltdown residue of moderate burnup (~1 a/o) samples has more numerous and larger voids and a density of about 8.3 g/cc, which is about half the density of unirradiated elements.

The void per gram of fuel is proportional to the burnup, within about 20%.

Uranium—molybdenum

1. Unirradiated Fermi pins withstood bursts up to 34-37 MW-sec total integrated power in TREAT without noticeable damage. Irradiated pins began to swell at 27 MW-sec, and failed at the melting point (about 29 MW-sec) by splitting of the cladding.

The short-time swelling upon meltdown, predicted on the basis of out-of-pile experiments, has been confirmed. If the densities determined after these TREAT

excursions are indeed typical of those for metallic fuel during the fuel failure and meltdown, a mechanism has been found which can limit considerably the amount of reactivity available upon meltdown of a fast reactor. In fact, extrapolation of the EBR-II element results suggests that a core of such fuel, if irradiated to a burnup of about 2 a/o, would undergo sufficient expansion upon meltdown to fill all the core spaces. Since EBR-II has a sizable negative sodium void coefficient of reactivity, this expansion would tend to shut down the reactor, at least temporarily. A reactivity addition could still occur upon meltdown for a reactor with a positive sodium void coefficient, of course. The short-term swelling reported for an EBR-II fuel segment of 1.24 a/o burnup heated in a furnace to 954°C⁴ is about 25% less than predicted by the relationship for the four failed EBR-II elements of this study. However, in another furnace study,³ performed with specimens of 0.14 a/o to 0.38 a/o burnup, minimum densities between 1.8 g/cc and 7.6 g/cc were observed. Final densities were higher (between 5.8 g/cc and 18.0 g/cc).

These specific results do not necessarily describe behavior for different burnups or the fuel density during the entire course of meltdown, and do not include possible effects of clustering of elements or of a sodium coolant.

REFERENCES

1. J. H. Monaweck, C. E. Dickerman and E. S. Sowa, *Behavior of Irradiated Metallic Fuel Elements Exposed to Nuclear Excursions in TREAT*, Trans. Am. Nucl. Soc., **6**, No. 2, 374 (1963).
2. D. G. Freas, A. Leatherman and J. E. Gates, *Meltdown Studies of Irradiated Uranium-10 w/o Molybdenum Fuel Pins*, BMI-PRDC-656 (1960).
3. J. F. Buddery and K. T. Scott, *A Study of the Melting of Irradiated Uranium*, J. Nucl. Mat. **5**, No. 1, 81 (1962).
4. J. H. Monaweck and E. S. Sowa, *Summary Report on Irradiation of Prototype EBR-II Fuel Elements*, ANL-6010 (1960).
5. E. S. Sowa and E. L. Kimont, *Development of a Process for Sodium Bonding of EBR-II Fuel and Blanket Elements*, ANL-6384 (1961).
6. R. J. Schiltz, F. L. Willis and J. H. Monaweck, *A Process for Remotely Encapsulating Pre-Irradiated Fuel Elements for Exposure in TREAT*, ANL-6752 (to be published).

III-34. Treat Study of the Penetration of Molten Uranium and Uranium-5 w/o Fission Alloy Through Type 304 Stainless Steel¹

C. M. WALTER* and C. E. DICKERMAN

The rate of penetration of fuel element cladding by molten fuel must be known, at least approximately, if analyses are to be made of the degree of coherence of fuel failure and the rate of fuel movement during the early stages of a meltdown-type accident. Transient experiments were run in TREAT to measure penetration rates of type 304 stainless steel by molten EBR-II Mark I fuel (U-5 w/o Fs alloy), under in-pile conditions with heat generated in the fuel, actual fuel element geometry, and representative fuel-cladding interface conditions including the sodium bond. Earlier, experiments had been performed isothermally and out-of-pile in a furnace, using a dip method in the temperature range 1100 to 1350°C.²

A temperature range from 1100 to 1250°C was investigated in-pile. Desired sample energy inputs were obtained by programming different TREAT initial reactivity inputs for self-limiting power bursts terminated by the prompt negative temperature coefficient of reactivity.³

Each reactor experiment was performed with a TREAT opaque meltdown capsule, modified to contain two half-length ERB-II-type samples, one with sodium bond and one without. The time of ejection of material from the cladding was marked by an electrical signal from a simple failure detector.

* Metallurgy Division.

The unbonded elements gave erratic results, which were attributed to excessive thermal stresses occurring in the cladding when hot fuel slumped against it.

For the less severe transients of the sodium-bonded elements, penetration times were about 1.5 sec, while penetration times for the more severe were about 1 sec. These data are in good agreement with the furnace results. The most severe excursions caused failure within 0.1 sec but previous calculations indicated that this could be caused by bursting of the cladding by internal pressure.

Two samples, run in a check experiment using a transparent meltdown capsule, confirmed the analyses of the opaque tests. These results indicate that the basic, out-of-pile laboratory experiments can give reliable safety information, but that they should be substantiated by the more realistic in-pile experiments for specific applications.

REFERENCES

1. C. M. Walter and C. E. Dickerman, *TREAT Study of the Penetration of Molten Uranium and U-5 w/o Fs Alloy Through Type 304 Stainless Steel*, Nucl. Sci. Eng. **18**, 518 (April 1964).
2. C. M. Walter and L. R. Kelman, *Penetration Rate Studies of Stainless Steel by Molten Uranium and Uranium-Fission Alloy*, J. Nucl. Mat. **6**, No. 3, 281, (1962).
3. C. E. Dickerman, R. D. Johnson and J. Gasidlo, *Kinetics of TREAT Used as a Test Reactor*, ANL-6458 (1962).

III-35. Photographic Experiments on Meltdown of Irradiated Metallic Fuel Pins¹

C. E. DICKERMAN and L. E. ROBINSON

Metallic uranium fuel pins containing appreciable fission gas inventories have been shown to swell significantly under transient nuclear heating to failure in meltdown experiments.² However, in evaluating the course of a hypothetical meltdown accident, it is necessary to know not only the total amount of fuel movement possible, but also the rates of movement and degree of coherence of the motion. Accordingly, meltdown experiments were performed in the Transient Reactor Test Facility (TREAT) using recently developed equipment³ which permits behavior of elements exposed in an inert gas atmosphere to be recorded by high speed color photography.

Two EBR-II and two Fermi A specimens were studied in order to observe directly the modes of failure and material motion. Each EBR-II element had been irradiated previously in the Materials Testing Reactor at a calculated maximum centerline temperature of 445°C to about 1 a/o burnup. Fermi A elements were irradiated to a maximum burnup of 0.5 a/o with a maximum calculated centerline temperature of 460°C.

Post-experiment conditions of the samples were consistent with those of the five irradiated pins run to failure in the earlier experiments,² if the difference in TREAT flux depression caused by substitution of the

transparent meltdown facility for the smaller opaque capsule is taken into account.

Photographs of each EBR-II sample showed the occurrence of preliminary failures, which were indicated by the release of small amounts of opaque vapor, before a single large failure with characteristic high-speed release of bond sodium which filled the capsule and prevented further observation. Unirradiated EBR-II specimens photographed during tests to failure have not shown these multiple failures.

One Fermi A sample received an energy input in the range between one initiating failure by swelling and clad splitting and one producing incipient fuel movement from the clad. The final sample appearance was intermediate between these two modes of behavior and there apparently was no delay between power transient and swelling. Upon failure, a thin opaque vapor, presumably from fission products volatile at around 1000°C, was expelled from the sample. The

other Fermi A sample, which was run to extensive failure, produced appreciably more vapor when it failed; however, fuel movement was not completely obscured and "frothy" fuel could be seen moving in discrete agglomerations. Mild expulsion of fuel in the form of globules through the clad was observed, with trajectories suggesting internal pressures of the order of magnitude of that from the hydrostatic molten uranium head of a few centimeters of Hg.

REFERENCES

1. C. E. Dickerman and L. E. Robinson, *Photographic Experiments on Meltdown of Irradiated Metallic Fuel Pins*, Trans. Am. Nucl. Soc. 7, No. 1, 137 (June 1964).
2. J. H. Monaweck, C. E. Dickerman and E. S. Sowa, *Behavior of Irradiated Metallic Fuel Elements Exposed to Nuclear Excursions in TREAT*, Trans. Am. Nucl. Soc. 6, No. 2, 374 (1963).
3. L. E. Robinson and C. August, *Transparent Facility for TREAT Meltdown Experiments on Pre-Irradiated Samples*, (to be published).

III-36. Calculations of Coherence of Failure in Hypothetical Meltdown Accidents in An EBR-II-like Reactor¹

D. V. GOPINATH,* C. E. DICKERMAN and L. BRYANT†

In the event of an accident in a fast reactor leading to fuel element failure, the time distribution in meltdown of different fuel elements could play a significant role in deciding the ultimate severity of the accident. If fuel element failure produces addition of reactivity and if many of the elements were to fail simultaneously, the rate of reactivity insertion could be large enough to lead to a destructive nuclear burst. For this reason, the time distributions of failure have been calculated for fuel pins in different positions in an Experimental Breeder Reactor-II-like core under a range of hypothetical accident conditions, using recently-developed theoretical techniques and data from transient experiments in the Transient Reactor Test Facility (TREAT).

Three general accident cases were studied:

- (1) Pump power failure without scram
- (2) Blockage of subassembly inlet orifice
- (3) Central subassembly dropped into a reactor which is critical at low power.

Feedback for an intact core was used in the analysis. However, the calculations did include spatial variations in power and coolant flow, transient heat trans-

fer, and propagation of failure from one pin to another. The transient heat transfer digital code "AR-GUS"² and an electronic analog technique operating on the logarithm of neutron density, combined with feedback from a transient temperature circuit,³ were used. Fuel failure data included failure thresholds for samples run in an inert gas atmosphere⁴ and in stagnant sodium,⁵ and the time required for cladding to be penetrated by molten fuel.⁶ Because reactivity effects caused by movements of material were neglected, the resulting spreads in failure time must be considered to be estimates.

Results of the calculations may be summarized as follows:

Case 1

Even if the (negative) temperature feedbacks are neglected and the power remains constant at full design level, spreads in failure can be as large as two seconds for a single subassembly and about three seconds for the core.

Case 2

If flow blockage occurs simultaneously for the entire core, the spread is about one second, when feedback

* Atomic Energy Establishment, Trombay, India.

† Applied Mathematics Division.

is included. Smaller spreads occur for individual sub-assemblies, or for the entire core if feedback is neglected.

Case 3

Simple kinetics calculations based on adiabatic fuel heating yield a spread of about 0.004 sec. More detailed calculations which include transient heat transfer indicate a spread about an order of magnitude greater.

This study spans a variety of conditions, ranging from an accident in which the duration of reactivity change due to failure is principally determined by the time for cladding to be penetrated by molten fuel, through an extreme case in which the time for movement of fuel must be combined with the spread in failure time in order to obtain the duration of reactivity change. In the less severe cases, variations in power and coolant flow within subassemblies are significant. Changes in assumptions on the rate of orifice block-

age and in the number of blocked subassemblies do not appear to change the results significantly for Case 2.

REFERENCES

1. D. V. Gopinath, C. E. Dickerman, and L. Bryant, *Calculations on Coherence of Failure in Hypothetical Meltdown Accidents in an EBR-II-Like Reactor*, Trans. Am. Nucl. Soc. 1, No. 1, 138 (1964).
2. D. F. Schoeberle, L. B. Miller, and J. Heestand, *A Method of Calculating Transient Temperatures in a Multi-Region, Axisymmetric, Cylindrical Configuration, The ARGUS Program, 1089/RP 248, Written in Fortran II, ANL-6654* (1963).
3. L. Bryant and D. V. Gopinath, *A Fast Reactor Excursion Simulator*, ANL-6798 (1964).
4. C. E. Dickerman, D. Okrent, and E. Sowa, *The Fast Reactor Safety Programme in TREAT*, Physics of Fast and Intermediate Reactors, IAEA, Vienna, III, 171 (1962).
5. C. E. Dickerman, E. S. Sowa, J. H. Monaweck, and A. Barsell, *In-Pile Experiments on Meltdown of EBR-II Mark I Fuel Elements in Stagnant Sodium*, Nucl. Sci. Eng., 18, No. 3, 319 (1964).
6. C. M. Walter and C. E. Dickerman, *TREAT Study of the Penetrating Uranium and U-5 w/o Alloy Through Type 304 Stainless Steel*, Nucl. Sci. Eng. (to be published).

III-37. Behavior of Uranium Sulfide Fast Reactor Type Fuel Specimens Under Transient Heating in TREAT¹

L. E. ROBINSON, C. E. DICKERMAN and C. AUGUST

Uranium monosulfide is a ceramic material with uranium atom density comparable to that of uranium dioxide, thermal conductivity and melting point similar to uranium carbide, and good compatibility with cladding materials and sodium.^{2,3} Early steady state irradiation studies have shown good dimensional stability and fission product retention for irradiations with high power generation ratings.⁴ As a continuation of the investigation of uranium monosulfide for use as reactor fuel, and extension of earlier transient tests on EBR-II-size UO₂ samples,⁵ transient irradiations were conducted on previously unirradiated uranium sulfide fuel specimens using the Transient Reactor Test Facility (TREAT).

Transient specimens consisted of pellets of approximately 95% theoretical density or higher, 0.381 cm in diameter, stacked in lengths of about 19.0 cm, and bonded with 1 atm of argon gas at room temperature to 0.022 cm thick tantalum cladding tubes with 0.436 cm outer dia. Samples were exposed to power pulses of 0.3–0.4 sec duration in standard TREAT transparent meltdown capsules in a helium atmosphere. Instrumentation consisted of a high speed motion picture

camera and fast response W-5% Re versus W-26% Re thermocouples spot welded to the cladding. The range of exposures is given in Table III-37-I.

Upon post-transient inspection, pellets from sample one appeared to be essentially unchanged from the pre-irradiation condition. In each of the remaining four specimens, however, fuel pellets were found fused together, and the highly oxidized surface prior to ex-

TABLE III-37-I. TREAT EXPOSURE CONDITIONS

Sample	Experiment	TREAT Energy Release, MW-sec.	Max. Cladding Surface Temperature, °C	Est. Max. Central US Temperature, °C
1	1	43	1060	1270
2	2	38	890	1060
2	3	60	1270	1520
3	4	60	1210	1450
3	5	87	1720	2060
4	6	111	2020	2440 ^a
5	7	136	2400	2462 ^a

^a The US melting point is 2463° C⁶. Because of the presence of appreciable quantities of the lower melting point UOS, some melting should have occurred for both samples 4 and 5.

posure had disappeared. Fuel cylinders from sample three had increased in diameter approximately 0.002–0.005 cm due to slumping while some melting occurred in samples four and five, both of which had undergone a mild cladding failure. The motion pictures of transients six and seven showed patches on the cladding, darker than the cladding as a whole, which appeared and moved downward as though produced by local fuel movement in contact with the cladding. Pellets from sample five showed evidence for fuel melting and freezing against the inside of the cladding.

In no case was there observed the central zone of loosely-bonded ceramic found to be typical of similar-sized gas-bonded UO_2 specimens, given transients with maximum cladding temperatures in the range covered by samples three and four. Tantalum-clad UO_2 samples exposed to a cladding temperature comparable to that of sample five failed extensively with expulsion of the ceramic fuel from the cladding.⁵

REFERENCES

1. L. E. Robinson, C. E. Dickerman and C. August, *Behavior of Uranium Sulfide Fast Reactor Type Fuel Specimens Under Transient Heating in TREAT*, Trans. Am. Nucl. Soc. 7, No. 1, 105 (1964).
2. Reactor Development Program Progress Report, ANL-6739, (1963).
3. P. D. Shalek, *Preparation and Properties of Uranium and Thorium Monosulfides*, J. Am. Ceram. Soc., 46(4), 155 (1963).
4. L. A. Neimark and P. D. Shalek, *The Irradiation Behavior of Uranium Monosulfide*, Trans. Am. Nucl. Soc. 6, No. 2, 372 (1963).
5. C. E. Dickerman, L. E. Robinson, E. S. Sowa and S. B. Skladzien, *Transient In-Pile Meltdown Experiments on Fast-Reactor-Type Uranium Oxide Fuel Elements in the Absence of Sodium*, Trans. Am. Nucl. Soc. 6, No. 1, 104 (1963).
6. E. D. Cater, *The Vaporization, Thermodynamics and Phase Behavior of Uranium Monosulfide*, ANL-6140 (1960).

III-38. In-pile Experiments on Meltdown of EBR-II Mark I Fuel Elements in Stagnant Sodium¹

C. E. DICKERMAN, E. S. SOWA,* J. H. MONAWECK* and A. BARSELL*

Experiments were performed in pile, in the TREAT reactor, to study the meltdown behavior under transient heating of EBR-II Mark I fuel elements contained in stagnant sodium. Threshold of failure, modes of failure, and post-experiment distribution of fuel were obtained for a range of experimental conditions. These included uniform axial power and an axial power profile shaped to approximate a typical power profile of a fast reactor core. Samples were exposed in a special capsule both with sodium initially at saturation conditions and with sodium pressurized to inhibit boiling. Sample temperatures were checked by means of central fuel thermocouples (of two different types), thermocouples in the sodium bond between fuel alloy and cladding, and thermocouples attached to the steel tube containing the sodium.

Experimental results were correlated against calculated sample temperatures. The power calibration used for the calculations was obtained from the thermocouple readings from the steel tube, which served as a short-term colormeter.

Results, related in terms of calculated maximum transient fuel-cladding interface temperatures, may

be summarized as follows, for fourteen 3% enriched specimens:

1. 800–913°C. No damage, except possibly slight alloying of fuel and cladding.
2. 985–1012°C. Failure threshold range.
3. 913–1004°C. The formation of voids in the fuel and extensive alloying of fuel and cladding.

In addition, one natural enrichment sample was run. Its maximum calculated interface temperature was 904°C, which falls at the upper end of range 1. Although its appearance could be classified as belonging to the third range, the discrepancy is only 9°C.

Thus, these results may be correlated in the same fashion as those obtained with single dry elements. Interface temperatures are also in good agreement with those established for dry elements.²

The two failures of elements with shaped axial power profile produced appreciably less concentration of fuel than found after similar tests run in the absence of sodium coolant.²

These tests show that the presence of a thin annulus of stagnant sodium does affect the course of failure. However, the results may be correlated in a fashion similar to that for dry experiments. The tests do not include possible effects due to appreciable quantities

* Reactor Engineering Division, Argonne National Laboratory.

of fission product gases, or flowing sodium environment, and are not necessarily typical of clusters of elements.

REFERENCES

1. C. E. Dickerman, E. S. Sowa, J. H. Monaweck and A. Barsell, *In-Pile Experiments on Meltdown of EBR-II*
2. C. E. Dickerman, E. S. Sowa, D. Okrent, J. Monaweck and L. B. Miller, *Studies of Fast Reactor Fuel Element Behavior under Transient Heating to Failure, I. Initial Experiments on Metallic Samples in the Absence of Coolant*, ANL-6334 (1961).

Mark I Fuel Elements in Stagnant Sodium, Nucl. Sci. Eng., **18**, No. 3, 319, (1964).

Section IV

Experimental Techniques and Facilities

Measured integral reactor physics parameters are necessary for either direct introduction into reactor design calculations or for comparison with values obtained theoretically using basic microscopic cross section data. In the latter case the objective is to verify either the cross section data or the calculational techniques. Integral parameters are obtained using special measurement techniques in exponential or critical facilities. The papers presented in this section deal with the development of such special techniques, facilities, and radiation detection devices. In addition, there are papers which discuss methods for the analysis and interpretation of experimentally determined quantities, and others which treat the development of special equipment for the detection of power reactor fuel element failures.

IV-1. Orthonormal Expansion of Neutron Spectra with Activation Measurements

R. GOLD

In many cases of interest, the measurement of neutron spectra with conventional detectors is not possible. Circumstances, such as hostile environs or severe space restrictions, usually leave no other recourse but to utilize an activation method. In this event, it is important to consider the different alternatives which activation methods may afford in the determination of (neutron) spectral information. The present investigation is concerned with one such method, namely, the utilization of activation measurements to determine an approximate expansion of the neutron spectrum with an orthonormal set of functions.¹

In this method, the flux of neutrons per unit energy interval, $\phi(\epsilon)$, is approximated by the form

$$\phi(\epsilon) \cong H_n(\gamma_1, \gamma_2 \cdots \gamma_n; \epsilon) = \sum_{i=1}^n \gamma_i u_i(\epsilon). \quad (1)$$

The set of functions $\{u_i(\epsilon)\}$ is orthonormal in the sense

$$(u_i, u_j) = \delta_{ij}, \quad i, j = 1, 2, \quad (2a)$$

where δ_{ij} is the customary Kronecker delta function and*

$$(u_i, u_j) = \int \rho(\epsilon) u_i(\epsilon) u_j(\epsilon) d\epsilon, \quad (2b)$$

with $\rho(\epsilon)$ the appropriate weight function. The set of coefficients $\{\gamma_i\}$ are determined by experimental activation measurements.

In order to determine the set of coefficients $\{\gamma_i\}$ in Eq. (1), we shall require an expression for the activation rate of neutrons, p_i , in the i^{th} foil material. This expression can be written in the form

$$p_i = \int_0^\infty \phi(\epsilon) g_i(\epsilon) d\epsilon, \quad i = 1, 2 \cdots n, \quad (3)$$

where $g_i(\epsilon) \equiv g(\mu_i, \tau_i)$ is the monoenergetic activation function for the i^{th} foil material. The argument of this function is a product of $\mu_i(\epsilon)$, the macroscopic activation cross section, and τ_i , the thickness of the i^{th} material. Different approximations of the monoenergetic activation function, $g_i(\epsilon)$, can be found in the literature. The correct approximation of this function should accurately account for flux perturbation and self-depression which arises due to the presence of the foil.

* The limits of the integration in Eq. (2b) are specified by the domain of orthogonality of the set of functions $\{u_i(\epsilon)\}$.

Two possible alternatives for the determination of the set $\{\gamma_i\}$ are considered separately below.

Method I

In what may be called the orthogonalized cross section expansion or the Gram-Schmidt method, one must make the assumption that $\mu_i \tau_i \ll 1, i = 1, 2 \cdots n$.[†] It follows that $g_i(\epsilon)$ may be approximated by

$$g_i(\epsilon) \cong \mu_i(\epsilon) \tau_i = n_i \sigma_i(\epsilon) \tau_i, \quad i = 1, 2, \cdots n, \quad (4)$$

where n_i is the number of nuclei per cc and $\sigma_i(\epsilon)$ is the activation cross section, respectively, for the i^{th} foil material. Using this approximation in Eq. (3), one may define the reduced activation integrals

$$p'_i = \int_0^\infty \phi(\epsilon) \sigma_i(\epsilon) d\epsilon, \quad i = 1, 2, \cdots n, \quad (5a)$$

where

$$p'_i = (n_i \tau_i)^{-1} \cdot p_i, \quad i = 1, 2, \cdots n. \quad (5b)$$

An additional assumption must also be employed. Namely, the set of n cross section functions $\{\sigma_i(\epsilon)\}$ are assumed to be linearly independent. Consequently, one can construct from these functions an orthonormal set $\{v_i(\epsilon)\}$ by the Gram-Schmidt process. Let this construction take the form

$$v_i(\epsilon) = \sum_{k=1}^n a_{ik} \sigma_k(\epsilon), \quad i, k = 1, 2, \cdots n, \quad (6a)$$

or in matrix notation

$$V(\epsilon) = A \Sigma(\epsilon), \quad (6b)$$

where A is the $n \times n$ matrix of the coefficients (a_{ij}) and $V(\epsilon)$ and $\Sigma(\epsilon)$ are column matrices containing elements of the sets $\{v_i(\epsilon)\}$ and $\{\sigma_i(\epsilon)\}$, respectively. Here the functions $\{v_i(\epsilon)\}$ satisfy the orthonormality condition

$$(v_i, v_j) = \int_0^\infty v_i(\epsilon) v_j(\epsilon) d\epsilon = \delta_{ij}, \quad i, j = 1, 2, \cdots n. \quad (7)$$

The solution of the system of Eqs. (6) and (6b), which must exist, is given by

$$\Sigma(\epsilon) = A^{-1} V(\epsilon), \quad (8)$$

[†] This assumption is easily satisfied, provided all foil material can be chosen sufficiently thin.

TABLE IV-1-I. ACTIVATION CROSS SECTIONS

Index	σ_i	Product	Half-Life	Reference
1	$U^{238}(n,f)$	Fission products	—	3
2	$S^{32}(n,p)$	P^{32}	14.22 day	3
3	$Al^{27}(n,p)$	Mn^{27}	9.5 min	4, 5
4	$Si^{28}(n,p)$	Al^{28}	2.3 min	4
5	$In^{115}(n,n')$	In^{115m}	4.5 h	3
6	$K^{39}(n,p)$	A^{39}	265.0 yr	4
7	$Al^{27}(n,\alpha)$	Na^{24}	15.0 h	4
8	$Li^6(n,\alpha)^a$	H^3	12.2 yr	3
9	$Np^{237}(n,f)$	Fission products	—	3
10	$P^{31}(n,p)$	Si^{31}	2.62 h	3

^a For a cadmium covered response, one can assume this reaction cross section is effectively zero below 0.5 eV.

where A^{-1} is the inverse of the matrix A . In order to obtain an approximation of the neutron spectrum in the form*

$$H_n(\epsilon) = \Gamma V(\epsilon), \quad (9)$$

where Γ is a row matrix of the elements $\{\gamma_i\}$, one uses Eq. (8) in Eq. (5). This substitution yields

$$P' = A^{-1}\Gamma, \quad (10)$$

where P' is a column matrix containing the measured reduced activation elements $\{p'_i\}$. The set of elements $\{\gamma_i\}$, of the column matrix Γ , are given by

$$\gamma_i = \int_0^\infty \phi(\epsilon) v_i(\epsilon) d\epsilon. \quad (11)$$

The solution of Eq. (10) for this unknown set is given by

$$\Gamma = AP'. \quad (12)$$

Using Eqs. (6b) and (12) in Eq. (9), one can write

$$H_n(\epsilon) = \tilde{P}' D \Sigma(\epsilon), \quad (13)$$

where D is a positive definite matrix given by

$$D = \tilde{A}A, \quad (14)$$

and n is the dimension of the system.

Method II

The second method, which may be called an approximation *in the mean*, or a *least-squares* expansion, also entails assumptions. Assuming that Eq. (1) is exact, multiplication of both sides of Eq. (1) by $g_k(\epsilon)$ and integration over the entire energy domain ($0 \leq \epsilon < \infty$) yields

$$P = B\Gamma, \quad (15)$$

* According to customary notation \tilde{M} represents the transpose of the matrix M .

where P is a column matrix with the measured activation elements $\{p_i\}$ and B is a square $n \times n$ matrix whose elements are defined as

$$b_{ki} = \int_0^\infty g_i(\epsilon) u_i(\epsilon) d\epsilon, \quad i, k = 1, 2, \dots, n. \quad (16)$$

In order to solve Eq. (15), it is necessary to employ a second assumption, namely, that the matrix B is non-singular. It follows that the solution of Eq. (15) is given by

$$\Gamma = B^{-1}P, \quad (17)$$

where B^{-1} is the inverse matrix of B . Using this result in Eq. (1), this approximation for the neutron spectrum may be written in the form

$$H_n(\epsilon) = \tilde{U}(\epsilon)B^{-1}P, \quad (18)$$

where $\tilde{U}(\epsilon)$ is a row matrix containing the set of elements $\{u_i(\epsilon)\}$.

Numerical Comparison of Methods I and II

Our numerical comparisons require the choice of a definite neutron spectrum. It is natural, therefore, to choose a spectrum which is representative of a class of spectra that often arise in practice. A spectrum of such general interest is that of the prompt neutrons accompanying the thermal neutron fission of U^{235} . For the analytical description of this spectrum, a modified form of the *Watt* fission spectrum² has been chosen and is given by

$$\phi(\epsilon) = ae^{-b\epsilon} \sinh(c\epsilon)^{1/2}, \quad (19a)$$

where

$$\begin{aligned} a &= 0.453 \\ b &= 1.035 \\ c &= 2.29. \end{aligned} \quad (19b)$$

$\phi(\epsilon)$ also satisfies the normalization condition

$$\int_0^\infty \phi(\epsilon) d\epsilon = 1. \quad (20)$$

Table IV-1-I enumerates the cross sections which are utilized in the subsequent calculations. Included in this table are the activation product, half-life of this product, and the reference from which the respective cross section has been obtained. In order to keep the numerical calculations tractable, the total number of cross sections utilized has been limited to ten. Inspection of Table IV-1-I reveals that most, if not all, of the cross sections chosen are frequently employed in practice.

In order to effectively compare these methods, the approximation cited in Eq. (4) for Method I has also been introduced in Method II. In this event, Eq. (15)

TABLE IV-1-II. REDUCED ACTIVATION INTEGRALS

Index	$p'_i \times 10^{24} \text{sec}^{-1}$
1	0.3090
2	0.0646
3	0.00352
4	0.00909
5	0.1719
6	0.0564
7	0.000583
8	0.3776
9	1.1920
10	0.02814

of Method II reduces to

$$P' = B' \Gamma, \quad (21)$$

where the matrix elements of B' are given by*

$$b'_{ki} = \int_0^\infty \sigma_k(\epsilon) u_i(\epsilon) d\epsilon. \quad (22)$$

The column matrix P' in Eq. (21) can be identified as the same matrix introduced in Eq. (10) of Method I. The elements of this matrix are the reduced activation integrals, p'_i , given in Eq. (5a). Using Eq. (5a), one can determine the elements of P' , for the spectrum defined in Eq. (19) and the cross sections given in Table IV-1-I. Table IV-1-II presents the evaluation of these matrix elements by numerical integration. This table furnishes, so to speak, a common starting point for our numerical comparison.

As a quantitative measure of the error attributed to a given approximation $H_n(\epsilon)$, we shall use the integral

$$E_n = \int_0^\infty |H_n(\epsilon) - \phi(\epsilon)| d\epsilon. \quad (23)$$

In view of the normalization condition, Eq. (20), one may regard E_n as the relative error associated with the given approximation $H_n(\epsilon)$. Equation (23) will be evaluated by numerical integration for the various approximations furnished by Methods I and II.

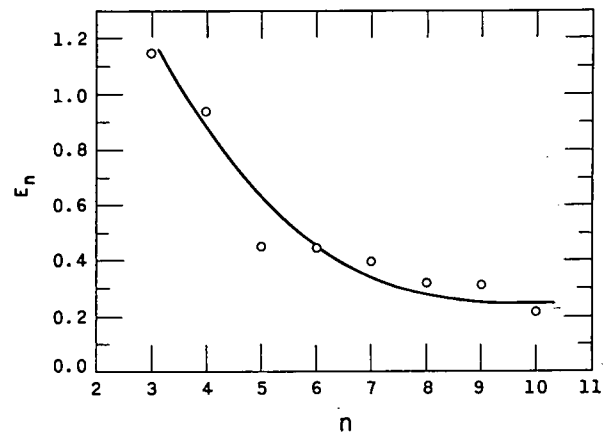
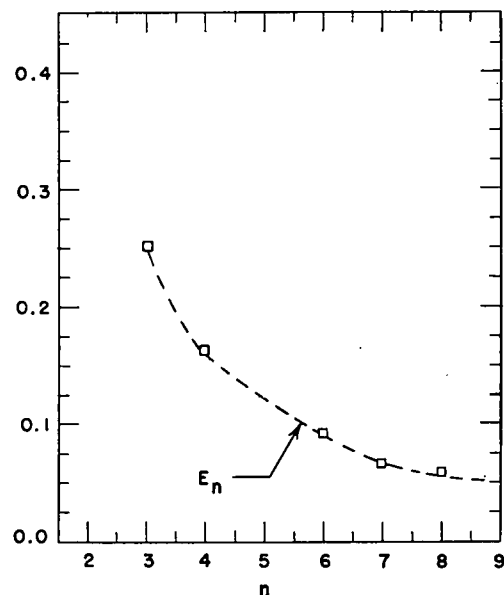
Computer programs have been developed for both Methods I and II.† The associated Laguerre polynomials of the second kind were chosen as the complete system of functions for the least-squares method. The results of these computations are presented below.

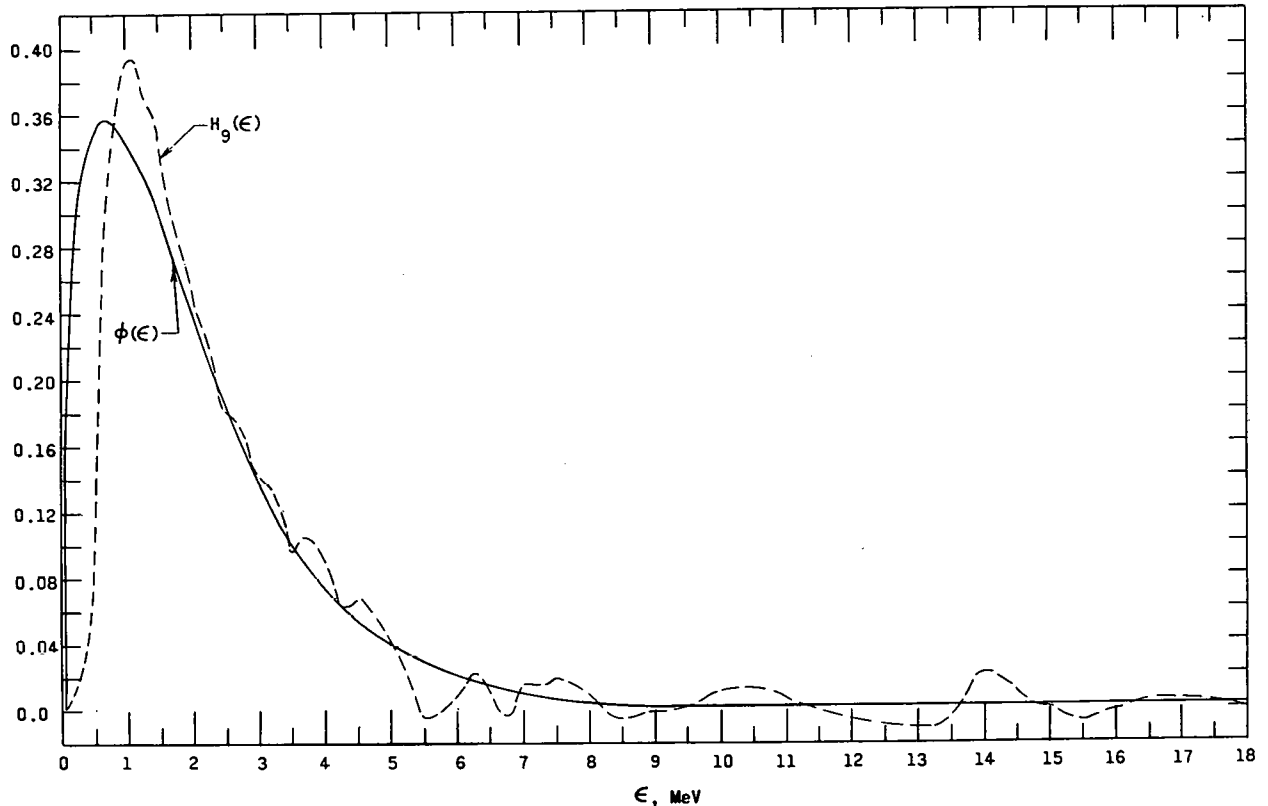
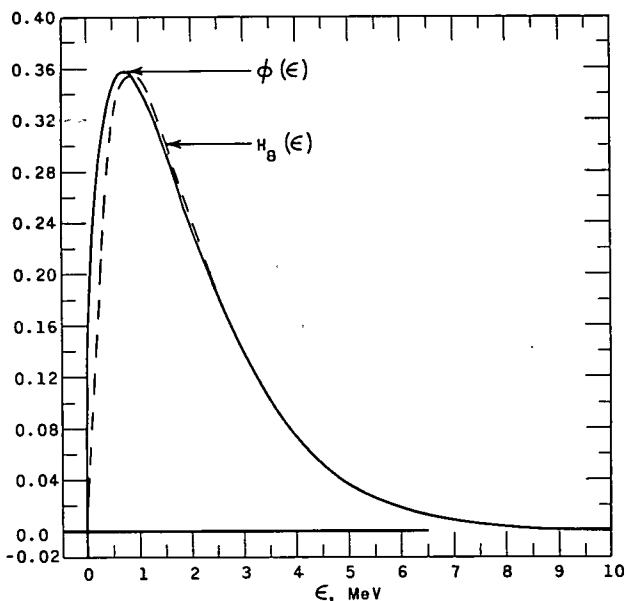
Figures IV-1-1 and IV-1-2 present E_n versus n for Methods I and II respectively. Figures IV-1-3 and IV-1-4 display the best approximations determined by these two methods, respectively, for the test problem employed.

* Method II, modified in this obvious way, would employ the matrices P' and B' instead of the matrices P and B , respectively.

† The computer program for Method I was facilitated by employing a SHARE subroutine.⁶

A comparison of the numerical results furnished by Methods I and II for our test problem reveals that the least-squares method affords better approximations. Figures IV-1-1 and IV-1-2 reveal that Method II possesses a much greater rate of convergence. In fact, applying Method II with only three or four cross sections (i.e., $n = 3$ or $n = 4$) will yield approximations which are as good as the limiting accuracy available from Method I. Furthermore, Method II possesses an additional advantage which is not revealed by the behavior of the relative error E_n , but which becomes apparent upon the direct examination of the approximations, $H_n(\epsilon)$. A comparison of Fig. IV-1-3 of Method I with Fig. IV-1-4 of Method II demonstrates that the Gram-Schmidt method does not yield the same smoothly varying approximations as those furnished by the least-

FIG. IV-1-1. E_n Versus n for Method I.FIG. IV-1-2. E_n Versus n for Method II.

FIG. IV-1-3. Comparison of $H_9(\epsilon)$ and $\phi(\epsilon)$ for Method I.FIG. IV-1-4. Comparison of $H_8(\epsilon)$ and $\phi(\epsilon)$ for Method II.

squares method. The maxima and minima and generally sharp variations that are exhibited in the Gram-Schmidt approximations are not only undesirable but unrealistic. Such erratic behavior must be classified as a general inadequacy of the approximations obtained from the Gram-Schmidt method.

REFERENCES

1. R. Gold, *Limitations in the Orthonormal Expansion of Neutron Spectra with Activation Measurements*, Nucl. Sci. Eng. (to be published).
2. L. Cranberg, et al., *Fission Neutron Spectrum of U^{235}* , Phys. Rev. **103**, 662-670 (1956).
3. D. J. Hughes and R. B. Schwartz, *Neutron Cross Sections*, BNL-325, 2nd Ed., (1958).
4. N. Tralli, et al., *Neutron Cross Section for Titanium, Potassium, Magnesium, Nitrogen, Aluminum, Silicon, Sodium, Oxygen, and Manganese*, UNC-5002, (1962).
5. E. S. Troubtzksy, *Fast Neutron Cross Sections of Iron, Silicon, Aluminum, and Oxygen*, NDA-2111-3, Vol. C, (1959).
6. P. J. Walsh and E. U. Haynsworth, *A General Purpose Orthonormalizing Code*, SHARE Program No. 850 (BS-ØRTH), Abstracts of the SHARE Programs for the IBM-704 (October 1961).

IV-2. An Iterative Solution of the Matrix Representation of Detection Systems

R. GOLD

Since ideal detection systems do not exist, the measurement of a spectrum of physical interest is often complicated by the problem of finding the actual spectrum from the observed experimental data. This unfolding problem can be conveniently formulated in terms of a matrix representation. In this approximation, one has

$$\mathbf{Y} + \mathbf{E} = \mathbf{A}\mathbf{X}, \quad (1)$$

where \mathbf{Y} , \mathbf{X} and \mathbf{E} are n element column vectors and \mathbf{A} is an $(n \times n)$ matrix. Here \mathbf{Y} represents the output data of the detection system and \mathbf{E} is the inherent experimental error in the measurement. The matrix \mathbf{A} is commonly called the response matrix of the detection system.

The solution of Eq. (1) for the unknown vector \mathbf{X} , which represents the desired spectrum, can be written as

$$\mathbf{X} = \mathbf{A}^{-1}(\mathbf{Y} + \mathbf{E}), \quad (2)$$

where \mathbf{A}^{-1} is the inverse matrix of \mathbf{A} . The crux of the present problem stems from the fact that the solutions determined by Eq. (2) are nonunique. This nonuniqueness property, which arises from the existence of the error vector \mathbf{E} , is complicated by the fact that most response matrices of interest are ill-conditioned.

Thus instead of a unique solution, one generally finds an infinite set of vectors

$$\chi = \{\mathbf{X} \mid \mathbf{Y} + \mathbf{E} = \mathbf{A}\mathbf{X}\}, \quad (3)$$

which satisfy Eq. (2). Consequently, one must employ subsidiary conditions to determine which element of the (generally infinite) set χ is the desired solution. For example, smoothness criteria have been utilized with some success.^{1,2} An iterative method has also been employed with limited success.^{3,4}

In this iterative method, the recursion relation between successive approximations of the elements of \mathbf{X} is given by

$$x_i^{(m+1)} = \frac{x_i^{(m)} y_i}{\sum_{j=1}^n a_{ij} x_j^{(m)}}, \quad i, j = 1, 2 \dots n. \quad (4)$$

Here the elements y_i , $i = 1, 2 \dots n$, of the output vector \mathbf{Y} contain the error inherent in the measurement and the set of coefficients $\{a_{ij}\}$ are, of course, those of the response matrix \mathbf{A} . The elements $x_i^{(m)}$, $i = 1, 2 \dots n$,

form the column vector $\mathbf{X}^{(m)}$, which is the m^{th} approximation of \mathbf{X} .*

While the iterative method has adequately treated the unfolding problem of the NaI(Tl) crystal detection system for gamma rays, it should be noted that only the triangular or quasi-triangular response matrix has been tested.⁴ To examine the more general case, the iterative method has been employed for a Li^6 solid state neutron spectrometer. The $\text{Li}^6(n, \alpha)\text{H}^3$ reaction is employed in conjunction with two separate silicon surface barrier detectors. Each of the two charged particles, which result from this reaction, impinge on each of the silicon surface barrier detectors and the output of these two detectors is summed. The resulting pulse is suitably amplified and fed to a multichannel analyzer for pulse height analysis.

Since a correction for the finite resolving power of this detector was desired, the response matrix was determined by measurements with a thermal neutron spectrum.† Table IV-2-I presents the first ten rows and columns of a (33×33) response matrix determined from such measurements. This matrix is typical of that which is found for many detectors, namely an (approximately) Gaussian representation of the response resolution. Since it is well known that matrices of this type are very poorly conditioned,⁵ this response matrix will provide a much more rigorous test for the iteration method than the quasi-triangular response matrix of the NaI(Tl) gamma-ray detection system.

The neutron measurements of interest were taken in the center of a fast critical reactor assembly. In order to unfold the experimental data, the representation was symmetrized. This is accomplished by multiplying the modified form of Eq. (1) on the left with $\tilde{\mathbf{A}}$, the transpose matrix of \mathbf{A} . (The modified form of Eq. (1) suppresses the error vector \mathbf{E} and therefore implies that the inherent error enters implicitly through the vector \mathbf{Y} .) One then treats the system

$$\mathbf{V} = \mathbf{B}\mathbf{X}, \quad (5a)$$

with

$$\mathbf{B} = \tilde{\mathbf{A}}\mathbf{A}, \quad (5b)$$

* A more detailed analysis of this iterative method, as well as an investigation of convergence properties, has been submitted for publication.

† Since the resolution of this detector was assumed independent of neutron energy, measurements at zero neutron energy (i.e., with thermal neutrons) define the response matrix completely.

TABLE IV-2-I. RESPONSE MATRIX FOR THE NEUTRON DETECTOR

Row No.	Column									
	1	2	3	4	5	6	7	8	9	10
1	1.0000	0.8142	0.5948	0.3585	0.1843	0.1338	0.0871	0.0622	0.0467	0.0345
2	0.8244	1.0000	0.8142	0.5948	0.3585	0.1843	0.1338	0.0871	0.0622	0.0467
3	0.5083	0.8244	1.0000	0.8142	0.5948	0.3585	0.1843	0.1338	0.0871	0.0622
4	0.2310	0.5083	0.8244	1.0000	0.8142	0.5948	0.3585	0.1843	0.1338	0.0871
5	0.0579	0.2310	0.5083	0.8244	1.0000	0.8142	0.5948	0.3585	0.1843	0.1338
6	0.0209	0.0579	0.2310	0.5083	0.8244	1.0000	0.8142	0.5948	0.3585	0.1843
7	0.0054	0.0209	0.0579	0.2310	0.5083	0.8244	1.0000	0.8142	0.5948	0.3585
8	0.0010	0.0054	0.0209	0.0579	0.2310	0.5083	0.8244	1.0000	0.8142	0.5948
9	0.0019	0.0010	0.0054	0.0209	0.0579	0.2310	0.5083	0.8244	1.0000	0.8142
10	0.0024	0.0019	0.0010	0.0054	0.0209	0.0579	0.2310	0.5083	0.8244	1.0000

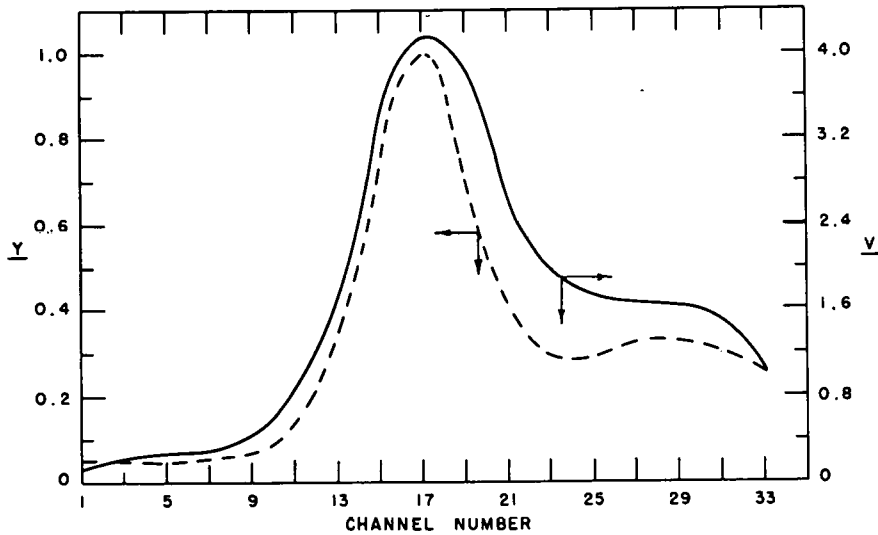


FIG. IV-2-1. The Li^6 Solid-State Detector Pulse Height Distribution or Y-Vector and the Symmetrized Experimental Data or V-Vector.

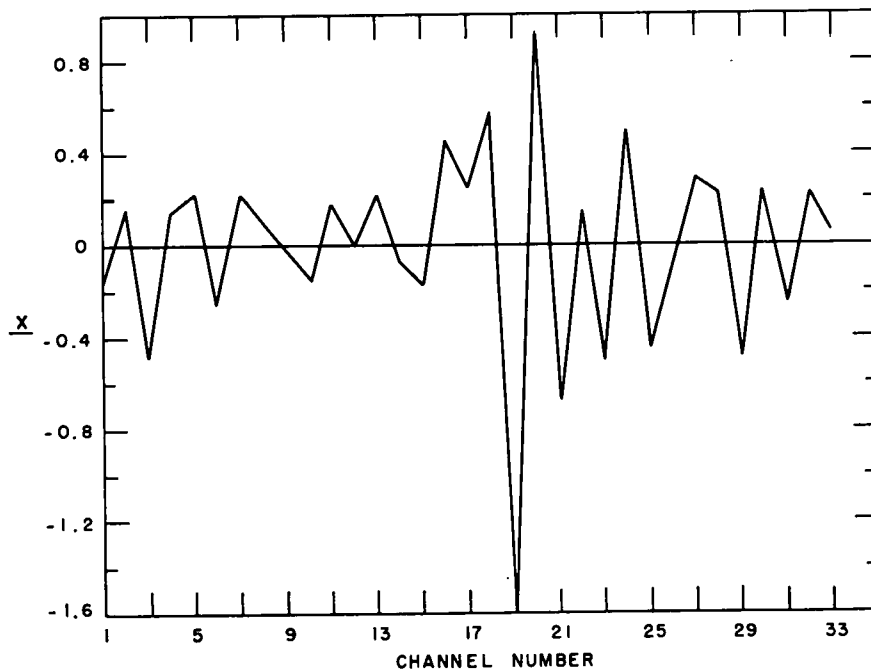


FIG. IV-2-2. The Exact Solution $X = A^{-1}Y$, Unfolded by the Inverse Response Matrix.

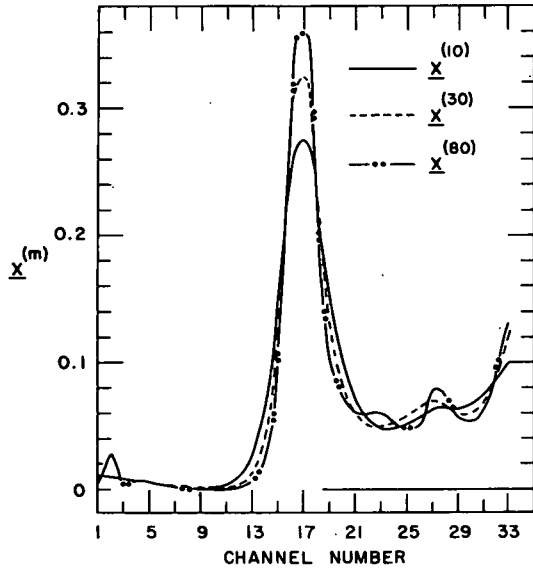


FIG. IV-2-3. The Iterative Approximations $X^{(10)}$, $X^{(30)}$, and $X^{(80)}$ of the Neutron Spectrum Obtained with the Initial Vector $X^{(0)} = \text{Constant}$.

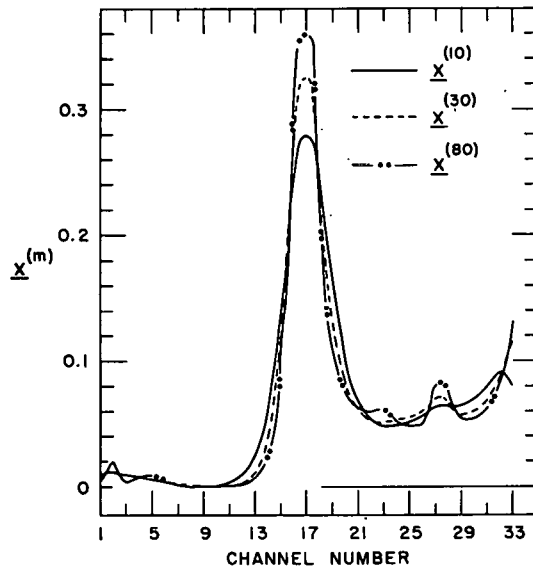


FIG. IV-2-4. The Iterative Approximations $X^{(10)}$, $X^{(30)}$, and $X^{(80)}$ of the Neutron Spectrum Obtained with the Initial Vector $X^{(0)} = V$.

and

$$V = \bar{A}Y. \quad (5c)$$

The vectors Y and V which result from the experimental data and the symmetrization process, respectively, are depicted in Fig. IV-2-1. As may now be anticipated, the exact solution $X = A^{-1}Y$, which is displayed in Fig. IV-2-2, proves to be completely unacceptable.

Figures IV-2-3 and IV-2-4 present the iterations $m =$

10, 30, and 80 obtained with two initial vectors $X^{(0)} = \text{constant}$ and $X^{(0)} = V$, respectively. The similarity exhibited in Figs. IV-2-3 and IV-2-4 demonstrates that the iterative approximations are rather insensitive to this particular change of initial vector. However, in contrast with earlier results found with the gamma ray response matrix, Figs. IV-2-3 and IV-2-4 do not demon-

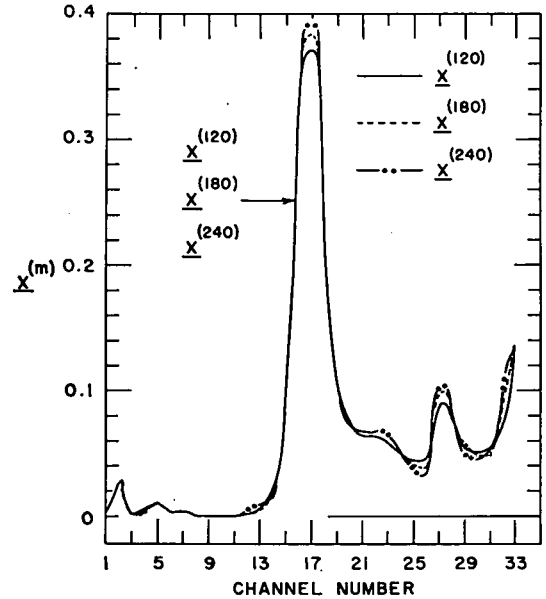


FIG. IV-2-5. The Iterative Approximations $X^{(120)}$, $X^{(180)}$, and $X^{(240)}$ of the Neutron Spectrum Obtained with the Initial Vector $X^{(0)} = \text{Constant}$.

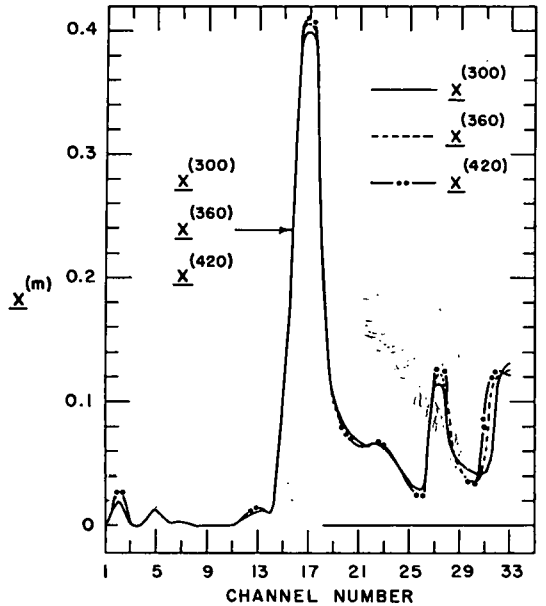


FIG. IV-2-6. The Iterative Approximations $X^{(300)}$, $X^{(360)}$, and $X^{(420)}$ of the Neutron Spectrum Obtained with the Initial Vector $X^{(0)} = \text{Constant}$.

strate adequate convergence for $m = 80$. Consequently, the investigation was extended and iterations up to $m = 420$ were examined. The iterative approximations obtained for $m = 120, 180, 240, 300, 360,$ and 420 with a constant initial vector are displayed in Figs. IV-2-5 and IV-2-6. Although these figures indicate some improvement for larger m , the adequacy of the convergence is still questionable.

On the brighter side, there is little question of the superiority of any of the presented iterative approximations as compared with the exact solution (viz. Fig. IV-2-2). Moreover, the peak which arises in the iterative approximations in the neighborhood of channel Nos. 27 and 28 corresponds to the resonance in the $\text{Li}^6(n,\alpha)\text{H}^3$ reaction at 0.26 MeV. In view of the drastic and unrealistic oscillation of the exact solution, no such comparable behavior can be observed in Fig. IV-2-2. Hence, while the resulting rate of convergence may

not be sufficient to permit a conclusive determination of the appropriate solution for this detection system, the iterative method is not completely without merit.

REFERENCES

1. G. Kreisel, *Some Remarks on Integral Equations With Kernels* $L(\xi_1 - x_1, \dots, \xi_n - x_n; \alpha)$, Proc. Roy. Soc. (London) Ser A, **197**, 160 (1949).
2. D. L. Phillips, *A Technique for the Numerical Solution of Certain Integral Equations of the First Kind*, J. ACM **9**, 84 (1962).
3. R. Gold and N. E. Scofield, *Iterative Solution of the Matrix Representation of Detection Systems*, Bull. Am. Phys. Soc. **2**, 276 (1960).
4. N. E. Scofield, *A Technique for Unfolding Gamma-Ray Scintillation Spectrometer Pulse-Height Distributions*, USNRDL-TR-447 (1960).
5. W. R. Dixon and J. H. Aitken, *The Resolution Correction in the Scintillation Spectrometry of Continuous X Rays*, Can. J. Phys. **36**, 1624 (1958).

IV-3. A Statistical Method for the Measurement of β_{eff}

R. A. KARAM

INTRODUCTION

There exists a number of methods by which the ratio of the effective delayed neutron fraction, β_{eff} , to the prompt generation time, ℓ , can be experimentally determined, but no technique of determining either quantity independently has seen widespread acceptance. Examples of such methods are the Rossi-alpha technique,¹ the source and power transfer function technique,² uniform $1/v$ poisoning,³ pulsed neutron techniques,⁴ and statistical techniques.^{5,6} Although the Rossi-alpha and the statistical method are based on the same principles, the techniques employed in the two methods are different. In this paper, the experimentally measurable variance-to-mean ratio is given in terms of β_{eff} and the excess reactivity, k_{ex} . By use of the inhour formula and the variance-to-mean relationship, unique values of β_{eff} and k_{ex} can be obtained independent of the neutron lifetime.

THEORY

It has been shown by C. de Hoffmann⁵ and later by W. Luckow and S. Churchill⁶ that the neutron population in the multiplying medium produces counts in a monitoring chamber whose variance, σ^2 , to mean, \bar{c} , ratio is

$$\frac{\sigma^2}{\bar{c}} = 1 + E \left[\frac{k'}{(1 - k')^2} \left(\frac{\bar{v}^2 - \bar{v}}{\bar{v}^2} \right) \left(1 - \frac{1 - e^{-\alpha T}}{\alpha T} \right) \right] \quad (1)$$

provided the counting time interval is short compared to the shortest delayed neutron half-life, but long compared to the prompt neutron generation time. In this expression:

E is the counter efficiency defined as the number of observed counts per fission in the reactor,

k' is the prompt multiplication factor, which to a good approximation is $(1 + k_{ex} - \beta_{eff})$,

\bar{v} is the average number of neutrons emitted per fission; (The values of \bar{v}^2 and \bar{v} reported by Diven, et al.,⁷ are used here.)

$$\alpha \text{ is the Rossi-alpha} \equiv \frac{\beta_{eff} - k_{eff}}{\ell},$$

T is the sampling time for counting.

In fast reactors, $\ell \sim 10^{-7}$ sec, and $\alpha \sim 10^5 \text{ sec}^{-1}$ so that T should be greater than $\sim 10^{-3}$ sec, and αT is sufficiently large compared to unity that the term containing the exponential can be dropped without introducing significant error into Eq. (1).

The counter efficiency can be eliminated from Eq. (1) by taking the ratio of two measurements: one at critical, and the other with the reactor subcritical. In principle, the experimentally measurable ratio

$$\frac{\left(\frac{\sigma^2}{\bar{c}} - 1 \right)_{\text{critical}}}{\left(\frac{\sigma^2}{\bar{c}} - 1 \right)_{\text{subcritical}}} \equiv \frac{(1 - \beta_{eff})(\beta_{eff} - k_{ex})^2}{\beta_{eff}^2(1 + k_{ex} - \beta_{eff})} \quad (2)$$

and the inhour equation⁸

$$k_{\text{eff}} = \frac{\ell}{\tau} + (1 + k_{\text{ex}}) \frac{\beta_{\text{eff}}}{\sum_1^m \beta_i} \sum_1^m \frac{\beta_i}{1 + \lambda_i \tau}, \quad (3)$$

can be solved simultaneously for unique values of β_{eff} and k_{ex} provided the reactor period, τ , corresponding to the k_{ex} of the subcritical reactor has been measured. It has been assumed that:

1. $\ell/\tau \approx 10^{-8}$ is small enough to be dropped from Eq. (3) without appreciable error,
2. All delayed neutron groups have equal importance weighting,
3. The sum of the absolute delayed neutron fractions, β_i , has been weighted for fissions in the various fissionable isotopes present.

Once β_{eff} and k_{ex} have been determined, the counter efficiency can be determined from Eq. (1) and the total number of fissions, and hence the reactor power, can be determined.

EXPERIMENTAL RESULTS

A 25-Mc time-gated scaler was used in conjunction with a large (2 in. diam \times 10 in. long) fission chamber in Assembly No. 2 of ZPR-VI to measure the total counts in a preselected time interval. A sufficiently large number of samples were taken for each time interval to determine the variance

$$\sigma^2 = \frac{1}{n-1} \left[\sum_1^n (c_i - \bar{c})^2 \right], \quad (4)$$

and the mean

$$\bar{c} = (1/n) \sum_1^n c_i. \quad (5)$$

A $\frac{1}{4}$ -in. thick jacket of polyethylene was used around the fission counter. Although the polyethylene may have produced an undesirable perturbation, its use appeared to be an expeditious means of obtaining the needed counter efficiency.

Table IV-3-I shows the data obtained as well as the derived σ^2/\bar{c} values. It is seen that variance-to-mean ratio increases as k_{ex} becomes more negative. This is opposite to the prediction of Eq. (1). It is also seen that the count rates are not in proportion to the reactor power and that the variance-to-mean ratio has an approximately linear proportionality to the reactor power. The first effect indicates the possibility of a counter dead time loss which is expected to be largest for the measurement at critical.* Since the fission rate in the

* Because of the inherent source of spontaneous fission neutrons, criticality usually cannot be established with any degree of certainty at power levels less than about 0.02 W. Even at this power, however, the expected counting rates

TABLE IV-3-I. EXPERIMENTAL VARIANCE-TO-MEAN DATA

Reactor Power, W	No. of Measurements	Counting Interval, msec	Mean Count, \bar{c} , count/time interval	σ^2/\bar{c}	Average Count Rate, count/sec	Normalization Factor
5.7×10^{-3}	334	100	1548.03	1.882	15,530	1.00
	291	10	154.89	1.756		
	287	1	15.62	1.904		
5.4×10^{-2}	253	100	7383.20	1.335	74,373	2.00
	267	10	739.76	1.240		
	281	1	75.31	1.287		
1.0×10^{-1}	305	100	12965.28	1.113	131,714	2.13
	338	10	1301.55	1.076		
	310	1	132.55	1.052		
	324	0.1	13.45	1.117		

Average σ^2/\bar{c}	Normalized σ^2/\bar{c}	k_{ex} , Ih
1.847	1.847	-90.3
1.287	2.574	0
1.103	2.345	0

reactor (and hence the power) is determined by the observed count rate, the efficiency of the counter at each power level was normalized to the lowest power level at which measurements are reported (0.0057 W, $k_{\text{ex}} = -90.3$ Ih) where the assumption of zero dead-time loss is appropriate. Since flux monitoring chamber currents are proportional to the reactor power, then the normalization factor is the ratio of percent increase in the mean count rate relative to their responses at 0.0057 W. The difference between the variance-to-mean ratios for the two measurements made at critical reflect the statistical error in the measurement, although it is somewhat larger than was expected.

If the normalized values of σ^2/\bar{c} obtained from the two measurements at critical are averaged and used in Eqs. (2) and (3) (k_{ex} was determined to be -90.3 Ih from the measured period and a calculated β_{eff}), the value of β_{eff} is found to be 0.0070 ± 0.0006 , a value which is very close to the calculated value of 0.0073 (one-dimensional 16-group diffusion code). Using $\beta_{\text{eff}} = 0.0070$, the counter efficiency was determined and the reactor power was found to be $(5.7 \pm 0.6) \times 10^{-3}$ W, which is in good agreement with a foil activation measurement of 6.4×10^{-3} W.

CONCLUSIONS

Being exploratory in nature, no attempt was made in this study to obtain precise values of the variance-

(~250,000 counts/sec) should not suffer appreciable dead-time losses in a 25-Mc scaler, and hence can only be attributed to the fission counter and its associated amplifier.

to-mean ratio, nor the exact simultaneous solution to Eqs. (2) and (3). Rather, the problem areas have been defined and the feasibility of an independent determination of β_{eff} and k_{ex} has been demonstrated. A major difficulty is a need for an efficiency normalizing factor because of the nonproportionality between the average count rate and the reactor power at the higher levels. The analysis is based on a one-group one-region reactor model and no account is made of the spatial and energy dependence of the detector efficiency. If the detector efficiency is much less than β_{eff}^2 , the variance-to-mean ratio is close to unity and statistically significant information about β_{eff} cannot be obtained. Also, at very large (negative) values of k_{ex} , the multiplication of the inherent source neutrons is very small or zero and the variance-to-mean ratio is again unity since the statistics are purely random and the distribution is a Poisson function.

The agreement between the measured and calculated values of β_{eff} and between the power calibration determined by statistical methods and that obtained by foil activation techniques is surprisingly good despite the seemingly bad experimental data. The statistical method outlined in this report appears to be a practical

technique for determining β_{eff} independent of the neutron lifetime.

REFERENCES

1. J. D. Ordhoff, *Prompt Neutron Periods of Metal Critical Assemblies*, Nucl. Sci. Eng. **2**, No. 4, 450 (1957).
2. C. E. Cohn, *A Simplified Theory of Pile Noise*, Nucl. Sci. Eng. **7**, No. 5, 472 (1960).
3. H. H. Hummel, C. E. Cohn, G. J. Fischer, W. Y. Kato, F. H. Martens, D. Meneghetti and B. J. Toppel, *Experimental and Theoretical Studies of the Coupled Fast-Thermal System ZPR-V*, Proc. 1958 Geneva Conference **12**, Paper No. 599, p. 166.
4. B. E. Simmons, *The Dynamic Reactivity Interpretation of Pulse Neutron Measurements*, Nucl. Sci. Eng. **5**, No. 4, 254 (1959).
5. F. de Hoffmann, *The Science of Nuclear Power*, (Addison-Wesley Publishing Company, Inc., Cambridge, Mass., 1949), p. 103.
6. W. K. Luckow and S. W. Churchill, *The Evaluation of Nuclear Reactor Parameters from Measurement of Neutron Statistics*, Trans. Am. Nucl. Soc. **1**, No. 2, 172 (1958).
7. B. C. Diven, et al., *Multiplicities of Fission Neutrons*, Phys. Rev. **101**, No. 3, 1012 (1956).
8. S. Glasstone and M. C. Edlund, *The Elements of Nuclear Reactor Theory*, (D. Van Nostrand Company, Inc., Princeton, 1952), p. 301.

IV-4. Analysis of Fast Neutron-Spectrum Measurements by Magnetic Analysis of Charged Particles Produced by Neutron Interactions

R. A. KARAM

INTRODUCTION

This study was undertaken to find out whether or not magnetic analysis of charged particles produced by fast neutrons can be used for spectrum measurement. It is found that under certain conditions magnetic analysis of either the α or the T produced by the reaction $\text{Li}^6(n, \alpha)T$ gives good neutron energy resolution if a beam geometry is used. However, the strength of the neutron beam required is above 10^{10} neutrons per cm^2/sec . This intensity requirement limits the use of this method to fast reactors that have fluxes of the order of 10^{14} neutrons per cm^2/sec inside the core.

There are several published reviews on recent developments of magnetic analyzers.¹⁻⁴ Several excellent designs of magnetic analyzers that can be adapted for this work are included in these reviews. In this paper a hypothetical design will be assumed in which the resolution and transmission are of the same magnitude,³ and are equal to 5×10^{-4} . It should be noted that a resolution of 0.1% and a transmission of 1.6% was achieved

with the "orange" toroids⁵ beta coincidence spectrometer.

DISCUSSION

Conservation of momentum and energy in the center of mass (CM) system provides the following relations:

$$m_1 V_1 = m_2 V_2, \quad (1)$$

$$m_3 V_3 = m_4 V_4, \quad (2)$$

and

$$\begin{aligned} \frac{1}{2} m_1 (V_1)^2 + \frac{1}{2} m_2 (V_2)^2 + Q \\ = \frac{1}{2} m_3 (V_3)^2 + \frac{1}{2} m_4 (V_4)^2, \end{aligned} \quad (3)$$

where the subscripts 1, 2, 3 and 4 refer to the neutron, Li^6 , T , and α , respectively. Q is the energy equivalence of the difference in masses between the incident plus target particles and the outgoing particles. The speed of the neutron in the CM system, V_1 , is related to the

speed of the neutron in the laboratory (L) system, V_n , by

$$V_1 = \frac{m_2 V_n}{m_1 + m_2}; \quad (4)$$

and similarly

$$V_2 = \frac{m_1 V_n}{m_1 + m_2}. \quad (5)$$

From Eqs. (1) to (5), it can easily be shown that the speed of the alpha particle in the CM system is

$$V_4 = \sqrt{\frac{9}{98} (V_n)^2 + \frac{6}{7} \frac{Q}{m_4}}, \quad (6)$$

and for the triton

$$V_3 = \sqrt{\frac{8}{49} (V_n)^2 + \frac{8}{7} \frac{Q}{m_3}}. \quad (7)$$

The transformation from the CM to the L coordinates is accomplished by the relation

$$(V_{4L})^2 = (V_4)^2 + (V_{CM})^2 + 2V_4 V_{CM} \cos \theta, \quad (8)$$

where θ is the angle in the CM system and (V_{4L}) is the speed of the alpha particle in the L system. It is obvious from Eq. (8) that V_{4L} is maximum when $\theta = 0$ and minimum when $\theta = 180$ deg. Thus, the speed of the alpha particle depends on the speed of the neutron and the angle between the direction of motion of the neutron and the alpha particle in the CM system.

If a Li-6 foil is exposed to an isotropic neutron flux, then the maximum and minimum speeds of the alpha particles produced by monoenergetic neutrons are [from Eqs. (6) and (8)]:

$$(V_{4L})_{max} = \sqrt{\frac{9}{98} (V_n)^2 + \frac{6}{7} \frac{Q}{m_4}} + \frac{V_n}{7}, \quad (9)$$

and

$$(V_{4L})_{min} = \sqrt{\frac{9}{98} (V_n)^2 + \frac{6}{7} \frac{Q}{m_4}} - \frac{V_n}{7}. \quad (10)$$

For example, the maximum and minimum energies of the alphas produced by 10 keV neutrons are calculated to be 2.10 and 1.98 MeV. Thus, it is obvious that with an isotropic neutron flux, one cannot get any resolution since the spread in the energy of the alpha particles produced by monoenergetic neutrons is considerably greater than the energy of the incident neutrons. However, if one uses a collimated beam of neutrons, then the maximum speed of the alphas is given by Eq. (9) and the spread of the speed is determined by the solid angle subtended by the slit width of the gap between the two pole pieces of the analyzing magnet. This spread is of the order of the resolution ($\sim 5 \times 10^{-4}$) if the maximum deviation of the alpha particle is only 8

deg from the direction of the incident neutron. Thus; for all practical purposes, $V_{4L} = V_4 + V_n/7$.

Upon differentiating Eq. (9) and with some rearranging, one obtains

$$\frac{dV_n}{V_n} = \frac{dV_{4L}}{V_{4L}} \left[\frac{2V_{4L}(7V_{4L} - V_n)}{V_n(2V_{4L} + V_n)} \right]. \quad (11)$$

If one replaces dV_n/V_n by $\Delta V_n/V_n$ and dV_{4L}/V_{4L} by $\Delta V_{4L}/V_{4L}$ and defines the neutron resolution as

$$R \equiv \frac{\Delta E_n}{E_n} = 2 \frac{\Delta V_n}{V_n}, \quad (12)$$

and the analyzing magnet resolution, R' , as $\Delta V_{4L}/V_{4L}$, then the neutron resolution based on the analysis of the alpha particles is

$$R = 2R' \left[\frac{2V_{4L}(7V_{4L} - V_n)}{V_n(2V_{4L} + V_n)} \right], \quad (13)$$

and that based on the analysis of triton is

$$R = 2R' \left[\frac{V_{3L}(7V_{3L} - V_n)}{V_n(V_{3L} + V_n)} \right]. \quad (14)$$

The resolutions, as expressed by Eqs. (13) and (14) are plotted in Fig. IV-4-1 as a function of the neutron energy; the value of R' was assumed to be 5×10^{-4} . For comparison, the resolution that is usually obtained by fast choppers is also shown in Fig. IV-4-1. It is seen that magnetic analysis gives better resolution at neutron energies above 20 keV. The resolution⁶ of the Van de Graaff is also shown in Fig. IV-4-1. It should be pointed out that the data of D. Hughes⁶ concerning the resolution of the Van de Graaff dates back to 1958. Currently, better resolution is being obtained by J. Rainwater, et al.,⁷ with the synchrocyclotron 200-m flight-path neutron velocity spectrometer.

For a beam geometry the reaction rate or the num-

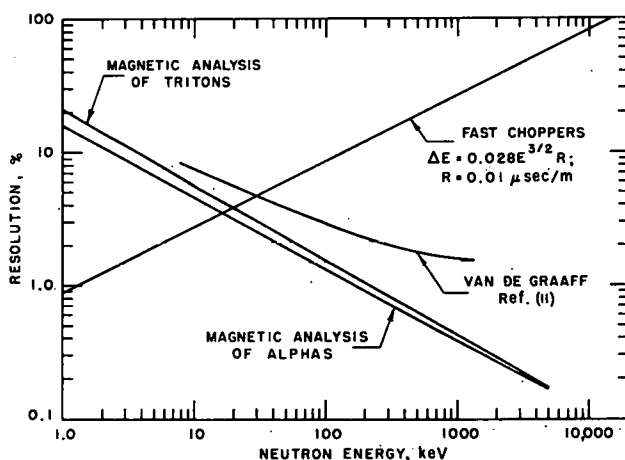


FIG. IV-4-1. Resolution Versus Neutron Energy.

ber of alphas or tritons that would be produced per sec can be expressed as

$$S = \phi(1 - e^{-\sigma Nt}), \quad (15)$$

where

S = number of alphas or tritons produced per sec

ϕ = neutrons per cm^2/sec (assumed to be 10^{10})

σ = microscopic cross section for the reaction $\text{Li}^6(n,\alpha)\text{T}$ (assumed to be 1 b)*

N = number of nuclei of Li^6/cm^3

t = thickness of Li^6 foil (assumed to be $2 \mu\text{g}/\text{cm}^2$)

With these assumed values it is found from Eq. (15) that S is $2000/\text{cm}^2\text{-sec}$. If a transmission of 5×10^{-4} is assumed, then 3600 counts per hour can be detected. This counting rate is small but not prohibitive. It should be noted that if such high resolution is not required, the counting rate can be increased by increasing the transmission at the expense of the resolution.

It is estimated that the average energy losses for the alphas and the tritons in the $2 \mu\text{g}/\text{cm}^2$ Li^6 foil due to straggling are 2 keV and 0.3 keV, respectively.† The straggling effect tends to decrease the resolution if thick foils are used.

For the case where the thickness of the foil is $2 \mu\text{g}/\text{cm}^2$, the spread in the speed of the charged particles due to straggling is slightly smaller than the resolving power (slightly over 2 keV) assumed for the magnetic analyzer. But, as the thickness of the foil increases, the straggling effect also increases to a point where it becomes the dominant factor in determining resolution. Because of this straggling, it is seen that the analysis of the tritons would be better than the alphas. In fact,

* The value of 1 b for σ corresponds to a neutron energy of 400 keV. This cross section is smaller at energies higher than 400 keV and larger at lower energies.⁸

† The estimate is based on a formula of Walter John.⁹

with triton analysis, the thickness of the Li^6 foil can be increased to $10 \mu\text{g}/\text{cm}^2$ without any ill effects. This will increase the counting rate to about 1.8×10^4 events per hour. The straggling effect for the tritons in a $10 \mu\text{g}/\text{cm}^2$ foil is estimated to be 1.5 keV. The magnetic separation of the alphas from the tritons is no problem unless there are neutrons of energies 1 keV and 7 MeV, in which case the alphas produced by 7 MeV neutrons will overlap the tritons produced by 1 keV neutrons. The overlapping may not be important because the Li^6 cross section at 1 keV is several orders of magnitude larger than the cross section at 7 MeV.

In conclusion, when high neutron flux beams from fast research reactors become available, this method of neutron spectrometry may prove to be useful.

REFERENCES

1. H. Hinterburger, *High-Sensitivity Mass Spectrometry in Nuclear Studies*, Ann. Rev. Nucl. Sci. **12**, 435-506 (1962).
2. C. A. McDowell, *Mass Spectrometry*, (McGraw-Hill Book Co., New York, 1963).
3. T. R. Gerholm, *Methods of Experimental Physics*, L. C. L. Yuan and Chien-Shiung Wu, Eds., (Academic Press, New York, 1961), Vol. 5, Part A, pp. 341-408.
4. J. D. Waldron, *Advances in Mass Spectrometry*, Proc. Conf. Univ. London, (Pergamon Press, London, 1959).
5. M. S. Freedman, et al., *Iron-Free Toroidal Beta-Beta Coincidence Spectrometer*, Nucl. Instr. **8**, 255 (1960); also cited in Ref. 3.
6. D. J. Hughes, *Progress in Nuclear Energy, Series C, Physics and Mathematics*, D. J. Hughes, J. E. Sanders and J. Horowitz, Eds., (Pergamon Press, New York, 1959), Vol. 3, 1-36.
7. J. Rainwater, et al., *Synchrocyclotron 200-Meter Flight Path Neutron Velocity Spectrometer*, Rev. Sci. Instr. **35**, No. 3, 263-275 (1964).
8. D. J. Hughes, B. A. Magurno and M. K. Brussel, *Neutron Cross Sections*, BNL-325, 2nd Ed., Supplement No. 1, (January 1, 1960).
9. American Institute of Physics Handbook, (McGraw-Hill Book Co., Inc., New York, 1957), pp. 8-23.

IV-5. Comparison of Linear and Square-Law Detectors for Noise Measurements¹

C. E. COHN

Since the measure of the intensity of a noise waveform is the mean square amplitude, it has been customary to make such measurements with square-law detectors. However, the accurate realization of such detectors is complex and expensive, so that it would be advantageous in many cases to use a linear detector, which is much simpler to realize accurately. It is easily shown that both types of detectors will yield the correct rms amplitude for pure Gaussian noise.

To compare the precision of the linear and square-law detectors, the analog-computer setup shown in Fig. IV-5-1 was used. Here a noise generator fed a tuned circuit analog which was a hybrid of the circuits presented by F. May and R. Dandl,^{2*} and P. Colburn and J. Hannaford.³ The square-law detector was an idealized-diode absolute-value circuit.⁴ The output of

* Note that this circuit has the disadvantage of nonzero response at zero frequency.

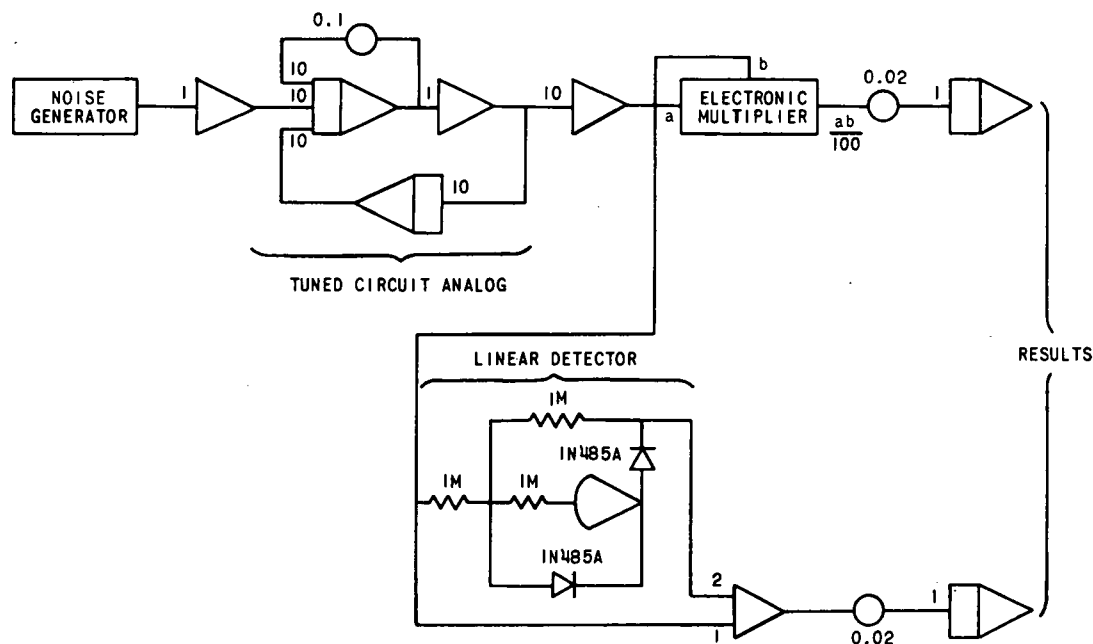


FIG. IV-5-1. Analog Setup for Detector Comparison.

each detector was integrated for 50 sec, after which the integrator outputs were read out, the integrators reset, and the integration repeated. A total of 182 replications were obtained.

The means and standard deviations of the estimates of the mean square amplitude of the noise derived from the output of each detector, in units of squared volts, are as follows:

Detector	Mean	Standard Deviation
Square-law	1833.6	360.2
Linear	1841.1	381.1

and the fractional deviations are as follows:

Square-law	0.196
Linear	0.207
Theoretical formula for square-law detector ⁵	0.200

This experiment thus indicates that the linear detector gives the same precision as the square-law detector.

It has been argued⁶ that the linear detector will not give correct readings of rms amplitude for non-Gaussian inputs. However, practically all experiments with atomic sources of noise involve pure Gaussian noise, so that objection would not apply for such experiments.

REFERENCES

1. C. E. Cohn, *Linear Detectors for Noise Measurements*, Rev. Sci. Instr. **35**, 638 (Note) (1964).
2. F. T. May and R. A. Dandl, *Active Filter Element and Its Application to a Fourier Comb*, Rev. Sci. Instr. **32**, No. 4, 387 (1961).
3. P. J. Colburn and J. Hannaford, *The Design and Testing of a Low-Frequency Spectrum Analyzer*, TRG Report 166 (CA), UKAEA (1962).
4. C. L. Johnson, *Analog Computer Techniques*, (McGraw-Hill, New York, 1956), 119.
5. D. Slepian, *Fluctuations of Random Noise Power*, Bell System Tech. J. **37**, No. 1, 163 (1958).
6. J. J. Davidson, *Average vs. rms Meters for Measuring Noise*, IRE Trans. Audio., Vol. AU-9, No. 4, 108 (July-August, 1961).

IV-6. Note on the Simulation of Higher-Order Linear Systems with Single Operational Amplifiers¹

C. E. COHN

Recently a number of authors^{2,3,4} have suggested the use of a single operational amplifier to simulate a higher-order linear system. The transfer function of such an arrangement is commonly derived assuming infinite operational-amplifier gain. However, it appears that such an assumption might not hold as well for these cases as it does for the usual first-order systems. This might be seen by looking at the simple second-order circuit shown in Fig. IV-6-1 which has been used⁵ as a tuned-circuit analog bandpass filter. The transfer function of this circuit is

$$\frac{e_o}{e_i} = \frac{G}{1 + jQ \left(\frac{\omega}{\omega_0} - \frac{\omega_0}{\omega} \right)}, \quad (1)$$

with resonant frequency

$$\omega_0 = (C_1 C_2 R_1 R_2)^{-1/2}. \quad (2)$$

With finite amplifier gain A taken into account,

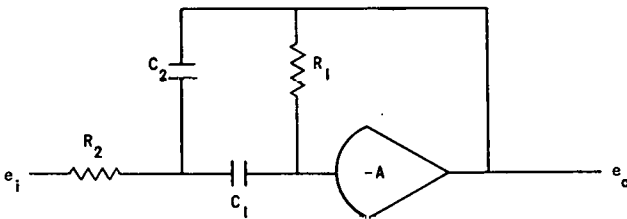


FIG. IV-6-1. Second-order Circuit Used as Tuned-Circuit Analog.

TABLE IV-6-I.

Q	R_1/R_2	$\frac{1}{2}(R_1/R_2) - 1$
1	4	1
2	16	7
5	100	49
10	400	199
20	1600	799
50	10000	4999
100	40000	19999

$$G = \left[\frac{1}{A} + \frac{A+1}{A} \cdot \frac{R_2}{R_1} \left(1 + \frac{C_2}{C_1} \right) \right] \quad (3)$$

and

$$Q = \sqrt{C_2 R_2 / C_1 R_1} \left[\frac{1}{A+1} + \frac{R_2}{R_1} \left(1 + \frac{C_2}{C_1} \right) \right]^{-1}. \quad (4)$$

Now it is readily shown that Q monotonically increases with R_1/R_2 and is a maximum for any value of that ratio when $C_1 = C_2$. With this latter condition, Eqs. (3) and (4) become

$$G = \left[\frac{1}{A} + 2 \frac{R_2}{R_1} \left(\frac{A+1}{A} \right) \right]^{-1}$$

$$= \frac{A}{A+1} \left[\frac{1}{A+1} + 2 \frac{R_2}{R_1} \right]^{-1},$$

$$Q = \sqrt{R_2/R_1} \left[\frac{1}{A+1} + 2 \frac{R_2}{R_1} \right]^{-1}.$$

For large A , the value of R_1/R_2 depends on the required Q according to the expression $R_1/R_2 = 4Q^2$. Now, for G and Q to be independent of A , and thus for the infinite-gain assumption to be valid, A must be very large compared to $(\frac{1}{2})(R_1/R_2) - 1$. Table IV-6-I shows values of this quantity for typical values of Q . For the higher values of Q , the requirement on amplifier gain is much more stringent than for the usual first-order circuits, where it must merely be large compared to unity. This can lead to noticeable degradation of circuit performance.

REFERENCES

1. C. E. Cohn, *Note on the Simulation of Higher-Order Linear Systems with Single Operational Amplifiers*, Proc. IEEE 52, 874 (Correspondence) (July, 1964).
2. A. Bridgeman and R. Brennen, *Simulation of Transfer Functions Using Only One Operational Amplifier*, WESCON Convention Record, (1957) Part 4, 273.
3. L. K. Wadhwa, *Simulation of Third-Order Systems with One Operational Amplifier*, Proc. IRE 50, No. 2, 201 (February, 1962).
4. G. K. Aggarwal, *On Fourth-Order Simulation by One Amplifier*, J. Electron. Control 15, No. 5, 449 (1963).
5. J. D. Cummins, *Frequency Spectrum of Calder Hall Reactor Noise*, AEEW-M-19, UKAEA (1960).

IV-7. Expediting Danger-Coefficient Measurements by Measuring Two Samples at Once

C. E. COHN¹

In danger-coefficient measurements, whether by autorod^{2,3} or pile oscillator, the required measuring time is related to the required precision by noise considerations. As a result, experiments involving measurement of very small reactivity changes are quite time-consuming and may involve integrated reactor powers which are not consistent with safe handling of fuel in critical assemblies. However, analysis indicates that it should be possible to use the measuring time more effectively and reduce fuel activation by measuring two samples at once.

Consider the three functions shown in Fig. IV-7-1. Here F_1 represents the reactivity as a function of time produced by a sample of reactivity ρ which is alternately inserted into the reactor for $T/2$ sec and removed for $T/2$ sec, and ρ_0 is the autorod reading with the sample removed. If the reading of an autorod on such a reactor is multiplied by weighting function W_1 and integrated over one cycle, the result will be $\rho T/2$, which is a measure of the sample reactivity. However, if F_1 is multiplied by weighting function W_2 and integrated, no output is obtained. If a second sample were alternately inserted and removed in such a way as to give reactivity profile F_2 equivalent to F_1 delayed by $T/4$ sec, then the integrated product of that profile with W_2 would give $\rho T/2$ and the integrated product with W_1 would give zero. If both samples were alternately inserted and removed and if the autorod reading were a linear superposition of the two reactivity profiles, the integrated product of the autorod reading with W_1 and W_2 would give a result proportional to the reactivity of only one sample, with no contribution from the other. Thus the two samples could be measured independently.

The functions shown in Fig. IV-7-1 would require some refinements to be useful for practical operation. The improved functions are shown in Fig. IV-7-2. Here F_1 and F_2 represent the reactivity introduced by each sample, while F is the overall reactivity. It has been pointed out in the references that weighting functions of the type shown as W_1 and W_2 are advantageous in rejecting extraneous reactivity drifts. An interval Δ would be provided at each sample-change time during which integration would be interrupted. This interval would have to be at least equal to the time required for changing samples plus the settling time of the autorod. Note that integration for one sample would be interrupted during the changing interval for the other sam-

ple. This would be done so that any asymmetry in the reactivity profiles of one sample for insertion and removal would not give a spurious contribution to the results for the other sample.

The results obtained from weighting functions of this type are given by

$$\int_0^{3T/2} F(t) W_1(t) dt = \left(\frac{T}{4} - \Delta \right) \rho_1,$$

$$\int_{T/4}^{7T/4} F(t) W_2(t) dt = \left(\frac{T}{4} - \Delta \right) \rho_2.$$

Thus each sample is measured independently of the other.

The application of this scheme to sinusoidal pile oscillators does not appear promising.

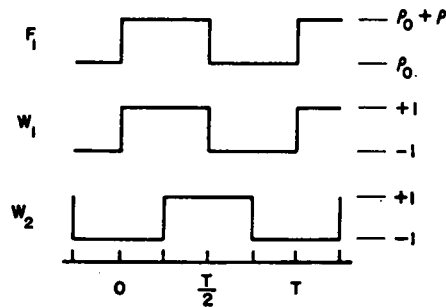


FIG. IV-7-1. Simplified Reactivity Profiles and Weighting Functions.

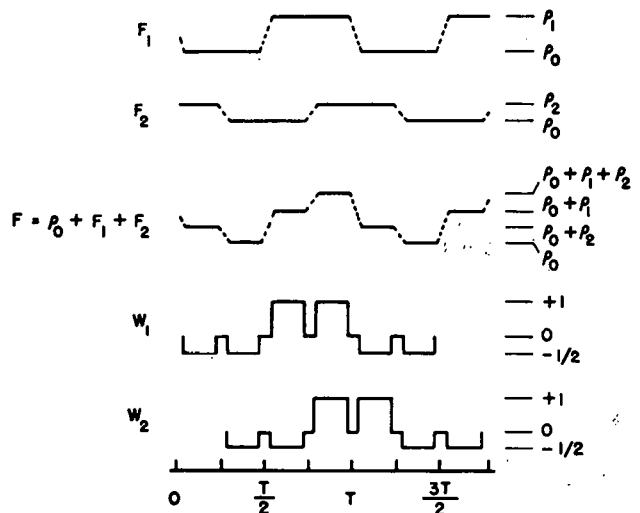


FIG. IV-7-2. Reactivity Profiles and Weighting Functions for Practical Operation.

REFERENCES

1. C. E. Cohn, *Expediting Danger-Coefficient Measurements by Measuring Two Samples at Once*, Nucl. Sci. Eng. **18**, No. 1, 140-142 (January, 1964).
2. E. F. Bennett and R. L. Long, *Noise Measurements on a Reactor Servo-Control System*, Trans. Am. Nucl. Soc. **5**, No. 1, 189 (June, 1962).
3. E. F. Bennett and R. L. Long, *Precision Limitations in the Measurement of Small Reactivity Changes*, Nucl. Sci. Eng., (in press).

IV-8. Argonne Fast Critical Facilities

W. Y. KATO, L. R. DATES, R. L. STOVER, W. G. KNAPP and G. K. RUSCH

The Argonne Fast Critical Facility, ZPR-VI, a large highly flexible zero power reactor which has been under construction since 1960 has been installed in Cell No. 5 of the Reactor Physics Laboratory to further the basic understanding of the physics of large dilute fast reactors. The facility became operational in July 1963 with its initial loading consisting of an all-uranium metal system with a U-238:U-235 atom ratio of 7.

The ZPR-VI facility¹ is shown in Fig. IV-8-1. It is a split-table horizontally-loaded critical facility. The facility consists of a large steel bed on which are mounted a stationary and a moveable table of 2.4 x 3.7 m dimensions. On each of the two tables is stacked 2025 stainless steel tubes (5 x 5 cm² x 1.2 m long) in a horizontal array supported on both sides by massive L-shaped cast steel supports. The array forms a 45-row by 45-column honeycomb-like matrix assembly and becomes a 2.4 m (8 ft) cube reactor when the two halves are brought together. The facility can be used to study reactors having core volumes as large as 3000 liters.

The reactor is controlled with the use of five horizontally actuated core removal type control-safety rods in each half of the assembly. In addition, there are six enriched B-10 filled safety rods in each half for use on assemblies having a degraded spectrum.

Various elements such as enriched, natural and depleted uranium, steel, aluminum, zirconium, graphite, iron oxide, niobium, and aluminum oxide—all in the form of small plates of 0.16 and 0.32 cm thick, 5 cm width, and lengths varying from 1 to 15 cm—are available for simulating the composition of different fast reactor systems. These materials are loaded into 5 x 5 cm² steel drawers to mockup the composition and geometry of reactors under investigation and the drawers are then inserted into the matrix assembly.

Following the installation of the mechanical and electrical components of the facility, a thorough operational testing and inspection program of the assembly was conducted. This program is outlined below.

BED AND TABLE ASSEMBLY

An investigation to determine the reaction of the assembly to a simulated matrix loading proceeded as follows:

1. Without Load
 - a. The mechanical operating system was thoroughly tested to verify dependability, accuracy, and conformity with specifications.
 - b. The loading surfaces of both the movable and stationary halves were checked for flatness with an Auto-Collimator.
2. With Load (82 metric tons—each half)
 - a. The complete mechanical system was again operated. No change in function or efficiency was noted after loading.
 - b. A recheck of the table loading surfaces revealed insignificant changes in individual table flatness. The movable table was observed to settle 0.005 cm more than the stationary table due to deflections in the roller bearing assemblies on which it rides.

It was concluded that the minor deflections demonstrated by the above tests would not effect the validity of the experimental data secured during the operation of the facility.

MATRIX ASSEMBLY AND TESTING

The matrix was constructed by stacking rows of tube bundles alternately so that the bundles were flush with the table interface. Lateral constraint was provided by holding knees. Figure IV-8-2 displays this arrangement.

Simulated core loadings in various configurations were assembled to test the integrity of the matrix complex. Generally, the greatest deflections were found to be at the center columns of tubes. As measurements moved toward the outer columns, deflections reduced because of the increased lateral support contributed by the very stiff holding knees. This condition, as expected, was most noticeable with the typical core

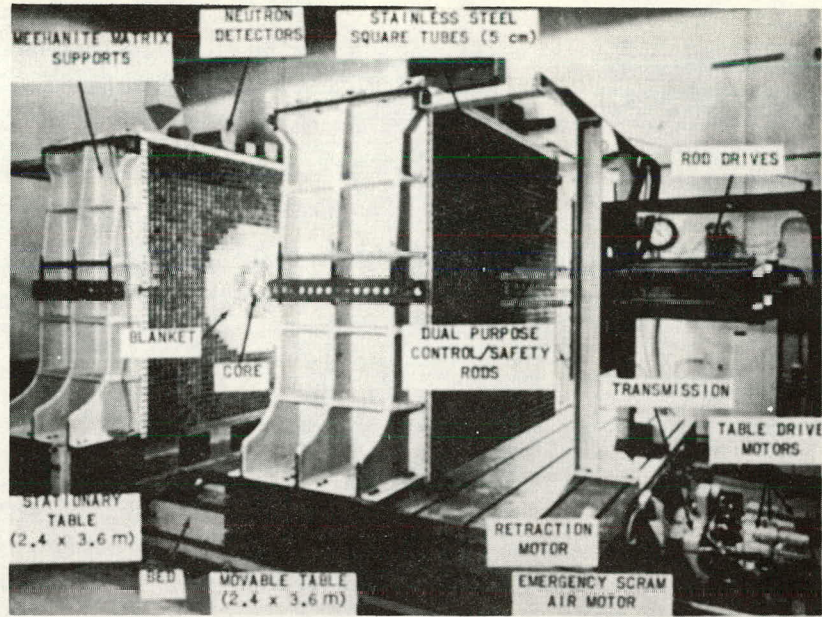


FIG. IV-8-1. Argonne Fast Critical Facility (ZPR-VI).

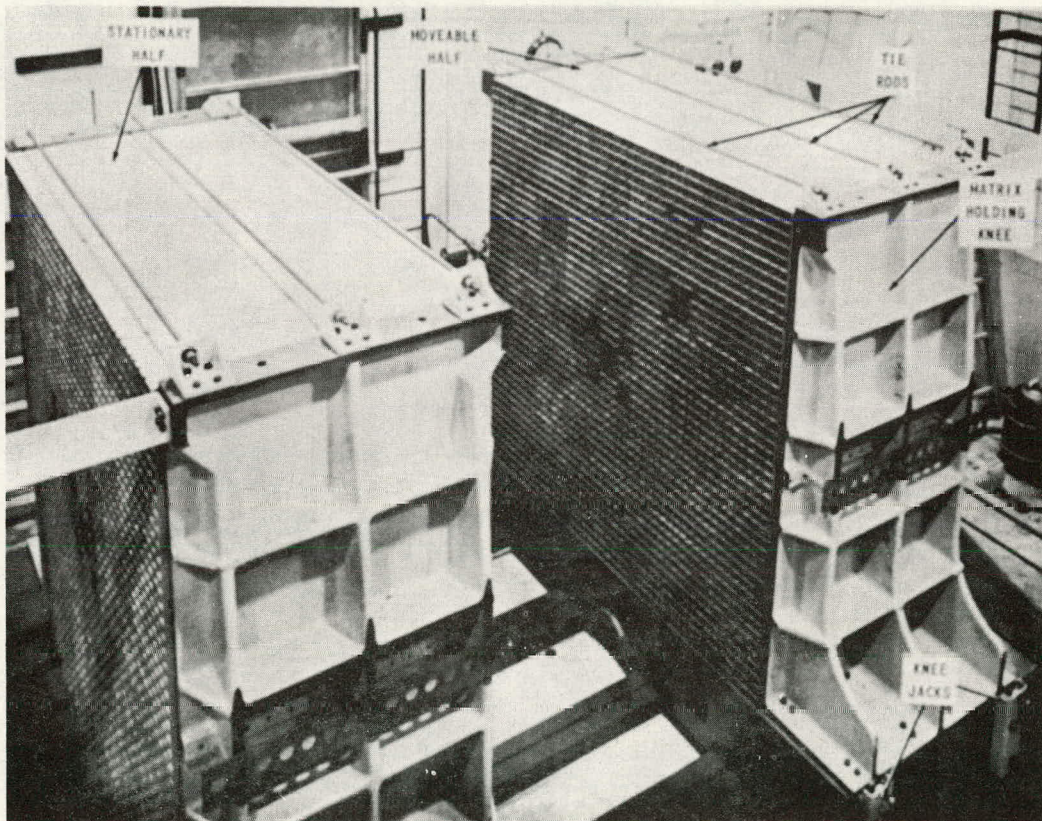


FIG. IV-8-2. Matrix Assembly.

loading where a concentrated load was applied on the central columns. A curve, shown on Fig. IV-8-3, exhibits the trend of deflections as measured over the height of the matrix at the central column.

CONTROL AND SAFETY ELEMENT TESTING

A mockup of actual operating conditions was used to test all rod drive mechanisms. Minor defects were detected and modifications were made until each

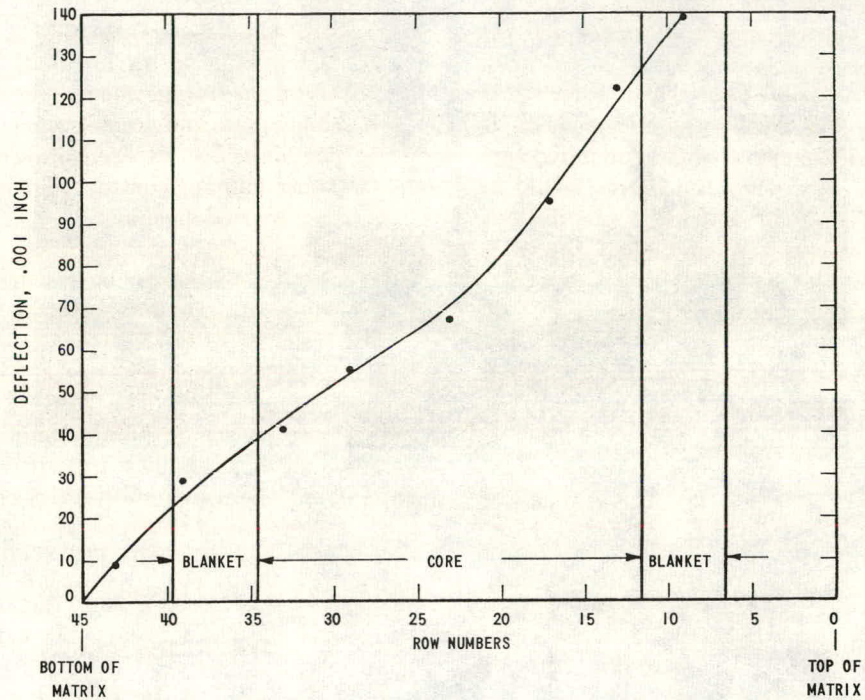


FIG. IV-8-3. Deflection at Vertical Centerline of Core (Column No. 23).

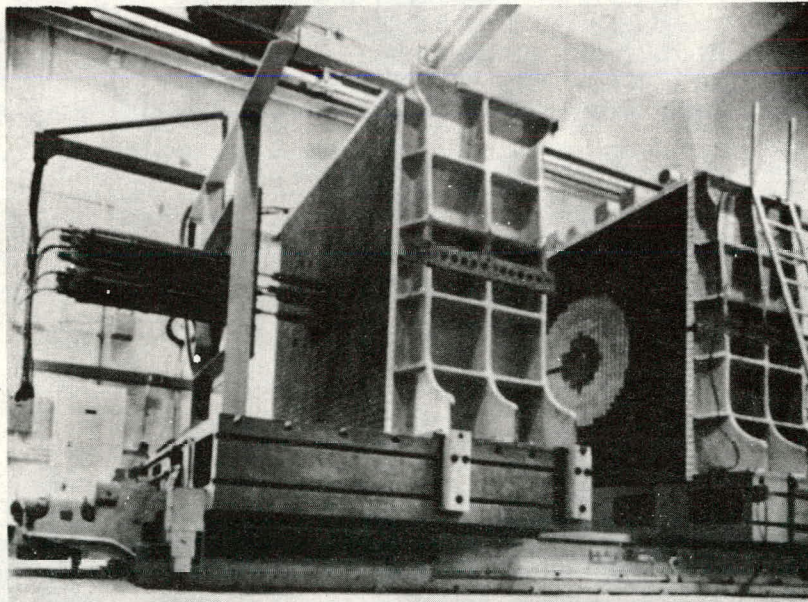


FIG. IV-8-4. Argonne Fast Critical Facility (ZPR-IX)

mechanism operated dependably at acceptable scram speeds.

NEUTRON SOURCE DRIVE TESTING

The complete system was operated with a "dummy" source loaded in the source capsule container and run through a series of insertion speed tests as it was made to travel through the flexible hose which connects to the insertion tube. The flexible hose was bent to various radii to impede the travel of the simulated capsule as would be the case when the source would be inserted into the reactors of varying configurations. No difficulty was experienced. When the hose was bent more than reasonably, the safety slip clutch served as a motor protector. It was established through these tests that the mechanism operated acceptably, and that the assembly should function dependably through the lifetime of the reactor.

CONTROL SYSTEM

A thorough check of all nine channels of neutron and gamma monitoring equipment was made. This consisted of basically measuring the stability, sensitivity, accuracy and response time of each electronic component. In addition, the electrical interlock circuitry was tested for proper operational use.

SUPPORT EQUIPMENT

The components listed below were built and tested and are considered ancillary devices to ZPR-VI:

1. Retractable loading platform
2. Danger coefficient sample changer and readout
3. Shim rod assembly
4. Television camera scanning trolley and operator
5. Reactor oscillator assembly
6. Analog table position readout
7. Argon gas storage and delivery system
8. Shield plate and accessories
9. Fat Man effect experimental equipment
10. Nonscramming control rod drive
11. Fuel coating machine
12. Fuel storage cages and racks
13. Fuel drawer conveying system
14. Working ramps and platforms.

The Argonne ZPR-IX, which is shown in Fig. IV-8-4, is a facility identical to the ZPR-VI, except for the matrix assembly. The ZPR-IX matrix of tubes and drawers is made of aluminum alloy instead of stainless steel to reduce parasitic absorption when systems which have a substantial component of thermal or epithermal neutrons are being studied. Construction began in 1960. The facility was complete and operational in February 1964.

REFERENCES

1. W. Y. Kato and L. R. Dates, *Design and Construction of the Argonne Fast Critical Facility (ZPR VI)*, Physics of Fast and Intermediate Reactors, IAEA, Vienna (1961), Vol. 1, pp. 295-312.

IV-9. Automatic Foil Activity Counting Facility and Data-Reduction Program

J. M. CHRISTENSON, K. E. PLUMLEE, W. R. ROBINSON and G. S. STANFORD

INTRODUCTION

Experiments using critical assemblies frequently involve interpreting large amounts of foil-activation data. The labor and investment necessary for foil-activation counting and processing have generally limited the amount of data obtained. As the number of samples to be counted increases, the desirability of having an automatic foil activity counting facility and data reduction program also increases. Recent improvements in these capabilities are described here.

AUTOMATIC FOIL ACTIVITY COUNTING FACILITY

There is in operation at Argonne a partially transistorized automatic foil-counting and recording facility.¹

The foil-activation data are taken from one to six counting channels operating in unison (normally sample changer, detector, amplifier, analyzer, scaler, and readout components). Five of the sample changers are single-counter units and one is a more heavily shielded double-counter arrangement, permitting a simultaneous count from the top and bottom of the foil. Sodium iodide gamma detectors and plastic beta scintillators can be interchanged. Output data are obtained on IBM-printed and punched cards which may be processed by a high speed computer.

A second automatic foil-counting facility has recently been placed in operation in anticipation of increased work loads as new experiments commence. Improvements in this system over the first system in-

clude capacity for larger counts, provision for automatic identification of samples and increased use of transistors.

In addition to the flexibility described in previously reported automatic counting systems,²⁻⁴ the following abilities were built into the facility to change counting intervals at will, to start or end traverses in any detector channel without complication, to take background counts intermixed at will between foil data, to preset counting intervals or preset count accumulation, and to provide for sealing data from various sources (other than foil-activation measurements). As an example of the latter, the scalers and automatic readout have been used in a manganese-bath experiment⁵ to measure ν , the number of neutrons per fission, for U-235 and Cf-252.

FOIL ACTIVITY DATA REDUCTION PROGRAM

The FORTRAN-II program for the IBM-704 computer produced tabulated and plotted data.⁶ The program is compatible with MONITOR operation⁷ and the logical flow is controlled entirely by input cards. Input cards consist of automatically produced "data" cards from the IBM-526 Summary Punch and manually produced "parameter" cards. All input cards are listed automatically in a self-identified format. Readout on the data cards include card number, elapsed time, counting internal time, scaler accumulation for up to six scalers operating in unison, and an identification column for each scaler. Parameter cards include a title card, cards to select the decay constant, reactor irradiation time, elapsed time from reactor shutdown to start of counting, coefficients for the scaler resolving time losses, resolution time, weight cards, and background adjustment cards. Parameter cards are necessary for each traverse being processed.

The program has a high degree of flexibility with numerous options depending upon the user's specific problem. Provisions are included for resolving time loss corrections, background adjustment, accidental coincidence corrections, decay corrections or alternatively concurrent normalization, weight corrections, averaging with deviation estimates, traverse normalization, and several choices of plotting. An outline of the options available is presented below.

RESOLVING LOSS CORRECTIONS

The resolving intervals are specified for each scaler on one of the parameter cards. Three constants of a polynomial equation (A , B , and C) are specified on an additional parameter card and may be adjusted to fit the characteristics of the counting system. The adjusted count is computed by the following formulation

$$\text{(Adjusted Count)} = \text{(Observed Count)} \cdot (1 + AR + BR^2 + CR^3) \quad (1)$$

where R is the observed count rate calculated by the computer.

BACKGROUND COUNT ADJUSTMENT

The background count adjustment may be either selected arbitrarily by the user or calculated by the program from background counts interspersed between foil activity counts.

ACCIDENTAL COINCIDENCE CORRECTIONS

Coincidence counting data, as is used for example in determining the relative amount of Pu-239 produced in irradiated foils, for initial conversion ratio (ICR) and for U-238 capture cadmium ratio (C_{28}) experiments, may be corrected for counts due to accidental coincidences.

DECAY CORRECTIONS

The decay constants for each scaler are specified on one of the parameter cards; consequently, the computer program is capable of processing data foils of six different decay constants concurrently. By special entries on the parameter card, foil data may be normalized against concurrently counted standard foils, rather than decay-corrected. This option is used with uranium fission product activities for which no single half-life is generally applicable. One or more sample changers are turned off after insertion of the reference foils which are counted repetitively. Data from these foils are recorded along with concurrently counted traverses in operating sample changers. Resolving loss adjustment and background subtraction are made with all concurrent normalized foils and standards. However, no provision has been made for differences in counter efficiencies, since the technique requires carefully matched counting channels and the normalization is heavily dependent on a fixed proportionality being maintained between scalers. Decay constants may be omitted when it is necessary to apply hand calculated time dependent corrections to the observed activities, as is the case for the fission product gamma activity correction factor in the ICR and C_{28} experiments. This feature also facilitates studies of the counting system sensitivity.

WEIGHT CORRECTIONS

Options available to the user include "no weight corrections," "normal weight corrections" (specific activity), and spatial weight corrections for gold and indium foils, either bare or cadmium-covered. The

formulas used for these special weight corrections are as follows: For cadmium-covered gold and indium foils

$$A_0 = A_m \frac{2 + H'F}{2 - H'F}. \quad (2)$$

For bare gold and indium foils

$$A_0 = A_m \left[1 - \frac{1}{CR} \left(\frac{2H'F}{2 + H'F} \right) \right]^{-1}. \quad (3)$$

Here A_m is the measured activation *per gram* of a foil whose weight is w , A_0 is the activation per unit weight that would have been observed for a foil of weight w_0 (having the same area), CR is the cadmium ratio for a foil of the thickness used, and F is a measure of the amount by which w differs from the nominal weight w_0 . F is defined by

$$F \equiv 2(w - w_0)/(w + w_0).$$

For the usual thicknesses of gold and indium (about 1 mil), it is ordinarily accurate enough to use the value of 0.44 for the correction factor H' . The formulas are adapted from the work reported in Ref. 8. Any effect of self-absorption of the radiation being counted is neglected; for beta-counted foils, additional self-absorption corrections would be required.

AVERAGING

A number of consecutive activities may be averaged. When this option is used, the average and the fractional standard deviation of the average is computed according to two hypotheses: (a) that the variation in the activities is due entirely to statistical variations in the count rate; and (b) that the variation in the activities is due entirely to statistical variations in the sensitivity of the counting equipment. The weighted average is computed from

$$\bar{X}_w = \frac{\sum_i \{X_i/S_r^2(X_i)\}}{\sum_i \{1/S_r^2(S_i)\}}, \quad (4)$$

and the relative error of the weighted average from

$$S_r(\bar{X}_w) = \left\{ \sum_i \{1/S_r^2(X_i)\} \right\}^{-1/2}, \quad (5)$$

where the $S_r(X_i)$'s are the estimated relative standard deviation of each X_i based on counting statistics alone:

$$S_r(X_i) \approx \left(\frac{\text{Total nonbackground counts used}}{\text{to determine the count rate } X_i} \right)^{-1/2}. \quad (6)$$

The mean is computed from

$$\bar{X}_M = (1/N) \sum_i^N (X_i), \quad (7)$$

and the relative root mean square deviation of X_i from

$$S_r'(X_i) = \frac{1}{\bar{X}_M} \left[\frac{1}{N} \sum_i (\bar{X} - X_i)^2 \right]^{1/2}. \quad (8)$$

$S_r(X_i)$ may be used to estimate the standard deviation of \bar{X}_M using the relationship

$$S_r(\bar{X}_M) = (N - 1)^{-1/2} S_r'(X_i). \quad (9)$$

NORMALIZED ACTIVITY

If a standard foil is indicated by a special entry in one of the identification columns on a data card, the traverse in which it is included will be normalized to this foil. If none is indicated, the computer selects the most active foil of the traverse for normalization.

DATA PLOTTING

The normalized activity of each point may be plotted and the magnitude of the point will be tabulated alongside. Special identification column entries will enable double or triple spacing on the plot.

COMPUTERS

Since the IBM-704 computer is to be phased out of operation the foil activity data-reduction program has recently been converted to the Control Data 3600 computer system.

REFERENCES

1. K. E. Plumlee and M. T. Wiggins, *Automatic Foil Activity Counting Facility and Data-Reduction Program*, ANL-6628 (1962).
2. H. A. Morewitz and R. F. Valentine, *A System of Obtaining and Reducing Neutron Flux Data from Critical Assemblies*, Nucl. Sci. Eng. 4, No. 1, 73-81 (1958).
3. K. E. Relf, *Counting Thousands of Samples in 12 Hours Automatically*, Nucleonics, 15, No. 4, 80-86 (1957).
4. R. T. Frost and E. B. Fehr, *Automatic Neutron Flux Scanner*, Nucleonics, 14, No. 3, 84-88 (1956).
5. A. DeVolpi, K. G. A. Porges and R. N. Larsen, *Mn-56 Coincidence Counting Facility*, ANL-6760 (1963).
6. C. E. Cohn, *Fortran Programming Technique for Graph Plotting on the IBM-704 Computer*, ANL-6161 (1960).
7. T. C. Barts and M. K. Butler, *OOPS Manual*, TM #27, Applied Math. Div. Argonne National Laboratory (November 1962).
8. G. S. Stanford, *Foil Data Thickness Corrections as Affected by Self-Shielding and Flux Depression*, TID-16733 (1962).

IV-10. A Calibrated Gamma Counting Facility

R. J. ARMANI

In order to determine disintegration rates of gamma-emitting radioisotopes, a calibrated gamma counting facility has been designed and assembled. The facility consists of a 3 in. x 3 in. NaI crystal and photomultiplier-tube package, transistorized preamplifier, high voltage supply, and a 400-channel pulse-height analyzer. The facility was initially assembled without shielding; however, subsequent addition of

shielding greatly reduced the background, thus enabling low activities to be counted with much improved accuracy. A lucite sample holder enables one to place a source in one of five reproducible positions, with the source-to-crystal distances ranging from 3 cm to 100 cm. This permits the counting of sources with activities from 10^2 decays/sec to 10^8 decays/sec with reasonable counting times.

An accuracy of the order of 2% to 4% is necessary to determine disintegration rates. With this objective, it was felt that the efficiency of counting could be determined by use of tables published by Heath.¹ The tables report efficiency as a function of gamma energy, distance from source to crystal, and crystal size. It was assumed that the NaI crystal was very close to the crystal cover, and that the transmission through the cover was 100%.

After counting a few samples, large discrepancies with the tabulated values were noted. There were no gamma standards immediately available to check the equipment. This resulted in a low confidence in the disintegration rates determined in much of the initial gamma counting done on detector materials used to monitor a radiation damage study.

Concurrently, the Working Group of the Irradiation Standards and Procedures Committee under the AEC Program on Radiation Damage to Reactor Structural Materials, concerned with standard methods of reporting experimental data, noted discrepancies in data reported to them. The discrepancies indicated errors in the determination of disintegration rates by gamma counting. In order to resolve the discrepancies, a foil intercalibration program was begun with eight laboratories participating, including Argonne National Laboratory (ANL).

Four pairs of foils were irradiated by Hanford and sent to the participating laboratories for analysis. The results reported by the laboratories are shown in Table IV-10-I. The discrepancies led to a meeting of the participants to discuss possible sources of errors, at which time it was decided to distribute a second set of foils for intercalibration.

The principal sources of error in the ANL counting facility were found to be source-to-crystal distance measurements and absorption in the crystal cover. These errors were discovered and corrected by means of calibrated gamma sources obtained from the National Bureau of Standards (NBS), by X-ray of the crystal package to determine the distance from the top

TABLE IV-10-I. FINAL REPORT: FIRST SAMPLE DISTRIBUTION

Irradiation Standards and Procedures Working Committee; Counting Intercalibration Program; Comparison of Results

Laboratory	Co ⁵⁹ (n, γ) Co ⁶⁰	Ni ⁵⁸ (n,p) Co ⁵⁸	Ti ⁴⁶ (n,p) Sc ⁴⁶	Fe ⁵⁴ (n,p) Mn ⁵⁴
A	1.06	1.04	0.58	1.14
	1.04	1.05	0.64	1.12
B	1.09	1.34	0.97	1.21
	1.02	1.25	1.20	0.91
C	1.06	1.26	1.27	1.23
	1.02	1.25	1.27	1.23
D	1.07	0.93	1.04	0.96
	1.015	0.94	0.98	0.88
E	1.00	1.64	1.31	1.58
	0.98	1.64	1.30	1.38
F	0.74	0.97	0.73?	0.95
	0.76	0.97	0.94	0.93
G	1.00	1.24	1.27	1.22
	1.01	1.26	1.19	1.23
H	1.03	1.42	Lost	1.40
	1.04	1.43	1.34	1.43
Average	0.99	1.23	1.09	1.18
Standard deviation	0.097	0.22	0.24	0.20

All numbers are ratios of count by the participating Laboratory to count at Hanford Atomic Power Operation.

TABLE IV-10-II. HANFORD-ANL COMPARISON: SECOND SAMPLE DISTRIBUTION

Material	Sample No.	Nuclide	ANL Activity, dis/sec	HAPO Activity, dis/sec
Ni	13-2	Co-58	2.83×10^4	2.78×10^4
	13-10	Co-58	2.84×10^4	2.77×10^4
AlCo	12-7	Co-60	2.63×10^3	2.60×10^3
	12-19	Co-60	2.64×10^3	2.59×10^3
Ti	6150-3	Sc-46	3.58×10^4	3.55×10^4
	6150-4	Sc-46	6.80×10^4	6.69×10^4
Fe	E-31-2A-3	Mn-54	9.81×10^3	9.88×10^3
	E-31-2A-4	Mn-54	9.41×10^3	9.41×10^3
	Sp-7-2	Mn-54	3.55×10^3	3.44×10^3

of the package to the top of the crystal, and by obtaining information from the manufacturer on the amount and type of material covering the crystal. The lucite sample holder mentioned above was placed on the crystal package to provide a reproducible geometry. Measurements were then made with the gamma standards. The results showed that the errors were now properly corrected.

By the time of the second foil exchange, the shield

and lucite sample holder had been added. There was much better agreement among the various laboratories during this exchange. The results obtained at ANL, shown in Table IV-10-II, were typical of those reported by all of the participants.

REFERENCES

1. R. L. Heath, *Scintillation Spectrometry Gamma-Ray Spectrum Catalogue*, IDO-16408 (July 1, 1957).

IV-11. Attenuation of Epicadmium Neutrons by Cadmium Foil Covers

G. S. STANFORD

INTRODUCTION

In striving for accurate quantitative interpretation of cadmium ratios, the fact must be considered that cadmium is neither perfectly opaque to thermal neutrons nor perfectly transparent to epithermal neutrons. As the thickness of the cadmium covering a foil decreases, the activation of the foil increases due to a combination of three effects: (1) the thermal activation increases; (2) the transmission of epithermal neutrons by the cadmium extends to lower energies; and (3) there is less attenuation by the cadmium of neutrons above the cutoff energy.

For a $1/v$ detector, the combined result of effects (2) and (3) determines the cutoff energy E_c , as frequently defined. It is convenient to use the cutoff energies as calculated for $1/v$ foils (see for example the Westcott calculations as plotted by N. Baumann¹), even for foils such as gold or indium which have large resonances. In such cases, however, it is necessary to make an additional correction for attenuation of epicadmium neutrons by the cadmium. As mentioned below, it is possible to calculate such correction factors, at least approximately, from the available cross section data.

Some measurements of the response of indium, and (to a lesser extent) gold, foils to variation in cadmium thickness have been reported by D. Martin² and by J. DeJuren and R. Paschall.³ From the measurements, a quantity F_{Cd} can be deduced, after the method of C. Tittle,⁴ by extrapolating the cadmium-covered foil activations to zero cadmium thickness. This extrapolated activation is presumed to be the epicadmium portion of the activation of a bare foil. However, it does not seem to have been widely recognized by users of the published F_{Cd} values that most of the slope of the curves is due to the decrease in cutoff energy as the cadmium

becomes thinner. For example, it is incorrect to apply F_{Cd} to the activation of a gold foil covered by 30-mil cadmium, while assuming that the cutoff energy remains unchanged at 0.62 eV. (An error of 10% in the cadmium cutoff energy is equivalent to an error of about 5% in the $1/v$ portion of a resonance integral.)

CALCULATIONS

In the ensuing discussion, the following definitions will be used:

E_c = cadmium cutoff energy for a $1/v$ detector,

A_n = non-thermal portion of the activation of a cadmium-covered foil,

A_f = activation that would be observed with an ideal filter which changes sharply from black to transparent at energy E_c ,

A_0 = extrapolation of A_f to zero cadmium thickness,

t = cadmium thickness,

x = foil thickness.

Two cadmium correction factors, F_{Cd} and F_t , will now be defined by the following equations:

$$A_0(x) = F_{Cd}(t,x) \cdot A_m(t,x), \quad (1)$$

$$A_f(t,x) = F_t(t,x) \cdot A_m(t,x). \quad (2)$$

The factor F_{Cd} was discussed above. F_t is a factor whose use does not involve an implicit change in cutoff energy; for a $1/v$ detector it is identically unity. F_t for gold and indium differs from unity because most of the epicadmium activation occurs near a large low-energy resonance where the removal cross section of cadmium is appreciable.

Table IV-11-I gives measured and calculated values of F_{Cd} for 2-mil indium, and in Fig. IV-11-1 some calculated values of F_{Cd} are plotted for a range of indium thicknesses. These plotted values are partly empirical,

TABLE IV-11-1. EPICADMIUM ATTENUATION FACTORS FOR 2-MIL INDIUM FOILS, ISOTROPIC FLUX

t , mils	E_c , eV ^a	F_{Cd} Measured (Ref. 3)	F_{Cd} Calculated ^b
0	0.40	1.0	1.0
5	—	1.013	—
10	0.478	1.025	1.029
15	0.516	1.038	1.042
20	0.555	1.051	1.056
25	0.591	1.064	1.069
30	0.622	1.077	1.079
35	0.651	1.090	1.091
40	0.678	1.103	1.101
50	0.726	1.128	1.122
60	0.767	1.150	1.140

^a For 1/v detector. From Westcott⁵ as plotted by Baumann.¹

^b Calculated entirely from cross section data, using 5.5 b for the value of the cadmium absorption cross section at the indium resonance.

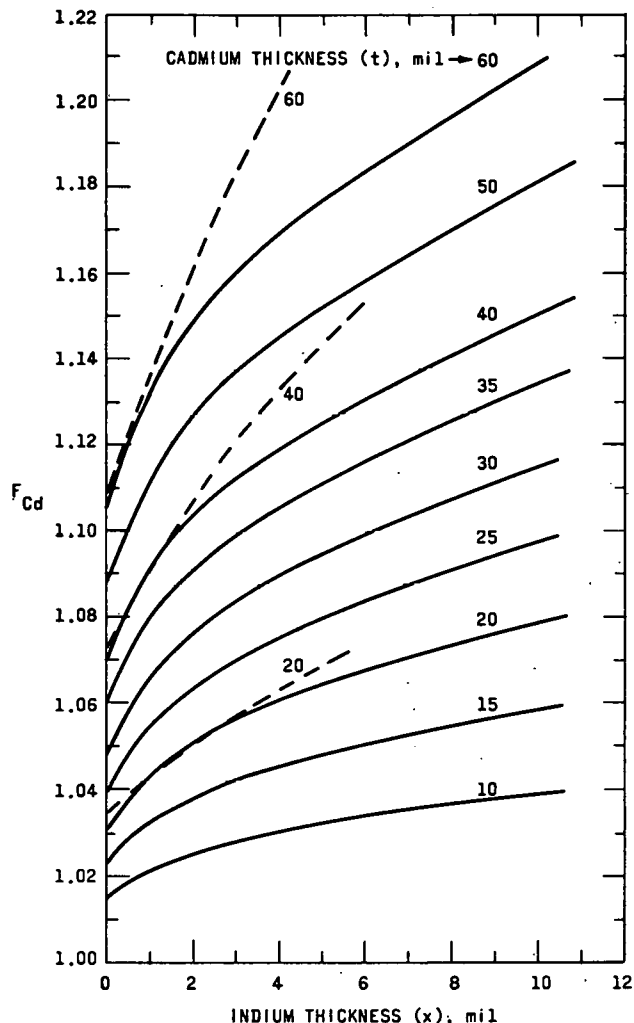


FIG. IV-11-1. The Factor F_{Cd} for Indium (Dashed lines are curves given by Tittle⁴).

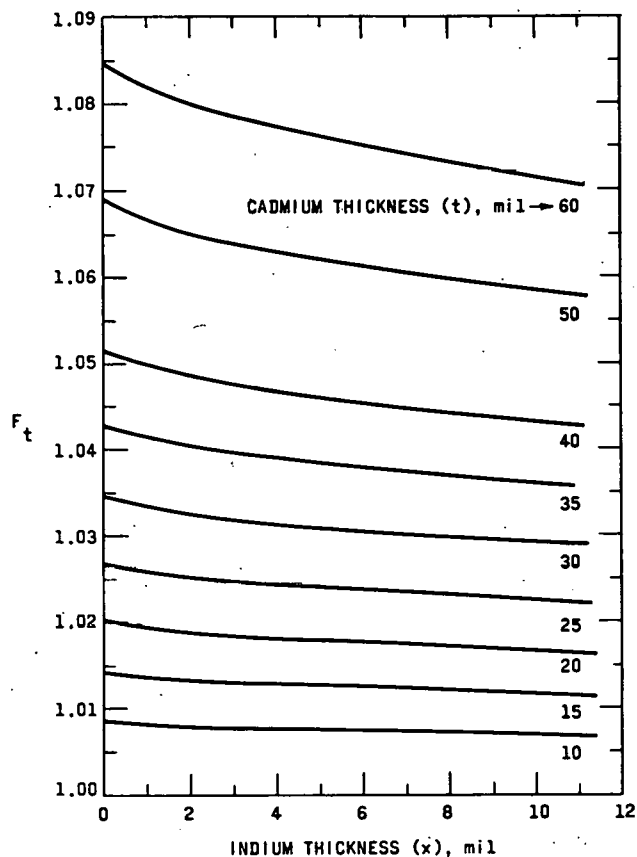


FIG. IV-11-2. Epicadmium Correction Factor F_t for Indium.

in that for each cadmium thickness a normalizing factor has been applied to force agreement with DeJuren and Paschall's measurements³ for 2-mil indium.

Figure IV-11-2 shows F_t for indium. These values are similarly partly empirical, being adjusted somewhat to agree with DeJuren and Paschall's measurements.

In Fig. IV-11-3 are plotted F_{Cd} and F_t for gold. Unlike the indium case, these curves are based entirely on calculations from cross section data. Some measurements taken with gold to check these curves are reported below.

One quantity that enters into the calculations for gold and indium is the value of the effective cross section of cadmium at the energy of the resonance. At the energy of the gold resonance (4.9 eV), σ_a is 0.2 b, and σ_s is 5 b. If the cadmium-covered foil is irradiated in a void, some of the resonance energy neutrons headed for the foil will be removed by scattering in the cadmium, so that its effective removal cross section will be greater than the absorption cross section. In making the calculations for Fig. IV-11-3 a value of 1.0 b was arbitrarily chosen for the Cd cross section.

If, on the other hand, the cadmium cover were to be

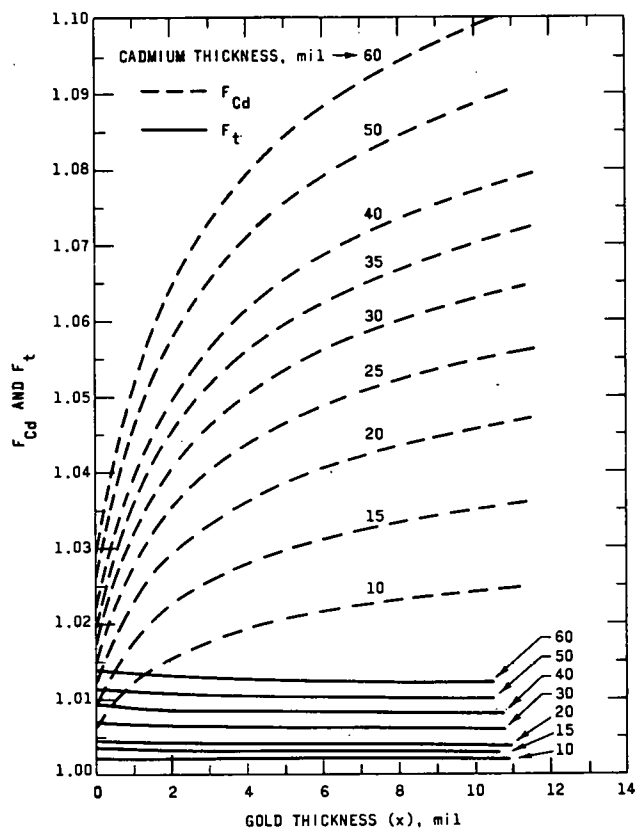


FIG. IV-11-3. Epicadmium Correction Factors for Gold (Calculated using $1b$ for the effective cross sections of cadmium at the energy of the gold resonance).

closely surrounded by a medium such as graphite or water, with a Σ_a comparable to, or larger than that of cadmium, the removal cross section should be the same as the cadmium absorption cross section. For such a case, the appropriate value of F_t can be determined from Fig. IV-11-3, using

$$(F'_t - 1) = (F_t - 1) \frac{\sigma_a}{1 \text{ barn}}, \quad (3)$$

where F'_t is the new value of F_t . Equation (3) is actually an approximation, sufficiently accurate for the purpose, for a more precise but more complicated expression. F_{Cd} can be recalculated from the information that for fixed foil thickness and fixed cadmium thickness, F_{Cd} is proportional to F_t .

MEASUREMENTS WITH CADMIUM-COVERED GOLD FOILS

By irradiating foils mounted on an aluminum wheel rotated in a cavity in the ATSR graphite stack, the data shown in Fig. IV-11-4 were obtained. The "calculated" curves are plots of $1/F_{Cd}$, taken directly from Fig. IV-11-3. For each gold thickness the measured activations have been normalized to agree with the

calculated curve in the neighborhood of 40–50 mils of cadmium. The agreement between measurement and calculation must therefore be judged on the basis of slope rather than magnitude.

The curves do in fact agree within the experimental scatter of the points, and it can easily be verified that this would not be the case for an attempt to match, say, the 4.8-mil data to the 1.2-mil calculation. It can also be seen that a linear extrapolation to zero cadmium thickness cannot in general be made (even with semi-log plotting).

It was also found that the choice of $1b$ for the removal cross section of the cadmium at the energy of the gold resonance was a good one, although perhaps not the best. However, calculations based on $0.2b$ and $2b$ gave decidedly poorer agreement.

DISCUSSION AND CONCLUSIONS

The agreement between calculation and measurement (see Table IV-11-I and Fig. IV-11-4) is good enough to give confidence in the calculational method. Both the calculations and the measurements on gold foils support Tittle's deductions⁴ that the correction factor F_{Cd} for gold and indium is in fact a rather strong function of the foil thickness. D. Trubey, T. Blosser and G. Estabrook's failure to observe this⁶ is not understood.

It also appears that the interrelationship between F_{Cd} and the cadmium cutoff energy has been insufficiently appreciated. Extrapolation of epicadmium ac-

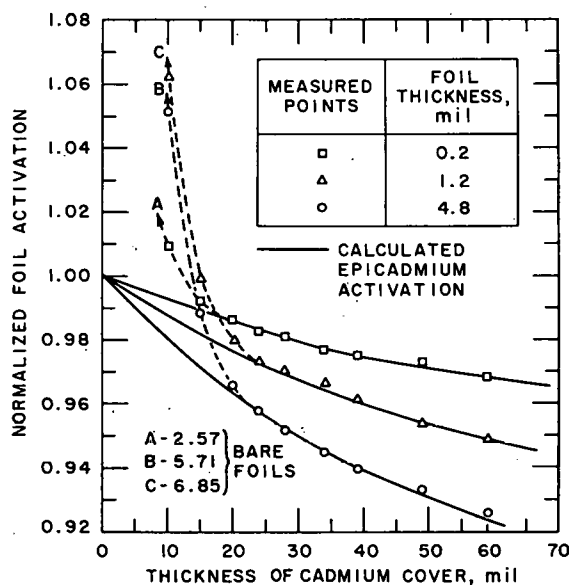


FIG. IV-11-4. Activations of Gold Foils as a Function of Cadmium Thickness for Three Foil Thicknesses. (Measured points have been normalized to agree with calculation at 40–50 mils. The 1.2-mil foils were exposed in a softer spectrum than the other two thicknesses.)

tivation to zero cadmium thickness, as done for instance in Fig. IV-11-4, involves extrapolating the cadmium cutoff energy to zero cadmium thickness, and the physical meaning of this is not exactly clear. The curves for F_{Cd} should be most useful for reducing to a common basis measurements that were made with differing thicknesses of cadmium. For this purpose the extrapolated value cancels out.

To correct for removal of epithermal neutrons by the cadmium while preserving a known cutoff energy, the plotted values of F_+ can be used, in conjunction with the cutoff energies from Table IV-11-I.

Finally, it is observed that the values of F_{Cd} for gold appear to be considerably higher than has previously² been indicated.

IV-12. The Activation of Gold Foils and Spheres for Non-Isotropic Neutron Incidence

F. H. HELM

INTRODUCTION

The self shielding of gold foils and the spatial distribution of activation in irradiated gold spheres were measured in various experimental geometric configurations which produce different conditions of angular incidence. A method has been developed to determine the angular distribution of the incident flux from these measurements.

THEORY

For an infinitely dilute absorbing sample, the activation is proportional to the unperturbed flux, ϕ_0 . In foils of finite thickness, t , the average flux, $\bar{\phi}$, through the foil volume is somewhat lower than its unperturbed value. The self shielding, G , is defined as the ratio of perturbed average flux to the unperturbed flux and, in an isotropic neutron field, is given as¹

$$G = (\bar{\phi}/\phi_0) = [\frac{1}{2} - E_3(t\Sigma_a)]/(t\Sigma_a), \quad (1)$$

where $E_3(t\Sigma_a)$ is an exponential integral for which the general definition is given by $E_n(x) = \int_1^\infty [e^{-xy}/y^n]dy$, and Σ_a is the microscopic absorption cross section of the foil material.

In a non-isotropic neutron field where the angular distribution is known, it is convenient to expand the angular flux in a cosine series with coefficients ϕ_n :

$$\phi(\theta) = \sum_n \phi_n \mu^n,$$

where $\mu = \cos \theta$ and θ is the angle between foil normal

REFERENCES

1. N. P. Baumann, *Resonance Integrals and Self-Shielding Factors for Detector Foils*, DP-187 (1963).
2. D. H. Martin, *Correction Factors for Cd-Covered Foil Measurements*, *Nucleonics* **13**, No. 3, 52-53 (1955).
3. J. A. DeJuren and R. K. Paschall, *Thermal Neutron Transmission through Cadmium-Covered Foils*, NAA-SR-7770 (1963).
4. C. W. Tittle, *Slow-Neutron Detection by Foils-II*, *Nucleonics* **9**, No. 1, 61-67 (1951).
5. C. H. Westcott, W. H. Walker and T. K. Alexander, *Effective Cross Sections and Cadmium Ratios for the Neutron Spectra of Thermal Reactors*, Proc., 1958 Geneva Conference, **15**, Paper No. 202, p. 70.
6. D. K. Trubey, T. V. Blosser and G. M. Estabrook, *Correction Factors for Foil-Activation Measurements of Neutron Fluxes in Water and Graphite*, ORNL-2842, 204-215 (1959).

and the neutron direction of travel. Each angular distribution is characterized by a set of coefficients, ϕ_n .

The corresponding expression for the self shielding is^{1,2}

$$G = \frac{(\sum_n \phi_n [1/(n+2) - E_{n+3}(t\Sigma_a)])}{(\sum_n [\phi_n t\Sigma_a / (n+1)])}. \quad (2)$$

In certain experiments (e.g., exposure to a beam) it is more convenient to divide the angular space into a number of increments³ of width $\Delta\mu_i = \mu_i - \mu_{i-1}$. With the proper choice of widths, the flux in each increment, ϕ_i , is approximately constant and the self shielding is

$$G = \left[\sum_i \phi_i \left\{ \mu_{i-1}^2 \left[\frac{1}{2} - E_3(t\Sigma_a/\mu_{i-1}) \right] - \mu_i^2 \left[\frac{1}{2} - E_3(t\Sigma_a/\mu_i) \right] \right\} \right] / \sum_i \phi_i t\Sigma_a \Delta\mu_i. \quad (3)$$

For a large (relative to $1/\Sigma_a$) gold sphere, few neutrons penetrate as deep as the center of the sphere and the activation of conic sections can be used as a qualitative measure of the angular flux in which the sphere was exposed.

MEASUREMENTS

Various non-isotropic neutron fields were experimentally produced by irradiating foils and spheres in the center of five-sided cubic Cd boxes in a thermal column of the Juggernaut reactor. The open side of

each box faced the reactor core. Measurements were taken in boxes of different sizes and with the box either voided or filled with graphite. The foils were oriented either parallel or vertical to the open face. Activation measurements were made for a series of foils whose thicknesses ranged from 0.00125 cm to 0.05 cm (0.5 to 20 mil) in each experimental geometric configuration. The difficult problem of extrapolating the measured data to infinite dilution¹ was circumvented by normalizing all measurements to the activation per unit mass and exposure of a 0.5 mil foil. This thickness of foil has a calculated self shielding in an isotropic flux [Eq. (1)] of $G = 0.98$ and is not very sensitive to non-isotropic neutron incidence. The use of this type of normalization is estimated to introduce less than $\frac{1}{2}\%$ error in the measured self shielding. The normalization to unit exposure was made by irradiating a 2-mil monitor foil simultaneously with each sample foil, but spatially isolated from the experiment.

Foils and spheres were gamma counted with a NaI scintillation counter. The foils were placed in an aluminum counting jig which provided a counting geometry reproducible to a few tenths of a per cent. A highly collimated configuration was used to measure the activation of small regions on the surface of the spheres. The scintillation counter was placed behind a pinhole in a $7\frac{1}{2}$ -cm thick lead shield and the sphere was rotated in front of the pinhole to determine the activation of the different regions.

RESULTS

Figure IV-12-1 shows the measured and calculated values of the self shielding for different thicknesses of foils in graphite-filled cadmium boxes of different dimensions for both parallel and vertical foil orientations. The calculated values were found from Eq. (2). The ϕ_n for each angular component of the flux was

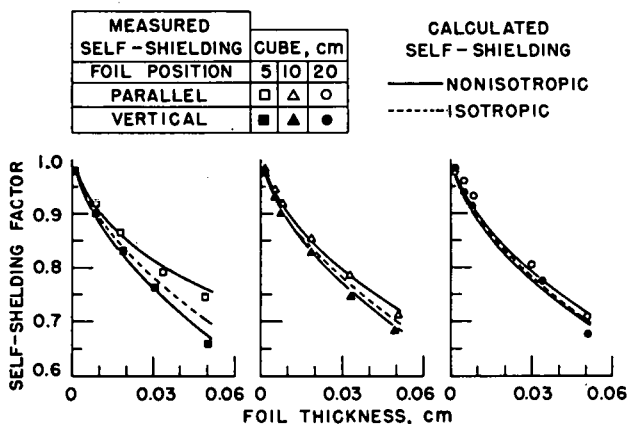


FIG. IV-12-1. Calculated and Measured Self-Shielding in Cadmium-Lined Graphite Cubes of Different Sizes.

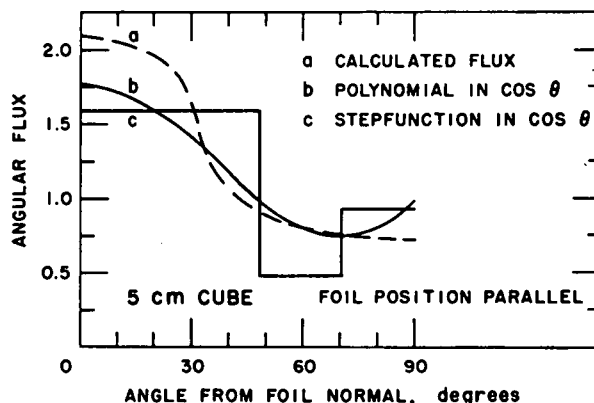


FIG. IV-12-2. Angular Flux Distribution in the Center of a Cadmium-Lined 5 cm—Graphite Cube: a) Calculated from the Scalar Flux Distribution; b) and c) Calculated from the Measured Self-Shielding of Foils Oriented Parallel to the Open Side.

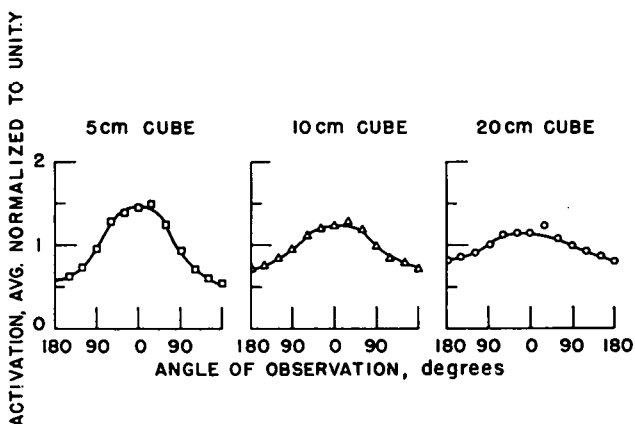


FIG. IV-12-3. Measured Activation of Gold Spheres, Activated in the Center of Cadmium-Lined Graphite Cubes of Different Sizes.

calculated from the scalar flux distribution through the box. The cosine series was limited to $n = 4$. The measured values of the self shielding for foils of different thicknesses were used in Eqs. (2) and (3) in order to generate systems of linear equations which allow the determination of the ϕ_n and ϕ_i . The corresponding angular distributions are shown as curves b and c of Fig. IV-12-2. The angular distribution as determined from the scalar flux measurements is shown as curve a. However, in order to yield good results, calculations of this kind require self shielding measurements of extreme accuracy—better than 0.1%. The accuracy of the present measurements was about 1% and the fitting procedure was limited to polynomials of the second order in $\cos \theta$ or step functions with three intervals.

Results of activation measurements with gold spheres in graphite are shown in Fig. IV-12-3. Although the results can only be interpreted qualitatively, they do

demonstrate the decrease in anisotropy with increasing box size.

Similar results were obtained with the gold spheres in the large (20 cm) voided cadmium box (shown in Fig. IV-12-4) where the incident flux is almost constant through the central 45 degree core and zero at all angles larger than 55 degrees. Results of foil measurements in this geometry are shown in Figs. IV-12-5 and IV-12-6. The difference between measured and calculated self shielding (Fig. IV-12-5) for parallel foil

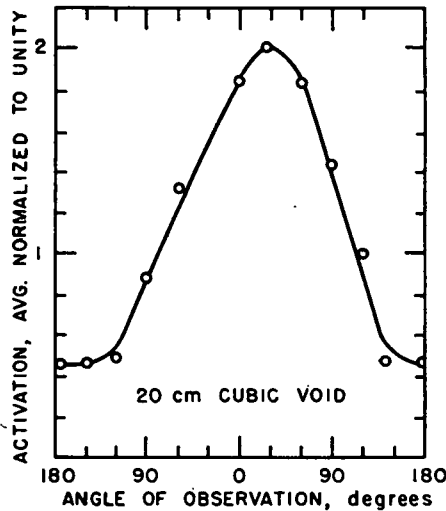


FIG. IV-12-4. Measured Activation of a Gold Sphere Activated in the Center of the Cadmium-Lined 20 cm-Void.

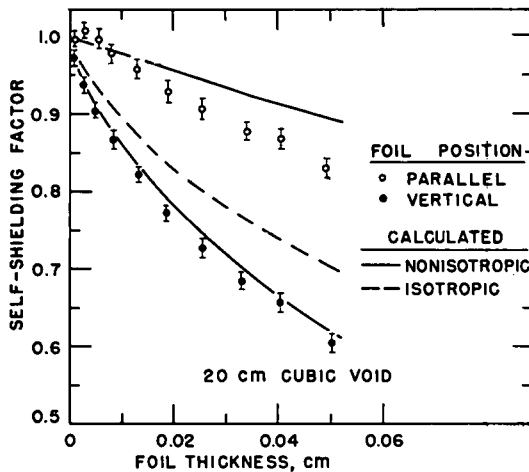


FIG. IV-12-5. Calculated and Measured Self-Shielding for the Cadmium-Lined 20 cm-Void.

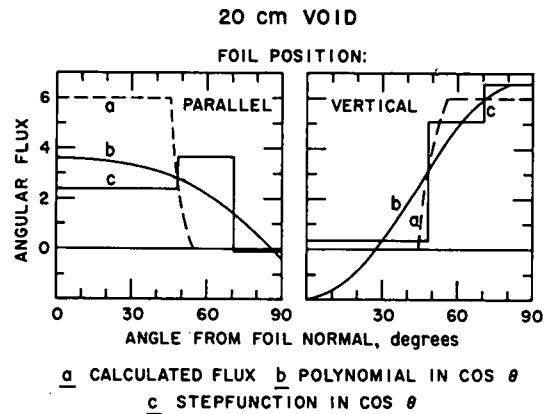


FIG. IV-12-6. Angular Flux Distribution in the Cadmium-Lined 20 cm-Void, as Calculated from the Experimental Geometry (a), and from the Measured Self-Shielding (b) and (c).

orientation is somewhat larger than was expected from the results in a graphite-filled box (Fig. IV-12-1). Only part of this discrepancy can be attributed to inaccurate foil positioning.

The angular distribution (Fig. IV-12-6) was determined in the same way in the case of the 5-cm graphite-filled cube (Fig. IV-12-2). The agreement between measured and calculated angular incidence is rather poor for parallel foil orientation, but surprisingly good for vertical orientation.

It can generally be concluded that the self shielding of foils in geometric configurations such as those studied here, can be predicted with an accuracy of about 1%. However, the reverse process, determining the angular distribution from the self shielding, gives only qualitative results. More detailed information could be gained by increasing the accuracy of the self shielding measurements. The method of activating spheres proved to be a convenient means of obtaining qualitative information about the angular distribution, despite the crude resolution of this technique.

REFERENCES

1. *Reactor Physics Constants*, ANL-5800, 2nd Ed., (1963) p. 669.
2. J. H. Broido and J. H. Ferziger, *A Technique for Measuring the Angular Distribution of Neutron Flux*, *Trans. Am. Nucl. Soc.* 5, No. 2, 385 (1962).
3. F. H. Helm, *Measurement of the Angular Distribution of Thermal Neutrons*, *Trans. Am. Nucl. Soc.* 6, No. 2, 237 (1963).

IV-13. A Study of the Applicability of Simple Reactor Kinetics to the Interpretation of Reactor Noise Experiments

C. E. COHN¹

INTRODUCTION

The results of reactor noise experiments are frequently interpreted in terms of the simple one-energy-group point-reactor kinetics model, even though the assumptions underlying this model are not valid for most reactors. However, a previous study² has shown that the predictions of an elementary reflected reactor model are identical with those of the simple model in situations of experimental interest. In this paper, that study is extended to other cases.

For each case, we calculate for each region or group the source transfer function. This is closely related to the reactivity transfer function (since a small reactivity change can be approximately considered as giving rise to a source of neutrons) and its square modulus carries the frequency dependence of the reactor noise spectrum.

TWO-GROUP POINT-REACTOR MODEL

The first case is a two-group point-reactor model where neutrons in either group can cause fission, and fission neutrons can be produced in each group. The criticality condition here is

$$k_1 Q_1 + k_2 Q_2 + k_2 P_{12} Q_1 = 1,$$

where k_1 and k_2 are the number of fission neutrons produced in each group per neutron lost, Q_1 and Q_2

$$\underline{N}_1 = \frac{S_1 \ell_1 [1 - k_2 G + j\omega \ell_2] + S_2 \ell_1 k_{21}}{(k_1 + k_2 - 2k_1 k_2) \left[\left(1 + \frac{j\omega (\ell_2 k_1 + \ell_1 k_2) + k_1 k_2 F}{k_1 + k_2 - 2k_1 k_2} \right) F + j\omega \ell^* \right] - \omega^2 \ell_1 \ell_2},$$

are the fractions of fission neutrons produced in each group ($Q_1 + Q_2 = 1$) and P_{12} is the probability that a neutron lost from group 1 will reappear in group 2. The $1/v$ lifetime is

$$\ell^* = \ell_1 (1 - k_2 Q_2) + \ell_2 (1 - k_1 Q_1),$$

where ℓ_1 and ℓ_2 are the lifetimes in groups 1 and 2. The source transfer functions are

$$\underline{N}_1 = \frac{S_1 \ell_1 [1 - k_2 Q_2 G + j\omega \ell_2] + S_2 \ell_1 k_2 Q_1 G}{D},$$

$$\underline{N}_2 = \frac{S_1 \ell_2 [k_1 Q_2 G + P_{12}] + S_2 \ell_2 [1 - k_1 Q_1 G + j\omega \ell_1]}{D},$$

where

$$D = [1 + j\omega (\ell_1 + \ell_2 - \ell^*)] F + j\omega \ell^* + \omega^2 \ell_1 \ell_2,$$

and

$$F = \sum_i \frac{j\omega \beta_i}{j\omega + \lambda_i}, \quad G = 1 - F.$$

Here \underline{N}_1 and \underline{N}_2 are the amplitudes of the sinusoidal components with frequency ω of the fluxes in groups 1 and 2, and \underline{S}_1 and \underline{S}_2 are the amplitudes of the fluctuating sources.

TWO-REGION ONE-GROUP MODEL

The second case involves a two-region reactor, and differs from the reflected-reactor model of Ref. 2 in that fission may occur in both regions. This is similar to the coupled-reactor model considered by R. Avery.³ The criticality condition is

$$(1 - k_1)(1 - k_2) = k_{12} k_{21},$$

where k_1 and k_2 are the number of fission neutrons produced in each region per neutron absorbed, and k_{12} and k_{21} are probabilities that a neutron lost from one region (denoted by the first subscript) will reappear on the other. The $1/v$ lifetime is

$$\ell^* = \frac{\ell_1 (1 - k_2) + \ell_2 (1 - k_1)}{k_1 + k_2 - 2k_1 k_2},$$

where ℓ_1 and ℓ_2 are the neutron lifetimes in the two regions. The source transfer function for region 1 is then

while the function for region 2 may be obtained merely by interchanging subscripts.

This model was tested on some noise data from the fast-thermal coupled critical experiment⁴ which was done on ZPR-III. This same data had also been tested with the reflected-reactor model of Ref. 2, and the results of the two were compared. The two-region model gives $\ell^* = 14.82 \mu\text{sec}$. This is to be compared with values of $12.7 \mu\text{sec}$ obtained from a $1/v$ calculation, $12.3 \mu\text{sec}$ from a uniform poisoning experiment, and $12.74 \mu\text{sec}$ calculated using the reflected-reactor model.

Figure IV-13-1 shows a plot of the noise data, together with the square modulus of the calculated transfer function. The transfer function calculated from the reflected-reactor model is also plotted on the figure.

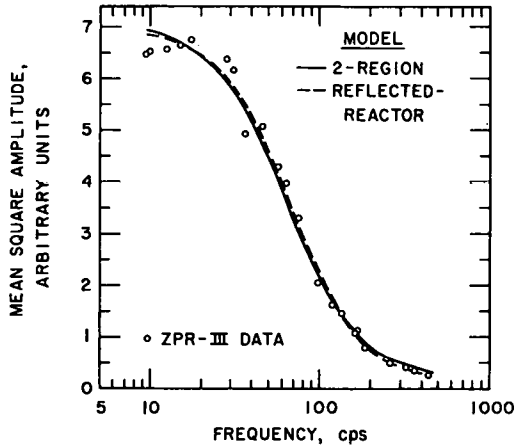


FIG. IV-13-1. Noise Spectrum for ZPR-III Coupled Critical Experiment.

It is apparent that the two calculated transfer functions are very similar, and each is a reasonable fit to the data. However, since the reflected-reactor model seems to give a better accounting of the prompt lifetime, it appears to be better suited to describe this system. (A comparison between the simple model and

$$\ell^* = \frac{\ell_1(k_2 + k_{32}k_{23} - 1) + \ell_2(k_1 + k_{31}k_{13} - 1) + \ell_3(1 - k_1)(1 - k_2)}{k_1(k_2 + k_{32}k_{23} - 1) + k_2(k_1 + k_{31}k_{13} - 1)}$$

the reflected-reactor model for this system was shown in Ref. 2.)

THREE-REGION ONE-GROUP MODEL

The third case is a variation of the one above, in which a third nonmultiplying region is interposed between the two multiplying regions. Neutrons may pass between the third region and either of the two multiplying regions in either direction, but neutrons may not pass between the multiplying regions directly. This model is applicable to the two-slab loading of an Argonaut type reactor. Such a configuration has in the past been described^{5,6,7,8} by a two-region model in which the effect of the intermediate region was represented by a time delay in the passage of neutrons between the two multiplying regions. When calculating a $1/v$ lifetime using this model, the intermediate region would give no contribution. This is not physically reasonable since the intermediate region would certainly be affected by a uniform poisoning. Therefore, the model presented here was developed in order to explore the significance of the $1/v$ lifetime. Note that this model provides no time delay between the multi-

$$D = k(1 - k_1) \left[\left(1 + \frac{j\omega[2\ell_1k_1 + 2\ell_3k_1(k_1 - 1)] - 2\omega^2\ell_1\ell_3k_1 + 2k_1^2(1 - j\omega\ell_3)F}{k_1(1 - k_1)} \right) F + j\omega\ell^* \right]$$

$$+ \omega^2[\ell_1^2 + 2\ell_1\ell_3(1 - k_1)] + j\omega^3\ell_1^2\ell_3.$$

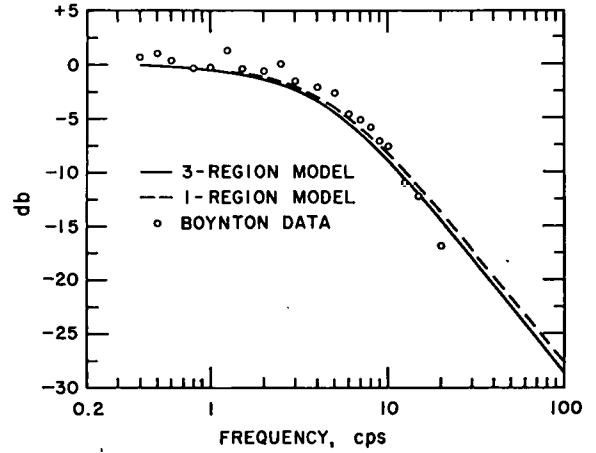


FIG. IV-13-2. Noise Spectrum in UFTR.

plying regions except for that afforded by the finite neutron lifetime in the intermediate region.

Here, the criticality condition is

$$(1 - k_1)(1 - k_2) = k_{23}k_{32}(1 - k_1) + k_{13}k_{31}(1 - k_2),$$

and the $1/v$ lifetime is

Most Argonaut reactor configurations which have been studied are symmetrical, i.e., the two multiplying regions are identical. In such cases the formulas can be somewhat simplified. Here

$$k_2 = k_1, \quad k_{23} = k_{13}, \quad k_{32} = k_{31}, \quad \text{and} \quad \ell_2 = \ell_1.$$

The above equations then become

$$1 - k_1 = 2k_{13}k_{31},$$

$$\ell^* = \frac{\ell_1}{k_1} + \frac{\ell_3(1 - k_1)}{k_1},$$

and the source transfer functions in regions 1 and 3 are

$$\underline{N}_1 = \frac{\underline{S}_1\ell_1H(1 + j\omega\ell_3) + \underline{S}_2\ell_1k_{31}k_{13} + \underline{S}_3\ell_1k_{31}H}{D},$$

$$\underline{N}_3 = \frac{(\underline{S}_1 + \underline{S}_2)\ell_3k_{13}H + \underline{S}_3\ell_3H^2}{D},$$

where

$$H = 1 - k_1G + j\omega\ell_1,$$

and

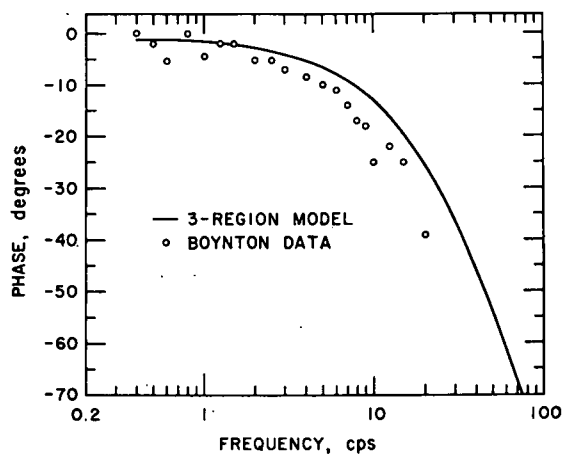


FIG. IV-13-3. Cross-Power Spectrum Between Fueled Regions in UFTR.

The transfer function for region 2 may be obtained from that for region 1 by interchanging subscripts 1 and 2.

This model follows the general pattern of behavior of the previous two cases. However, if k_1 or k_2 become close to unity, the denominators of the transfer functions as well as the numerators will deviate from the simple model at frequencies small compared to the reciprocals of the lifetimes.

The model was tested on some results obtained by A. Boynton⁸ at the University of Florida Training Reactor (UFTR).*

The aforementioned data comprises power and cross-power spectra of the neutron level fluctuations in the two multiplying regions resulting from a white-noise reactivity signal in one of them. Figure IV-13-2 shows the power spectrum of the fluctuations in the excited region, while Fig. IV-13-3 shows calculated and meas-

* The data designated as "Run CC" were used here.

ured values for the phase of the cross-power spectrum. The slight difference between the calculated curve for the one-region and three-region models in Fig. IV-13-2 shows that a slight systematic error is made when the one-region model is used to determine ℓ^* from a transfer function measurement. The agreement between observation and theory in Figs. IV-13-2 and IV-13-3 is considered adequate in view of the arbitrary nature of the parameters used in deriving the theoretical results.

REFERENCES

1. C. E. Cohn, *A Study of the Applicability of Simple Reactor Kinetics to the Interpretation of Reactor Noise Experiments*, Symposium on Noise Analysis in Nuclear Systems, Univ. of Florida, Gainesville, November 4-6, 1963 (Proceedings to be published).
2. C. E. Cohn, *Reflected-Reactor Kinetics*, Nucl. Sci. Eng., **13**, No. 1, 12 (May 1962).
3. R. Avery, *Theory of Coupled Reactors*, Proc. 1958 Geneva Conf., **12**, Paper No. 1858, p. 182.
4. R. Avery, C. Branyan, G. Brunson, C. Cohn, G. Fischer, H. Hummel, W. Kato, F. Kirn, D. Meneghetti, F. Thalgott and B. Toppel, *Coupled Fast-Thermal Power Breeder Critical Experiments*, Proc. 1958 Geneva Conf., **12**, Paper No. 2160, p. 151.
5. G. C. Baldwin, *Kinetics of a Reactor Composed of Two Loosely Coupled Cores*, Nucl. Sci. Eng. **6**, No. 4, 320 (October, 1959).
6. R. A. Danofsky and R. E. Uhrig, *The Kinetic Behavior of the Coupled Regions of the UTR-10 Reactor*, Nucl. Sci. Eng. **16**, No. 2, 131 (June, 1963).
7. R. W. Badgley and R. E. Uhrig, *Power Spectral Density Measurements in a Subcritical Nuclear Reactor*, Nucl. Sci. Eng. **19**, No. 2, 158 (June, 1964).
8. A. R. Boynton, *Evaluation of Parameters in a Two Slab Reactor by Random Noise Measurements*, Ph.D. Thesis, Univ. of Florida, Gainesville, (1962). A. R. Boynton and R. E. Uhrig, *Evaluation of Two Region Reactor Parameters by Random Noise Measurements*, Nucl. Sci. Eng., **18**, No. 2, 220 (February, 1964).

IV-14. Errors in Noise Measurements Due to the Finite Amplitude Range of the Measuring Instrument¹

C. E. COHN

One of the features of Gaussian random noise is the nonzero probability of observing amplitudes which exceed any finite bound. However, no measuring instrument can handle an infinite amplitude, but all instruments have a finite amplitude range beyond which they do not respond. Since the portions of the

noise having amplitudes above this range are lost, all measurements of average amplitude are too low.

The data presented in this paper are intended to assist in correcting experimental results for clipping errors. Detection of noise in the presence of saturation has been considered previously,² but results

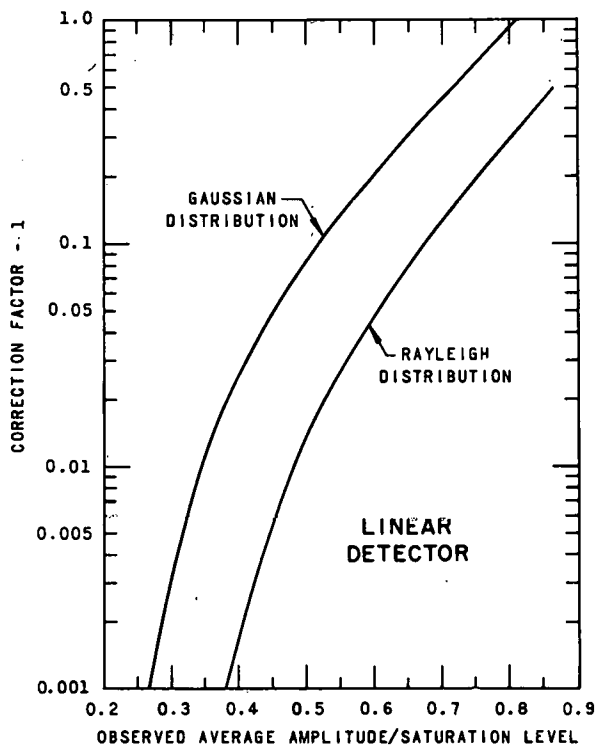


FIG. IV-14-1. Correction Factors for the Linear Detector.

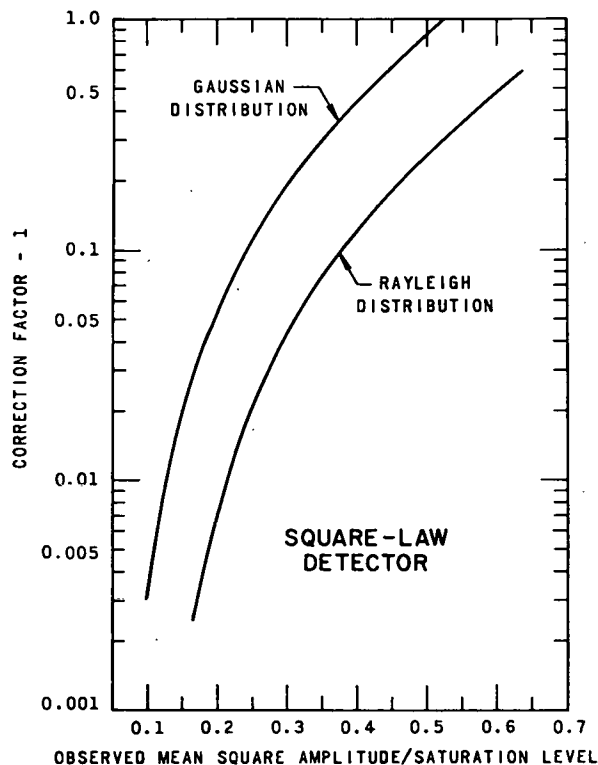


FIG. IV-14-2. Correction Factors for the Square-Law Detector.

have not been presented in a form convenient for the present purpose. The treatment here assumes that the instrument behaves ideally for all amplitudes below a saturation level and that the output remains at this level for all greater amplitudes.

Four cases are considered here. Two of these involve Gaussian noise with a linear rectifier and a square-law detector, while the other two assume the Rayleigh distribution with the same detector types. The latter two cases apply to envelope detection of narrow-band noise where the clipping element follows the detector.

Note that this treatment assumes that the frequency response of the instrument is flat between the clipping element and the detector. Cases where this does not hold would require a much more complicated treatment.^{2,3}

Case 1. Linear Rectifier, Gaussian Distribution

The correction factors for this case are shown in Fig. IV-14-1. The abscissa is the ratio of the observed average amplitude to the saturation level. The ordinate is the correction factor by which the observed average amplitude is to be multiplied.

Case 2. Square-Law Detector, Gaussian Distribution

The correlation factors for this case are shown in Fig. IV-14-2. The abscissa is the ratio of the observed

average square amplitude to the output saturation level, and the ordinate is the correction factor.

Case 3. Linear Detector, Rayleigh Distribution

The correction factors for this case are also shown in Fig. IV-14-1.

Case 4. Square-Law Detector, Rayleigh Distribution

The correction factors for this case are also shown in Fig. IV-14-2.

These calculations show that saturation effects are significant even for saturation levels several times the average amplitude. Also, it is easily seen that the linear detector is less affected by this error than is the square-law detector.

REFERENCES

1. C. E. Cohn, *Errors In Noise Measurements Due to the Finite Amplitude Range of the Measuring Instrument*, Rev. Sci. Instr. **35**, No. 6, 701-703 (June, 1964).
2. D. Middleton, *The Response of Biased, Saturated Linear and Quadratic Rectifiers to Random Noise*, J. Appl. Phys. **17**, No. 10, 778 (October, 1946).
3. J. H. Laning, Jr. and R. H. Battin, *Random Processes in Automatic Control*, (McGraw-Hill Book Company, Inc., New York, 1956), pp. 164, 167-171, 361-365.

IV-15. Improvements in Particle and Radiation Detection

A. DEVOLPI and K. PORGES

There are three classes of instrument development currently receiving attention: (1) equipment associated with a high precision coincidence counting facility; (2) improvements in background, noise, and resolution response of existing detectors; and (3) special monitors for reactor-oriented experiments.

The coincidence counting facility^{1,2} provides the capability of accurate counting of a variety of radioisotopes, chiefly by beta-gamma coincidence (Figs. IV-15-1, IV-15-2, and IV-15-3) with 4π liquid scintillation detection. Mn-56 can be detected with about 40% efficiency by Cherenkov radiation. By substituting a recessed plastic scintillator for the liquid, a 5-mil manganese foil has been monitored with 73% effectiveness. About 98% of all decays from Mn⁵⁶SO₄ may be registered when small aliquots are dissolved in a water-alcohol-dioxane scintillating mixture. The beta channel, which has a total background rate of less than 1 count/sec, is operated at room temperature with a 100-nsec gate time. A tunnel diode discriminator fires directly without any additional amplification on anode pulses. Phototubes were selected for high gain and low noise.

An interesting extension has been found in the direct counting of rather large samples (about 7 g) of Na-23 as NaNO₃ in H₂O by Cherenkov light in beta-gamma coincidence. The Na-23 (n, γ) reaction is a useful measure of neutrons existing in a fast spectrum reactor at about 3 keV. In this case because of flux, cross section, material perturbations, and background considerations, other methods of assay would be marginal.

Resolution and counting efficiency obtainable in a given spectrometer is often limited by noise and background, as well as by inherent instabilities of the detector and electronic chain, aside from the statistics associated with each pulse. In the case of the "Hornyak button",³ for example, a circuit has been developed which removed noise and gamma background pulses while passing characteristic ZnS(Ag) scintillations with risetimes of about 2.5 nsec³ (See paper No: IV-23). Investigations extended into various transparent media associated with scintillation detectors reveal that much can be done to eliminate the effect of extraneous pulses. There are many interactions from background radiation which result in scintillation or Cherenkov light derived from light pipes, the phototube face, and other clear materials. Three events lead to very narrow fast decaying pulses, akin to noise pulse shapes, which are readily distinguishable from acti-

vated scintillator decays. In addition, there is a wide range of efficiency of light output. Paraffin, an epoxy sample, and polyethylene demonstrated rather large peak amplitudes, while glass, quartz, and lucite exhibited somewhat smaller conversion efficiencies. These results were obtained with a 70-keV electron beam. It was also found that the range of decay times varied widely from epoxy (2.5 nsec) to paraffin (24 nsec). At the same time 3.5 nsec risetimes were observed in ZnS(Ag) when small integrating time constants were used. An attempt was made to use various filters to optimize the ratio of light obtained from ZnS(Ag) versus other transparent media, but no enhancement resulted.

Experiments undertaken in the vicinity of nuclear reactors, particularly those involving beams extracted from the core, require special attention to details of background rejection, stability, and response. Not only is the above-mentioned Hornyak button work related to this problem area, but other developments in the use of fission chambers and attendant coincidence circuitry are applicable. Construction of thinly coated ionization fission fragment counters with fast risetimes

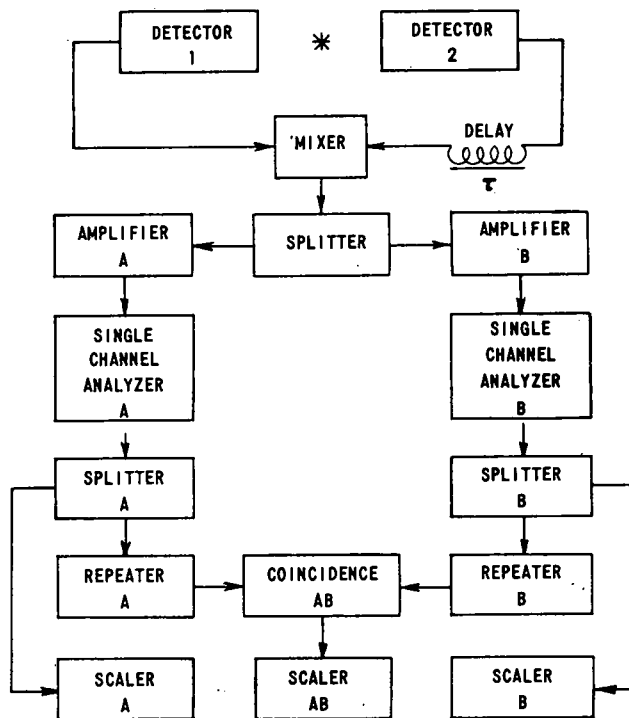


FIG. IV-15-1. Delay-mixing-splitting Technique Using Two Amplifiers.

$\gamma\gamma$ AND $\beta\gamma$ SIGNAL CIRCUITS

RG	Z_0
—	58
□	71
■	114
▨	176
	Z_0
	50 Ω
	93 Ω
	185 Ω
	2200 Ω

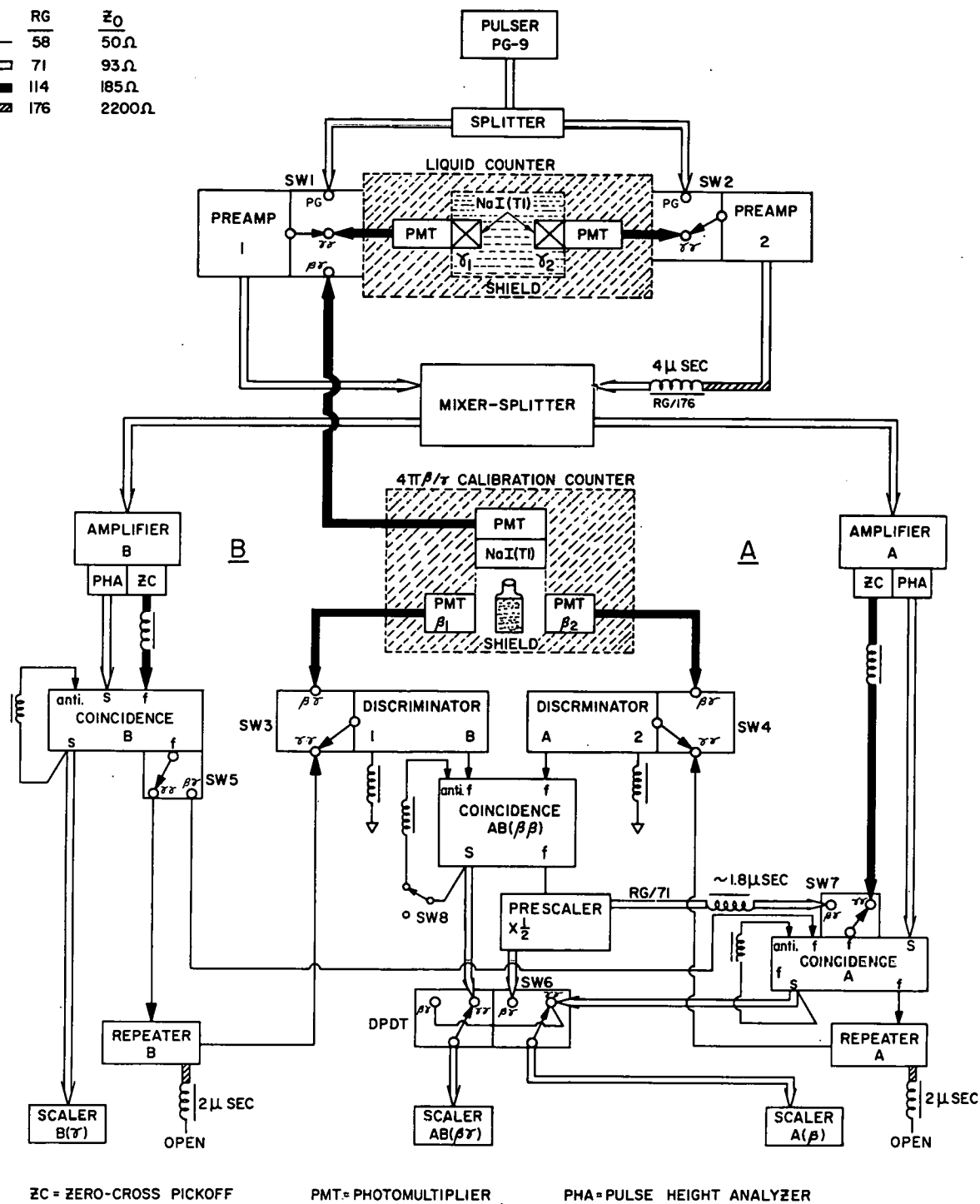
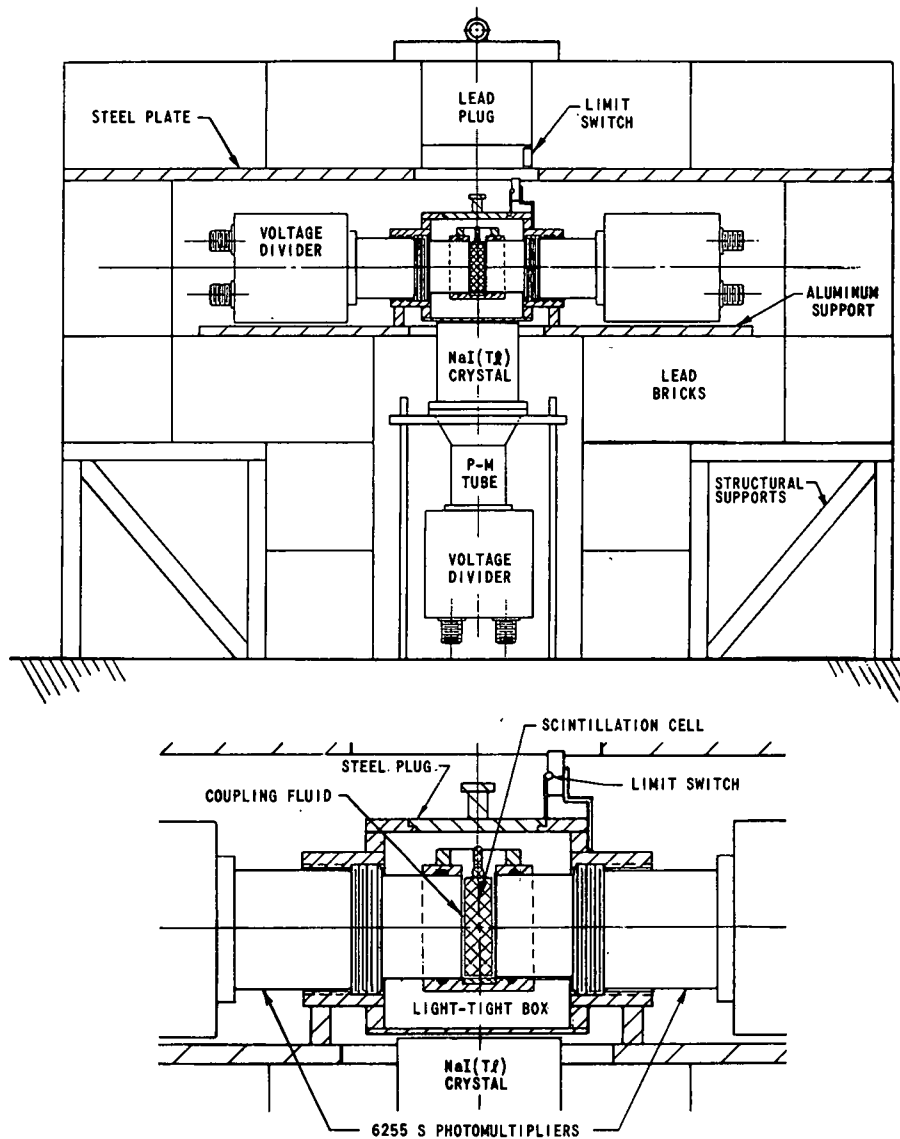


FIG. IV-15-2. Complete Signal-processing Network for $\gamma\gamma$ and $\beta\gamma$ Coincidence Counting.

FIG. IV-15-3. $\beta\gamma$ Coincidence Arrangement.

has been achieved. Pulse rates of 25,000 counts/sec were counted at efficiencies approaching 100% when combined with fast amplifiers, discriminators, and scalars. By using a neutron-fission coincidence, the fission rates could be evaluated to a high precision. A fast system for counting Cf-252 spontaneous fission has also been prepared.

The recent availability of a fast feedback-stabilized current amplifier⁴ has opened the domain of ionization counters operating with fast rise and collection times. Some fission fragment ionization counters, designed for fast electron collection, have been operated with computed RC risetimes of 100 psec. Natural pulse widths are 10–20 nsec. Signal amplitudes are

enough above noise to permit operation on a plateau in integral bias. No pre- or post-amplification is required to bring the lowest energy fragments from Cf-252 into the 100-mV range of the tunnel diode discriminator used in testing. By impedance matching at the amplifier input, very long lengths of coaxial cable may be interposed between the detector and the amplifier, suffering only the characteristic frequency-dependent attenuation of the cable.

A typical pulse profile obtained is presented in Fig. IV-15-4. Observe that the pulse width is a little over 20 nsec and the risetime around 3 nsec. The width is consistent with a drift velocity for electrons approaching 10^7 cm/sec. Since, at present, the amplifier limits

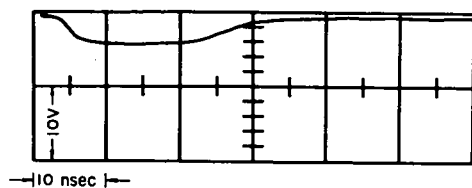


FIG. IV-15-4. Methane Flow Ionization Counter: Cf²⁵² Fission Fragment.

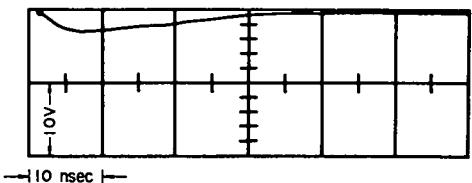


FIG. IV-15-5. Pulse After 39 ft of RG/58 Methane Flow Ionization Counter: Cf²⁵² Fission Fragment.

upper frequency response, much larger counter capacities may be tolerated while still maintaining fast risetimes.

Figure IV-15-5 demonstrates the effect of inserting a 39 Ω series resistor to obtain an input impedance of 50 Ω and then coupling the counter to the amplifier with almost 40 ft of RG/50 cable. Since this coaxial cable does not have especially good transmission bandwidth, some degradation of risetime is noticeable.

An examination of a boron-lined gas-filled cylindrical counter with 1-mil anode wire, operating in the proportional region, disclosed similar sharply rising current pulses of short duration. However, in view of

the time lag involved between the initiation of the nuclear ionization track and the commencement of the multiplication process in the proximity of the central wire, one must be cautious in fast timing applications.

These investigations demonstrate that a rather simple detection system can provide extensive benefits when operating in the vicinity of high radiation sources, when very rapid time references are required, and when high counting rates must be handled. Only a low voltage ionization counter and a coaxial cable, items rather immune to radiation damage, need be inserted into a nuclear reactor vessel or in the proximity of an accelerator beam. The single active electronic amplifier may be at some distance, readily accessible for maintenance. Since this current amplifier has a large ac and dc feedback ratio (about 20 dB), relatively stable operation may be expected. The high count rate capabilities follow from the natural pulse widths which may, within the available parameters, be adjusted for small deadtimes.

REFERENCES

1. A. De Volpi, K. G. Porges and R. N. Larsen, *Mn-56 Coincidence Counting Facility*, ANL-6760 (1963).
2. K. G. Porges, A. De Volpi and R. N. Larsen, *Electronic Design of an Absolute Counting System for Mn-56*, Nucl. Instr. Methods (to be published).
3. W. F. Hornyak, *A Fast Neutron Detector*, Rev. Sci. Instr. **23**, 264 (1952).
4. A. De Volpi, K. G. Porges and C. Rush, *Subnanosecond RC Risetimes from Ionization Counters*, Bull. Am. Phys. Soc. **9**, 46 (1964).

IV-16. Automated Data Acquisition and Processing with An On-Line Computer

J. F. WHALEN, J. W. MEADOWS, A. B. SMITH and W. F. MILLER*

The staff of the Applied Nuclear Physics section was among the first to realize the potential of and to apply the small digital computer to data acquisition in the nuclear laboratory. Several years of experience have clearly shown that such devices can, when properly applied, greatly improve the experimental productivity. This has been true in the diverse range of experimental activities that are encountered in the nuclear data studies that characterize this group's activities. In addition to the on-line data acquisition and processing, a degree of fully automated operation has been achieved. This operation is in the sense of industrial process

control and includes the use of the computing systems to acquire, process, and interpret the incoming experimental information; to execute the executive decisions made, as programmed, by the computer; and to control the nuclear accelerator by the computer. Thus the laboratory operations are a closed loop. The justification for this automation is twofold: improved quality of information and appreciable economy resulting from improved utilization of manpower and equipment. The success of the computer control concept has been such as to urgently warrant its extension to as much of the experimental program as possible.

The principles underlying the above computer utilization and the detailed technical design have been de-

* Applied Mathematics Division.

scribed in a number of professional journals and conferences. Representative examples include the following:

*On-Line Operation of a Digital Computer in Nuclear Physics Experiments*¹

The instrumentation necessary for coupling a commercial digital computer to several nuclear physics experiments in an "on-line" operation has been designed and constructed. Multiparameter experiments utilizing the "on-line" operation include fission fragment mass ratio measurements, neutron time-of-flight measurements and the measurement of prompt $\bar{\nu}$ for fissionable materials.

*Extensive Experience with an On-Line Computer in a Nuclear Laboratory*²

A multiparameter system for the storage and analysis of data in a low energy nuclear laboratory was constructed. Digital arithmetic functions, storage, and control are exercised by a CDC-160A computer. The logic and the design of this apparatus (including input-output devices) is described. Examples of on-line fission and fast neutron experiments taken from eighteen months of successful operation are given.

*A Computer Controlled Display System for Nuclear Experiments*³

The basic characteristics and requirements for a nuclear display system are presented covering the topics of versatility, storage requirements, and the proper balance between fixed wired controls and computer programmed controls. An existing computer-controlled displayed system is described showing modes of display and calibration techniques. A new display system being designed is also discussed. This system incorporates a small buffer magnetic drum memory for display data storage which can be used as an auxiliary memory for the computer since it has

random access for both the read and write modes. A method of identifying for the computer particular data points or areas of interest is also available.

*On-Line Data Acquisition and Feedback to Accelerator Control—A Status Report*⁴

The principles underlying the utilization of an on-line computer system for data acquisition, processing, and analysis, and for accelerator control in a nuclear data laboratory are delineated. The system components and their correlation including nucleonic apparatus, the digital computer, and the nuclear accelerator (pulsed Van de Graaff) are described. Particular attention is given to the relation of the digital system to the analog operation of the accelerator. Experience with the data acquisition and processing portions of the system, and, to a lesser extent, with the accelerator control is described. Specific examples dealing with: a) fast neutron time-of-flight, and b) total neutron cross sections using pulsed and steady beams are given. Final remarks deal with the simultaneous utilization of the digital system from two geographically isolated accelerator laboratories and with the digitalization of the basic accelerator operation.

REFERENCES

1. J. F. Whalen, J. W. Meadows and R. N. Larsen, *On-Line Operation of a Digital Computer in Nuclear Physics Experiments*, Rev. Sci. Instr. **35**, No. 6, 682 (1964).
2. J. W. Meadows, J. F. Whalen and A. B. Smith, *Extensive Experience with an On-Line Computer in a Nuclear Laboratory*, EANDC Conf. Automatic Acquisition and Reduction of Nuclear Data, Karlsruhe, July 13-16, 1964.
3. J. F. Whalen, *A Computer Controlled Display System for Nuclear Experiments*, EANDC Conf. Automatic Acquisition and Reduction of Nuclear Data, Karlsruhe, July 13-16, 1964.
4. W. F. Miller, J. W. Meadows, J. F. Whalen and A. B. Smith, *On-Line Data Acquisition and Feedback to Accelerator Control—A Status Report*, EANDC Conf. Automatic Acquisition and Reduction of Nuclear Data, Karlsruhe, July 13-16, 1964.

IV-17. Development of Solid State Fission Counters

G. W. MAIN

During the past year a series of small solid state fission counters have been developed for use in the ZPR-VI and ZPR-IX reactors. Their development was due to the desire for an absolute fission counter which was small enough that it would cause no significant perturbation of reactor flux. A solid state counter

seemed well suited for this job because its size and shape could be varied to adapt to almost any desired geometry. Other characteristics of these counters, such as charge collection times of the order of a few nsec and a much larger output pulse for a given incident particle energy than conventional gas-type

counters, were also desirable features. In addition, this type of fission counter was mechanically simple to construct, and it was expected to be trouble-free in use. A major shortcoming of this type of counter is its susceptibility to radiation damage. The first signs of radiation

damage to the silicon detector is a broadening of the energy-distribution curve for the particles. When the detectors are new, there is a large separation between the activity from the alphas and the fission fragments. As long as it is possible to discriminate between the

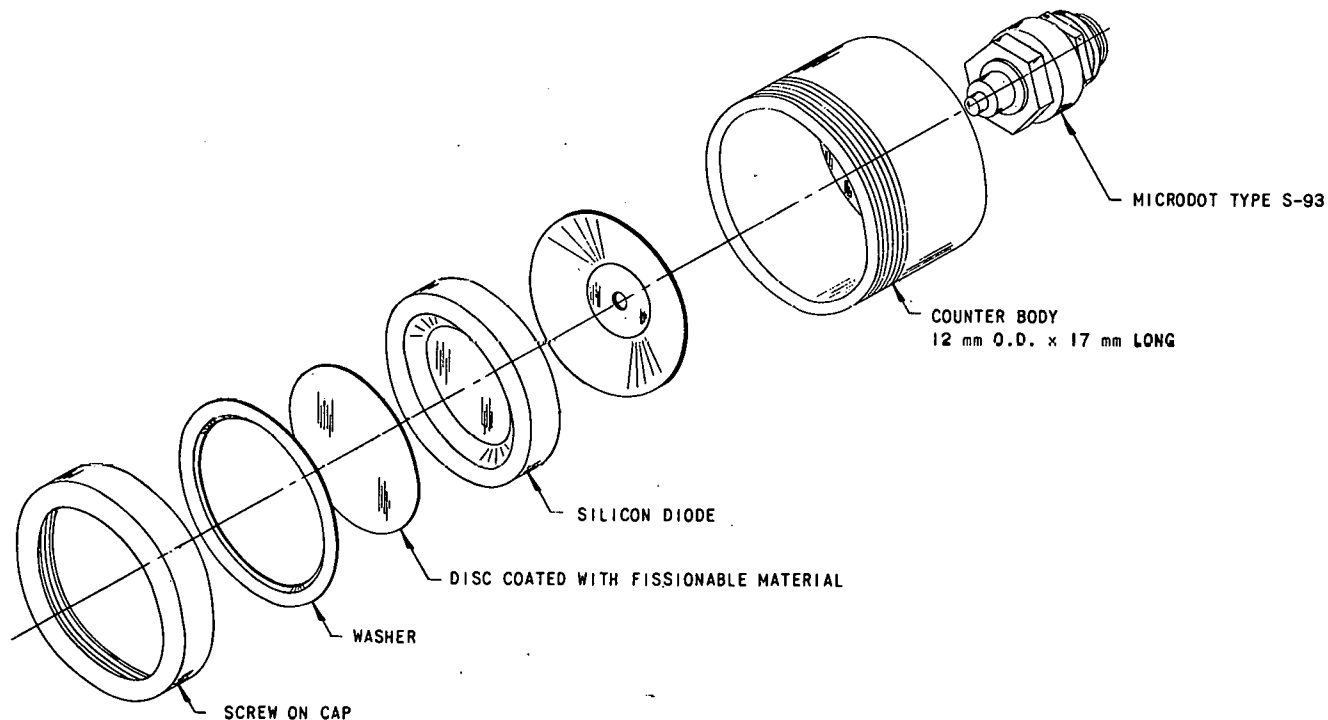


FIG. IV-17-1. Solid State Fission Detector A.

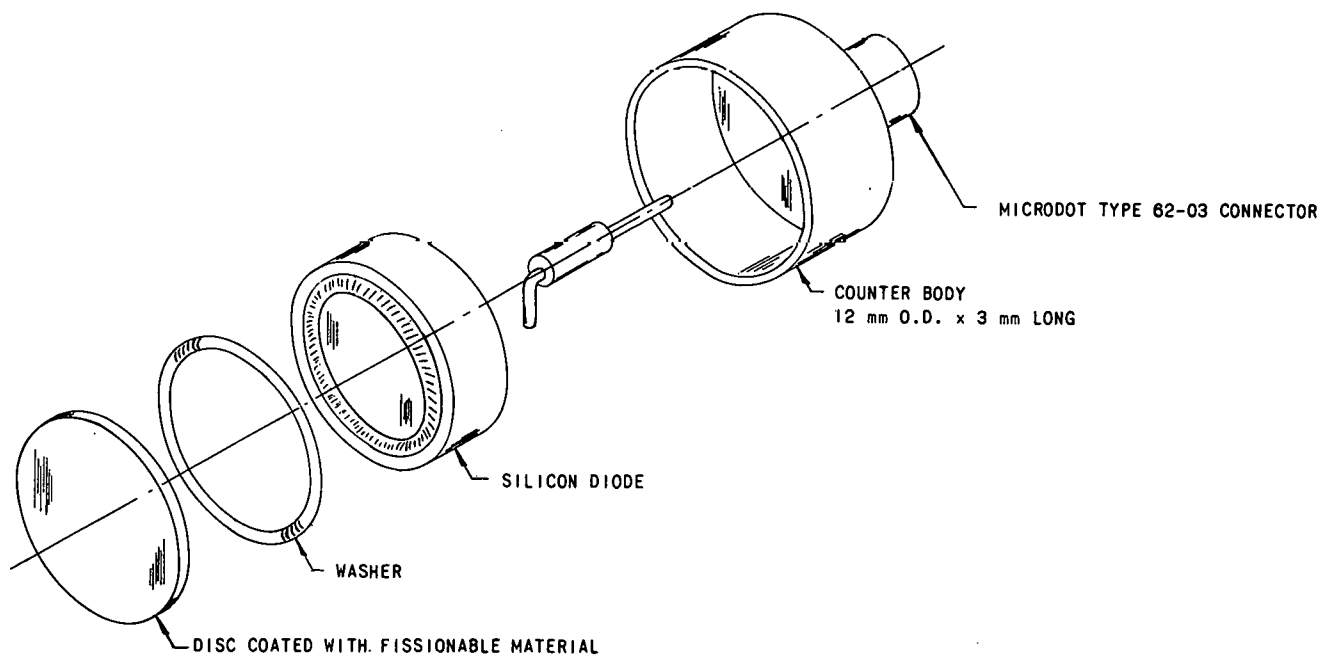


FIG. IV-17-2. Solid State Fission Detector B.

alphas and the fission fragments, the detector is usable for our purposes, even though the resolution is quite poor.

Surface-barrier type silicon detectors were used in the construction of all the counters. This type of detector is relatively simple to construct and is somewhat cheaper than the diffused junction type. The surface-barrier type is adequate for this application since high resolution is not required.

Early models of silicon detectors were made at ANL and the counters made from these detectors performed well. The first units were cylinders 11.5 mm in diameter and 2.5 mm long, (see Fig. IV-17-1). The sensitive area was approx 75 mm², although this varied somewhat for various counters. A thin stainless steel disc on which was deposited a thin layer (<150 µg/cm²) of uranium or other fissionable material was placed against the sensitive area. The sandwich was then sealed into a thin-walled aluminum case 12 mm in diameter and 3 mm long, which had a cable connector built into one end. The detectors built in this fashion operated well and no problems were encountered in their use.

A second set of counters was made (see Fig. IV-17-2) using commercially available silicon detectors. These counters were designed so that only the detector was sealed inside the case, while the disc containing the fissionable material was held in place by a screw-on

cap. This permitted removal of the disc when the counter was not in use, thus preventing radiation damage to the detector from some of the highly radioactive isotopes which were used. In addition, this approach reduced the number of detectors which were required. The modified counters were also 12 mm in diameter, but were about 70 mm long due to the use of a different type of cable connector.

The discs containing the fissionable material were all made in the same manner. The material was electroplated onto an area of the disc, the area being somewhat smaller than the sensitive area of the detector. After plating, the disc was alpha counted to determine the amount of material deposited. If the activity was very high, the residual plating solution was counted. Plating efficiencies were normally of the order of 95%–98%. Nine different isotopes were used in the counters, (U-233, U-234, U-235, U-236, U-238, Np-237, Pu-239, Pu-240, and Am-241), and the same plating procedure was used for each isotope.

These counters have been used extensively in the ZPR-VI and ZPR-IX facilities for making fission ratio measurements. The results obtained are consistent with those from radiochemical measurements as well as with the larger gas flow counters. There has been no indication of significant amounts of radiation damage to the silicon detectors to the present time.

IV-18. Preparation of Source and Source Mount for Beta Counting on a 4π Proportional Counter

D. M. SMITH

Assuming that the electronics of a 4π proportional counter are in good order, the main difficulty encountered in 4π beta counting is caused by absorption. Absorption in the source mount is small for all but the softest beta emitters,^{1,2} if thin source mounts are used. Self-absorption is the principal uncertainty in 4π counting. For accurate determination of the activity of a beta emitter it is desirable to minimize absorption. A method for preparation of extremely thin samples and supports, to minimize absorption and thus improve the accuracy of 4π counting, is described here.

The 4π proportional counter in use is spherical, with an inside diameter of 7.2 cm. A central plane is occupied by the sample holder, which is a disc of 7.2-cm diameter with a 3.8-cm hole in the middle. Across the hole is stretched a thin membrane rendered con-

ductive by a thin coating of gold, in the center of which the sample to be counted is deposited.

To minimize source mount absorption the thinnest films possible must be used. Aluminum foil has been used but it is very brittle at low superficial densities and also it is not very resistant to acids which may be present in the sample. Synthetic resins have been used for films, the best appearing to be a polyvinyl-chloride-acetate copolymer, VYNS, described by B. Pate and L. Yaffe.³ Such films with superficial densities as low or lower than one microgram per square centimeter can be made, although films of superficial density of 5–10 µg/cm² exhibit less fragility. These films exhibit excellent tensile strength and excellent chemical resistance to acids and alkalis in all concentrations.

VYNS is a finely ground, white powder. The most

convenient solvent has been found to be cyclohexanone, requiring about two volumes of solvent to one volume of resin for complete dissolution. The first addition of solvent to the resin produces a gel, which dissolves in several days with the further addition of solvent. This saturated solution forms a convenient stock solution which may be diluted before use with about two parts solvent to one part stock solution to give a workable solution. The correct consistency of the solution is important for good films and can be determined by the trial and error method of making films. Roughly, the consistency is similar to that of a thin oil.

To make the film, a drop of the solution is allowed to flow onto the surface of a pan of distilled water by placing the drop of solution on the side of the pan just above the level of the water. The solution will flow out over the surface of the water and form a film large enough for several 4π plates. The films can be placed on aluminum discs by gently dropping the discs onto the surface of the film while it is in the water and then by carefully sliding the discs from the water. With good technique, several dozen 4π plates per hour can be obtained by this method. The superficial densities of the films can be estimated by the refraction colors, which are listed in Table IV-18-I.³

It has been observed that after several films have been made in a fresh pan of water, the films tend to become thicker. Apparently, this is caused by the water becoming contaminated by solvent. This can be prevented by frequently changing the water or by "cleaning" the surface of the water by drawing a paper towel across the surface.

To render the films conductive, the discs with their adhering films are placed in a vacuum plating unit where gold is distilled onto both sides of the films. In general, the slower the evaporation rate, the more uniform the film. The progress of distillation of the gold may be followed visually by observing the color of the film by reflected light. If the VYNS film is initially

uncolored (about $10 \mu\text{g}/\text{cm}^2$), the color intensity will change to a faint purple at $\sim 1 \mu\text{g}/\text{cm}^2$ of gold. The distillation rate of the gold may also be followed by measuring the resistance across an insulator placed in the vacuum plating unit near the films being coated. A resistance of $10 \text{ M}\Omega$ indicates about $10 \mu\text{g}/\text{cm}^2$ of gold. Five to ten $\mu\text{g}/\text{cm}^2$ of gold on each side of the plates is sufficient for counting.

In minimizing self-absorption in the source itself, sample deposits must be kept to the bare minimum. Specific activities of the samples must be high enough so that deposits of solids are no greater than $5 \mu\text{g}$, preferably less (about $2 \mu\text{g}$) for low-energy beta emitters.

The usual method of depositing an aliquot of a dissolved active sample onto a 4π plate and evaporating it has been found to be inappropriate for low-energy emitters. Relatively large, nonuniform crystals are formed and as a result, efficiencies are low and inconsistent.

If the aliquot is delivered into a small amount of silica sol on a source mount and then evaporated, the efficiencies are found to be higher and much more consistent.⁴ Upon evaporation, the individual silica particles seem to act as crystallizing agents with the result that many relatively small crystals are formed instead of a few large crystals.

The silica sol is a $1:10^4$ aqueous dilution of a colloidal silica solution known as Ludox SM (DuPont). Ten to twenty μl of the diluted solution is optimum for most isotopes and adds only about 0.2 to 0.4 μg of residual silica to the sample.

A 5% insulin solution used as a wetting agent improves the uniformity of the samples, but the resultant heavy addition of solids partially offsets the beneficial properties of the insulin.

REFERENCES

1. H. H. Seliger and A. Schwebel, *Standardization of Beta-Emitting Nuclides*, *Nucleonics* **12**, No. 7, 54-63 (1954).
2. B. D. Pate and L. Yaffe, *Disintegration-Rate Determination by 4π Counting. Part II. Source Mount Absorption Correction*, *Can. J. Chem.* **33**, No. 5, 929-937 (May, 1955).
3. B. D. Pate and L. Yaffe, *A New Material and Techniques for the Fabrication and Measurement of Very Thin Films for Use in 4π -Counting*, *Can. J. Chem.* **33**, No. 1, 15-23 (January, 1955).
4. J. S. Merritt, J. G. V. Taylor and R. J. Campion, *Self-Absorption in Sources Prepared for 4π -Beta Counting*, *Can. J. Chem.* **37**, No. 6, 1109-1114 (June, 1959).

TABLE IV-18-I. SUPERFICIAL DENSITY OF VYNS FILMS

Density of Film, $\mu\text{g}/\text{cm}^2$	Color	Density of Film, $\mu\text{g}/\text{cm}^2$	Color
1	Dark gray	30	Purple
5	Light gray	35	Blue
10	White	40	Yellow
20	Light yellow	45	Red
25	Yellow-brown		

IV-19. 4π Recoil Counter Neutron Spectrometers

E. F. BENNETT

INTRODUCTION

A proportional counter will multiply ionization created by fast charged particles. This multiplication occurs in an avalanche of electrons initiated when electrons from the primary ionization have drifted close to the anode wire under the influence of the applied field. The multiplication process is almost noiseless and this fact, together with the possibility of including radiation sources homogeneously throughout the gas volume, explains the continued interest in these devices. Solid state detectors, by contrast, do not apparently possess a usable linear avalanche mechanism so that ionization equivalent to 10–20 keV or less is not seen above system noise.

Neutrons are detected by interacting with nuclei. For one reason or another the resolution of practical exoergic reaction counters will not usually be less than about 100 keV Full Width-Half Maximum (FWHM). Add to this the hypersensitivity (as $1/\sqrt{E}$) of exoergic charged particle reactions to slow neutrons and one finds that the resulting ionization spectrum does not lend itself at all well to providing neutron spectral information below about 100 keV.

Instead of an exoergic reaction, one may study proton recoils from hydrogen included in the counter filling gas. A problem arises immediately, however, for no longer are pulses large as compared to gamma-ray-induced background. Gamma events are found over almost all of the ionization spectrum where interpretation in terms of neutron spectrum is easiest but this problem may be surmounted by pulse shape discrimination against the gamma-induced events.^{1,2}

The 4π recoil proportional counter with shape discrimination against gamma background lends itself best to measurements below about 1 MeV. The low energy response cannot be extended indefinitely, however, since a proton having energy less than the ionization potential of the gas in which it stops (about 15 eV) will create no ion pair and hence will be undetected, let alone measured (a single ion pair is sufficient to detect an event but a large number are needed to define the energy in a statistically meaningful way). A quantity $W(E)$ represents the average energy loss for fast protons in the gas, per ion pair. Without knowledge of the way W varies with energy, no way exists to relate measured ionization to proton energy. W is known for some gases above 10 keV or so, but adequate data below this energy are lacking.

Another problem encountered is in detector calibration over the range of its use. Proportional counters are not absolute ionization detectors; they must be calibrated relative to a source of known energy and ionization. Once this has been done, the counter will produce pulses proportional to ionization over a range of ionizations generally adequate for spectroscopy. A difficulty arises if it is necessary to change to another range. The best thing would be to have a suitable standard for each multiplication range, but this may be difficult and so an accurate means of predicting changes in gas multiplication with counter voltage is required.

Also there is the problem of space-charge saturation. If one tries to get big pulses, far from noise, by running up the gas multiplication, it could happen that the avalanche saturates, making the induced pulse less than it should be. This kind of nonlinear effect would introduce systematic errors which, at all costs, are to be avoided.

Even with clean, undistorted proton recoil spectra, one is left with a rather peculiar distribution compared with the more common structural variations with energy. Because of the systematics of n - p scattering, a complicated neutron spectrum will lead to a recoil proton spectrum increasing monotonically as energy decreases. The recoil-proton spectrum, $D(E)$, is a convolution over the neutron spectrum, $\phi(E)$, and the n - p scattering cross section, $\sigma(E)$, according to the well-known result

$$D(E) \sim \int_E^\infty \phi(E') \sigma(E') \frac{dE'}{E'}. \quad (1)$$

Ocular demonstration of neutron spectrum is lost and one must resort to the derivative of the proton distribution to extract a neutron spectrum. This appears a worse state of affairs than it actually is, however. Even a modest computer will provide straight line fits to input data and the precision with which details of n - p scattering are known eliminates any significant error, other than a statistical one, from the analysis.

Any discussion of detector resolution or efficiency must consider details of the differentiation as well as the intrinsic resolving power.³ It is by no means true, however, that the peculiar differentiation requirement will invariably be the one which limits resolution. It is not difficult to think of situations in which a 4π recoil counter, by virtue of its high rate of detection, pro-

duces spectra having resolution and statistical accuracy superior to telescopic arrangements which select only forward scatters.

In any case, there is no possibility of any kind of collimation at low energies because the range of protons is too short. It is not possible to decrease indefinitely the gas pressure because a minimum amount of gas is always required to quench the multiplication process.

These then are some of the problems to be faced in using the 4π recoil counter. Needless to say, most have been considered previously but low level work has been done principally with noble gases for beta measurements rather than with hydrogen for proton recoils. There is a large difference, for example, between W for an electron in a noble gas and a proton of the same energy in hydrogen.

To study a few of these problems, measurements were made on the characteristic $1/E$ neutron slowing down spectrum, a spectrum which can be reasonably anticipated under some rather general conditions. For an infinite moderator, say graphite or heavy water (or mixtures of these), and for neutron energies below 100 keV where the scattering cross section is unchanging and isotropic, the neutron spectrum from a uniformly distributed source (of energy in excess of 100 keV) will assume a $1/E$ spectral shape. This quite general result also holds well for finite media and for point sources where source energies are again in excess of 100 keV and source and detector are well separated. For the results presented here a graphite- D_2O block (1.5 x 1.5 x 1.5 m) was used in two different ways in conjunction with a plutonium-beryllium neutron source of 1×10^7 neutrons/sec. The source could be immersed in the D_2O providing well-thermalized neutrons for counter calibration via the $N^{14}(n,p)C^{14}$ reaction with nitrogen included in the filling gas. The source could then be placed in the graphite stack to get a suitably intense $1/E$ flux. Source and detector were separated by about 25 cm.

Studying a $1/E$ spectrum is admittedly not very interesting, except insofar as it reveals information concerning the counter. A $1/E$ spectrum turns out to be rather well suited for this purpose, however, and results obtained are sufficient to permit studies in other more interesting cases.

The counter configuration considered here is the simplest possible, consisting of a fine wire anode (0.0254-mm diameter) at high potential on the axis of a grounded cylindrical cathode. The field near the ends of the counter is defined by hypodermic needles extending into the body a distance of a counter diameter from the end seals. Both counter body and anode wire can be made of stainless steel and so no springs, etc.,

are needed to maintain wire tension under differential temperature expansion of wire and body. Results reported here were taken with a counter having a 2.54-cm radius, 0.8-mm wall thickness, and a 15-cm effective length.

CALIBRATION

The proportional counter must be calibrated against a standard of known ionization. Any source of known ionization will do, but, since recoil protons will originate uniformly over the gas volume, a calibration source consisting of monoenergetic protons uniformly dispersed over the volume will furnish not only calibration but a realistic measure of line width as well. For this reason a small amount of nitrogen gas was included in the counter, providing ionization equivalent to a 615-keV proton from the reactor $N^{14}(n,p)C^{14}$ when the counter was exposed to a thermal neutron flux.

Fragments from the $N^{14}(n,p)C^{14}$ reaction will release approximately $615,00 \div 36 = 1.71 \times 10^4$ electrons in hydrogen. Having calibrated the counter with this reaction, one may study a spectrum over a range of ionization near 1×10^4 , but to extend the calibration to fewer initial ion pairs an accurate dependence of multiplication on voltage is needed. W. Diethorn⁴ has observed that the ratio of the log of the gas multiplication, A , to the voltage, V , is linear with $\log V$, a result in good agreement with experimental results for all of the gases and mixtures so far tested. It is fortunate that an accurate means of predicting changes of A with voltage exists for it makes possible a reliable gas gain value at any counter voltage after calibrating with a single standard ionization source.

Because most of the previous multiplication versus voltage work has been done with noble gas mixtures, it was felt that an additional test using a predominantly hydrogen filling would be useful, especially one in which the largest possible range of A was covered. Using the $N^{14}(n,p)C^{14}$ reaction with 1.7×10^4 initial electrons, it was found to be impossible to increase multiplication in excess of about 100 without introducing an effect which caused the proton line to undergo a rapid broadening with increase in voltage. The reason for this is apparently a space-charge saturation phenomenon caused by the very large ($\sim 2 \times 10^6$) number of collected electrons. In order to study A versus V for larger A , one must start with fewer initial electrons. By introducing ultra-violet light into the counter, single electrons were ejected randomly from the cathode by the method of S. Curran, *et al.*⁵ The pulse height distribution is quite broad due to statistical effects, but it is easy to determine the mean value and this was done as a function of voltage, which now

had to be set quite high. The counter used for these tests had one atmosphere of H_2 , 20 cm of CH_4 and 10 cm of N_2 . It was not convenient to operate at higher pressures because of limitations on high tension operation of the counter. Results of a calibration are plotted in Fig. IV-19-1 for A greater than 10. The Diethorn prescription appears to do quite well over the whole range of gas multiplication.

GAMMA REJECTION

Measurements of proton recoils are, unfortunately, obscured by the background of electrons from gamma rays which invariably accompany neutron flux. There is a region of ionization in a counter of given size and gas pressure beyond which electron events are ordinarily negligible relative to proton events. This region is, however, that in which proton tracks are a significant fraction of counter dimensions and so the recoil spectrum is distorted by wall- and end-effects. A Monte Carlo type of calculation is then necessary for interpretation of data. Because of the sensitivity of the Monte Carlo calculation to flux anisotropy, one must use spherical proportional counters⁶ to make the calculation generally useful. Gas pressure can be minimized, but cannot be reduced below the point where quenching is no longer adequate.

In the presence of intense gamma fields, the Monte Carlo approach for a low pressure system appears to be the only feasible one. If, however, the total rate of occurrence of all events is not greater than about 2000/sec, each event can be "examined" individually and a decision made as to its origin.³ The gas pressure problem then reverses; best results are achieved by keeping the pressure as high as possible. The reason is that gammas generate electrons predominately in the counter wall and so the total number of electrons does not depend upon pressure. The ionization distribution of electron-induced events rises sharply as ionization increases from zero, goes through a broad maximum depending on counter size and pressure, and falls off to zero again. Increasing pressure shifts the distribution to a higher mean ionization, but does not change the total rate of events. Recoil proton rates, on the other hand, will increase with pressure so that the over-all neutron-to-gamma ratio improves as pressure rises. In addition to good neutron-to-gamma ratios, one would like as low an absolute gamma rate as possible; hence counter surface area should be small. The combination of small size and high pressure promises best over-all performance and this is also the configuration desired for a probe in general. With high gas pressures, an energy range where end- and wall-effect distortion is negligible can be used and one need only differentiate proton spectra to derive neutron spectra. Gas purity,

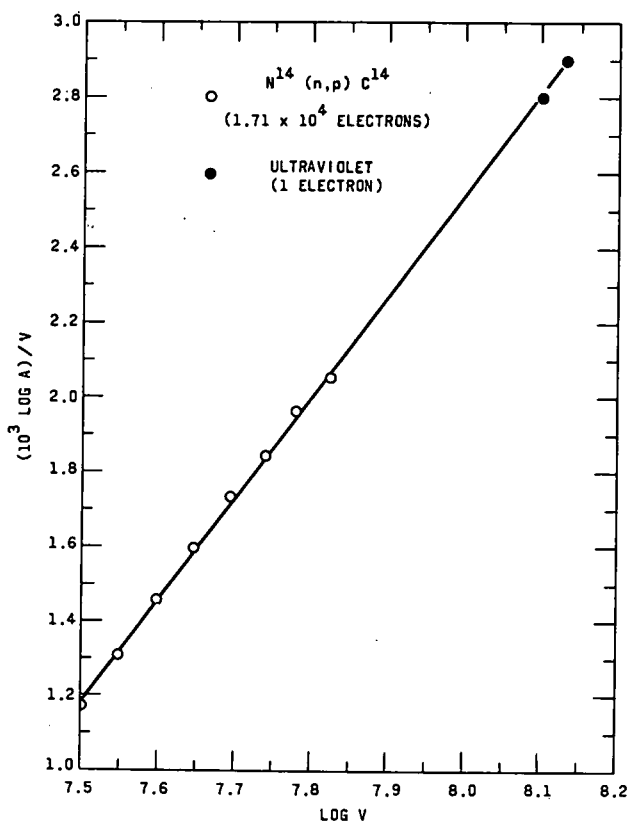


FIG. IV-19-1. Counter Ionization Calibration Plotted as (Log A)/V Versus Log V.

high voltage, space charge saturation, and electron drift velocity limit the useful counter size and pressures.

Shape rejection of electron events, which is the technique used in this study, is based upon the large difference in specific ionization between a recoil proton and an electron of the same ionization. The electron crosses the counter along a chord and so the projection on the radius of the ionization created is, on the average, a substantial fraction of counter radius. The proton recoil, on the other hand, has negligible range so that its ionization is highly localized spatially. Electrons arriving at the anode over a short time interval, as for a proton recoil, induce a pulse that rises much more rapidly than will the pulse from a broadly distributed gamma-induced electron event of low specific ionization.

COUNTER RESPONSE TO A 1/E NEUTRON FLUX

Proton recoil spectra were recorded with a counter (3 atm H_2) exposed to the 1/E slowing-down spectrum obtained by placing a plutonium-beryllium α -n source (10^7 /sec) in a mixed graphite and D_2O block. Gamma background, which was everywhere comparable to or

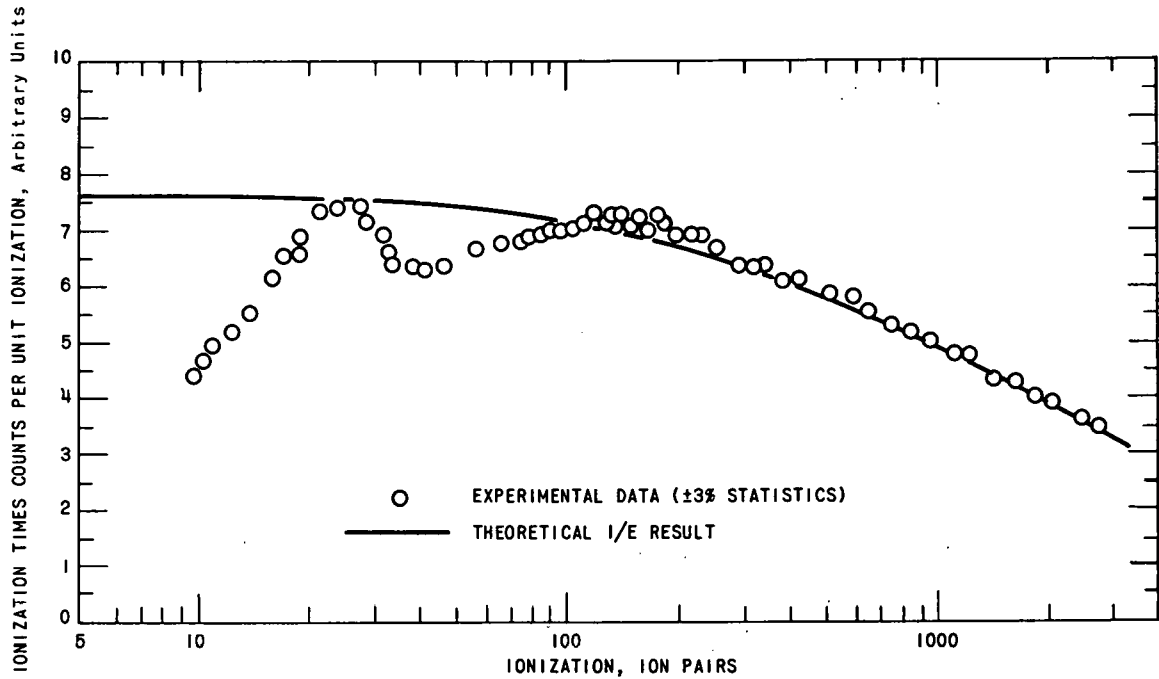


FIG. IV-19-2. Experimental Distribution of Ionization from a Counter Exposed to a $1/E$ Neutron Flux.

in excess of recoil proton rates, was removed by shape discrimination.

The proton recoil spectrum, which one would expect to observe in response to a $1/E$ neutron flux, can be calculated from the neutron proton scattering cross section⁷ along with Eq. (1).

Figure IV-19-2 is the experimentally observed proton recoil ionization distribution. The ordinate is actually the product of ionization by ionization spectrum and the predicted shape is also shown where the value 36.0 eV/ion pair has been assumed for the region in excess of 300 pairs. Agreement for $I > 350$ pairs is good, as would be expected, but below this a complicated dependence of W on E is apparent.

To calculate $W(E)$ one may integrate the equality

$$N(I)dI = D(E)dE, \quad (2)$$

where $N(I)$ and $D(E)$ are distributions in ionization and energy, and obtain

$$\int_I^{E_0/W_0} N(I)dI = \int_E^{E_0} D(E)dE, \quad (3)$$

where E_0 is any energy (~ 10 keV) beyond which W can be assumed to have its asymptotic value W_0 . An analytic result for the integral of $D(E)$ can be derived using Eq. (1). This can be compared with numerical integrals over $N(I)$ using the observed spectrum, and the value of E for which integrals are equal is the energy corresponding to ionization I .

Having evaluated I versus E , one may determine $W(E)$ from the definition (Eq. 2)

$$W(E) = \frac{dE}{dI} = \frac{N(I)}{D(E)}. \quad (4)$$

Data in Fig. IV-19-2 can be analyzed in this manner for W down to an ionization of about 40 pairs (~ 1.5 keV). Below this, as can be seen, the distribution goes through a peak with maximum near 25 pairs. At least

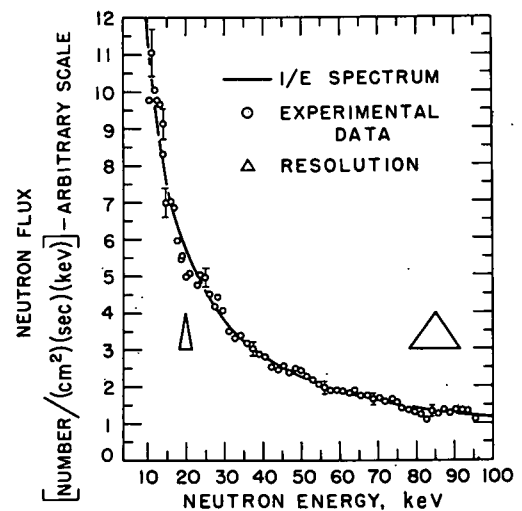


FIG. IV-19-3. Neutron Spectrum Measurement of a $1/E$ Slowing-Down Spectrum.

part of the distribution in this region is probably due to recoil deuterons following thermal neutron capture on hydrogen in the counter.

The simple $1/E$ observation which can be done using a conventional "hand" neutron source not only supplies W , but provides a convenient means of testing counting procedures and techniques generally for systematic errors that would be difficult to discover in the low energy region by other means.

MEASURED $1/E$ SPECTRUM

In order to demonstrate a spectrum measured with the 4π recoil counter, a measurement of the $1/E$ neutron spectrum is shown in Fig. IV-19-3 over the interval 10 to 100 keV, an interval not requiring a correction for ion pairs versus energy. The corresponding proton recoil distribution was accumulated in an hour at an average recoil rate of 250/sec. The average rate of rejected gamma background was 500/sec. Differentiation of the recoil proton distribution (Eq. 1) was done for successive increments of 16% of energy and the intrinsic counter width was estimated at about 13%. Calculations³ indicate that a resultant width of 16% is appropriate for the neutron spectrum and this width has been included in the figure. Statistical accuracy ranged from $\pm 4\%$ to $\pm 8\%$ and, although the ordinate

scale is arbitrary, all information exists to determine fluxes absolutely if desired.

REFERENCES

1. E. F. Bennett, *Proportional Counter Proton-Recoil Spectrometer with Gamma Discrimination*, Rev. Sci. Instr. **35**, 1153 (1962).
2. E. F. Bennett, *Gamma-Ray Discrimination in Proton Recoil Proportional Counters*, Proc. Sym. Neutron Detection Dosimetry and Standardization, Harwell, Dec. 10-14, 1962 (IAEA, Vienna, 1963), Vol. II. Neutron Dosimetry, pp. 341-349.
3. E. F. Bennett, *A Study of the $1/E$ Slowing Down Neutron Spectrum Using 4π Recoil Proportional Counters*, ANL-6897 (to be published).
4. W. Diethorn, *A Methane Proportional Counter System for Natural Radio-Carbon Measurements*, NYO-6628 (March 1956).
5. S. C. Curran, A. L. Cockroft and J. Angus, *Investigation of Soft Radiation by Proportional Counters—V. Use as a Detector of Ultra-Violet Quanta and Analysis of the Gas Multiplication Process*, Phil. Mag. **7**, 929 (1949).
6. P. W. Benjamin, *The Use of Proton-Recoil Methods for Measuring Neutron Spectra in a Fast Reactor*, Proc. Sym. Neutron Detection Dosimetry and Standardization, Harwell, Dec. 10-14, 1962 (IAEA, Vienna, 1963), Vol. I. Neutron Dosimetry, pp. 307-318.
7. J. L. Gammel, *The n - p Total and Differential Cross Sections in the Energy Range 0-40 MeV*, Fast Neutron Physics, J. B. Marion and J. L. Fowler, Eds., (Interscience Publishers, Inc., New York, 1963), Part II p. 2185.

IV-20. In-Core Fast Neutron Spectroscopy

E. F. BENNETT and J. HAUGSNES

The measurement of uncollimated neutron spectra in the range from 1 keV to 1 MeV with a recoil proton proportional counter employing gamma rejection by means of pulse-shape discrimination has been investigated.^{1,2,3} Even though the gamma-induced events in the detector are ultimately rejected, the associated electronic circuitry must examine each event and decide whether to accept or to reject it. For the electronic circuitry to function as designed, the total count rate (neutrons plus gammas) should be less than about 2000 counts/sec. The possible use of this spectrometer in the core of a zero power reactor was investigated by making some preliminary count rate measurements.

A proportional counter had been constructed to fit into the standard 5.1×5.1 -cm matrix fuel drawer for ZPR-VI and ZPR-IX. The counter had a center wire 0.0025-cm diameter and a grounded case 3.5 cm i.d. by 14 cm long. Steel capillary tubing was slipped over

the ends of the center wire to define an active counter length of about 7.6 cm (active volume of about 73 cm^3). The filling gas was 3 atm of H_2 plus 100 mm-Hg of CH_4 (for quenching) plus 100 mm-Hg of N_2 (for calibrations by means of the n,p reaction).

This detector was placed in one of the halves of ZPR-VI Assembly No. 2—a 650-liter core with the following volume fractions: 17% stainless steel, 36% sodium, 15% carbon, 5% U-235, and 21% U-238. The core had a depleted uranium blanket. Count rates were taken about 70 h after a reactor run of about 40 min at a power level of about 50 W.

With the reactor halves separated and with no neutron sources, the total background gamma count rate in the detector was 2700, 1300, and 500 counts/sec, at the center of the core, at the edge of the core, and in the blanket, respectively.

Then the reactor sources were inserted into the

halves, and the halves were driven together leaving the reactor still subcritical. Under these conditions, the detector count rate in the center of the core was 6000 counts/sec and some data were taken with a two-dimensional analyzer which sorts events by risetime and pulse height.

For those pulses with heights corresponding to the ionization produced by a 5 to 10-keV recoil proton, the rise time distribution was separated into neutron and gamma events with the former comprising about 30% of the total number of events. The neutron peak was smeared out (presumably the effect of the excessive count rate) so that some uncertainty occurred in subtracting the gammas. For ionization levels above or below those chosen here, the separation should be better.

Further studies will be made of the possible use of this spectrometer in-core. Some new chambers have been fabricated, filled, and calibrated. The center wires are still 0.0025 cm in diameter but the inside diameter has been reduced to 2.5 cm and the active length to 5.9 cm. One detector has been filled with 3 atm of H_2 plus 100 mm-Hg of CH_4 and 100 mm-Hg of N_2 . The other has been filled with 3 atm of CH_4 plus 100 mm-Hg of N_2 . The former counter will be used for spectrum measurements in the region from 0.8 to 100 keV and the latter for measurements in the region from 100 keV to 1 MeV. Figure IV-20-1 shows the arrangement of the detector, lead shield, and first tube of the preamplifier in the fuel drawer.

No special effort was made to minimize the over-all size of these probes and their associated electronics

since the purpose of this work is to establish limitations associated with in-core proportional counter use, especially as to response to gamma background (natural and from the irradiation history of the core), quality of measured neutron spectra, and sensitivity of spectral shape to the perturbation caused by the probe.

The neutron count rate in the new H_2 -filled chamber will be approximately 40% of that in the original chamber (because of the reduced active volume) but this count rate is still more than adequate to get good statistics for neutron spectra. More importantly, the gamma counting rate will be reduced by approximately 45% because the surface area of the active volume in the new detector is approximately 55% that of the original detector. A small additional thickness of lead can be fitted around the new chambers which will reduce the transmission of the prompt and fission product gamma flux from 70 to 50%. Further reduction in the detector counting rate will be attempted by using unirradiated fuel, and possibly some extra lead, in the fuel drawers adjacent to the detector. In addition, it is feasible to wait for longer periods of time after relatively high power reactor runs.

Finally, it is possible to reduce the absolute count rate by decreasing the effective chamber dimensions further but this is not a trivial change. In order to keep end and wall effects negligible, the filling gas pressure would have to be increased correspondingly but this will require an increase in the counter high voltage to maintain the same gas multiplication. Higher voltages would require more attention to the design of the counter and associated cables.

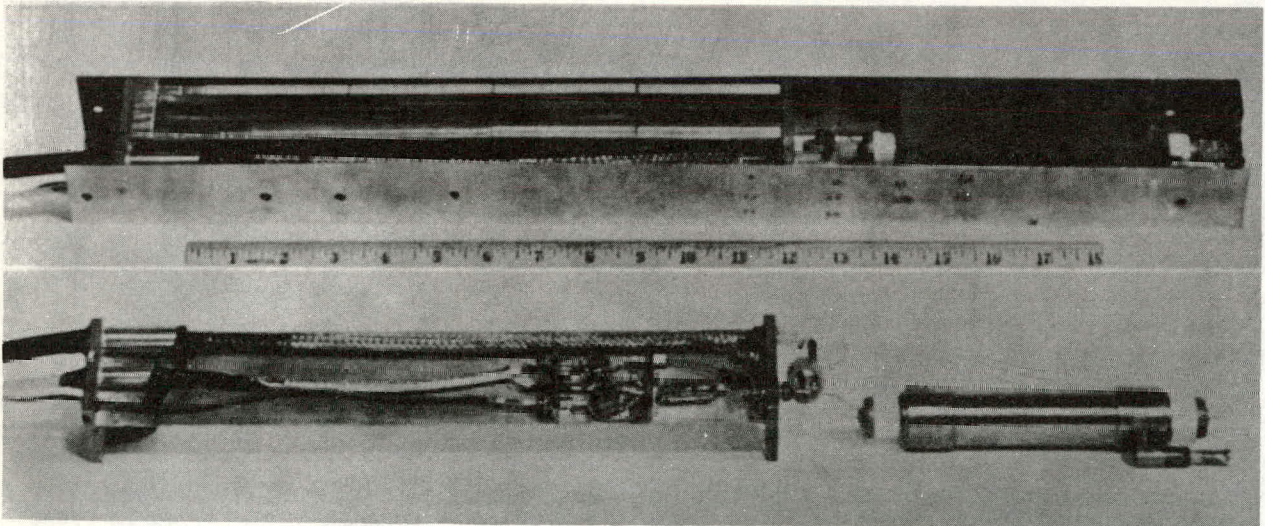


FIG. IV-20-1. Arrangement of the Recoil Proton Proportional Counter, Lead Shield, and Preamplifier in a ZPR-VI Fuel Drawer.

REFERENCES

1. E. F. Bennett, *Proportional Counter Proton-Recoil Spectrometer with Gamma Discrimination*, Rev. Sci. Instr. **33**, 1153-1160 (November, 1962).
2. E. F. Bennett, *Gamma-Ray Discrimination in Proton Recoil Proportional Counters*, Proc. Sym. Neutron Detection Dosimetry and Standardization, Harwell, Dec. 10-14, 1962 (IAEA, Vienna, 1963), Vol. II, pp. 341-349.
3. E. F. Bennett, *A Study of the 1/E Slowing Down Neutron Spectrum Using 4π Recoil Proportional Counters*, ANL-6897 (to be published).

IV-21. A Study of Rossi-Alpha Measurements in Critical Facilities

E. H. HELM

Rossi-alpha^{1,2} measurements were made in several of the ANL critical facilities using a new time analyzer designed and constructed by the Electronics Division.

The first measurements were made in the Argonne Thermal Source Reactor, a low power, water reflected, water moderated and fully enriched fueled reactor. The neutron detecting fission chamber was located at the core-reflector interface. To minimize the number of uncorrelated counts, the measurements were performed at very low levels with the reactor 0.3% sub-critical.

After an initial fast decay* the prompt decay constant assumed an approximately constant value which was determined to be

$$\alpha = (108 \pm 31)/\text{sec.}$$

From the definition of the Rossi-alpha,

$$\alpha \equiv (\beta_{\text{eff}} - k_{\text{ex}})/\ell,$$

the prompt lifetime was found to be

$$\ell = 105 \pm 33 \mu\text{sec},$$

assuming a delayed neutron fraction of 0.008. This may be compared with the value $\ell = 69.4 \mu\text{sec}$ measured earlier using the pile noise method.³ The large discrepancy between the two values could be entirely due to statistical errors. It is possibly somewhat increased by the different counter locations and by the use of different reflectors at the thermal column face.

* An explanation of this effect was later given by R. A. Karam.⁴

Subsequently the same measurements were made in the fast critical facilities ZPR-VI and ZPR-IX. Because of the shorter prompt neutron lifetime, there is less overlap of the prompt chains and therefore a smaller fraction of uncorrelated counts. Therefore, in these fast reactors, measurements can be performed with much better statistics.

Measurements in Assembly No. 1 of ZPR-VI (a 138 liter core composed of U-235 and U-238 in a ratio of 1:7) gave for Rossi-alpha a value of

$$\alpha = (10.8 \pm 0.7) 10^4/\text{sec}^{-1}.$$

This was in good agreement with the value measured for ZPR-III Assembly No. 11, which had the same composition.⁵

Furthermore, a core similar to Assembly No. 1 of ZPR-VI, but with an aluminum reflector, (see Paper No. III-12), gave the Rossi-alpha as

$$\alpha = (7.78 \pm 0.34) 10^4/\text{sec}^{-1}$$

REFERENCES

1. J. D. Orndoff, *Prompt Neutron Periods of Metal Critical Assemblies*, Nucl. Sci. Eng. **2**, No. 4, 450 (1957).
2. G. S. Brunson, R. Curran, S. G. Kaufmann, J. McMahon and L. Pahis, *Measuring the Prompt Period of a Reactor*, Nucleonics **15**, No. 11, 132 (1957).
3. W. K. Luckow, *The Evaluation of Nuclear Reactor Parameters from Measurements of Neutron Statistics*, Thesis, University of Michigan, 56 (1958).
4. R. A. Karam, *Measurement of Rossi-Alpha and Reflected Reactors*, Trans. Am. Nucl. Soc. **7**, (to be published).
5. G. S. Brunson, R. N. Curran, J. M. Gasidlo and R. J. Huber, *A Survey of Prompt Neutron Lifetimes in Fast Critical Systems*, ANL-6681 (1963).

IV-22. Radiochemical Measurement Techniques in ZPR VI and IX

R. J. ARMANI

The fission rates in U-235 and U-238 and the capture rate in U-238 were measured at various points and for various core configurations in ZPR-VI and -IX. These measurements were made by irradiating enriched (93% U-235) and depleted (0.2% U-235) uranium foils, and using radiochemical techniques to separate the activity. In addition, the ratio of U-238 effective fission cross section to U-235 effective fission cross section and the ratio of U-238 effective capture cross section to U-235 effective fission cross section were calculated from the irradiation. The sensitivity of this technique is such that fissions and captures as small in number as 10^8 each may be detected to an accuracy of $\pm 3\%$, not including the uncertainty in the fission yields. The uncertainty in the fission ratio and the capture-to-fission ratio is of the order of $\pm 10\%$ due to the uncertainty in the foil enrichment or depletion, fission yields, and decay constants.

The fission rates were measured by inserting uranium foils in the core and irradiating for a known period of time. The foils were then removed from the core and dissolved in hydrochloric acid. The fission product Mo-99 was extracted by solvent extraction and prepared in a form suitable for counting. The activity was determined by counting with an end-window flow counter previously calibrated as a function of sample thickness.

Assuming that the irradiation time is short compared with the half life of Mo-99, the fission rate $N\phi\sigma$ is calculated from the following equation:

$$N\phi\sigma = \frac{A^{Mo}}{(1 - e^{-\lambda T})} = \frac{A^{Mo}}{Y\lambda T},$$

where N = number of target atoms, ϕ = neutron flux, σ = fission cross section, A^{Mo} = Mo-99 activity at the end of the irradiation, Y = fission yield of Mo-99 (6.3% for U-238 and 6.1% for U-235), λ = decay constant for Mo-99, and T = irradiation time.

Capture rates were determined by irradiation of depleted uranium foils. The foils were allowed to decay for a time sufficiently long to allow essentially all of the U-239 to decay to Np-239, at which time the Np-239 was extracted.

The foils were dissolved in hydrochloric acid and a known activity of Np-237 was added in order to determine the chemical yield. The neptunium was ex-

tracted by ion exchange and deposited on a platinum disc. The Np-237 activity was determined by alpha counting and the chemical yield was calculated. The Np-239 activity was determined by beta counting with a previously calibrated end-window flow counter.

Assuming an irradiation time T small compared with the half life of Np-239 and allowing sufficient time for all of the U-239 to decay to Np-239 before performing the analysis, the capture rate, $N_{28}\phi\sigma_c^{28}$, is calculated from the following equation:

$$N_{28}\phi\sigma_c^{28} = \frac{A_{39}(\lambda_{29} - \lambda_{39})}{\lambda_{29}[1 - \exp(-\lambda_{39}T)] \exp(-\lambda_{39}T)} \\ \cong \frac{A_{39}(\lambda_{29} - \lambda_{39}) \exp(\lambda_{39}t)}{\lambda_{29}\lambda_{39}T}$$

Here N_{28} = number of U-238 target atoms, ϕ = neutron flux, σ_c^{28} = capture cross section of U-238, A_{39} = activity of Np-239 at time t after irradiation, λ_{29} = decay constant for U-239, and λ_{39} = decay constant for Np-239.

The fission ratio $\bar{\sigma}_f^{28}/\bar{\sigma}_f^{25}$ and the capture-to-fission ratio $\bar{\sigma}_c^{28}/\bar{\sigma}_f^{25}$ were both determined by irradiating one enriched and one depleted uranium foil in the same position. A fission analysis was performed on both foils and a capture analysis was performed on the depleted foil. The fission ratio is calculated from the following equation:

$$\frac{\bar{\sigma}_f^{28}}{\bar{\sigma}_c^{25}} = \frac{Y^{25}(N_1^{25} - RN_2^{25})}{Y^{28}(RN_2^{28} - N_1^{28})}$$

Here $R = A_1^{Mo}/A_2^{Mo}$, $\bar{\sigma}_f^{28}$ and $\bar{\sigma}_f^{25}$ = fission cross sections for U-238 and U-235, Y^{28} and Y^{25} = fission yields for Mo-99 for U-238 and U-235, N_1^{28} and N_1^{25} = number of U-238 and U-235 atoms in the depleted foil, N_2^{28} and N_2^{25} = number of U-238 and U-235 atoms in the enriched foil, and A_1^{Mo} and A_2^{Mo} = activity of Mo-99 in the depleted and enriched foils at the end of irradiation.

The capture-to-fission ratio is calculated from the following equation:

$$\frac{\bar{\sigma}_c^{28}}{\bar{\sigma}_f^{25}} = \frac{N_2^{25} A_{39} e^{\lambda_{39}t} \lambda Y^{25}}{N_1^{28} A_2^{Mo}}$$

Here λ = decay constant for Mo-99 and all other symbols are as previously defined.

IV-23. Rejection of Gamma Background in Hornyak Fast Neutron Detectors

K. PORGES, A. DEVOLPI and P. POLINSKI*

"Hornyak button" scintillation detectors¹ for fast neutrons, which are essentially dispersions of small zinc-sulfide crystals in lucite or similar hydrogenous and transparent media, are designed to have inherently reduced response to gamma radiation. Typical Compton electrons released by incident gamma rays have ranges considerably in excess of the size of the zinc-sulfide crystals and thus yield only weak zinc-sulfide light pulses. This is in contrast to recoil protons released by incident neutrons, whose ranges are compar-

the photo-tube. The relative amount of light in such pulses is, of course, very small in comparison to the light emitted over, say, a few microseconds by a zinc-sulfide crystal. Integration at the photo-multiplier anode, followed by amplification at ordinary (1 Mc) bandwidths will therefore effectively eliminate this undesirable background. This stratagem becomes inadmissible, however, when the time of arrival of the neutrons must be known accurately, e.g. for certain types of coincidence experiments, or when the gamma back-

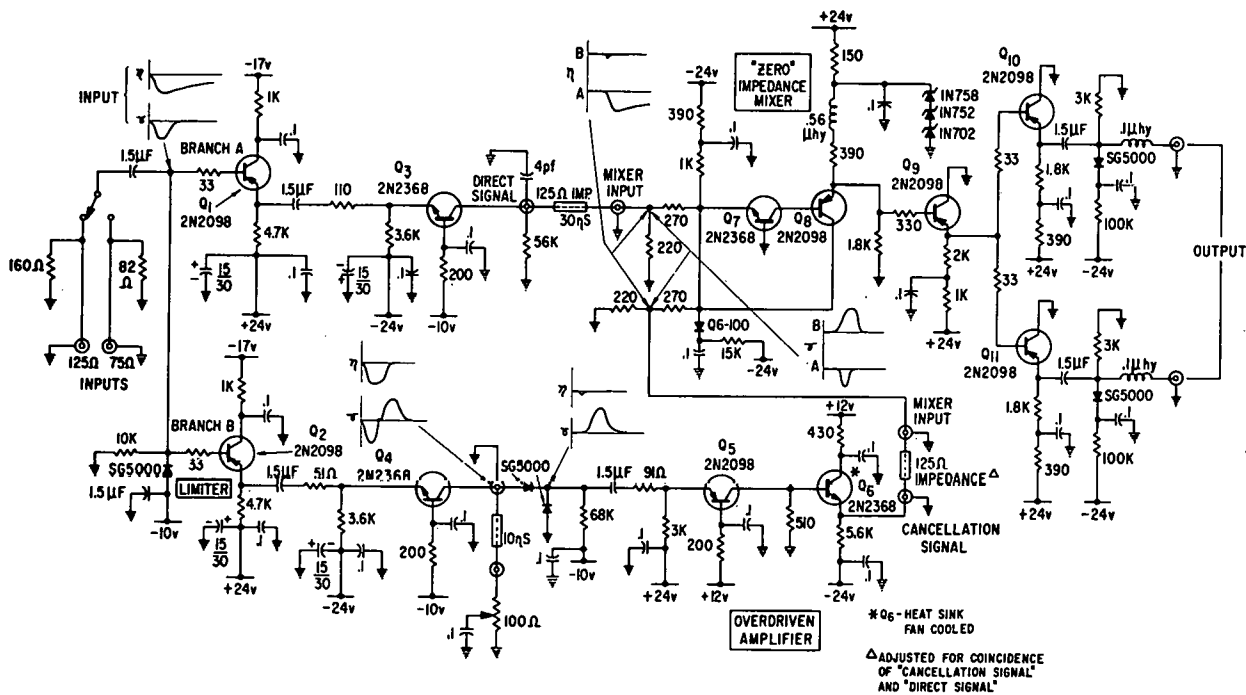


Fig. IV-23-1. Gamma Cancellation Circuit

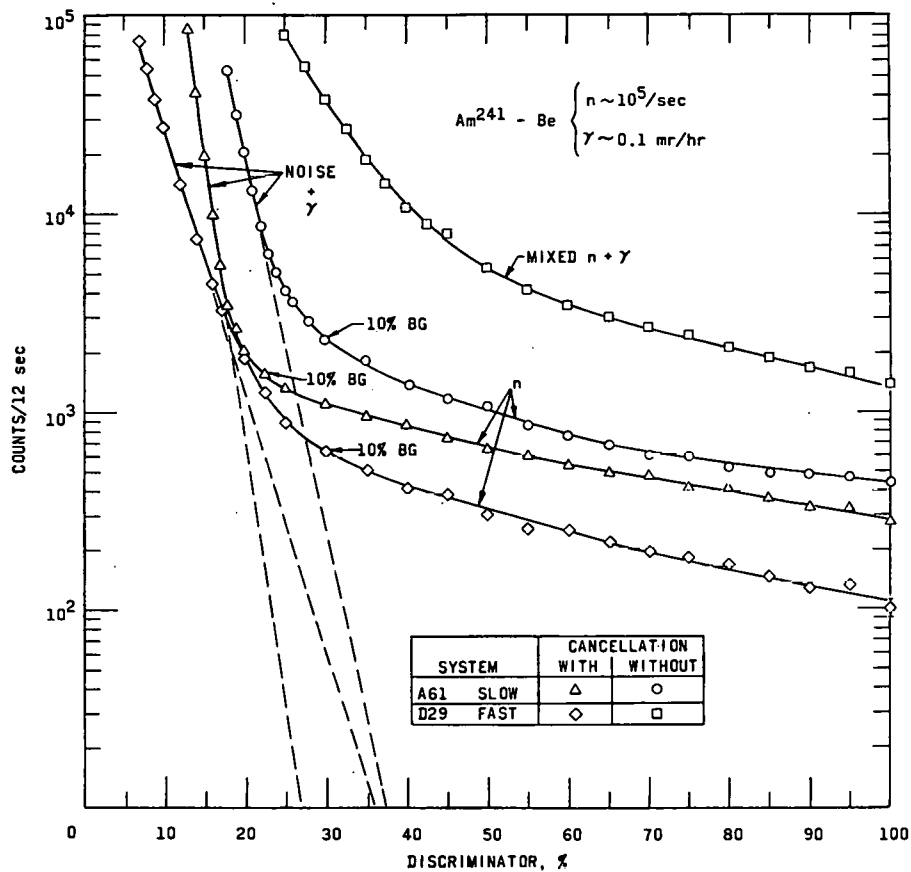
able to crystal size. However, observation of the anode pulses of a "fast" photomultiplier coupled to a Hornyak button in the presence of a neutron source with an oscilloscope of large bandwidth shows, in addition to pulses which have the typical decay periods of zinc sulfide, the presence of very fast-decaying pulses. The fastest of these have decay periods of about 70 nsec. These short pulses (whose shape is similar to that of photocathode noise pulses) appear to be caused by scintillation and Cherenkov light, caused mainly by gamma radiation in the various media which are both exposed to such radiation and seen by the cathode of

ground is strong enough to result in considerable pileup with 1 μ sec integration.

For this contingency, a cancellation circuit was devised which takes advantage of the appreciable difference in length of the background pulses and the shortest (70 nsec) zinc-sulfide decay component.

A simple passive circuit, devised for this purpose was reported previously.² Further work on this scheme during the current year has resulted in significant improvement of background rejection. A new cancellation circuit, shown in Fig. IV-23-1, splits the anode signal into two branches. In one branch, the signals are strongly differentiated through a shorted delay line, somewhat longer than the background pulses. Re-

* Electronics Division, Argonne National Laboratory.

FIG. IV-23-2. Integral Bias Curves Using Am²⁴¹-Be Neutrons.

fections are adjusted such that the background pulses are effectively inverted, while the long-tailed zinc-sulfide pulses are just cancelled and do not cross the zero line. After processing by a diode network which passes only the inverted echo pulses due to background, the latter are amplified and mixed with the other branch, which contains only a cable delay of slightly more than twice the differentiating cable mentioned above, and suitable isolation and impedance matching stages. The background pulses are thus effectively cancelled, while zinc-sulfide scintillation pulses are passed. The effect of the circuit on pulses due to mixed neutron and gamma radiation is shown in Fig. IV-23-2, which allows comparison of discrimi-

nator bias curves taken with fast electronics (the cancellation circuit has a bandwidth of 150 Mc) and with integration (1 Mc bandwidth). It is apparent that the cancellation circuit provides about the same gamma discrimination as integration, yet provides output pulses of 2.5 nsec risetime, suitable for fast coincidence work.

REFERENCES

1. W. F. Hornyak, *A Fast Neutron Detector*, Rev. Sci. Instr. **23**, 264 (1952).
2. A. DeVolpi and K. G. Porges, *Rejection of Gamma Background Radiation Pulses in Hornyak Buttons*, IRE, Trans. Nucl. Sci., NS-9, No. 3, 320-326 (1962).

IV-24. EBR-II Fuel Element Failure Detector

K. G. PORGES

The rapid detection of fuel element cladding failures has been of considerable concern to the designers of power reactors, both for reasons of personnel safety and for the prevention of possibly serious damage to the plant. Over the last several years, a number of different cladding failure detection systems have been developed and installed for specific reactors. Since cladding failures are, or at least are hoped to be, rather infrequent in occurrence, actual performance data for this equipment accumulate only very slowly, and fairly elaborate laboratory tests as well as loop experiments must be resorted to in order to establish some confidence in an initial installation. Thus, the fuel cladding failure detection system for EBR-II was designed on the basis of a laboratory facility in which the radiation background and detection geometry of the actual site can be exactly reproduced. An initial installation is now operational. Further development work is, however, planned with a view of improving the sensitivity as well as reliability of this equipment, and of establishing its characteristic signal in case of a cladding failure. Some of this information will be sought by means of equipment installed on a new fuel failure experimental loop in the TREAT reactor.

The method employed by this equipment—the detection of delayed neutrons emitted by fission products—is essentially unaffected by substantial gamma backgrounds. For that reason, this method is the only immediately applicable one for sodium-cooled reactors, as the 15-hour Na-24 activity allows no hope for the direct detection of fission product beta or gamma activity injected into the coolant as a result of a cladding failure.

The amount of delayed neutron precursor fission products which is injected into the coolant as a result of the cladding rupture of a single fuel pin can be estimated reasonably well. A large degree of uncertainty attaches, however, to the degree of dissemination of this spike in the flowing coolant as it passes through the upper plenum and heat exchanger, at which point it is sampled—with an efficiency which is also largely conjectural—by a bypass loop. Approximately 17 sec after leaving the core, a certain fraction of the fission product spike thus passes through a 1-m long section of the 5 cm diameter sampling loop which is surrounded by a graphite stack. BF_3 , boron-lined and fission detectors count the delayed neutrons which

are emitted and moderated in the stack. A simple calculation, subject to the large uncertainties alluded to above, predicts a total source strength of 1 to 3×10^6 delayed neutrons per cladding failure. The object of the testing program, completed several months ago, was therefore to ascertain the over-all efficiency of an optimum arrangement of detectors and graphite, as well as to ascertain the neutron detection efficiency and gamma background sensitivity of several types of counters, using electronic amplification at different bandwidths. In addition, a group of high-efficiency, fast fission chambers was developed which will be used in the facility when they become available.

The electronic circuitry which processes the signals developed in these detectors was designed to have a bandwidth of more than 30 Mc, in order to be able to keep pulses short and thus reduce pileup due to the strong gamma background. Preamplifiers are located adjacent to the detectors; amplifiers and discriminators (one for every two detector channels) nearby; together with temperature reading circuits and test equipment. The discriminators are designed to drive several hundred feet of cable, in order to deliver digital information to the record/display unit which is located in the main control room of the reactor. The latter unit was designed to allow a faithful display of the instantaneous count rate in two count channels; it makes use of a magnetic tape loop buffer memory and a fast oscillograph, which is turned on by a trip circuit whenever the count rate exceeds a certain level. Owing to a short delay in the tape, the oscillographic record begins just ahead of the excursion, which is thus completely out. This unit appears to have several features which may make it useful in other applications.

The record must still be interpreted by operating personnel, in conjunction with other instrument channels in the control console, to determine whether a fuel failure may be assumed to have occurred, and moreover whether this failure appeared to have been of "benign" type (a slow leak in the cladding of one or several fuel elements) or of the more serious type (a cladding rupture resulting in the emission of debris). The difficulty of this determination may be materially reduced through foreknowledge of the typical "signature" of different types of cladding failures; this information will become available through the "TREAT" loop experiments mentioned above.

IV-25. Fuel Meltdown Monitoring in TREAT by Fast Neutron Detection

A. DeVOLPI

Calculations and experiments are underway to examine the feasibility of monitoring fuel element transient meltdowns in TREAT by means of fast neutron detectors. The results of one experiment are displayed in Fig. IV-25-1, which shows the count rate obtained by scanning a single channel collimator across the test fuel pin plane. The monitor was a "Hornyak button"¹ fast neutron detector, in contrast to the previous Argonne-Naval Research Laboratory effort with gamma ray detection.² For this steady-state test the neutron detector was located over 13 ft from the source plane.

Presently under design is a 320-channel collimator intended to provide 1-msec time resolution and 0.15-in. horizontal space resolution for the duration of a typi-

cal transient. Cost of electronic processing equipment per channel is an important aspect of development effort. The readout system consists of acquisition of a linear neutron signal, amplification, discrimination, and digitizing of an electrical signal to yield a light output of uniform amplitude. The light flashes from each channel are photographed in a fast framing camera to provide what amounts to an inexpensive high-duty-cycle, two-parameter analyzer.

To understand operation of the system, visualize a 2 x 20 in. plane containing the fuel pin, which is situated in the center of the TREAT core in the through slot. The plane is subdivided for detection purposes into a 14 x 23 element matrix, and each element is the focal point of one channel of the collimator. Associated

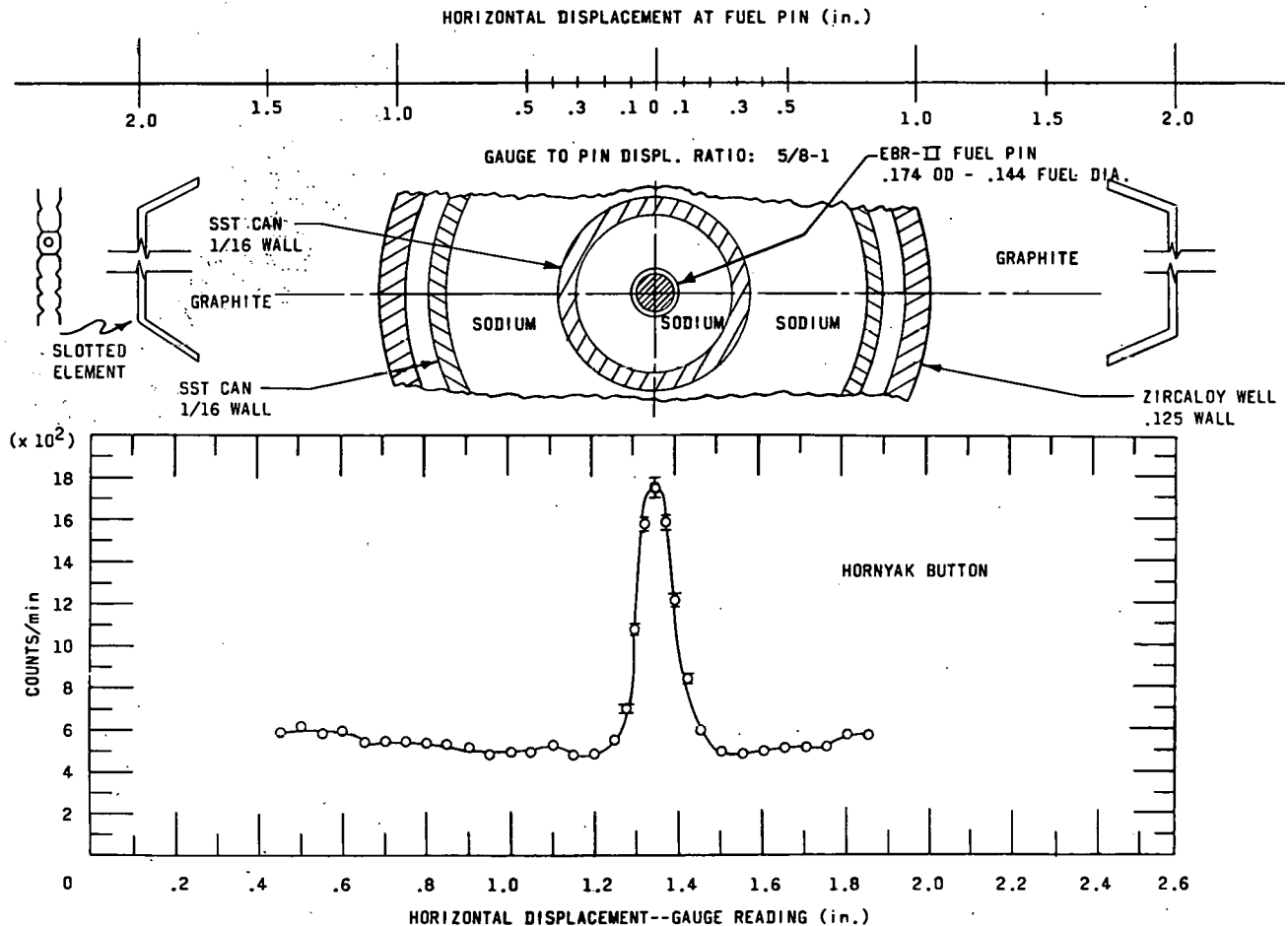


FIG. IV-25-1. Fast Neutrons Emanating from Fuel Pin Region During 90-kW Steady-State Scan by Single Channel Collimator Located 13 ft from Test Plane.

with each collimator slot is a "Hornyak button" neutron detector, each channel containing its own electronic processing package and subsequent indicating light. The light flashes every time a fast neutron is recognized by the channel discriminator. Dead time per channel is less than 5 μ sec. A panel containing an array of all 320 lights is arranged to allow photographing by a fast framing camera. With framing rates of 1000/sec, each picture contains a 14 x 23 pattern of exposures, each exposure being proportional to the total number of neutrons detected in the corresponding channel in a millisecond. The photographic film functions as 320 digitized fast recorder traces compressed onto a single roll, although a linear relationship between exposure and film density does not necessarily

exist. Thus both space and time information are inexpensively recorded in a system permitting over 10^7 total counts/sec. Initially the recorded data will be examined qualitatively for preliminary evaluation of the transient. If it is found that more detailed inspection of all or a portion of the film is required, an automatic densitometer program can be established by making use of experience and equipment available in Argonne's High Energy Physics Division.

REFERENCES

1. W. F. Hornyak, *A Fast Neutron Detector*, Rev. Sci. Instr. **23**, 264 (1952).
2. Beach, L. A., et al., *Gamma-Ray Scanning Techniques for Fast Breeder Reactor Safety Studies*, NRL Report 5625, (July 12, 1961).

Section V

Miscellaneous

The first five papers report attempts to extend and improve the accuracy of general reactor physics theory. Two papers on experimental work illustrate the exploratory work necessary to evaluate the possible extent of applications of reactor technology and to define in more exact fashion the problems that exist.

Concepts and evaluations of proposals involve preliminary analytical work to define possible objectives and probable areas of difficulty. Frequently this work is highly speculative. Five papers of this type are included here: three deal with applications in outer space, one with meteorology and one on research tools.

The heavy emphasis on computing work in reactor physics is represented by eight papers. These include numerical analysis, work applicable to a variety of problems, and code development, wherein a specific problem is resolved. Associated with this work is the compilation of basic data for use in analysis. Three such activities are reported; one associated with the Nuclear Cross Sections Advisory Group and two with the Reactor Physics Constants Center.

An activity of an analytic nature engendered by project work is the development of computing techniques for the solution of elasticity problems in cylindrical coordinates. This section closes with descriptions of two component developments which grew out of the needs of programmatic work, and are applicable to a wide range of experimental activities.

V-1. Some Problems in Reactor Theory

BERNARD I. SPINRAD

SUMMARY

Three different problems are reported here: the formulation of reactor lifetime; the significance of diffusion boundary conditions; and the physical interpretation of mathematical transforms appearing in the one-velocity neutron transport equations.

With regard to reactor lifetime, it is shown that, in a multiplying system, the "transport retardation" is of opposite sign from the corresponding term in a source-sink system, and yields a small correction which reduces the lifetime.

Internal boundaries in media to which diffusion theory is applied have an overdetermined set of continuity conditions arising from applying exact conditions. The situation is thus analogous to the case of vacuum boundary conditions. It is shown that the acceptance of continuity of flux and of current in directions normal to boundaries is physically reasonable. It follows that neutron currents may be subject to refraction.

The Laplace transform of the one-velocity, one-dimensional Milne problem is shown to be directly related to the outgoing angular flux. For the more general one-velocity, slab transport problem, it is shown that treatment of the problem by Fredholm methods avoids most of the undesirable aspects normally associated with the method of discrete ordinates.

THE EQUATIONS DEFINING REACTOR LIFETIME

The system of equations representing the lifetime of a reactor system are developed here. These are presented in full generality. Their examination, even at a cursory level, reveals that more common formulations rest on a very great number of approximations, each of which must be justified anew for a given experimental situation.

DEFINITION OF LIFETIME

We define lifetime by a conceptual experiment:

Let a reactor be delayed critical. Then convert all delayed neutrons into prompt neutrons. The reactor will still be critical. Now increase ν for all fissions by a ratio $\delta\nu/\nu$. Let $\delta\nu/\nu$ be very small, so that after a very long time observation is still possible, and let there be no power feedbacks.

A mean lifetime exists if, in this conceptual experiment, the power of the reactor approaches asymptotically

a definite shape in space and increases as a single exponential in time. This means that, ultimately, the neutron density in phase-space and time may be written as:

$$n(\mathbf{v}, \mathbf{r}, t) = n(\mathbf{v}, \mathbf{r}, t) e^{\alpha t} \quad (1)$$

This situation is assumed to exist, α being some constant.

Then, lifetime may be defined as:

$$\ell \equiv (\delta\nu/\alpha\nu), \quad (2)$$

ℓ may be (and usually is) a function of $\delta\nu/\nu$.

Therefore, we define a limiting lifetime as:

$$\ell(0) = \lim_{(\delta\nu/\nu) \rightarrow 0} \left(\frac{1}{\alpha} \frac{\delta\nu}{\nu} \right). \quad (3)$$

FLUX AND ADJOINT EQUATIONS FOR A MULTIPLYING SYSTEM WITHOUT SOURCE

The time dependent Boltzmann equation in an isotropic system without sources is:

$$\begin{aligned} & \frac{1}{v} \frac{d}{dt} \phi(\mathbf{r}, v, \Omega, t) + \Omega \cdot \nabla \phi(\mathbf{r}, v, \Omega, t) + \Sigma(\mathbf{r}, v) \phi(\mathbf{r}, v, \Omega, t) \\ &= \frac{1}{4\pi} \chi(v) \iint dv' d\Omega' \nu(\mathbf{r}, v') \Sigma_f(\mathbf{r}, v') \phi(\mathbf{r}, v', \Omega') \\ &+ \iint dv' d\Omega' \Sigma_s(\mathbf{r}, v') \phi(\mathbf{r}, v', \Omega') S(\mathbf{r}, v', \Omega' \cdot \Omega, v) \end{aligned} \quad (4)$$

where

- $\phi(\mathbf{r}, v, \Omega)$ = flux density in position, speed, neutron direction and space
- v = neutron speed
- Ω = neutron direction
- \mathbf{r} = position in space
- t = time
- Σ = total cross section
- Σ_s = scattering cross section
- Σ_f = fission cross section
- ν = neutrons born/fission (fission assumed isotropic)
- $\chi(v)$ = fission spectrum

$S(\mathbf{r}, v', \Omega' \cdot \Omega, v)$ = probability that a neutron scattered at $(\mathbf{r}, v', \Omega')$ emerges in differential phase space $(\mathbf{r}, v + dv, \Omega + d\Omega)$. That this is a function of $\Omega' \cdot \Omega$ is a result of the isotropic nature of the system.

Equation (4) is incomplete without boundary conditions. These are:

1. Continuity of $\phi(\mathbf{r}, \nu, \Omega, t)$ along the line $S = R + \lambda \Omega$ where λ is variable.

2. Vacuum boundary conditions at the ultimate extremities of the system, for all time.

3. ϕ not identically zero

For the critical system, $\nu = \nu_c$, $\phi = \phi_c$, and we may equate the time-dependent term to zero.

In what follows, an operator notation is used.

X is the operator converting a flux to a fission source:

$$X\phi \Rightarrow \frac{\chi}{4\pi} \iint \nu_c \Sigma_f \phi dv' d\Omega'; \quad (5)$$

S is the operator converting a flux to a scattered flux:

$$S\phi \Rightarrow \iint \Sigma_s \phi S dv' d\Omega'. \quad (6)$$

Then in the critical case, Eq. (4) may be written.

$$\Omega \cdot \nabla \phi_c + \Sigma \phi_c - X\phi_c - S\phi_c = 0. \quad (7)$$

The critical adjoint equation may also be written

$$-\Omega \cdot \nabla \phi_c^+ + \Sigma \phi_c^+ - X^+ \phi_c^+ - S^+ \phi_c^+ = 0. \quad (8)$$

The adjoint equation has adjoint-vacuum boundary conditions and the same continuity and non-zero conditions as the flux equation. The adjoint operators X^+ and S^+ are:

$$X^+ \phi^+ \Rightarrow \frac{\nu_c \Sigma_f(v)}{4\pi} \iint \chi \phi^+ dv' d\Omega', \quad (9)$$

$$S^+ \phi^+ \Rightarrow \Sigma_s(v) \iint \phi^+ S(\mathbf{r}; \nu, \Omega \cdot \Omega', \nu') dv' d\Omega'. \quad (10)$$

If Eq. (1) is satisfied, it may be substituted into Eq. (4) along with the simplifying notation previously defined, to yield

$$\Omega \cdot \nabla \phi + \Sigma \phi - X\phi - S\phi = (\delta\nu/\nu)X\phi - (\alpha/\nu)\phi. \quad (11)$$

We now multiply Eq. (11) by ϕ_c^+ on both sides, and integrate over space, speed, and direction. The left-hand side becomes

$$\iiint \phi_c^+ (\Omega \cdot \nabla + \Sigma - X - S) \phi d\mathbf{r} dv d\Omega,$$

which, deriving from our selection of adjoint, is the same as

$$\iiint \phi (-\Omega \cdot \nabla + \Sigma - X^+ - S^+) \phi_c^+ d\mathbf{r} dv d\Omega.$$

This last is identically zero.

Then, from Eq. (2)

$$\ell = \frac{\iiint \frac{1}{\nu} \phi_c^+ \phi d\mathbf{r} dv d\Omega}{\iiint \phi_c^+ [X\phi] d\mathbf{r} dv d\Omega}. \quad (12)$$

As $(\delta\nu/\nu) \rightarrow 0$, $\phi \rightarrow \phi_c$, so that from Eq. (3),

$$\ell(0) = \frac{\iiint \frac{1}{\nu} \phi_c^+ \phi_c d\mathbf{r} dv d\Omega}{\iiint \phi_c^+ [X\phi_c] d\mathbf{r} dv d\Omega}. \quad (13)$$

Equations (12) and (13) are exact relations. It now remains to approximate ϕ_c and ϕ_c^+ .

CONSISTENT P-1 APPROXIMATION

Since diffusion theory is used widely to obtain results for specific systems, the consistent P-1 approximation is important. The simplest correct reduction is to assume that:

$$\phi(\mathbf{r}, \nu, \Omega) = (1/4\pi)[F(\mathbf{r}, \nu) + 3\Omega \cdot \mathbf{J}(\mathbf{r}, \nu)] \quad (14)$$

where F is the scalar flux and \mathbf{J} is the current.

Substituting Eq. (14) into Eq. (4), using $\alpha\phi/\nu$ to replace $d\phi/dt$, and integrating over $d\Omega$ gives:

$$\begin{aligned} \nabla \cdot \mathbf{J}(\mathbf{r}, \nu) + \left[\Sigma(\mathbf{r}, \nu) + \frac{\alpha}{\nu} \right] F(\mathbf{r}, \nu) \\ = \chi(\nu) \int dv' \nu(\mathbf{r}, \nu') \Sigma_f(\mathbf{r}, \nu') F(\mathbf{r}, \nu') \\ + \int dv' \int d\Omega' \int \alpha \Omega' \cdot \frac{\Sigma_s(\mathbf{r}, \nu')}{4\pi} \\ \cdot [F(\mathbf{r}, \nu') + 3\Omega' \cdot \mathbf{J}(\mathbf{r}, \nu')] S(\mathbf{r}; \nu', \Omega \cdot \Omega', \nu). \end{aligned} \quad (15)$$

S may now be expanded in Legendre polynomials of $\Omega' \cdot \Omega$. That is,

$$S = \frac{f(\mathbf{r}; \nu', \nu)}{4\pi} + \frac{3}{4\pi} g(\mathbf{r}; \nu', \nu) \Omega' \cdot \Omega + \dots \quad (16)$$

Note that $\iint S d\Omega dv$ is the probability that a neutron when scattered lands at some speed-angle point. This probability is unity. Hence,

$$\int f(\mathbf{r}; \nu', \nu) dv = 1. \quad (17)$$

Also, $\iint S(\Omega' \cdot \Omega) d\Omega dv$ is the mean scattering cosine, which will be written as $\bar{\mu}(\mathbf{r}, \nu')$. It thus follows that:

$$\int g(\mathbf{r}; \nu', \nu) dv = \bar{\mu}(\mathbf{r}, \nu'). \quad (18)$$

The substitution of Eq. (16) into Eq. (15) and per-

formance of the indicated integrations yields:

$$\begin{aligned} \nabla \cdot \mathbf{J}(\mathbf{r}, \nu) + \left[\Sigma(\mathbf{r}, \nu) + \frac{\alpha}{\nu} \right] F(\mathbf{r}, \nu) \\ = \chi(\nu) \int dv' \nu(\mathbf{r}, \nu') \Sigma_f(\mathbf{r}, \nu') F(\mathbf{r}, \nu') \\ + \int dv' \Sigma_s(\mathbf{r}, \nu) F(\mathbf{r}, \nu') f(\mathbf{r}, \nu', \nu). \end{aligned} \quad (19)$$

More complicated algebra follows the premultiplication of Ω into Eq. (4) before integrating. The result is displayed here:

$$\begin{aligned} \frac{1}{3} \nabla F(\mathbf{r}, \nu) + \left[\Sigma(\mathbf{r}, \nu) + \frac{\alpha}{\nu} \right] \mathbf{J}(\mathbf{r}, \nu) \\ = \int dv' \Sigma_s(\mathbf{r}, \nu') \mathbf{J}(\mathbf{r}, \nu') g(\mathbf{r}, \nu', \nu). \end{aligned} \quad (20)$$

Define operators X , \mathfrak{F} , \mathfrak{G} so that

$$\begin{aligned} X(\mathbf{r}) \Psi &\equiv \chi(\nu) \int dv' \nu(\mathbf{r}, \nu') \Sigma_f(\mathbf{r}, \nu') \Psi(\mathbf{r}, \nu'), \\ \mathfrak{F}(\mathbf{r}) \Psi &\equiv \int dv' \Sigma_s(\mathbf{r}, \nu') \Psi(\mathbf{r}, \nu') f(\mathbf{r}, \nu', \nu), \\ \mathfrak{G}(\mathbf{r}) \Psi &\equiv \int dv' \Sigma_s(\mathbf{r}, \nu') \Psi(\mathbf{r}, \nu') g(\mathbf{r}, \nu', \nu). \end{aligned} \quad (21)$$

In the definitions [Eq. (21)], the operators are position-dependent. Only if the sigmas, ν , f , and g are independent of position are X , \mathfrak{F} , and \mathfrak{G} also position-independent.

Returning to the argument, we may now write symbolically:

$$\nabla \cdot \mathbf{J} + [\Sigma + (\alpha/\nu) - X - \mathfrak{F}] F = 0, \quad (22)$$

$$\frac{1}{3} \nabla F + [\Sigma + (\alpha/\nu) - \mathfrak{G}] \mathbf{J} = 0. \quad (23)$$

Equations (22) and (23) are a pair of coupled integro-differential equations. Their canonical boundary- and continuity-conditions are:

(i) Continuity of F

(ii) Continuity of \mathbf{J} over all regions in which physical properties are continuous, and of the component of \mathbf{J} normal to all surfaces across which properties change abruptly

(iii) F proportional to the normal component of \mathbf{J} at all external surfaces of the system. That is

$$F dS + \lambda \mathbf{J} \cdot d\mathbf{S} = 0 \quad (24)$$

at all external surfaces, dS

A diffusion operator, \mathfrak{D} , is now defined such that

$$-\mathfrak{D} \nabla F \equiv \mathbf{J} \quad (25)$$

in terms of which Eq. (23) becomes the defining equa-

tion for \mathfrak{D} :

$$\left\{ \frac{1}{3} - [\Sigma + (\alpha/\nu) - \mathfrak{G}] \mathfrak{D} \right\} \nabla F = 0 \quad (26)$$

and Eq. (22) becomes

$$\nabla \cdot \mathfrak{D} \nabla F - [\Sigma + (\alpha/\nu) - X - \mathfrak{F}] F = 0. \quad (27)$$

Note that the existence of a solution \mathfrak{D} of Eq. (26) is required without at this time requiring that this solution be unique.

We now search for adjoints to Eq. (27) at criticality. Such an adjoint is

$$\nabla \cdot \mathfrak{D}_c^+ \nabla F_c^+ - [\Sigma - X^+ - \mathfrak{F}^+] F_c^+ = 0. \quad (28)$$

We must, however, determine a defining equation for \mathfrak{D}_c^+ and suitable boundary conditions (in addition to continuity of F_c^+ and $\mathfrak{D}_c^+ \nabla F_c^+$).

A suitable defining equation is:

$$\left\{ \frac{1}{3} - (\Sigma - \mathfrak{G}^+) \mathfrak{D}_c^+ \right\} \nabla F_c^+ = 0 \quad (29)$$

and useful boundary conditions are:

$$F_c^+ \mathfrak{D}_c \nabla F_c \cdot d\mathbf{S} = F_c \mathfrak{D}_c^+ \nabla F_c^+ \cdot d\mathbf{S}. \quad (30)$$

The critical equations are also displayed as

$$\left\{ \frac{1}{3} - (\Sigma - \mathfrak{G}) \mathfrak{D}_c \right\} \nabla F_c = 0, \quad (31)$$

$$\nabla \cdot \mathfrak{D}_c \nabla F_c - [\Sigma - X_c - \mathfrak{F}] F_c = 0. \quad (32)$$

We are now ready to multiply Eq. (27) by F_c^+ and integrate. Then, remembering that $X = X_c + (\delta\nu/\nu) X_c$

$$\begin{aligned} \iint F_c^+ \nabla \cdot \mathfrak{D} \nabla F d\mathbf{r} d\nu - \iint F_c^+ (\Sigma - X_c - \mathfrak{F}) F d\mathbf{r} d\nu \\ = \iint F_c^+ [(\alpha/\nu) - (\delta\nu/\nu) X_c] F d\mathbf{r} d\nu. \end{aligned} \quad (33)$$

After some manipulation, including the application of boundary conditions (which cause the surface terms to cancel),

$$\begin{aligned} - \iint (\nabla F_c^+ \cdot \mathfrak{D} \nabla F - \nabla F \cdot \mathfrak{D}_c^+ \nabla F_c^+) d\mathbf{r} d\nu \\ = \iint F_c^+ [(\alpha/\nu) - (\delta\nu/\mu) X_c] F d\mathbf{r} d\nu. \end{aligned} \quad (34)$$

Use is made of Eqs. (26) and (29), from which may be derived, after appreciable algebra:

$$\begin{aligned} \iint (\nabla F \cdot \mathfrak{D}_c^+ \nabla F_c^+ - \nabla F_c^+ \cdot \mathfrak{D} \nabla F) d\mathbf{r} d\nu \\ = 3 \iint (\alpha/\nu) (\mathfrak{D}_c^+ \nabla F_c^+) \cdot (\mathfrak{D} \nabla F) d\mathbf{r} d\nu. \end{aligned} \quad (35)$$

The technique used in the derivation of Eq. (35) is to pre-multiply Eq. (26) by $\mathfrak{D}_c^+ \nabla F_c^+$, Eq. (29) by $\mathfrak{D} \nabla F$, and subtract.

From Eqs. (34) and (35) we get, finally:

$$\ell = \frac{\int F_c^+(1/v)F - 3 \int (\mathfrak{D}_c^+ \nabla F_c^+) (1/v) (\mathfrak{D} \nabla F)}{\int F_c^+ X_c F}, \quad (36)$$

$$\ell(0) = \frac{\int F_c^+(1/v)F_c - 3 \int (\mathfrak{D}_c^+ \nabla F_c^+) (1/v) \cdot (\mathfrak{D}_c \Delta F_c)}{\int F_c^+ X_c F_c}. \quad (37)$$

THE ONE GROUP REACTOR

In the one-group case, \mathfrak{D} reduces to D , a constant over any one region. The integrals involved in evaluating ℓ and $\ell(0)$ become simple volume integrals. Moreover, \mathfrak{D}^+ also reduces to D , and the one-group equations may be used to yield:

$$\ell = \frac{1}{\nu \Sigma_f} \frac{\int_{\text{reactor}} F^2 dV - \int_{\text{reactor}} 3 |D \nabla F|^2 dV}{\int_{\text{core}} F^2 dV}. \quad (38)$$

If, in addition, the reactor is unreflected and is large enough so that the simple boundary condition $F(S) = 0$ is approximately valid,

$$\begin{aligned} \ell &= \frac{1}{\nu \Sigma_f} \left(1 + 3D^2 \frac{\int F \nabla^2 F dV}{\int F^2 dV} \right) \\ &= \frac{1}{k_\infty \Sigma_a \nu} (1 - 3D^2 B^2). \end{aligned} \quad (39)$$

Thus, in this case, the lifetime is reduced from that of the usual formulation ($\ell = 1/k_\infty \Sigma_a \nu$) by the factor $(1 - 3D^2 B^2)$. The reason for the appearance of this term is that the "perturbation" α/v , which has the effect of bringing the time-dependent equations into a pseudo-critical form, acts identically as though an incremental $1/v$ poison were introduced into the system. In diffusion theory (consistent P -1, rather than asymptotic), this introduction modifies both the neutron absorption cross section and the transport cross section. In a word, the introduction of time dependence—or of $1/v$ poison—is a double perturbation on the system.

The result has been obtained before¹ for a source-sink system. The result displayed here differs from that cited because, in a multiplying system, the effective absorption cross section is negative.

DISCUSSION

Equations (36) and (37) are the proper consistent P -1 diffusion equations for reactor lifetime. The second

term in the numerator of these equations may be significant for reactors where B^2 is large. These are, however, reactors for which diffusion theory is not applicable. The proper transport equations, Eqs. (12) and (13), must be used in these cases. The transport-theory fluxes and adjoints cannot be reliably approximated by diffusion forms without including current-like terms.

DIFFUSION THEORY CONTINUITY CONDITIONS AND NEUTRON CURRENT REFRACTION

The Boltzmann equation for neutron transport deals primarily with flux rays $[\phi(\mathbf{r}, \Omega)]$ which are defined as continuous only along the path of neutron travel. This path is the line $\mathbf{r} + s\Omega$, s being a scalar variable.

In the reduction of this problem by the method of spherical harmonics (or any method differential in space), the differential flux in space is integrated over appropriate angular coordinates to get total flux, current, etc. This integration introduces formal continuity in space to the integrated variable, in the same sense that a Fourier series representation of a discontinuous function is continuous for any finite truncation. Similarly, an angular distribution continuity is introduced as a formal matter.

These continuities cause difficulties. The most extreme case is the determination of black body boundary conditions: here, as is well known, no finite angular distribution series can reproduce the true conditions; hence there is a degree of arbitrariness to any boundary condition used. This confusion is constrained only by physical reasonableness—a non-formal addendum to the problem.

Within the body of a uniform scattering region, simple continuity of all of the flux components is also a mathematically simple and physically reasonable condition. In fact it is physically correct and causes no problems. Indeed, in any system where variation of cross sections is smooth, no problem exists. However, the same difficulties which plague the Milne problem reappear at any boundary where physical properties are discontinuous. The particular difficulty with which this note is concerned is the apparent irrelevance of current continuity, for components parallel to boundaries, in diffusion theory.

FORMULATION

The neutron flux as a function of position and direction is approximated in diffusion theory by the equation:

$$4\pi\phi(\mathbf{r}, \Omega) = F(\mathbf{r}) + 3\Omega \cdot \mathbf{J}(\mathbf{r}) \quad (40)$$

where $F(\mathbf{r})$ and $\mathbf{J}(\mathbf{r})$ are described as the total flux and diffusion-theory current, respectively.

From Eq. (40) and the Boltzmann equation (one-group, steady-state isotropic system)

$$\begin{aligned} \Omega \cdot \nabla \phi(\mathbf{r}, \Omega) + \Sigma \phi(\mathbf{r}, \Omega) \\ = \frac{C}{4\pi} \int \Sigma(\mathbf{r}) \phi(\mathbf{r}, \Omega') S(\mathbf{r}, \Omega' \cdot \Omega) d\Omega' \end{aligned} \quad (41)$$

with S as a (normalized) scattering function and C being secondary for collision, we may derive the diffusion equations:

$$\nabla \cdot \mathbf{J} + \Sigma(1 - C)F = 0, \quad (42)$$

$$\frac{1}{3} \nabla F + \Sigma(1 - \bar{\mu}C)\mathbf{J} = 0. \quad (43)$$

$\bar{\mu}$ is the mean cosine of the change of neutron direction per secondary neutron emitted.

From Eq. (43), Fick's Law is obtained:

$$\mathbf{J} = -D \nabla F, \quad D = \frac{1}{3\Sigma(1 - \bar{\mu}c)}. \quad (44)$$

The original Boltzmann equation continuity condition requires that F and \mathbf{J} be continuous in \mathbf{r} , if Eq. (40) is a good approximation. Since \mathbf{J} is a vector, we have, in general, four continuity conditions in P -1 diffusion theory.

Now let us look at a boundary, across which D , as defined by Eq. (44), is discontinuous. Conservation of neutrons demands that the component of \mathbf{J} normal to the boundary be continuous. However, continuity of tangential components of \mathbf{J} (defined by Fick's law) and continuity of flux are incompatible, as may be readily seen by the following argument:

Let \mathbf{h} be a vector parallel to the boundary

$$\mathbf{h} \cdot \mathbf{J} = -D\mathbf{h} \cdot \nabla F = -D(\partial F / \partial X_h),$$

where X_h is a position variable along \mathbf{h} .

Thus, the component of \mathbf{J} in the \mathbf{h} direction will vary at a rate proportional to that of F in the same direction; but the constant of proportionality will be different on the two sides of the boundary, given different D . In consequence, $\mathbf{h} \cdot \mathbf{J}$ and F on the two sides of the boundary cannot be simultaneously identical except at isolated points, or unless they are both constant.

The situation may be resolved—and correctly, considering the nature of the approximation in Eq. (40)—by taking D as both a dyadic and a variable in \mathbf{r} . When this is done, the inconsistency disappears. It is to be noted, however, that this is done by accepting continuity of flux, and altering the definition of current. This leads to acceptable solutions of physical problems.

Another way of resolving the problem is by continuing to treat D as a scalar, but letting it vary continuously over a small buffer zone. This, too, yields acceptable physical solutions, and permits F and all three com-

ponents of \mathbf{J} to be continuous. However, it introduces rotational properties into the system; for:

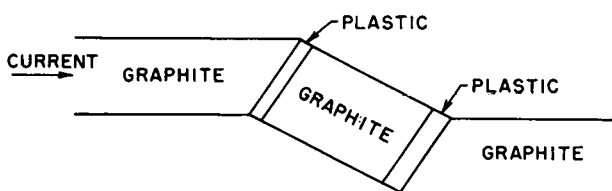
$$\begin{aligned} \nabla \times \mathbf{J} = \nabla \times D \nabla F = \nabla D \times \nabla F + D(\nabla \times \nabla F) \\ = \nabla D \times \nabla F \end{aligned} \quad (45)$$

since F is a continuous scalar.

Physically, this implies that a neutron current is capable of being refracted.

A POSSIBLE APPLICATION

If this rotational property is real, neutron current refraction might be useful for zigzagging a thermal column to avoid core X-ray or fast neutron background. Consider a graphite thermal column with two sheets of water or plastic as indicated:



It is possible that this system, even considering neutron absorption in the plastic, would transmit more neutrons more uniformly than the system without inserts.

THE MILNE PROBLEM

The Milne problem may be written as the solution of

$$\mu \frac{\partial}{\partial x} \phi(x, \mu) + \phi(x, \mu) = \frac{1}{2} \int_{-1}^1 \phi(x, \mu) d\mu \quad (46)$$

subject to the boundary conditions that:

$$\int_{-1}^1 \mu \phi(x, \mu) d\mu = -1, \quad (47)$$

$$\phi(0, \mu) = 0 \quad \text{for } \mu > 0. \quad (48)$$

The solution of this problem is given by:

$$\int_{-1}^1 \phi(x, \mu) d\mu = 3x + a + \psi(x) \quad (49)$$

where " a " is a constant (equal to 0.7104...) and ψ a function which falls off more rapidly than e^{-x} .

ψ may be represented as an integral:

$$\psi = \int_1^{\infty} e^{-px} f(p) dp,$$

and therefore the question arises as to whether e^{-px} , ($p > 1$) can in any sense be treated as an eigenfunction of the problem. K. Case² has demonstrated that it can be. His proof is very abstract, and thereby loses some contact with physical reality. An argument which justi-

fies treating e^{-pz} as an eigenvalue, and which has a closer relation to the physical problem, is given below:

If

$$\phi(x, \mu) = \int e^{-pz} f(p, \mu) dp,$$

such that

$$\int_{-1}^1 f(p, \mu) d\mu = f(p)$$

then substitution into Eq. (46) yields

$$(1 - \mu p)f(p, \mu) = \frac{1}{2} \int_{-1}^1 f(p, \mu) d\mu. \quad (50)$$

Equation (50) must have a solution for e^{-pz} to be an eigenfunction.

In the method of discrete ordinates, the integral on the right hand side of Eq. (50) is approximated by a suitable summation formula:

$$\frac{1}{2} \int_{-1}^1 f(p, \mu) d\mu \approx \sum_{i=1}^n a_i f(p, \mu_i). \quad (51)$$

Then Eq. (50) becomes, for each μ_i ,

$$(1 - \mu_i p)f(p, \mu_i) = \sum_{j=1}^n a_j f(p, \mu_j). \quad (52)$$

Equation (52) is a set of homogeneous equations in the variables $f(p, \mu_i)$, and has a solution only for certain values of p , the eigenvalues of the algebraic system [Eq. (52)].

The foregoing method is essentially the method of Fredholm and it bypasses the usual problem of principal-value integration.

A physical description analogous to the Fredholm method is that the functional in the integral is represented as a bar diagram in the variable μ , both within and outside the integral.

It is well known that, as the number of points (n) in the μ integral increases, the eigenvalues p_k approach 0 for the lowest value and for the rest cluster, more or less uniformly, in the region $1/p = (0, 1)$. These eigenvalues are, of course, mathematical artifacts; but this does not prevent the solutions by such artifice from being perfectly reasonable approximate solutions. The main physical point is to adhere to a bar diagram description of μ -variation; any other technique is a violation of the basis of the approximation.

It is now possible to describe the sense in which the e^{-pz} are eigenfunctions of the transport problem. They are eigenfunctions in the sense that the discrete ordinate approximations of very large order have eigenfunctions $e^{-p_k z}$ with some p_k as close as is necessary to any arbitrary p . The integral:

$$\int e^{-pz} f(p, \mu) dp$$

is essentially an approximation to a sum

$$\sum_i e^{-p_i z} a_i(p_i) f_i(p_i, \mu_k)$$

which is in its turn an approximation to the true solution.

Note that there is no physical necessity for f to be continuous in μ ; merely integrable. It is nevertheless true that f approaches a continuous function in μ (except at a vacuum boundary) as " n " becomes large.

$f(p)$ has other interesting properties. It may be represented as the solution of an integral equation. The Milne problem may be written alternately as:

$$\begin{aligned} \Phi(x) &\equiv \int_{-1}^1 \phi(x, \mu) d\mu \\ &= \frac{1}{2} \int_0^\infty \Phi(y) E_1 |x - y| dy \end{aligned} \quad (53)$$

with

$$E_1(z) \equiv \int_1^\infty \frac{e^{-uz} du}{u}. \quad (54)$$

Then, since

$$\Phi(x) = \int_0^\infty f(p) e^{-pz} dp, \quad (55)$$

$$\begin{aligned} \int_0^\infty f(p) e^{-pz} dp &= \frac{1}{2} \int_0^\infty f(p) dp \\ &= \int_1^\infty \frac{du}{u} \left\{ \frac{e^{-pz}}{u+p} + \frac{e^{-uz} - e^{-pz}}{p-u} \right\}. \end{aligned} \quad (56)$$

In Eq. (56), the main difficulty in reduction arises from the fact that, while the term $(e^{-uz} - e^{-pz})/(p-u)$ is non-singular, any attempt at successive quadrature by integrating first over the variable not containing an exponential leads to difficulties. This is avoided by observing that the integral over $dpdu$ is trivially different from the integral obtained by excluding the strip $-\epsilon < p - u < \epsilon$ from the integration.

We use the notation:

$$\begin{aligned} \text{Pr} \left\{ \int_a^b \frac{f(s) ds}{s-t} \right\} &\equiv \text{Lim}_{\epsilon \rightarrow 0} \left\{ \int_a^{t-\epsilon} \frac{f(s) ds}{s-t} \right. \\ &\quad \left. + \int_{t+\epsilon}^b \frac{f(s) ds}{s-t} \right\}. \end{aligned} \quad (57)$$

After some manipulation of Eq. (56), we arrive at:

$$\begin{aligned} \int_0^\infty f(p) e^{-pz} dp &= \int_0^\infty f(p) e^{-pz} \left\{ \frac{1}{2p} \ln \frac{p+1}{|p-1|} \right\} \\ &\quad + \frac{1}{2} \int_1^\infty \frac{du}{u} e^{-uz} \text{Pr} \left\{ \int_0^\infty \frac{f(p) dp}{p-u} \right\}. \end{aligned} \quad (58)$$

If, in Eq. (58), P and u are interchanged in the last integral—a change which is merely one of notation—we finally obtain:

$$\int_0^\infty f(p) e^{-px} dp = \int_0^\infty f(p) e^{-px} \left\{ \frac{1}{2p} \ln \frac{p+1}{|p-1|} \right\} + \frac{1}{2} \int_1^\infty \frac{dp}{p} e^{-px} \text{Pr} \left\{ \int_0^\infty \frac{f(u) du}{u-p} \right\}. \quad (59)$$

Finally, Eq. (59) may be rewritten as:

$$f(p) \left(1 - \frac{1}{2p} \ln \frac{1+p}{1-p} \right) = 0 \quad \text{for } (p < 1) \\ f(p) \left(1 - \frac{1}{2p} \ln \frac{p+1}{p-1} \right) = \frac{1}{2p} \text{Pr} \left\{ \int_0^\infty \frac{f(u) du}{u-p} \right\} \quad \text{for } (p > 1). \quad (60)$$

$f(p)$ is also a generating function for the Laplace transform of the Milne problem. If

$$\mathcal{L}(q) \equiv \int_0^\infty e^{-qx} \Phi(x) dx \quad (61)$$

then

$$\mathcal{L}(q) \equiv \int_0^\infty f(p) dp / (p+q). \quad (62)$$

A simple interpretation of $\mathcal{L}(q)$ [which is related to (p) by Eq. (62)] is given below.

Multiply Eq. (46) by $e^{x/\mu}$ on both sides, and, for μ negative, integrate from x to ∞ . Then,

$$\phi(x, \mu) = -\frac{1}{2\mu} \int_x^\infty e^{-(x-y)/\mu} \Phi(y) dy \quad (63) \\ \text{for } (\mu < 0).$$

Then, for $x = 0$

$$-2\mu\phi(0, \mu) = \int_0^\infty e^{y/\mu} \phi(y) dy, \quad (64) \\ (\mu < 0).$$

Letting $-\mu = 1/q$

$$\frac{2}{q} \phi(0, -1/q) = \int_0^\infty e^{-qv} \Phi(y) dy = \mathcal{L}(q), \quad (65) \\ (1 < q < \infty).$$

Thus, the Laplace transform of the total flux, is, for $q > 1$, simply related to the angular distribution of the emerging current.

REFERENCES

1. A. M. Weinberg and E. P. Wigner, *The Physical Theory of Neutron Chain Reactors*, (The University of Chicago Press, Chicago, 1958) p. 235 et seq.
2. K. M. Case, *Elementary Solution of the Transport Equations and Their Applications*, Ann. Phys. 9, No. 1, 1 (1960).

V-2. Effects of Resonance Interference*

C. N. KELBER

Neutrons, propagating in a medium composed of a mixture of isotopes, are absorbed in isotope resonances. If two or more isotopes have resonances which are close in energy, the absorption rate in each resonance is influenced by the absorption rate in neighboring resonances.

Thus, in mixtures of U-235 and U-238, the absorption rate in U-235 resonances from 4.8 to 8.8 eV is strongly influenced by the absorption rate in the large U-238 resonance at 6.7 eV.

A computer code, 1559/RE, has been written to investigate various approximate solutions to the problem. A report on a typical version of this code has been published.²

1559/RE is an experimental IBM-704 code in FORTRAN language to compute the resonance integrals of

isotopes in mixtures in the presence of hydrogenic moderation. There may be up to four isotopes, each with no more than 75 resolved resonance levels. Doppler broadening and interference scattering are included. No estimate is made of contributions from unresolved resonances. Typical running times are 30 min (no Doppler broadening) to 90 min (with Doppler broadening) for problems involving 67 levels and unit lethargy widths.

Two approximations have been investigated to date; the narrow resonance (moderator) approximation and the infinite mass approximation.

EQUATIONS SOLVED—NARROW RESONANCE APPROXIMATION

The collision density is given by an integral equation involving scattering by atoms of all species.³ In this ap-

* See also, Ref. 1.

proximation it is assumed that all atoms are heavy or light (moderator) and in the moderator terms the collision density is replaced by its asymptotic form. In using the code the moderator constants should be adjusted to give the correct asymptotic form.

Code 1559/RE solves the equations:

$$F(u) = \frac{1}{\alpha} \int_{u-\Delta}^u F(u') a(u') du' + \frac{\Sigma_m}{E(u)}, \quad (1)$$

$$\text{RESINT}(i,j) = N_i \int_{u(E_U)}^{u(E_L)} F(u) E(u) \frac{\sigma_{ji}}{\Sigma_i} du \quad (2)$$

where RESINT is the resonance integral times the atomic density.

$F(u)$ = collision density at lethargy u per unit energy

E_U = upper energy limit (eV)

E_L = lower energy limit (eV)

$E(u) = e^{-u} E_U$

Σ_m = "moderator" scattering cross section

α = heavy atom scattering term,

$$\alpha = 4A/(A+1)^2$$

Δ = maximum logarithmic decrement in lethargy from heavy atom scattering

N_i = number of atoms of isotope i per barn-cm

σ_{ji} = absorption ($j = a$) or fission ($j = f$) cross section of isotope i at energy $E(u)$

$a(u)$ = heavy atom scattering cross section divided by the total cross section

The Doppler broadened line shapes are obtained from the W subroutine of H. Thacher and D. O'Shea.⁴

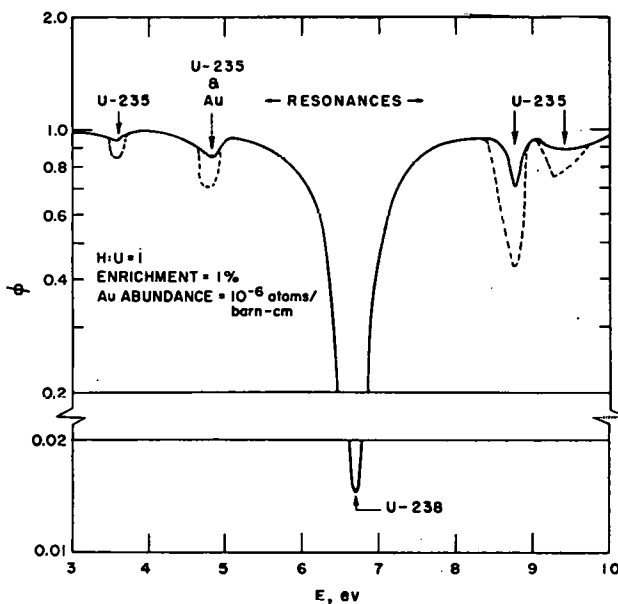


FIG. V-2-1. Flux Per Unit Lethargy in an H/U Mixture.

EQUATIONS SOLVED—INFINITE MASS APPROXIMATION

In this case, scattering by the heavy atoms is neglected. The equation solved is:

$$(d\psi/du) + (\Sigma_a/\Sigma)\psi = 0,$$

$$\psi = \Sigma(0) \quad \text{at } u = 0$$

where

u = lethargy

ψ = collision density per unit lethargy

Σ_a = total absorption cross section

Σ = total cross section

It is assumed that

$$\psi = \psi(u_i) + \frac{u - u_i}{u_{i+1} - u_i} [\psi(u_{i+1}) - \psi(u_i)],$$

$$u_i \leq u \leq u_{i+1}.$$

The machine equation is then

$$\psi(u_{i+1}) = \psi(u_i) [1 + 0.5\delta R(i)] / [1 - 0.5\delta R(i+1)]$$

where

$$\delta = u_{i+1} - u_i = \text{constant},$$

$$R(i) = \Sigma_a[u(i)] / \Sigma[u(i)].$$

In all other respects this version of the code is similar to the narrow resonance version.

TYPICAL RESULTS

An interesting case to study is a low enrichment, high conversion lattice. A mixture of water and uranium in equal volumes was taken as an example. (Rod size effects were neglected at this point.) The temperature was 0°K and the heavy atom scattering mass was 238. Three U-235 enrichments were studied: 1, 2, and 3%. In addition, Au at 10^{-6} atoms/(b-cm) was included to study the response of a typical monitor foil.

The narrow resonance version of the code was used to calculate the real fluxes, and these are plotted, for 1% enrichment, in Fig V-2-1. Also shown on Fig. V-2-1 are the changes in the flux when calculated at 3% enrichment. The flux perturbations from the various resonances are clearly seen. Note also the affect of the 6.68 eV U-238 resonance and the 4.84 eV U-235 resonance on the Au resonance at 4.91 eV. The Au resonance integral over the energy range indicated is given in Table V-2-I for the various enrichments. The shielding is due mostly to U-238, but there is a small effect from U-235.

Figure V-2-2 is a graph of the U-235 resonance integral as a function of enrichment. Based on moderator scattering per U-235 atom, a larger variation in the cross section as well as a larger cross section would be

TABLE V-2-I. RESONANCE INTEGRAL OF DILUTE GOLD IN IN H:U = 1 MIXTURE. ENERGY RANGE 3-10 eV

Enrichment, %	Resonance Integral, barns
1	1357
2	1337
3	1333

Resonance integral over this energy range and 1/E spectrum: 1445 b.

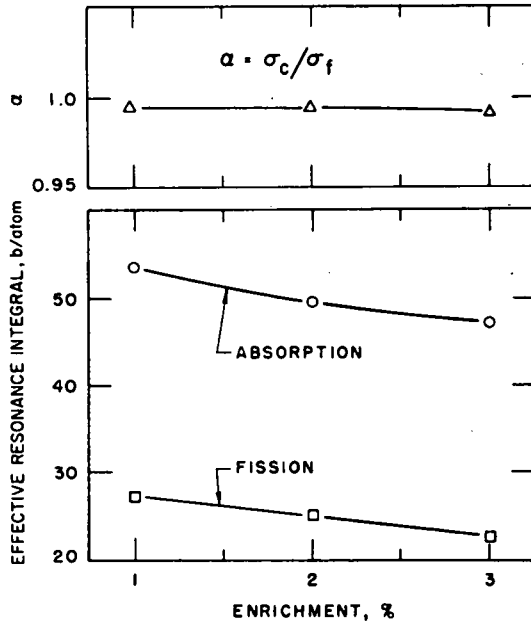


FIG. V-2-2. Effective Resonance Integrals of U-235 in H:U = 1 Mixture; and α of U-235.

expected. The U-238 dominates the spectrum suppressing the scattering effect. Shielding by the U-238 amounts to about 20% of the cross section.⁵ The capture to fission ratio (α) in U-235 is practically constant as a function of enrichment (Fig. V-2-2).

For check purposes, infinite dilution integrals were calculated by using small abundances and these were checked against results obtained by use of the code RP-266,¹⁶ a code designed especially for computing infinite dilution integrals. For U-235, agreement was better than 0.1%

A somewhat different effect is encountered in the statistical region. J. Codd and P. Collins⁷ have studied the effects of accidental overlap in this region with regard to overlap.

In order to compare results with those of Codd and Collins, a study was made of a U-238:Pu-239 = 7 mixture in the presence of 525 b scattering per Pu-239 atom. The cavalier treatment of light atom scattering is hardly justified here, but the principal results are not

much affected by this approximation since we are concerned with the resonance integral over a narrow range only.

The notion is that in the statistical region (i.e., several hundred eV and up) any averaging procedure must take into account the chances that a U-238 and Pu-239 resonance (say) will have the same resonant energy or very nearly so. Then the one will shield the other and the effective resonance integrals will be reduced. More important, as the temperature and, hence, Doppler broadening, increase the mutual shielding will change and thus the Doppler coefficient will be changed.

Following Codd and Collins, it was supposed that at 1000 eV U-238 has a resonance level described by the average U-238 parameters; and that at a nearby energy there is a Pu-239 level characterized by average Pu-239 parameters. The Pu-239 resonance integral from 980 to 1020 eV as a function of the separation of the two levels was studied next. To compare with the results of Codd and Collins the Pu-239 resonance integral was normalized to 1 at a separation of +5 eV. Since interference scattering is included in this description (Codd and Collins did not) negative separation has also been studied to include the asymmetry caused by this term. Finally it was assumed that the U-238 resonances are 18 eV apart

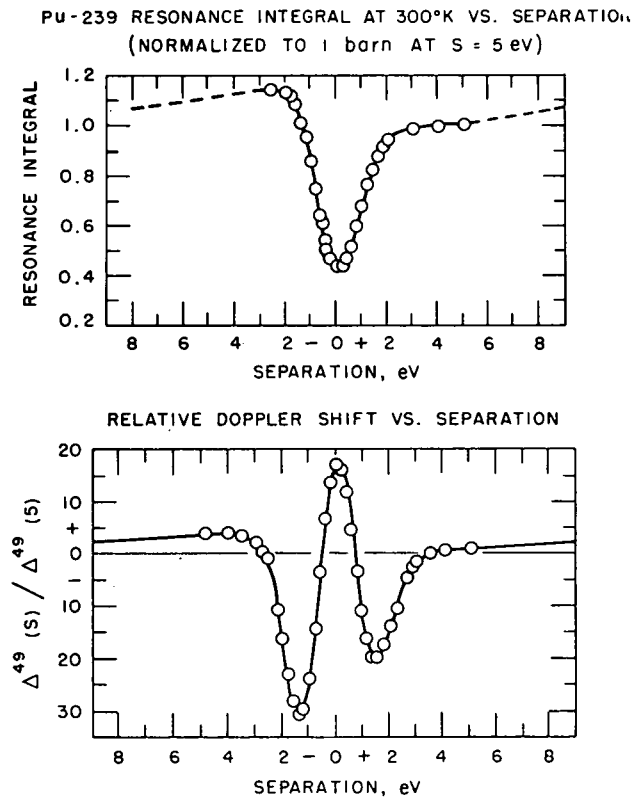


FIG. V-2-3. Overlap Effects in Pu-239 at 1 keV.

and this was used to extrapolate the resonance integral in the intervals $(-9, -5)$ and $(+5, +9)$ eV separations. The results are shown in Fig. V-2-3.

These results agree well with those of Codd and Collins over the range 0.2 eV to 5 eV as expected. The asymmetric effect of interference scattering is clearly shown in the figure. Moreover, this is an interference effect in both senses of the use of the term; i.e., interference between potential and resonant scattering and interference with resonance absorption in another isotope.

Again following the example of Codd and Collins, the change in Pu-239 resonance integral for a temperature change from 300°K to 600°K as a function of level separation was computed. Again the normalization is 1 at a separation of +5 eV. The asymmetry is marked here; and extrapolating to -9 , and $+9$ eV, as before, it is found that the Doppler shift averaged over separation is -1.33 times the Doppler at 5 eV.

This work is part of a continuing study of resonance absorption.

REFERENCES

1. C. N. Kelber, *Fluxes and Reaction Rates in the Presence of Interfering Resonances*, Trans. Am. Nucl. Soc., 6, 2, 273 (1963).
2. C. N. Kelber, *1559/RE: A Code to Compute Resonance Integrals in Mixtures*, ANL-6709 (1963).
3. L. W. Nordheim, *A Program of Research and Calculations of Resonance Absorption*, GA-2527 (August 28, 1961). *The Theory of Resonance Absorption*, Proceedings of Symposium in Applied Mathematics, Vol. XI, Nuclear Reactor Theory, pp. 58-88 (1961).
4. D. O'Shea and H. C. Thacher, Jr., *Computation of Resonance Line Shape Functions*, Trans. Am. Nucl. Soc. 6, No. 1 (1963).
5. C. N. Kelber, *Resolved Resonance Integrals at 0° K for U²³⁵*, Argonne National Laboratory, Reactor Physics Constants Center, Newsletter No. 8 (October 1, 1962).
6. P. J. Persiani, Argonne National Laboratory (private communication).
7. J. Codd and P. J. Collins, *Plutonium 239 and Uranium 238 Resonance Interaction Effects in a Dilute Fast Reactor*, EAES Symposium, Advances in Reactor Theory, Karlsruhe, 23-24, (April, 1963).

V-3. Resonance Parameter Analysis

E. N. PENNINGTON

A Fortran code has been written to determine single level Breit-Wigner resonance parameters from experimental data on total cross sections at various energies. Initial guesses are supplied for the resonance parameters and a least-squares fit is made to improve on the initial values. Cross section contributions from potential scattering and the tails of resonances outside the energy range under consideration are kept constant throughout the calculations. Angular momentum values of $\ell = 0, 1, 2$ are allowed. Estimates of errors in the derived resonance parameters are computed. Since the code is

designed to fit data in the keV region supplied by the Applied Nuclear Physics Section using a Van de Graaff accelerator, Doppler broadening and instrument resolution effects are not included. Doppler effects for the resonances under study are quite negligible, and resolution effects are small.

Test problems were run for which the "experimental" cross sections were computed by a preliminary Fortran code. The calculated resonance parameters converge rapidly to the correct values for these problems.

V-4. An Importance-Weighting Procedure for Averaging Group Parameters in Multigroup Diffusion Theory

DAVID H. SHAFTMAN and H. GREENSPAN*

INTRODUCTION

For much of the analysis of a reactor physics nature, it is useful to perform computations using a multigroup

diffusion theory where the number of groups is not very large. This is particularly the case in two or more dimensions, where the machine time and cost involved in solving multigroup problems, even with a very fast computer, might not be justified by the purpose of the com-

* Applied Mathematics Division.

putation. It is of interest, therefore, to develop methods of reducing the total number of neutron energy groups, with the constraint that the percentage error in a specific computed parameter be kept small. In such programs as MUFT¹ and GAM,² the fewer-group parameters are obtained as flux-weighted averages of multigroup parameters, where the multigroup fluxes are fundamental-mode solutions of the consistent P -1 or B -1 equations for some uniform bare reactor. In the following paragraphs, an importance-weighting procedure is developed formally from a perturbation-theory model. The application of this procedure will be to reduce the number of neutron energy groups, so as to synthesize N groups from M groups, $N \leq M$. The method applies also to the derivation of average parameters for N -group theory from the case of the continuous flux spectrum, if the continuous solution is available.

In developing the fewer-group parameters, the constraint will be the attempted preservation of the value of the effective multiplication factor, k_{eff} . This is not to say that the fewer-group model will yield precisely the same value of k_{eff} , other than in special cases such as the case of a uniform bare reactor. Indeed, the method must be tested in a number of different problems, to determine how effective it is in preserving the numerical magnitude of k_{eff} . These tests are in limbo until the completion of current work on a multigroup program which will permit the assignment of fission-spectrum distributions which are functions of the energy of the incident neutron. This flexibility is essential to the use of the proposed importance-weighting procedure, as will be shown in the following development.

Now, the full use of such a weighting procedure is not well defined, for at least it must be determined empirically how well the method works in relatively simple cases, e.g., one-dimensional reactor systems. The hope is that from a multigroup solution of one reactor problem, and the subsequent derivation of fewer-group parameters, other, similar reactors may be analyzed using the fewer-group theory. For example, perhaps one-dimensional solutions could be used to provide the group parameters to be used in fewer-group solutions of 2-dimensional problems.

The use of importance-weighting procedures, in this connection, is not new. A number of reactor physicists have proposed that adjoint-flux weighting be applied. Among them are D. S. Selengut,³ and B. H. Duane,⁴ in the U.S.; K. Parker,⁵ in the U. K.; and A. I. Novozhilov and S. B. Shikhov,⁶ and S. B. Shikhov and V. B. Troyanskii,⁷ in the U.S.S.R. The work reported below is new in the treatment of spatial averaging of group cross sections.

A GENERALIZED GROUP-SYNTHESIS METHOD FOR MULTIGROUP DIFFUSION THEORY

The basic multigroup system will consist of M coupled, homogeneous, linear differential equations of second order, describing an "equilibrium" condition of gain rates and loss rates of the neutron population in each elementary volume of a multi-zone reactor, where each zone is of a uniform material composition. Scattering from any one group to any other group is permitted. Provision is made for a dependence of the distribution of fission spectrum neutrons upon the group index of the incident neutron. If the reactor is not critical, in its final form, k_{eff} will be determined as the number by which each $\nu_k \chi(k, j)$ (the coefficient for transfer from fission events in group k to source neutrons in group j) is divided so as to make the new, fictitious system critical.

In this section, a procedure will be detailed for a reduction in the number of neutron energy groups, from M group to N groups, $N \leq M$. Such a procedure has been referred to variously as "group collapsing" or "group contracting", although in the process the energy spans of the groups increase, if changed at all. The method is alluded to here as a "group-synthesis" procedure.

One defining principle of a group-synthesis procedure is that the (multigroup) value of k_{eff} is to be invariant. The second condition which the group-synthesis method is to satisfy is that two successive group syntheses— N_1 groups to N_2 groups, followed by N_2 groups to N_3 groups—are to provide the same N_3 -group nuclear parameters as a single group synthesis from N_1 groups to N_3 groups. These conditions will be satisfied only approximately, in general, and exactly for the special case of a fundamental-mode spectrum.

In the following equations,

$$(1/4\pi)\Sigma_{(\cdot),j}^{(0)} T_{(\cdot)}^{(0)}(j \rightarrow k) \equiv (1/4\pi)\Sigma_{(\cdot)}^{(0)}(j \rightarrow k)$$

is the coefficient of the P_0 term of a terminated "Legendre expansion" of the macroscopic cross section, $\Sigma_{(\cdot)}(j \rightarrow k)$, for a particular mode of neutron transfer from group j to group k . The symbol (\cdot) denotes elastic transfer or inelastic transfer, for which the normalization is

$$\sum_{k=1}^M T_{(\cdot)}^{(0)}(j \rightarrow k) = 1;$$

or $(n, 2n)$ transfer, in which case

$$\sum_{k=1}^M T_{(\cdot)}^{(0)}(j \rightarrow k) = 2.$$

The total elastic, inelastic, and $(n, 2n)$ cross sections are denoted by $\Sigma_{el,j}^{(0)}$, $\Sigma_{in,j}^{(0)}$, and $\Sigma_{(n,2n),j}^{(0)}$, respectively.

DERIVATION OF THE GROUP-SYNTHESIS FORMULAS, STARTING WITH THE M-GROUP REAL-FLUX EQUATIONS

The basic multigroup diffusion equations for the real fluxes ϕ_j are:

$$\begin{aligned}
 0 = & \nabla \cdot D_j \nabla \phi_j - \phi_j \left[\Sigma_{c,j} + \Sigma_{f,j} \right. \\
 & + \frac{1}{2} \sum_{k=1}^M \Sigma_{(n,2n),j}^{(0)} T_{(n,2n)}^{(0)}(j \rightarrow k) \\
 & + \sum_{k=1}^M \Sigma_{in,j}^{(0)} T_{in}^{(0)}(j \rightarrow k) \\
 & \left. + \sum_{k=1}^M \Sigma_{el,j}^{(0)} T_{el}^{(0)}(j \rightarrow k) \right] \\
 & + \sum_{k=1}^M \phi_k \left[\frac{\chi(k,j) \nu_k \Sigma_{f,k}}{k_{eff}} + \Sigma_{(n,2n),k}^{(0)} T_{(n,2n)}^{(0)}(k \rightarrow j) \right. \\
 & \left. + \Sigma_{in,k}^{(0)} T_{in}^{(0)}(k \rightarrow j) + \Sigma_{el,k}^{(0)} T_{el}^{(0)}(k \rightarrow j) \right]; \\
 & 1 \leq j \leq M
 \end{aligned} \quad (1)$$

(Note that, in this model, the $(n,2n)$ source terms are treated as additional "slowing-down" terms rather than as fission-like source terms. For additional discussion of this model, refer to Paper No. II-1.)

Symbolically, this may be written:

$$0 = \nabla \cdot D_j \nabla \phi_j - \Sigma_{out,j} \phi_j + \sum_{k=1}^M \Sigma_{source}(k \rightarrow j) \phi_k. \quad (2)$$

The system of equations for the adjoint neutron flux is, symbolically:

$$0 = \nabla \cdot D_j \nabla \phi_j^* - \Sigma_{out,j} \phi_j^* + \sum_{k=1}^M \Sigma_{source}(j \rightarrow k) \phi_k^*. \quad (3)$$

Using the (unnormalized) real and adjoint multi-

$$\begin{aligned}
 0 = & \bar{D}_n \nabla^2 \Phi_n - \bar{\Sigma}_{R,n} \Phi_n + \sum_{k=1}^N \Phi_k \\
 & \cdot \left\{ \frac{(\nu \Sigma_f)_k \chi(k,n)}{k_{eff}} + \overline{\Sigma_{(n,2n),k}^{(0)} T_{(n,2n)}^{(0)}(k \rightarrow n)} + \overline{\Sigma_{in,k}^{(0)} T_{in}^{(0)}(k \rightarrow n)} + \overline{\Sigma_{el,k}^{(0)} T_{el}^{(0)}(k \rightarrow n)} \right\}
 \end{aligned} \quad (8)$$

group fluxes determined from the solution of Eq. (2) and of Eq. (3), respectively, the balance equation for coarse-group n ($1 \leq n \leq N$) is obtained by multiplying the p th equation in Eq. (2), term by term, by ϕ_p^* ; integrating over the zone; and summing over p , for $\alpha_n + 1 \leq p \leq \alpha_{n+1}$. (The notation requires that $\alpha_1 = 0$ and $\alpha_{N+1} = M$.)

Now define the point functions Φ_n and Φ_n^* by:

$$\Phi_n \equiv \sum_{p=\alpha_n+1}^{\alpha_{n+1}} \phi_p; \quad \Phi_n^* \equiv \sum_{p=\alpha_n+1}^{\alpha_{n+1}} \phi_p^*. \quad (4)$$

Define $\bar{\Sigma}_{R,n}$ by:

$$\bar{\Sigma}_{R,n} \int_{zone} \Phi_n \Phi_n^* dr \equiv \sum_{p=\alpha_n+1}^{\alpha_{n+1}} \int_{zone} \Sigma_{out,p} \phi_p \phi_p^* dr \quad (5)$$

where $\Sigma_{out,p}$ is the total isotropic cross section for group p . Each of the corresponding coarse-group weighted average loss rates is defined by an equation similar to Eq. (5).

Define $\overline{(\nu \Sigma_f)_k \chi(s,n)}$ by:

$$\begin{aligned}
 \overline{(\nu \Sigma_f)_k \chi(s,n)} \int_{zone} \Phi_s \Phi_n^* dr \\
 \equiv \sum_{p=\alpha_n+1}^{\alpha_{n+1}} \sum_{k=\alpha_s+1}^{\alpha_{s+1}} \int_{zone} \chi(k,p) \nu_k \Sigma_{f,k} \phi_k \phi_p^* dr
 \end{aligned} \quad (6)$$

Similarly, average cross sections for transfers by $(n,2n)$, elastic scattering, and inelastic scattering from one coarse group to another are defined [as in Eq. (6)] in the adjoint-weighted mean.

The coarse-group average diffusion coefficients are defined, zone by zone, as follows:

$$\begin{aligned}
 \bar{D}_n \int_{zone} (\nabla^2 \Phi_n) \Phi_n^* dr \\
 \equiv \sum_{p=\alpha_n+1}^{\alpha_{n+1}} \int_{zone} D_p (\nabla^2 \phi_p) \phi_p^* dr.
 \end{aligned} \quad (7)$$

Thus, if $\nabla^2 \phi_p = -B^2 \phi_p$, where B^2 is a constant independent of p , then

$$\bar{D}_n = \frac{\sum_{p=\alpha_n+1}^{\alpha_{n+1}} \int_{zone} D_p \phi_p \phi_p^* dr}{\int_{zone} \left(\sum_{p=\alpha_n+1}^{\alpha_{n+1}} \phi_p \right) \left(\sum_{k=\alpha_n+1}^{\alpha_{n+1}} \phi_k^* \right) dr}$$

With these definitions for coarse-group parameters, Eq. (1) is replaced by $(1 \leq n \leq N)$:

which is correct at least in the adjoint-weighted mean, as may be shown by multiplying the p th equation of Eq. (8) by Φ_n^* , integrating over the zone, and then making use of the above definitions [Eqs. (4) to (7)].

By definition, Φ_n is the sum of the fluxes of the included fine groups. For the idealized, fundamental-mode spectrum, the functions

$$\Phi_n \equiv \sum_{p=\alpha_n+1}^{\alpha_{n+1}} \phi_p$$

constitute a solution for Eq. (8), and k_{eff} is invariant

with respect to group synthesis. For the more general situation, however, these Φ_n 's do not satisfy Eq. (8) exactly, only in the weighted mean.

DERIVATION OF THE GROUP-SYNTHESIS FORMULAS:
VIA THE MULTIGROUP ADJOINT FLUXES

In the preceding subsection, group-synthesis formulas were obtained from algebraic operations on and integrations of the multigroup real-flux equations. Alternatively, one could start with the adjoint system and perform similar operations to obtain such formulas. If the methods were entirely consistent, the numerical values of corresponding parameters would be equal.

The multigroup diffusion equations for the system adjoint to Eq. (1) are given by Eq. (3) which, in detail are:

$$0 = \nabla \cdot D_j \nabla \phi_j^* - \phi_j^* \left[\Sigma_{c,j} + \Sigma_{f,j} + \frac{1}{2} \sum_{k=1}^M \Sigma_{(n,2n),j}^{(0)} T_{(n,2n)}^{(0)}(j \rightarrow k) + \sum_{k=1}^M \Sigma_{i_n,j}^{(0)} T_{i_n}^{(0)}(j \rightarrow k) + \sum_{k=1}^M \Sigma_{el,j}^{(0)} T_{el}^{(0)}(j \rightarrow k) \right] + \sum_{k=1}^M \phi_k^* \left[\frac{\chi(j,k) \nu_j \Sigma_{f,j}}{k_{eff}} + \Sigma_{(n,2n),j}^{(0)} T_{(n,2n)}^{(0)}(j \rightarrow k) + \Sigma_{i_n,j}^{(0)} T_{i_n}^{(0)}(j \rightarrow k) + \Sigma_{el,j}^{(0)} T_{el}^{(0)}(j \rightarrow k) \right]. \quad (9)$$

Multiply the p th equation of Eq. (9), term by term, by ϕ_p ; integrate over the zone; and sum over p , $\alpha_n + 1 \leq p \leq \alpha_{n+1}$.

Define $\bar{\Sigma}_{R,n}^*$ by:

$$\bar{\Sigma}_{R,n}^* \int_{\text{zone}} \Phi_n^* \Phi_n dr \equiv \sum_{p=\alpha_n+1}^{\alpha_{n+1}} \int_{\text{zone}} \Sigma_{\text{out},p} \phi_p^* \phi_p dr. \quad (10)$$

(Note: Thus, $\bar{\Sigma}_{R,n}^* = \bar{\Sigma}_{R,n}$.)

Define $(\nu \Sigma_f)_n \chi(n,s)^*$ by:

$$\overline{(\nu \Sigma_f)_n \chi(n,s)^*} \int_{\text{zone}} \Phi_s^* \Phi_n dr \equiv \sum_{p=\alpha_n+1}^{\alpha_{n+1}} \sum_{k=\alpha_s+1}^{\alpha_{s+1}} \int_{\text{zone}} \chi(p,k) \nu_p \Sigma_{f,p} \phi_p^* \phi_k^* dr. \quad (11)$$

The other "source" components of Eq. (9) are defined by equations similar to Eq. (11). The individual removal components of $\Sigma_{\text{out},p}$ yield coarse-group average cross sections defined by equations similar to Eq. (10).

Define \bar{D}_N^* by:

$$\bar{D}_N^* \int_{\text{zone}} (\nabla^2 \Phi_n^*) \Phi_n dr \equiv \sum_{p=\alpha_n+1}^{\alpha_{n+1}} \int_{\text{zone}} D_p (\nabla^2 \phi_p^*) \phi_p dr. \quad (12)$$

Then, in the weighted mean, using these coarse-group adjoint parameters:

$$0 = \bar{D}_N^* \nabla^2 \Phi_n^* - \bar{\Sigma}_{R,n}^* \Phi_n^* + \sum_{k=1}^N \Phi_k^* \left\{ \frac{(\nu \Sigma_f)_n \chi(n,k)^*}{k_{eff}} + \overline{\Sigma_{(n,2n),n}^{(0)} T_{(n,2n)}^{(0)}(n \rightarrow k)^*} + \overline{\Sigma_{i_n,n}^{(0)} T_{i_n}^{(0)}(n \rightarrow k)^*} + \overline{\Sigma_{el,n}^{(0)} T_{el}^{(0)}(n \rightarrow k)^*} \right\}. \quad (13)$$

which may be shown by multiplying the p th equation of Eq. (13) by Φ_n and integrating over the zone.

REMARKS ON EQS. (8) AND (13)

The question at issue is under what conditions is the N -group system given by Eq. (13) the adjoint to Eq. (8)? In other words, if we first transform from the M -group real-flux equations to the M -group adjoint system and then group-synthesize to N groups, do we get the same equations—with the same parameters—as by group-synthesizing first to the N -group real system and then formally transforming to the N -group adjoint system?

In Eq. (6), make a uniform interchange of group indexes n and s , on the left hand side; and interchange the summation indexes p and k on the right hand side. The

result is:

$$\overline{(\nu \Sigma_f)_n \chi(n,s)} \int_{\text{zone}} \Phi_n \Phi_s^* dr \equiv \sum_{p=\alpha_n+1}^{\alpha_{n+1}} \sum_{k=\alpha_s+1}^{\alpha_{s+1}} \int_{\text{zone}} \chi(p,k) \nu_p \Sigma_{f,p} \phi_p^* \phi_k^* dr$$

which is precisely the equation for $\overline{(\nu \Sigma_f)_n \chi(n,s)^*}$ —Eq. (11).

Similar proofs apply to the other "source" terms of Eq. (13).

By definition, $\bar{\Sigma}_{R,n} = \bar{\Sigma}_{R,n}^*$. It is the leakage term which causes the real mischief. If $\bar{D}_n = \bar{D}_n^*$, as defined by Eqs. (7) and (12), for all n , $1 \leq n \leq N$, this group-synthesis procedure preserves "idempotence of order 2", i.e., it preserves the property that the system which is adjoint to the "adjoint" system is the original system of equations. Of course this would mean also that the same equations would be obtained whether one started with the real multigroup equations or with the adjoint multigroup system.

In general, $\bar{D}_n \neq \bar{D}_n^*$. Therefore, strictly speaking, the proofs which purportedly demonstrated that $\bar{\Sigma}_{R,n} = \bar{\Sigma}_{R,n}^*$, etc., involved an approximation. Although Φ_n and Φ_n^* are not adjoint to one another, they have been used

as if they were, in speaking of the correctness of Eqs. (10) and (13) "in the weighted mean".

It should be noted, however, that this problem exists for linear flux weighting, as well, for then, except in the case of a fundamental-mode spectrum, the definition of a *zone-average* coarse-group diffusion coefficient would require an integration, for example:

$$\bar{D}_n \int_{\text{zone}} \nabla^2 \bar{\Phi}_n dr \equiv \int_{\text{zone}} \sum_{p=\alpha_n+1}^{\alpha_{n+1}} D_p \nabla^2 \phi_p dr$$

and

$$\bar{D}_n^* \int_{\text{zone}} \nabla^2 \bar{\Phi}_n^* dr \equiv \int_{\text{zone}} \sum_{p=\alpha_n+1}^{\alpha_{n+1}} D_p \nabla^2 \phi_p^* dr.$$

With

$$\bar{\Phi}_n \equiv \sum_{p=\alpha_n+1}^{\alpha_{n+1}} \phi_p \quad \text{and} \quad \bar{\Phi}_n^* \equiv \sum_{p=\alpha_n+1}^{\alpha_{n+1}} \phi_p^*$$

there is no assurance that $\bar{D}_n = \bar{D}_n^*$. Indeed, in this case, in general $\bar{\Sigma}_{R,n} \neq \bar{\Sigma}_{R,n}^*$, et cetera.

Since there is no clear choice to be made between \bar{D}_n and \bar{D}_n^* , perhaps it would be advantageous numerically to define the average diffusion coefficients, \hat{D}_n , by:

$$\hat{D}_n \equiv \frac{\bar{D}_n + \bar{D}_n^*}{2}, \quad (14)$$

whence

$$\hat{D}_n \equiv \frac{1}{2} \left\{ \frac{\sum_{p=\alpha_n+1}^{\alpha_{n+1}} \int_{\text{zone}} D_p (\nabla^2 \phi_p) \phi_p^* dr}{\int_{\text{zone}} \left(\sum_{p=\alpha_n+1}^{\alpha_{n+1}} \nabla^2 \phi_p \right) \left(\sum_{p=\alpha_n+1}^{\alpha_{n+1}} \phi_p^* \right) dr} + \frac{\sum_{p=\alpha_n+1}^{\alpha_{n+1}} \int_{\text{zone}} D_p (\nabla^2 \phi_p^*) \phi_p dr}{\int_{\text{zone}} \left(\sum_{p=\alpha_n+1}^{\alpha_{n+1}} \nabla^2 \phi_p^* \right) \left(\sum_{p=\alpha_n+1}^{\alpha_{n+1}} \phi_p \right) dr} \right\}. \quad (15)$$

TRANSITIVITY OF THE GROUP-SYNTHESIS OPERATOR

The group-synthesis procedure is said to be "transitive" if successive group syntheses—from N_1 groups to N_2 groups to N_3 groups—yield the same equations as the direct synthesis from N_1 to N_3 .

To demonstrate transitivity, start with Eq. (8), and define \bar{D}_n by:

$$\bar{D}_n \int_{\text{zone}} (\nabla^2 \bar{\Phi}_n) \bar{\Phi}_n^* dr \equiv \sum_{q=\beta_n+1}^{\beta_{n+1}} \int_{\text{zone}} \bar{D}_q (\nabla^2 \bar{\Phi}_q) \bar{\Phi}_q^* dr \quad (16)$$

where

$$\bar{\Phi}_n \equiv \sum_{q=\beta_n+1}^{\beta_{n+1}} \bar{\Phi}_q \quad \text{and} \quad \bar{\Phi}_n^* \equiv \sum_{q=\beta_n+1}^{\beta_{n+1}} \bar{\Phi}_q^* \quad (17)$$

with $\bar{\Phi}_q$ and $\bar{\Phi}_q^*$ defined by Eq. (4).

Using Eq. (7),

$$\begin{aligned} \bar{D}_n \int_{\text{zone}} (\nabla^2 \bar{\Phi}_n) \bar{\Phi}_n^* dr \\ = \sum_{q=\beta_n+1}^{\beta_{n+1}} \sum_{p=\alpha_q+1}^{\alpha_{q+1}} \int_{\text{zone}} D_p (\nabla^2 \phi_p) \phi_p^* dr. \end{aligned} \quad (18)$$

If the double summation, on the right hand side of Eq. (18), includes all fine groups, p , in the range $\Delta_n + 1 \leq p \leq \Delta_{n+1}$, then Eq. (18) may be written as the single summation

$$\bar{D}_n \int_{\text{zone}} (\nabla^2 \bar{\Phi}_n) \bar{\Phi}_n^* dr = \sum_{p=\Delta_n+1}^{\Delta_{n+1}} \int_{\text{zone}} D_p (\nabla^2 \phi_p) \phi_p^* dr \quad (19)$$

where

$$\bar{\Phi}_n \equiv \sum_{p=\Delta_n+1}^{\Delta_{n+1}} \phi_p \quad \text{and} \quad \bar{\Phi}_n^* \equiv \sum_{p=\Delta_n+1}^{\Delta_{n+1}} \phi_p^*.$$

Note that Eq. (19) is the definition of the average diffusion coefficient for the n th group resulting from group synthesis from N_1 groups to N_3 groups.

Similarly, it may be shown that successive group syntheses provide the appropriate N_3 -group weighted reaction rates and group fluxes, and transitivity is proved.

REFERENCES

1. R. L. Hellens, R. W. Long and B. H. Mount, *Multigroup Fourier Transform Calculation Description of MUFT III Code*, WAPD-TM-4, (July, 1956). Also: H. Bohl, Jr., E. N. Gelbard and G. H. Ryan, *MUFT-4 Fast Neutron Spectrum Code for IBM-704*, WAPD-TM-72, (July, 1957).
2. G. D. Joann and J. S. Dudek, *GAM-1; A Consistent P_1 Multigroup Code for the Calculation of Fast Neutron Spectra and Multigroup Constants*, GA-1850, (June, 1961).
3. D. S. Selengut, *Variational Analysis of Multi-Dimensional Systems*, Trans. Am. Nucl. Soc. 2, No. 1, 58 (June, 1959).
4. B. H. Duane, *Neutron and Photon Transport; Plane-Cylinder-Sphere; GE-ANPD Program S; Variational Optimum Formulation*, XDC 59-9-118, (January, 1959).
5. K. Parker, *A Punched-Card Library of Neutron Cross Sections and Its Use in the Mechanized Preparation of Group Cross Sections for Use in Monte Carlo*, Carlson S_8 and Other Multi-Group Neutronics Calculations on High-Speed Computers, Physics of Fast and Intermediate Reactors, Vol. 1, IAEA, Vienna, 1962.
6. A. I. Novozhilov and S. B. Shikhov, *A Method of Averaging Nuclear Constants in Fast Reactor Calculations, Taking into Account Neutron Weighting*, translated by N. Kemmer; J. Nucl. Energy: P. A & B 16, pp. 137-141 (1962).
7. G. I. Marchuk, *Methods for Nuclear Reactor Calculations*, (Gos Atom Izdat, Moscow, 1961).

V-5. Neutron Attenuation Calculations and Intercomparison

M. GROTENHUIS,* C. N. KELBER, A. E. MCARTHY and A. D. ROSSIN†

In connection with general shielding work and the Neutron Attenuation Intercomparison sponsored by the Shielding Division of the American Nuclear Society, solutions to all of the ANS study problems were determined by Argonne and submitted to a Committee of the ANS Shielding Division. Results were displayed and compared at the November, 1963, ANS meeting in New York. The study is described in Ref. 1.

The set of four problems consisted of: 1) a point source, 2) a system mocking up a large graphite reactor and shield, 3) an H₂O moderated system, and 4) a small fast core with an optimized shield.

In the first calculations, solutions were obtained by using the RE-122 diffusion code with sixteen energy groups to find flux distributions through different shield configurations. Also, DSN problems were run for some of the solutions.

Alternate solutions were determined by replacing the two high energy groups with a source term calculated by removal theory. The fast neutron flux at the surface of the core was determined from an average source value. The average source value was obtained by using the source distribution designated for the problem. The lower energy fluxes obtained from the diffusion solution for the edge of the core were used as inner boundary conditions for the lower energy groups in the alternate solutions.

Three geometries were analyzed in the problems:

* Personnel Division, Argonne National Laboratory.

† Metallurgy Division, Argonne National Laboratory.

spherical, finite cylinder with prescribed axial distribution, and finite cylinder with prescribed radial distribution. Three reactor types were represented: graphite moderated, water moderated, and fast. And three shields were represented: graphite-concrete, iron-water, and BeO-LiH. In addition to these complex-shield problems, three simple cases of point isotropic sources in infinite homogeneous media were included as fiducial calculations.

The following information was requested as solutions of the problems: 1) fast neutron spectra and dose rates at specified points within the shields; 2) neutron absorption rates at these same points; 3) radiative capture rates as functions of position in the reactor vessels; and 4) leakage rates from the shields.

In general, the "exact" methods—Moments, Monte Carlo, Niobe, and Transmission Matrix—agreed fairly well, although not quite as well as expected. The results obtained from the combination removal-diffusion theory methods were about as expected, a reasonable overestimate. Diffusion theory problems were included for comparative purposes and the calculated values were low at deep penetration. The results for all methods differed by factors of ten to one hundred at deep penetration except for the case of a LiH shield for which the range of values varied by 10⁵.

REFERENCE

1. R. L. Ashley and W. E. Kreger (Eds.), *Neutron Attenuation in Optically Thick Shields*, ANS-SD-1 (April, 1964).

V-6. Thermionic Energy Conversion With a Plasma Thermocouple

H. K. RICHARDS

Several facets of the problems involved in converting thermal to electrical energy using a plasma thermocouple (thermionic converter) have been investigated experimentally as part of a continuing effort.^{1,2} The area reported herein covers a performance comparison among sodium, potassium, and cesium plasmas between a tantalum emitter and a molybdenum collector at high temperature and low pressure, and various gap sizes.

NATURE OF INVESTIGATION

The thermionic converter is arranged so that the space charge between the emitter and collector is neutralized by means of alkali ions and the collector work function is reduced to the work function of the neutral alkali metal. The fission heat source is simulated by using electrically heated emitter materials with the fissionable material omitted. Using this arrangement the following behavioral characteristics are

determined experimentally for each of the three alkali metals:

1. dc and rf power, current, and voltage relations as a function of gap width and vapor pressure.
2. Interaction of dc and rf outputs.
3. Relation between electron and ion currents.

In each case the temperature of the alkali metal is adjusted to give the desired vapor pressure.

THE CONVERTER AND EQUIPMENT

Experiments have been performed with a uranium-zirconium carbide emitter in which it was found that the material changed composition.³ To avoid this difficulty, a tantalum emitter has been chosen to eliminate the influence of such variation on the characteristics measured. A molybdenum collector and guard-ring are arranged so that the gap between emitter and collector can be altered over the range 0-2 mm.

The emitter-collector can be observed through a sapphire window with an optical pyrometer. The collector and guard-ring is oil cooled. The alkali vapor is introduced from a trap, and its pressure is controlled by the oil bath over the temperature range 0-320° C. Figure V-6-1 is a schematic representation of the experimental set up.

The voltage current characteristics are measured with an X-Y recorder at the collector, with rf chokes separating the rf output from dc. The rf was connected over capacitances to a section with a scope and VTV meter. This section could remain open, loaded with an inductance-free load, or it could be short-circuited independent of the dc section. The effect of rf open (O) or short-circuited (S) could be observed on the dc characteristics.

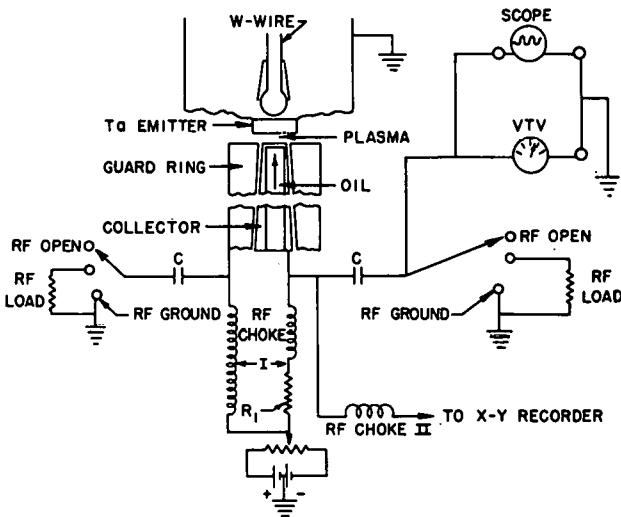


FIG. V-6-1. Circuit Diagram of the Experimental Arrangement.

$$p(\text{Cs}) = 1.1 \times 10^{-4} \text{ mm Hg}$$

$$n_{\text{Cs}} = 3.1 \times 10^{12} \text{ atoms/cc}$$

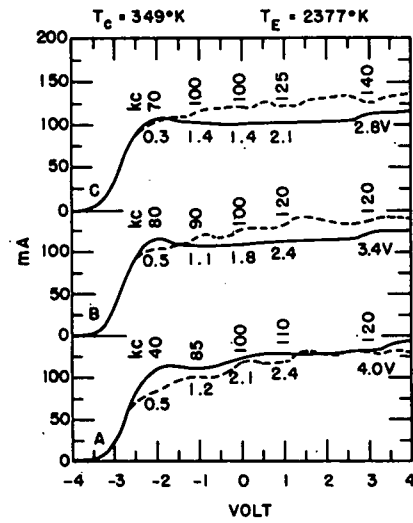


FIG. V-6-2. Cesium Cell Characteristics. (rf open-dashed curves. rf shorted-solid curves.)

TABLE V-6-I. CESIUM CELL CHARACTERISTICS

Run No.	$J_c, \frac{\text{mA}}{\text{cm}^2}$		$J_i, \frac{\text{mA}}{\text{cm}^2}$		J_c/J_i	P_{max}, mw		Emitter-Collector Distance, mm
	Meas	Calc	Meas	Calc		dc	rf	
A	260	420	2.5	2.9	104	240	1	0.5
B	260	420	3.0	2.9	87	240	10	1.0
C	260	420	2.4	2.9	108	240	20	2.0

$p(\text{Cs}) = 1.1 \times 10^{-4} \text{ mm}$; $n_{\text{Cs}} = 3.1 \times 10^{12} \text{ atoms/cc}$; $T_c = 349^\circ \text{ K}$; $T_e = 2377^\circ \text{ K}$.

MEASUREMENTS AND RESULTS

CESIUM CELL

Figure V-6-2 shows the dc characteristic behavior of the cesium cell for the indicated vapor pressure and density. The currents are plotted against the applied voltage for rf open and rf shorted for three emitter-collector distances. The observed rf's in kc are shown above and the corresponding RMS voltages below each characteristic curve. It is evident that energy conversion occurs only at the negative portion of the characteristics, with a maximum found at about -2.6 V for dc. However, the rf power maximum was found at zero volts or slightly less.

The characteristics are tabulated, as shown in the last column of Table V-6-I, for emitter-collector distances of 0.5, 1.0 and 2.0 mm. Columns 2 and 3 show

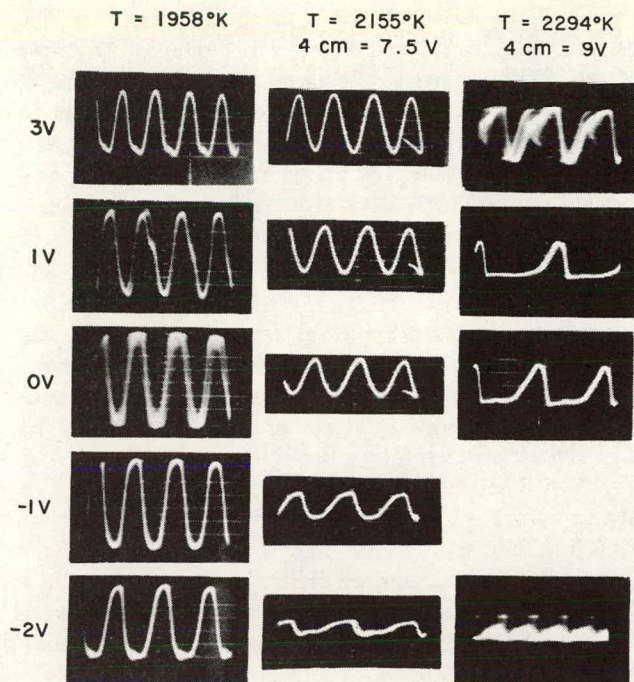


FIG. V-6-3. Cs-rf Oscillations.

the measured and calculated* emitter current, the next two columns measured and calculated ion currents, the sixth column gives the ratio of measured electron to ion current, and the next two columns give the dc and rf power output. The emitter temperature was constant for all measurements. Other measurements were made with different emitter temperatures and cesium pressure. The result for cesium showed that the maximum dc power occurred at about -2.6 to -2.7 V. Assuming that the emitter work function is about 4.2 V, this indicates a collector work function of 1.5 to 1.6 V. Experiments at different emitter temperatures and pressures not exceeding 10^{-2} mm Hg (dry emitter) show about the same result. As can be seen, the table shows fair agreement between calculated and measured values for J_e (emitter current) and J_i (ion current). Since for a neutral plasma $J_e/J_i = 496$, the plasma here is ion rich. Referring to Fig. V-6-2, it is interesting to note that the dc characteristics with rf open and shorted are not identical. The rf frequencies decrease with decreasing dc voltage. Also, negative portions of the characteristics are observed. The rf power increases with increasing emitter-collector distance up to 2 mm, while for higher cesium pressures the dc power decreases with distance.

The oscillations which are not observed for very ion-rich plasma, increase with increasing electron

* The calculations are carried out² on the basis of text book theory.

density, reach a maximum, and decrease again for very electron-rich plasma. The rf power in a Cs cell reaches 20% of the dc power. The rf frequencies decrease usually with decreasing applied dc voltage.

Figure V-6-3 shows the rf oscillation characteristics over a range of $+3$ to -2 applied volts at 3 emitter temperatures. The horizontal scale is $1 \mu\text{sec}/\text{cm}$. As is seen for the highest temperature, the amplitudes exceed 4 V, i.e., they are higher than the 3.87-V ionization voltage of cesium.

POTASSIUM CELL

Experiments with the potassium cell followed the same procedure as for the cesium cell. Since the melting and evaporation temperatures are higher, the cell had to be operated at higher temperature to yield the same vapor pressures.

Since the cesium ionization voltage is lower than the tantalum work function, the Saha-Langmuir equation⁴ predicts nearly 100% ionization. However, for potassium, a much lower rate, about 33%, can be expected. For cell temperatures exceeding 100°C , the ion density

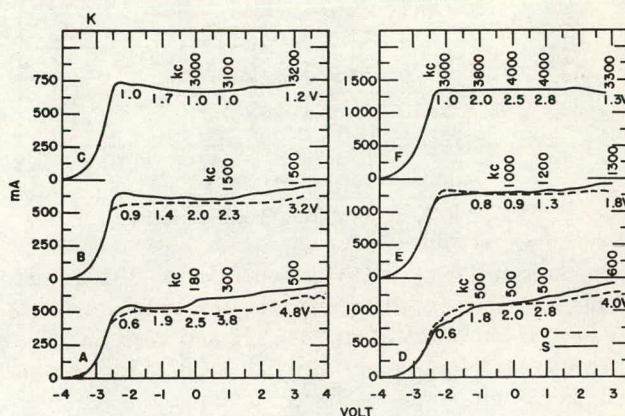


FIG. V-6-4. Potassium Cell Characteristics.

TABLE V-6-II. POTASSIUM CELL CHARACTERISTICS

No.	$J_e, \frac{\text{mA}}{\text{cm}^2}$		$J_i, \frac{\text{mA}}{\text{cm}^2}$		J_e/J_i	P_{max}, mW		Emitter-Collector Distance, mm
	Meas	Calc	Meas	Calc		dc	rf	
A ^a	1200	700	11	14.7	109	1200	250	2.0
B ^a	1200	700	14	14.7	86	1560	60	1.0
C ^a	1200	700	12	14.7	100	1750	—	0.5
D ^b	2800	1700	20	19.3	140	1900	240	2.0
E ^b	2800	1700	20	19.3	140	2860	100	2.0
F ^b	2800	1700	16	19.3	175	3100	50	0.5

^a $T_E = 2446^\circ \text{K}$; $T_C = 435^\circ \text{K}$; $p(\text{K}) = 1 \times 10^{-3}$ mm Hg; $n(\text{K}) = 2.3 \times 10^{13}$.

^b $T_E = 2529^\circ \text{K}$; $T_C = 440^\circ \text{K}$; $p(\text{K}) = 1.5 \times 10^{-3}$ mm; $n(\text{K}) = 3.0 \times 10^{13}$.

TABLE V-6-III. SODIUM CELL CHARACTERISTICS

No.	$J_e, \frac{\text{mA}}{\text{cm}^2}$		$J_i, \frac{\text{mA}}{\text{cm}^2}$		J_e/J_i	P_{max}, mW		Emitter-Collector Distance, mm
	Meas	Calc	Meas	Calc		dc	rf	
A	850	660	4.0	3.0	212	800	50	2
B	1150	660	4.0	3.0	288	1210	—	1
C	1500	600	4.6	3.0	326	1595	—	0.5
D	2000	3200	7.0	5.0	286	4000	—	0.5
E	2000	3200	10.0	5.0	200	3800	—	1
F	2000	3200	12.0	5.0	167	2850	—	2

$$T_C = 571^\circ \text{K}; T_E = \begin{cases} 2424^\circ \text{K (A-C)} \\ p(\text{Na}) = 1.2 \times 10^{-2} \text{ mm} \\ n_{\text{Na}} = 2 \times 10^{14} \\ 2624^\circ \text{K (D-F)} \end{cases}$$

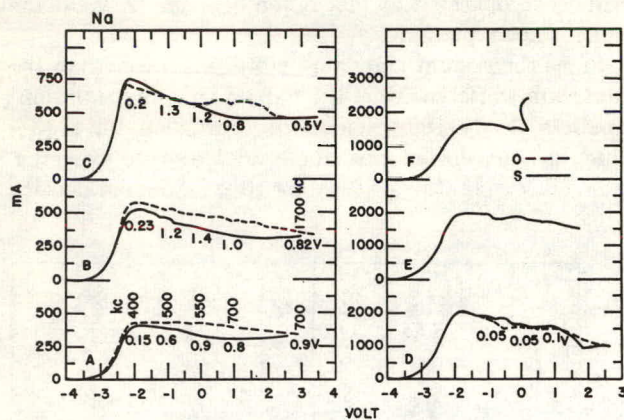


FIG. V-6-5. Sodium Cell Characteristics.

was sufficient for neutralization. Figure V-6-4 and Table V-6-II show the characteristics and data for a potassium cell operated at 2446°K and 2529°K . The characteristics look essentially like those of the cesium cell. For 2 mm emitter-collector distance the rf power maximum exceeds 20% of the dc power maximum, reaching 25% on occasion. It appears that the potas-

sium cell produces relatively more rf power than the cesium cell. The other data are self-evident. The knees of the characteristic are situated at about -2.5 V , i.e., the dc power is slightly less than for cesium, due to the higher work function of potassium deposited at the collector. At pressures of about $5 \times 10^{-3} \text{ mm Hg}$ and higher, the dc power decreases rapidly at emitter-collector distances greater than 1 mm.

SODIUM CELL

Since the ionization voltage for sodium is 5.12, the Saha-Langmuir equation⁴ predicts less than 1% ionization even for high emitter temperatures. The sodium cell must be operated at temperatures above 520°K . The characteristics values listed in Table V-6-III, and Fig. V-6-5 show that the knees of the characteristics are at about -2 V , i.e., the power maximum is about 20% less than with cesium and potassium. Neutralization of the plasma required higher vapor pressures than for the cesium and potassium cells. rf oscillations were observed in a manner similar to the other alkaline metals.

While the power output is lower due to the higher ionization voltage, a sodium cell could be operated with a higher collector temperature because of its lower back emission.

REFERENCES

1. H. K. Richards, *Thermionic Energy Conversion for DC and High Frequency Power Output*, Proc., Conference on Direct Energy Conversion, ANL-6802, (1963) p. 152.
2. H. K. Richards, *DC and High Frequency Voltage and Power Output and Interaction in Cesium, Potassium and Sodium Thermionic Converters*, Proc., Symposium on High Temperature Conversion-Heat to Electricity, TID-7687, 161 (February, 1964).
3. L. Young and F. D. Carpenter, *Materials Problems in Cesium Thermionic Converters*, J. Electrochem. Soc. **108**, 1079 (1961).
4. I. Langmuir and K. H. Kingdon, Phys. Rev. **34**, 129 (1929).

V-7. Flux Monitoring of Radiation Damage Experiments

R. J. ARMANI and A. D. ROSSIN*

A program of radiation effects on reactor structural materials is in progress. Damage to structural materials is being studied as a function of the fast neutron dose received. In order to determine fast neutron dose,

both the spectrum and the flux intensity must be determined, usually by means of one or more threshold detectors. A number of methods are available to determine experimentally the fast spectrum by use of threshold detectors.¹ These methods require knowledge of detector cross sections as a function of neutron en-

* Metallurgy Division, Argonne National Laboratory.

ergy, most of which are known only to a limited accuracy.

The neutron dosimetry measurements for this program were made in EBWR, EBR-I, and in two locations in CP-5. In each case, the fast neutron spectrum was calculated by the DSN neutron transport code with 20 energy groups of equal lethargy width from 10 MeV down to 0.067 MeV. Capsules containing threshold detectors were irradiated in these locations to determine flux intensity and to verify the calculated spectrum. Verification of the spectrum was accomplished by calculating activation rates from the spectrum and cross sections of the threshold detectors, and comparing the predicted with the measured activation rates. The flux intensity was determined from the measured activation rates and the detector cross sections.²

The threshold detectors were chosen to be compatible with the high temperatures and high intensity neutron fluxes encountered in the irradiation locations. Samples of nickel, iron, U-238, and Th-232 were used in metallic form. The U-238 and Th-232 were jacketed in cadmium to reduce activation products produced by the neutron-gamma reaction and to retard oxidation. Sulfur was used in the form of $\text{Al}_2(\text{SO}_4)_3$, and later as Li_2SO_4 because of desirable thermal properties and the dilution of the sulfur. In EBWR and CP-5, Co-59 was included to determine the thermal flux level. The cobalt was in the form of an aluminum alloy containing 0.1% cobalt.

Dosimetry packages were inserted in the four reactor locations either before or after specimens of

structural material were irradiated, to determine the neutron environment there. During irradiation of the specimens, nickel was included for determination of flux intensity. Advantage was also taken of the fact that the specimens were type SA-212 B steel whose composition is well known. The Mn-54 activity found in the specimens and produced by $\text{Fe}^{54}(n,p)\text{Mn}^{54}$ reaction was determined. Thus the sample itself also acted as a threshold detector.

Using the average cross sections found in the literature,¹ some disagreement was found in the information obtained using Fe-54, Ni-58, Ti-46, and S-32. A measurement of the average cross section of the above detectors was made in EBR-I just prior to its deactivation. Using S-32 as the reference, the measurement indicated the cross sections to be about 15% higher than the published values. Inconsistent results have also been observed elsewhere.³ Previous measurements had been made relative to the $\text{Al}^{27}(n,\alpha)\text{Na}^{24}$ reaction. More measurements are being made in JUGGERNAUT to determine the source of this discrepancy.

REFERENCES

1. J. Moteff, *Neutron Flux and Spectrum Measurement with Radioactives*, Nucleonics 20, No. 12, 56-60 (December 1962).
2. A. D. Rossin and R. J. Armani, *Fast Neutron Dosimetry for Radiation Damage Studies*, Proc. Sym. Neutron Detection Dosimetry and Standardization, Harwell, Dec. 10-14, 1962 (IAEA, Vienna, 1963), Vol. II. Neutron Detection, pp. 293-304.
3. R. Barrall, Illinois Institute of Technology Research Institute (private communication).

V-8. Comparison of Accelerators and Reactors for Steady Neutron Flux Production

C. N. KELBER

The thermal neutron flux produced per source neutron is independent of the origin of the neutron provided the spectrum of source neutrons is substantially constant. Thus charged particle beams bombarding heavy elements produce neutrons which can be used for research.

In advanced research reactors, the maximum thermal flux per source neutron per cc is 33 (HFIR) to 50 (AARR) n/cm²-sec. Similar calculations have been performed for accelerators having typical Pb or U-238 annular targets with H₂O internal thimbles and D₂O external reflectors to evaluate, in part, the effects of

structure, geometry, and spatial distribution. It is found that the optimum target of U-238 for a 500 MeV beam yields above 20 n/cm²-sec per source neutron per cc, while the optimum U-238 target at 1 BeV yields 47.5 n/cm²-sec per source neutron per cc.

The basic reason for the change in going from 500 MeV to 1 BeV is the increase in source size and total source. Unlike a reactor, going to targets larger than those quoted at given energy does not increase the total source appreciably; hence, the use of the term "optimum."

The energy release in the target per source neutron

TABLE V-8-I. ENERGY RELEASE PER SOURCE NEUTRON^a

Process	Number of Source Neutrons Produced	Energy Release (MeV) Per Reaction	
		Lower estimate	Upper estimate
<i>One incident proton, energy: 500 MeV, optimum target</i>			
Cascade	0.5	50	100 (+ pions)
Evaporation	4.3	10	20
Fission	8.3	200 per fission ($\nu = 3$)	
Totals	13.1	621	689
Energy release/source neutron		47	52
<i>One incident proton, energy: 1 BeV, optimum target^b</i>			
Cascade	1.4	50	100 (+ pions)
Evaporation	5.4	10	20
Fission	23.0	200 per fission ($\nu = 3$)	
Totals	29.8	1657	1781
Energy release/source neutron		56	60

^a Prepared with the generous help of A. B. Smith.

^b In addition, half the beam energy is dissipated outside the target.

is estimated in Table V-8-I. The estimates are obviously crude. In uranium fission, the energy dissipated per source neutron is about 80 MeV. In the U-238 targets listed here, the figures range from 47 to 52 MeV per neutron for 500 MeV incident protons and from 56 to 60 MeV for 1 BeV incident protons. Not included in these estimates is the pion energy carried off in the cascade process. About half the energy release in the evaporation process is in the form of energetic protons. While the fission process contributes the overwhelming part of the energy release, it also contributes most of the neutrons. (It has probably been underestimated here.) Thus, there is likely to be no advantage in going to target materials with higher fission thresholds.

Since the neutron flux produced per unit source density is the same in the accelerator as in the reactor, and since the energy release per source neutron is of the same order as in a nuclear reactor, it is concluded there is little significant advantage to this method. Improved knowledge of yields and energy release may markedly change the picture. It is unlikely that there can be a change by more than a factor of 2 to 5.

Late experimental results indicate the neutron yield may be only half that indicated here.

V-9. Evaluation of a Rotating Power Generating System

A. J. ULRICH, J. C. CARTER, R. O. BRITTAN and R. G. POST*

A concept of an electrical power generation system has been proposed which uses centrifugal forces to circulate the working fluid against the generator load and hydraulic pressure drops. The principal interest is that the system can operate in a zero gravity field. This is a report on the course and status of the evaluation of the system concept proposed originally by A. J. Ulrich.

DESCRIPTION OF THE CONCEPT

In its original form, the concept called for rotating a natural circulation closed flow circuit consisting of a nuclear reactor heat source in a peripheral position and a separator-condenser heat sink near the axis, connected by a riser and downcomer which passes through a magnetic field. The working fluid is a conducting metal, having a liquid-vapor phase in the riser and a

liquid phase in the downcomer. The centrifugal force field, whether or not in the presence of a gravitational force field, acts to a greater degree on the dense fluid in a downcomer than on the two-phase fluid in the riser. The net force circulates the fluid, replacing a pump, against the hydraulic pressure drops and impedance load of the MHD generator. Thus the generator is a liquid metal analog of the ordinary turboelectric generator, with the electrically conducting liquid metal acting as the rotor. The circuit is diagrammed in Fig. V-9-1.

The concept is proposed as a means of providing high flow velocity against the large flow impedance imposed by the electric power generator. The centrifugal force field, in addition, promotes higher heat transfer rates than can occur in a normal gravitational field and eliminates the need for a pump.

The cycle begins as heat is added by the nuclear reactor to the liquid metal before it enters the riser.

* Univ. of Arizona.

The centrifugal force field diminishes in intensity toward the axis of rotation, so that at some point in the riser the coolant reaches and drops below saturation pressure. There ensues a region of two-phase flow at much reduced density. The two-phase fluid enters the separator-condenser wherein the vapor phase rejects heat to the sink and condenses. The liquid leaving enters the downcomer or high density leg. It is accelerated non-linearly by the centrifugal force field, which is increasing in intensity as the periphery is approached. The fluid is at maximum velocity and pressure as it encounters the magnetic field of the generator near the periphery. After inducing conversion of the fluid work energy to electrical energy, the fluid returns along the periphery to the reactor heat source.

In the original concept, the heat source was visualized as a nuclear reactor, and the variable impedance load as an MHD generator using a liquid metal as conductor passing through the magnetic field. However, the problems of importance in making the evaluation do not lie with the reactor or the MHD generator at this stage, but rather with the behavioral aspects of the system. In particular, can the coolant be circulated against a high resistance with reasonable efficiency and stability? Because of this question the concept has been generalized to examining a rotating natural circulation heat transfer loop with heat source, sink and flow impedance.

In the early stages of the evaluation, it was felt that: 1) If adequate circulation could be realized, an energy converter could be incorporated, whether it be an MHD generator or a turbo-generator. 2) The original concept of a complete reactor on the outer portion of a single fluid loop could be modified to an annular core with multiple fluid loops to realize compactness.

EVALUATION WORK

It was recognized at once that an evaluation from a purely analytic standpoint would be very complex and uncertain. In general, one must deal with a non-uniform force field superimposed on the gravitational force field. The centrifugal and Coriolis forces would modify void formation, two phase flow, the processes of separation and condensation and the heat transfer in an unknown way. The variation in position of the liquid-vapor interface or slug flow might lead to inertial instabilities as a result of mass imbalances. These could make the concept unattractive.

Because of these complications it was planned to combine experimental and analytical approaches to assist in the evaluation. The goal is that of describing the behavior and performance of the system in terms

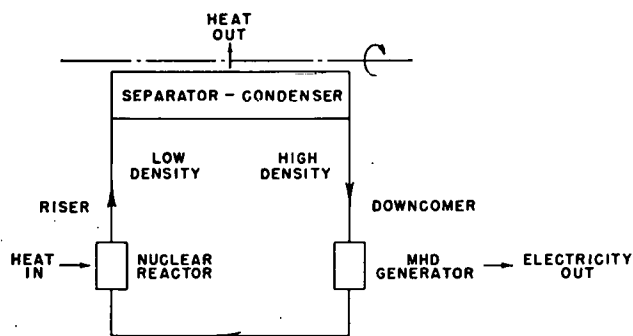


FIG. V-9-1. Diagram of Basic Concept.

of the principal parameters: heat source strength, angular velocity, flow impedance, system pressure and temperature. It will thus be possible to determine the feasibility of the concept and to suggest and optimize practical designs incorporating the basic principles.

The requirements of the evaluation call for construction and operation of a rotating heat transfer loop in which the reactor heat source is simulated by an electric heater, the MHD generator by a variable impedance valve, and the metal working fluid by water. This "proof-of-principal" test will develop the phenomenology, provide a check on the analysis, and establish the stability characteristics. Our efforts have been concentrated on this experimental work.

Arrangements have been made to carry out the experimental studies. The apparatus evolved is that shown schematically in Fig. V-9-2.

Two identical loops are arranged axisymmetrically to provide mass balance and incidentally to double the data output. It is necessary to measure mass flow rates, temperatures, pressures, condensing heat transfer rates, and the limits of flow stability as heat input, angular velocity, and impedance are varied. The axis of rotation must be either horizontal or vertical, at will. In the horizontal position the relative gravitational force field then alternates direction, providing a perturbation suitable for measuring the transfer function. It immediately became evident that the requirement of making measurements and observations, and transmitting the data to a fixed observer posed a formidable set of problems. All efforts for some time may be concentrated on their solution.

To this end, four methods of measuring the mass flow have been devised and are being checked out sequentially until a satisfactory system is found.

AN ELECTROLYTIC METHOD OF FLOW MEASUREMENT

A pulse of DC current between two electrodes produces a local change in conductivity in the liquid. The

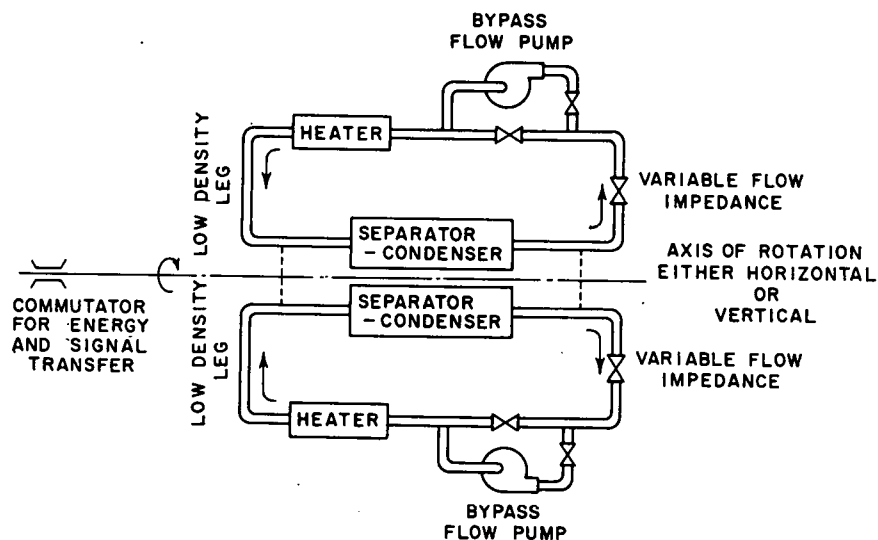


FIG. V-9-2. Schematic of Experimental Set-up.

region of perturbed conductivity is carried downstream to the conductivity measuring cell. The time interval between the DC pulse and the change in conductivity cell measurement is the ratio of the distance between the electrodes and the cell to the linear flow velocity. With a proper choice of the electrochemical system, a pair of electrodes downstream from the cell will reverse the electrochemical reaction and no net chemical change will result. The silver compound (or other) which is added to the water may separate at the point that vaporization occurs and concentration will not remain steady. However, the resultant change in conductivity will be spread out in time and the observed change in conductivity will still be sharply evident. The magnitude of the change is unimportant. Crudding in the boiling leg can be cleaned up from time to time.

A TRACER METHOD

In one version, a solid bead whose density is closely matched with that of water (e.g., polystyrene bead with filler) is injected into the liquid stream. The bead is illuminated by a light source as it passes a small transparent section. The light reflected from the passing bead is transmitted by a light pipe to a point on or near the axis of rotation where it is viewed by a photomultiplier not rotating with the apparatus. The detector receives pulses from at least two positions along the system, so that the stream velocity is given by the time delay. One disadvantage is that corrections must be made for the velocity profile of the channel. Another is that the transient response is poor. Still a third disadvantage is the problem of removing the beads. Beads could be screened, extracted, and re-

turned to the injector. A variation using a radioactive bead can also be considered.

A HEAT BALANCE METHOD FOR DETERMINING MASS FLOW RATE

Steam (or vapor) produced in the loop is bled off at the separator, and makeup water is subcooled. Stream temperature is measured upstream and downstream from the point at which makeup water is injected. With the temperature and mass of the makeup water and the two stream temperatures, the stream velocity can be computed. Complete mixing must be realized. This method of course works only in the steady state and has no transient response. However, it is an absolute method which can be used to calibrate other methods having reasonable transient response.

AN ORIFICE PLATE OR VENTURI WITH UPSTREAM AND DOWNSTREAM PRESSURE MEASUREMENTS

If used in the ordinary way two complications arise: (1) The Coriolis force causes added vortices and pressure gradients to occur at constrictions. In particular, vortices are produced in restrictions in pipes parallel to the rotational axis, whereas both vortices and pressure gradients are produced at restrictions in pipes perpendicular to the rotational axis. This means that the orifice plate must be calibrated for the angular velocity of the system as well as translational velocity of the fluid, perhaps using water from an external source. (2) The other complication is that the pressure value of a unit length of fluid in a radial manometer tube depends on angular velocity, radial position, and relative size and direction of the earth's gravitational

field. The complications due to angular velocity and radial position are eliminated if a separate gas pressure source is applied to each tube to bring the levels to the same radius. The desired pressure drop is the difference in gas pressures. To avoid making gravitational corrections, the two null points must lie in the same horizontal plane as well as at the same radius. The levels might be observed with a stroboscope.

It has been pointed out that uneven or damaging bearing friction loads on the rotor of a conventional flow meter would make it useless for measurement in a rotating system.

Serious analytical work has not yet been begun. The

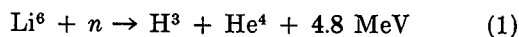
planned program of analytical work is based on the assumption that the system will behave properly. Parametric studies will allow choice of optimum position and operating conditions for the various components. From these, an evaluation of the potential efficiencies and minimum weights can be made. Transfer functions for the various components and the entire system may be obtained by perturbing the analytical model and using experimental data when available. Finally, predictions of the useful pressures which can be developed will be attempted as a function of heat source strength, rotational velocities and other parameters.

V-10. Investigation of a Direct Nucleonic Process in the Production of High Temperature Effluent

M. B. RODIN and J. C. CARTER

A conceptual study was initiated during the year on a novel nuclear propulsion system for use in space. The system is designed to react excess neutrons with Li-6 atoms in a reactor. The resultant energy liberated by the reaction heats the unreacted lithium to produce a very high temperature gas. This gas is then expanded through a nozzle to provide thrust. In operation, the lithium must be continually fed into the reactor as it is discharged through the nozzle. The gas temperature, theoretically, can reach levels well above those achieved in conventional convection cooled systems and are comparable in level with those achieved in some electrically energized systems. The proposed system, however, does not require the use of heavy generating and conditioning equipment and is limited to developing modest thrust levels.

Li is one of a number of substances having the necessary physical and nuclear properties suitable for the proposed concept. The reaction



produces two particles, an alpha and a triton, having a combined kinetic energy of 4.8 MeV. These particles, in collisions with other neutral target atoms, convert the kinetic energy to heat.

Li-6 has a very high cross section for thermal neutrons and a relatively low molecular weight. Since the specific impulse of a propellant varies as the square root of the ratio of the absolute temperature to the

molecular weight of the substance, it is well suited for this application. In addition, the isotopic abundance of Li-6 in natural lithium is 7.8%. Thus the cost of using either partially or fully enriched material is sufficiently low to consider its use on a once-through basis.

The current study has been basically limited to investigating the parameters concerned with establishing neutron and heat balances, with some attention being given to the over-all system design. Subsequent studies will include detailed studies of engineering and material problems, use of Li compounds such as LiH, potential applications, and the generation of pertinent experimental data.

A number of reactor configurations were investigated using the RE-122 Diffusion Code. Criticality calculations were made for both spherical and cylindrical geometries using a Pu-239 fueled annulus with an internal moderating region and either a heavy metal or moderating reflector. The annulus is operated in a fast neutron spectrum and the lithium is irradiated in the moderator regions. Idealized studies indicate that, depending upon the system studied, an average as high as one to two neutrons are absorbed in Li-6 for every fission in Pu-239. Optimization studies are in progress to more firmly establish the ratio of absorptions in Li-6 to fissions in Pu-239 for more sophisticated systems.

In order to effectively utilize the neutron production, it is necessary to contain the Li-6 target gas under high pressure during the heating process. Since the gas

temperatures in some regions of the reactor are well above tolerance for any container material, some method for protecting the material must be made. External wall cooling techniques developed to protect the inside surfaces of rocket nozzles, which operate under similar but not as severe conditions, are being investigated for this application. The heat losses through the wall, however, must be minimal at the same time. Since

experimental values for the thermophysical properties are not known for lithium gas under the design conditions, heat balances were based upon values determined by extrapolation and calculation. In addition, the effects of disassociation, radiation, particle impingement, and possibly ion bombardment of the wall are considered in determining the heat balance of the system.

V-11. Zero Gradient Synchrotron Vertical Beam Study

H. MOSES,* R. L. MARTIN,† J. KASTNER* and A. J. ULRICH

The feasibility of using a vertical proton beam generated by the Zero Gradient Synchrotron to produce an ionized column in the atmosphere which in turn might be used for meteorological research has been investigated.¹

The use of a high-energy proton or electron beam, directed vertically to act as a probe for the study of atmospheric processes was proposed. An outstanding feature of such an atmospheric probe would be its capability to ionize a column of air repeatedly in a few microseconds and in approximately the same place.

There are a number of potential uses of an atmospheric ionized column for meteorological research. Such investigations may include the artificial initiation of lightning, the production of atmospheric ozone resulting from lightning, and the line spectra associated with the lightning channel. Furthermore, a method might be possible whereby a combination of the high-energy particle beam and infrared techniques may be used to determine the air circulation within a thunderstorm. There may be possible uses of a high-energy particle beam for aerospace sciences, such as the study of whistlers and electromagnetic radiation phenomena associated with the aurora and air glow.

An IBM-704 program was developed to compute proton flux, ionization rate in the atmosphere, electron density produced, the degree of ionization and the electrical conductivity of the air as a function of height and time after the proton beam entered the atmosphere. Because of the simplified model used, the answers obtained were recognized as being approximate but they were considered to be adequate for investigations of feasibility and evaluation.

The central effort of the study in 1964 was the determination of whether the proton beam could cause a lightning stroke from a thunderstorm cell passing overhead. The electrical conductivity of the ionized

column, although much better than that of normal air, was still extremely low compared to that of a good electrical conductor and therefore could not be important in the process. The electric field due to the proton space charge in the beam was shown to be negligible, as was that due to the bremsstrahlung from scattered electrons. The problem was reduced to the calculation of the charge separation in the ionized column due to ion drift, and the distortion of the electric field below the thunderstorm cell due to the unneutralized space charge thus produced. The free electrons liberated by ionization have a very short lifetime in air because they almost immediately attach themselves to oxygen. Consequently, the appropriate drift velocity for the negative charges is that of negative ions rather than free electrons. Recombination of the plasma then occurs between positive ions and negative ions rather than electrons.

A number of exploratory calculations were made. In a representative calculation a beam of 10^{13} protons emerged in 100 μ sec, and the recombination coefficient was taken to be 1.6×10^{-6} cm³/sec. Three values were chosen for the electric field due to the thunderstorm cell: 100 V/cm, 1000 V/cm and 10,000 V/cm. In each case the electric field distortion amounted to about 1% of the undistorted electric field. Therefore, in terms of the mechanisms which have been investigated thus far the frequency of lightning strikes is not likely to be significantly increased above normal because of the presence of the proton beam produced by this method of operation of the ZGS. Other experimental procedures to increase the electric field distortion are being considered.

REFERENCE

1. H. Moses, R. L. Martin, J. Kastner and A. J. Ulrich, *Manned Ionized Columns in the Atmosphere—a New Tool for Meteorological Research*, Radiological Physics Division Summary Report, July 1962 through June 1963, ANL-6769 (1963), p. 220.

* Radiological Physics Division.

† Particle Accelerator Division.

V-12. Evaluation of a Thermionic Diode for Space Power Using a Liquid Metal Electron Collector

A. J. ULRICH

The conventional plasma thermocouple or thermionic energy conversion diode has a solid metal electron collector. Cesium vapor at a pressure of a few millibars or less is widely used to provide ions for electron space charge neutralization. Under usual conditions, a layer of cesium coats the collector, so that electrically the collector appears to be cesium. This suggests the use of a diode with a liquid metal collector material such as cesium, rubidium, or potassium and their alloys, separated from the hot emitter by the vapor film produced in film boiling.¹⁻⁵

To investigate the feasibility of this concept, a series of experiments was performed. It was established that stable film boiling was possible for ranges of emitter temperatures and cesium and potassium vapor pressures which are useful for thermionic diodes. The range of subcooling of the liquid metal which was permissible was not prohibitively narrow. The spacing between emitter and liquid metal decreased as subcooling increased. It was estimated to be about 0.1 mm when the submersion was small, but the relationship between spacing and subcooling was not determined in these experiments.

Upon shutdown the transient behavior of electron bombardment heat to the emitter did not immediately lead to the violent nucleate boiling which was anticipated. For a step function shutdown the time lag before violent nucleate boiling occurred might be of the order of 20 sec for a fission-heated diode.

The few millimeters of submersion which can be tolerated indicates that a thermionic reactor cannot be made simply by plunging an array of fission heated emitters into a tank of flowing liquid metal. On the other hand, the submersion which is possible shows that diodes could indeed still continue to operate if radiation damage were to warp the emitters badly. In addition the concept gives promise of ameliorating the electron emitter evaporation problem.

Thermionic reactor fuel elements usually contain many diodes in series, all supplied with cesium vapor from a common source capsule containing liquid cesium which is usually located at the end of the fuel element (see Fig. V-12-1). The cesium vapor pressure in the diodes is determined by the temperature of the cesium liquid in the capsule. This same basic fuel element can be used in a film boiling liquid metal design to produce power in the zero gravity field of space. By controlling the temperature of the electron collec-

tors within $\pm 10^\circ$ K, liquid cesium alloy may be condensed on them in any desired thickness, the vapor being transported from the capsule at the end of the element. Use of vapor transport is mentioned in the discussion following presentation of the paper cited in Ref. 4. The spacing between emitter and liquid collector is then determined by the subcooling which is imposed.

This improvement in a space application requires chiefly more precise control of collector temperatures, a modified startup and shutdown schedule to avoid nucleate boiling and development of a new thermal divider, to exclude nucleate boiling from the boundaries of the collector surface. Preliminary work on this type of divider has been reported.⁶

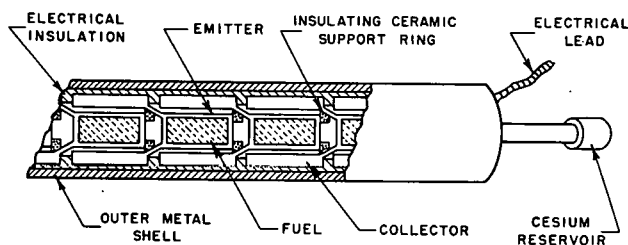


Fig. V-12-1. Cross Section of a Typical In-Core Thermionic Fuel Element.

An auxiliary benefit may be a much more reliable thermal bond between the collector and the coolant channel.

These problems are being approached from other directions. The use of a cesium coated refractory metal clad on the fuel as an emitter eliminates the evaporation problem and gives an added advantage of a variable work function. This is very satisfactory but it required a closer electrode spacing, which makes the radiation damage problem more critical. The radiation problem is currently being studied independently as a fundamental problem. If the study does not result in an adequate reduction of radiation damage, it will be necessary to develop other means of avoiding diode shorting.

REFERENCES

1. J. C. Fischer, *Thermionic Generator*, U.S. Pat. 3,002,116 (September 26, 1961).
2. A. J. Ulrich, *Thermionic Energy Conversion Diode Using a Film Boiling Liquid Metal Anode*, J. Appl. Phys. **33**, No. 5, 1896 (May, 1962).

3. P. Brosens and G. N. Hatsopoulos, *Thermionic Energy Converter with a Liquid Collector*, *Advanced Energy Conversion* **3**, No. 1, 387 (1963).
4. A. J. Ulrich, *Thermionic Energy Conversion Diodes Using a Film Boiling Liquid Metal Electron Collector*, *Advanced Energy Conversion* **3**, No. 1, 397 (1963).
5. A. J. Ulrich, *Stability of a Thermionic Energy Conversion Diode Using a Liquid Metal Electron Collector*, *Bull. Am. Phys. Soc.* **8**, Paper W7, 445, (June, 1963).
6. A. J. Ulrich, *Thermionic Energy Conversion Diode Using a Film Boiling Liquid Metal Anode—Progress from February 1961 to September 1961*, ANL-6465, (1961) p. 10.

V-13. Numerical Integration by Iterative Procedures and by Rational Osculatory Interpolation

H. C. THACHER, JR.

Studies of methods of estimating integrals from numerical data resulted in three publications, two with regard to functions of many variables, and one on functions which are well represented as ratios of polynomials.

The first paper on multivariate quadrature¹ describes a combination of the multivariate quadrature method of Thacher and Milne² and Thacher's iterative algorithm³ for integrating functions of a single variable. The resulting algorithm is convenient for estimating the integral of the interpolating polynomial from data at any set of points sufficient to define the polynomial uniquely.

The difficult combinatorial problem of selecting sets of points which satisfy this criterion, i.e., which are degree- n independent, is somewhat alleviated by the theorem:

Let T be any linear transformation which is non-singular with respect to the set of points $\{x_j\}$. Then for all n , $\{x_j\}$ and $\{Tx_j\}$ are either both degree- n dependent or degree- n independent.

Since the lattice points of a simplicial grid of n points on an edge are known to be degree- n independent, this theorem permits the generation of a large variety of other independent sets of points.

The second paper on multivariate quadrature⁴ is devoted to the integration of functions which cannot be represented effectively by a single approximation over the entire region of integration. Under these circumstances, it is advisable to subdivide the region into several subdomains, and to use a fairly low-degree approximating function over each subdomain. A quadrature formula accurate for all quadratics in s variables has been found which requires knowledge of the integrand at one point on each face of an s -dimensional hyperparallelepipedon, and at one interior point. Since the values of the function associated with points on opposite faces of the subdomain appear with weights of equal magnitude but opposite sign, their contributions

cancel, and the integral over the entire region requires only one function value per subdivision, plus one point from each subdivision of the surface of the region. An extensive series of trials indicated that the new method is more efficient than simple Monte Carlo, except when fewer than 300 points are allowed. For smooth functions, however, multiple Gaussian formulas are even more efficient.

In integrating ordinary differential equations by predictor-corrector methods, the corrector formula is ordinarily an open integration formula, that is, the integral from x_1 to x_0 is expressed in terms of the values of the integrand at x_0, x_1, \dots, x_n , and of the integral at x_1, \dots, x_n . These formulas have previously been derived on the assumption that the integral can be adequately represented by a polynomial over the range x_0, x_n . Badly behaved functions are often far better represented by ratios of polynomials than by polynomials, and an integration formula which is exact for rational functions would be of interest for numerical solution of differential equations. In 1961, Thacher⁵ and Salzer⁶ independently discovered algorithms for rational osculatory interpolation, which could be used as closed, predictor formulas. However, their algorithms were not applicable unless function values were specified. A family of open quadrature formulas has now been discovered which are exact whenever the integral is a rational function.

The first member of this family is:

$$y(x_0) = y(x_1) + (x_0 - x_1) \operatorname{sgn}(f_1) \sqrt{f_0 f_1} \quad (1)$$

where f_i is the derivative of $y(x)$ at the point x_i and $\operatorname{sgn}(x < 0) = -1$, $\operatorname{sgn}(x = 0) = 0$, and $\operatorname{sgn}(x > 0) = +1$. This formula is analogous to the trapezoidal rule with the arithmetic mean replaced by the geometric mean. Aside from its interest for numerical solution of differential equations, Eq. (1) leads to a variety of interesting approximations for elementary

functions, including

$$\ln x \cong x^{1/2} - x^{-1/2} \quad (2)$$

with an error $-\frac{1}{24}(x-1)^3 + O(x^4)$;

$$\tan x \cong x \frac{\left(1 + \frac{5}{12}x^2 \sqrt{1 - \frac{4}{25}x^2 - \frac{x^2}{12}}\right)}{1 - \frac{x^4}{6}} \quad (3)$$

with an error $+\frac{2}{7575}x^7 + O(x^9)$.

The three-point formula is considerably more complicated, and requires special treatment when the data are consistent with two distinct rational functions. These cases have been analyzed in detail.⁷

V-14. Evaluation of Functions by Shifted Chebyshev Polynomials

H. C. THACHER, JR.

Evaluation of functions requires a large fraction of the time in most scientific computer programs, and improvements in techniques for this task are of general value. For the common elementary functions, considerable effort has been devoted to computing the coefficients of polynomials, or of ratios of polynomials, which minimize the maximum deviation from the desired function over a suitable range. For the less familiar transcendental functions, this effort is rarely expended, and users are content with truncated power series, or other infinite expansions. Clenshaw¹ has recently advocated an intermediate form of machine table, the truncated expansion in Chebyshev polynomials. These expansions converge rapidly for many functions—more rapidly in fact than expansion alternates in sign in a manner which is very close to that which characterizes minimum deviation polynomials and rational approximations.

When the function to be approximated has a rapidly convergent power series, it is possible to rearrange this series to obtain the coefficients in the Fourier-Chebyshev series. This is the basis of Lanczos' familiar economization procedure. When the power series converges slowly, or fails to converge over part of the range, direct rearrangement is unsatisfactory, and Clenshaw recommends other, more complicated devices. In a recent paper² it has been shown that the Fourier-Chebyshev coefficients can be obtained by rearranging slowly-convergent or even divergent power series by

REFERENCES

1. H. C. Thacher, Jr., *Numerical Integration and Differentiation of Functions of Several Independent Variables by an Iterative Procedure*, J. Soc. Ind. Appl. Math. **11**, 614-622 (1963).
2. H. C. Thacher, Jr. and W. E. Milne, *Interpolation in Several Variables*, J. Soc. Ind. Appl. Math. **8**, 33-42 (1960).
3. H. C. Thacher, Jr., *An Iterative Method for Quadratures*, Comput. J. **5**, 270-271 (1962).
4. H. C. Thacher, Jr., *An Efficient Composite Formula for Multi-dimensional Quadrature*, Comm. ACM, **7**, 23-25 (1964).
5. H. C. Thacher, Jr., *A Recursive Algorithm for Rational Osculatory Interpolation*, J. Soc. Ind. Appl. Math. Rev. **3**, 359 (1961).
6. H. E. Salzer, *Note on Osculatory Rational Interpolation*, Math. Comput. **16**, 486 (1962).
7. H. C. Thacher, Jr., *Closed Rational Integration Formulas*, Comput. J., (to be published).

suitable use of summation procedures. Briefly, let

$$f(x) = \sum_{r=0}^{\infty} a_r x^r = \sum_{q=0}^{\infty} c_q T_q(x) \quad (1)$$

where the prime on the second summation indicates that the first term is to be halved, and let $\nu_{r,q}$ be the coefficient of the q th Chebyshev polynomial, $T_q(x)$, in the expression of x^r in terms of Chebyshev polynomials. Then

$$c_q = \sum_{r=q}^{\infty} a_r \nu_{r,q} \quad (2)$$

If the power series converges rapidly, only a few terms of Eq. (2) will be significant. If many terms of Eq. (2) are significant, one of the many summation devices, such as the Euler summation formula, or the ϵ algorithm may be applied to estimate the sum. As examples, the coefficients in the expansion of $\ln(1+x)$ in shifted Chebyshev polynomials were found correct to 6D from the first 10 terms of the power series, and acceptable values were even obtained for $\ln(1+3x)$ where the power series converges only over $\frac{1}{3}$ of the range. The technique was also used successfully to obtain an expansion of the dilogarithm function.

Expansions in Chebyshev polynomials converge slowly, and are therefore inefficient, in the neighborhood of a singularity. Under these circumstances, rational approximations are apt to be definitely superior. The flexibility, stability, and convenience of the Chebyshev

expansion can be retained to a large extent, while gaining the power of the rational form of approximation, by making a rational transformation of the independent variable. For example, the Fourier-Chebyshev series for the natural logarithm in the form

$$\ln(1+x) = \sum_{r=0}^{\infty} c_r T_r^*(x) \quad (3)$$

requires 25 terms to achieve 20D accuracy. By rearranging the power series

$$\ln x = 2 \left(\frac{x-1}{x+1} \right) \sum_{k=1}^{\infty} \frac{1}{2k+1} \left(\frac{x-1}{x+1} \right)^{2k}$$

an expansion

$$\ln x = \left(\frac{x-1}{x+1} \right) \sum_{k=0}^{\infty} c_k T_{2k} \left(\frac{x-1}{sx+1} \right)$$

was obtained, where s is selected so that the variable in the polynomial ranges between -1 and 1 as x ranges

between $\sqrt{1/R}$ and \sqrt{R} . For $R = 2$, $s = 0.1715 \dots$, and for $R = 10$, $s = 0.5194 \dots$. In the former case, 12 terms are sufficient to give 28 significant digit accuracy, and 9 to give 20S accuracy. For the decimal range, 24 terms give 28S accuracy and 16 give 20S accuracy. This example illustrates the great potential advantages of transformations of the independent variable, a device which has been somewhat neglected in the practice of approximation. The study of these transformations is being extended to a variety of other functions for which Clenshaw found slow convergence of the Fourier-Chebyshev coefficients.

REFERENCES

1. C. W. Clenshaw, *Chebyshev Series for Mathematical Functions*, National Physical Laboratory Mathematical Tables, Vol. 5 (Her Majesty's Stationary Office London, 1962), pp. 1-4, 25.
2. H. C. Thacher, Jr., *Conversion of a Power to a Series of Chebyshev Polynomials*, Comm. ACM 7, 181-182 (1964).

V-15. Generalized Recursive Interpolation

P. M. LUKEHART

Most widely known interpolation procedures use polynomials as basis functions and many of these procedures are applicable only for equally-spaced points. Although these are sufficient in many cases there are many other cases for which they are not the best. For example, if it is known that the desired function approaches some finite value in the limit or that it is periodic, polynomial approximations are not efficient. It is obvious that equally-spaced data are not always available, especially when the data are experimental.

H. Thacher¹ has developed a generalized method which is flexible enough to be useful in almost all cases in which the data and results are function values, at least in exploratory analysis. It is desirable to generalize the approach further to allow more general linear functionals than function values both as data and as results. A linear functional, L_i , is simply a method for associating with any function, f , a scalar value, $L_i f$. The functional must satisfy the relation,

$$L_i(a_1 f_1 + a_2 f_2) = a_1 L_i f_1 + a_2 L_i f_2 \quad (1)$$

where f_1, f_2 are functions and a_1, a_2 are scalars. The most common linear functionals are derivatives and definite integrals and of course, function values.

The problem is: given a set of linear functionals, $L_i f$, $i = 1, 2, \dots, n$, on a function f , to construct a

sequence of estimates, LR_k , $k = 1, 2, \dots, n$, of the functional, $L_j f$, such that

$$L_i R_k(x) = L_i f, \quad (i = 1, 2, \dots, k). \quad (2)$$

Let us consider a set of basis functions, $\Omega_j(x)$, which satisfy the conditions:

$$L_i \Omega_j(x) = 0, \quad (i = 1, 2, \dots, j-1) \quad (3)$$

$$L_j \Omega_j(x) \neq 0. \quad (4)$$

Let $R_1(x)$ be a function such that $L_1 R_1(x) = L_1 f$. Then the sequence of functionals generated recursively by

$$LR_j(x) = LR_{j-1}(x) + a_j L_j \Omega_j(x) \quad (5)$$

where

$$a_j = \frac{L_j f - L_j R_{j-1}(x)}{L_j \Omega_j(x)}$$

satisfy Eq. (2).

The $\Omega_j(x)$ may be any functions which satisfy the conditions Eqs. (3) and (4). A fairly general set may be constructed in the form $\Omega_1(x) = 1$ and

$$\Omega_j(x) = [g_j(x) - g_j(x_{j-1})] \Omega_{j-1}(x) \quad (6)$$

where the $g_j(x)$ are arbitrarily chosen except that $g_j(x_i) \neq g_j(x_{j-1})$ for $i \geq j$.

A few examples have been studied where the $g_j(x)$ are all the same. If $g(x) = x$ the basis functions are polynomials in x and an ordinary polynomial function is obtained. If $g(x) = x^n$ the approximation function is a polynomial in x^n . For a trigonometric interpolation an appropriate function would be $g(x) = \cos x$. If the base points are chosen as the zeros of the first neglected Chebyshev polynomial this turns out to be a Chebyshev approximation in $\cos x$. It is also possible to use $g(x) = \sin x$.

The linear operation of differentiation is not difficult

regardless of the form of the $g_j(x)$, since the expression for $\Omega_j(x)$ can be differentiated as:

$$\Omega_j'(x) = [g_j(x) - g_j(x_{j-1})]\Omega'_{j-1}(x) + g'_j(x)\Omega_{j-1}(x) \quad (7)$$

However, the examples given are also easily integrated. In choosing the function, $g(x)$ to be used in an integration problem it will be necessary that $\int_a^x [g(x)]^n dx$ be integrable.

REFERENCES

1. H. C. Thacher, Jr., Argonne National Laboratory, (private communication).

V-16. Kutta-Merson Solutions of Differential Equations

P. M. LUKEHART

The Kutta-Merson¹ method for solving systems of ordinary first-order differential equations is of the Runge-Kutta type but, by evaluating an extra iterative function, gives a fairly good bound on the truncation error. Thus by adjusting the interval of calculation the error may be kept within a specified bond.

An Algol version of the method was published² and has been transcribed into a number of other languages for use on different computers at the Laboratory. The program will solve a system of first-order equations $y_i = f_i(t, y_1, y_2, \dots, y_n)$ where initial values of all variables, t, y_1, y_2, \dots, y_n , are given. An interval, h , is specified at which results are printed but the working interval is adjusted by the program to keep the error below the specified limit and to compensate for the behavior of the function at any place in the range.

The Kutta-Merson method has been found to be quite useful in a wide variety of applied problems. Among them is the problem of constructing an analytic model to describe the boiling coolant pressure pulse for a known power pulse in a reactor. Manipulation of the basic equations leads to a second order non-linear differential equation:

$$\begin{aligned} \frac{d^2 P}{dt^2} &= \left(\frac{2}{P} - \frac{bm_0c}{\alpha} \right) \left(\frac{dP}{dt} \right)^2 + q_1 \left(\frac{b}{\alpha} - \frac{2}{\beta} \right) \frac{dP}{dt} \\ &+ \left(\frac{bm_0cq_1}{\alpha\beta} \right) P \frac{dP}{dt} + \left(\frac{1}{\beta} \frac{dq_1}{dt} - \frac{bq_1^2}{\alpha\beta} \right) P \\ &+ \frac{A^2 P^2}{Gb\alpha\beta} (P_0 - P) \\ \alpha &= m_0 - b \int_0^t q_1(\xi) d\xi + m_0cb(P - P_0) \end{aligned}$$

$$\beta = \int_0^t q_1(\xi) d\xi + m_0cP_0$$

$$q_1 = q_1(t)$$

where $P(t)$ = pressure as a function of time

P_0 = initial pressure

$q_1(t)$ = power entering system as a function of time

A = constant effective cross-sectional area of coolant in heated section

m_0 = total liquid-vapor mass in system

G = average value of the product of the vapor's specific volume and corresponding pressure

c = average value of the amount of energy required to raise the temperature of unit liquid mass sufficiently to cause unit pressure increase

$\beta(t)$ = total energy in system as a function of time

b = average value of the reciprocal of the enthalpy of vaporization.

This equation can be further manipulated into five first-order differential equations so that it may be solved by the Kutta-Merson method.

REFERENCES

1. L. Fox, *Numerical Solution of Ordinary and Partial Differential Equations*, (Pergamon Press, New York, 1962), p. 24.
2. P. M. Lukehart, *Algorithm 218-Kutta-Merson*, Comm. ACM, 6, No. 12, 37-38 (1963).

V-17. Nuclear Data Compilation Activities

A. B. SMITH and W. G. VONACH

The proper reporting of results is inherent to the research activity. In addition to this requisite, appreciable effort has been expended upon compilation activities of a more general nature. Primary of these is the Compilation of Requests for Nuclear Cross Sections (WASH-1047). This compilation has been formulated on punched cards. In this format it is possible to rapidly update and produce the printed document, utilizing data processing equipment, correlate the request compilation with known information (The BNL Sigma Center), and assay the requests in the context of the national requirements and capabilities for the production of basic nucleonic data. This compilation provides the nuclear physics community with an up-to-date

listing of the cross sections needed in the applied nuclear energy program and a measure of their relative importance. In addition, it is hoped that it will become a valuable tool for the guidance of the long range cross section program of this country.

It is noteworthy that the neutron cross section field is one of the few scientific disciplines where a common computer language is employed to describe the physical phenomena (The Request Compilation, CINDA bibliography, and the data compilation at Sigma Center). This common language is fundamental to the referencing and transfer of the necessary large amounts of data.

V-18. Reactor Physics Constants Center

L. J. TEMPLIN

The primary objective of the Reactor Physics Constants Center is the periodic compilation and publication of the latest and best values of the constants and formulae which are necessary to calculate reactor characteristics. In addition to providing a unified compilation of pertinent data, the precepts of the Center are: (1) to encourage critical comparison of experiment with theory; (2) to encourage critical analysis of experimental techniques; (3) to encourage critical evaluations of contradictory data; (4) to call attention to areas where further experimental and theoretical work will be most profitable; and (5) to promote standardization in definitions of reactor physics parameters.

The first compilation was published in 1958 as "Reactor Physics Constants," ANL-5800. Again, late in 1960, a group of reactor physicists from the original Reactor Engineering Division and mathematicians from the Applied Mathematics Division undertook to review and evaluate more than fifteen hundred reports and books for the purpose of publishing an updated compilation. Additionally, a considerable amount of information was acquired by direct communication with both U.S. and European scientists. In late 1963, "Reactor Physics Constants," ANL-5800 Second Edition, was successfully published and distributed.

V-19. Resonance Integrals for Dilute Solution

P. J. PERSIANI, A. E. MCARTHY and J. J. KAGANOVE*

Many nuclei of interest to reactor physicists require the introduction of negative energy levels in

* Applied Mathematics Division, Argonne National Laboratory.

order to describe the experimental low energy neutron cross section data.¹ To investigate the contribution of these levels to the resonance integral for infinite dilution, the capture and fission integrals were evaluated

by relaxing the usual assumption that the cut-off energy be much lower than the lowest resonance energy level.

In the single-level Breit-Wigner approximation, the integral which includes negative energy levels is

$$I_{\infty,x}(P) = \int_{E_c}^{\infty} \sigma_x \frac{dE}{E} \\ = \frac{\pi \hbar^2}{2m} \sum_{i=1}^N g_i \Gamma_{n_i}^0 \Gamma_{x_i} \\ \int_{E_c}^{\infty} \frac{dE}{E^{3/2} [(E - PE_i)^2 + \frac{1}{4}(E^{1/2} \Gamma_{n_i}^0 + \Gamma_{f_i} + \Gamma_{\gamma_i})^2]} \quad (1)$$

where P is (+1) and (-1) for positive and negative energy levels respectively, and x denotes the reaction process of interest ($x = c$, radiative capture and $x = f$, fission). The definitions of the remaining symbols are those commonly used.

The solution for equation (1) was coded for the IBM-704 and designated as ANL-RE-266.

The contribution from the unresolved levels includes the effect of the fluctuation of the reduced neutron widths as given by C. Porter and R. Thomas.² The statistical distribution of the fission widths was neglected. This error could be masked by the error introduced in not utilizing the multi-level formalism for nuclei with fission channels.^{3,4} The sensitivity of the resonance integral to the details of the level formula has not been investigated.

Calculation of the capture and fission cross sections as a function of energy, in the one level approximation, has also been programmed into the code. This serves as a check on the choice of parameters, when a choice exists, by comparing the computed cross section with the experimental data.

A continuing search is being made in the literature and recently reported experimental and calculated data have been listed in Ref. 5. The computed values obtained by the above code are included in this publication. The experimental data are supplemental to the data reported in Ref. 6 and the computed values supersede those of Ref. 6.

In Table V-19-I are listed separately and in more detail the computed and experimental resonance integrals for those nuclei whose negative energy level parameters are available.

The negative energy level parameters used for U-235 were those reported by J. Harvey and J. Sanders.⁷ The positive level parameters used were essentially a combination of those listed in BNL-325 2nd Ed. supplement 1, and the data of W. Havens, *et al.*⁸ This choice of parameters gives a computed fission cross section, in the energy region of 0.025 eV to 0.44 eV, in very good agreement with the data in BNL-325. The con-

tribution of the bound levels (52.8 b) to the fission resonance integral, brings the computed value into better agreement with the experimental value of 271 ± 11 b.^{9,10}

The parameter data of L. Bollinger, *et al.*,¹¹ were used in computing the resonance integrals of Pu-239. The bound level contributes 13.6 b, giving a total of 280 b for the fission integral. Although this is in fair agreement with the experimental value of 327 ± 22 b,¹⁰ the computed fission cross section does not agree too well with the BNL-325 data in the energy region from 0.025 eV to 0.44 eV. The computed cross section values were somewhat lower. This discrepancy results from the failure of the single level Breit-Wigner formalism to adequately describe the cross section for the fissile isotopes.

In the absence of fission channels, the radiative capture cross section can be adequately described by the sum of single level Breit-Wigner terms. For these nuclei, one should expect a higher degree of consistency between the computed cross sections and resonance integrals with the respective experimental data.

The negative level parameters used for Th-232 and U-234 were those reported by G. Cooper, *et al.*¹² The positive level parameters for U-234 were taken from BNL-325 and for Th-232 the data used was that of J. Desjardins, *et al.*¹³ The experimental value for the resonance integral of U-234 is not available for comparison.

In the case of Th-232, the bound level is found to contribute 1.2 b to the capture integral. The total integral, i.e., resolved and unresolved, of 94 b lies be-

TABLE V-19-I. FISSILE ISOTOPES, CUTOFF ENERGY 0.44 eV

	U-235		Pu-239	
	$I_{\infty,f}$, b	$I_{\infty,c}$, b	$I_{\infty,f}$, b	$I_{\infty,c}$, b
(+) levels	153.9	135.4	189.9	147.7
(-) levels	52.8	9.0	13.6	3.4
Unresolved	57.7	43.8	76.7	30.4
Total	264.4	188.3	280.2	181.5
Experimental values	271 ± 11		327 ± 22	

NON-FISSILE ISOTOPES, $I_{\infty,c}$, CUTOFF ENERGY 0.44 eV

	Th-232	U-234	Dy-164
(+) levels	89.6	634.0	19.6
(-) levels	1.2	9.2	351.7
Unresolved	3.2	18.1	10.8
Total	94.0	661.4	382.1
Experimental values	110		482 ± 33
	85		

tween the two experimental values of 85 b¹⁴ and 110 b.¹⁵

The Dy-164 bound level was determined by R. Sher, *et al.*,¹⁶ using a fitting procedure which did not require specifying the radiation width. The total capture integral was found to be 416 b when the radiation width was taken to be that of the positive level, $\Gamma_\gamma = 115$ mV. However using this width in the Breit-Wigner formula, the computed cross section was in complete disagreement with the experimental data in the energy region from 0.25 eV to 2.0 eV. It was found that a radiative width of 76 mV was in excellent agreement with the data. This width then yielded a resonance integral of 382 b which is approximately 100 b less than the experimental value of 482 ± 33 b reported by G. Jacks.¹⁷ Part of this discrepancy may be resolved if the experimental method of determining integrals, particularly for strong non $1/v$ behavior, is modified to include cadmium difference ratios rather than cadmium ratios. The bound level in Dy-164 comprises 92% of the resonance integral.

The computations indicate that negative energy levels may contribute appreciably to resonance integrals. It should then be expected that these levels would also contribute to resonance integrals for finite dilutions and heterogeneous mixtures.

REFERENCES

1. P. J. Persiani, J. J. Kaganove and A. E. McArthur, *The Contribution of Negative Energy Levels to Resonance Integrals*, Trans. Am. Nucl. Soc. **6**, No. 1, 39 (June, 1963).
2. C. E. Porter and R. G. Thomas, *Fluctuations of Nuclear Reaction Widths*, Phys. Rev. **104**, 483 (1956).
3. E. Vogt, *Resonance Theory of Neutron Cross Sections of Fissionable Nuclei*, Phys. Rev. **112**, 203 (1958); Phys. Rev., **118**, 724 (1960).
4. C. W. Reich and M. S. Moore, *Multilevel Formula for the Fission Process*, Phys. Rev. **111**, 929 (1958); Phys. Rev. **118**, 718 (1960).
5. Reactor Physics Constants Center Newsletter No. 10 (April, 1963).
6. Reactor Physics Constants Center Newsletter No. 1 (June, 1961).
7. J. A. Harvey and J. E. Sanders, *Progress in Nuclear Physics, Physics and Mathematics*, (McGraw-Hill Book Co., Inc., New York, 1955).
8. W. W. Havens, Jr., *et al.*, *Resonance Fission Widths of U-235 for Levels from 6 eV to 50 eV*, Phys. Rev. **116**, 1538 (1959); see also *Multi-Region Reactor Lattice Studies. Microscopic Lattice Parameters in Single- and Multi-Region Cores; A Comparison of Theory and Experiment*, WCAP-1434 (June, 1961).
9. R. L. Maklin and H. S. Pomerance, *Resonance Capture Integrals*, Proc., 1955 Geneva Conference, **5**, Paper No. 96, p. 883.
10. J. Hardy, Jr., D. Klein and G. G. Smith, *The Resonance Fission Integrals of U-235, Pu-239, Pu-241*, Nucl. Sci. Eng. **9**, No. 3, 341-345, (March, 1961).
11. L. M. Bollinger, *et al.*, *The Slow Neutron Cross Section of Plutonium-239*, Proc., 1958 Geneva Conference, **15**, Paper No. 687, p. 127.
12. G. S. Cooper, J. D. Garrison and H. A. Hines, *The Negative Energy Resonance Parameters of Th-232 and U-234*, Trans. Am. Nucl. Soc. **4**, 271 (November, 1961).
13. J. S. Desjardins, *et al.*, WASH-1029, *Reports to the AEC Nuclear Cross Sections Advisory Group*, p. 19 (September, 1960).
14. F. J. Johnston, J. Halperin and R. W. Stoughton, *The Thermal Neutron Absorption Cross Section of Th-233 and the Resonance Integrals of Th-232, Th-233 and Co 59*, J. Nucl. Energy, Part A, Reactor Science, **11**, 95-100 (1960).
15. R. B. Tattersall, *et al.*, *Pile Oscillator Measurements of Resonance Absorption Integrals*, AERE-R/2387 (August, 1959).
16. R. Sher, *et al.*, *Low Energy Neutron Cross Sections of Dy-164*, Nucl. Sci. Eng., **11**, No. 4, 369-376 (1961).
17. G. M. Jacks (Transmitted by J. L. Crandall) Savannah River, 1960 (private communication).

V-20. A Fortran Code for Cylindrical Lattice Collision Probabilities (B692/RP)

E. M. PENNINGTON

Fortran codes have been written which compute first collision probabilities for either a two-region or a three-region unit cells in cylindrical geometry. It is assumed that neutrons incident on the boundary of the unit cell from the inside are returned isotropically rather than with mirror image reflection. Reference 1 presents the derivation of the equations involved along with a description of the Fortran codes (B692/RP) including listings and sample input and output sheets.

Reference 2 compares collision probabilities using the assumption of isotropic return and the Wegner-Seitz unit cell approximation for a two-region lattice with results using Fukai's exact method and other approximate methods. In Fukai's method the neutron paths in the actual lattice are considered without the unit cell approximation. The B692/RP collision probabilities are in rather good agreement with Fukai's exact values. Also in Ref. 2, collision probabilities for the

TABLE V-20-I. THERMAL FLUX RATIOS FOR HI-C AND BORAX-V LATTICES
(Data in part from Ref. 2)

Core and Lattice	Flux Ratio	27 Group THERMOS	One Group THERMOS	B692/RP	Core and Lattice	Flux Ratio	27 Group THERMOS	One Group THERMOS	B692/RP
BORAX-V } 1.27 cm □	$\bar{\phi}_2/\bar{\phi}_1$	1.1150	1.1125	1.1173	Hi-C Al } 1.166 cm Δ	$\bar{\phi}_2/\bar{\phi}_1$	1.0853	1.0865	1.0870
	$\bar{\phi}_3/\bar{\phi}_1$	1.2535	1.2462	1.2394		$\bar{\phi}_3/\bar{\phi}_1$	1.1286	1.1299	1.1299
BORAX-V } 1.27 cm Δ	$\bar{\phi}_2/\bar{\phi}_1$	1.1124	1.1105	1.1142	Hi-C SS } 1.166 cm Δ	$\bar{\phi}_2/\bar{\phi}_1$	1.0781	1.0789	1.0801
	$\bar{\phi}_3/\bar{\phi}_1$	1.2299	1.2249	1.2203		$\bar{\phi}_3/\bar{\phi}_1$	1.1375	1.1391	1.1397
Hi-C Al } 1.24 cm □	$\bar{\phi}_2/\bar{\phi}_1$	1.0894	1.0890	1.0902	Hi-C Al } 1.127 cm Δ	$\bar{\phi}_2/\bar{\phi}_1$	1.0831	1.0848	1.0858
	$\bar{\phi}_3/\bar{\phi}_1$	1.1572	1.1551	1.1497		$\bar{\phi}_3/\bar{\phi}_1$	1.1271	1.1299	1.1260
Hi-C SS } 1.24 cm □	$\bar{\phi}_2/\bar{\phi}_1$	1.0819	1.0815	1.0836	Hi-C SS } 1.127 cm Δ	$\bar{\phi}_2/\bar{\phi}_1$	1.0772	1.0785	1.0798
	$\bar{\phi}_3/\bar{\phi}_1$	1.1709	1.1687	1.1634		$\bar{\phi}_3/\bar{\phi}_1$	1.1367	1.1395	1.1363
Hi-C Al } 1.27 cm Δ	$\bar{\phi}_2/\bar{\phi}_1$	1.0880	1.0879	1.0887					
	$\bar{\phi}_3/\bar{\phi}_1$	1.1486	1.1477	1.1413					
Hi-C SS } 1.27 cm Δ	$\bar{\phi}_2/\bar{\phi}_1$	1.0807	1.0807	1.0824					
	$\bar{\phi}_3/\bar{\phi}_1$	1.1615	1.1607	1.1544					

two-region cell are used along with the flat flux approximation in calculating thermal disadvantage factors which are compared with those from discrete ordinate calculations using various boundary conditions. For the three-region cell average thermal fluxes are compared with those computed by the THERMOS code. The results obtained are in good agreement with those from the W-DSN code with the isotropic boundary condition or from the DTK or THERMOS codes with an extra scattering region as proposed by H. Honeck.³ Such agreement is expected for lattices where

the flat flux approximation is justified. Fluxes for the three-region lattices as obtained using both THERMOS and B692/RP are given in Table V-20-I.

REFERENCES

1. E. M. Pennington, *Cylindrical Lattice Collision Probability Codes, B692/RP*, ANL-6836 (1964).
2. E. M. Pennington, *Collision Probabilities in Cylindrical Lattices*, Nucl. Sci. Eng. **19**, 215 (1964).
3. H. C. Honeck, *Some Methods for Improving the Cylindrical Reflecting Boundary Condition in Cell Calculations of the Thermal Neutron Flux*, Trans. Am. Nucl. Soc. **5**, No. 2, 350 (1962).

V-21. Foil Activation Programs, B512/RP

E. M. PENNINGTON

Programs have been written in Fortran which calculate cutoff energies and various activation integrals for covered foils in slab geometry. The derivation of the equations involved and the description of the programs, including listings and input and output sheets, are given in Ref. 1. The original versions of the programs were roughly equivalent to those described in Ref. 2. In these versions, cutoff energies were calculated for a slab $1/\nu$ absorbing foil between covers having a cross section consisting of a single Breit-Wigner resonance. Either an isotropic or beam flux was used, with the energy dependence being a Maxwellian plus a

$1/E$ tail. When the programs were later modified to conform to the IBM-704 monitor system, a number of features were added.

Both the slab absorbing foil and covers are of arbitrary thicknesses and have absorption cross sections consisting of a $1/\nu$ part and/or Breit-Wigner resonances. The angular dependence of the neutron flux is either isotropic or beam; whereas the energy dependence is either Maxwellian with several epithermal options including a $1/E$ form, or a flux input for a suitable number of energy values. A rough treatment of outer flux depression is available in the isotropic flux

case. Absorption integrals above and below the cutoff energy are calculated for both the bare and covered absorbing foil; and, in the analytical flux case, for both Maxwellian and epithermal components. An optional output of various functions at each energy involved in the integrations is available.

V-22. Multigroup Constants Code MC'

D. M. O'SHEA

A FORTRAN program to compute multigroup constants from evaluated monochromatic data has been written for the CDC-3600. Given the users input specification, the code will extract the basic cross section data from a library stored on magnetic tape. The program will then form group cross sections for a suitably large number of fine groups, and finally average these constants over either a specified or calculated spectrum. An ELMOE¹ type calculation may be done if desired.

Doppler broadened cross sections over the resolved resonance region are calculated for a homogeneous mixture. The method follows the intermediate representation of E. Cohen and R. Goldstein.² The interference between resonance and potential scattering, and the interference with overlapping resonances in other isotopes is allowed.

The average cross section, $\bar{\sigma}_{ci}$, for a fine group over the region of resolved resonances is expressed as

$$\bar{\sigma}_{ci} = \int_{E_i}^{E_{i+1}} \frac{\sigma_c(E) dE}{\Sigma_i(E)} / \int_{E_i}^{E_{i+1}} \frac{dE}{\Sigma_i(E)}$$

where the integration is carried out over the limits of the fine group.

In order to reduce the computation time, the code uses the Romberg integration method.³ In this method the number of points in the interval and the degree of the approximating polynomial are successively doubled until convergence of the integral is obtained. The method retains the values of the ordinates previously computed for use in the current calculation.

Doppler line shape functions are computed by the continued fraction expansions described in Ref. 4.

Cross sections which are smoothly varying over energy are represented in the library by the coordinates of end points of linear segments taken from log E -log σ , log E -linear σ , or linear E -linear σ graphs.

REFERENCES

1. E. M. Pennington and W. L. Boettinger, *Foil Activation Programs, B612/RP, ANL-6822* (1964).
2. G. D. Hickman and W. B. Leng, *The Calculation of Effective Cutoff Energies in Cadmium, Samarium, and Gadolinium*, *Nucl. Sci. Eng.* **12**, 523 (1962).

Fine group cross sections are obtained by interpolation over the fine group limits.

Data on the average number of neutrons emitted per fission is represented by polynomial fits to the data. The coefficients for these polynomials are stored in the library.

Inelastic scattering matrices are computed from excitation functions for individual levels. The statistical model is used above the region of resolved level. Level excitation data and data on nuclear temperature are represented in the library by linear segments from the graphs of these functions.

The fission spectrum source for a fine group is represented by a function of the type

$$F_j = A \int_{\text{group } j} e^{-BE} \sinh \sqrt{CE} dE$$

where A , B , and C are constants. An analytic representation for the integral is used.

The elastic scattering treatment of light elements has been adapted from the ELMOE program. Modifications have been made to remove the restriction that all materials must scatter an integral number of groups. The present ELMOE library of Legendre coefficients is used.

Calculation of the weighting spectrum is presently done in the ordinary P-1 approximation. The program assumes data is available for either a fine group width, or a coarse group width of some integral multiple of fine group widths, or both. The data required for individual fine groups are the capture and fission cross sections from the resolved resonance calculation, and the elastic transfer and transport cross sections for the materials that are treated in the ELMOE manner. All other data are specified for coarse groups.

The number of groups which may be used in the calculation of the weighting spectrum is almost arbitrary.

trary, since the program is designed to do the calculation in segments. Elastic scattering matrices are read in for each new segment. The inelastic and elastic scattering source from higher energies is retained in fast memory.

The final averaged group constants are punched on cards. The cross sections may be punched out in formats suitable for direct use in the RE-122, DSN, or CRAM neutronics codes.

A library of evaluated cross section data has been assembled for use in conjunction with the MC² program. Cross section data over the range of 0.4 eV-10 MeV has been collected from data current to about March 1964. Materials in the library are B, B-10, C, O, Na, Al, S, Cl, K, Ti, V, Cr, Fe, Ni, Zr, Nb, Mo, Ta, W, Re, Pb, Bi, Th, U-233, U-234, U-235, U-236, Pu-239, Pu-240, Pu-241, Pu-242, and Fission Products.

The experimental data are supplemented by theo-

retical analyses where necessary. The documentation for the library, and a 26 group cross section set generated largely by the MC² program will appear in Ref. 5.

REFERENCES

1. A. L. Rago and H. H. Hummel, *ELMOE: An IBM-704 Program Treating Elastic Scattering Resonances in Fast Reactors*, ANL-6805 (1964).
2. R. Goldstein and E. R. Cohen, *Theory of Resonance Absorption of Neutrons*, Nucl. Sci. Eng. **13**, No. 2, 132-140 (1962).
3. F. L. Bauer, H. Rutishauser and E. Stiefel, *Proc. of Fifteenth Symposium in Applied Math*, Am. Math. Soc. **15**, 199-218 (1962).
4. D. M. O'Shea and H. C. Thacher, Jr., *Computation of Resonance Line Shape Functions*, Trans. Am. Nucl. Soc. **6**, 36 (June, 1963).
5. D. M. O'Shea, H. H. Hummel, W. B. Loewenstein and D. Okrent, *Twenty-Six Group Cross Sections*, ANL-6858 (to be published).

V-23. Ancillary Computing Programs

L. C. KVITEK

FIZZ (IBM-704 PROGRAM 2184/RP)

This code employs the results of multigroup diffusion theory calculations to calculate various reaction rates for use in determining the neutron balance. Fission and capture rates, breeding ratios and regional leakages are evaluated. The code can utilize energy group flux integrals from a multigroup analysis. It can also utilize point by point flux values and perform the appropriate volume integration prior to determining the total reaction rates.

DEL (IBM-704 PROGRAM 2184/RP)

DEL is a multigroup perturbation theory program. It utilizes point by point real and adjoint fluxes and performs appropriate integrations to give a problem normalization as well as individual perturbations. These include fission, absorption, elastic spectral degradation, inelastic spectral degradation and leakage. Programming is now complete for sphere, infinite cylinder and infinite slab. Revisions are under way to include adaptation to finite cylinders and slabs.

V-24. Solution Techniques for Elasticity Problems in Cylindrical Coordinates

C. K. YOUNGDAHL

PREFACE

To preface this section, some remarks on the state-of-the-art of the field of classical linear elasticity are in order. Although there is a large number of approximate solutions to elasticity problems, exact solutions are rare and are mostly for problems involving very simple geometries and/or one dimensional variations.

This is mainly due to the lack of any systematic procedure for solving problems, forcing the solver to rely upon his personal experience and mathematical intuition to enable him to superimpose existing solutions for similar problems plus something additional conjured from his own imagination, to produce a solution for a new problem.

The use of stress functions in elasticity appears at first glance to bring the solution of problems out of the realm of applied ingenuity into the realm of applied mathematics. The Galerkin stress function is a single biharmonic function related to the displacement and stresses in such a way that the equilibrium equations are automatically satisfied. Alternatively, the stresses and displacements can be expressed in terms of the newer Papkovitch stress functions (four in number), and equilibrium will be satisfied if these are harmonic. Since a great deal is known about biharmonic and harmonic functions it would appear that solutions of problems could be obtained in a routine manner; however, the difficulty is that there is still no way of systematically satisfying the boundary conditions. Unfortunately, transform techniques, which have proven quite successful in other fields for incorporating boundary conditions into solutions, just do not work here because the boundary conditions expressed in terms of the stress functions are not transformable.

A technique has been devised for constructing the Papkovitch stress functions in such a way that the resulting boundary conditions have the form one would have expected if the normal transform or Fourier series (which may be thought of as finite transforms) methods had worked. Then from this point on, the solution simply involves the routine use of transform methods, and although the algebra usually becomes quite complicated, one can proceed confidently to a correct answer. The stress functions involve known functions suitable to the body shape and arbitrary functions determined from the boundary conditions. If the boundary is simple, the arbitrary functions can be solved for explicitly in terms of the known functions, and the solution will be in closed form. Considering geometries that lend themselves readily to cylindrical coordinates (r, θ, z) , infinitely long circular cylinders, infinitely long circular tubes, the elastic space with an infinitely long circular hole, and the infinite plate all fall into the category of bodies with simple boundaries. Now consider problems where the body has a complex boundary but where the solution is independent of one of the coordinates or a known function of it. The arbitrary functions can then be expressed in terms of known functions and one arbitrary function. The latter is the solution to an equation of the form

$$A(i) = L(i) + \sum_{m=1}^{\infty} A(m) \sum_{n=1}^{\infty} F(m, n, i) \quad (1)$$

where $L(i)$ is derived from the loading, $F(m, n, i)$ involves known functions only, and $A(i)$ is the unknown function to be solved for. In some cases $A(i)$ may be a set of coefficients which might more conveniently be denoted by A_i , while in others it may be a function of a continuous variable, denoted by $A(i)$, and the sum over m becomes an integration; this depends on the finiteness of the boundaries involved. For instance, restricting the listing to geometries amenable to cylindrical coordinate representation, we have the following cases:

1. For a finite circular cylinder or a finite circular tube, Eq. (1) becomes

$$A_i = L_i + \sum_{m=1}^{\infty} A_m \sum_{n=1}^{\infty} F_{mni} \quad (2)$$

2. For a semi-infinite circular cylinder or tube, Eq. (1) becomes

$$A_i = L_i + \sum_{m=1}^{\infty} A_m \int_0^{\infty} F_{mi}(n) dn \quad (3)$$

3. For an infinite plate of finite thickness with a circular hole perpendicular to its surfaces, Eq. (1) becomes

$$A(i) = L(i) + \int_0^{\infty} A(m) \sum_{n=1}^{\infty} F_n(m, i) dm \quad (4)$$

4. For the half-space with an infinite circular hole perpendicular to its surface, Eq. (1) becomes

$$A(i) = L(i) + \int_0^{\infty} A(m) \int_0^{\infty} F(m, n, i) dn dm \quad (5)$$

Because of the cylindrical geometries, F would in general be a function of the Bessel functions of the first and second kinds and the modified Bessel function of the first and second kinds. The functions $L(i)$ or L_i would be obtained from transformations or Fourier series representation of the loading.

The three following problems of this general type have been considered.

1. Half-Space with a Hole. This problem is reported in Paper No. V-24a.

2. Thermoelastic Problem for Fuel Rod with Cladding. This problem is reported in Paper No. V-24b.

3. Thermal Stresses in Reactor Fuel Plates. This problem is reported in Paper No. V-24c.

V-24a. The Exact Elastic Stress Distribution in the Vicinity of a Hole in a Thick Plate Loaded in Uniaxial Tension

INTRODUCTION

Obtaining the exact three-dimensional solutions of plane problems in elasticity is usually a very difficult matter. Consequently, standard two-dimensional approximations to these problems have been formulated. There exists a large body of literature dealing with methods for obtaining these two-dimensional approximate solutions and presenting such solutions to particular problems. However, without available exact solutions for comparison, there is no way of determining the accuracy, and thereby the limitations, of the approximate methods.

In this report, the exact three-dimensional solution to a non-trivial plane problem is developed. Numerical results for the stress distribution in the vicinity of the surface of the elastic body are presented, since it is in this region that the plane approximations are poorest. The stresses at and near the surface are found to be strongly dependent on the Poisson's ratio of the elastic material; this is of significance for photo-elastic work, where experiments usually must be performed using materials with different Poisson ratios than those of common structural metals.

The particular problem treated in this study is the nature of the stress concentration caused by a circular hole, such as a rivet hole or port, in a plate which is being pulled in one direction.

For a plate which is very thin compared to the diameter of the hole the appropriate plane stress solution gives useful results for the average stresses through the thickness, but it is not an exact solution of the problem since the boundary conditions on the hole are not satisfied. On the other hand, the corresponding plane strain solution gives results which are valid near the center plane of a thick plate, but it does not satisfy the boundary conditions on the plate surfaces. E. Sternberg and M. Sadowsky¹ give an approximate solution to the problem using energy methods for an infinite plate of arbitrary thickness.

In all of the above, however, there is a blurring, or averaging, of the stresses, particularly in the vicinity of the edge created by the intersection of the hole and the plate. This local stress concentration is really the heart of the problem.

To isolate the edge effect, it is assumed here that the plate's dimensions are very large compared with the diameter of the hole. The plate then becomes a semi-infinite elastic medium with a circular hole drilled perpendicular to its bounding plane. The half-space is loaded at infinity in uniaxial tension in a direction per-

pendicular to the axis of the hole. The exact three-dimensional solution of this non-axially-symmetric elasticity problem is obtained through the use of the Papkovitch stress functions² and pseudo-transform techniques involving the Fourier Transform Inversion Theorem and Weber's Integral Theorem. These techniques lead to a single integral equation which is solved numerically on the IBM-704. Computations are also performed to numerically check the satisfaction of the boundary conditions (and thereby the validity of the solution) and to find the desired stress distribution on the hole. A summary of the method and results is given here.

STATEMENT OF THE ORIGINAL PROBLEM

Consider a homogeneous, isotropic, elastic body occupying the region $0 \leq z < \infty$, $1 \leq r < \infty$, which, at infinity, is in a state of uniform uniaxial tension of intensity τ acting in the x direction (see Fig. V-24a-1). The displacement vector field and the stress tensor field associated with this loaded body must satisfy equations of equilibrium, stress-displacement relations, and boundary conditions. In cylindrical coordinates r , θ , z the equilibrium equations of elasticity for zero body forces are

$$\left. \begin{aligned} \frac{\partial \tau_{rr}}{\partial r} + \frac{1}{r} \frac{\partial \tau_{r\theta}}{\partial \theta} + \frac{\partial \tau_{rz}}{\partial z} + \frac{\tau_{rr} - \tau_{\theta\theta}}{r} &= 0, \\ \frac{\partial \tau_{r\theta}}{\partial r} + \frac{1}{r} \frac{\partial \tau_{r\theta}}{\partial \theta} + \frac{\partial \tau_{\theta z}}{\partial z} + \frac{2\tau_{r\theta}}{r} &= 0, \\ \frac{\partial \tau_{rz}}{\partial r} + \frac{1}{r} \frac{\partial \tau_{\theta z}}{\partial \theta} + \frac{\partial \tau_{zz}}{\partial z} + \frac{\tau_{rz}}{r} &= 0, \end{aligned} \right\} \quad (1)$$

where τ_{rr} , $\tau_{\theta\theta}$, τ_{zz} are the normal components of the stress tensor and $\tau_{r\theta}$, $\tau_{\theta z}$, τ_{rz} are the shear components. A typical stress-displacement relation is

$$\tau_{rr} = \mu \left(\frac{2 - \alpha}{\alpha - 1} \nabla \cdot \mathbf{u} + 2 \frac{\partial u_r}{\partial r} \right). \quad (2)$$

Here \mathbf{u} is the displacement vector having components u_r , u_θ , u_z ; μ is the shear modulus and

$$\alpha = 2(1 - \nu) \quad (3)$$

where ν is Poisson's ratio. The boundary conditions which the stress field must satisfy are:

Zero loading on the surface of the hole

$$\tau_{rr} = \tau_{rz} = \tau_{r\theta} = 0 \quad \text{on } r = 1, \quad z \geq 0. \quad (4)$$

Zero loading on the bounding plane

$$\tau_{zz} = \tau_{\theta z} = \tau_{rz} = 0 \quad \text{on } z = 0, \quad r \geq 1. \quad (5)$$

A state of uniaxial tension at infinity

$$\left. \begin{aligned} \tau_{rr} &\rightarrow \frac{1}{2}\tau(1 + \cos 2\theta) \\ \tau_{\theta\theta} &\rightarrow \frac{1}{2}\tau(1 - \cos 2\theta) \\ \tau_{r\theta} &\rightarrow -\frac{1}{2}\tau \sin 2\theta \\ \tau_{zz}, \tau_{\theta z}, \tau_{rz} &\rightarrow 0 \end{aligned} \right\} \text{as } r \rightarrow \infty \text{ and for } z \geq 0 \quad (6)$$

PARTIAL SOLUTION AND RESIDUAL PROBLEM

Consider the displacement and stress fields given by

$$\left. \begin{aligned} u_r^P &= \frac{\tau}{4\mu} \left[\frac{\alpha r}{4 - \alpha} + \frac{1}{r} + \left(r + \frac{2\alpha}{r} - \frac{1}{r^3} \right) \cos 2\theta \right] \\ u_\theta^P &= -\frac{\tau}{4\mu} \left[r + \frac{2(\alpha - 1)}{r} + \frac{1}{r^3} \right] \sin 2\theta \\ u_z^P &= -\frac{\tau}{2\mu} \frac{2 - \alpha}{4 - \alpha} z \\ \tau_{rr}^P &= \frac{\tau}{2} \left[1 - \frac{1}{r^2} + \left(1 - \frac{4}{r^2} + \frac{3}{r^4} \right) \cos 2\theta \right] \\ \tau_{\theta\theta}^P &= \frac{\tau}{2} \left[1 + \frac{1}{r^2} - \left(1 + \frac{3}{r^4} \right) \cos 2\theta \right] \\ \tau_{zz}^P &= \frac{\tau(\alpha - 2)}{r^2} \cos 2\theta \\ \tau_{r\theta}^P &= -\frac{\tau}{2} \left(1 + \frac{2}{r^2} - \frac{3}{r^4} \right) \sin 2\theta \\ \tau_{\theta z}^P &= \tau_{rz}^P = 0 \end{aligned} \right\} \quad (7)$$

where the superscript *P* denotes a partial solution.

These satisfy the system of differential equations indicated by Eqs. (1) and (2) and the boundary conditions (4), (6) and the last two of Eq. (5); in other words, the solution given by Eq. (7) meets all the requirements except that it gives a τ_{zz} stress of $\tau[(\alpha - 2)/r^2] \cos 2\theta$ on the bounding plane rather than a stress-free surface. Note that this will be the exact solution if $\alpha = 2$ (Poisson's ratio equals zero).

Let the superscript *R* denote the residual problem obtained by subtracting the solution [Eq. (7)] from the original problem; that is,

$$u_r^R = u_r - u_r^P, \quad \tau_{rr}^R = \tau_{rr} - \tau_{rr}^P, \quad \text{etc.} \quad (8)$$

Then, by the principle of superposition applicable to linear elasticity, this residual stress state should satisfy the field Eqs. (1), (2) and the boundary conditions

$$\tau_{rr}^R = \tau_{rz}^R = \tau_{r\theta}^R = 0 \quad \text{on } r = 1, \quad z \geq 0 \quad (9)$$

$$\tau_{zz}^R = \frac{(2 - \alpha)}{r^2} \cos 2\theta, \quad \tau_{\theta z}^R = \tau_{rz}^R = 0 \quad (10)$$

on $z = 0, \quad r \geq 1$

$$\tau_{rr}^R, \tau_{\theta\theta}^R, \tau_{zz}^R, \tau_{r\theta}^R, \tau_{\theta z}^R, \tau_{rz}^R \rightarrow 0 \quad \text{as } r \rightarrow \infty. \quad (11)$$

Hence, this solution added to Eq. (7) will be the solution to the original problem.

PAPKOVICH STRESS FUNCTIONS

If the displacement vector is represented as

$$2\mu\mathbf{u} = \nabla(\Phi + \mathbf{x} \cdot \Psi) - 2\alpha\Psi \quad (12)$$

where \mathbf{x} is the position vector, Φ is a scalar function, and Ψ is a vector function with cartesian components Ψ_x, Ψ_y, Ψ_z , then equilibrium will be satisfied if

$$\nabla^2\Phi = \nabla^2\Psi = 0. \quad (13)$$

The functions Φ, Ψ_x, Ψ_y and Ψ_z are called the Papkovich stress functions.² It is well known that for an axially-symmetric problem Ψ_x and Ψ_y can be taken to be zero without any loss of generality. Earlier investigators have tried to solve this non-axially-symmetric problem in an analogous way by, in effect, working with two functions ϕ and ψ related to Φ and Ψ_x through*

$$\left. \begin{aligned} \Phi(r, \theta, z) &= \tau\phi(r, z) \cos 2\theta \\ \Psi_x(r, \theta, z) &= \tau\psi(r, z) \cos 2\theta \end{aligned} \right\} \quad (14)$$

However, it can be shown that a third function is necessary for a complete solution. This function, χ , is related to Ψ_x and Ψ_y by

$$\left. \begin{aligned} \Psi_x(r, \theta, z) &= \tau\chi(r, z) \cos \theta \\ \Psi_y(r, \theta, z) &= -\tau\chi(r, z) \sin \theta \end{aligned} \right\} \quad (15)$$

Substituting Eqs. (14), (15) into Eq. (13), it is found that equilibrium will be satisfied if

$$\nabla_2^2\phi = \nabla_2^2\psi = \nabla_1^2\chi = 0 \quad (16)$$

where

$$\nabla_n^2 F = \frac{\partial^2 F}{\partial r^2} + \frac{1}{r} \frac{\partial F}{\partial r} + \frac{\partial^2 F}{\partial z^2} - \frac{n^2}{r^2} F. \quad (17)$$

The displacement components are expressed in terms of ϕ, ψ and χ through the substitution of Eqs. (14) and (15) into Eq. (12); for example,

$$u_r = \frac{\tau}{2\mu} \left[\frac{\partial}{\partial r} (\phi + r\chi + z\psi) - 2\alpha\chi \right] \cos 2\theta. \quad (18)$$

The corresponding stresses can then be found from the stress-displacement relations; for example

$$\begin{aligned} \frac{\tau_{rr}}{\tau} &= \left[\frac{\partial^2}{\partial r^2} (\phi + r\chi + z\psi) \right. \\ &\left. + (\alpha - 2) \left(\frac{\partial\chi}{\partial z} - \frac{\chi}{r} \right) - (\alpha + 2) \frac{\partial\chi}{\partial r} \right] \cos 2\theta. \end{aligned} \quad (19)$$

Solutions to Eq. (16) can be obtained in a straightforward manner through the use of separation of variables or transform methods, yielding combinations of

* The τ factor is included to make ϕ and ψ dimensionless.

Bessel functions, exponentials, and trigonometric functions. However, the boundary conditions on ϕ , ψ and χ derived from Eqs. (9), (10), (11) and relations such as Eq. (19), are coupled differential equations which are not separable or transformable, necessitating a departure from standard methods. A systematic technique has been developed for constructing the stress functions ϕ , ψ and χ to arrive at forms of solution not obtainable by transform methods but which when substituted into the boundary conditions yield relations which can be inverted using standard transform inversion theorems. Space limitations prohibit a discussion here of the method of constructing the stress functions and the rationale behind it. Suffice it to say that the correct form for this problem is

$$\left. \begin{aligned} \phi(r,z) &= \int_0^\infty \left\{ \left[A(\gamma) - \frac{2}{\alpha} C(\gamma) \right] K_2(\gamma r) \cos \gamma z \right. \\ &\quad + \left[B(\gamma) - \frac{1}{\alpha} C(\gamma) \right] \\ &\quad \cdot [\gamma r K_2'(\gamma r) \cos \gamma z - \gamma z K_2(\gamma r) \sin \gamma z] \\ &\quad \left. + (1 - \alpha) \gamma^2 G(\gamma) \Omega_2(\gamma, r) e^{-\gamma z} \right\} d\gamma \\ \psi(r,z) &= \int_0^\infty \left\{ \left[B(\gamma) - \frac{1}{\alpha} C(\gamma) \right] \gamma K_2(\gamma r) \sin \gamma z \right. \\ &\quad \left. + \gamma^3 G(\gamma) \Omega_2(\gamma, r) e^{-\gamma z} \right\} d\gamma \\ \chi(r,z) &= \frac{1}{\alpha} \int_0^\infty C(\gamma) \left[\frac{2}{r} K_2(\gamma r) + \gamma K_2'(\gamma r) \right] \\ &\quad \cdot \cos \gamma z d\gamma \\ \Omega_2(\gamma, r) &= Y_2'(\gamma) J_2(\gamma r) - J_2'(\gamma) Y_2(\gamma r). \end{aligned} \right\} \quad (20)$$

The functions J_2 , Y_2 and K_2 are the Bessel function of the first kind, Bessel function of the second kind, and modified Bessel function of the second kind, respectively.³ Primes denote differentiation with respect to the argument. The arbitrary functions, A , B , C and G are to be determined from the boundary conditions.

Using the differentiation and recursion relations⁴ for the Bessel functions, it can be shown that Eqs. (20) satisfy Eq. (16). The last two of boundary conditions (10) are automatically satisfied by Eq. (20), while boundary conditions (11) also hold because of the behavior of the Bessel functions⁵ as $r \rightarrow \infty$. This leaves the four boundary conditions given by Eq. (9) and the first of Eq. (10) to be satisfied by a proper choice of the four functions A , B , C and G .

Originally, the function Ω_2 was defined as

$$Y_2(\gamma) J_2(\gamma r) - J_2(\gamma) Y_2(\gamma r).$$

Although this leads to a quite satisfactory solution from

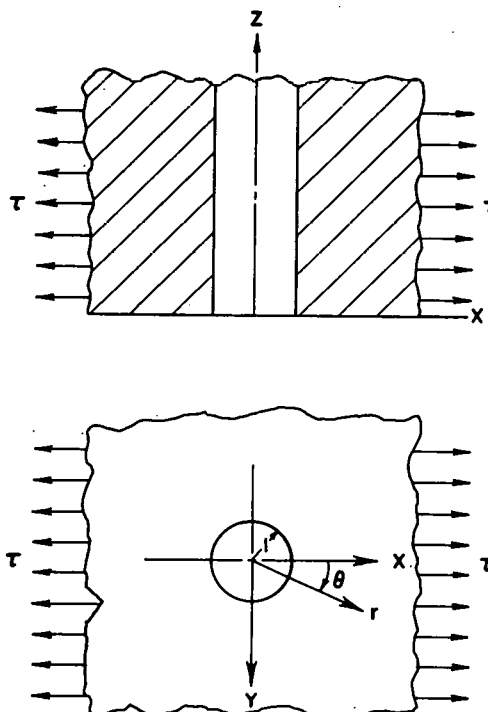


FIG. V-24a-1. Half-Space with a Circular Hole.

the theoretical standpoint, the resulting integrals for the stresses converge too slowly to be readily evaluated numerically. Defining Ω_2 as in Eq. (21) gives results which are much more convenient for computational purposes. This will be discussed further in the section on numerical results.

DETERMINATION OF A , B , C AND G FROM THE BOUNDARY CONDITIONS

The three boundary conditions (9) are each handled in a similar fashion. Therefore, for the sake of brevity, only one will be considered in detail. Consider the first of Eq. (9); i.e.,

$$\tau_{rr}^R(r, \theta, z) \Big|_{\substack{r=1 \\ z \geq 0}} = 0. \quad (22)$$

Substituting Eq. (20) into Eq. (19) and evaluating at $r = 1$, it is determined that Eq. (22) is equivalent to

$$\left. \begin{aligned} &\int_0^\infty \{ A(\gamma) [\gamma^2 + 4 - K(\gamma)] + B(\gamma) \\ &\quad [(\alpha - 1)\gamma^2 - 4 + (\gamma^2 + 4)K(\gamma)] \\ &\quad + C(\gamma) [-2(\gamma^2 + 2) - 2K(\gamma)] \} \\ &\quad \cdot K_2(\gamma) \cos \gamma z d\gamma \\ &= \frac{2}{\pi} \int_0^\infty \gamma G(\gamma) [4(\alpha - 1 - \gamma z) \\ &\quad + \gamma^2(\gamma z - 1)] e^{-\gamma z} d\gamma, \quad z \geq 0 \end{aligned} \right\} \quad (23)$$

where

$$K(\gamma) = \frac{\gamma K_2'(\gamma)}{K_2(\gamma)}. \tag{24}$$

Multiply Eq. (23) by $(2/\pi) \cos \eta z$, integrate with respect to z from 0 to ∞ , and use the Fourier cosine transform inversion theorem* to obtain

$$\left. \begin{aligned} & A(\eta) [\eta^2 + 4 - K(\eta)] \\ & + B(\eta) [(\alpha - 1)\eta^2 - 4 + (\eta^2 + 4)K(\eta)] \\ & + C(\eta) [-2(\eta^2 + 2) - 2K(\eta)] \\ & = \frac{8}{\pi^2 K_2(\eta)} \int_0^\infty G(\gamma) \left[2\alpha - (\eta^2 + 4) \right. \\ & \left. \cdot \left(\frac{\gamma^2}{\gamma^2 + \eta^2} \right) \right] \left(\frac{\gamma^2}{\gamma^2 + \eta^2} \right) d\gamma. \end{aligned} \right\} \tag{25}$$

The other two of Eq. (9) lead to two more algebraic equations for A , B and C in terms of integrals of G . These three simultaneous equations are then solved in a routine fashion; for example $A(\gamma)$ is given by

$$\left. \begin{aligned} A(\gamma) = \frac{16\alpha}{\pi^2 K_2(\gamma) \Delta(\gamma)} \{ & (2\gamma^2 + 3)(\gamma^2 + 4) \\ & - \gamma^2 K(\gamma) - \gamma^2 K^2(\gamma) + \alpha[-\gamma^2 \\ & + (\gamma^2 + 6)K(\gamma) + 3K^2(\gamma)] \} \\ & \cdot \int_0^\infty G(\eta) \frac{\eta^2}{\gamma^2 + \eta^2} d\eta + \frac{8}{\pi^2 K_2(\gamma) \Delta(\gamma)} \\ & \cdot \{ -(\gamma^2 + 4)f(\gamma) + \alpha[4\gamma^2 \\ & - (\gamma^4 + 8\gamma^2 + 24)K(\gamma) - 2(\gamma^2 + 6) \\ & \cdot K^2(\gamma)] \} \int_0^\infty G(\eta) \left(\frac{\eta^2}{\gamma^2 + \eta^2} \right)^2 d\eta \end{aligned} \right\} \tag{26}$$

where

$$f(\gamma) = (\gamma^2 + 2)(\gamma^2 + 6) - 2\gamma^2 K(\gamma) \tag{27}$$

and

$$\left. \begin{aligned} \Delta(\gamma) = & [\gamma^2 + 4 - K^2(\gamma)]f(\gamma) \\ & + \alpha[-4\gamma^2 + 8(\gamma^2 + 3)K(\gamma) \\ & - \gamma^2 K^2(\gamma) - 6K^3(\gamma)]. \end{aligned} \right\} \tag{28}$$

The remaining boundary condition is [see Eq. (10)]

$$\tau_{rz}(r, \theta, z) \Big|_{\substack{z=0 \\ r \geq 1}} = \tau(2 - \alpha) \frac{\cos 2\theta}{r^2}. \tag{29}$$

* This may be summarized⁶ as

$$F(\eta) = \frac{2}{\pi} \int_0^\infty \int_0^\infty F(\gamma) \cos \gamma z \cos \eta z d\gamma dz.$$

This becomes

$$\left. \begin{aligned} \int_0^\infty \gamma^4 G(\gamma) \Omega_2(\gamma, r) d\gamma = & \frac{2 - \alpha}{r^2} \\ & + \int_0^\infty \{ A(\gamma) \gamma^2 K_2(\gamma r) + \gamma^2 B(\gamma) \\ & \cdot [(\alpha + 2)K_2(\gamma r) + \gamma r K_2'(\gamma r)] \\ & - 2\gamma^2 C(\gamma) K_2(\gamma r) \} d\gamma, \quad r \geq 1. \end{aligned} \right\} \tag{30}$$

Weber's Integral Theorem⁷ treats integrals of functions similar to Ω_2 [namely, $Y_n(\gamma)J_n(\gamma r) - J_n(\gamma)Y_n(\gamma r)$]. A corresponding theorem can be proved for kernels like Ω_2 and leads to the relation

$$\left. \begin{aligned} F(\xi) \{ [J_2'(\xi)]^2 + [Y_2'(\xi)]^2 \} \\ = \int_1^\infty \int_0^\infty \gamma r F(\gamma) \Omega_2(\gamma, r) \Omega_2(\xi, r) d\gamma dr \end{aligned} \right\} \tag{31}$$

which is of the form of a transform inversion theorem. In solving an axially-symmetric elasticity problem, K. Blenkarn and J. Wilhoit⁸ use a similar relation involving J_0, J_1, Y_0, Y_1 rather than J_2, J_2', Y_2, Y_2' .

Multiplying Eq. (30) by $r\Omega_2(\xi, r)$, integrating from 1 to ∞ with respect to r , and applying Eq. (31) gives the transformed boundary condition

$$\left. \begin{aligned} G(\xi) \xi^6 \{ [J_2'(\xi)]^2 + [Y_2'(\xi)]^2 \} = & \frac{4(2 - \alpha)}{\pi} \\ & - \frac{2}{\pi} \int_0^\infty \left\{ A(\gamma) K(\gamma) + B(\gamma) \left[\gamma^2 + 4 \right. \right. \\ & \left. \left. + \alpha K(\gamma) + 2K(\gamma) \left(\frac{\xi^2}{\gamma^2 + \xi^2} \right) \right] \right. \\ & \left. - 2C(\gamma) K(\gamma) \right\} \gamma^2 \left(\frac{\gamma^2}{\gamma^2 + \xi^2} \right) K_2(\gamma) d\gamma. \end{aligned} \right\} \tag{32}$$

The substitution of Eq. (26) and similar expressions for $B(\gamma)$, $C(\gamma)$ into Eq. (32) results in an integral equation for G . This equation is

$$\left. \begin{aligned} G(\xi) \xi^6 \{ [J_2'(\xi)]^2 + [Y_2'(\xi)]^2 \} \\ = \frac{4(2 - \alpha)}{\pi} + \int_0^\infty G(\eta) L(\xi, \eta) d\eta \end{aligned} \right\} \tag{33}$$

with the symmetric kernel $L(\xi, \eta)$ being given by

$$\left. \begin{aligned} L(\xi, \eta) = \frac{32\alpha}{\pi^3} \int_0^\infty \frac{\gamma^2}{\Delta(\gamma)} g\left(\frac{\gamma}{\xi}\right) g\left(\frac{\gamma}{\eta}\right) \left\{ F_1^0(\gamma) \right. \\ & \left. + 2 \left[g\left(\frac{\gamma}{\xi}\right) + g\left(\frac{\gamma}{\eta}\right) \right] F_2^0(\gamma) \right. \\ & \left. + g\left(\frac{\gamma}{\xi}\right) g\left(\frac{\gamma}{\eta}\right) F_3^0(\gamma) d\gamma \right\} \end{aligned} \right\} \tag{34}$$

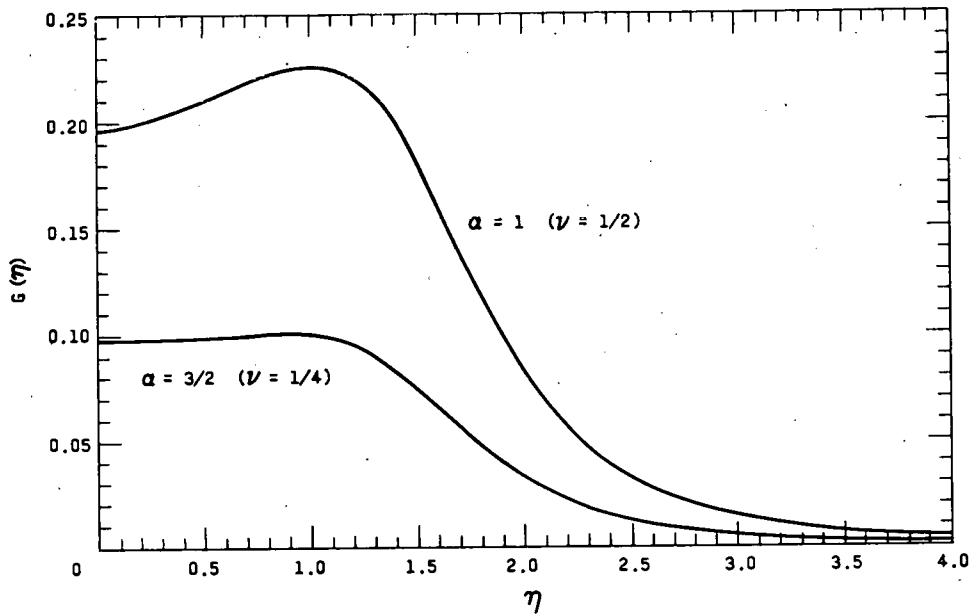


FIG. V-24a-2. $G(\eta)$ for Poisson's Ratios of 1/2, 1/4.

with

$$\left. \begin{aligned} g(x) &= (x^2 + 1)^{-1} \\ F_1^0(\gamma) &= -\gamma^2(\gamma^2 + 4) + (\gamma^2 - 3\alpha)K^2(\gamma) \\ F_2^0(\gamma) &= -\gamma^2K(\gamma) + (\gamma^2 + 3)K^2(\gamma) \\ F_3^0(\gamma) &= -\alpha^{-1}f(\gamma)K^2(\gamma). \end{aligned} \right\} \quad (35)$$

The integral equation (33) was solved numerically on the IBM-704 for $G(\eta)$ using Poisson's ratios of $\frac{1}{2}$ and $\frac{1}{4}$ (see Fig. V-24a-2). The stresses and displacements can be expressed in terms of G through the relations among the stresses, displacements and the Papkovitch stress functions, since A , B and C are known functions of G . A resulting typical stress is

$$\frac{\tau_{zz}^R}{r \cos 2\theta} = \int_0^\infty G(\eta) T_{zz}(\eta, r, z) d\eta \quad (36)$$

where

$$\left. \begin{aligned} T_{zz}(\eta, r, z) &= \frac{16\alpha}{\pi^2} \int_0^\infty \frac{\gamma^2}{(\Delta\gamma)} g\left(\frac{\gamma}{\eta}\right) \left[f_1(\gamma) \frac{K_2(\gamma r)}{K_2(\gamma)} \right. \\ &+ f_2(\gamma) \frac{rK_2'(\gamma r)}{K_2'(\gamma)} \left. \right] \cos \gamma z d\gamma + \frac{8}{\pi^2} \int_0^\infty \frac{\gamma^2}{\Delta(\gamma)} \\ &\cdot g^2\left(\frac{\gamma}{\eta}\right) \left[f_3(\gamma) \frac{K_2(\gamma r)}{K_2(\gamma)} + f_4(\gamma) \frac{rK_2'(\gamma r)}{K_2'(\gamma)} \right] \\ &\cdot \cos \gamma z d\gamma + \eta^4 (1 + \eta z) \Omega_2(\eta, r) e^{-\eta z} \end{aligned} \right\} \quad (37)$$

and

$$\left. \begin{aligned} f_1(\gamma) &= -(\gamma^4 + 9\gamma^2 + 12) \\ &+ 3(\gamma^2 + 2 - \alpha)K(\gamma) \\ f_2(\gamma) &= F_2^0(\gamma) \\ f_3(\gamma) &= [\gamma^2 + 4 - 2K(\gamma)]f(\gamma) \\ &+ 4\alpha[-\gamma^2 + (\gamma^2 + 3)K(\gamma)] \\ f_4(\gamma) &= -K^2(\gamma)f(\gamma). \end{aligned} \right\} \quad (38)$$

Since the techniques employed here are somewhat unusual, particularly the application of Eq. (31), and since a numerical solution of the integral equation must be resorted to, an independent check of the results is highly desirable. It can be shown that the governing field equations and the boundary conditions (9) are satisfied for any function G , provided G is such that all the integrals involved exist. The solution will check therefore if the boundary condition on $z = 0$ is satisfied, namely $\tau_{zz}^R = \tau(2 - \alpha)r^{-2} \cos 2\theta$. This calculation was made by putting $z = 0$ into Eq. (37) and evaluating the resultant expression on the computer for a number of values of r (see Table V-24a-I). This check also provides an estimate of the upper limit of the error in the solution since the stresses on $z = 0$ are the most difficult to evaluate numerically. Hence, stresses computed at other points should be more accurate than the τ_{zz}^R stress at $z = 0$.

In order to determine the stress concentration effect, the non-zero stresses on the hole, $\tau_{\theta\theta}$, τ_{zz} , $\tau_{\theta z}$, were computed for various values of z near $z = 0$ (see Figs. V-24a-3 and V-24a-4).

TABLE V-24a-I. CHECK OF THE BOUNDARY CONDITION

r	$\frac{\tau_{zz}^R}{\tau \cos 2\theta}$			
	Poisson's ratio = $\frac{1}{4}$		Poisson's ratio = $\frac{1}{2}$	
	Theoretical value	Calculated value	Theoretical value	Calculated value
1.0	0.50000	0.49982	1.00000	0.99947
1.02	0.48058	0.47815	0.96117	0.95090
1.1	0.41322	0.41363	0.82644	0.82720
1.2	0.34722	0.34792	0.69444	0.69644
1.4	0.25510	0.25557	0.51020	0.51106
1.6	0.19531	0.19533	0.39063	0.39061
1.8	0.15432	0.15439	0.30864	0.30866
2.0	0.12500	0.12517	0.25000	0.25031

ANALYSIS PERTAINING TO NUMERICAL COMPUTATIONS

The numerical computations consist of three main parts: solving the integral equations [Eq. (33)] for G ; checking the boundary conditions on τ_{zz}^R by evaluating Eq. (36) at $z = 0$ for various values of r ; and finding the stresses $\tau_{zz}^R, \tau_{\theta\theta}^R, \tau_{\theta z}^R$ on the hole for various values of z by evaluating Eq. (36) and similar expressions for $\tau_{\theta\theta}^R, \tau_{z\theta}^R$ at $r = 1$. As mentioned previously under Papkovitch stress functions the problem was originally solved with Ω_2 defined in a different manner. The numerical solution for the corresponding G function was obtained with no difficulty but the check of the boundary condition proved to be intractable. The reason was that, for this formulation, the $G(\eta)$ function does not assume its asymptotic behavior until large values of η are reached (approximately $\eta > 1500$); this, and the slow convergence of the integral in Eq. (36) for $z = 0$ necessitated numerical integration to large values of η . The oscillating character of T_{zz} [Eq. (37)] due to the Ω_2 term requires that very small increments of η be taken; even then the differences between the contributions of adjacent positive and negative loops of the integrand are too small to permit any accuracy in the final results. Therefore, although it is quite possible that the G function obtained was correct and accurate, no confidence could be placed in the solution to the original formulation because of the inability to check the boundary condition. The solution outlined in this report was then constructed and, despite its being very similar in appearance to the first formulation, theoretical rates of convergence, etc., were found to be more amenable to numerical evaluation.

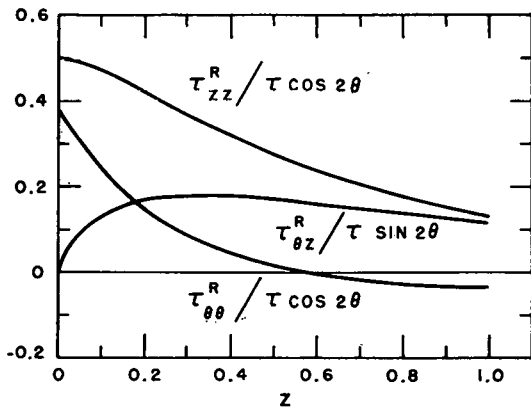


FIG. V-24a-3. Stresses on Hole for Poisson's Ratio = 1/4.

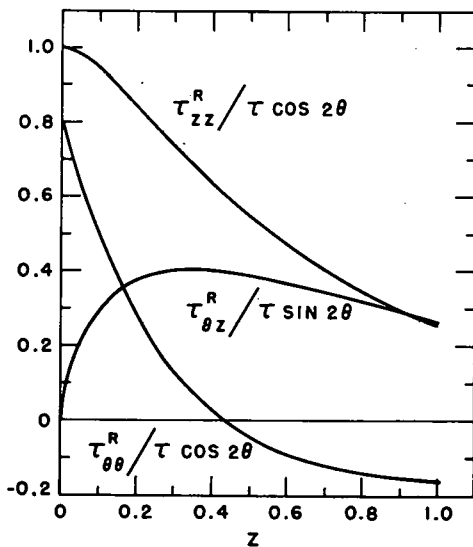


FIG. V-24a-4. Stresses on Hole for Poisson's Ratio = 1/2.

A preliminary numerical solution indicated the shape of the G function, but it was felt that the numerical methods employed were too crude to give reasonable accuracy; in addition, the check of the boundary condition still defied straight-forward numerical evaluation. It appeared necessary, therefore, to analyze more thoroughly the numerical problems involved and to devise special techniques where necessary.

Space limitations preclude a discussion of all the laborious details involved in the rearrangement of the desired integrals into forms more amenable to numerical evaluations. One technique frequently employed was to add and subtract a function from the integrand in such a way that the difference between the original integrand and the function was small and could be more easily integrated numerically than the original function itself, while the integration of the added function could be performed analytically in closed form. To use this technique effectively, however, a great deal must be known about the integrands, which are quite complicated in appearance. It was necessary to find the

asymptotic expansions of all integrands; this was especially tedious because of the $[\Delta(\gamma)]^{-1}$ factor in Eqs. (34) and (37). Since $\Delta(\gamma)$ is a function of α , all coefficients in the asymptotic expansion are functions of Poisson's ratio. It becomes evident that one of the reasons for the integrations being so difficult to do by straight-forward numerical methods is that some of the integrands are quite similar to the sine integral, cosine integral, and exponential integrals, which are very difficult to evaluate directly from their integral definitions. Another difficulty that became apparent was a serious loss in accuracy in some of the integrations due to subtraction of almost equal quantities over part on the range of integration. These situations were isolated and appropriate series expansions were determined to replace the original functions.

A curve fitting technique was developed for the intermediate integration ranges. Parts of the integrands which involve complicated combinations of Bessel functions [F_1^0 , F_2^0 , F_3^0 , in Eq. (34) for example] were evaluated at a number of points using tabular values.⁹ Series expansions in positive and negative powers were fitted to these points such that the resulting integrations could be performed in closed form. The accuracy of this technique for desk computer calculation turned out to be quite good, but it was not used for later computer work.

The final form of $L(\xi, \eta)$ used for computer programming purposes is

$$L(\xi, \eta) = \frac{32\alpha}{\pi^3} \left[L^0(\xi, \eta) + L^s(\xi, \eta) + L^\infty(\xi, \eta) \right] \quad (39)$$

with

$$L^0(\xi, \eta) = \int_0^\infty g\left(\frac{\gamma}{\xi}\right) g\left(\frac{\gamma}{\eta}\right) \cdot \left\{ -1 + 2 \left[g\left(\frac{\gamma}{\eta}\right) + g\left(\frac{\gamma}{\xi}\right) \right] (\alpha - \gamma) + g\left(\frac{\gamma}{\xi}\right) \cdot g\left(\frac{\gamma}{\eta}\right) \left[\gamma^3 + (1 - \alpha)\gamma^2 + \left(\frac{47}{8} - 2\alpha + \alpha^2\right)\gamma + \left(-\frac{15}{4} - \frac{3}{4}\alpha + 3\alpha^2 - \alpha^3\right) \right] \right\} d\gamma \quad (40)$$

$$L^s(\xi, \eta) = \int_0^{10} g\left(\frac{\gamma}{\xi}\right) g\left(\frac{\gamma}{\eta}\right) \left\{ F_1(\gamma) + \left[g\left(\frac{\gamma}{\xi}\right) + g\left(\frac{\gamma}{\eta}\right) \right] F_2(\gamma) + g\left(\frac{\gamma}{\xi}\right) g\left(\frac{\gamma}{\eta}\right) F_3(\gamma) \right\} d\gamma \quad (41)$$

$$L^\infty(\xi, \eta) = \int_{10}^\infty g\left(\frac{\gamma}{\xi}\right) g\left(\frac{\gamma}{\eta}\right) \left\{ F_1^\infty(\gamma) + \left[g\left(\frac{\gamma}{\xi}\right) + g\left(\frac{\gamma}{\eta}\right) \right] F_2^\infty(\gamma) + g\left(\frac{\gamma}{\xi}\right) g\left(\frac{\gamma}{\eta}\right) F_3^\infty(\gamma) \right\} d\gamma. \quad (42)$$

In Eq. (41) F_1 , F_2 and F_3 are defined by

$$\left. \begin{aligned} F_1(\gamma) &= \frac{\gamma^2}{\Delta(\gamma)} F_1^0(\gamma) + 1 \\ F_2(\gamma) &= 2 \left[\frac{\gamma^2}{\Delta(\gamma)} F_2^0(\gamma) + \gamma - \alpha \right] \\ F_3(\gamma) &= \frac{\gamma^2}{\Delta(\gamma)} F_3^0(\gamma) - \gamma^3 + (\alpha - 1)\gamma^2 \\ &\quad + \left(-\frac{47}{8} + 2\alpha - \alpha^2 \right) \gamma \\ &\quad + \left(\frac{15}{4} + \frac{3}{4}\alpha - 3\alpha^2 + \alpha^3 \right) \end{aligned} \right\} \quad (43)$$

with F_1^0 , F_2^0 , F_3^0 given by Eq. (35). The functions F_1^∞ , F_2^∞ , F_3^∞ in Eq. (42) are the asymptotic expansions of the corresponding functions F_1 , F_2 , F_3 ; each is of the form

$$F_m^\infty = \sum_{n=1}^N \frac{b_{mn}}{\gamma^n}. \quad (44)$$

For instance, for $\alpha = 1$ (the coefficients in the asymptotic expansion are functions of Poisson's ratio),

$$\left. \begin{aligned} F_1^\infty(\gamma) &= \frac{6}{\gamma} - \frac{3}{\gamma^2} - \frac{36.75}{\gamma^3} + \frac{92.25}{\gamma^4} \\ &\quad + \frac{181.828125}{\gamma^5} - \frac{1403.4375}{\gamma^6} \\ &\quad + \frac{1676.0566}{\gamma^7} + \frac{9726.75}{\gamma^8}. \end{aligned} \right\} \quad (45)$$

The major contribution to the kernel, except for small values of both ξ and η , is from L^0 . The integration in Eq. (40) can be done in closed form and gives, for $\alpha = 1$,

$$\left. \begin{aligned} L^0(\xi, \eta) &= \frac{\pi}{8} \left[\frac{3\xi\eta}{\xi + \eta} - \frac{5\xi^2\eta^2}{(\xi + \eta)^3} \right] \\ &\quad + \frac{\xi^2\eta^2}{(\xi^2 - \eta^2)^3} \left\{ -2.4375(\xi^4 - \eta^4) \right. \\ &\quad \left. + [2(\xi^2 - \eta^2)^2 + 9.75\xi^2\eta^2] \log \frac{\xi}{\eta} \right\} \\ &\quad + \frac{\xi^4\eta^4}{(\xi^2 - \eta^2)^3} \left[(\xi^2 + \eta^2) \log \frac{\xi}{\eta} \right. \\ &\quad \left. - (\xi^2 - \eta^2) \right], \quad \xi \neq \eta \end{aligned} \right\} \quad (46)$$

$$L^0(\eta, \eta) = 0.109375\pi\eta - 0.1875\eta^2 + \frac{1}{12}\eta^4.$$

The integration for L^∞ of Eq. (42) can also be performed in closed form for each term in the asymptotic expansion F_1^∞ , F_2^∞ , F_3^∞ ; for example, the contribution of the term with coefficient b_{31} to $L^\infty(\xi, \eta)$ is

$$b_{31} \left\{ \begin{aligned} & \frac{\xi^4 \eta^4}{(\xi^2 - \eta^2)^3} \left[\xi^{-2} \log \frac{100 + \xi^2}{100} \right. \\ & \left. - \eta^{-2} \log \frac{100 + \eta^2}{100} \right] + \frac{\xi^4 \eta^4}{2(\xi^2 - \eta^2)^2} \\ & \cdot \left[-\frac{1}{\xi^2(100 + \xi^2)} - \frac{1}{\eta^2(100 + \eta^2)} \right. \\ & \left. + \frac{1}{\xi^4} \log \frac{100 + \xi^2}{100} + \frac{1}{\eta^4} \log \frac{100 + \eta^2}{100} \right] \Big\}, \end{aligned} \quad (47)$$

$\xi \neq \eta$

and

$$b_{31} \left[-\frac{1}{2} \left(\frac{\eta^2}{100 + \eta^2} \right) - \frac{1}{4} \left(\frac{\eta^2}{100 + \eta^2} \right)^2 \right. \\ \left. - \frac{1}{6} \left(\frac{\eta^2}{100 + \eta^2} \right)^3 + \frac{1}{2} \log \frac{100 + \eta^2}{100} \right], \quad (48)$$

$\xi = \eta.$

The remaining part of the kernel, L' , was integrated numerically using γ intervals of 0.1 and Simpson's rule.

To check the boundary condition it is necessary to evaluate Eq. (36) at $z = 0$. To facilitate the computation, T_{zz} of Eq. (37) is put into the following form for $z = 0$:

$$T_{zz}(\eta, r, 0) = B(\eta, r) + W(\eta, r) + J(\eta, r) \quad (48)$$

where

$$\left. \begin{aligned} B(\eta, r) &= \frac{8}{\pi^2} \int_0^\infty g \left(\frac{\gamma}{\eta} \right) \\ & \cdot \left[2\alpha F_4(\gamma, r) + g \left(\frac{\gamma}{\eta} \right) F_5(\gamma, r) \right] d\gamma, \\ W(\eta, r) &= \frac{8}{\pi^2} \int_0^\infty g \left(\frac{\gamma}{\eta} \right) \\ & \cdot \left[2\alpha H_4(\gamma, r) + g \left(\frac{\gamma}{\eta} \right) H_5(\gamma, r) \right] d\gamma, \\ J(\eta, r) &= \eta^4 \Omega_2(\eta, r). \end{aligned} \right\} \quad (49)$$

In Eq. (49)

$$\left. \begin{aligned} F_4(\gamma, r) &= \frac{\gamma^2}{\Delta(\gamma)} \left[f_1(\gamma) \frac{K_2(\gamma r)}{K_2(\gamma)} \right. \\ & \left. + f_2(\gamma) \frac{r K_2'(\gamma r)}{K_2'(\gamma)} \right] - H_4(\gamma, r), \\ F_5(\gamma, r) &= \frac{\gamma^2}{\Delta(\gamma)} \left[f_3(\gamma) \frac{K_2(\gamma r)}{K_2(\gamma)} \right. \\ & \left. + f_4(\gamma) \frac{r K_2'(\gamma r)}{K_2'(\gamma)} \right] - H_5(\gamma, r), \\ H_4(\gamma, r) &= r^{-1/2} e^{-\gamma(r-1)} [\gamma A_1(r, \alpha) + A_2(r, \alpha)], \\ H_5(\gamma, r) &= r^{-1/2} e^{-\gamma(r-1)} [\gamma^3 A_3(r, \alpha) + \gamma^2 A_4(r, \alpha) \\ & \quad + \gamma A_5(r, \alpha) + A_6(r, \alpha)]. \end{aligned} \right\} \quad (50)$$

The $A_j(r, \alpha)$ functions are derived from the asymptotic expansions of $K_2(\gamma r)/K_2(\gamma)$, $rK_2'(\gamma r)/K_2'(\gamma)$, f_1, f_2, f_3, f_4 and $\Delta(\gamma)$, and are such that F_4 and F_5 become very small as γ becomes large. Their exact definitions are lengthy.

In Eq. (49), the integral for $B(\eta, r)$ was evaluated by numerical means; the integration for $W(\eta, r)$ was obtained in the closed form

$$W(\eta, r) = \sum_{j=1}^6 B_j(r, \alpha) D_j[\eta(r-1)] \quad (51)$$

where the B_j are related to the A_j , and the D_j are defined by

$$\left. \begin{aligned} D_1(x) &= x[\sin x Ci(x) - \cos x si(x)], \\ D_2(x) &= -x^2[\cos x Ci(x) \\ & \quad + \sin x si(x)], \\ D_3(x) &= \frac{x^2}{2} [1 - D_1(x)], \\ D_4(x) &= \frac{1}{2} [D_1(x) + D_2(x)], \\ D_5(x) &= \frac{x^2}{4} [D_1(x) - D_2(x)], \\ D_6(x) &= \frac{x^2}{6} [D_2(x) - D_3(x)]. \end{aligned} \right\} \quad (52)$$

The function $Ci(x)$ and $si(x)$ are the cosine integral and sine integral, defined by¹⁰

$$\left. \begin{aligned} Ci(x) &= -\int_x^\infty \frac{\cos t}{t} dt, \\ si(x) &= \int_x^\infty \frac{\sin t}{t} dt. \end{aligned} \right\} \quad (53)$$

The $D_j(x)$ functions are defined in such a way that they approach unity as x becomes large. The $J(\eta, r)$ term in Eq. (48) was evaluated using the computer subroutines for the Bessel functions involved in Ω_2 for small η and using the asymptotic expansion for large η ; this expansion is of the form

$$\left. \begin{aligned} \Omega_2(\eta, r) &\approx \left[\frac{1}{\eta} + \frac{C_3(r)}{\eta} + \frac{C_5(r)}{\eta} + \dots \right] \\ &\cdot \cos[\eta(r-1)] + \left[\frac{C_2(r)}{\eta^2} + \frac{C_4(r)}{\eta^4} + \dots \right] \\ &\quad \cdot \sin[\eta(r-1)]. \end{aligned} \right\} \quad (54)$$

The expressions for the desired stresses on the hole, $\tau_{zz}, \tau_{\theta\theta}, \tau_{zz}$, were similarly reformulated. Since all were treated in much the same way, only τ_{zz} will be discussed here. The form of T_{zz} at $r = 1$ (which was found to be practical for numerical computation) was

$$T_{zz}(\eta, 1, z) = S_{zz}(\eta, z) + V_{zz}(\eta, z) + \bar{V}_{zz}(\eta, z) \quad (55)$$

with

$$\left. \begin{aligned} S_{zz}(\eta, z) &= \frac{8}{\pi^2} \int_0^\infty g\left(\frac{\gamma}{\eta}\right) \left[2\alpha F_6(\gamma) \right. \\ &\quad \left. + g\left(\frac{\gamma}{\eta}\right) F_7(\gamma) \right] \cos \gamma z d\gamma, \\ V_{zz}(\eta, z) &= \frac{8}{\pi^2} \int_0^\infty g\left(\frac{\gamma}{\eta}\right) \left[2\alpha + g\left(\frac{\gamma}{\eta}\right) (-\gamma^2 \right. \\ &\quad \left. - \frac{15}{2} + 6\alpha - \alpha^2) \right] \cos \gamma z d\gamma \\ &\quad + \eta^4 (1 + \eta z) \Omega_2(\eta, 1) e^{-\eta z}, \\ \bar{V}_{zz}(\eta, z) &= \frac{8}{\pi^2} \int_0^\infty g^2\left(\frac{\gamma}{\eta}\right) (\alpha - 1) \gamma \cos \gamma z d\gamma \end{aligned} \right\} (56)$$

where

$$\left. \begin{aligned} F_6(\gamma) &= \frac{\gamma^2}{\Delta(\gamma)} [f_1(\gamma) + f_2(\gamma)] - 1, \\ F_7(\gamma) &= \frac{\gamma^2}{\Delta(\gamma)} [f_3(\gamma) + f_4(\gamma)] + \gamma^2 \\ &\quad + (1 - \alpha)\gamma + \left(\frac{15}{2} - 6\alpha + \alpha^2\right). \end{aligned} \right\} (57)$$

The integration for S_{zz} was performed numerically while that for V_{zz} , \bar{V}_{zz} was obtained in closed form. Using¹¹ $\Omega_2(\eta, 1) = 2/(\pi\eta)$,

$$\left. \begin{aligned} V_{zz}(\eta, z) &= \frac{2}{\pi} \left[2\eta^4 z + \left(-\frac{15}{2} + 6\alpha - \alpha^2\right) \eta^2 z \right. \\ &\quad \left. + \left(-\frac{15}{2} + 10\alpha - \alpha^2\right) \eta \right] e^{-\eta z}, \\ \bar{V}_{zz}(\eta, z) &= \frac{2}{\pi} (\alpha - 1) \eta^2 (1 - \eta z \{e^{-\eta z} E^*(\eta z) \\ &\quad + e^{\eta z} [-Ei(-\eta z)]\}) \end{aligned} \right\} (58)$$

where $-Ei(-x)$ and $E^*(x)$ are the exponential integrals defined by¹²

$$\left. \begin{aligned} -Ei(-x) &= \int_x^\infty \frac{e^{-t}}{t} dt, \\ E^*(x) &= -\int_x^\infty \frac{e^{-t}}{t} dt \end{aligned} \right\} (59)$$

\bar{V}_{zz} was evaluated by hand calculation using tabulated values.^{13, 14, 15}

COMPUTER PROGRAMS

The following computer programs were devised by the author for solution of the integral equation, check of the boundary condition, and evaluation of stresses on the hole.

SOLUTION OF THE INTEGRAL EQUATION [EQ. (33)]

Program 8*

The integral equation was solved with $\alpha = 1$, (Poisson's ratio equals $\frac{1}{2}$) for $G(\eta)$ at 75 points given by [0(0.25)5], [5(0.5)10], [10(1)20], [20(5)100], [100(100)-200], where $[a(b)c]$ indicates that the range of a to c was covered in steps of size b . The use of the standard library subroutines for the arctangent and logarithm needed for the calculation of L^∞ proved too inaccurate for some values of the arguments since almost equal quantities were subtracted from them; power series expansions were therefore substituted where necessary. The subroutine *MATINV* was used to solve the resulting 75 simultaneous algebraic equations. Calculating the kernel $L(\xi, \eta)$ using Eqs. (39), (40), (41), and (42) proved to be more accurate and much faster than straightforward integration using Eq. (34). The results of this program are shown in Fig. V-24a-2 for small η ; for large η , $G(\eta) \approx 0.625\eta^{-4}$.

Program 8A

This is the same as Program 8 except that $\alpha = \frac{3}{4}$ (Poisson's ratio equals $\frac{1}{4}$). It was originally planned to write a program to solve the integral equation for arbitrary α , but the coefficients of the asymptotic expansions needed to evaluate L^∞ are complicated functions of α . There seems to be no reasonable way to multiply and divide asymptotic expansions on the computer, and by hand it is much easier to evaluate the coefficients for a particular value of α than for arbitrary α . The function G found by this program is shown in Fig. V-24a-2 for small η ; for large η it behaves as $0.16\eta^{-4}$.

CHECK OF THE BOUNDARY CONDITIONS

Program 6

The functions $J(\eta, r)$, $\Omega_2(\eta, r)$ were calculated for various η, r combinations. The library subroutine for the Bessel functions was used for small arguments and the asymptotic expansion, Eq. (54), for large arguments.

Program 5

This program determined the contribution to $B(\eta, r)$ [see Eq. (49)] of the numerical integration over γ from 0 to 10.

* The program numbers were chosen quite arbitrarily and do not indicate any logical or chronological order; rather, Program 3 is composed of instructions numbered in the 300's, etc., in order that blocks of instructions could be reused in later programs where the same functions were needed again.

Program 10

The D_i functions of Eq. (52) were programmed here. At first the standard FORTRAN subroutine for the cosine integral and sine integral was used but it proved to be too inaccurate. A new subroutine was therefore devised which provides at least five significant figure accuracy for all the D_i functions over the entire range of the argument.

Program 16

Based on Program 6, this program* finds the integral $\int_0^{20} G(\eta)J(\eta,r)d\eta$ for various values of r .

Program 15

Based on Program 5, this program calculates the integral $\int_0^{20} G(\eta)B^r(\eta,r)d\eta$, where B^r is the part of B of Eq. (49) due to γ between 0 and 10.

Program 9

The integral $\int_0^{20} G(\eta)B^\infty(\eta,r)d\eta$ is calculated in a manner similar to Program 15. B^∞ is the contribution to B due to $\gamma > 10$. Asymptotic expansions for F_4 and F_6 are used to avoid the subtraction of nearly equal quantities in the integrand. The contribution of this program is small unless r is near unity.

Program 10A

The integral $\int_0^{20} C(\eta)W(\eta,r)d\eta$ is calculated, using the results of Program 10.

Program 14

The integrals $\int_0^{100} G(\eta)J(\eta,r)d\eta$ and $\int_0^{100} G(\eta)W(\eta,r)d\eta$ are calculated.

The sums of the results of Programs 16, 15, 9, 10A, 14 and the factor mentioned in the footnote are summarized in Table V-24a-I, for $\alpha = 1$ and $\frac{3}{2}$.

EVALUATION OF THE STRESSES ON THE HOLE

Program 2

The program finds $S_{zz}^c(\eta,z)$, $S_{\theta\theta}^c(\eta,z)$, $S_{\theta z}^c(\eta,z)$ for $\alpha = 1$ and $\frac{3}{2}$, where S_{zz}^c is the contribution to S_{zz} of Eq. (56) due to integration over γ from 0 to 10, etc.

Program 3

Same as Program 2 except that γ is integrated over the range 10 to 100. Asymptotic expansions are used for F_6 and F_7 .

* Note that for $\eta > 20$, where $G(\eta) = c\eta^{-4}$ and Ω_2 can be approximated by Eq. (54), the integral can be evaluated in closed form. The contribution of the integral for this range of η is small except when r is near unity.

Program 4

This program evaluates $V_{zz}(\eta,z)$ of Eq. (58).

Program 7

The results of Programs 2, 3 and 4 are added, multiplied by $G(\eta)$ for $\alpha = 1$ and $\frac{3}{2}$ respectively and integrated over η between 0 and 20.

Program 3A

Here the contribution to S_{zz} for $100 \leq \gamma \leq 2000$ was calculated and the result multiplied by $G(\eta)$ and integrated over η . This contribution was found to be negligible except for z very close to zero.

Program 17

The integral $\int_0^{1900} G(\eta)V_{zz}(\eta,z)d\eta$ was evaluated and found to be a large contributor to the resultant stresses for small z .

The results of Programs 7, 3A and 17 were added to the hand calculations for $\int_0^{20} G(\eta)\bar{V}_{zz}d\eta$, $\int_0^{20} G(\eta)\bar{V}_{\theta\theta}d\eta$ and $\int_0^{20} G(\eta)\bar{V}_{\theta z}d\eta$ to give the stresses on the hole. These stresses are shown in Figs. V-24a-3 and V-24a-4.

REFERENCES

1. E. Sternberg and M. A. Sadowsky, *Three-Dimensional Solution for the Stress Concentration Around a Circular Hole in a Plate of Arbitrary Thickness*, J. Appl. Mech. **16**, 1, 27 (1949).
2. I. S. Sokolnikoff, *Mathematical Theory of Elasticity*, (McGraw-Hill Book Co., Inc., New York, 1956), 2nd Ed., p. 331.
3. G. N. Watson, *Bessel Functions*, (Macmillan Co., New York, 1948), pp. 40, 63, 77.
4. *Ibid.*, pp. 32, 66, 79.
5. *Ibid.*, Chap. 7.
6. I. N. Sneddon, *Fourier Transforms*, (McGraw-Hill Book Co., Inc., New York, 1951), Chap. 1.
7. G. N. Watson, *op. cit.*, p. 468.
8. K. A. Blenkarn and J. C. Wilhoit, *Stresses Due to a Band of Normal Stress at the Entrance of a Circular Hole*, J. Appl. Mech. **29**, 4, 647 (1962).
9. *British Association Mathematical Tables—Bessel Functions, Parts I, II*, (University Press, Cambridge, 1950).
10. Bateman Manuscript Project, *Higher Transcendental Functions*, (McGraw-Hill Book Co., Inc., New York, 1953) Vol. II, p. 145.
11. *Ibid.*, p. 79.
12. *Ibid.*, p. 143.
13. J. Miller and R. P. Hurst, *Simplified Calculation of the Exponential Integral*, MTAC **12**, 187 (1958).
14. Works Projects Administration, *Tables of Sine, Cosine and Exponential Integrals*, Vol. I, II.
15. Works Projects Administration, *Tables of the Exponential Functions*.

V-24b. Thermoelastic Problem for Fuel Rod with Cladding

The purpose of this analysis is to find the thermal stresses and displacements in a fuel rod clad with a material having different elastic properties due to an arbitrary temperature distribution in the fuel and cladding. The stresses are important from the element failure standpoint and the displacements are desirable in analyzing reactor control and feedback. To simplify the algebra involved it is assumed that the rod is infinitely long, the temperature distribution is axi-symmetric (a function of r and z but not θ), and the surface loading and temperature distribution are symmetrical about $z = 0$. In addition it is assumed that the temperature distribution and surface loading possess the required transforms and series representations, which assumption will certainly be met by any physically realistic distributions.

Although this problem could be attacked directly, it turned out to be easier to solve some simpler problems first and utilize the results of these to obtain the solution to the desired problem. The end result is the same but solving the simpler problems leads to convenient groupings of terms that considerably simplify the intermediate algebra involved in the more complicated problem. The simpler axi-symmetric problems are:

THE INFINITE CYLINDER $r \leq a$ WITH ARBITRARY SURFACE LOADING AND TEMPERATURE DISTRIBUTION

The boundary conditions are:

$$\begin{aligned} \tau_{rr} &= f_1(z) \\ \tau_{rz} &= f_2(z) \quad \text{on } r = a \end{aligned} \quad (1)$$

Its temperature distribution is assumed to have a Fourier Bessel series of the form:

$$T(r,z) = C_0(z) + \sum_{j=1}^{\infty} C_j(z) J_0(\alpha_j r), \quad J_0(\alpha_j a) = 0 \quad (2)$$

and also to possess a Fourier cosine transform with respect to z .

THE INFINITE CYLINDER $r \leq a$ WITH ARBITRARY SURFACE DISPLACEMENTS AND TEMPERATURE DISTRIBUTION

The boundary conditions are:

$$\begin{aligned} u_r &= f_3(z) \\ u_z &= f_4(z) \quad \text{on } r = a \end{aligned} \quad (3)$$

and the temperature distribution has the same properties as in A.

THE INFINITE TUBE $a \leq r \leq b$ WITH ARBITRARY TRACTIONS ON BOTH SURFACES AND ARBITRARY TEMPERATURE DISTRIBUTION

The boundary conditions are:

$$\begin{aligned} \tau_{rr} &= f_5(z) \\ \tau_{rz} &= f_6(z) \quad \text{on } r = a \\ \tau_{rr} &= f_7(z) \\ \tau_{rz} &= f_8(z) \quad \text{on } r = b. \end{aligned} \quad (4)$$

The temperature distribution is assumed to possess a Fourier cosine transform and a series representation of the form:

$$\begin{aligned} T(r,z) &= C_0(z) + \bar{C}_0(z) \log r \\ &+ \sum_{j=1}^{\infty} C_j(z) [J_0(\beta_j r) Y_0(\beta_j b) - Y_0(\beta_j r) J_0(\beta_j b)] \end{aligned} \quad (5)$$

where

$$J_0(\beta_j a) Y_0(\beta_j b) - Y_0(\beta_j a) J_0(\beta_j b) = 0.$$

THE INFINITE TUBE $a \leq r \leq b$ WITH ARBITRARY DISPLACEMENTS ON THE INNER SURFACE, ARBITRARY TRACTIONS ON THE OUTER SURFACE, AND ARBITRARY TEMPERATURE DISTRIBUTION

The boundary conditions are:

$$\begin{aligned} u_r &= f_9(z) \\ u_z &= f_{10}(z) \quad \text{on } r = a \\ \tau_{rz} &= f_{11}(z) \\ \tau_{rr} &= f_{12}(z) \quad \text{on } r = b \end{aligned} \quad (6)$$

The temperature distribution is assumed to have the same properties as under: *The Infinite Tube $a \leq r \leq b$ with Arbitrary Tractions on Both Surfaces and Arbitrary Temperature Distribution.*

Because of the simple boundaries involved, all these solutions were obtained in closed form. The experience gained in solving these sub-problems was then used in obtaining the solution to the desired problem, due account being taken of the different elastic properties of the rod and cladding. Using the single and double prime to refer to the rod and cladding respectively, we have

for the boundary conditions

$$\left. \begin{aligned} \tau'_{rr} &= \tau''_{rr} \\ \tau'_{rz} &= \tau''_{rz} \\ u'_r &= u''_r \\ u'_z &= u''_z \end{aligned} \right\} \text{ on } r = a$$

$$\left. \begin{aligned} \tau''_{rr} &= F_1(z) \\ \tau''_{rz} &= F_2(z) \end{aligned} \right\} \text{ on } r = b$$

The temperature distribution in the rod and cladding was assumed to possess the representations under the following respective headings: *The Infinite Cylinder* $r \leq a$ with *Arbitrary Surface Loading and Temperature Distribution*; and *The Infinite Tube* $a \leq r \leq b$ with *Arbitrary Traction on Both Surfaces and Arbitrary Temperature Distribution*.

V-24c. Thermal Stresses in Reactor Fuel Plates¹

The elastic stresses and displacements in a rectangular prism of dimensions $2a$, $2b$ and $2c$ due to an arbitrary temperature distribution and arbitrary normal surface loading are found. To make the problem two-dimensional, it is assumed that all quantities are independent of the coordinate measured in the direction of dimension $2c$. The arbitrary normal surface tractions are assumed to have Fourier series expansions and the arbitrary temperature distribution to have a double Fourier series expansion. As expected, the exact solution of the problem involves solving an equation of the form of Eq. (1) Paper No. V-24 for an infinite set of coefficients. These coefficients are then substituted into Fourier series type expressions for the stresses and displacements.

The work on this problem then continues in two different directions. First, it is assumed that the rectangular prism is a fuel plate of width $2c$, thickness $2a$, and length $2b$. Approximations to the exact solution are then derived based on the large ratio of b/a normally found for fuel plate proportions. The first approximation is such that the governing differential equations are satisfied exactly but the boundary conditions only approximately. The closeness of this approximation can thus be studied and numerically evaluated. This is in contrast to most thin plate approximations, where, since the exact solution is not known, the degree of approximation can only be estimated. A further approximation is derived which is simpler in form but invalid near the ends of the plate (an application of St. Venant's Principle). A side result gleaned from these

approximations is the information that the stresses due to the variation of the temperature in the direction of the plate length are negligible compared to the stresses due to the variation through the plate thickness. Although this conclusion has been drawn before, in this case a numerical measure of the degree of the approximation can be obtained due to the availability of the exact solution.

Large ratios of b/a having been treated, it was then decided to go to the other extreme and take $b = a$. In other words, the elastic body became a block of square cross-section. For this case geometrical approximations are out of the question and the exact solution must be dealt with.

Since imposed surface shearing loads are not included in the original formulation of the rectangular prism thermoelastic problem, the problem for a constant temperature prism with these loads applied was also solved. The resulting stresses and displacements can then be superimposed on the solution to the previous problem because of the linearity of the governing equations.

In addition, rather than prescribing the normal surface loading as in the original problem statement, the thermoelastic problem where the surface displacements are prescribed was solved.

REFERENCES

1. C. Youngdahl, *Basic Material Resulting from ANL Rocket Study*, ANL-6656, (1963), Chap. VII.

V-25. Gain Stabilization of Analog Amplifiers in the Nanosecond Regime

K. G. PORGES and J. BJORKLAND*

Many nuclear and reactor physics experiments require the amplification of analog signals from a nuclear detector (fast-rising voltage or current pulses) at bandwidths of the order of 200 Mc/sec, either in order to maintain precise timing or to keep pulse widths short and thus avoid pileup and overloading. Amplification of this sort is needed to allow conversion of the analog information (i.e., pulse height and/or shape) to the digital regime through discriminators, such that further processing can then be done by digital logic systems (coincidence circuits, time analyzers, etc.). With the advent of tunnel diode discriminators, with thresholds of the order of 100 mV, the necessary gain (of the order of 60 dB) can be obtained with a few chain amplifiers, which have been available commercially for some time. Transistorized amplifiers of adequate bandwidth have been developed more recently.

At the large bandwidths considered here, it becomes difficult to stabilize the amplifier gain and, to some extent, the discriminator threshold, in such a way as to make these insensitive to changes and fluctuations in circuit element characteristics. In fact, the gain of most wide-band amplifiers (especially of those of chain or distributed type) is not stabilized at all. In many experiments, this lack of stability is not of serious consequence, since the prevalence of high count rates which may have been the motivation for employing such an amplifier also results in a very rapid accumulation of data. Occasionally, however, one is faced with a situation in which gain stability is required in spite of a high count rate. For instance, in a coincidence experiment in which the other channel, or channels, are counting relatively rare events, it may be necessary to run the experiment for many hours. At the same time, the fast-counting channel may be looking at a widely distributed pulse height spectrum, such that gain drifts have a relatively strong effect on channel efficiency.

In the course of planning such an experiment, it was found desirable to devise some convenient means of testing the gain stability of several commercially available types of wide-band amplifiers. The circuitry developed for that purpose was then slightly modified to serve as an external channel gain regulator.¹ Its operation is briefly described in what follows.

Two slightly different dc voltages, E and $E + \Delta E$, derived from a divider across the supply, are used to

charge two cables, which are alternatively discharged into the following add-split network by two mercury-wetted reed switches driven by a clock at a suitable frequency (10 pulses/sec to 1 pulse/sec). The splitter thus applies a train of alternating "high" and "low" pulses of about 20-nsec length to the amplifier input as well as to a sorting logic.

The divider and attenuator are adjusted to make the pulse height difference ΔE , after reamplification, straddle the discriminator level (which has been previously adjusted to any desired point with respect to the signal pulse height spectrum). "High" pulses normally pass the discriminator and are applied to three coincidence circuits, C_1 , C_2 , and C_3 . In C_1 , these pulses go into anticoincidence input in such a way as to veto the corresponding pulses which have been routed to a coincidence input of this circuit through a delay, splitter, flipflop, and pulse shaper from the other pulser output. Conversely, in C_3 , discriminator output pulses are vetoed by the corresponding direct pulses, such that only detector pulses are counted in the scaler. As concerns C_2 , suppose that the amplifier gain momentarily increases, or that the discriminator level falls, and the next "low" pulse is therefore passed; then, coincidence circuit C_2 receives pulses at both inputs and fires, actuating a stepping device which increases the negative grid bias on one of the chain amplifiers by a suitable amount. This process is repeated until the pulses once more straddle the discriminator level. Whenever the gain momentarily falls, or the discriminator triggering point goes up, C_1 , which now receives no veto input from the next "high" pulse, delivers an output which drives the bias in the opposite sense. In order to keep a record of such excursions, the outputs of C_1 and C_2 may be also fed to a chart recorder, through suitable shaping circuits. All sensitive components of the system are either passive or digital and hence are insensitive over a fairly wide range to temperature, supply voltage and other environmental changes.

When the unit is used in the AGC (automatic gain control) mode, it is necessary to detach the grid bias supply of one of the chain amplifiers used, and connect the grid base to the AGC circuit instead. For this reason, it was thought to be more convenient to apply the error signal to the pulses instead of to the amplifier bias when the unit is used for bench testing of amplifier gain stability. This required wiring a 40-

* Electronics Division.

position, 2-wafer switch which can be driven in either direction through separate stepping relays in such a way that the voltage difference between the two wipers remains constant throughout the range of the divider at twice the size of the step. By means of additional switches, the current through this adjustable divider may be changed to obtain various values of $\Delta E/E$.

When the unit is switched into the AGC mode, ΔE can be more simply adjusted by means of a helipot.

REFERENCES

1. K. G. Porges and J. Bjorkland, *Gain Stabilization of Analogue Amplifiers in the Nanosecond Regime*, Proc. Intern. Symp. Nucl. Electron. Paris, 811-818 (1963).

V-26. A Simple, Compact Control Rod Drive Using a Stepping Motor

E. F. GROH and C. E. COHN¹

Figure V-26-1 shows a control rod drive used on the AARR critical. The drive achieves considerable reduction in size and cost by the use of a stepping motor. The rod is connected to a double-strand roller chain which passes over a sprocket driven by the motor. As the rod rises, the slack in the chain forms a loop, as shown in Fig. V-26-2. A chain separator and chain guard prevent tangling.

The rod is scrambled by removing the dc power from the motor windings. The holding torque of the motor then falls to a residual-magnetism level of one-eighth of the energized value. This is insufficient to support the rod, which promptly drops. As the rod nears bottom, the slack in the chain is taken up, and the kinetic energy is absorbed by a pair of shock absorbers.

The control circuit for the drive includes four reed

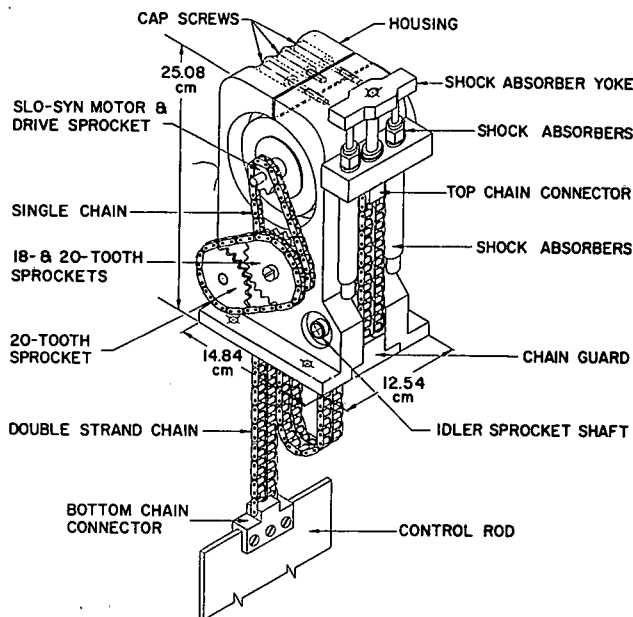


Fig. V-26-1. Over-all View of Rod Drive.

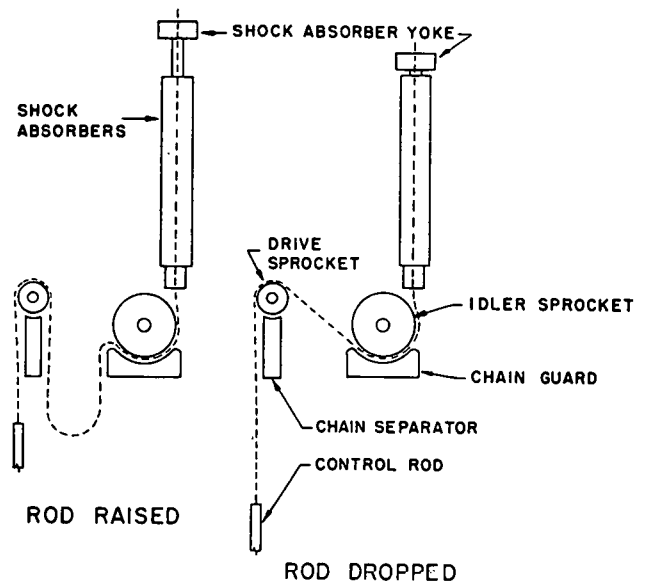


Fig. V-26-2. Schematic Diagram Showing Path of Chain.

relay modules used as flip-flops. These control the power to the motor windings. When triggered by a pulse generator, the modules change state and switch power between windings in such a sequence as to move the rod up or down as desired. Each revolution of the motor shaft is divided into 400 steps. The gearing between the motor and the drive sprocket is such that each step corresponds to 0.1 mm of rod motion, with a systematic error no greater than 0.2×10^{-3} mm per step. Reproducibility of positioning has been measured to be within 0.005 cm for a total travel of 45 cm. The rod position indicator is a counter with add and subtract coils, which counts the stepping pulses. The register count increases or decreases by one whenever the rod moves up or down by one step.

The unit was life-tested by repeatedly raising a 13-kg weight to a height of 60 cm and then scrambling. This was done over 30,000 times with no evidence of

malfunction or deterioration. Total drop time for this configuration is 0.45 sec. after power is removed from the motor. For a 45 cm drop, it is 0.3 sec. The over-all size shown in Fig. V-26-1 may be compared to that of the ZPR-I type which measures 41 x 46 x 90 cm.

REFERENCES

1. E. F. Groh and C. E. Cohn, *A Simple, Compact Control Rod Drive Using A Stepping Motor*, Trans. Am. Nucl. Soc. 6, No. 1, 70 (June 1963). Also, Nucl. Sci. Eng., (to be published).

Section VI

Publications and Reports, Reactor Physics Division

(APRIL 1, 1963 TO APRIL 1, 1964)

Open-Literature

- Armani, R. J., E. F. Bennett, M. W. Brenner, M. M. Bretscher, C. E. Cohn, R. J. Huber, S. G. Kaufmann and W. C. Redman, *Improved Techniques for Low Flux Measurement of Prompt Neutron Lifetime, Conversion Ratio and Fast Spectra*, Proc. IAEA Symp. on Exponential and Critical Experiments, Amsterdam, September 2-6, 1963, Vol. 1, pp. 227-259.
- Baird, Q. L. and A. R. Boynton, *Bucklings, Disadvantage Factors and δ^{28} Measurements in Some Undermoderated Slightly Enriched Cores*, Trans. Am. Nucl. Soc. **6**(2), 248 (November 1963).
- Bennett, E. F. and R. L. Long, *Precision Limitations in the Measurement of Small Reactivity Changes*, Nucl. Sci. Eng. **17**(3), 425-432 (November 1963).
- Cohn, C. E., *Expediting Danger-Coefficient Measurement by Measuring Two Samples at Once*, Nucl. Sci. Eng. **18**(1), 140-142 (January 1964).
- Cox, S. A., *Neutron Activation Cross Sections for Br^{79} , Br^{81} , Rh^{103} , In^{115} , I^{127} and Ta^{181}* , Phys. Rev. **133**, B378-B383 (January 27, 1964).
- Cox, S. A., *Elastic Neutron Scattering From Fe, Ni and Cu*, Bull. Am. Phys. Soc. **8**, 478 (August 1963) Abstract.
- Crane, J. L. and R. C. Doerner, *Thermal Self-Shielding and Edge Effects in Absorbing Foils*, Nucl. Sci. Eng. **16**(3), 259-262 (July 1963).
- DeVolpi, Alexander, K. G. Porges and C. J. Rush, *Subnanosecond RC Rise Times from Ionization Counters*, Bull. Am. Phys. Soc. **9**, 46 (January 1964) Abstract.
- Dickerman, C. E., E. S. Sowa, J. H. Monaweck and A. W. Barsell, *In-Pile Experiments on Meltdown of EBR-II. Mark I Fuel Elements in Stagnant Sodium*, Nucl. Sci. Eng. **18**(3), 319-328 (March 1964).
- Dwyer, T. P., *Certification of Algorithm 210-Hermite Interpolation*, Comm. ACM **6**(10), 619 (October 1963).
- Engelbrecht, C. A., *Nuclear Photoproduction of Neutral Pions*, Bull. Am. Phys. Soc. **9**, 80 (January 1964) Abstract.
- Fischer, G. F., H. H. Hummel, J. R. Folkrod and D. A. Meneley, *Doppler Coefficient Measurements for U^{238} in Fast Reactor Spectra*, Nucl. Sci. Eng., **18**(2), 290-292 (February 1964) Letter.
- Friedman, A. M., J. W. Meadows, A. B. Smith, P. R. Fields, John Milsted and J. F. Whalen, *Fission Fragment Kinetic Energies of Cf^{246} , Cf^{248} and Cf^{254}* , Phys. Rev. **131**, 1203 (August 1, 1963).
- Gemmell, D. S., L. L. Lee, Jr., J. P. Schiffer and A. B. Smith, *The $Fe^{54}(d,n)Co^{55}$ Reaction*, Bull. Am. Phys. Soc. **9**, 92 (January 1964) Abstract.
- Gold, R. and Calvin Wong, *Disintegration of the Deuteron in a Coulomb Field*, Phys. Rev. **132**, 2586-2599 (December 15, 1963).
- Grench, R. E. and H. C. Thacher, Jr., *An Act-III Debugging Aid*, Proc. 6th Ann. Mtg. of POOL, Los Angeles, California, April 2-4, 1963. Commercial Computer Division, General Precision Co., Burbank, California, 1964. pp. 44-45.
- Helm, F. H. *Measurements of the Angular Distribution of Thermal Neutrons*, Trans. Am. Nucl. Soc. **6**(2), 237 (November 1963).
- Kelber, C. N., *Fluxes and Reaction Rates in the Presence of Interfering Resonances*, Trans. Am. Nucl. Soc. **6**(2), 273 (November 1963).
- Loewenstein, W. B., *The Control of Fast Reactors; Current Methods and Future Prospects*, IAEA Symp. on Physics and Material Problems of Reactor Control Rods, Vienna, November 11-15, 1963; Abstracts of Papers, SM-46/15.
- Lukehart, P. M., *Algorithm 218. Kutta-Merson*, Comm. ACM **6**, 737-738 (December 1963).
- Madell, J. T., *Application of Nuclear Power to an Oceanographic Research Submarine*, Proc. Torpedo Propulsion Conference, July 23-26, 1963, U. S. Naval Underwater Ordnance Station, Newport, Rhode Island, Vol. 2, Paper No. 10 (Classified).
- Meadows, J. W., G. R. Ringo and A. B. Smith, *Neutron Production by 450-MeV Protons*, Nucl. Instr. Methods **25**(2), 349-352 (1964).
- Moldauer, P. A., *Problem of Measurement*, Am. J. Phys. **32**, 172 (1964).
- Moldauer, P. A., *Spatial Distribution of the Absorptive Interaction for Low-Energy Neutrons*, Bull. Am. Phys. Soc. **9**, 170-171 (February 1964) Abstract.
- Moldauer, P. A., *Optical Model Interpretation of Neutron Strength Functions*, Intern. Conf. on Nuclear Physics with Reactor Neutrons, October 15-17, 1963, ed. F. E. Throw. ANL-6797 (1963), pp. 358-362. Bull. Am. Phys. Soc. **9**, 178 (February 1964) Abstract.
- Moldauer, P. A., *Nuclear Cross Section Fluctuations*, Phys. Letters **8**, 70-72 (January 1964).
- Moldauer, P. A., *Optical Model of Low Energy Neutron Interactions with Spherical Nuclei*, Nucl. Phys. **47**(1), 65-92 (August 1963).
- Moldauer, P. A., *Resonance Statistics and Average Cross Sections*, Proc. Symp. on Statistical Properties of Atomic and Nuclear Spectra, Stony Brook, New York, May 3, 1963; State University of New York, Stony Brook, 1963; Paper No. 5.
- Monaweck, J. H., C. E. Dickerman and E. S. Sowa, *Behavior of Irradiated Metallic Fuel Elements Exposed to Nuclear Excursions in TREAT*, Trans. Am. Nucl. Soc. **6**(2), 374 (November 1963).
- Okrent, David, *Recent Developments in the Physics and Safety of Large Fast Power Reactors*, Trans. Am. Nucl. Soc. **6**(2), 360 (November 1963).

- Okrent, David, *Nuclear Considerations on the Selection of Materials for Fast Power Reactors*, IMD Spec. Reprt Ser. No. 12, Vol. 9, Nuclear Metallurgy; AIME, New York, 1963; pp. 1-56.
- Plumlee, K. E., Q. L. Baird, G. S. Stanford and P. I. Amundson, *Critical Experiment with BORAX-V Superheater Elements*, Trans. Am. Nucl. Soc. 6(2), 217 (November 1963); also, ANL-6691 (1963).
- Porges, K. G. A. and J. A. Bjorkland, *Gain Stabilization of Analogue Amplifiers in the Nanosecond Regime Nuclear Electronics*, Proc. Third Intern. Symp. on Nuclear Electronics, Paris, November 25-27, 1963; European Nuclear Energy Agency, 1964, pp. 811-818.
- Redman, W. C., K. E. Plumlee and Q. L. Baird, *Power Reactor Design at Zero Power*, Proc. IAEA Symp. on Exponential and Critical Experiments, Amsterdam, September 2-6, 1963, Vol. 1, pp. 3-27.
- Reitmann, Daniel, C. A. Engelbrecht and A. B. Smith, *Scattering of Fast Neutrons from Natural Zr and Nb*, Nucl. Phys. 48(4), 593-607 (1963).
- Rossin, A. D., *Degradation of Impact Energy of Steel as a Function of Neutron Exposure*, Trans. Am. Nucl. Soc. 6(2), 389 (November 1963).
- Rossin, A. D., *A Monitoring Technique for Radiation Damage Experiments, Neutron Dosimetry*; Proc. IAEA Symp. on Neutron Detection, Dosimetry and Standardization, Harwell, December 10-14, 1962, pp. 515-520 (published 1963).
- Rossin, A. D., *Significance of Neutron Spectrum on Radiation Effects Studies*, Proc. Symp. of Radiation Effects on Metals and Neutron Dosimetry, Los Angeles, October 2-3, 1962. A.S.T.M., Philadelphia, 1963. pp. 115-132.
- Rossin, A. D. and R. J. Armani, *Fast Neutron Dosimetry for Radiation Damage Studies, Neutron Dosimetry*; Proc. IAEA Symp. on Neutron Detection, Dosimetry and Standardization, Harwell, December 10-14, 1962, pp. 293-304 (published 1963).
- Smith, A. B., *The Scattering of Fast Neutrons from W^{184}* , Z. Physik 175, 242-256 (1963).
- Smith, A. B., *The Scattering of Fast Neutrons from Natural Uranium*, Nucl. Phys. 47, 633-651 (1963).
- Smith, A. B., *Elastic Scattering of Fast Neutrons from U^{235}* , Nucl. Sci. Eng. 18(1), 126-129 (January 1964).
- Spinrad, B. I., *Calculations for Lattice Parameters, Heavy Water Lattices: Second Panel Report*, Vienna, February 18-22, 1963; Tech. Report Ser. No. 20 Intern. Atomic Energy Agency, Vienna 1963. pp. 39-41.
- Srinivasan, A. V., *Buckling Load of Bars with Variable Stiffness—A Simple Numerical Method*, AIAA Journal 2, 139-140 (1964).
- Stupegia, D. C., A. B. Smith and K. L. Hamm, *Fast Neutron Capture in Th^{232}* , J. Inorg. Nucl. Chem. 25, 627-630 (June 1963). (TID-17651).
- Thacher, H. C., Jr., *Certification of Algorithm 167—Calculation of Confluent Divided Differences* (W. Kahan and I. Farkas); *Certification of Algorithm 168—Newton Interpolation with Backward Divided Differences* (W. Kahan and I. Farkas); *Certification of Algorithm 169—Newton Interpolation with Forward Divided Differences* (W. Kahan and I. Farkas); Comm. ACM 6, 523 (September 1963).
- Thacher, H. C., Jr., *Certification of Algorithms 134 and 158—Exponentiation of Series* (Henry E. Fettis); Comm. ACM 6, 390 (July 1963).
- Thacher, H. C., Jr., *Certification of Algorithm 163—Modified Hankel Function* (Henry E. Fettis); Comm. ACM 6, 522 (September 1963).
- Thacher, H. C., Jr., *An Efficient Composite Formula for Multi-dimensional Quadrature*, Comm. ACM 6, 356-357 (July 1963).
- Thacher, H. C., Jr., *Table Errata—Jahnke-Emde Lösche Tables of Higher Functions*, 6th Ed. McGraw-Hill Book Co., New York: 1960. Math. Comput. 17(84), 485-486 (October 1963).
- Thacher, H. C., Jr., *Numerical Integration and Differentiation of Functions of Several Independent Variables by an Iterative Procedure*, J. Soc. Ind. Appl. Math. 11(3), 614-622 (September 1963).
- Thacher, H. C., Jr., *Certification of Algorithm 8—Euler Summation*, Comm. ACM 6, 663 (November 1963).
- Thacher, H. C., Jr., *Algorithm 215—Shanks*, Comm. ACM 6, 662 (November 1963).
- Thacher, H. C., Jr., *Certification of Algorithm 118—Reversion of Series* (Henry E. Fettis); Comm. ACM 6, 745 (December 1963).
- Thacher, H. C., Jr., *An Efficient Composite Formula for Multi-dimensional Quadrature*, Comm. ACM 7, 23-25 (January 1964).
- Thacher, H. C., Jr., *Conversion of a Power Series to a Series of Chebyshev Polynomials*, Comm. ACM 7, 181-182 (March 1964).
- Wimunc, E. A., M. Petrick, W. C. Lipinski and H. P. Iskenderian, *Performance Characteristics of EBWR from 0-100 MWt.*, Proc. IAEA Conf. on Operating Experience with Power Reactors, Vienna, June 4-10, 1963; pp. 344-404.

Reports

- Bryant, L. T. and D. V. Gopinath, *A Fast Reactor Excursion Simulator*, ANL-6798 (1963).
- Butler, D. K., *Fission Cross Section of Pu^{238}* , The AEC Nuclear Cross Sections Advisory Group Meeting at the University of Colorado, August 13-14, 1963. WASH-1044, p. 2 Abstract.
- Carter, J. C., D. W. Sparks and J. H. Tessier, *The Steady State and Transient Kinetics of EBR-I, Mark-III*, ANL-6851 (1964).
- Cohn, C. E., G. H. Golden, B. M. Hoglund, W. B. Loewenstein, G. S. Rosenberg, D. W. Sparks and C. K. Youngdahl, *Basic Material Resulting from ANL Rocket Study*, ANL-6656 (1963).
- Cox, S. A., *Good Resolution Studies of Elastic Neutron Scattering for Fe*, The AEC Nuclear Cross Sections Advisory Group Meeting at the University of Colorado, August 13-14, 1963. WASH-1044, p. 2 Abstract.
- Cox, S. A., *Fast Neutron Capture Cross Sections*, The AEC Nuclear Cross Sections Advisory Group Meeting at the University of Colorado, August 13-14, 1963. WASH-1044, p. 13 Abstract.
- DeVolpi, A. and K. G. Porges, *Direct and Absolute Measurement of Average Yield of Neutrons from Thermal Fission of U^{235}* , Intern. Conf. on Nuclear Physics with Reactor Neutrons, October 15-17, 1963, ed. F. E. Throw. ANL-6797 (1963). pp. 450-454. Bull. Am. Phys. Soc. 9, 180 (February 1964). Abstract.
- DeVolpi, A., K. G. Porges and R. N. Larson, *Mn^{56} Coincidence Counting Facility*, ANL-6760 (1963).
- Dickerman, C. E., *Reactor Safety Experiments*, Argonne National Laboratory Reviews 1(1), 11-14 (September 1963).
- Dickerman, C. E., E. S. Sowa, L. E. Robinson and D. V. Gopinath, *Meltdown Studies*, Proc. Conf. on Breeding, Economics and Safety in Large Fast Reactors, Argonne National Laboratory, October 7-10, 1963. ANL-6792 (1963), pp. 99-112.
- Fischer, G. J., H. H. Hummel, J. R. Folkrod and D. A. Meneley,

- Experimental Results for U²³⁵ Doppler Measurements in Fast Reactor Spectra*, Proc. Conf. on Breeding, Economics and Safety in Large Fast Power Reactors, Argonne National Laboratory, October 7-10, 1963. ANL-6792 (1963) pp. 885-896.
- Gemmell, D. W., L. L. Lee, Jr., J. P. Schiffer and A. B. Smith, *A Study of (d,n) Reactions on Fe⁵⁴ and Ni⁵⁸, Nuclear Spectroscopy with Direct Reactions. I. Contributed Papers*. Ed. F. E. Throw, ANL-6848 (1964) pp. 98-103.
- Gopinath, D. V. and C. E. Dickerman, *Calculations of Coherence of Failure for Hypothetical Meltdown Accidents in an EBR-II Like Reactor*, ANL-6844 (1964).
- Hummel, H. H. and A. L. Rago, *Effect of Parameter Variation in Doppler Effect Calculations*, Proc. Conf. on Breeding, Economics and Safety in Large Fast Power Reactors, Argonne National Laboratory, October 7-10, 1963. ANL-6792 (1963) pp. 747-764.
- Hummel, H. H., K. E. Phillips and A. L. Rago, *Calculations of Sodium Void Reactivity Effect for Large Fast Oxide Reactors in Spherical and Slab Geometry*. Proc. Conf. on Breeding, Economics and Safety in Large Fast Power Reactors, Argonne National Laboratory, October 7-10, 1963. ANL-6792 (1963) pp. 65-74.
- Hwang, R. N., *An Improved Method of Doppler-Effect Calculation for Fissile Materials in the Intermediate Energy Reaction*, Proc. Conf. on Breeding, Economics and Safety in Large Fast Power Reactors, Argonne National Laboratory, October 7-10, 1963. ANL-6792 (1963) pp. 727-746.
- Iskenderian, H. P., *Use of Depleted Uranium in Thermal Reactors with Slightly Enriched Fuel to Achieve High Neutron Economy and High Burnup*, ANL-6843 (1964).
- Kato, W. Y., G. J. Fischer and L. R. Dates, *Safety Analysis Report, Argonne Fast Critical Facility (ZPR-VI)*, ANL-6271 (1963).
- Kelber, C. N., *1559/RE: A Code to Compute Resonance Integrals in Mixtures*, ANL-6709 (1963).
- MacFarlane, D. R., *A 200-Watt Conduction-Cooled Reactor Power Supply for Space Application*, ANL-6694 (1963).
- Meneghetti, David, *Introductory Fast Reactor Physics Analysis*, ANL-6809 (1963).
- Okrent, D., *Proceedings of the Conference on Breeding, Economics, and Safety in Large Fast Power Reactors*, October 7-10, 1963, Argonne National Laboratory, ANL-6792 (1963).
- Pennington, E. M., *Cylindrical Lattice Collision Probability Codes, B692/RP*, ANL-6836 (1964).
- Pennington, E. M. and J. A. Bjorkland, *Foil Activation Programs, B512/RP*, ANL-6822 (1964).
- Persiani, P. J., *Reactivity Coefficient Measurements in FARET*, Proc. Conf. on Breeding, Economics and Safety in Large Fast Power Reactors, Argonne National Laboratory, October 7-10, 1963. ANL-6792 (1963) pp. 873-884.
- Plumlee, K. E., *Critical Experiment with BORAX-V Internal Superheater*, Proc. 8th Nuclear Superheat Mtg., Idaho Falls, March 20-22, 1963. COO-267 (April 5, 1963) pp. 58-59.
- Plumlee, K. E., Q. L. Baird, G. S. Stanford and P. I. Amundson, *Critical Experiment with BORAX-V Internal Superheater*, ANL-6691 (1963).
- Rago, A. L. and H. H. Hummel, *ELMOE, an IBM-704 Program Treating Elastic Scattering Resonances in Fast Reactors*, ANL-6805 (1964).
- Reactor Physics Constants*, ANL-5800, 2nd ed. (1963).
- Reitmann, D. and A. B. Smith, *Time-of-Flight Measurements—Differential Elastic Scattering*, The AEC Nuclear Cross Sections Advisory Group Meeting at the University of Colorado, August 13-14, 1963. WASH-1044, p. 2. Abstract.
- Reitmann, D., C. A. Engelbrecht and A. B. Smith, *Inelastic Neutron Scattering*, The AEC Nuclear Cross Sections Advisory Group Meeting at the University of Colorado, August 13-14, 1963. WASH-1044, p. 5. Abstract.
- Reitmann, D. and A. B. Smith, *Total Cross Sections*, The AEC Nuclear Cross Sections Advisory Group Meeting at the University of Colorado, August 13-14, 1963. WASH-1044, p. 13 Abstract.
- Richards, H. K., *High Temperature Conversion—Heat to Electricity*, A Symposium on High Temperature Conversion—Heat to Electricity, Tucson, Arizona, February 19-21, 1964. TID-7687, pp. 161-199.
- Richards, H. K., *Thermionic Energy Conversion for DC and High Frequency Power Output* AMU-ANL Conference on Direct Energy Conversion, November 4-5, 1963. ANL-6802 (1963) pp. 152-160.
- Sanathanan, C. K. and J. Koerner, *Transfer Function Synthesis as a Ratio of Two Complex Polynomials*, ANL-6716 (1963).
- Schoeberle, D. F., J. M. Heestand and L. B. Miller, *A Method of Calculating Transient Temperatures in a Multiregion, Axisymmetric, Cylindrical Configuration. The Argus Program, 1089/RE248, Written in Fortran II*. ANL-6654 (1963).
- Smaardyck, A., T. R. Bump, J. H. Handwerk, W. J. Kann, E. L. Martinec, P. J. Persiani, G. F. Popper and S. B. Skladzien, *Interim Report: Faret Experimental Program*, ANL-6708 (1963).
- Smith, A. B., *Recent Changes in Heavy Element Cross Sections*, Proc. Conf. on Breeding, Economics and Safety in Large Fast Power Reactors, Argonne National Laboratory, October 7-10, 1963. ANL-6792 (1963) pp. 29-50.
- Smith, A. B., ed., *Reports to the AEC Nuclear Cross Sections Advisory Group Meeting at E. I. du Pont de Nemours and Co., Savannah River Laboratory, January 28-30, 1964*. WASH-1046.
- Smith, A. B., ed., *The AEC Nuclear Cross Sections Advisory Group Meeting at the University of Colorado*, August 13-14, 1963. WASH-1044.
- Smith, A. B., *Fast Neutron Scattering from Ta¹⁸¹*, ANL-6727 (1963).
- Spinrad, B. I., *Symposium Introduction*, A Symposium on High Temperature Conversion—Heat to Electricity, Tucson, Arizona, February 19-21, 1964. TID-7687, pp. 1-9.
- Spinrad, B. I., L. E. Link and J. T. Weills, *A Study of the Future Economic Prospects for Fast Reactors*, Proc. Conf. on Breeding, Economics and Safety in Large Fast Power Reactors, Argonne National Laboratory, October 7-10, 1963. ANL-6792 (1963) pp. 455-472.
- Spinrad, B. I., *Why Study Direct Conversion?* AMU-ANL Conference on Direct Energy Conversion, November 4-5, 1963. ANL-6802 (1963) pp. 3-14.
- Thacher, H. C., Jr. and R. E. Grench, *A Primer on the ACT-III Compiler for the LGP-30 Digital Computer*, ANL-6697 (1963).
- Whalen, J. F., *Accelerator Programs: Instrumentation*, The AEC Nuclear Cross Sections Advisory Group Meeting at the University of Colorado, August 13-14, 1963. WASH-1044, p. 13 Abstract.
- Wimunc, E. A., M. Petrick, W. C. Lipinski and H. P. Iskenderian, *Performance Characteristics of EBWR from 0-100 Mw.t*. ANL-6775 (1963).